AUSTRALIAN NATIONAL ANTARCTIC RESEARCH EXPEDITIONS

# ANARE RESEARCH NOTES 80

Australian upper atmospheric and magnetospheric physics research in Antarctica, 1991

Edited by Gary Burns

ANTARCTIC DIVISION
DEPARTMENT OF THE ARTS, SPORT,
THE ENVIRONMENT, TOURISM AND TERRITORIES

*ANARE RESEARCH NOTES (ISSN 0729-6533)*

This series allows rapid publication in a wide range of disciplines. Copies of this and other *ANARE Research Notes* are available from the Antarctic Division. Any person who has participated in Australian National Antarctic Research Expeditions is invited to publish through this series. Before submitting manuscripts authors should obtain a style guide from:

The Publications Office
Antarctic Division
Channel Highway
Kingston
Tasmania 7050
Australia

Published June 1990
ISBN: 0-642-16286-7

CONTENTS

# AUSTRALIAN UPPER ATMOSPHERIC AND MAGNETOSPHERIC PHYSICS RESEARCH IN ANTARCTICA, 1990

Edited by Gary Burns

Antarctic Division
Department of the Arts, the Environment, Tourism and Territories
Kingston, Tasmania, Australia

## PREFACE

The papers in this collection were presented at the Solar Terrestrial and Space Physics conference held at La Trobe University, Victoria between 5 and 9 February 1990. One paper with solely 'non-Australian' authorship (Olson et al.) appears contrary to the title of this anthology by virtue of its general interest.

The editor wishes to thank those researchers who have availed themselves of this opportunity to publish their research in this collective form. A number of Antarctic Division staff have contributed to getting the papers into a uniform format, and to them goes the editors thanks. Ms A. Gingell undertook the task of transfering the bulk of the texts to 'Mackintosh' format. Mr D. Ratcliffe and Mr. R. Walsh assisted with incorporating equations into the retyped manuscripts.

The majority of the papers are preliminary and are intended as an indication of some of the current directions of Australian upper atmospheric and space physics. It is anticipated that the results will appear in appropriate journals.

# 1. THE ORIGIN OF HIGH LATITUDE PC1 BURSTS RECORDED BY GROUND BASED INDUCTION MAGNETOMETERS LOCATED NEAR THE POLAR CUSP

H.J. Hansen[1], B.J. Fraser[1], F.W. Menk[1], Y. Hu[1], P.T. Newell[2], C.-I. Meng[2] and R.J. Morris [3]

[1]Physics Department
University of Newcastle
NSW 2308
Australia

[2]Applied Physics Laboratory
The John Hopkins University
Laurel Md. 20707
USA

[3]Antarctic Division
Kingston Tas 7050
Australia

ABSTRACT

Dayside Pc1/2 geomagnetic pulsation bursts (including IPRP) have been studied using a three station array of induction magnetometers located at high latitudes (L ~ 8 to 38). For selected intervals, it has been found that when these emissions are recorded at Davis (magnetic latitude 74.6°, L=14), the low altitude cleft, detected on the DMSP-F7 satellite was always located poleward and within 2° of Davis' latitude. Associated variations in the form of solitary pulses, when recorded, lead the Pc1 burst by ~240 s. These magnetic pulses are often associated with riometer absorption events, and therefore the precipitation of fluxes of keV electrons. The Pc1 bursts are interpreted as resulting from ion-cyclotron waves which have propagated to the ionosphere from the low latitude boundary layer.

## 1.1 INTRODUCTION

Pc1/2 (0.2 to 5 Hz) magnetic variations detected on ground based magnetometers are believed to be the ionospheric effects of left hand ion-cyclotron waves that have propagated from their source in the equatorial magnetosphere. Pc1 emissions are categorised according to their dynamic frequency-time characteristics. Structured 'pearl' (Kawamura et al. 1982, Fraser et al. 1984) bursts are mostly received from the plasmapause region; unstructured hydromagnetic chorus (Fukunishi et al. 1981, Hayashi et al. 1981) from the auroral oval region and intervals of rising or variable period (Morris et al. 1982, Matveeva et al. 1976) from the polar cusp.

In this paper, high latitude magnetic pulses of time durations between 120 and 300 s and associated Pc1 bursts (Arnoldy et al. 1988) are investigated. It was have found that the magnetic impulses have measurable riometer absorption events associated with them. The onset of this absorption precedes the Pc1 burst by time intervals between 60 and 240 s. In addition, the Pc1 bursts are of rising or constant period, and are received at Davis only when the location of the low altitude cleft is just poleward of Davis.

## 1.2 MULTISTATION ARRAY

The observations were recorded on induction magnetometers at Mawson, Davis and Casey in the Australian Antarctic Territory. Figure 1 shows the location of each station. Mawson (situated at ~70°S latitude - MLAT) is, during the dayside, located at the foot of field lines equatorward of the cleft in the plasmatrough. Davis (at ~75°S MLAT) is, near local noon, beneath the average position of the dayside cleft/cusp; the region through which high fluxes of magnetosheath particles have direct access to ionospheric altitudes. Those locations on the earth that rotate beneath the cusp are shown by the speckled region. Casey (at ~80°S MLAT) is, near noon, situated beneath polar mantle field lines.

## 1.3 DATA RECORDING AND ANALYSIS

The magnetic variations described here are presented as amplitude-time variations. The magnetometer at each site comprises two induction coils, one aligned in the north-south (the Ḣ component) and the other in the east-west (the Ḍ component) direction with respect to the geomagnetic field. The magnetic variations are modulated on a 25 Hz carrier and stored on slow speed magnetic tape. Amplitude variations in real time are recorded on charts directly after amplification from coils at both Davis and Casey. From the Mawson recordings, the authors extracted the amplitude-time variations through digitising the magnetic variation signal from slow speed tape.

Associated 30 MHz riometer absorption measurements were made at Davis (Dilong and Burns 1988).

During the intervals analysed, low altitude particle data were measured on the low altitude DMSP-F7 satellite. This satellite is in sun synchronous polar orbit at 840 km altitude (Newell and Meng 1988).

The present data set comprises five selected intervals during the October/November 1985 period when this Pc1 activity was observed.

## 1.4 OBSERVATIONS

The attention was focused on Pc1 bursts, recorded at Davis between 0300 and 1500 UT. A particular case study is first presented for which the observations are typical of the complete data set.

Figure 2 displays induction magnetometer traces recorded from Casey to Mawson at 0738 UT on 20 October 1985. Three traces (i) to (iii) show the Ḋ variations at Casey, Davis and Mawson respectively. The Ḣ records exhibit similar activity.

In Figure 2, trace (i) indicates the magnetic pulsation activity at Casey. Casey is, on average, poleward of the polar cusp. At 0736 UT, a magnetic pulse occurs (~100 nT). It is important to note there is no evidence of Pc1 activity. Trace (ii), the Davis recordings, indicate the pulsation activity at locations near the average latitude of the cusp and cleft. Contrasting with trace (i), trace (ii) shows a burst of ~1 nT peak-to-peak variations occurring on the tail of a peak-to-peak pulse of about 100 nT. The magnetic pulse occurs concurrently with that recorded at Casey. Trace (iii) then displays simultaneous recordings of pulsation activity at Mawson station. This suggests that the event is not only confined to cusp and cleft latitudes, but that similar pulsation activity is received within the magnetosphere. Trace (iii) also shows a solitary pulse preceding the Pc1 burst by about 60 s. Absolute magnetometer records reveal the pulse is approximately 50 nT in amplitude. At both Davis and Mawson, the period of the Pc1 variations is estimated to be about 5 s.

There is precipitation of keV electrons in the ionosphere about Davis which is associated with the magnetic pulse that precedes the Pc1 burst. In Figure 2, trace (iv) displays the 0.1 to 1 Hz activity filtered from trace (ii). Initially, the Pc1 emission exhibits a period, measured from these traces of about 4 s (±0.3 s) corresponding to a frequency of 0.25 Hz. After maximum amplitude, the period changes to 5 s (±0.3 s). Thus, this emission may be classified as a pulsation interval of rising period or falling frequency (Morris et al. 1982). Trace (v) of Figure 2 depicts the 30 MHz riometer activity at Davis and an associated absorption event of greater than 0.3 dB is present. The Pc1 burst reaches maximum amplitude about 90 s after the onset of the absorption event.

Fifteen Pc1 bursts and associated magnetic pulses, recorded at Davis during five chosen days are listed in Table 1. These observations are now summarised. The events occur predominantly in the post-dawn to pre-noon sector (column 2). Frequencies exhibited by the bursts range between 0.2 and 0.3 Hz, with the exception of two events (column 3). Magnetic impulses lead the Pc1 emissions for 13 of the events (column 4). Associated riometer absorption is identified on at least 9 of these occasions (column 5). The time delays between onset of absorption events and the corresponding Pc1 bursts at Davis are mostly between 180 and 240 s (column 6). The average energy of cleft ions measured on DMSP for those passes closest in UT to each event is listed in column 7.

The DMSP-F7 satellite provides information on where the low altitude cleft and cusp is located relative to Davis. For the 20 October 1985 interval, Figure 3 shows the latitude where boundary plasma signatures are found. Three passes are displayed. For all of these, the satellite passed through boundary plasmas on about the same MLT meridian (~0900 MLT). The time of the event described in Figure 2 is indicated by the vertical arrow and other Pc1 bursts were recorded during the interval labelled I. Clearly Davis lies beneath boundary layer particle signatures (BP) while this type of Pc1 bursts is received.

Detailed particle spectra for a later pass at 0850 UT are displayed in Figure 4. This shows that during interval I, the low latitude boundary layer particle signatures are situated above Davis. The satellite passed through boundary layer plasma (BP) in the vicinity of Davis at about 0905 UT. BP particles are magnetosheath like, but with smaller number and energy fluxes and higher energies than those found in the cusp (Newell and Meng 1988). The spectrogram displays BP plasma between 73°S and 76°S MLAT. Thus, these particles are found on field lines which straddle Davis' latitude.

## 1.5 DISCUSSION AND INTERPRETATION

These results are consistent with an ion-cyclotron instability mechanism occurring in the equatorial low latitude boundary layer. Wavegrowth from boundary layer ions is possible if, near the equatorial plane ($7<Re<10$) and in regions of background cold plasma, ion-cyclotron waves of the observed frequencies grow at the expense of the transverse energy manifest in the gyrating motion of the ions. Figure 5 depicts four curves which display the variation in energy of ions in cyclotron resonance at 0.3 Hz in the equatorial plane as a function of L-value. The four curves indicate differences in this variation according to different cold plasma densities in the interaction region. These densities are indicated in the figure. The energy range of boundary plasma measured by DMSP is shaded and where these values intersect the curves, it is shown at what geocentric distances wavegrowth at 0.3 Hz is possible. This is between 7 and 9 Re, locations at which the dayside low latitude boundary layer is found.

The magnetic impulses are most likely ionospheric current variations caused by induced field aligned current/particle precipitation. In the equatorial magnetosphere, such field aligned currents can be established by compressions (Olson and Lee 1983), FTE's (Arnoldy et al. 1988) or field-line resonances (Potemra et al. 1989). These phenomena are able to change the pitch angle anisotropy of ions, particularly those in the vicinity of the dayside boundary layer region. Ion-cyclotron wavegrowth in the Pc1 range of frequencies can result from the anisotropy change and after these waves have propagated to the ionosphere, they are detected on the ground based induction magnetometers as the observed Pc1 activity.

The time delays between the absorption events and the Pc1 bursts point to an equatorial source rather than a low altitude one.

The hard electron precipitation indicates that the field aligned current has been established. This goes in hand with the pitch angle anisotropy in the equatorial plane being affected such that the ion-cyclotron instability is able to develop. The electrons are more mobile than both the resonant ions and the ion-cyclotron waves and consequently reach the ionosphere ~120 s before the waves. Calculations confirm the plausibility of this scenario, which is summarised schematically in Figure 6. Electrons are first received at the ionosphere, and are measured as absorption events by the riometer. The ion-cyclotron waves then arrive and they are detected as Pc1 bursts by the induction magnetometers.

## 1.6 ACKNOWLEDGMENTS

The Casey and Davis magnetic variation and riometer data were made available by Antarctic Division. The Mawson magnetograms were provided by Dr.P.A. Hopgood, Bureau of Mineral Resources. The authors acknowledge Australian Research Council and Antarctic Science Advisory Committee for financially supporting this research and thank the University of Newcastle for travel grant assistance.

## 1.7 REFERENCES

Arnoldy, R.L., Engebretson, M.J. *and* Cahill, L.C. Jr. (1988). Bursts of Pc1-2 near the ionospheric footprint of the cusp and their relationship to flux transfer events. *Journal of Geophysical Research 93*:1007-1016.

Dilong, X. *and* Burns, G.B. (1988). Riometer absorption morphology at Davis and Casey stations. *ANARE Research Notes Number 61*. 33 pp.

Fraser, B.J., Kemp, W.J. *and* Webster, D.J. (1984). Pc1 pulsation source regions and their relationship to the plasmapause. *Proceedings of the Conference of Achievements of the International Magnetospheric Study, ESA-SP217*. Graz, Austria. Pp. 609-613.

Fukunishi, H., Toya, T.H., Koike, K., Kuwashima, M. *and* Kawaruma, M. (1981). Amplification of hydromagnetic emissions based on frequency time spectra. *Journal of Geophysical Research 86*:9020-9039.

Hayashi, K., Kokubun, T., Oguti, T., Tsuruda, K., Machida, S., Kitamura, T., Saka, O. *and* Watanabe, T. (1981). The extent of Pc1 source region at high latitudes. *Canadian Journal of Physics 59*:1097-1105.

Kawamura, M., Kuwashima, M. *and* Toya, T. (1982). Comparative study of magnetic Pc1 pulsations observed at low and high latitudes: source region and generation mechanism of periodic hydromagnetic emissions. *Memoirs of the National Institute of Polar Research 221*:3-16.

Matveeva, E.T., Troitskaya, V.A. *and* Feygin, F.Z. (1976). Intervals of pulsations of rising periods (IPRP) in the polar caps. *Planetary and Space Science 24*:673-678.

Morris, R.J., Cole, K.D., Matveeva, E.T. *and* Troitskaya, V.A. (1982). Hydromagnetic whistles at the dayside cusp. *Planetary and Space Science 30*:113-127.

Newell, P.T. *and* Meng, C.-I. (1988). The cusp and cleft boundary layer: low altitude identification and statistical local time variation. *Journal of Geophysical Research 93*:14549-14556.

Olson, J.V. *and* Lee, L.C. (1983). Pc1 wave generation by sudden impulses. *Planetary and Space Science 31*:295-302.

Potemra, T.A., Luhr, H., Zanetti, L.J., Takahashi, K., Erlandson, R.E., Marklund, G.T., Block, G.T., Blomberg, L.G. *and* Lepping, R. (1989). Multi-satellite and ground based observations of transient ULF waves. *Journal of Geophysical Research 94*:2543-2554.

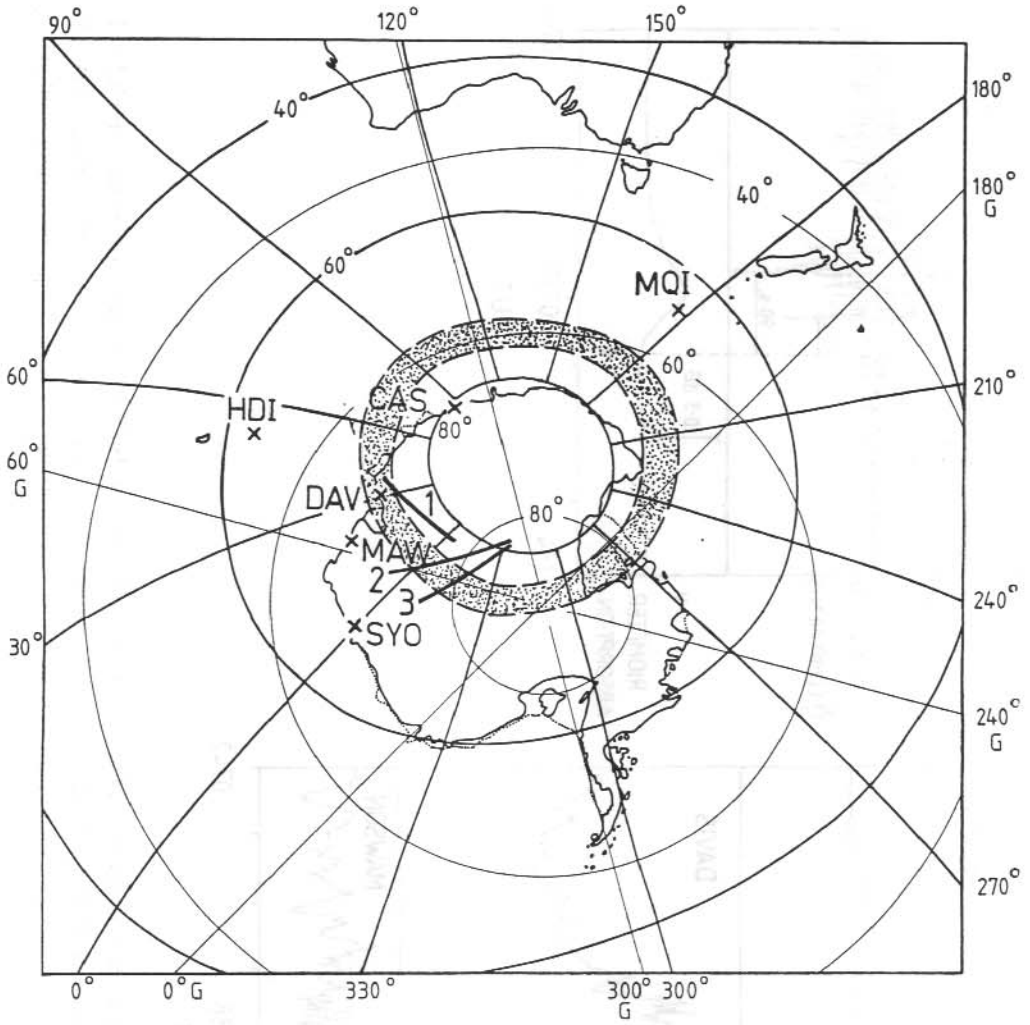


Figure 1. The locations of Casey (CAS), Davis (DAV) and Mawson (MAW). The bold/fine curves indicate geomagnetic/geographic coordinates. The shaded region indicates those locations on Earth that rotate beneath the average local noon location of the dayside cusp. Traces 1 to 3 show DMSP-F7 satellite passes at about 710, 0830 and 1030 UT respectively on 20 October, 1985.

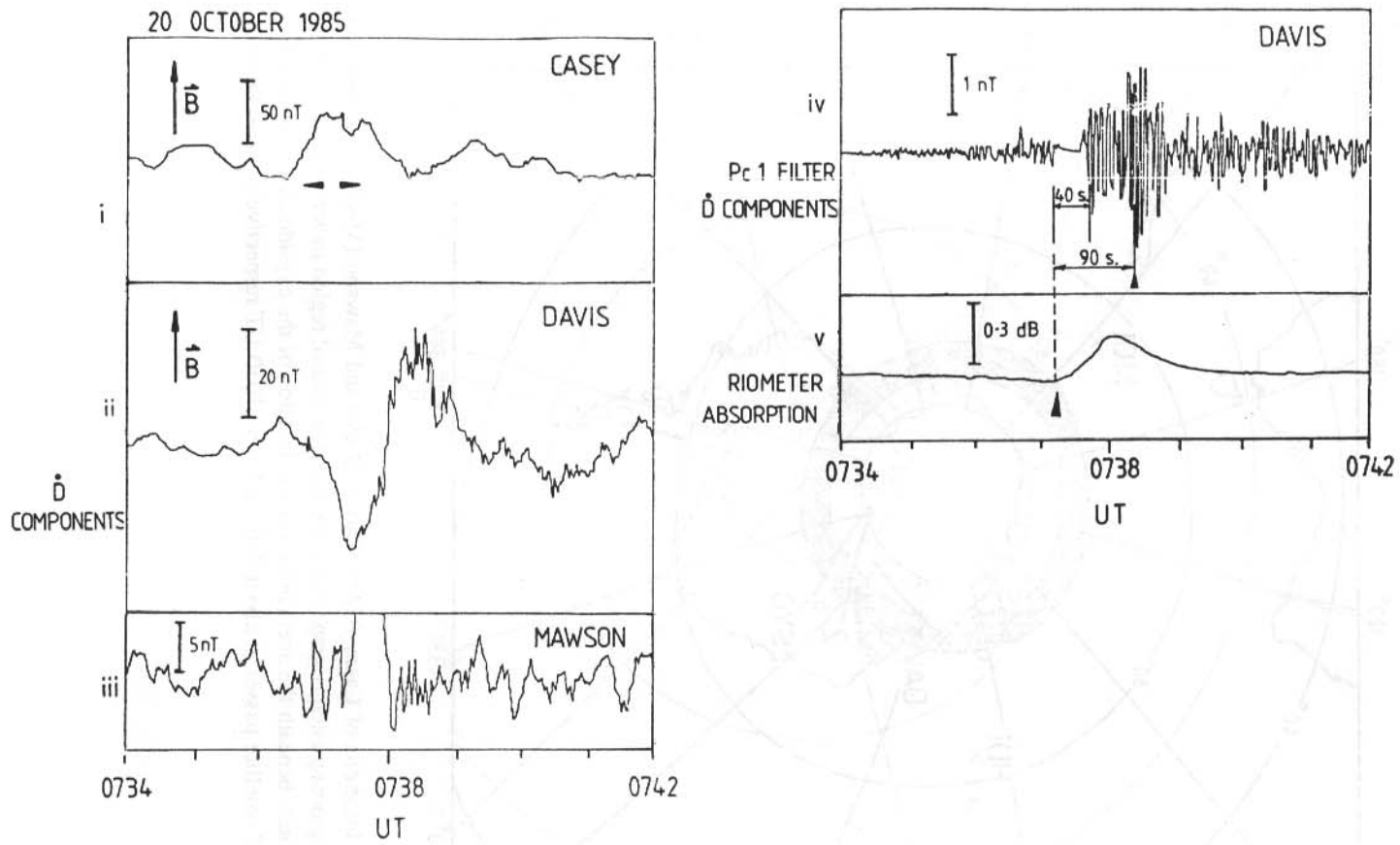


Figure 2. (i) to (iii) are the Ḋ magnetic variations between 0734 and 0744 UT on 20 October, 1985 (Casey, Davis, Mawson). (iv) 0.1 to 1 Hz is filtered Ḋ component variations between 0734 and 0742 UT on 20 October, 1985 (Davis). (v) variations in the corresponding 30 MHz riometer signal. An absorption event of at least 0.3 dB is displayed beginning 90 s before the Pc1 burst reaches maximum amplitude.

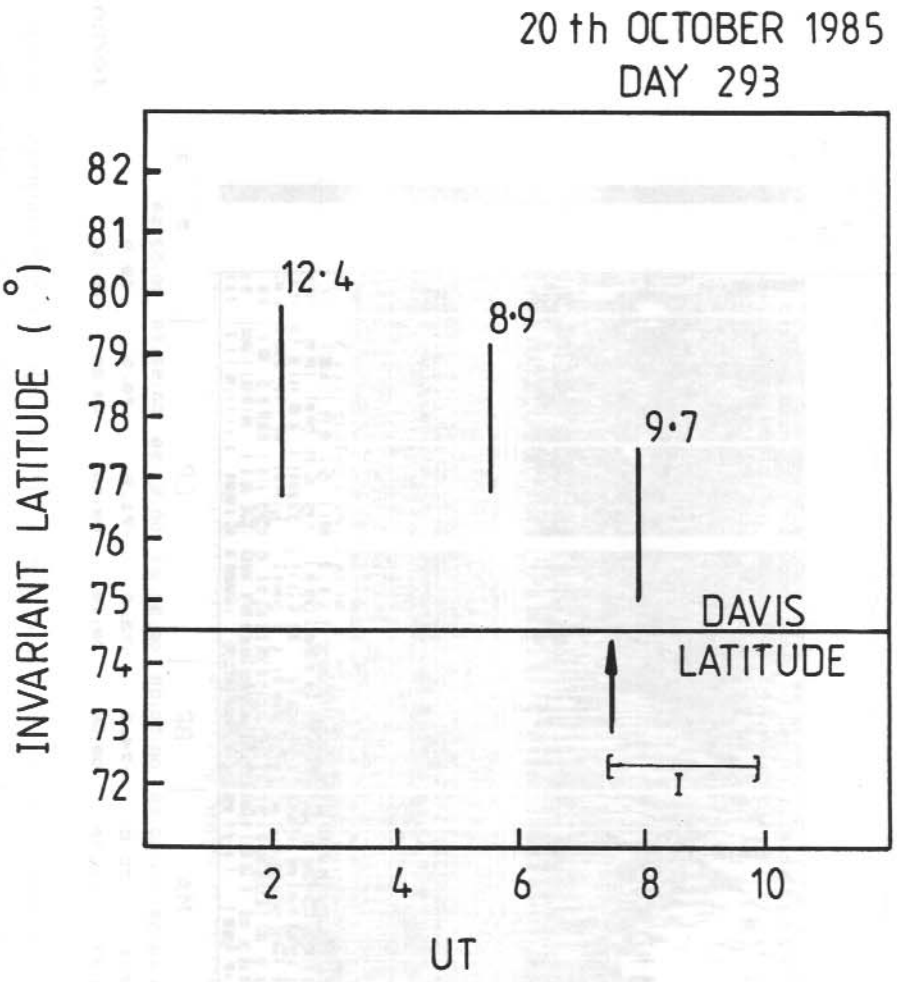


Figure 3. DMSP-F7 satellite locations of the low altitude cleft and cusp for the 3 passes at 0710, 0850 and 1030 UT on 20 October 1985. Davis' MLAT is indicated by the horizontal line. The interval, during which Pc1 bursts are received at Davis, is labelled I.

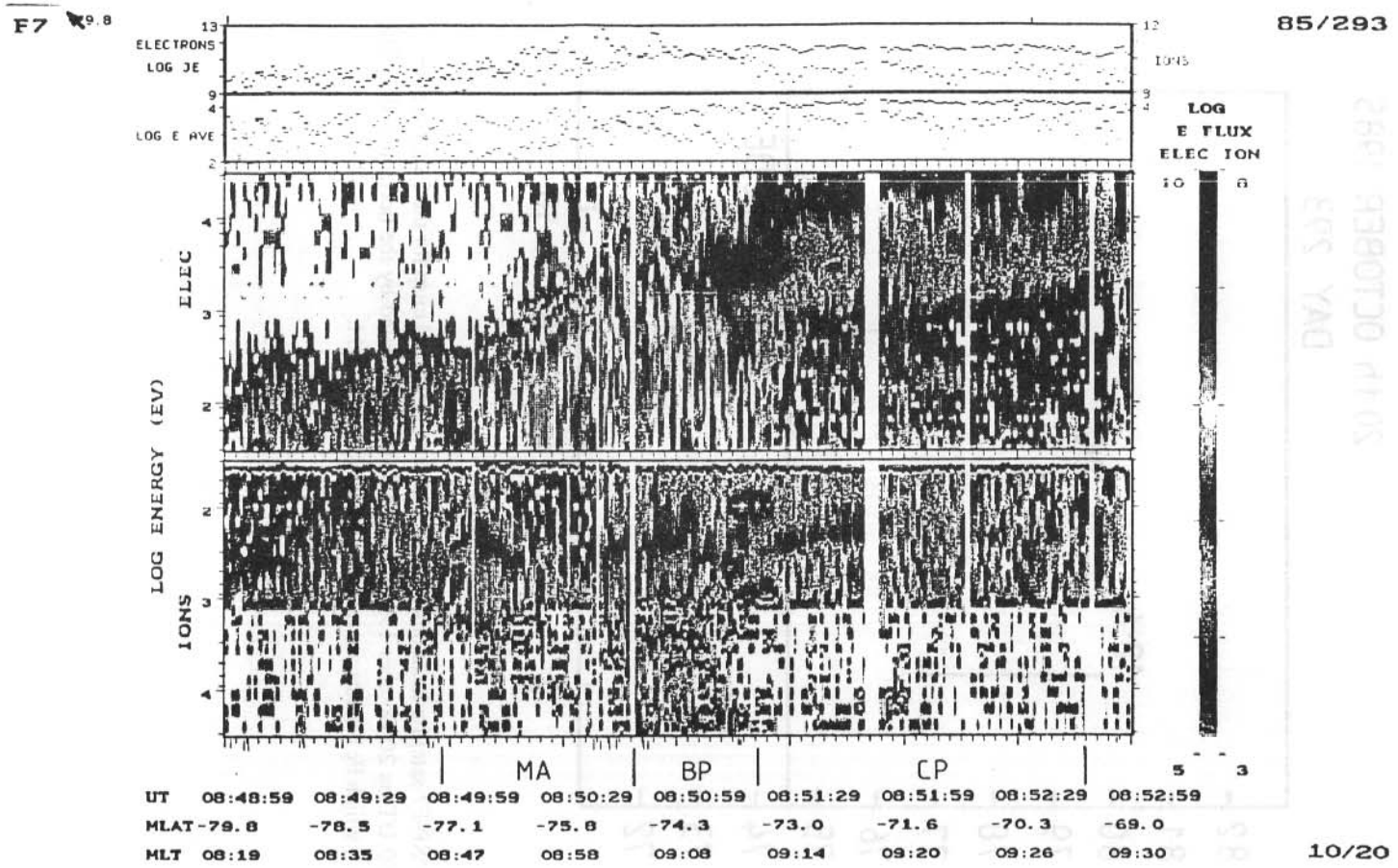


Figure 4. DMSP-F7 satellite particle spectra—pre-noon pass through cleft and cusp at 0850 UT on 20 October 1985. Top panel—electron and ion energy fluxes, average energy, electron/ion energy and flux distribution is a function of position of geomagnetic and geographic coordinates.

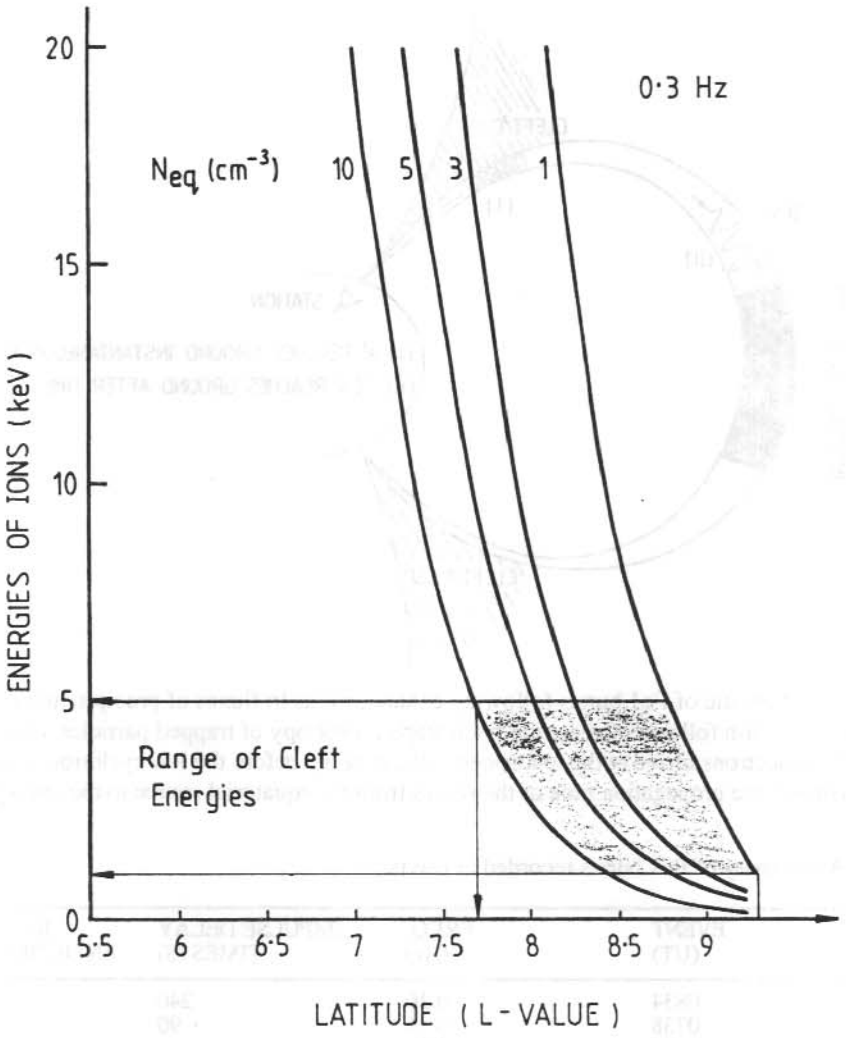


Figure 5. The variation in energy of ions resonant with 0.3 Hz ion-cyclotron waves in the equatorial plane as a function L value. Curves are shown for equatorial cold plasma densities expected in the vicinity of the low latitude boundary layer.

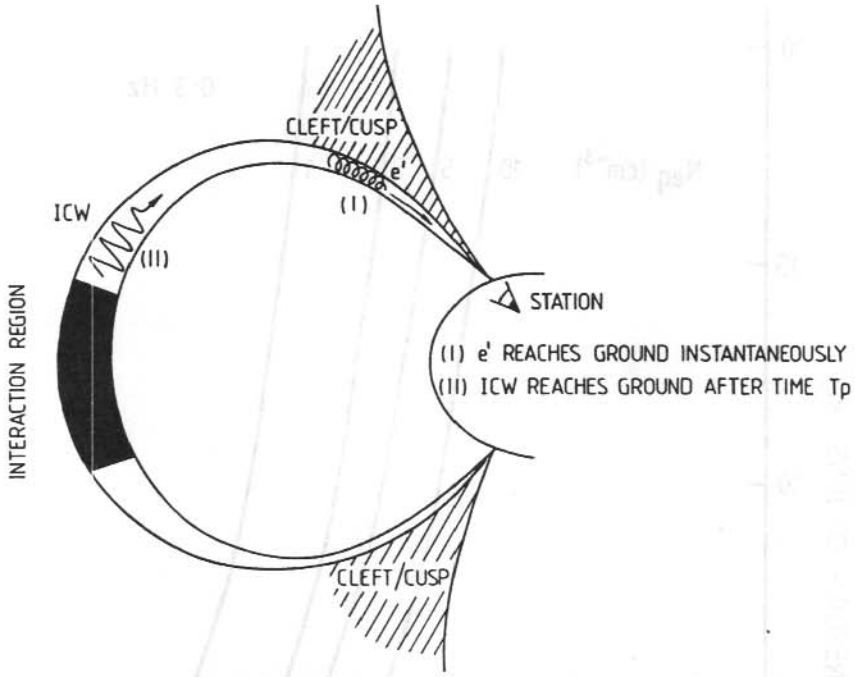


Figure 6. A schematic of Pc1 bursts following enhancements in fluxes of precipitating particles. Particle precipitation follows increases in pitch angle anisotropy of trapped particles, of electrons and ions. The electrons arrive at the ionosphere, (i) a time Tp before the ion-cyclotron waves, (ii) Tp approximates the propagation time of the waves from the equatorial source to the ionosphere.

Table 1. A summary of Pc1 bursts recorded at Davis.

| DAY 1985 | EVENT (UT) | FREQ. (Hz) | IMPULSE DELAY TIMES (S) | ION CLEFT ENERGIES (KEV) |
|---|---|---|---|---|
| 15 Oct. | 0834 | 0.20 | 240 | 2.8 |
| 20 Oct. | 0738 | 0.26 | 90 | 5.1 |
| | 0840 | 0.26 | - | 2.1 |
| | 0943 | 0.30 | - | 2.1 |
| 25 Oct. | 0513 | - | 180 | 4.7 |
| | 0617 | - | 60 | 2.5 |
| | 0722 | 0.25 | 240 | 2.5 |
| 4 Nov. | 0528 | 0.20 | 200 | 3.7 |
| | 0645 | 0.25 | - | 3.7 |
| | 0752 | 0.25 | 120 | 5.2 |
| | 0850 | 0.87 | - | 5.2 |
| | 0939 | 0.40 | - | 4.0 |
| | 1040 | 0.30 | 200 | 4.0 |
| 09/10 Nov. | 2300 | 0.20 | - | 3.7 |
| | 0610 | 0.20 | 120 | 4.3 |

## 2. SPECTRAL CHARACTERSTICS AND SOURCE REGIONS OF HIGH LATITUDE 2.5-0.1 Hz (Pc1-2) ULF WAVES

F.W. Menk[1], B.J. Fraser[1], H.J. Hansen[1], P.T. Newell[2], C.-I. Meng[2] and R.J. Morris[3]

[1]Physics Department
University of Newcastle
NSW 2308
Australia

[2]Applied Physics Laboratory
The Johns Hopkins University
Laurel Md 20707
USA

[3]Antarctic Division
Kingston Tas 7050
Australia

ABSTRACT

Dynamic spectra of 2.5-0.1 Hz ULF pulsations recorded with an array of six antarctic stations ranging in latitude from 62.3°S to 80.6°S invariant have been examined in order to identify the various spectral regimes present and to determine their likely magnetospheric source regions. These were deduced using DMSP satellite, long period pulsation, riometer and ground ionosonde data. General properties and specific examples are discussed. Broadband Pc1 noise is characteristic of the cusp itself, while narrowband unstructured Pc2 (0.1-0.2 Hz), and quasi-structured chorus type emissions occur preferably just equatorward of the cleft. Short Pc1 bursts including intervals of pulsations of rising period (IPRP) are another common feature at cleft latitudes. Propagation from lower latitudes does not seem to be the major source of cusp and cap Pc1 (0.2-2.5 Hz) signals. The Pc1 noise associated with the cusp constitutes part of the broadband wave spectrum recorded on the ground and on satellites, and could be generated by instabilities associated with shear in ion flow near the cusp boundary. Antisunward convecting plasma features in the boundary layer may give rise to the short Pc1 bursts. The dispersive plasmatrough Pc1-2 may be reconciled with ion-cyclotron generation if heavy ion effects are considered.

### 2.1 INTRODUCTION

The study of high latitude magnetic pulsation signatures is important in explaining the mechanisms by which ULF wave energy can penetrate the magnetospheric and ionospheric environments. There also exists the possibility of using ground-based measurements of ULF

pulsations as a simple diagnostic of high latitude magnetospheric dynamics. Ground magnetometer spectra may be used to distinguish wave processes associated with different particle signatures when the observatories are located beneath or near the energy deposition region.

The spectrum of ULF pulsations recorded at spaced ground stations is both complex and varied. The 5-0.1 Hz frequency range (Pc1-2) is of special interest because at polar cleft and cusp latitudes this is occupied by several different phenomena (Fraser-Smith 1982, Arnoldy et al. 1986, 1988, Olson 1986). These include short-lived emissions with varied dispersion characteristics (Matveeva et al. 1976, 1978, Morris and Cole 1985), and long-lived unstructured noise-like emissions (Fukunishi et al. 1981, Heacock 1974).

Although morphological properties of these pulsations have been generally established, it is not clear whether phenomena which exhibit different spectral properties arise independently or are manifestations of the same process. This paper presents results from a multistation study of Pc1-2 emissions in the polar cleft and cusp regions, with the aim of identifying the different pulsation signatures recorded at these latitudes. By using satellite particle data and ground magnetograms, riometer data and ionograms, the location of the Pc1-2 source region, projected to ionospheric altitudes, can be determined.

## 2.2 DATA RECORDING AND ANALYSIS

Five Pc1-2 pulsation recording stations were operated by Antarctic Division and the University of Newcastle in Antarctica over the 1986-87 austral summer. These stations span 62-81° invariant latitude and 12 hours in local time (Table 1, Figure 1). At each station, 3-0.01 Hz ULF emissions in the H and D components were detected with induction coil sensors and recorded on paper chart and slow speed analogue FM tape. Data retrieval included replaying each tape and digitally sampling the demodulated sped-up signal. Data were then processed by FFT using a dedicated PC to provide dynamic spectra that were recorded on film. Data were effectively sampled over the 2.5-0.1 Hz range at a real time rate of 10 Hz in 256-point blocks with a step size of 128 points between blocks. Sensitivity of the record-replay system was typically 0.05 nT $Hz^{-1}$ and time resolution of the spectra is 60 seconds. Pulsation data were obtained in similar form from the Japanese station, Syowa (SYO), courtesy of the National Institute of Polar Research, Tokyo.

The following data were also used to identify the regions under which the ULF waves were recorded: SYO, MAW and DAV fluxgate magnetometer chart records; DAV ionograms; DAV and CAS 30 MHz riometer records, and topside particle data from the DMSP-F7 ion and electron counter experiments. The latter were examined in the form of colour spectra of particle energies and fluxes for orbits passing over or near the MAW-DAV-CAS array.

Table 1. Antarctic Pc1-2 ULF pulsation ground stations.

| Code | Station | Geographic | | Corr. Geomagnetic | | Invariant | | Approx. Magnetic Noon | L-value |
|---|---|---|---|---|---|---|---|---|---|
| | | Lat.°S | Long.°E | Lat.°S | Long.°E | Lat.°S | Long.°E | | |
| HDI. | Heard Is. | 53.0 | 73.5 | 62.1 | 123.5 | 62.3 | 60.4 | 0945UT | 4.7 |
| MQI. | Macquarie Is. | 54.5 | 159.0 | 64.5 | 246.8 | 64.5 | 177.7 | 0015UT | 5.4 |
| SYO | Syowa (Japan) | 69.0 | 39.6 | 66.1 | 70.9 | 66.0 | 1.2 | 115OUT | 6.2 |
| MAW | Mawson | 67.6 | 62.8 | 60.3 | 89.5 | 70.1 | 19.6 | 1019UT | 8.6 |
| DAV | Davis | 68.6 | 78.0 | 74.5 | 103.0 | 74.5 | 29.6 | 0926UT | 14.0 |
| CAS | Casey | 66.2 | 110.3 | 80.8 | 153.6 | 80.6 | 85.3 | 0525UT | 37.8 |

## 2.3 SPECTRAL CHARACTERISTICS

Table 1 shows that the stations HDI, SYO, MAW, DAV and CAS are each about 1-2 hour apart in local time and 4-5° in latitude. Both temporal and spatial features are thus present in data comparisons, as well as effects associated with changes in magnetic activity. Dynamic spectra covering the Pc1-2 range (2.5-0.1 Hz)Ḣ component were examined from all stations for the days 26 November to 7 December 1986 inclusive, in order to identify the range of spectral features recorded on the ground under quiet and moderately disturbed summer conditions.

In general, Pc1-2 emissions at the plasmatrough stations MQI, HDI and SYO exhibited similar characteristics, whilst at the subcleft station, MAW, additional features were also observed. The MAW records always contained the greatest diversity of spectral features. Emissions at these stations exhibited distinct, bandlimited discrete spectral characteristics, including repetitive dispersion features. Activity at the polar cleft and cusp stations DAV and CAS occurred predominantly in broad, diffuse bands centered around geomagnetic noon, and may generally be reconciled with the broadband wave spectrum recorded by polar orbiting satellites (Erlandson et al. 1989).

The spatial and temporal distribution of the observed spectral features is summarised in Figure 2 and Table 2.

## 2.4 SOURCE REGION LOCATION

Multipoint ground and satellite data were jointly examined for the days 1, 3 and 4 December 1986 in order to identify the ionospheric projection of the cusp and cleft, and hence identify the likely ULF wave source region. Since the results are self-consistent, details for one day only, 3 December, are presented.

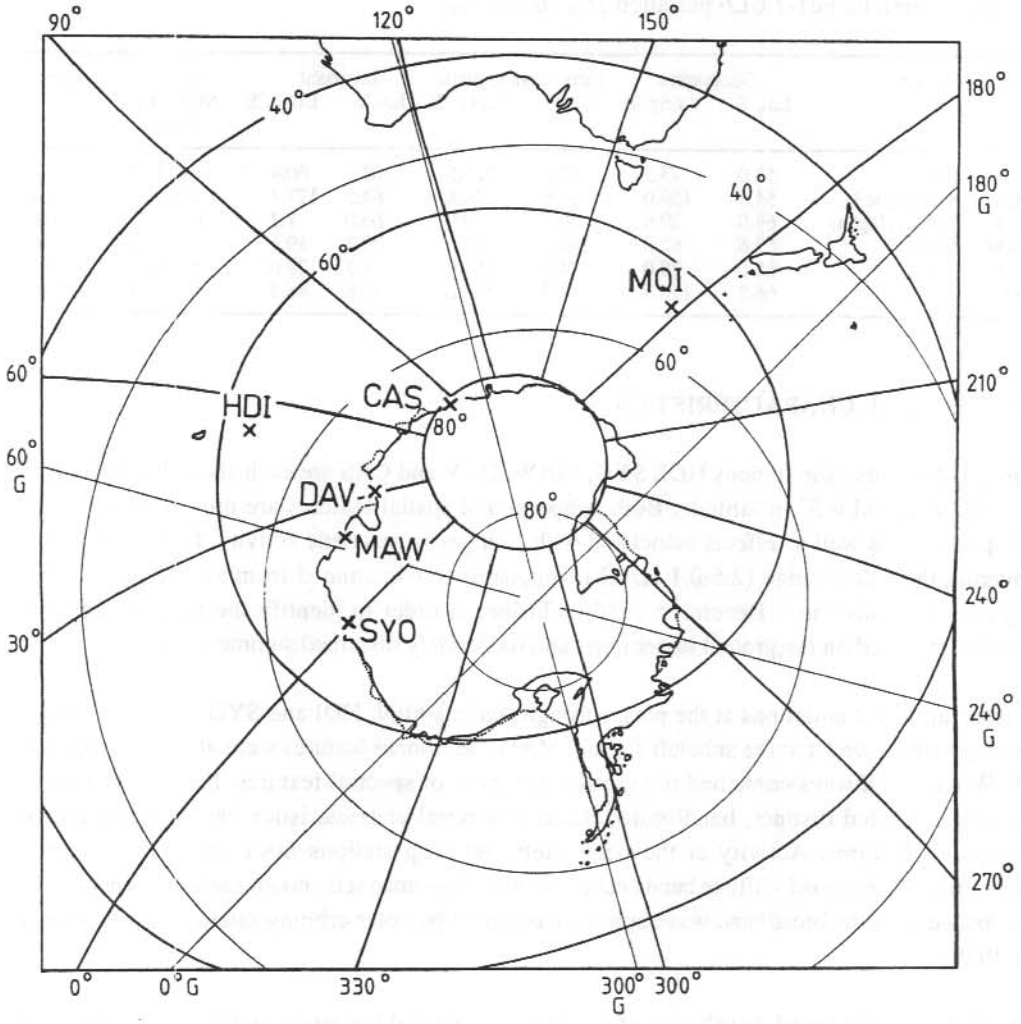


Figure 1. Map showing locations of ground stations used in this study. Coordinate systems are geographic and invariant (light and heavy lines respectively).

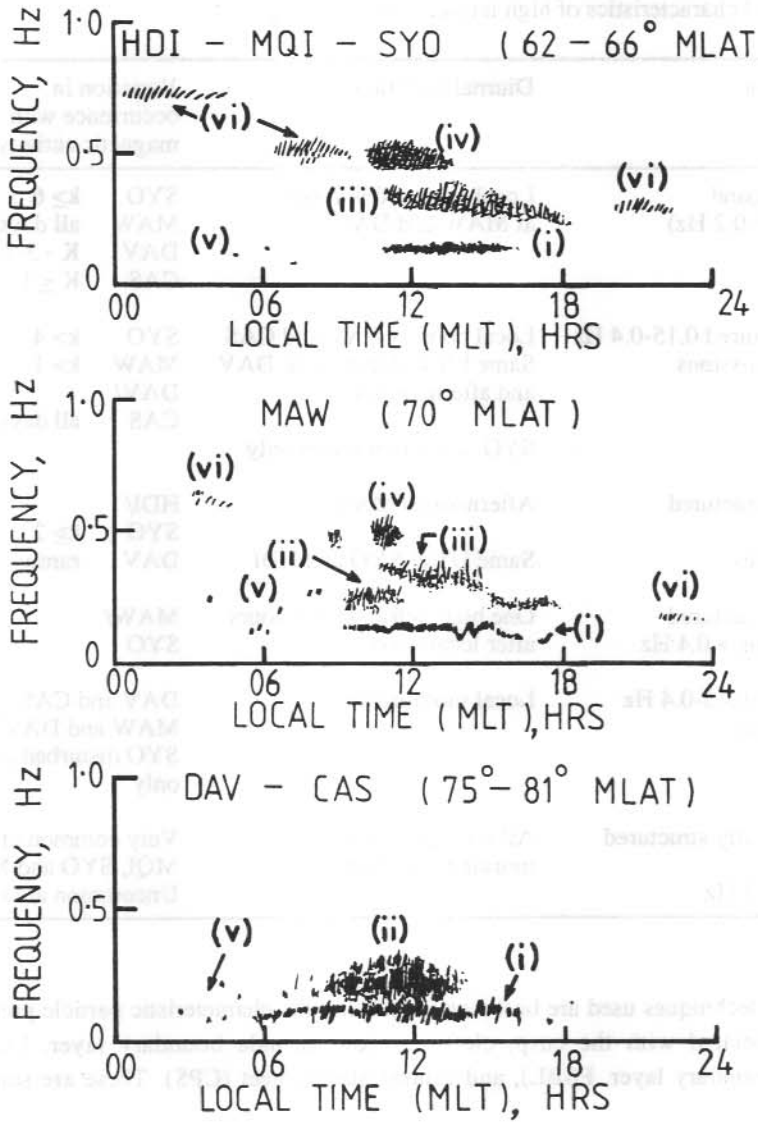


Figure 2. Schematic representation of Pc1-2 activity observed over 11 summer days at polar ground stations under quiet to moderately disturbed conditions. Local magnetic times shown.

Legend: (i) Narrowband Pc2 (0.1-0.2 Hz) emissions
(ii) Unstructured 0.15-0.4 Hz noise-like emissions
(iii) Quasi-structured hm (hydromagnetic) chorus (Fukunishi et al. 1981)
(iv) Quasi-structured emissions >0.4 Hz (Fukunishi et al. 1981)
(v) Discrete 0.15-0.4 Hz emissions (Morris and Cole 1985)
(vi) Periodically structured Pc1 >0.2 Hz

Table 2. Spatial characteristics of high latitude Pc1-2 activity.

| | Emission | Diurnal variation | Variation in occurrence with magnetic activity |
|---|---|---|---|
| (i) | Narrowband Pc2 (0.1-0.2 Hz) | Local noon ± few hours at MAW and DAV | SYO $k \geq 6$<br>MAW all days<br>DAV K - 3-4<br>CAS $K \leq 1$ |
| (ii) | Unstructured 0.15-0.4 Hz noise emissions | Local noon at DAV and CAS<br>Same UT at MAW as at DAV and afternoon sector<br>SYO, afternoon sector only | SYO $k > 4$<br>MAW $k > 1$<br>DAV/ CAS all days |
| (iii) | Quasi-structured hm chorus | Afternoon at MAW<br>Same UT at SYO and HDI | HDI/ SYO $k \geq 2$<br>DAV rarely |
| (iv) | Quasi-structured emissions > 0.4 Hz | One hour before to 3-4 hours after local noon | MAW/ SYO |
| (v) | Discrete 0.15-0.4 Hz emissions | Local morning hours | DAV and CAS<br>MAW and DAV<br>SYO disturbed conditions only |
| (vi) | Periodically structured Pc1 > 0.2 Hz | All hours, especially morning and evening | Very common at HDI, MQI, SYO and MAW<br>Uncommon at DAV, CAS |

The analytical techniques used are based on identifying the characteristic particle precipitation signature associated with the cusp, cleft (i.e. low latitude boundary layer, LLBL, and plasmasheet boundary layer, PSBL), and central plasmasheet (CPS). These are summarised below:

1. DAV ionograms: E and F layer signatures of precipitating magnetosheath-like particles, such as the slant-E condition (SEC) and F-layer irregularity zone (FLIZ) respectively (Pike 1971, Piggott 1975, Stiles et al. 1977).

2. DAV and CAS 30 MHz riometer: enhanced electron precipitation (<1 dB) around local magnetic noon is a cusp identifier (Olson 1986).

3. MAW, DAV and CAS magnetograms: long period Pc5 and IPCL (~2-10 min) pulsations are characteristic of the nearby cusp (Rostoker et al. 1972). Their local time of occurrence and amplitude can be used as a guide to the proximity of the cusp (Bol'shakova and Troitskaya 1977).

4. DMSP satellite particles: spectra of ion and electron energies and fluxes from the 840 km altitude polar orbiting satellite show signatures identified with the mantle, cusp, LLBL, PSBL and CPS regions (Newell and Meng 1988). Figure 3 shows two examples for the 0329 and 0510 UT, 3 December passes, 1.2 hours east of CAS and between DAV and CAS respectively.

These data were combined to locate the ionospheric projection of the cusp and cleft on 1, 3 and 4 December 1986 at MAW-CAS longitudes. Figure 4 shows the resultant cusp/cleft location map for 3 December 1986. The different mapping techniques yield self-consistent results, lending confidence to the cusp and cleft determinations.

The occurrence of the different types of Pc1-2 emissions summarised in Figure 2 were compared with the cusp and cleft projections (Figure 4) on an event-by-event basis. Emissions with different spectral characteristics were found to be associated with different particle signatures and hence distinct magnetospheric source regions. These results are summarised in Table 3.

## 2.5 GENERATION MECHANISMS

The different Pc1-2 spectral characteristics and inferred source region projections suggest possible wave generation mechanisms. These are ordered by region of occurrence as follows:

1. *Plasmapause and plasmatrough* (HDI, MQI, SYO, MAW):
   Ion-cyclotron instability between ULF waves and Doppler-shifted ions near the equatorial plane results in successive amplification of bouncing wavepackets whose dispersion characteristic can be used as a plasma diagnostic (eg. Fraser 1976). This mechanism is likely to be associated with hm chorus and other periodically structured dispersive Pc1 emissions at plasmatrough stations. Emissions may propagate between these stations in the ionospheric duct (Manchester 1970). The narrowband Pc2 emissions could also be generated by an ion-cyclotron mechanism if heavy ion effects are considered (Fraser and McPherron 1982, Inhester et al. 1984).

2. *Cleft/boundary layers* (MAW, DAV):
   Boundary layer instabilities are of concern here. These include waves generated in association with tailward convecting plasma perturbations of solar wind origin in the presence of spatially varying magnetic field and plasma parameters. The resultant emissions may include short discrete bursts with variable dispersion properties (Cole et al. 1982).

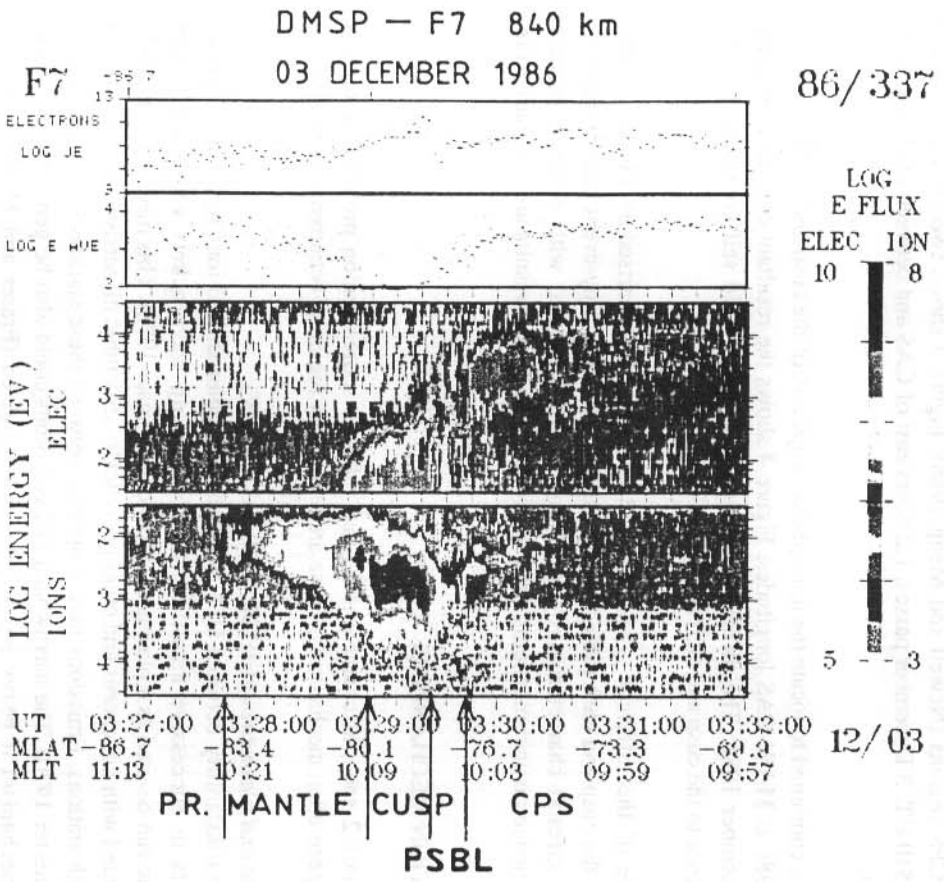


Figure 3. Examples of DMSP satellite spectra for 03 December, 1986, showing electron and ion energy flux (upper panels), average energy, particle energy and flux distribution with corrected geomagnetic latitude (MLAT).
(a) 0329 UT Southern hemisphere orbit. (continued)

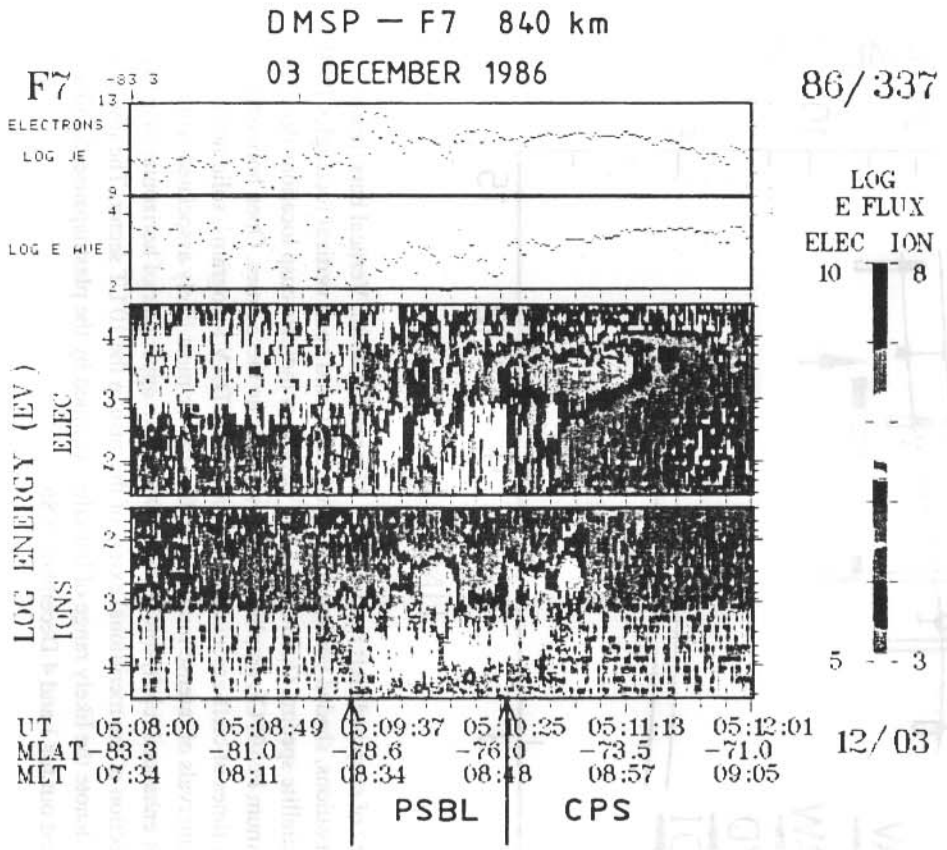


3(b). 0510 UT Southern hemisphere orbit.

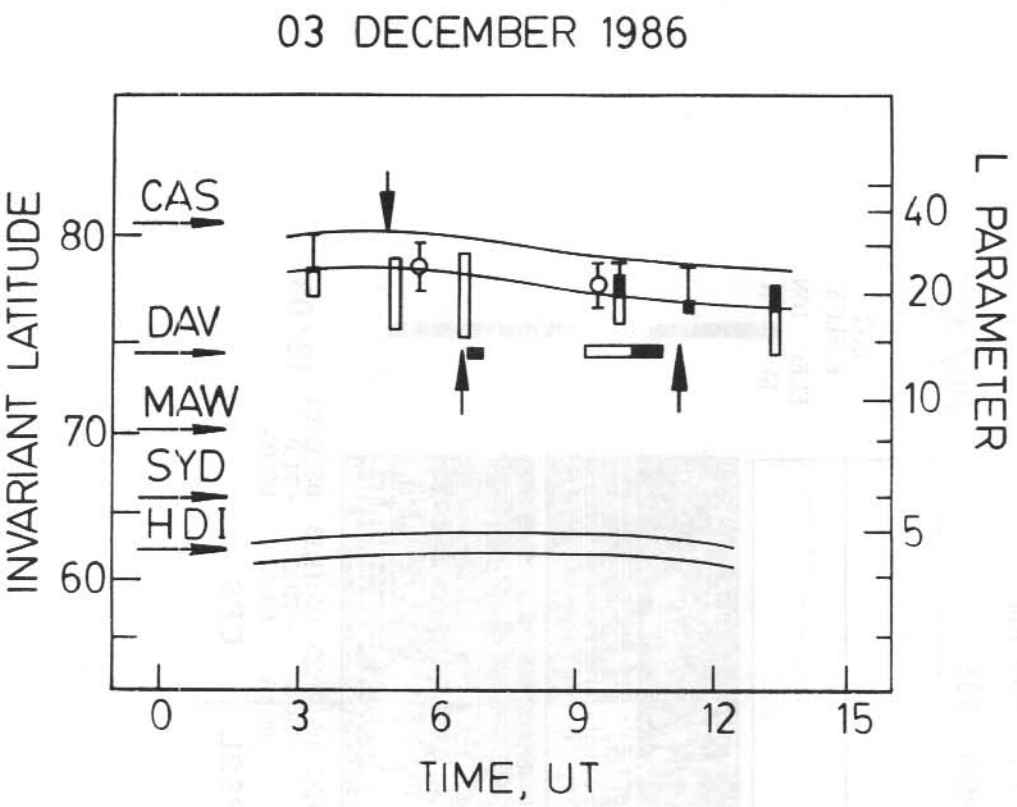


Figure 4. Summary of cusp and cleft mapping, for 3 December 1986. Vertical bars denote satellite cusp observations, shaded vertical rectangles LLBL and open vertical rectangles PSBL determined from satellite spectra. Open circles and error bars indicate cusp locations deduced from time of maximum Pc5/IPCL amplitudes: arrows indicate these times. Open horizontal rectangles indicate times of cleft-associated irregularities on DAV ionograms; solid horizontal rectangles denote intervals of intense ionospheric disturbance most likely associated with closest approach of enhanced (cleft) ionisation to DAV. The upper pair of horizontal lines are the estimated projection of the meridional extent of the cusp in the 10 LT sector. The lower pair of horizontal lines denote the likely range of latitudes occupied by the plasmapause. Similar mapping was carried out for 1 and 4 December 1986.

Table 3. Pc1-2 source region locations.

| | Emission | Spectral appearance | Preferred region of occurence |
|---|---|---|---|
| (i) | Narrowbrand Pc2 | Unstructured narrow band, 0.1-0.2 Hz; frequency | Under and a few degrees equatorward for PSBL in noon sector |
| (ii) | Unstructured 0.15-0.4 Hz noise emissions | Unstructured patchy broad noise-like band, 0.2-0.3 Hz at SYO and MAW, 0.15-0.4 HZ at DAV and CAS | Within -2° of poleward edge of cusp. Duration correlated with azimuthal width of cusp. |
| (iii) | Quasi-structured hm chorus | Mixture of period frequency-structured elements and a band of unstructured noise 0.25-0.5 Hz | Within plasmatrough, few degrees poleward of plasmapause in afternoon sector, typically 68-70° geomag. latitude |
| (iv) | Quasi-structured emissions >0.4 Hz | Mixture of structured hm periodic emissions and diffuse noise. | As for (iii) above |
| (v) | Discrete 0.15-0.4 Hz | Discrete packets or trains of packets, 0.15-0.4 Hz, with constant or varying frequency within both the packet and/or the train. | Cleft to -5-6° equatorward of cusp; also occasionally in cap. Morning sector. |
| (vi) | Periodically structured Pc1 >0.2 Hz. (pearls) | Periodic frequency-structured elements often exhibiting dispersion characteristics | Plasmatrough and near poleward edge of plasmapause; prenoon and late afternoon sector |

3. *Cusp* (DAV, CAS):

Any mechanism capable of generating broadband ULF noise must be considered. Likely candidates include the Kelvin-Helmholtz instability at the plasma flow shear associated with the cusp boundary; drift-wave instability; variations in ionospheric current systems driven by FTE-like transients; and multiple X-line magnetic reconnection processes (D'Angelo 1977, Arnoldy et al. 1988, Lanzerotti et al. 1986, Lee et al. 1988).

## 2.6 CONCLUSIONS

1. High latitude Pc1-2 (2.5-0.1 Hz) ULF emissions fall at summertime into spectrally distinct regimes corresponding to the observation of narrowband Pc2, broadband unstructured 0.15-0.4 Hz noise, quasi-structured hm chorus, short Pc1 bursts, and dispersive periodically structured Pc1 emissions at ground observatories.

2. Several independent techniques were used to locate the ionospheric projection of the cusp and cleft/boundary layer, based on their particle signatures. These include ground magnetometer, riometer, ionosonde and topside ion and electron data. Self-consistent results in mapping these locations point to diagnostic applications.

3. Spectral properties of Pc1-2 ULF waves at polar latitudes can be ordered according to the projection of the cusp and cleft to ionospheric altitudes, permitting wave source region identification.

4. Consequently, likely generation mechanisms may be proposed.

Future work should focus on identifying multistation polarisation properties with specific case studies in order to determine interstation propagation characteristics and clarify the associated wave generation mechanism.

## 2.7 ACKNOWLEDGMENTS

The magnetic pulsation and related ground data were obtained by members of the 1986 ANARE. Davis ionograms were kindly supplied by the director of the Ionospheric Prediction Service, Sydney. Syowa pulsation dynamic spectra were made available by the National Institute of Polar Research, Tokyo. This work was supported by funding obtained under the Antarctic Science Advisory Committee (ASAC) and Australian Research Council (ARC) schemes.

## 2.8 REFERENCES

Arnoldy, R.L., Cahill, L.J. Jr., Eather, R.J. *and* Engebretson, M.J. (1986). Greater than 0.1 Hz ULF magnetic pulsations measured at South Pole. *Journal of Geophysical Research 91*:5700-5710.

Arnoldy, R.L., Cahill, L.J. Jr., Engebretson, M.J., Lanzerotti, L.J. *and* Wolfe, A. (1988). Review of hydromagnetic wave studies in the Antarctic. *Reviews of Geophysics 26*:181-207.

Bol'shakova, O.V. *and* Troitskaya, V.A. (1977). Dynamics of the day cusp, according to observations of long-period geomagnetic pulsations. *Geomagnetism and Aeronomy 17*:722-725.

Cole, K.D., Morris, R.J., Matveeva, E.T., Troitskaya, V.A. *and* Pokhotelov, O.A. (1982). The relationship of the boundary layer of the magnetosphere to IPRP events. *Planetary and Space Science 30*:129-136.

D'Angelo, N. (1977). Plasma waves and instabilities in the polar cusp: a review. *Review of Geophysics and Space Physics 15*:299-307.

Erlandson, R.E., Zanetti, L. *and* Potemra, T.A. (1989). Magnetic-field fluctuations from 0 to 26 Hz observed from a polar-orbiting satellite. *IEEE Transactions on Plasma Science 17*:196-200.

Fraser, B.J. (1976). Pc1 geomagnetic pulsation source regions and ionospheric waveguide propagation. *Journal of Atmospheric and Terrestrial Physics 38*:1141-1146.

Fraser, B.J. *and* McPherron, R.L. (1982). Pc1-2 magnetic pulsation spectra and heavy ion effects at synchronous orbit: ATS6 results. *Journal of Geophysical Research 87*:4560-4566.

Fraser-Smith, A.C. (1982). ULF/lower-ELF electromagnetic field measurements in the polar caps. *Reviews of Geophysics and Space Physics 20*:497-512.

Fukunishi, H., Toya, T., Koike, K., Kuwashima, M. *and* Kawamura, M. (1981). Classification of hydromagnetic emissions based on frequency-time spectra. *Journal of Geophysical Research 86*:9029-9039.

Heacock, R.R. (1974). Midday Pc1-2 pulsations observed at a subcleft location. *Journal of Geophysical Research 79*:4239-4245.

Inhester, B., Wedeken, U., Korth, A., Perraut, S. *and* Stokholm, M. (1984). Ground-satellite coordinated study of the April 5, 1979 events: observation of $O^+$ cyclotron waves. *Journal of Geophysics 55*:134-141.

Lanzerotti, L.J., Lee, L.C., Maclennen, C.G., Wolfe, A. *and* Medford, L.V. (1986). Possible evidence of flux transfer events in the polar ionosphere. *Geophysical Research Letters 13*:1089-1092.

Lee, L.C., Shi, Y. *and* Lanzerotti, L.J. (1988). A mechanism for the generation of cusp region hydromagnetic waves. *Journal of Geophysical Research 93*:7578-7585.

Manchester, R.N. (1970). Propagation of hydromagnetic emissions in the ionospheric duct. *Planetary and Space Science 18*:299-307.

Matveeva, E.T., Troitskaya, V.A. *and* Feygin, F.Z. (1976). Intervals of pulsations with rising periods (IPRP) in polar caps. *Planetary and Space Science 24*:673-678.

Matveeva, E.T., Troitskaya, V.A. *and* Feygin, F.Z. (1978). Isolated bursts of type Pc1b geomagnetic pulsations at high latitudes. *Geomagnetism and Aeronomy 18*:75-79.

Morris, R.J. and Cole, K.D. (1985). Pc1-2 discrete regular daytime pulsation bursts at high latitudes. *Planetary and Space Science 33*:53-67.

Newell, P.T. *and* Meng, C.-I. (1988). The cusp and cleft/boundary layer: low altitude identification and statistical local time variation. *Journal of Geophysical Research 93*:14549-14556.

Olson, J.V. (1986). ULF signatures of the polar cusp. *Journal of Geophysical Research 91*:10056-10062.

Piggott, W.R. (1975). High-latitude supplement to the URSI handbook on ionogram interpretation and reduction. *World Data Center A for STP, NOAA, Boulder, Colorado.*

Pike, C.P. (1971). A latitudinal survey of the daytime polar F layer. *Journal of Geophysical Research 76*:7745-7753.

Rostoker, G., Samson, J. *and* Higuchi, Y. (1972). Occurrence of Pc 4,5 micropulsation activity at the polar cusp. *Journal of Geophysical Research 77*:4700-4706.

Stiles, G.S., Hones, E.W. Jr., Winningham, J.D., Lepping, R.P. *and* Delana, B.S. (1977). Ionosonde observations of the northern magnetospheric cleft during December 1974 and January 1975. *Journal of Geophysical Research 82*:67-73.

# 3. Pc1-2 CONTINUOUS DAYTIME MAGNETIC PULSATIONS A SIGNATURE OF THE POLAR CUSP/CLEFT

R.J. Morris[1] and K.D. Cole[2]

[1]Antarctic Division
Kingston Tas 7050
Australia

[2]La Trobe University
Bundoora Vic 3083
Australia

ABSTRACT

New observational and dynamical morphological results of high-latitude Pc1-2 (0.2-10 s) magnetic pulsations observed at Davis (invarient 74.6° S), Antarctica during solar maximum, are presented. An interesting regime of Pc1-2 containing structured, semi-structured and unstructured, long duration ($\tau$ ~ 1-10 hours) magnetic pulsation bands (T ~ 2-10 s), which appear to maximise in occurrence frequency and amplitude under the projection of the dayside polar cusp/cleft, are examined. An account of these emissions is given, including; periods, amplitudes, duration, diurnal and seasonal distributions, polarisation, power spectra and their association with magnetic activity ($K_p$). Moreover a review of the literature reveals the necessity for a universal convention to clear up the apparent paradox and confused nomenclature existing in the literature on high-latitude Pc1-2 magnetic pulsations. This study concludes that Pc1-2 magnetic pulsations as reported provide a ground diagnostic estimate as to whether a station lies under the projection of the polar cusp/cleft.

## 3.1 INTRODUCTION

Despite the somewhat limited high-latitude ground-based research conducted on the spectrum of pulsations emanating from the polar cusp/cleft, several new pulsation regimes in the Pc1-2 (0.2-10 s) range have been reported in the last decade, viz., IPRP (Matveeva et al. 1976, Morris et al. 1982, Cole et al. 1982, Morris and Cole 1985), Pc1b (Matveeva et al. 1978) or IPCP (Morris and Cole 1985), Pc1 Structured (Heacock et al. 1970), Pc1-2 Non-structured (Bolshakova et al. 1980) and Serpentine Emission (SE) (Gul'elmi and Dovbnya 1974, Morris and Cole 1987). The paucity of scientific literature on polar cusp/cleft and polar cap magnetic pulsations can most likely be attributed to some extent, to logistical difficulties restricting the number of suitable Arctic and Antarctic observatories.

Newell and Meng (1988) have provided clear experimental evidence which overwhelmingly distinguishes the dayside cusp and the cleft as two separate entities, based upon average ion and

electron energies ($E_i$ and $E_e$) as detected by the Defense Meteorological Satellite Program (DMSP) F7. Newell and Meng (1988) defined several objective criteria to determine whether a region had cusp or cleft (or both) status, whereby the low altitude cusp was defined to be the region of more direct entry of magnetosheath plasma with both 300 eV < $E_i$ < 3000 eV and $E_e$ < 220 eV; and the cleft was defined as the region of entry of LLBL plasma if either 3000 eV < $E_i$ < 6000 eV or 220 eV < $E_e$ < 600 eV hold. These authors concluded that the cusp is sharply peaked at noon, with a latitudinal width of 0.8°-1.1° MLAT which is independent of MLT and has an ion precipitation number flux approximately 3.6 times that of the cleft, which is comparable to that of the magnetosheath. Conversely, they found that the probability of observing the cleft maximises a few hours away from noon, having a pronounced minimum near noon with a latitudinal thickness that varies inversely with time measured from noon. Correlation studies between cusp position and variations in $D_{st}$, AE and IMF $B_z$ have demonstrated an equatorward positional movement of the cusp/cleft for increasing negative values of these parameters with an associated decrease in the width (Meng 1982, Winningham and Heelis 1983), a similar effect has also been reported for increasing levels of $K_p$ (Winningham 1972, Meng 1984).

Although the positional and dimensional variability of the polar cusp/cleft in response to both solar and terrestrial perturbations can be monitored by low-altitude DMSP snapshots, the terrestrial observer still has no categorical knowledge as to whether their ground observatory lies under the projection of the polar cusp/cleft regions of the magnetosphere. Investigations of high-latitude magnetic pulsation regimes, i.e. Pc1-2 continuous and discrete emissions, have revealed a possible connection between their morphological characteristics and the location of the projection of the polar cusp/cleft regions (Bolshakova et al. 1980, Morris and Cole 1985). Such observations are extremely significant since ground signatures of magnetic pulsation emissions could provide a continuous monitor of the ground projection of the polar cusp and cleft, and thus afford a ground diagnostic tool on aspects of the magnetosphere.

This paper presents new morphological and dynamical analyses of the too little documented high-latitude Pc1-2 continuous magnetic pulsation band as observed at the typical polar cusp/cleft station, Davis (gg 68.6° S, 78.0° E; $\Lambda \sim 74.6°$ S). An investigation of thirteen months induction magnetometer data (March 1981 to February 1982 augmented with 1985 data) revealed the existence of at least three sub-classes of Pc1-2 continuous magnetic pulsation emissions, which the authors have tentatively called: Pc1-2 Structured, Pc1-2 Semi-Structured and Pc1-2 Unstructured, in the absence of a universally recognised classification scheme. The proposed nomenclature is based upon qualitative signatures recognisable on both amplitude-time chart records and frequency-time dynamic spectra. Figure 1 illustrates a schematic cartoon of the high altitude magnetospheric plasma environs and their perceived mapping down the polar cusp/cleft topology (top), and subsequent ground projection for the latitude of Davis (at local magnetic noon), where the arrows point to the proposed source regions of the reported sub-classes of Pc1-2 continuous magnetic pulsations (bottom).

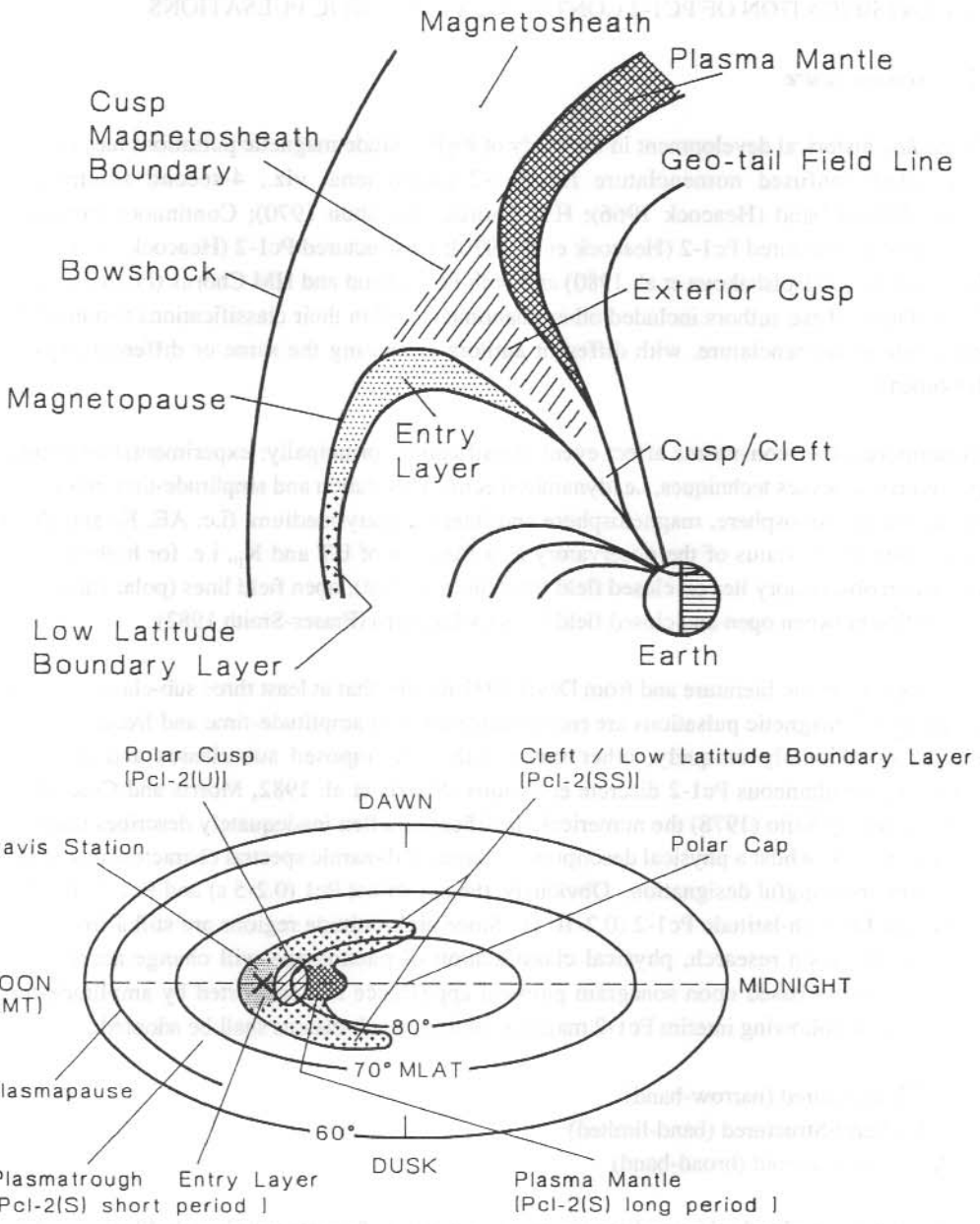


Figure 1. (Top) A schematic cartoon illustrating the high-altitude magnetospheric plasma environs and their perceived mapping down to the polar cusp/cleft topology, and (bottom) subsequent ground projection for the latitude of Davis (at local magnetic noon), where the arrows point to the proposed source regions of the reported sub-classes of Pc1-2 continuous magnetic pulsations .

## 3.2 CLASSIFICATION OF PC1-2 CONTINUOUS MAGNETIC PULSATIONS

### 3.2.1 *Nomenclature*

The *ad hoc* historical development in the study of high-latitude magnetic pulsations has, resulted in a rather confused nomenclature for Pc1-2 phenomena, viz., 4-second summertime micropulsation band (Heacock 1966); HM Chorus (Kokubun 1970); Continuous Emissions (Saito 1969); Structured Pc1-2 (Heacock et al. 1970); Unstructured Pc1-2 (Heacock 1974); Non-structured Pc1-2 (Bolshakova et al. 1980) and both Pc1-2 band and HM Chorus (Fukunishi et al. 1981). Often, these authors included other phenomena within their classifications resulting in a near circle of nomenclature, with different authors discussing the same or different physical phenomena.

Furthermore, other constraints affect event classification, principally: experimental equipment sensitivities; analyses techniques, i.e. dynamic spectrum resolution and amplitude-time resolution; the state of the ionosphere, magnetosphere and interplanetary medium, (i.e. AE, $K_p$ and IMF); and the latitudinal status of the observatory as a function of UT and $K_p$, i.e. for high-latitudes whether an observatory lies on closed field lines (auroral oval), open field lines (polar cap) or lies in transition between open and closed field lines (polar cusp) (Fraser-Smith 1982).

It is evident from the literature and from Davis 1981 results, that at least three sub-classes of high-latitude Pc1-2 magnetic pulsations are recognisable on both amplitude-time and frequency-time records; occasionally uniquely, other times with superimposed sub-classes and generally containing simultaneous Pc1-2 discrete emissions (Morris et al. 1982, Morris and Cole 1985). As discussed by Saito (1978) the numerical classification often inadequately describes magnetic pulsation events, whilst a physical description in terms of dynamic spectral characteristics affords a clear and meaningful designation. Obviously, the numerical Pc1 (0.2-5 s) and Pc2 (5-10 s) are inadequate for high-latitude Pc1-2 (0.2-10 s). Since high-latitude regions are still a frontier for magnetic pulsation research, physical classification of phenomena will change accordingly. Hence, primarily based upon sonagram physical appearance and supported by amplitude-time signatures, the following interim Pc1-2 magnetic pulsation sub-classes shall be adopted:

1. Pc1-2 Structured (narrow-band)
2. Pc1-2 Semi-Structured (band-limited)
3. Pc1-2 Unstructured (broad-band)

Representative amplitude-time and sonagram presentations of events are given in Figures 2, 3 and 4, respectively. The authors believe that the majority of documented high-latitude Pc1-2 phenomena could be incorporated within these sub-classes.

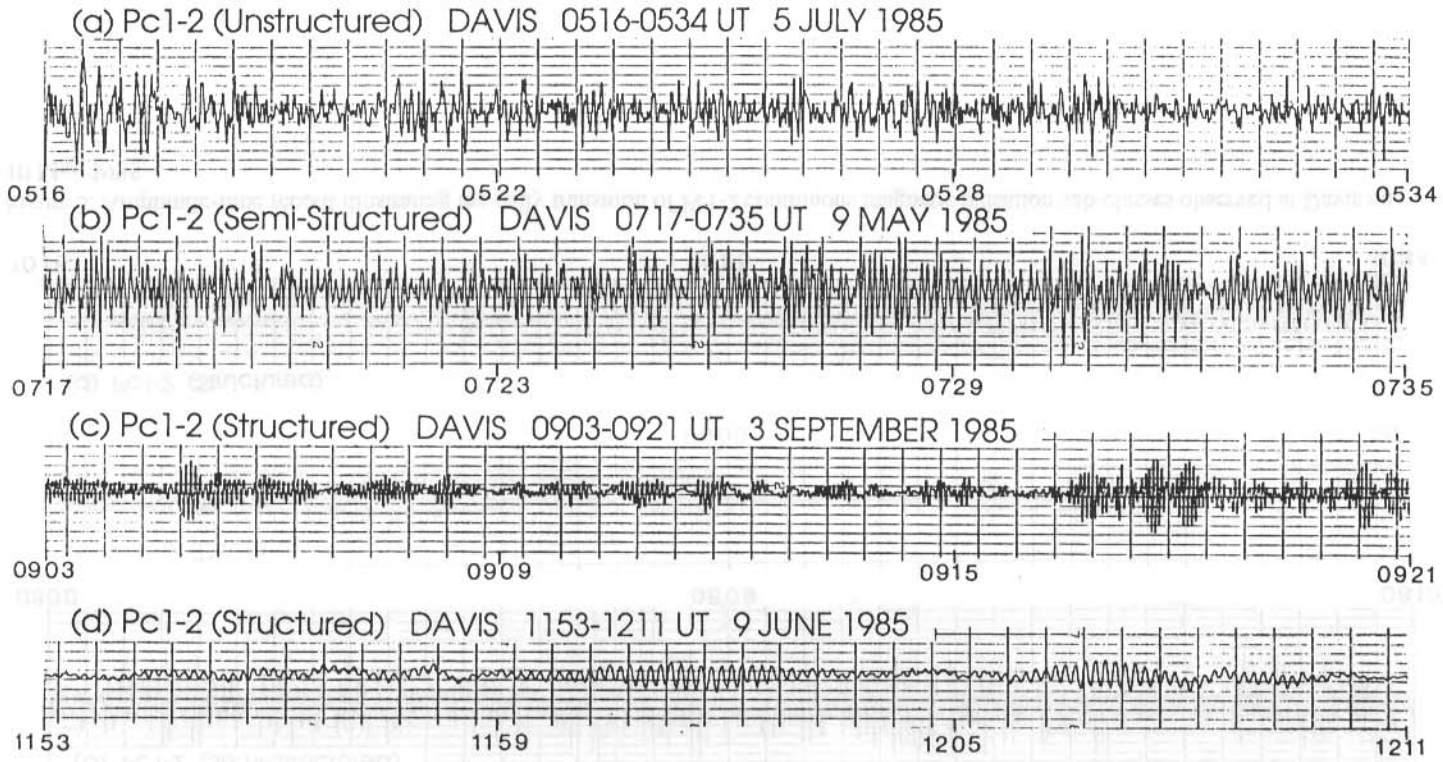


Figure 2. Composite amplitude-time records for Davis 1985 Pc1-2 continuous magnetic pulsations, illustrating three observed regimes: (a) Pc1-2 Unstructured, (b) Pc1-2 Semi-Structured and (c), (d) Pc1-2 Structured.

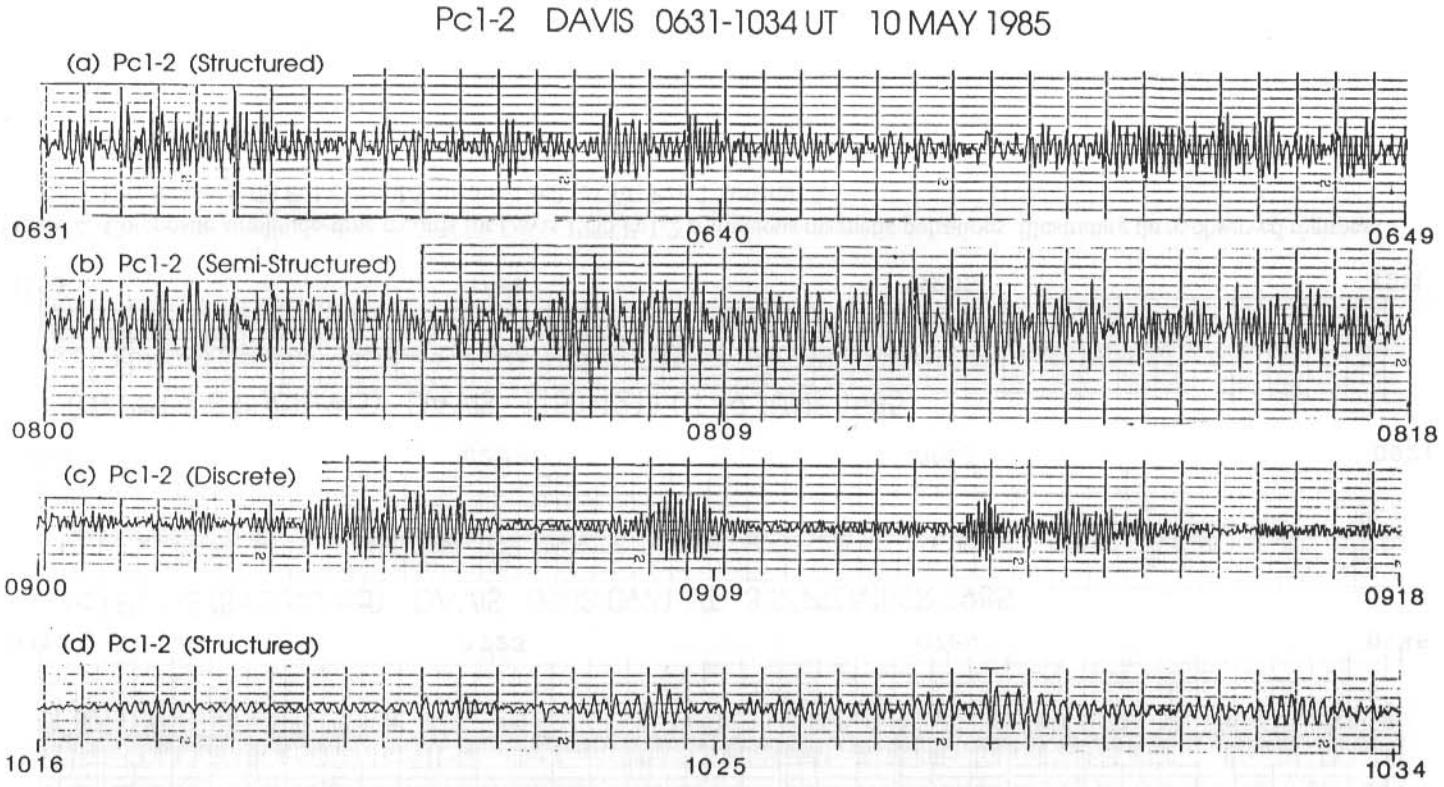


Figure 3. Amplitude-time record illustrating the daily transition of Pc1-2 continuous magnetic pulsation sub-classes observed at Davis on 10 May 1985.

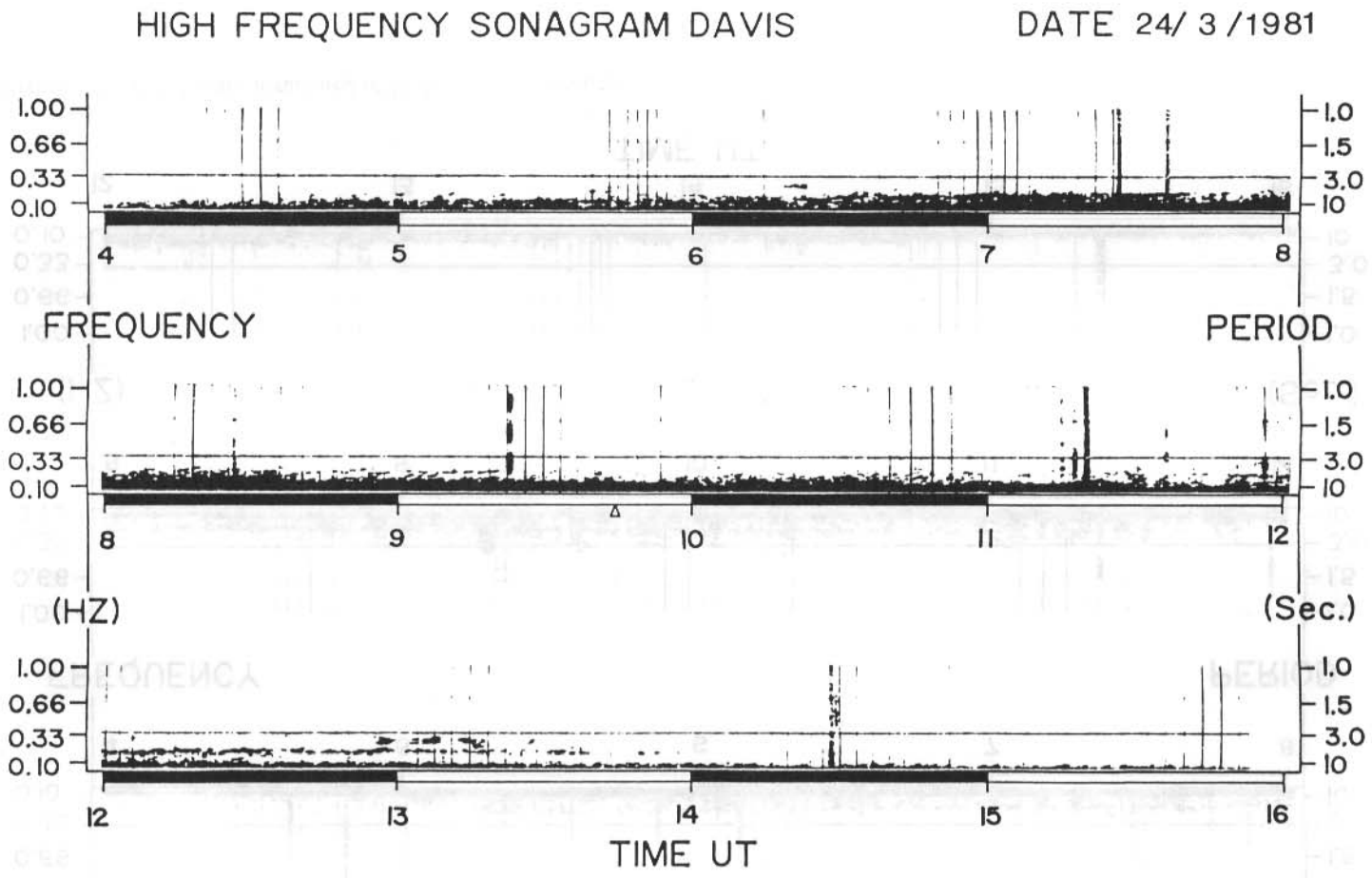


Figure 4. Sonagrams of illustrative Davis Pc1-2 continuous magnetic pulsations: (a) Pc1-2 Structured of 24 March 1981. (continued)

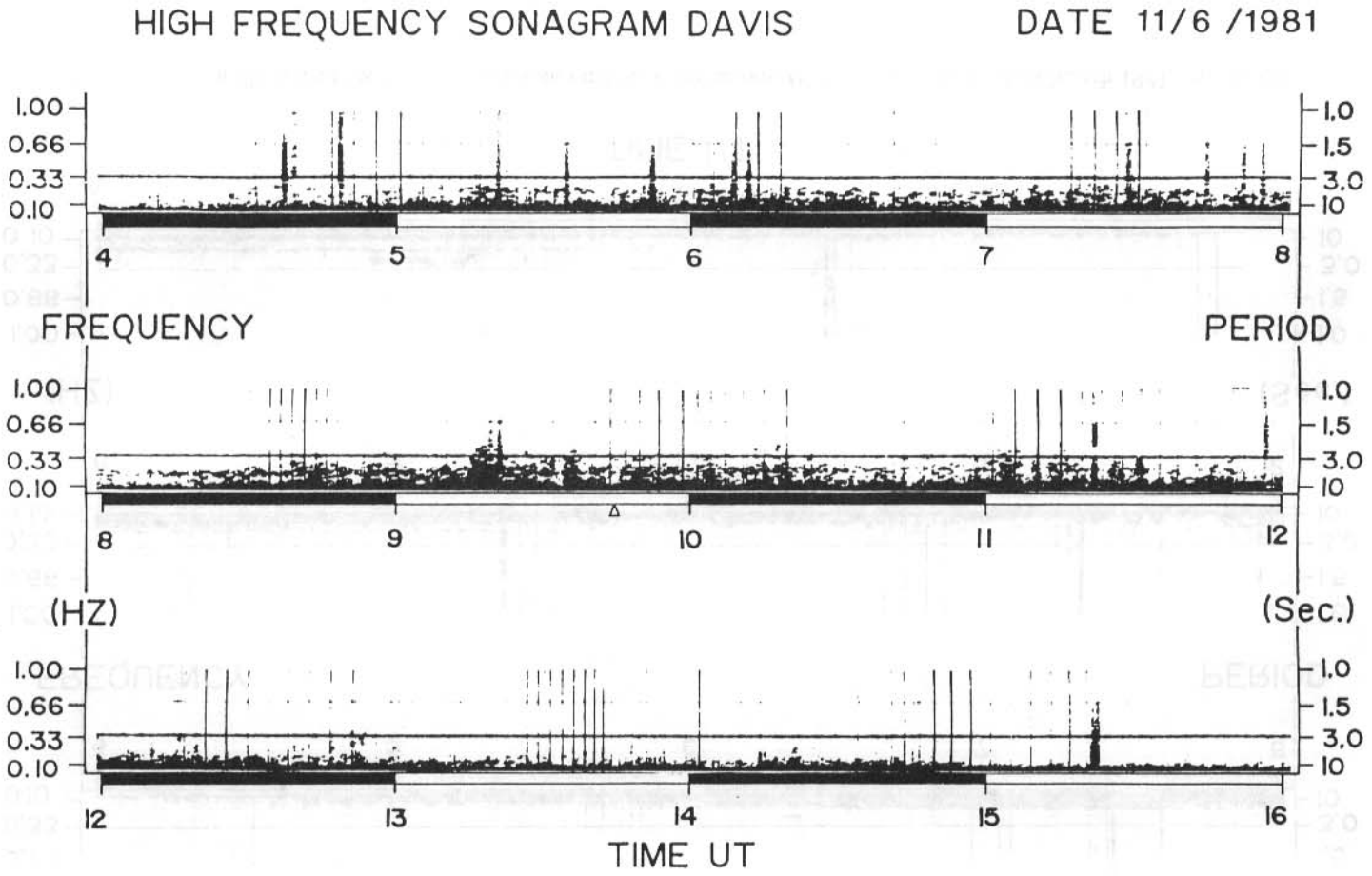


Figure 4(b). Pc1-2 Semi-Structured of 11 June 1981. (continued)

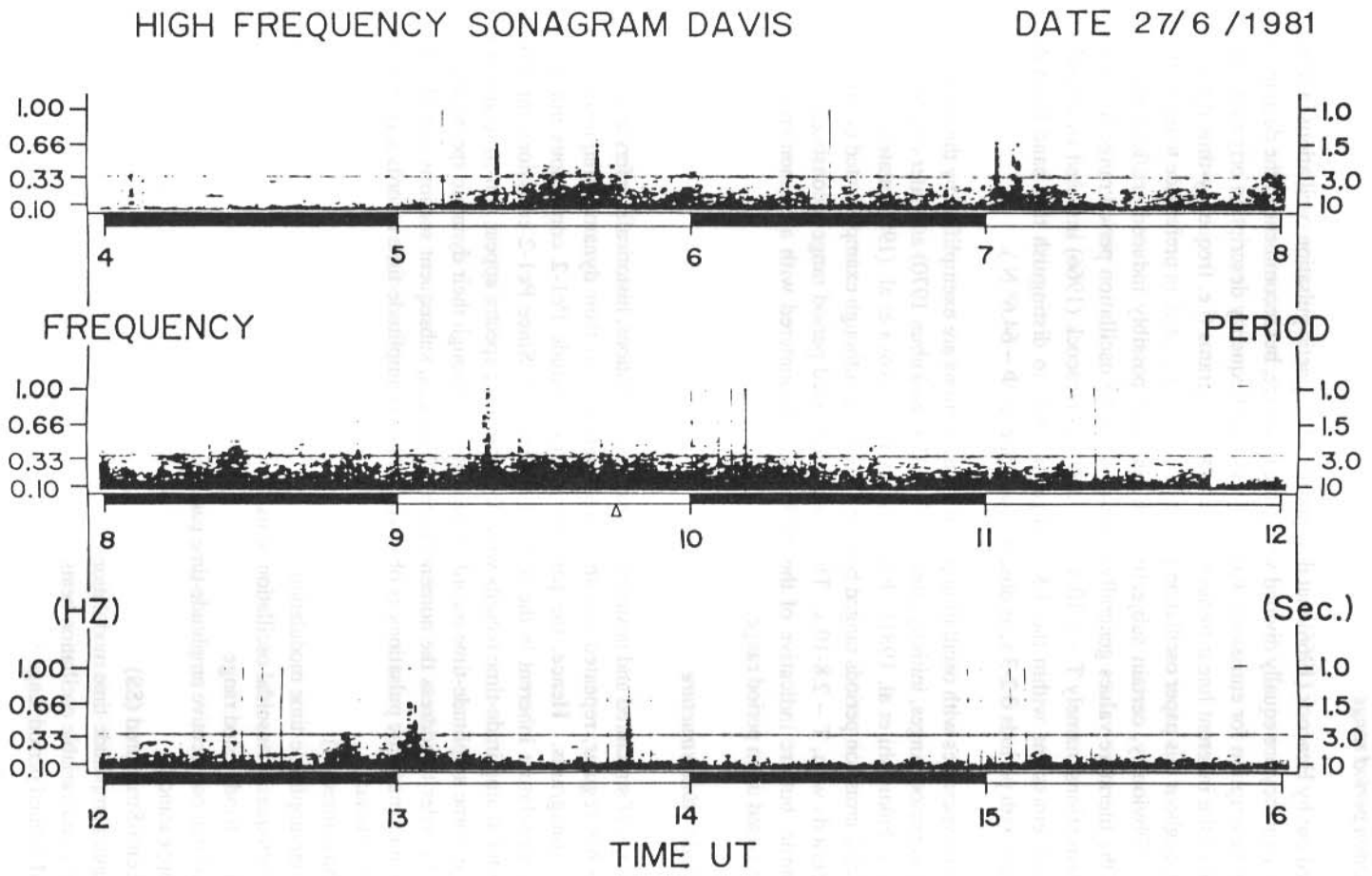


Figure 4(c). Pc1-2 Unstructured of 27 June 1981.

### 3.2.2 *Oscillation period range*

It was pointed out by Heacock (1966) that descriptions of magnetic pulsation oscillations in terms of period or frequency are equally divided within the literature, but recommended the desirability of the period description for emissions with T > 1 s. The frequency description originated as a consequence of the inherent linear frequency scale on sonagrams (i.e. frequency-time dynamic spectra). Throughout this paper oscillation periods are generally cited, in preference to oscillation frequencies. Obviously, certain subjective criteria have possibly induced artificial ranges, nonetheless the literature values generally correspond to the oscillation period range for Davis 1981 Pc1-2 emissions, namely T ~ 2-10 s. For instance, Heacock (1966) imposed an artificial limit on Pc1-2 emissions within the 3-8 s range, in order to distinguish this band from the classical pearls with periods 0.2-3 s, as observed at College ($\Phi \sim 64.6°$ N ).

Additional idiosyncrasies with oscillation period classifications are exemplified by the evolution of HM Chorus period ranges, initially cited as, T ~ 2-5 s (Kokubun 1970) and later extended to, T ~ 1.25-10 s (Fukunishi et al. 1981). Furthermore, Bolshakova et al. (1980) stated that non-structured Pc1-2 emission periods ranged between, T ~ 4-8 s, although examples cited clearly had oscillation periods with, T ~ 2.8-10 s. The above-mentioned period range inconsistencies are purely semantic, but are indicative of the difficulties encountered with a phenomenological classification based upon period range.

### 3.2.3 *Amplitude - time structure*

The terminology of structured and unstructured magnetic pulsations, historically refers to whether an emission has regular, repeated and structured elements on their dynamic frequency-time spectra, i.e. sonagrams. Hence, the paradox in high-latitude Pc1-2 continuous magnetic pulsation nomenclature inherent in the scientific literature! Since Pc1-2 emissions can have smooth structured amplitude-time records while their dynamic spectra appear non-structured and vice versa, i.e. some amplitude-time records appear noisy, although their dynamic spectra appear structured. In order to address the nomenclature difficulties, subsequent sections will classify Pc1-2 continuous magnetic pulsations as observed on Davis amplitude-time records according to the following criteria:

1. Pc1-2 - Structured (S)
   (i) regular amplitude-time modulation
   (ii) smooth quasi-sinusoidal oscillation beats
   (iii) narrow-band period range
   (iv) individual consecutive amplitude-time packets
   (v) Pc appearance
2. Pc1-2 - Semi-Structured (SS)
   (i) irregular amplitude-time modulation
   (ii) messy and variable oscillation beats
   (iii) band-limited period range

(iv) individual amplitude-time packets often overlap
(v) Pc and Pi appearance

3. Pc1-2 - Unstructured (U)
   (i) amplitude-time modulation not apparent
   (ii) noisy to non-existent oscillation beats
   (iii) broad-band period range
   (iv) individual amplitude-time packets indistinguishable
   (v) almost Pi appearance containing impulsive bursts

A composite amplitude-time diagram illustrating the three Pc1-2 continuous magnetic pulsation sub-classes is given in Figure 2, where the interval 0516-0534 UT on 5 July 1985 illustrates Pc1-2(U); the interval 0717-0735 UT on 9 May 1985 illustrates Pc1-2(SS) and the intervals 0903-0921 UT on 3 September 1985 and 1155-1211 UT on 9 June 1985 illustrates Pc1-2(S) emissions observed at Davis. This diagram exemplifies the subjectivity in classification encountered, where the transition from Pc1-2(U) to Pc1-2(SS) is often subtle and the transition from Pc1-2(SS) to Pc1-2(S) is similarly subtle. Furthermore, the two Pc1-2(S) emissions cited are physically different in appearance and contain different characteristic oscillation periods (i.e. T ~ 3.5 s (short period) on 3 September 1985 and T ~ 8.0 s (long period) on 9 June 1985). The possibility of additional sub-classes within the Pc1-2(S) continuous band as classified above must not be overlooked.

Figure 3 illustrates a typical daily transition of Pc1-2 continuous magnetic pulsations observed at Davis on 10 May 1985, where during the interval 0631-0649 UT, Pc1-2(S) emissions occurred, during the interval 0800-0818 UT, Pc1-2(SS) emissions occurred, while during the interval 0900-0918 UT, Pc1-2 discrete emissions were observed and throughout the interval 1016-1034 UT, Pc1-2(S) emissions were observed. This example illustrates the degree of complexity and subjectivity involved in the diurnal classification of Pc1-2 continuous magnetic pulsations observed at the cusp/cleft latitude station, Davis.

3.2.4 *Frequency - time structure*

The continuous dynamic spectrum analysis (CDSA) technique developed at La Trobe University by Menk (1981) was utilised in the analyses of the Davis 1981 magnetic pulsation data set. The CDSA sonagrams have been presented as 35 mm contact prints, where the vertical axes correspond to frequency, 0.1-1.0 Hz (or period 10-1.0 s) and the horizontal axes correspond to universal time (UT). The power spectral density of the sonagram is proportional to the trace intensity. Illustrative Davis 1981 sonagrams are given in Figures 4(a-c), which show three distinctive Pc1-2 continuous magnetic pulsation regimes, viz., Pc1-2(S), Pc1-2(SS) and Pc1-2(U).

Pc1-2(S) magnetic pulsations contain a narrow frequency band with discrete elements of variable gradients, whose elements are semi-continuous in the time domain. The mean emission

frequency is variable from event to event and sometimes during the course of a day. The obvious difference of this class of Pc1-2 continuous magnetic pulsations from the classical Pc1 pearl emission is that the frequency-time elements are not periodic with time. An illustrative sonagram of the Pc1-2(S) regime observed at Davis on 24 March 1981 (0000-1600 UT), is given in Figure 4(a). This event contained three intervals of Pc1-2(S) occurrence (~ 0600-0745 UT; ~ 0830-0920 UT and ~ 1150-1420 UT), where the frequency width, $\Delta f \leq 0.06$ Hz and the emissions central frequency, f ~ 0.14 Hz (T ~ 7 s). Notice that the degree of structure changes during the course of the event, viz., during the interval 0600-0745 UT, the frequency-time elements merge forming a near-continuous band centred at ~ 0.14 Hz (7 s), whereas throughout the intervals 0830-0920 UT and 1150-1420 UT, individual discrete frequency-time elements of variable gradient form a semi-continuous narrow-band in the time domain. For this event Pc1-2 discrete emissions overlap the Pc1-2(S) band between ~ 1230 UT and 1330 UT, which is characteristic for all these Pc1-2 sub-classes.

Pc1-2(SS) magnetic pulsations are comprised of band-limited emissions with sporadic discrete elements, irregularly spaced forming a near-continuous band in the time domain, containing distinct upper and lower frequency boundaries. The emission frequency bandwidth is both variable within a specific event and from event to event. An illustrative sonagram of the Pc1-2(SS) regime observed at Davis on 11 June 1981 (0000-1600 UT) is given in Figure 4(b). The variable band-limited emission is clearly observed between 0500 UT and 1200 UT, with a central emission frequency, f ~ 0.15 Hz (T ~ 6.9 s), containing upper and lower frequency borders of 0.27 Hz (3.7 s) and 0.09 Hz (11.5 s) respectively. The band thickness $\Delta f$, ranged between 0.06 and 0.18 Hz for this particular event.

Pc1-2(U) magnetic pulsations are characterised by a broad-band frequency noise which contains distinctive discrete frequency-time elements, irregularly spaced in the frequency-time domain. This class of emission has a variable upper-frequency boundary and often no definitive lower-frequency boundary is visible, that is, the emission band merges with the background low frequency continuum. An illustrative sonagram for the Pc1-2(U) regime observed at Davis on 27 June 1981 (0000-1600 UT) is given in Figure 4(c). This event clearly depicts the broad-band nature, 0.1-0.4 Hz (10-2.5 s) of the emission and shows how the lower-frequency border merges with the background continuum. Furthermore, Pc1-2 discrete emissions with variable gradients overlap this event. It should be noted that a degree of subjectivity is involved in differentiating between Pc1-2(SS) and Pc1-2(U) emissions and that in such cases, both the amplitude-time and frequency-time records must be examined.

The above three examples have been cited in order to illustrate the three tentative sub-classes of Pc1-2 magnetic pulsations observed at the high-latitude station, Davis. It is apparent that classifications based upon both amplitude-time and frequency-time formats are complimentary. Our analyses also indicate that additional sub-categories of Pc1-2(S) emissions are observed, however this will remain the subject for future investigation.

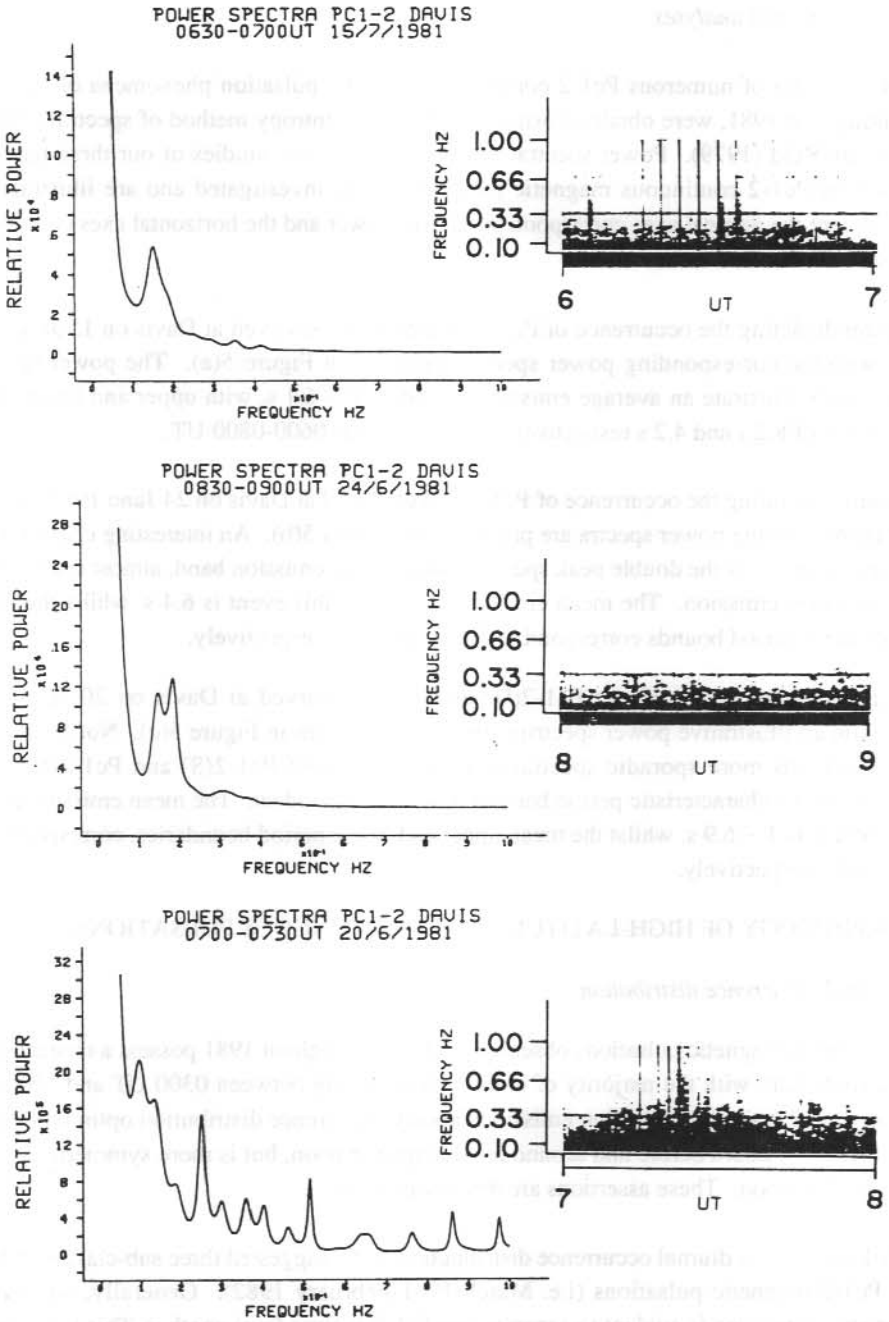


Figure 5. Power spectra and associated sonagrams for Pc1-2 continuous magnetic pulsation subclasses observed at Davis: (a) Pc1-2 Structured of 15 July 1981, (b) Pc1-2 Semi-Structured of 24 June 1981, and (c) Pc1-2 Unstructured of 20 June 1981.

3.2.5 *Power spectral analyses*

The power spectra of numerous Pc1-2 continuous magnetic pulsation phenomena observed at Davis throughout 1981, were obtained using the maximum entropy method of spectral analysis developed by Reid (1979). Power spectra of representative case studies of our three tentative sub-classes of Pc1-2 continuous magnetic pulsations were investigated and are illustrated in Figure 5, where the vertical axes correspond to relative power and the horizontal axes correspond to frequency (Hz).

A sonagram depicting the occurrence of Pc1-2(S) emissions observed at Davis on 15 July 1981 together with the corresponding power spectra are given in Figure 5(a). The power spectral analyses clearly illustrate an average emission period of T ~ 6.1 s, with upper and lower mean period bounds of 8.2 s and 4.2 s respectively, for the interval 0600-0800 UT.

A sonagram illustrating the occurrence of Pc1-2(SS) observed at Davis on 24 June 1981 together with the corresponding power spectra are presented in Figures 5(b). An interesting characteristic of this specific event, is the double peak spectral nature of the emission band, almost suggesting a double resonance emission. The mean emission period for this event is 6.4 s, whilst the upper and lower mean period bounds correspond to 10.1 s and 4.8 s respectively.

Finally, a sonagram exemplifying Pc1-2(U) emissions observed at Davis on 20 June 1981 together with an illustrative power spectrum are similarly given in Figure 5(c). Notice that this spectrum contains more sporadic spectral peaks than those of Pc1-2(S) and Pc1-2(SS) sub-classes, although a characteristic period band of 3.0-15.3 s is evident. The mean emission period for this event was T ~ 6.9 s, whilst the mean upper and lower period boundaries, corresponded to 9.7 s and 4.6 s respectively.

3.3 MORPHOLOGY OF HIGH-LATITUDE PC1-2 CONTINUOUS PULSATIONS

3.3.1 *Diurnal occurrence distribution*

Pc1-2 continuous magnetic pulsations observed at Davis throughout 1981 possess a characteristic diurnal distribution, with the majority of emissions occurring between 0300 UT and 1200 UT. Hence, the Pc1-2 magnetic pulsation emissions hourly occurrence distribution optimises during the daytime, ~ 3-4 hours before and around local magnetic noon, but is more symmetrical about local geographic noon. These assertions are discussed below.

Figure 6 illustrates the diurnal occurrence distribution for the suggested three sub-classes of high-latitude Pc1-2 magnetic pulsations (i.e. March 1981-February 1982). Generally, no obvious characteristic distinction is evident to separate one Pc1-2 regime from another. This is the prime consideration for incorporating the general morphologies of these three Pc1-2 continuous magnetic pulsations in this paper. However, all three Pc1-2 emissions generally occur between 0300 UT and 1200 UT, exhibiting the following (subjective) infrastructure:

1. Unstructured Pc1-2 emission occurrence peaks between 0400 UT and 1000 UT, with a spike at 0700 UT, i.e. generally before local magnetic noon.
2. Semi-structured Pc1-2 emission occurrence peaks between 0500 UT and 1200 UT, with a spike at 0600 UT, i.e. generally before and marginally after local magnetic noon.
3. Structured Pc1-2 emission occurrence peaks between 0300 UT and 1000 UT, with a spike at 0600 UT, i.e. a flat distribution before local magnetic noon.

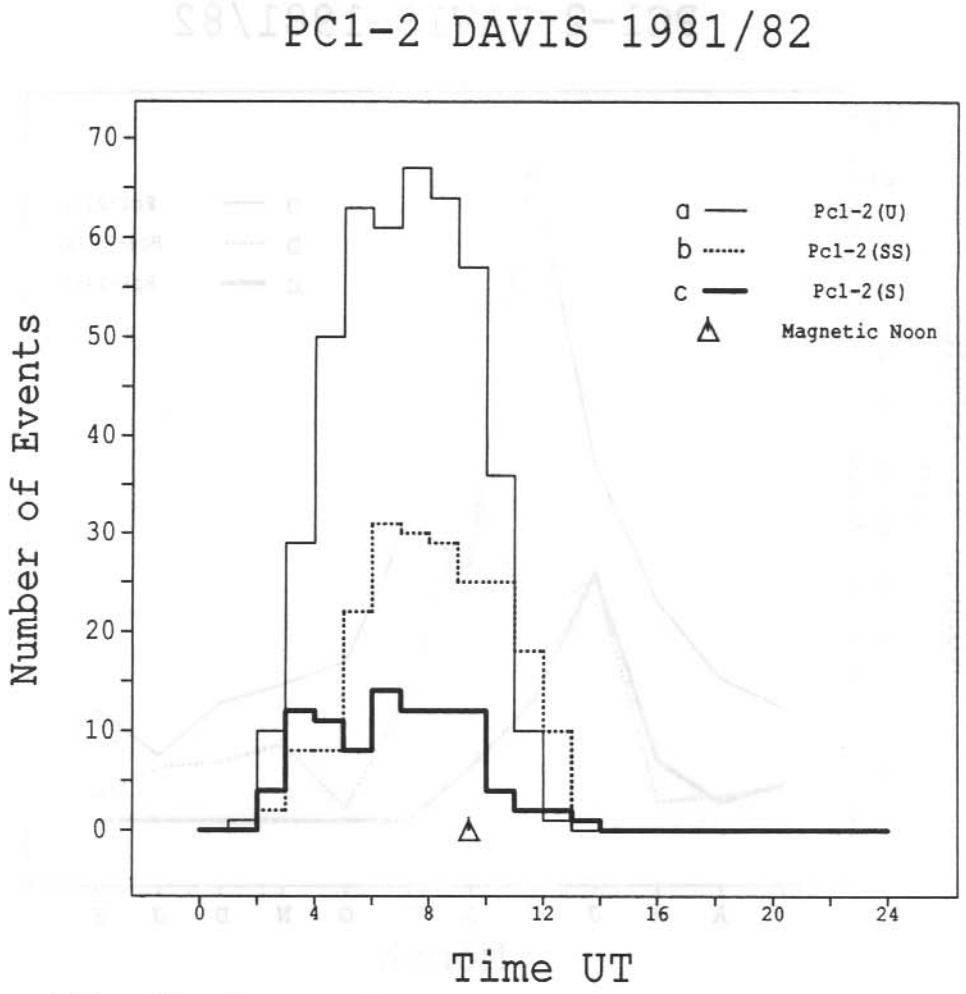


Figure 6. Plots of diurnal occurrence frequency distribution for sub-classes of Pc1-2 continuous magnetic pulsations observed at Davis during 1981/82: (a) Pc1-2 Unstructured, (b) Pc1-2 Semi-Structured, and (c) Pc1-2 Structured.

Furthermore, Figure 6 illustrates the peak hourly occurrence distribution has the ratio 4 : 2 : 1, for Unstructured : Semi-structured : Structured, Pc1-2 magnetic pulsations respectively. The Davis 1981 diurnal occurrence distributions are comparable to those cited in the literature on an invariant latitude criterion. Satellite verification of simultaneous *in situ* and ground based Pc1-2 magnetic pulsation distributions are urgently required, so that ground observations of Pc1-2 emissions can be convincingly used as a diagnostic tool for polar cusp/cleft position location. Furthermore, the infrastructure of the three possible Pc1-2 magnetic pulsations sub-classes should be developed *once* a universal classification scheme has been implemented.

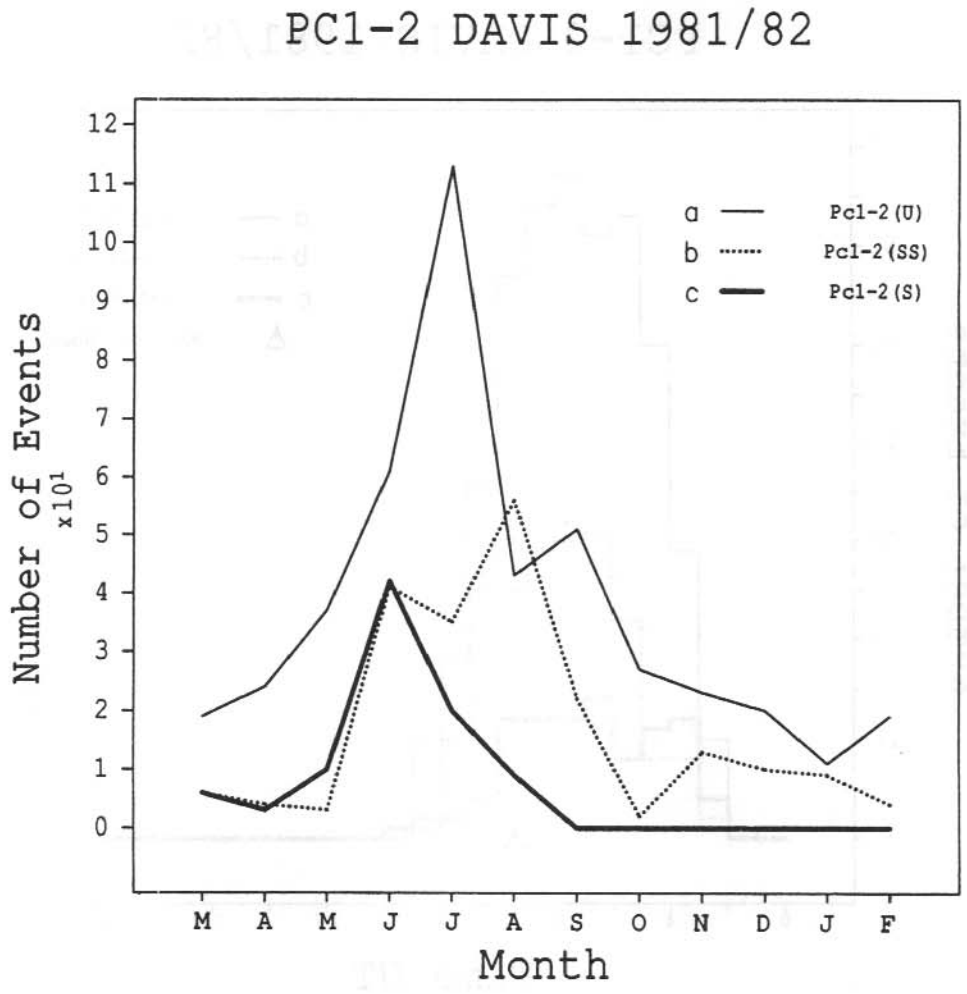


Figure 7. Plots of seasonal occurrence distribution for sub-classes of Pc1-2 continuous magnetic pulsations observed at Davis during 1981/82: (a) Pc1-2 Unstructured, (b) Pc1-2 Semi-Structured, and (c) Pc1-2 Structured.

3.3.2 *Seasonal occurrence distribution*

Figure 7 illustrates the seasonal occurrence distribution for the three proposed sub-classes of high-latitude Pc1-2 magnetic pulsations. Clearly all three sub-classes of Pc1-2 emissions exhibit distinctive winter maximums in their seasonal occurrence distributions. Only marginal differences in the peak occurrence month are evident, viz., Pc1-2 Unstructured/July, Pc1-2 Semi-Structured/August and Pc1-2 Structured/June; however, these discrepancies are not deemed significant, when considering the subjective classification technique employed.

Contrary to these observations, Bolshakova et al. (1980) found from the average results over many years, that Mirny ($\Lambda \sim 77.1°$ S) had a summer maximum in occurrence distribution an order of magnitude greater than in winter. This morphological paradox must be resolved and perhaps indicates an asymmetry in the source region or propagation path for high-latitude Pc1-2 magnetic pulsations.

3.3.3 *Amplitudes*

Amplitudes of Pc1-2 magnetic pulsations observed at Davis 1981 were less than 1.4 nT, but generally less than 0.6 nT, with peak occurrence between 0.05 and 0.25 nT. Figure 8(a) illustrates the histogram of hourly occurrence N, as a function of amplitude (nT), for Davis 1981 Pc1-2 emissions. Davis 1981 amplitude ranges are comparable to those cited in the literature for high-latitude Pc1-2 magnetic pulsations.

The diurnal amplitude variation against UT plotted in Figure 8(b) for June 1981 Davis Pc1-2 emissions, clearly exhibits a daytime amplitude maximum around and before local magnetic noon. A pronounced winter seasonal amplitude maximum was observed, analogous to their seasonal occurrence distribution. For each month the best three illustrative Pc1-2 emissions, as observed on 35 mm high frequency sonagrams (0.1-1 Hz), for $K_p \sim 0$-2, had their amplitude-time records scaled. The mean of these three values was plotted against month of observation, and the results are presented in Figure 8(c). Note, the range of amplitudes varied between 0.16 nT in summer (February) and 0.62 nT in winter (June), with maximal amplitudes occurring between May and September, with a broad minimum in amplitudes occurring between October and April.

There exists a significant seasonal morphological incongruence, between Davis (southern hemisphere) winter maximal amplitudes for Pc1-2 magnetic pulsations and the summer maximum amplitudes for these emission as presented in the literature. The northern hemisphere (summer) and the southern hemisphere (winter) amplitude maximum or coincidence can be explained; however, some difficulties arise interpreting the opposite seasonal observations between the southern hemisphere stations Davis and Mirny.

As previously mentioned the Pc1-2 emission amplitudes increase with increasing magnetic activity as illustrated in Figure 8(d), which represents a scatter plot of amplitude in nT, as a function of the magnetic index $K_p$, for Davis June 1981 Pc1-2 emissions.

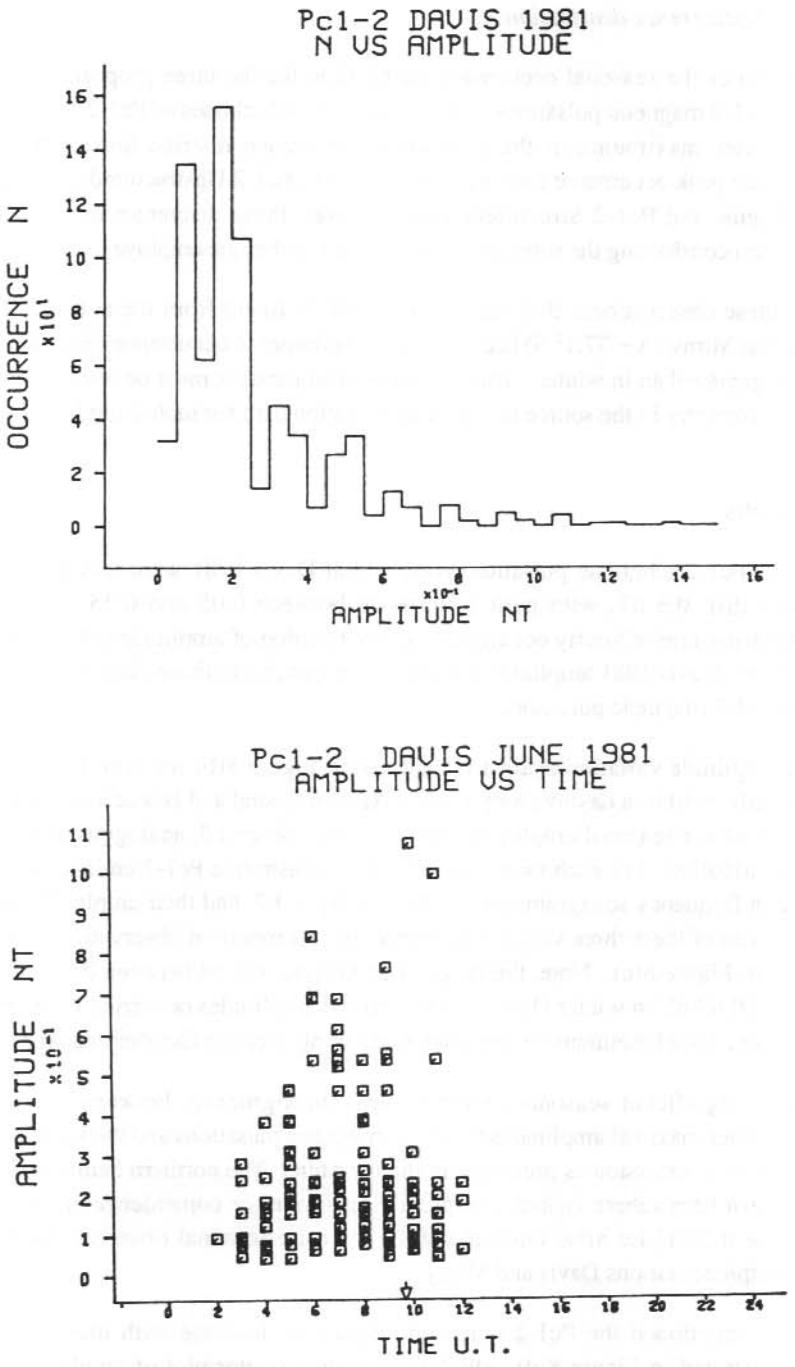


Figure 8. Morphology of Davis 1981 Pc1-2 continuous magnetic pulsations: (a) hourly occurrence vs amplitude, (b) diurnal amplitude variation for June 1981. (continued)

### 3.3.4 *Duration*

No distinction between the three sub-classes of high-latitude Pc1-2 magnetic pulsations has been attempted. The duration interval for Pc1-2 magnetic pulsations observed at Davis throughout 1981 was less than 12 hours ($\tau < 12$ hours) with a pronounced peak between 3 and 8 hours. Furthermore, a summer/winter asymmetry in duration was evident, where for summer (December), $\tau < 5$ hours and for winter (June), $\tau < 10$ hours, with peak durations between, $2 < \tau < 4$ hours and $5 < \tau < 8$ hours, for summer and winter respectively. However, values in the literature generally ranged between $\tau \leq 3$ and $\tau \leq 9$ hours, which are comparable to values of $\tau \leq 12$ hours observed for Davis 1981 high-latitude Pc1-2 magnetic pulsations.

### 3.3.5 *Relationship to magnetic activity ($K_p$)*

Figure 9 illustrates the hourly occurrence N, for Pc1-2 magnetic pulsations as a function of $K_p$, for Davis 1981. It clearly exhibits a predominant occurrence distribution for $K_p < 3$, with a distinctive maximum for $K_p \sim 2^-$. It is evident that functional relationships exist for the occurrence of Pc1-2 magnetic pulsation sub-class and amplitude (nT), with both the source region latitude and the level of magnetic agitation ($K_p$). Previous discussion revealed that Pc1-2 emission amplitudes increase monotonically with increasing magnetic activity ($K_p$).

### 3.3.6 *Polarisation*

The polarisation of numerous Pc1-2 continuous magnetic pulsation emissions observed at Davis throughout 1981 were investigated by replaying the Ḣ and Ḋ magnetic components, recorded on fast frequency modulated tape, through an X-Y recorder. Unfortunately, only Pc1-2 emissions with good quality records (i.e. tapes void of signal drop-out and noise) could be analysed. Hence, some of the excellent Pc1-2 emissions observed on 35 mm sonagrams and amplitude-time charts could not be examined. Furthermore, compounding the degree of difficulty of Pc1-2 emission polarisation analyses, it was observed that unstructured and semi-structured Pc1-2 regimes produce extremely noisy ellipsoids, which are impossible to classify as either right-handed (R) or as left-handed (L).

However, in all, some 16 days of Pc1-2 magnetic pulsation emissions had their polarisation sense investigated. Of these; 6 days contained pure L-waves, 8 days contained persistent L-waves with occasional bursts of R-waves (i.e. transitional emissions), and finally 2 days contained persistent R-waves. It is thought that the dominant L-wave characteristic of high-latitude Pc1-2 emissions are a manifestation of Alfvén waves. Thus, the transitional L-wave to R-wave and the persistent R-waves are a response to transient magnetospheric parameters along the wave propagation path or alternately, due to ionospheric irregularities producing, discrete and quasi-permanent reversals in the polarisation sense of these Pc1-2 emissions. Obviously more research into the polarisation of high-latitude Pc1-2 magnetic pulsation emissions in both latitude and longitude and especially between the ground and the source region, i.e. *in situ* satellite observations, are urgently required.

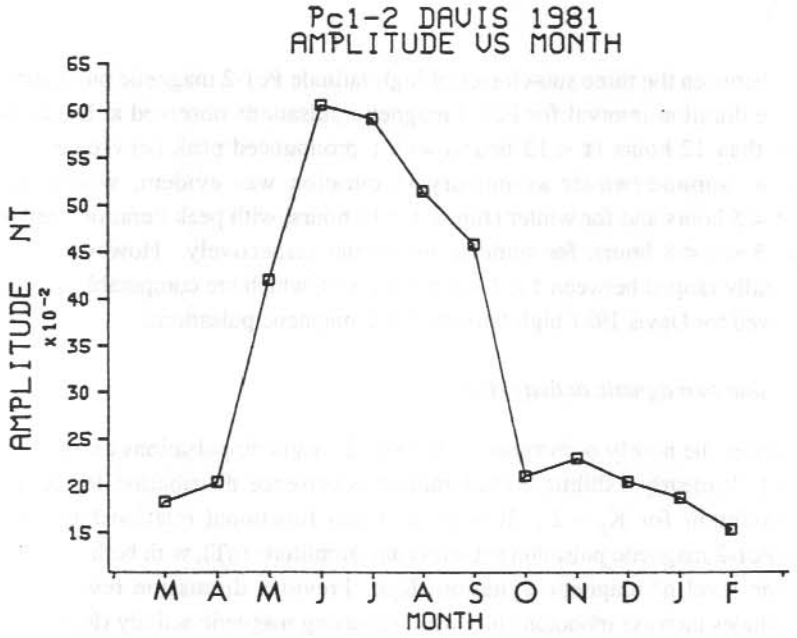


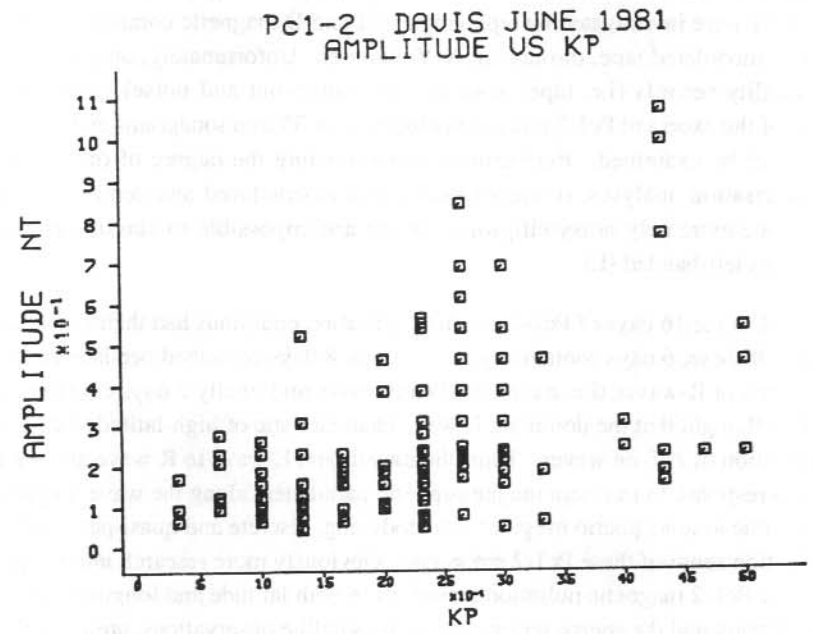


Figure 8(c). Amplitude vs month, and (d) amplitude vs $K_p$ for June 1981.

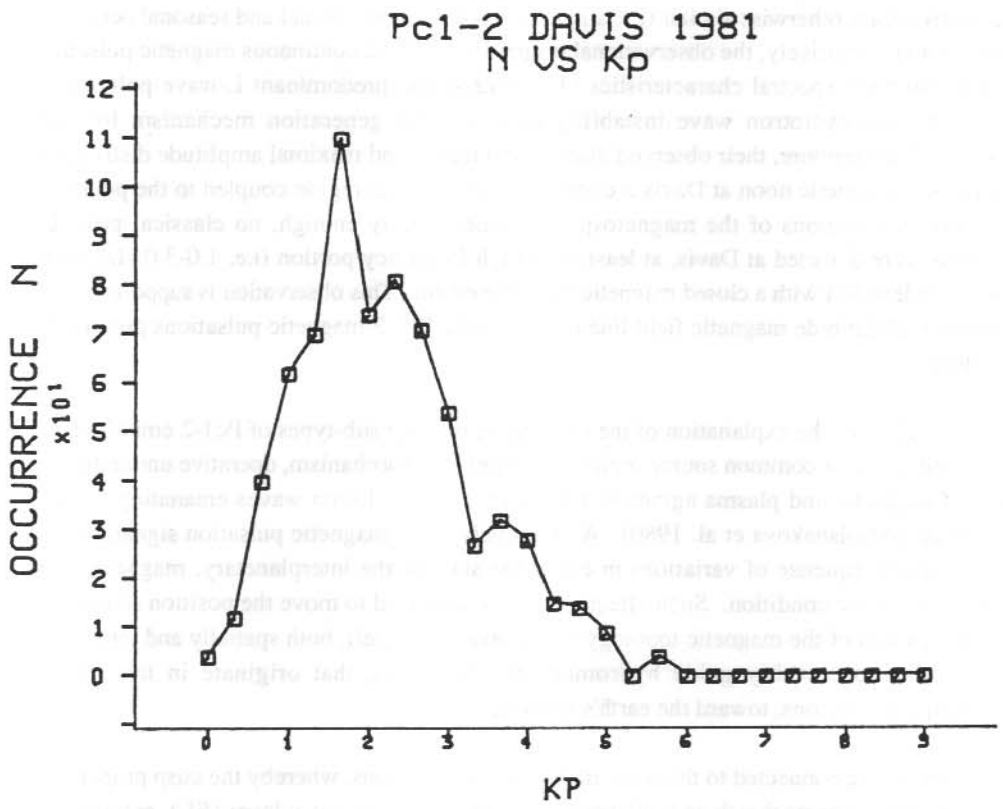


Figure 9. Plot of number vs $K_p$ for Davis 1981 Pc1-2 continuous magnetic pulsations.

## 3.4 DISCUSSION

The new morphological characteristics of high-latitude Pc1-2 continuous magnetic pulsations presented generally compliment and extend those cited in the literature, except for the seasonal asymmetry in their occurrence distribution for the two southern hemisphere sites, Davis (winter) and Mirny (summer). This apparent paradox could be related to a solar cycle effect on the position of the projection of the polar cusp/cleft for the different observation intervals or may indicate a longitudinal asymmetry in the latitude of the proposed source region, the polar cusp/cleft! Alternatively, this paradox may be related to the observation of Meng (1989) who reported an approximate ~ 1° poleward displacement of the summer position of the dayside noon transition region for quiet magnetic conditions, relative to the winter position.

It was further demonstrated that at least three sub-types are evident, i.e. Pc1-2 (Structured), Pc1-2 (Semi-Structured) and Pc1-2 (Unstructured), which exhibit different spectral characteristics (i.e. amplitude-time, frequency-time and power spectra). However, their morphological

characteristics are otherwise similar (i.e. amplitude, polarisation, diurnal and seasonal occurrence distributions). Intuitively, the observational properties of Pc1-2 continuous magnetic pulsations, in particular their spectral characteristics (T ~ 2-12 s) and predominant L-wave polarisation, suggest the ion cyclotron wave instability as a possible generation mechanism for these emissions. Furthermore, their observed diurnal occurrence and maximal amplitude distributions around local magnetic noon at Davis are indicative of a source region coupled to the polar cusp and polar cleft regions of the magnetosphere. Interestingly enough, no classical pearl Pc1 emissions were detected at Davis, at least their high frequency portion (i.e. 1.0-3.0 Hz), which have been identified with a closed magnetic field line origin. This observation is supportive of the proposed high-latitude magnetic field line origin for the Pc1-2 magnetic pulsations presented in this study.

One possibility for the explanation of the occurrence of three sub-types of Pc1-2 emissions may be reconciled with a common source region and generation mechanism, operative under different levels of magnetic and plasma agitation, for instance ion cyclotron waves emanating from the exterior cusp (Bolshakova et al. 1980). Alternatively, such magnetic pulsation signatures may result as a consequence of variations in either the state of the interplanetary, magnetospheric and/or ionospheric condition. Such effects would be expected to move the position of the focus of the projection of the magnetic topology of the polar cusp/cleft, both spatially and temporally, which could conceivably guide hydromagnetic emissions, that originate in the adjacent magnetospheric regions, toward the earth's surface.

These regions are connected to the outer magnetopause environs, whereby the cusp proper maps directly to the magnetosheath and adjacent layers including the entry layer (EL), exterior cusp (EC) and plasma mantle (PM), and the polar cleft maps into the low latitude boundary layer (LLBL), as illustrated in Figure 1 (top). It is within high L-value open magnetic field and plasma environs, that the authors suggest, provide the source region for the reported Pc1-2 magnetic pulsation emissions, where the plasma parameters, i.e. hot anisotropic and cold plasmas are of sufficient energy, and moreover the appropriate magnetic field **B** strengths prevail, to enable ion cyclotron wave generation of emissions with periods of T ~ 2-12 s (Cole et al. 1982, Kaye and Kivelson 1979, Inhester et al. 1984).

Perhaps the following conjecture for source regions of the three sub-types of Pc1-2 continuous magnetic pulsation emissions applies, in relation to the proposed magnetic cusp movements, viz., Pc1-2(S) either originate under or are ducted from the plasmapause (short period) or within the polar cap (long period); Pc1-2(SS) either originate under or are ducted from the polar cleft region; and Pc1-2(U) either originate under or are ducted from the polar cusp region of the magnetosphere, as schematically depicted in Figure 1 (bottom). In any case the necessary plasma parameters as detected on satellites (Crooker et al. 1977) and as theoretically modelled (Fairfield 1968) prevail for the development of ion cyclotron waves, in these high L-value magnetospheric regions.

Although a theoretical explanation of Pc1-2 magnetic pulsation emissions as reported in this paper is discussed in terms of ion cyclotron wave instabilities, several alternate source regions and generation mechanisms are also feasible:

1. ULF waves originating upstream of the bow shock region could permeate the magnetopause and subsequently propagate down the polar cusp and polar cleft.
2. ULF waves originating in the distant geo-tail region of the magnetosphere could conceivably propagate to the polar cap region.
3. A local ionospheric source, particularly for the Pc1-2(U) sub-class, whereby particles of magnetosheath origin precipitate down the polar cusp/cleft region and the associated FAC structures provide the appropriate momentum and energy, to redistribute the ionospheric Hall and Pedersen conductivities (i.e. $\Sigma_H$ and $\Sigma_P$) and the ensuing Hall and Pedersen current flows, which subsequently manifest as magnetic pulsation signatures below the ionosphere (Burns and Cole 1985).

All these possibilities deserve further examination. In any case, the question as to whether the three sub-classes of Pc1-2 emissions have a common source region, i.e. microscopic variations of a common macroscopic source region and mechanism, or are separate phenomena generated by independent mechanisms operative at different source regions, must await future simultaneous ground-array and *in situ* satellite investigation (Fraser and Morris 1987).

## 3.5 ACKNOWLEDGMENTS

The assistance of Antarctic Division staff and fellow members of the Davis 1981 and 1985 ANARE is gratefully acknowledged. The work of K.D. Cole was supported by a grant from the Australian Research Grants Committee.

## 3.6 REFERENCES

Burns, G.B. *and* Cole, K.D. (1985). Ionospheric sources of Pi(c) pulsations. *Journal of Atmospheric and Terrestrial Physics 47*:587-599.

Bolshakova, O.V., Troitskaya, V.A. *and* Ivanov, K.G. (1980). High-latitude Pc1-2 geomagnetic pulsations and their connection with location of the dayside polar cusp. *Planetary and Space Science 28*:1-7.

Cole, K.D., Morris, R.J., Matveeva, E.T., Troitskaya, V.A. *and* Pokhotelov, O.A. (1982). The relationship of the boundary layer of the magnetosphere to IPRP events. *Planetary and Space Science 30*:129-136.

Crooker, N.U. (1977). Explorer 33 entry layer observations. *Journal of Geophysical Research 82*:515-522.

Fairfield, D.H. (1968). Average magnetic field configuration of the outer magnetosphere. *Journal of Geophysical Research 73*:7329-7338.

Fraser-Smith, A.C. (1982). ULF/lower-ELF electromagnetic field measurements in the polar caps. *Reviews of Geophysics and Space Physics 20*:497-512.

Fraser, B.J. *and* Morris, R.J. (1987). Australia's magnetospheric research in Antarctica. In: Burns, G.B. *and* Craven, M. (Eds). *ANARE Research Notes Number 48*:236-245.

Fukunishi, H., Toya, T., Koike, K., Kuwashima, M. *and* Kawamura, M. (1981). Classification of hydromagnetic emissions based on frequency-time spectra. *Journal of Geophysical Research 86*:9029-9039.

Gul'elmi, A.V. *and* Dovbnya, B.V. (1974). Hydromagnetic emissions of the interplanetary plasma. *Astrophysics and Space Science 31*:21-29.

Heacock, R.R. (1966). The 4-second summertime micropulsation band at College. *Journal of Geophysical Research 71*:2763-2775.

Heacock, R.R. (1974). Midday Pc1-2 pulsations observed at a subcleft location. *Journal of Geophysical Research 79*:4239-4245.

Heacock, R.R., Hessler, V.P. *and* Olesen, J.K. (1970). The 2-0.1 Hz polar cap micropulsation activity. *Journal of Atmospheric and Terrestrial Physics 32*:129-138.

Inhester, B., Wedeken, U., Korth, A., Perraut, S. *and* Stockholm, M. (1984). Ground satellite coordinated study of the April 5, 1979 events: observation of cyclotron waves. *Journal of Geophysics 55*:134-141.

Kaye, S.M. *and* Kivelson, M.G. (1979). Observations of Pc1-2 waves in the outer magnetosphere. *Journal of Geophysical Research 84*:4267-4276.

Kokubun, S. (1970). Fine structure of ULF emissions in the frequency range of 0.1~2Hz. *Report on Ionospheric Space Research 24*:24-44. Japan.

Matveeva, E.T., Troitskaya, V.A. *and* Feygin, F.Z. (1976). Intervals of pulsations with rising periods (IPRP) in polar caps. *Planetary and Space Science 24*:673-678.

Matveeva, E.T., Troitskaya, V.A. *and* Feygin, F.Z. (1978). Isolated bursts of type Pc1b geomagnetic pulsations at high latitudes. *Geomagnetism and Aeronomy 18*:75-78. (English Edition)

Meng, C.-I. (1982). Latitudinal variation of the polar cusp during a geomagnetic storm. *Geophysics Research Letters 9*:60-63.

Meng, C.-I. (1984). Dynamic variation of the auroral oval during intense magnetic storms. *Journal of Geophysical Research 89*:227-235.

Meng, C.-I. (1989). Auroral oval configuration during the quiet condition. In: P.E. Sandholt and A. Egeland (Eds.) *Electromagnetic Coupling in the Polar Clefts and Caps* Pp. 61-86.

Menk, F.W. (1981). *Mid-latitude geomagnetic pulsation phenomena at solar maximum.* PhD thesis, La Trobe University.

Morris, R.J. *and* Cole, K.D. (1985). Pc1-2 discrete regular daytime pulsation bursts at high latitudes. *Planetary and Space Science 33*:53-67.

Morris, R.J. *and* Cole, K.D. (1987). "Serpentine emission" at the high latitude Antarctic station, Davis. *Planetary and Space Science 35*:313-328.

Morris, R.J., Cole, K.D., Matveeva, E.T. *and* Troitskaya, V.A. (1982). Hydromagnetic "whistles" at the dayside cusps: IPRP events. *Planetary and Space Science 30*:113-127.

Newell, P.T. *and* Meng, C.-I. (1988). The cusp and the cleft/boundary layer: low-altitude identification and statistical local time variation. *Journal of Geophysical Research 93*:14549-14556.

Reid, J.S. (1979). Confidence limits and maximum entropy spectra. *Journal of Geophysical Research 84*:5289-5301.

Saito, T. (1969). Geomagnetic pulsations. *Space Science Reviews 10*:319-412.

Saito, T. (1978). Long-period irregular magnetic pulsations, Pi3. *Space Science Reviews 21*:427-467.

Winningham, J.D. (1972). Characteristics of magnetosheath plasma observed at low altitudes in the dayside magnetospheric cusps. In: D. McCormac (Ed.) *Earth's Magnetospheric Processes*. Pp. 68-80.

Winningham, J.D. *and* Heelis, R.A. (1983). The low altitude cleft: plasma entry and magnetospheric topology. In: B. Hultqvist and T. Hagfors (Eds.) *High-Latitude Space Plasma Physics* Nobel Foundation Symposium. Pp. 57-72.

# 4. AMPLIFICATION OF Pc1-2 WAVES ALONG A GEOMAGNETIC FIELD LINE

Y.D. Hu[1], B.J. Fraser[1] and J.V. Olson[2]

[1]Physics Department
University of Newcastle
Newcastle NSW 2308
Australia

[2]Geophysical Institute
University of Alaska
Fairbanks AL 99775
USA

ABSTRACT

The amplification of electromagnetic ion-cyclotron waves are considered along a geomagnetic field line in the earth's multicomponent magnetosphere, assuming that the waves propagate parallel to the background magnetic field. The energetic ring-current protons (energy~10-100 keV) can resonate with the waves not only in the equatorial region, but also off the equator. The wave instability stimulated by these protons may occur in separated regions on and/or off the equator. The positions of the wave source regions along the field line depend on the concentration of cold heavy ion species. The off-equator wave sources significantly affect generation/amplification and propagation of Pc1-2 waves in the magnetosphere. The off-equator wave source provides an important contribution to the Pc1-2 wave spectrum observed at the foot of the field line on the ground or in the high latitude magnetospheric region by elliptically orbiting spacecraft.

## 4.1 INTRODUCTION

Pc1-2 geomagnetic pulsations recorded on the ground are electromagnetic ion-cyclotron waves generated in the magnetosphere. These waves propagate along a geomagnetic field line away from the wave source region. One of the most important considerations in the generation/amplification and propagation of electromagnetic ion-cyclotron waves in the magnetosphere is the locations of the wave source regions along wave paths. In previous theoretical studies on electromagnetic ion-cyclotron waves in the magnetosphere, the source region was normally assumed to be on or very close to the geomagnetic equator (Cornwall 1965). This assumption is reasonable for a plasma with only one ion species. The amplification is caused by a resonant interaction, in which the parallel velocity of the interacting ions $V_R$ satisfies $F-kV_R/2\pi-F_c=0$, where $F_c$ is the gyrofrequency of the interacting ion, and k and F are wave number and frequency respectively. In the magnetosphere, the ions which provide the free energy to stimulate the waves are the energetic and anisotropic protons in the ring current (energy~10-100 keV, $T_\perp/T_\parallel \sim 2$). In a proton-electron plasma, the parallel resonant energy of the interacting proton is

$$E = 0.5V_R^2 m_{H^+} = 0.5(1-F_c/F)^2 V_a^2 (1-F/F_c) m_{H^+} \quad (1)$$

where the Alfven velocity is $V_a = B_o/(4\pi n_e m_{H^+})^{1/2}$, $B_o$ is a background magnetic field, and $n_e$ is the electron number density. In the magnetosphere, the density of background electrons increases rapidly with geomagnetic latitude, $\lambda$, along a field line. E, therefore, has a minimum value on the geomagnetic equator and then increases rapidly with latitude along the field line. This implies that in the equatorial region more ions may interact with the waves, because the number density of the interacting ions becomes small when their kinetic energy becomes high. Through calculations using magnetospheric parameters and a dipole geomagnetic model, it can be shown that when F~1Hz (~$F_c$) and E~10-100 keV, the interacting region occurs only at or close to the equator. Calculations on the growth rate for the instability also show that the peak of the instability is at the equator, and the growth rate decreases rapidly with increasing latitude (Liemohn 1967).

Observations have shown that heavy ions, such as $He^+$ and $O^+$, are important constituents of the magnetospheric plasma near the plasmapause and at geostationary orbit. The ratios $n_{He^+}/n$, and $n_{O^+}/n_e$ are typically of order of 0.1 (Geiss et al. 1978). The presence of heavy ion species modifies the propagation of ion-cyclotron waves (Smith and Brice 1964). By using observations on GEOS-1, -2 and ATS-6, many authors (Young et al. 1981, Fraser and McPherron 1982, Roux et al. 1982) have studied the effects of heavy ion species in the magnetospheric plasma on the propagation and generation of ion-cyclotron waves. In these studies, it was assumed that the source region of the ion-cyclotron instability was located only at or close to the equator. Based on this assumption, a model was suggested to explain the ion-cyclotron waves in the magnetosphere (Young et al. 1981, Roux et al. 1982, Rauch and Roux 1982). Also, influenced by this assumption, the studies of the ion-cyclotron instability have been focused only on one location in the magnetosphere: the equator (Gomberoff and Neira 1983, Kozyra et al. 1984). However, an equatorial source may not explain all the properties of the waves in the magnetosphere. The instability will be shown that it may also peak in regions off the equator, leading to several separated source regions along the wave path. The locations of these source regions and the growth rates in these regions will depend on the concentrations of the heavy ion species. The equatorial region is still important for wave amplification, but the off-equator source regions must also be considered.

## 4.2 RESONANT ENERGY

Let us consider the parallel resonant energy of the interacting ring-current protons in the presence of $He^+$ and $O^+$ ions. This will introduce the possibility that the interaction takes place off the equator. For electromagnetic left-hand ion-cyclotron waves propagating along the background magnetic field, the local dispersion relation is

$$V_p^2 \equiv (2\pi F/k)^2 = c^2 \left( 1 + \sum_i \frac{\eta_i c^2}{V_a^2 \left( \frac{1}{M_i} - \frac{F}{F_c(H^+)} \right)} \right)^{-1} \quad (2)$$

where $\eta_i=n_i/n_e$, $M_i=m_i/m_{H^+}$, i=$H^+$, $He^+$ and $O^+$ ion species and c is the velocity of light. It is well known that the presence of $He^+$ and $O^+$ ions leads to two stop bands in F-k space. If the authors consider the waves with F~$F_c$(i), the stop bands in which the left-hand waves cannot exist, and the pass bands in which the waves may appear, are illustrated as follows:

$O<F<F_c(O^+)$: pass band, the $O^+$ wave branch,
$F_c(O^+)\le F\le F_{cf}(O^+)$: stop band,
$F_{cf}(O^+)<F<F_c(He^+)$: pass band, the $He^+$ wave branch,
$F_c(He^+)\le F\le F_{cf}(He^+)$: stop band,
$F_{cf}(He^+)<F<F_c(H^+)$: pass band, the $H^+$ wave branch,
$F\ge F_c(H^+)$: stop band.

Two cut-off frequencies, $F_{cf}(O^+)$ and $F_{cf}(He^+)$, are the real solutions of the equation $\sum_i c^2\eta_i^2[V_a^2(1/M_i-F/F_c(H^+))]^{-1}=-1$ (i.e. $Vp\to\infty$). All characteristic frequencies increase with increasing $\lambda$ because of the increase of $B_o$. The stop and pass bands also vary along the field line.

Here the authors consider a dipole magnetic field line at geostationary orbit (L~6.6) with the densities of cold ions assumed to be $n_i(\lambda)/n_i(0)\sim B_o(\lambda)/B_o(0)$, and use typical equatorial parameters for a cold magnetospheric plasma: $n_{H^+}=7\ cm^{-3}$, $n_{He^+}=2cm^{-3}$, and $n_{O^+}=1cm^{-3}$. The resulting characteristic frequencies vary along the field line as shown in Figure 1.

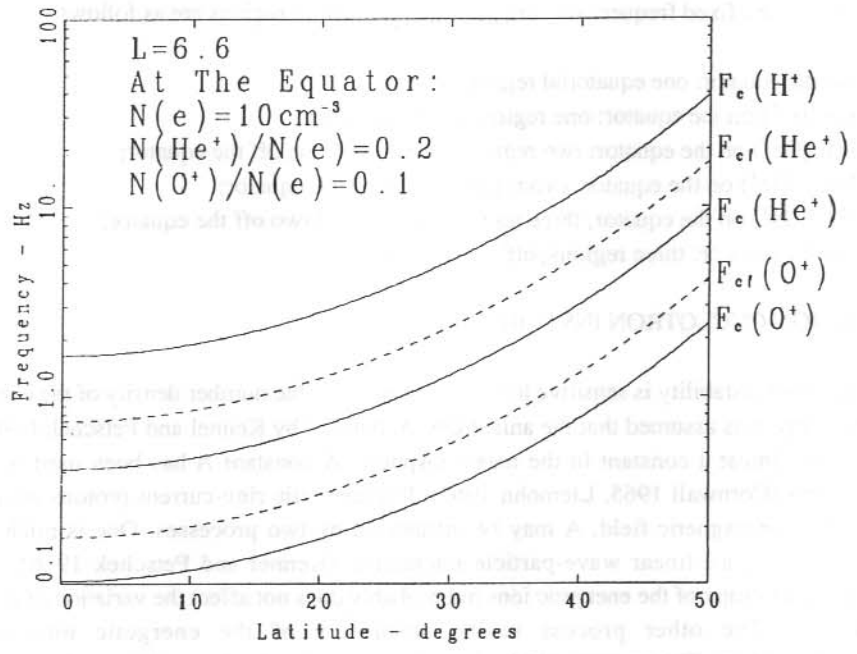


Figure 1. The variations of cut-off frequencies $F_{cf}$ and gyrofrequencies $F_c$ along a dipole geomagnetic field line at L=6.6.

From (2), the proton parallel resonant energy E is obtained as

$$E = 0.5c^2(1-F_c(H^+)/F)^2\left[\ 1 + (c^2/V_a^2)\ \sum_i \eta_i/(1/M_i - F/F_c\ (H^+))\right]^{-1} m_{H^+} \qquad (3)$$

Figure 2 illustrates the variation of E with latitude along the L=6.6 field line for various frequencies. It can be seen that E always increases with latitude for all wave frequencies, but the interaction regions may be located at different latitudes. In Figure 2(a), if $F<F_c(O^+)$ on the equator (F=0.02, 0.07, 0.103 Hz cases), then 10-100 keV ring-current protons resonate with the $O^+$ wave branch in the equatorial region. If $F>F_c(O^+)$ on the equator (F=0.11-2.0 Hz cases), the resonance takes place away from the equatorial region. Note that the waves with frequencies in the stop bands on the equator (F=0.11, 0.14, 0.5, and 2.0 Hz cases) will interact with ring-current protons off the equator. Figure 2(b) shows the interaction with the $He^+$ wave branch. When $F_{cf}(O^+)<F<F_c(He^+)$ on the equator (F=0.18-0.4 Hz cases), the interaction occurs in the equatorial region; when $F>F_c(He^+)$ on the equator (F=0.5-2.0 Hz cases), the energetic protons resonate with the $He^+$ wave branch off the equator. This is similar to the $O^+$ wave branch case. For the interaction with the $H^+$ wave branch, Figure 2(c) makes it clear that, when $F_{cf}(He^+)<F<F_c(H^-)$ on the equator (F=0.75-1.5 Hz cases), the interaction between the energetic protons and the $H^+$ wave branch is possible only in the equatorial region. When $F>F_c(H^+)$ (F=2-3 Hz cases) on the equator, the interaction may appear off the equator.

In summary, for any fixed frequency F, the potential interaction regions are as follows:

$F<F_c(O^+)$ on the equator: one equatorial region;
$F_c(O^+)\le F<F_{cf}(O^+)$ on the equator: one region, off the equator;
$F_{cf}(O^+)\le F<F_c(He^+)$ on the equator: two regions, one on and one off the equator;
$F_c(He^+)\le F<F_{cf}(He^+)$ on the equator: two regions, both off the equator;
$F_{cf}(He^+)\le F<F_c(H^+)$ on the equator, three regions, one on and two off the equator;
$F\ge F_c(H^+)$ on the equator: three regions, off the equator.

## 4.3 LOCAL ION CYCLOTRON INSTABILITY

The ion-cyclotron instability is sensitive to the anisotropy and the number density of the energetic ions. In the study, it is assumed that the anisotropy A, defined by Kennel and Petschek (1966), is assumed to be almost a constant in the magnetosphere. A constant A has been used in some previous papers (Cornwall 1965, Liemohn 1967). For energetic ring-current protons which are trapped in the geomagnetic field, A may be influenced by two processes. One is pitch angle scattering by the quasi-linear wave-particle interaction (Kennel and Petschek 1966), which decreases the anisotropy of the energetic ions but probably does not affect the variation of A along the field line. The other process is the absorption of the energetic ions in the ionosphere/atmosphere. This process will lead to a loss-cone distribution and A may become very large near the absorption point. However, if the absorption altitudes are of the order of 100 km, the influence of this absorption on A can be neglected in the magnetosphere.

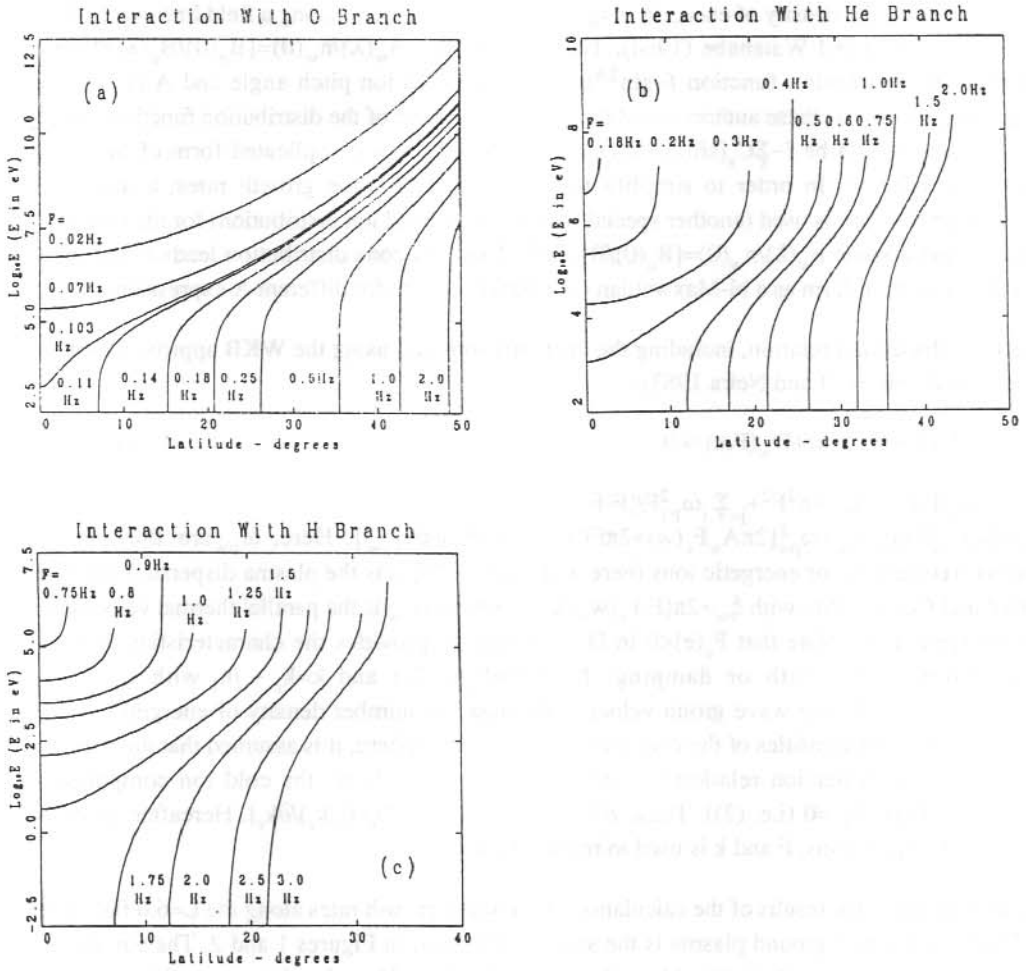


Figure 2. The parallel resonant energy of the protons interacting with (a) the $O^+$ wave branch (b) the $He^+$ wave branch and (c) the $H^+$ wave branch.

The variation of the density of energetic ring-current protons, $n_w(\lambda)$, along a field line was studied by Parker (1957) and Watanabe (1964). They showed that $n_w(\lambda)/n_w(0)=[B_o(0)/B_o(\lambda)]^A$ for a trapped ion distribution function $f\sim\sin^{2A}\psi$, where $\psi$ is an ion pitch angle and A is also the anisotropy. However, these authors noted that the general form of the distribution function for the trapped ions should be $f\sim\sum_s C_s[\sin 2\psi/B_o(\lambda)]^s$, which leads to a complicated form of the wave dispersion relation. In order to simplify the calculation of wave growth rates, a loss-cone distribution function is used (another special solution of trapped ion distribution) for the energetic protons, and assume $n_w(\lambda)/n_w(0)=[B_o(0)/B_o(\lambda)]^A$. This loss-cone distribution leads to the same dispersion relation form as a bi-Maxwellian distribution, except for different A expressions.

The local dispersion relation, including the energetic ions and using the WKB approximation, is written as (Gomberoff and Neira 1983):

$$D(F,k) = D_c(F,k)+D_w(F,k) = 0 \qquad (4)$$

where $D_c(F,k)=c^2k^2-4\pi^2F^2+\sum_{j=e,i}\omega_{pj}^2F/[F-F_c(j)]$, and $D_w(F,k)=-\sum_w\{\omega_{pw}^2A_w+\omega_{pw}^2[2\pi A_wF_c(w)+2\pi F(A_w+1)]Z(\xi_w)/k\alpha_{|w}\}$. Here, $\omega_{pw}$ are the angular plasma frequencies for energetic ions (here $w=H^+$), and $Z(\xi_w)$ is the plasma dispersion function (Fried and Conte 1961) with $\xi_w=2\pi[F-F_c(w)]/k\alpha_{|w}$ where $\alpha_{|w}$ is the parallel thermal velocity for the energetic ions. Note that $F_c(e)<0$ in $D_c$. Solving (4) provides the characteristics of wave propagation and growth or damping. Note $F=F_r+j\gamma/2\pi$ and $k=k_r+jk_i$ with $k_i\approx-\gamma/V_g$, $|\gamma|<<2\pi F_r$ and $V_g$ the wave group velocity. Because the number density of energetic ions is much less than the densities of the cold ions in the magnetosphere, it is assumed that the solution of $k_r$ from the dispersion relation for known $F_r$ depends only on the cold ion components. Therefore, $D_c(F_r,k_r)=0$ (i.e. (2)). Thus, $\gamma/V_g\approx\mathrm{Im}D_w(F_r,k_r)/[\partial D_c(F_r,k_r)/\partial k_r]$. Hereafter, in order to simplify expressions, F and k is used to replace $F_r$ and $k_r$.

Figure 3 displays the results of the calculation of the wave growth rates along the L=6.6 field line. In Figure 3, the background plasma is the same as that used in Figures 1 and 2. The parameters used for the energetic protons are: A(equator)=0.75, $T_{|}$=25 keV, and $n_w$(equator)=0.1 $cm^{-3}$. The absorption point is located at latitude 64.5° (altitude ~100 km). Hence, the absorption by the ionosphere/atmosphere does not affect the anisotropy of the energetic protons in the magnetosphere, so that A remains almost constant (~0.75). The maximum frequency, at which the wave becomes unstable ($\gamma>0$), is $F_m=AF_c(H^+)/(A+1)\approx0.43F_c(H^+)$. This frequency varies with latitude since $B_o$ changes. Figure 3 shows that wave growth in the plasma system considered here can occur off the equator. When $F<F_c(O^+)$ on the equator (F=0.1 Hz curve in Figure 3(a)), the wave amplification occurs only in the equatorial region. However, when $F_c(O^+)<F<F_{cf}(O^+)$ on the equator (F=0.15 and 0.2 Hz curves in Figure 3(a)), the wave grows in a region off the equator. The wave amplification is caused by interaction of the energetic protons with the $O^+$ wave branch. When $F_{cf}(O^+)<F<F_c(He^+)$ on the equator (F=0.3 Hz curve in Figure 3(a)), the wave grows in two regions, one on and the other off the equator. When $F_c(He^+)<F<F_{cf}(He^+)$ on the equator (F=0.5 and 0.7 Hz curves in Figure 3 (a)), the wave is destabilized in two regions, both off the equator. In the last two cases, the source region closer to the equator results from

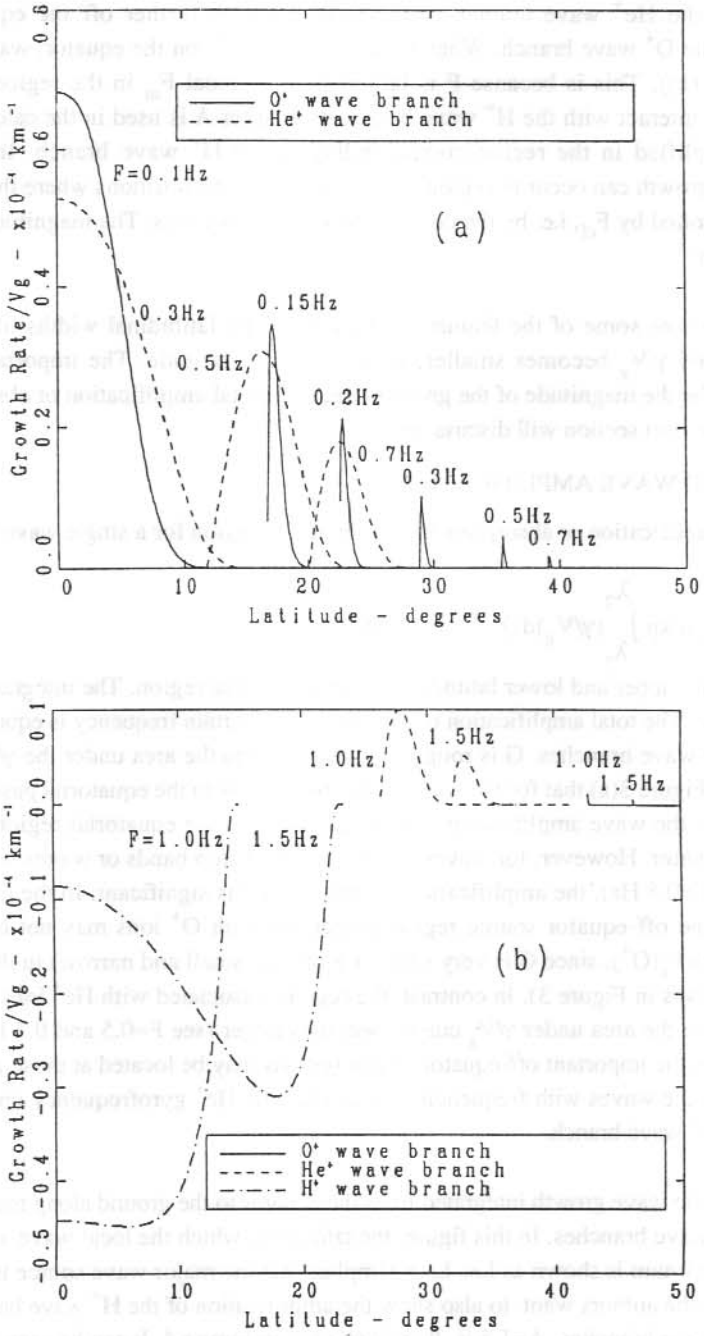


Figure 3. $\gamma/V_g$ versus latitude for the three wave branches. (a) $0.1 \leq F \leq 0.7$Hz and (b) F=1.0 and 1.5 Hz.

interaction with the $He^+$ wave branch, and the other region further off the equator, from interaction with the $O^+$ wave branch. When $F_{cf}(He^+)<F<F_c(H^+)$ on the equator, wave damping occurs (Figure 3 (b)). This is because F is larger than the local $F_m$ in the region where the energetic protons interact with the $H^+$ wave branch. If a larger A is used in the calculation, the wave can be amplified in the region corresponding to the $H^+$ wave branch. In summary, significant wave growth can occur in regions off the equator. The positions where the waves are growing are controlled by $F_{cf}$, i.e. by the concentrations of heavy ions. The magnitude of $\gamma/V_g$ is about $10^{-6}$-$10^{-5}$ $km^{-1}$.

It is important to note some of the features in Figure 3. The latitudinal widths of the source regions narrow and $\gamma/V_g$ becomes smaller, with increasing latitude. The important physical quantity may not be the magnitude of the growth rate, but a total amplification or absorption in a source region. The next section will discuss this.

4.4 INTEGRATED WAVE AMPLIFICATION

The wave total amplification or absorption in an interaction region for a single wave branch may be defined as

$$G = 20 \log_{10}[\exp \int_{\lambda_1}^{\lambda_2} (\gamma/V_g) ds] \qquad \text{(dB)} \qquad (5)$$

where $\lambda_1$ and $\lambda_2$ are upper and lower latitude limits of the source region. The integration in (5) is along the field line. The total amplification or absorption at a certain frequency is equal to the sum of G for the three wave branches. G is roughly proportional to the area under the $\gamma/V_g$ curve. It can be seen from Figure 3(a) that for the waves with frequencies in the equatorial pass bands (e.g. F=0.1 and 0.3Hz), the wave amplification is more effective in the equatorial region than in the regions off the equator. However, for waves in the equatorial stop bands or waves with $F>F_m$ on the equator (e.g. F=0.5 Hz), the amplification off the equator is significant. In the geostationary magnetosphere, the off-equator source region associated with $O^+$ ions may not be important unless F is close to $F_c(O^+)$, since G is very small (i.e. $\gamma/V_g$ is small and narrow) in this case (e.g. F>0.5Hz solid curves in Figure 3). In contrast, the regions associated with $He^+$ ions will show a significant G, since the area under $\gamma/V_g$ curves becomes larger (see F=0.5 and 0.7 Hz curves in Figure 3(a)). Thus, the important off-equator source regions may be located at those geomagnetic latitudes at which the waves with frequencies larger than the $He^+$ gyrofrequency on the equator are in the local $He^+$ wave branch.

Figure 4 displays the wave growth integrated from the equator to the ground along the L=6.6 field line for the three wave branches. In this figure, the latitude at which the local wave amplification $\gamma/V_g$ becomes maximum is shown as Lm. Lm>0 implies that the major wave source is located off the equator. Since the authors want to also show the amplification of the $H^+$ wave branch as well as the other two wave branches, A=1.5 is, therefore, used in Figure 4. It can be seen from Figure 4 that before the integrated amplification G maximises, Lm becomes larger than zero (Figure 4, see the points where the Lm curves start to increase). This means the wave source moves away

from the equator. For the $O^+$ wave branch, if F is high, the G is very small (~0), although $L_m$ is large. This confirms that the off-equator source associated with the $O^+$ wave branch is not important, as discussed above. The importance of the off-equator source for the $He^+$ and/or $H^+$ wave branches can be seen in Figure 4. For example, for a frequency of F=0.5Hz, point B in Figure 4 shows the G for the $He^+$ wave branch is ~2 dB (as a comparison the largest G is ~8 dB for this wave branch). This amplification mainly occurs at latitude ~16° (A in Figure 4).

The importance of the off-equator source is mentioned. This does not mean the equatorial source is not significant. Figure 4 shows that the largest amplification for the three wave branches occurs over latitudes ~5-10°, close to the equator. But at some frequencies (e.g. F~0.5 Hz in Figure 4) as mentioned before, the significant amplification occurring off the equator will make an important contribution to the wave spectrum.

## 4.5 DISCUSSION

Previous studies of wave instabilities in a multicomponent magnetosphere were focused on a single source region at the equator. In their study, the authors find that waves may be generated and amplified at different locations along the field line. Thus, a broad band of waves can be expected to be generated in the magnetosphere, although some modes may be weaker than others. At any fixed location, the favoured unstable frequency depends on $\gamma/V_g$ at that location. For any fixed wave frequency, the favoured source region depends on the amplification G at the wave frequency, and the location of the unstable region is determined by the cold heavy ion concentration. This allows us to compare observations at different positions along the field line.

The possibility of multiple source locations is important and should be included in any theory of propagation and generation/amplification for ion-cyclotron waves in an inhomogeneous magnetospheric plasma. For those waves generated in the equatorial region, previous propagation theory is valid (Roux et al. 1982, Rauch and Roux 1982). However, those waves propagating away from off-equator source regions must also be considered. These waves may propagate to high latitudes along the field line, and also to the equatorial region continuing on into the other hemisphere. It is noted that the propagation of these waves towards the equator, the damping of the waves caused by the energetic protons is important (see the $H^+$ wave branch in Figure 3(b)).

Generally, the damping by the energetic ring-current protons is not significant for waves propagating from a low latitude to a high latitude along a field line, since $F/F_m$ decreases during propagation. But this damping will become important for waves propagating towards the equator, since $F_m$ decreases during the propagation, and should be considered further. Also, there is another important damping effect on equatorward propagation of waves with $F \leq F_c(q)$, where $F_c(q)$ is the local gyrofrequency of heavy ion species (i.e. $q=O^+$ and $He^+$). These waves may reach a location where $F=F_c(q)$, since $B_o$ decreases. Near this location, the interaction between the waves and cold (or thermal) heavy ions leads to a strong absorption of wave energy (Mauk 1982).

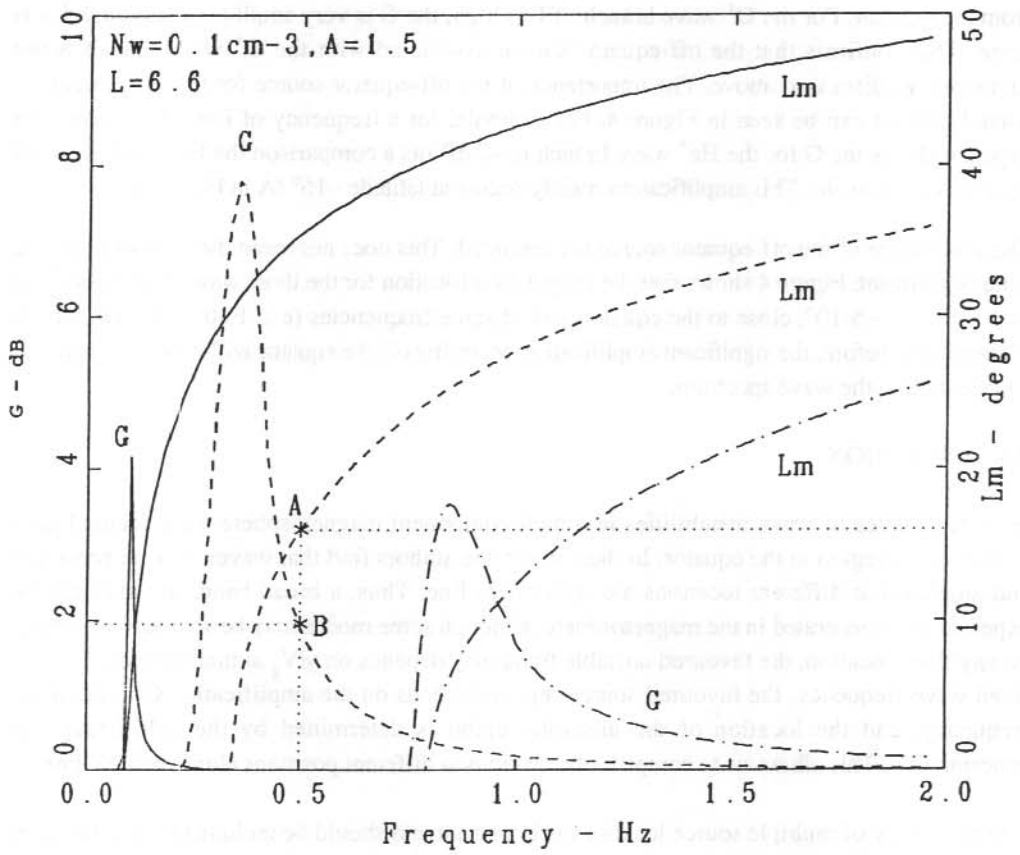


Figure 4. Integrated growth rate (G) and the latitude where the local wave growth becomes maximum ($L_m$) plotted as a function of frequency. The integration is along the L=6.6 field line. The plasma parameters are the same as in the other figures except A=1.5. The solid, dash, and dash-point lines are for the $O^+$, $He^+$ and $H^+$ wave branches respectively.

When a satellite is located at a geomagnetic latitude $\Lambda \sim 10°$, the waves produced over latitudes $0<\lambda<\Lambda$ would be expected to contribute to the wave spectrum observed at the satellite (Figure 3(a)). However, because the waves generated over these latitudes have $F \sim F_c(q)$, the wave energy is, in fact, absorbed by magnetospheric thermal heavy ions through a quasilinear resonant process (Gendrin and Roux 1980) or a non-resonant phase bunching process (Hu and Fraser 1990). So these waves would hardly be expected to contribute significantly to the wave spectrum. Observations at geostationary orbit over a latitude range 0° to ~10° have confirmed that the wave spectrum is dominated by the waves generated on the equator, and the wave spectral gaps relate to the equatorial non-propagation stop bands (Young et al. 1981, Fraser and McPherron 1982, Roux

et al. 1982). However, when a satellite is located at higher latitude and/or observes waves with frequencies corresponding to the equatorial stop bands, off-equator sources could be responsible.

Wave observations on the ground have not shown the spectral gaps which correspond to the equatorial stop bands observed by satellites. Perraut et al. (1984) showed that the spectral peaks seen on the ground were generally at lower frequencies than those seen by GEOS satellites at or near the geostationary orbit, and often occurred in the equatorial $He^+$ stop band. These authors explained their results by invoking wave tunnelling through an off-equator region, where the wave frequency matches a local bi-ion hybrid frequency. This region behaves as a "lowpass filter" for the waves. However, this lowpass filter effect is valid only for the waves with frequencies above the equatorial heavy ion stop bands. If off-equator wave sources are considered, the observation at the bottom of the field line above the ionosphere is the result of the waves generated/amplified and propagated in the inhomogeneous magnetospheric plasma. The wave power spectrum recorded there is determined by G which is dependent on the plasma parameters along the field line. At L~6.6, it has been shown that G is large in the equatorial $He^+$ stop band, because of the contribution of off-equator sources. As a consequence, the spectral gap near the equatorial $He^+$ gyrofrequency may not be seen at the bottom of the field line above the ionosphere. These waves can propagate through the ionosphere to the ground. Thus, the off-equator sources provide an additional explanation as to why the waves observed near the equator have different frequencies from the associated waves observed on the ground.

Furthermore, it is noted that for waves with frequencies near $F_c(He^+)$ on the equator, the amplification in the $O^+$ wave branch is not important. Thus, when $F<F_c(He^+)$ on the equator, the waves seen on the ground may behave similarly to the waves appearing at the equator. However, when $F>F_c(He^+)$ on the equator, particularly when F is in the equatorial stop band of $He^+$ ions, these two kinds of waves may behave differently. Statistical studies have shown the existence of similarities and differences in diurnal occurrence of ground-satellite ion-cyclotron wave observations (Bossen et al.1976, Perraut et al. 1984). However, it should be remembered that the comparison between ground and satellite observations should include the effects of the propagation in the ionospheric F2 region waveguide which distributes wave energy over a wide area (Tepley and Landshoff 1966, Manchester 1968). As a consequence, ground observed waves may originate from a distant field line source. For some individual ground-satellite observed events, the off-equator source effect can probably be identified. However, for a statistical study such as diurnal occurrence, the effects caused by three factors, namely the off-equator sources, the lowpass filter and the ionospheric wave-guide, are combined. Thus, the off-equator source effect may contribute only partly to the explanation of ground observations. A better position to observe the waves generated by off-equator sources may be in the high latitude magnetospheric region by elliptically orbiting spacecraft, where the influence of the ionospheric waveguide is not present. In such a region, the observed waves corresponding to the equatorial stop bands could be traced to the off-equator sources, and those corresponding to the equatorial $H^+$ and $He^+$ wave branches could result from the combination of a small fraction of equatorial waves tunnelling through the $He^+$ and $O^+$ stop bands and waves generated off the equator. Such studies could be

undertaken using wave and particle data from the VIKING spacecraft or in the future from the CRRES spacecraft.

In conclusion, this study shows that the peaks of the growth rate of the ion-cyclotron instability may occur off the equator. These off-equator sources are the result of the interaction of energetic ring-current protons with local $H^+$, $He^+$ and/or $O^+$ wave branches. The effects due to off-equator sources can significantly modify the generation/amplification and propagation of the ion-cyclotron waves in the inhomogeneous magnetospheric plasma. In further studies, the authors plan to investigate a more general plasma system, including multiple energetic ion species, and oblique propagation.

## 4.6 ACKNOWLEDGMENTS

This research is supported by Research Grants from the Australian Research Council and the University of Newcastle. Thanks are due to J.C. Samson for helpful discussions.

## 4.7 REFERENCES

Bossen, M., McPherron, R.L., *and* Russell, C. T. (1976). Simultaneous Pc1 observations by the synchronous satellite ATS-1 and ground stations: implications concerning IPDP generation mechanisms. *Journal of Atmospheric and Terrestrial Physics 47*:1157-1167.

Cornwall, J.M. (1965). Cyclotron instabilities and electromagnetic emission in the ultra low frequency and very low frequency ranges. *Journal of Geophysical Research 70*:61-69.

Fraser, B.J. *and* McPherron, R.L. (1982). Pc1-2 magnetic pulsation spectra and heavy ion effects at synchronous orbit: ATS 6 results. *Journal of Geophysical Research 87*:4560-4566.

Fried, B.D. *and* Conte, S.D. (1961). *The Plasma Dispersion Function.* Academic Press, New York.

Geiss, J., Balsiger, H., Eberhardt, P., Walker, H.-P., Weber, L., Young, D.T. *and* Rosenbauer, H. (1978). Dynamics of magnetospheric ion composition as observed by the GEOS mass spectrometer. *Space Science Reviews 22*:357-374.

Gendrin, R. *and* Roux, A. (1980). Energization of helium ions by proton-induced hydromagnetic waves. *Journal of Geophysical Research 85*:4577-4586.

Gomberoff, L. *and* Neira, R. (1983). Convective growth rate of ion cyclotron waves in a $H^+$-$He^+$ and $H^+$-$He^+$-$O^+$ plasma. *Journal of Geophysical Research 88*:2170-2174.

Hu, Y.D. *and* Fraser, B.J. (1990). Transverse phase bunching: an interaction between magnetospheric thermal heavy ions and ion cyclotron waves. *ANARE Research Notes Number 80.*

Kennel, C.F. *and* Petschek, H.E. (1966). Limit on stably trapped particle fluxes. *Journal of Geophysical Research 71*:1-28.

Kozyra, J.U., Cravens, T.E., Nagy, A.F., Fontheim, E.G. *and* Ong, R.S.B. (1984). Effects of energetic heavy ions on electromagnetic ion cyclotron wave generation in the plasmapause region. *Journal of Geophysical Research 89*:2217-2233.

Liemohn, H.B. (1967). Cyclotron-resonance amplification of VLF and ULF whistlers. *Journal of Geophysical Research 72*:39-55.

Manchester, R.N. (1968). Correlation of Pc1 micropulsations at space stations. *Journal of Geophysical Research 73*:3549-3556.

Mauk, B.H. (1982). Helium resonance and dispersion effects on geostationary Alfvén/ion cyclotron waves. *Journal of Geophysical Research 87*:9107-9119.

Parker, E.N. (1957). Newtonian development of the dynamical properties of ionized gases of low density. *Physical Review 107*:924-933.

Perraut, S., Gendrin, R., Roux, A. *and* de Villedary, C. (1984). Ion cyclotron waves: direct comparison between ground-based measurements and observations in the source region. *Journal of Geophysical Research 89*:195-202.

Rauch, J.L. *and* Roux, A. (1982). Ray tracing of ULF waves in a multicomponent plasma: consequences for the generation mechanism of ion cyclotron waves. *Journal of Geophysical Research 87*:8191-8198.

Roux, A., Peraut, S., Rauch, J.L., de Villedary, C., Kremser, G., Korth, A. and Young, D.T. (1982). Wave-particle interaction near $\Omega_{He^+}$ observed on board GEOS 1 and 2, 2, Generation of ion cyclotron waves and heating of $He^+$ ions. *Journal of Geophysical Research 87*:8147-8190.

Smith, R.L., *and* Brice, N. (1964). Propagation in multicomponent plasmas. *Journal of Geophysical Research 69*:5029-5040.

Tepley, L.R. *and* Landshoff, R.K. (1966). Waveguide theory for ionospheric propagation of hydromagnetic emissions. *Journal of Geophysical Research 71*:1499-1504.

Watanabe, T. (1964). Distribution of charged particles trapped in a varying strong magnetic field (one dimensional case) with applications to trapped radiation. *Canadian Journal of Physics 42*:1185-1194.

Young, D.T., Perraut, S., Roux, A., de Villedary, C., Gendrin, R., Korth, A., Kremser, G. *and* Jones, D. (1981). Wave-particle interaction near $\Omega_{He^+}$ observed on GEOS 1 and 2, 1, Propagation of ion cyclotron waves in $He^+$-rich plasma. *Journal of Geophysical Research 86*:6755-6772.

# 5. TRANSVERSE PHASE BUNCHING: AN INTERACTION BETWEEN THERMAL HEAVY IONS AND ION-CYCLOTRON WAVES

Y.D. Hu and B.J. Fraser
Department of Physics
University of Newcastle
Newcastle NSW 2308
Australia

ABSTRACT

Using test particle simulation and analytical approximations, the authors investigated a non-resonant interaction of low energy (1-10ev) ions with electromagnetic monochromatic ion-cyclotron waves propagating along a uniform magnetic field in a cold multicomponent plasma. A periodic phase bunching process, which is mainly due to transverse wave electric and Lorentz forces, occurs during the interaction. This transverse phase bunching causes an ion acceleration mainly perpendicular to the uniform magnetic field. The wave propagation effect and the transverse Lorentz force play important roles in controlling the behaviour of the phase bunching. It is found that the period of the phase bunching is about $2\pi/ | k[v_{\|o}+ (\Omega-\omega)/k] |$, where k and $\omega$ are the wave number and angular frequency, $v_{\|o}$ and $\Omega$ are the ion initial velocity parallel to the background magnetic field and the angular gyrofrequency respectively. These results are applied to explain the heating of thermal $He^+$ ions observed at the geostationary orbit in the earth's magnetosphere. Using realistic magnetospheric parameters, it is shown that only $He^+$ ions can be effectively energised by the phase bunching, provided that wave frequencies are near the gyrofrequency of $He^+$ ions. In the presence of a 1-5 nT magnetic wave field, the thermal (1-10ev) $He^+$ ions can be accelerated up to suprathermal energies (10-100ev). The explanation of other important features of thermal and suprathermal $He^+$ ion observations, including the modulation of a suprathermal $He^+$ flux observed on ATS-6 and GEOS satellites, are also discussed. The agreement between theory and observation supports the suggestion that the transverse phase bunching process is responsible for the heating of thermal $He^+$ ions in the magnetosphere.

## 5.1 INTRODUCTION

The wave-particle interaction between heavy ions, such as $He^+$ and $O^+$, and ion-cyclotron waves (ICWs) observed in the magnetosphere is a two-way process. On the one hand, the presence of heavy ion species affects the generation/amplification and propagation of the ICWs in the inhomogeneous magnetosphere (Hu et al. 1990). On the other hand, there exist inverse effects of the intense ICWs on the dynamics and the distribution of the heavy ions.

When one considers the effect of the ICWs on heavy ions, the physical picture is not clear. Observations on GEOS-1, -2 and ATS-6 satellites have confirmed that the thermal (1-10ev) $He^+$ ions in the geostationary magnetosphere are accelerated up to suprathermal energies (E~10-100ev) (Mauk and McPherron 1980, Young et al. 1981, Mauk et al. 1981, Roux et al. 1982). From these studies the authors conclude the following observational characteristics:

1. Only thermal $He^+$ ions are effectively accelerated up to 10-100ev energies, in the presence of thermal $H^+$, $He^+$, and $O^+$ ions in the magnetosphere.
2. Observations of suprathermal $He^+$ ions are coincident with the ICWs.
3. Heating of the $He^+$ ions is mainly in the perpendicular direction.
4. The count rates of the suprathermal $He^+$ ions recorded by low-energy detectors are modulated. This modulation may have frequencies close to the $He^+$ gyrofrequency $F_c$ ($He^+$) (Mauk et al. 1981) or to F, the frequency of simultaneously recorded ICWs (Young et al. 1982). Anti-phased modulations are observed by two detectors with the same pitch angle view (~88°) but in opposite directions (Mauk et al. 1981). The impulsive modulation of the suprathermal $He^+$ ions is detected only by the detector viewing large pitch angles (88°±3° for ATS-6, and ~90° for GEOS-1 and -2). The detectors viewing pitch angles of 15° and 117° have recorded no modulation of the suprathermal ion flux.

To understand the observations of the inverse interaction, two explanations have been suggested. One involves quasilinear diffusion theory (Gendrin and Roux 1980). This considers a resonant interaction between $He^+$ ions and the ICWs. However, observations in the magnetosphere show that this resonant interaction may not occur at the geostationary orbit. The large amplitude ICWs normally occur at F~O. $8F_c(He^+)$, or $F \gtrsim F_{cf}$ ($He^+$)>$F_c(He^+)$ (Young et al. 1981, Fraser and McPherron 1982). Here $F_{cf}$ (ion) is the cut-off frequency associated with individual heavy ion species. Using a cold plasma dispersion relation, the authors can estimate that the resonant parallel velocity of the $He^+$ ions would be ~$10^2$ km $sec^{-1}$, which is too high for the $He^+$ ions in the thermal energy range to reach. Furthermore, the quasilinear theory requires a wide band of wave frequencies, whereas wave observations show only quasi-monochromatic spectra.

The other theory considers the non-linear coherent interaction between a monochromatic or quasi-monochromatic ICW and the thermal $He^+$ ions. Two processes have been used to interpret the heating of $He^+$ ions. One considers the $He^+$ ion trapped by the wave field (Roux et al. 1982). The other process is a phase bunching. Because the parallel ion velocity $v_{\parallel}$, in this phase bunching process may not be equal to the resonant drift velocity $V_R$, the interaction can be nonresonant (Mauk 1982). Strictly, the wave trapping and phase bunching are two different concepts. The authors will show that both types of $He^+$ ions, trapped and untrapped by the wave field, are equally important for the acceleration of the $He^+$ ions during the phase bunching process.

Mauk (1982) has used a simple model to study the phase bunching without consideration of the effects of wave propagation and the Lorentz force. His calculations gave only a restricted view of how the ion phase angles are bunched and perpendicular velocities increased. In that model the phase bunching was considered a non-periodic process. Berchem and Gendrin (1985) have undertaken parameter analysis on the phase bunching process by using a phase diagram in ion velocity space drawn from two motion invariants. However, the phase diagram analysis could not give a complete view of the time evolution of the phase bunching process, because the phase bunching exhibits a temporal behaviour. Besides, some of the Berchem and Gendrin explanations of the supra-thermal $He^+$ ion modulations observed on ATS-6 and GEOS-1 need more discussion in detail.

## 5.2 BASIC EQUATIONS AND CONCEPTS

### 5.2.1 *Wave propagation characteristics*

Firstly, it is necessary that the wave dispersion relation is reviewed. It is well-known that the presence of $He^+$ and $O^+$ ions causes two stop bands in the dispersion space (k-F space) of the left-hand polarised ICWs. The details of these stop bands have been discussed in another article in this issue (Hu et al. 1990). Separated by these stop bands, the ICWs have three pass bands. When the same parameters are used for the bulk magnetospheric plasma at the equatorial geostationary orbit as those used in Hu et al. (1990), the characteristic frequencies are: $F(H^+)=2.13Hz$, $F_c(He^+)=0.53Hz$, $F_c(O^+)=0.13Hz$, $F_{cf}(He^+)=0.96Hz$, and $F_{cf}(O^+)=0.23Hz$. Thus the three wave pass branches are $0.96Hz<F<2.13Hz$ (the $H^+$ wave branch), $0.23Hz<F<0.53Hz$ (the $He^+$ wave branch), and $F<0.13Hz$ (the $O^+$ wave branch).

### 5.2.2 *Basic equations of motion for test ions*

An ICW propagates along a static magnetic field $\mathbf{B}_o$ ($\mathbf{B}_o=B_o\mathbf{e}_z$,$\mathbf{k}=k\mathbf{e}_z$) with transverse electric field $\mathbf{E}_w$ and magnetic field $\mathbf{B}_w$ (Figure 1, $\mathbf{e}$ defines a unit vector). Consider a test ion with velocity $\mathbf{v}=v_\perp\mathbf{e}_\perp+v_\parallel\mathbf{e}_z$. In a fixed coordinate system in Figure 1, $\psi$ is the angle of $\mathbf{e}_\perp$ with respect to a fixed transverse direction (Y axis). Suppose the phase of $\mathbf{B}_w$ is $\varphi=kz-\omega t$ and the ion phase angle $\theta=\psi-\varphi$. The nonrelativistic equation of motion for the test ion is

$$\frac{d\theta}{dt} = \omega - kv_\parallel - \Omega + \frac{\Omega_w(v_\parallel - v_p)\cos\theta}{v_\perp} \tag{1}$$

$$\frac{dv_\perp}{dt} = \Omega_w (v_\parallel - V_p)\sin\theta \tag{2}$$

$$\frac{dv_\parallel}{dt} = -\Omega_w v_\perp \sin\theta \tag{3}$$

where $\Omega_w=\Omega B_w/B_o$, $\Omega$ is the gyrofrequency of the test ion in $\mathbf{B}_o$, and $\omega=2\pi F$.

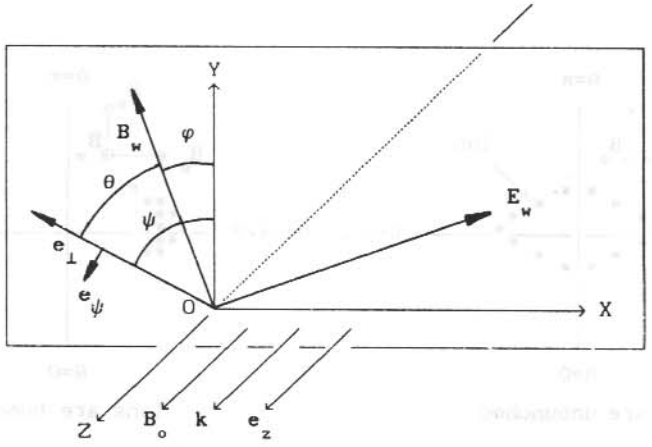


Figure 1. The coordinate system used for test ions.

There are four forces acting on the test ion. The first force is $qc^{-1}v_{\perp}\mathbf{e}_{\perp}x\mathbf{B}_o$, which leads to the normal cyclotron motion, appearing as $-\Omega$ in the right hand side (RHS) of (1). The second force is $qc^{-1}v_{\perp}\mathbf{e}_{\perp}x\mathbf{B}_w$, which leads to acceleration in the longitudinal direction as described by (3). The third and fourth forces are $qc^{-1}v_{\parallel}\mathbf{e}_z x\mathbf{B}_w=\Omega_w V_{\parallel}$ $(\sin\theta\mathbf{e}_{\perp}+\cos\theta\mathbf{e}_{\psi})$ and $q\mathbf{E}_w=-V_p\Omega_w$ $(\sin\theta\mathbf{e}_{\perp}+\cos\theta\mathbf{e}_{\psi})$ respectively, which accelerate the ion transversely, and also cause the phase angle change as described by the last term on the RHS of (1). The parallel Lorentz force does not correspond directly to the the change of $\theta$. However, the variation of $\theta$ is affected by $v_{\parallel}$. This is the result of wave propagation and the transverse Lorentz force (the third force). For Mauk's model ($k=0$ or $v_{\parallel}\equiv 0$) and the resonant interaction ($\omega-kv_{\parallel}-\Omega=0$), the wave propagation effect disappears. However, it will be shown that $v_{\parallel}$ can increase up to $\sim 2v_{\parallel o}$ (subscript o describes an initial value) during the phase bunching, and the influence of $v_{\parallel}$ through wave propagation (i.e. $kv_{\parallel}$) on $d\theta/dt$ thus should be considered.

### 5.2.3 *Phase bunching*

Phase bunching defines the process in which many test ions with various initial phase angles are bunched, after a certain time, around a particular ion phase angle. Figure 2 shows a schematic illustrating this. It is noted that phase bunching is different from wave trapping. Wave trapping is defined as a bounded phase angle oscillation of an individual ion in the wave field. Normally, both trapped and untrapped ions may have contributions to the phase bunching. There may be a wave trapping, however, without phase bunching (Matsumoto 1979).

Basically, the test ions are accelerated longitudinally and transversely during phase bunching. According to the dominant direction of the acceleration, one can classify phase bunching processes into two types: transverse and longitudinal phase bunching. Matsumoto et al. (1974) has classified the phase bunching for resonant electron-VLF interactions. Now this classification to the non-resonant ion-ULF interaction is extended.

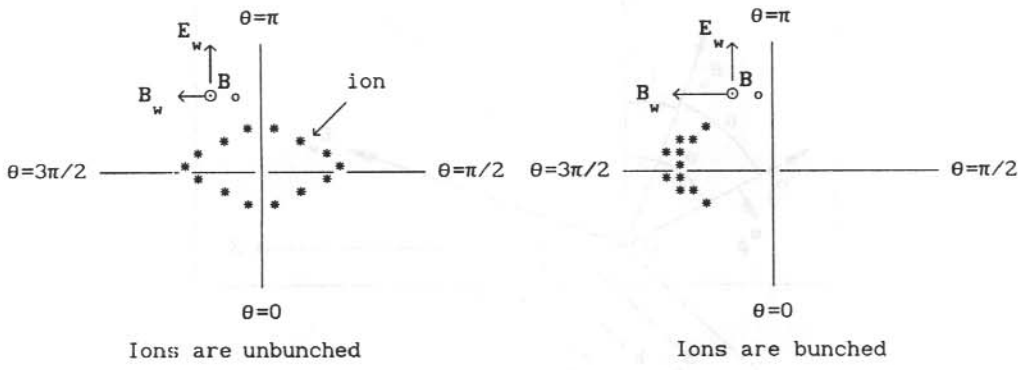


Figure 2. What is the phase bunching?

Whether a phase bunching process is transverse or longitudinal depends on the ratio of the wave transverse Lorentz-electric force to the parallel Lorentz force. For the interaction of the magnetospheric thermal ions with the ICWs, this ratio is much greater than 1 (Mauk 1982). Therefore, if phase bunching occurs in the interaction, it will be a transverse phase bunching.

The authors now provide a physical view of how the ion phase angles are bunched. Suppose a left-hand wave propagates parallel to $\mathbf{B}_o$. Because the total transverse force has a radial component, the test ions sense an extra centripetal acceleration. Thus, all test ions migrate quickly to $\theta=3\pi/2$ to minimise the centripetal acceleration (Mauk 1982). Therefore, the phase bunching starts at $\theta\sim3\pi/2$. Near this bunched phase angle, the angular velocity $d\theta/dt \approx \omega-kv_{\parallel}-\Omega$, and the bunched ions shift to $\pi/2$ through $\pi$ when $\omega-kv_{\parallel}-\Omega < 0$ (the $He^+$ and $O^+$ wave branches), or through $2\pi$ (or 0) when $\omega-kv_{\parallel}-\Omega>0$ (the $H^+$ wave branch). During the rotation of $\theta$ from $3\pi/2$ to $\pi$ or $2\pi$, $v_{\perp}$ is parallel to $\mathbf{E}_w$, and the ions are, therefore, accelerated and $v_{\perp}$ increases greatly. During the rotation of $\theta$ from $\pi$ or $2\pi$ to $\pi/2$, the ions are decelerated, but the value of $v_{\perp}$ remains large. Since $v_{\perp}$ is large during the rotation of $\theta$ from $3\pi/2$ to $\pi/2$, (1) gives $d\theta/dt\approx\omega-kv_{\parallel}-\Omega$. This indicates that the rotation of the phase angle depends roughly only on the value of $\theta$ around which the ions start to be bunched (i.e. $\sim3\pi/2$). Therefore, all ions have approximately the same angular velocity of $\theta$ during the shift of $\theta$ from $3\pi/2$ to $\pi/2$, and the ions thus remain bunched in phase angle. When $\theta$ passes $\pi/2$, the value of $v_{\perp}$ becomes so small that the last term on the RHS of (1) becomes important. In this case, the change of $\theta$ becomes sensitive to the individual initial conditions, and then the ions tend to become unbunched. When unbunched, the ions repeat the above process to form another period of phase bunching.

## 5.3 ANALYTICAL APPROXIMATION

Neglecting the longitudinal Lorentz force, then $v_{\parallel}\approx v_{\parallel o}$ and equations (1) and (2) can be solved analytically. Noting $u_o= v_{\parallel o}-(\omega-\Omega)/k$ and $w_o= v_{\parallel o}-\omega/k$, the solutions are

$$\theta = \tan^{-1}\left(\frac{\frac{\Omega_w w_o}{ku_o}\sin(ku_o t) + v_{\perp o}\sin(ku_o t-\theta_o)}{\frac{\Omega_w w_o}{ku_o}[1-\cos(ku_o t)]- v_{\perp o}\cos(ku_o t-\theta_o)}\right) \tag{4}$$

and

$$v_{\perp} = \left[\left(\frac{2\Omega_w w_o \sin(ku_o t/2)}{ku_o}\right)^2 + \frac{4\Omega_w w_o v_{\perp o}}{ku_o}\sin(ku_o t/2)\sin(ku_o t/2 - \theta_o) + v_{\perp o}^2\right]^{1/2} \tag{5}$$

### 5.3.1 *Phase Bunching Period*

The solutions for $v_{\perp}$ and $\theta$ are periodic functions of time. The period of the ion motion is

$$T = \frac{2\pi}{|ku_o|} = \frac{2\pi}{|kv_{\parallel o} + (\Omega-\omega)|} \tag{6}$$

The test ions with the same $v_{\parallel o}$ have a constant period. This means that if a group of ions with the same $v_{\parallel o}$ are phase bunched during the movement in the wave field, this phase bunching is also a periodic process with the same period T. Strictly, for different ion groups with different $v_{\parallel o}$, the phase bunching behaves differently. The phase bunching period is influenced by the initial kinetic energy and pitch angle, which determine $v_{\parallel o}$. However, all test ions have the same period when $kv_{\parallel o} \ll |\Omega-\omega|$. So, if the ions exhibit phase bunching, this process will be independent of the initial conditions. In this case, T becomes

$$T \approx 1/|F-F_c|. \tag{7}$$

This simplified result has been obtained by Berchem and Gendrin (1985). If $\omega$ tends to $\Omega$ (i.e. $|k|$ tends to $\infty$, see the wave dispersion relation) or $v_{\parallel o}$ is large, then $T \rightarrow 2\pi/|kv_{\parallel o}|$. It is necessary to point out that the phase bunching period cannot be compared directly with the period of the observed modulation of suprathermal ions. This will be discussed again later.

### 5.3.2 *Maximum $v_\perp$ during phase bunching*

From equation (5), the maximum $v_\perp$ can estimated during phase bunching as

$$v_{\perp m} \sim \left| \frac{2\,\Omega_w w_o}{ku_o} + v_{\perp o} \right| = \left| \frac{2\Omega_w(v_{\parallel o}-V_p)}{kv_{\parallel o}+(\Omega-\omega)} + v_{\perp o} \right| \tag{8}$$

Normally $v_{\perp o} \ll v_{\perp m}$. If it can be assumed $|kv_{\parallel o}| \ll |\Omega-\omega|$ and $v_{\parallel o} \ll V_p$, then

$$v_{\perp m} \sim \left| \frac{2\Omega_w V_p}{\Omega - \omega} \right|. \tag{9}$$

## 5.4 NUMERICAL SIMULATION

### 5.4.1 *Behaviour of* $\theta$

In these simulations, the test ion species is $He^+$. Figure 3 shows the time behaviour of $\theta$ for 18 test $He^+$ ions with the same initial kinetic energy ( $E_{\parallel o}$ 5ev) and pitch angle ($\alpha_o$=45°) but different $\theta_o$. The values of $\theta_o$ for these 18 ions are uniformly distributed from $\pi/36$ to $23\pi/12$. When $F<F_c$ (i.e. the $He^+$ and $O^+$ wave branches, middle and bottom panels of Figure 3), the bunching occurs firstly around $\theta \sim 3\pi/2$, then the bunched $\theta$ decreases. The test ions remain bunched while $\theta$ for all ions decreases to $\pi/2$. After passing $\pi/2$, the values of $\theta$ for the test ions quickly diffuse again, and then enter another period. In the $F>F_c$ case (i.e. the $H^+$ wave branch, top panel of Figure 3), the phase angles become bunched at $3\pi/2$, and the bunching continues as $\theta$ increases to $\pi/2$ through $2\pi$. These behaviours agree well with the theoretical interpretations. It is found that both types of ions, trapped and untrapped by the wave field, are phase bunched. This can be seen in the middle and bottom panels of Figure 3, in which the tapped ions are shown as lines and the untrapped ions as points.

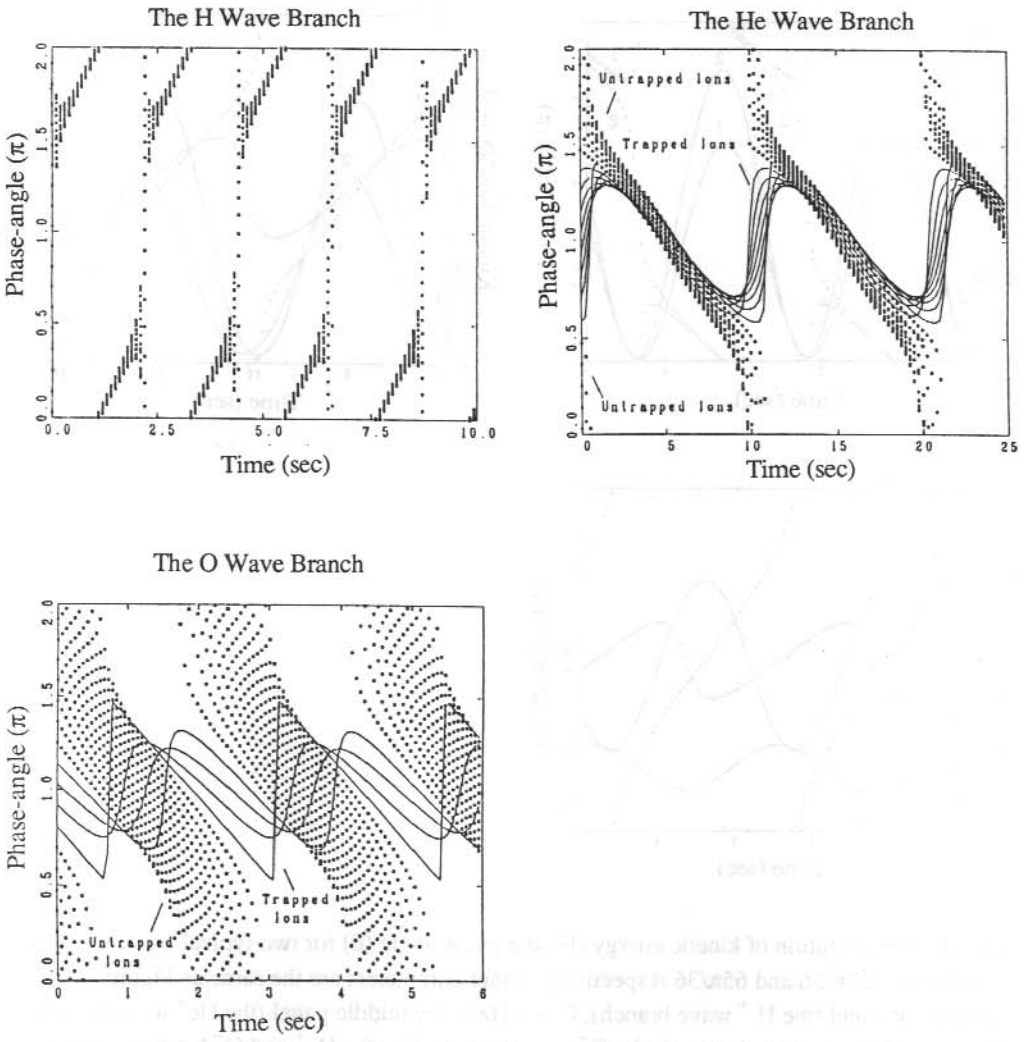


Figure 3. Time behaviour of θ for 18 test $He^+$ ions in the wave field with $B_w$=5nT. $\theta_o$ of 18 ions is uniformly distributed from π/36 to 23π/12. F=1.0 Hz for the $H^+$ wave branch in the top panel, F=0.5 Hz for the $He^+$ wave branch in the middle panel, and F=0.12 Hz for the $O^+$ wave branch in the bottom panel.

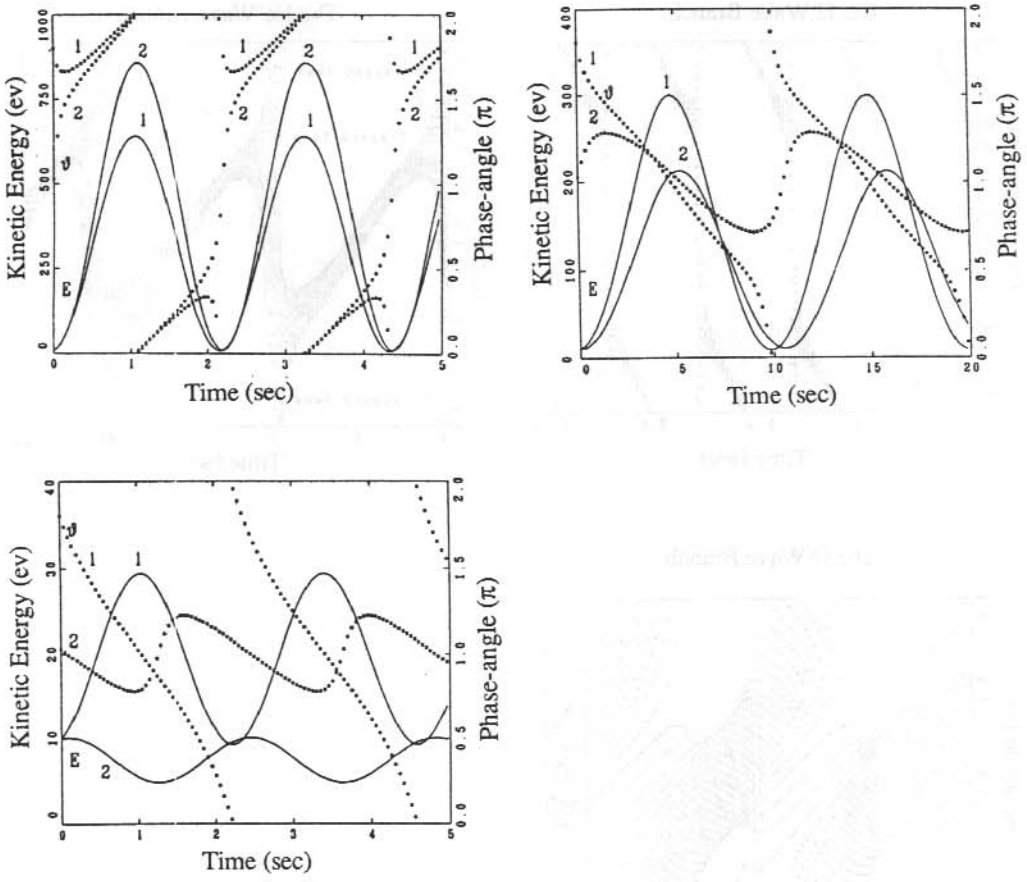


Figure 4. The evolution of kinetic energy (E) and phase angle (θ) for two typical test ions. Ions 1 and 2 have $\theta = 37\pi/36$ and $65\pi/36$ respectively. Other parameters are the same as Figure 3. F=1.0 Hz in the top panel (the $H^+$ wave branch), F=0.5 Hz in the middle panel (the $He^+$ wave branch), and F=0.12 Hz in the bottom panel (the $O^+$ wave branch). For the $He^+$ and $O^+$ branches, ion 1 is untrapped and ion 2 is trapped, while for the $H^+$ branch, ion 1 is trapped and ion 2 is untrapped.

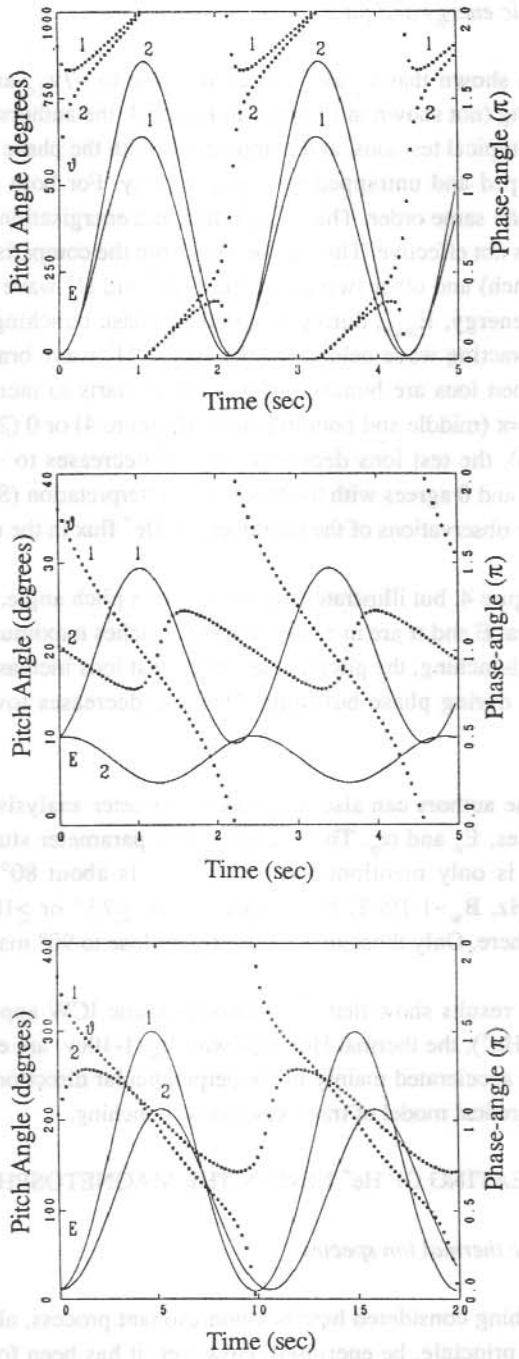


Figure 5. The same as Figure 4, but illustrating the evolution of the test ion pitch angles ($\alpha$).

5.4.2 *Behaviour of kinetic energy and pitch angle*

These simulations have shown that $v_\perp$ and $v_\parallel$ can increase to ~$7v_{\perp o}$ and ~$2v_{\parallel o}$ respectively during the phase bunching (not shown in figures). In Figure 4, the authors depict the total kinetic energy evolution of two typical test ions, and compare this with the phase angle evolution. These two ions belong to trapped and untrapped ions respectively. For both test ions, the resultant energy of the ions is of the same order. The acceleration and energisation of the $He^+$ ion species by the $O^+$ wave branch is not effective. This can be seen from the comparison between the bottom panel (the $O^+$ wave branch) and other two panels (the $He^+$ and $H^+$ wave branches) in Figure 4. The maximum kinetic energy, $E_{max}$, during a period of phase bunching is of order $10^2$ev for $E_{\parallel o}$=5ev, when the interacting wave belongs to the $He^+$ or $H^+$ wave branches (top and middle panels of Figure 4). When ions are bunched at $\theta \sim 3\pi/2$, E starts to increase rapidly, and then becomes maximum at $\theta=\pi$ (middle and bottom panels of Figure 4) or 0 ($2\pi$) (top panel of Figure 4). After passing $\pi$ or 0, the test ions decelerate, and E decreases to ~$E_o$. This relationship between the phases of E and $\theta$ agrees with the theoretical interpretation (Section 2.3), and can be used to explain the phase observations of the suprathermal $He^+$ flux in the magnetosphere.

Figure 5 is similar to Figure 4, but illustrates the evolution in pitch angle, $\alpha$. Comparing Figures 4 and 5, it can be seen that E and $\alpha$ are in phase. When E reaches maximum, $\alpha$ is also maximum. At the start of the phase bunching, the pitch angles of the test ions increase very rapidly to $\alpha_{max}$, then remain at $\alpha \sim \alpha_{max}$ during phase bunching. When E decreases towards $E_o$, $\alpha$ decreases rapidly to $\alpha_{min} \sim \alpha_o$.

Using the simulation, the authors can also undertake parameter analysis on $E_{max}$ and $\alpha_{max}$ for various wave frequencies, $E_o$ and $\alpha_o$. The details of this parameter study will be reported in another paper. Here it is only mentioned that the $\alpha_{max}$ is about 80° or 100°, if the wave frequency is ~0.30-1.6Hz, $B_w$~1-10nT, $E_o$~1-10ev and $\alpha_o \lesssim 75°$ or $\gtrsim 105°$, which are typical values in the magnetosphere. Only those ions whose $\alpha_o$ is close to 90° may have $\alpha_{max} \sim 90°$.

In summary, simulation results show that if a monochromatic ICW appears with frequency at ~(0.75-0.85)$F_c$ or ~$F_{cf}(He^+)$, the thermal $He^+$ ions with $E_o$~1-10ev, are effectively energised to $\gtrsim 10E_o$. The test ions are accelerated mainly in the perpendicular direction. The phase behaviour agrees well with the theoretical model of transverse phase bunching.

## 5.5 APPLICATION: HEATING OF $He^+$ IONS IN THE MAGNETOSPHERE

5.5.1 *Heating of multiple thermal ion species*

Because the phase bunching considered here is a nonresonant process, all ion species including $H^+$, $He^+$ and $O^+$ can, in principle, be energised. However, it has been found that the $He^+$ ions display a suprathermal flux modulation, when the ion detector views a large pitch angle (~90°), whereas thermal protons are hardly affected (Roux et al. 1982). This result suggests that the

heating of thermal ions is a mass dependent process. The authors will show that only $He^+$ ions can be effectively accelerated by the nonresonant transverse phase bunching process. For typical wave frequencies, the evolution of kinetic energy of the $H^+$, $He^+$, and $O^+$ ions are displayed in Figure 6. Each ion species has two test ions with $E_o$=2 and 12ev respectively. They used $\theta_o=37\pi/36$ for all test ions, and note that the influence of $\theta_o$ on E is negligible since ion energisation occurs mainly during the phase bunching, which is independent of $\theta_o$. From the top panel of Figure 6 (F=.5Hz, the $He^+$ wave branch), it can be seen that the energisation of $H^+$ and $O^+$ ions can be ignored compared with the energisation of the $He^+$ ions when $F \lesssim F_c(He^+)$. If $F \gtrsim F_{cf}(He^+)$, the energisation of the $He^+$ ions is still more effective than that of the $H^+$ ions and much more effective than that of the $O^+$ ions (bottom panel of Figure 6). Although the kinetic energy for the $H^+$ test ion species is considerable, the pitch angle is about 70°. In this case, the detector with a 90° pitch angle view cannot record these energised $H^+$ ions. Thus, even though the transverse phase bunching is a nonresonant process, it only provides a suprathermal $He^+$ ion flux when $F \lesssim F_c(He^+)$ or $F \gtrsim F_{cf}(He^+)$, although all thermal ions $H^+$, $He^+$ and $O^+$ are present.

### 5.5.2 *Modulation of suprathermal $He^+$ ion flux*

#### Observable Suprathermal $He^+$ Ion Flux

When the pitch angle view of a detector is ~90°, only ions with large $\alpha_o$ (>75°) may be detected because their $\alpha_{max}$ can reach 90° as mentioned in Section 4. Therefore, the detector records, in this case, only those ions whose pitch angles are already large before energisation. Mauk et al. (1981) reported that when the pitch angle view of a detector is small (15°), there was no detection of the suprathermal $He^+$ flux. This result is predicted by the transverse phase bunching process. Because $\alpha$ and E are in phase and $\alpha$ increases rapidly at the start of the phase bunching, the accelerated suprathermal ions cannot have pitch angles smaller than 75°-80°. Now, the authors have seen that not only the energy response, but also the pitch angle view of the detector control the detection of the ion flux. For example, suppose the energy response range of a detector is $E_2$ to $E_1$ ($E_1>E_2$), and the pitch angle view range is $\alpha_2$ to $\alpha_1$ ($\alpha_1>\alpha_2$). These response ranges constitute an 'observable window'. If an ion can pass through this window (i.e. $E_{max}>E_1$ and $\alpha_{max}>\alpha_1$), this ion may be detected twice per phase bunching period. If an ion can just enter the window ($\alpha_1>\alpha_{max}>\alpha_2$ and $E_1>E_{max}>E_2$), this ion may be detected once per phase bunching period.

#### Phase Relation

Mauk and McPherron (1980) found that two detectors on ATS-6 looking in opposite directions (i.e. $\theta$ anti-phased) recorded anti-phased modulations. From the $\alpha$-$\theta$ and E-$\theta$ relations (Figures 4 and 5), it can be seen that if the phase difference of $\theta$ is $\pi$ which corresponds to two opposing detectors, the $\alpha$ and E are also anti-phased. Thus, the observed signatures are also anti-phased. The acceleration of ions through a quasilinear process does not show similar characteristics. Therefore, this phase relation confirms the occurrence of the transverse phase bunching during the ion acceleration.

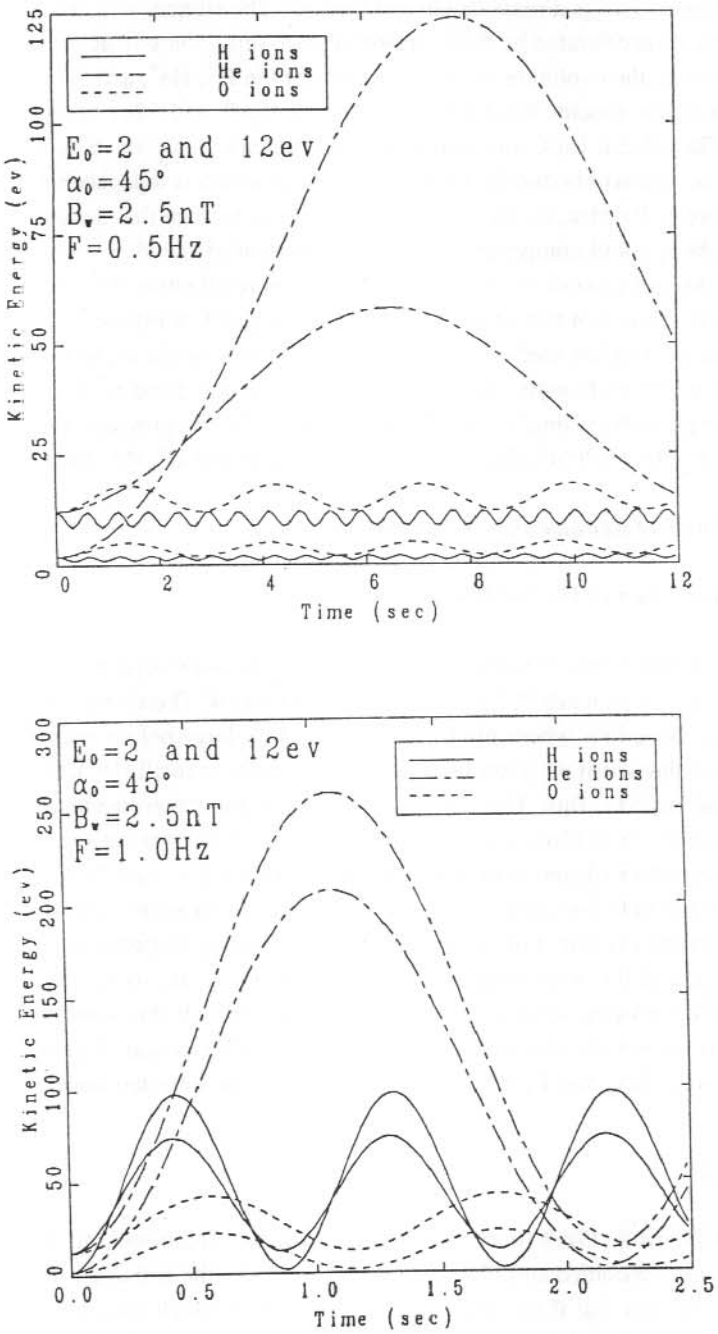


Figure 6. The energisation of three ion species by ion-cyclotron waves. Each ion species has two test ions. One has $E_o$=2ev, the other has $E_o$=12ev. $\alpha_o$=45° for all ions. $B_w$=2.5nT. F=0.5Hz in the top panel and F=1.0Hz in the bottom panel.

Modulation Frequency

Normally, the modulation frequency of the impulses was observed in the satellite frame of reference. This frequency cannot be directly compared with the phase bunching frequency. If it is assumed the phase bunching, which leads to the suprathermal $He^+$ modulation, is caused by a wave of the $He^+$ branch, $\theta$ decreases with time from $3\pi/2$ to $\pi/2$. An ion detector with a pitch angle view of ~90° will record a large flux when the detector points $\theta^*+\varphi$, where $\theta^*$ is the value of $\theta$ around which the ions are phase bunched. $\theta^*$ decreases with time. For a detector spinning with the satellite such as ICE on GEOS-1, the observed modulation frequency should approximate $F+F_b-F_s$ (for ions detected once per phase bunching period) or $F+2F_b-F_s$ (for ions detected twice per phase bunching period), where $F_s$ and $F_b$ are the satellite spin and phase bunching frequencies respectively. Here the authors suppose the spin of the satellite is right-hand. If the interacting wave is associated with the $H^+$ branch, a similar analysis can be undertaken, remembering $\theta^*$ is an increasing function of time. Thus, the authors see that the observed modulation frequencies are the result of coupling amongst F, $F_s$ and $F_b$.

If F had been reported with the ion modulation, it could estimate $F_b$ from the observations, and then compare this result with results from the simulation or analytical expressions. From the observations on ATS-6 and GEOS-1, $F_b$ may be of the order of 0.2-0.4 Hz, i.e. the bunching period may be 2.5-5 seconds. This agrees with the simulation results. However, to confirm this, more observations are needed.

## 5.6 CONCLUSION

The motion of test ions (E~1-10ev) have been considered in the ion-cyclotron electromagnetic wave field in the earth's multicomponent plasma. Through the evolution of the wave-particle interaction the authors have studied the basic characteristics and time behaviours of a periodical transverse phase bunching. This phase bunching process is due to transverse wave electric and Lorentz forces. The transverse phase bunching energises and accelerates the ions mainly in perpendicular directions. If $B_w$~1-5nT, $E_o$~1-10ev and F is near $F_c$ ($He^+$), then $E_{max}$ of the $He^+$ ions can reach ~100ev. The frequency of phase bunching $F_b$ is approximately $|kv_{\|o} + (\Omega-\omega)|/2\pi$ and the simulation has confirmed this frequency. The simulation also shows the pitch angle of the ions is ~80° for small or medium initial pitch angle cases. When $\alpha_o$ becomes large, the pitch angle for bunched ions may reach ~90°. The authors have used these results to explain the heating of thermal $He^+$ ions and suprathermal $He^+$ modulation observed in the geostationary region of the magnetosphere. The authors have also shown that only $He^+$ ion species can be accelerated effectively by the observed ion-cyclotron waves through the phase bunching. Both the pitch angle and kinetic energy of the ions will affect the observation of the suprathermal flux. The observed phase relation confirms that the suprathermal ion modulation is caused by the phase bunching process. It has also been pointed out that the observed modulation frequencies are a consequence of the coupling of F, $F_s$ and $F_b$.

## 5.7 ACKNOWLEDGMENTS

This work is supported by Research Grants from the Australian Research Council and the University of Newcastle.

## 5.8 REFERENCES

Berchem, J. *and* Gendrin, R. (1985). Nonresonant interaction of heavy ions with electromagnetic ion cyclotron waves. *Journal of Geophysical Research 90*:10945-10960.

Fraser, B.J. and McPherron, R.L. (1982). Pc1-2 Magnetic pulsation spectra and heavy ion effects at synchronous orbit: ATS 6 results. *Journal of Geophysical Research 87*:4560-4566.

Gendrin, R. *and* Roux, A. (1980). Energization of helium ions by proton-induced hydromagnetic waves. *Journal of Geophysical Research 85*:4577-4586.

Hu, Y.D., Fraser, B.J. *and* Olson, J.V. (1990). Amplification of Pcl-2 waves along a geomagnetic field line. In: Burns. G.B. (Ed.). *ANARE Research Notes Number 80.*

Matsumoto, H. (1979). Nonlinear whistler-mode interaction and triggered emission in the magnetosphere: a review. In: Palmadesso, P. J. and Papadopoulos, K. (Eds). *Wave Instabilities in Space Plasmas*. Pp. 163-190.

Matsumoto, H., Hashimoto, K. *and* Kimura, I. (1974). Two types of phase punching in the whistler mode wave-particle interaction. *Journal of Geomagnetism and Geoelectricity 26*:365-383.

Mauk, B.H. *and* McPherron, R.L. (1980). An experimental test of the electromagnetic ion cyclotron instability within the earth's magnetosphere. *Physics Fluids 23*:2111-2127.

Mauk, B.H., McIlwain, C.E. *and* McPherron, R.L. (1981). Helium cyclotron resonance within the earth's magnetosphere. *Geophysical Research Letters 8*:103-106.

Mauk, B.H. (1982). Electromagnetic wave energization of heavy ions by the electric 'phase bunching' process. *Geophysical Research Letters 9*:1163-1166.

Roux, A., Perraut, S., Rauch, J.L., de Villedary, C., Kremser, G., Korth, A. *and* Young, D.T. (1982). Wave-particle interaction near $\Omega_{He}$+ observed on board GEOS 1 and 2, 2, generation of ion cyclotron waves and heating of $He^+$ ions. *Journal of Geophysical Research 87*:8147-8190.

Young, D.T., Perraut, S., Roux, A., de Villedary, C., Gendrin, R., Korth, A., Kremser, G. *and* Jones, D. (1981). Wave-particle interactions near $\Omega_{He}$+ observed on GEOS 1 and 2, 1, propagation of ion cyclotron waves in $He^+$-rich plasma. *Journal of Geophysical Research 86*:6755-6772.

# 6. A PERSONAL COMPUTER INDUCTION MAGNETOMETER SYSTEM FOR RECORDING GEOMAGNETIC PULSATIONS

B.J. Fraser, P.W. McNabb, F.W. Menk and C.L. Waters
Department of Physics
University of Newcastle
NSW 2308
Australia

ABSTRACT

An economical and compact two component induction magnetometer system to record geomagnetic pulsations in the 0.003 - 0.4 Hz frequency range has been designed around a PC XT/AT microcomputer. The heart of the system is a plug in card containing 8 bit A/D converters, buffer storage and a crystal controlled clock (1 in $10^7$ accuracy) for timing purposes. Using advanced signal processing techniques, data compression and preprocessing of the digital data are carried out. This low-cost system may be a viable alternative to a fluxgate instrument in many Solar Terrestrial Energy Program (STEP) ground-based applications.

## 6.1 INTRODUCTION

Geomagnetic pulsations in the Pc1-5 frequency bands (2mHz - 5 Hz) observed at the earth's surface generally result from hydromagnetic wave resonances or ion-cyclotron waves originating in the magnetosphere (Orr 1973, Hughes 1983). The temporal and spatial structure of these waves, as seen on the ground, is of great importance in determining their source and propagation mechanisms and complement spacecraft observations (Perraut et al. 1984, Fraser et al. 1989).

At low and equatorial latitudes ground-based observations provide the only means of studying ULF wave phenomena, while at middle and high latitudes they augment spacecraft studies and allow a close monitoring of boundary regions such as the plasmapause and polar cusp. For these reasons many experiments over recent years have involved the recording of Pc1-5 pulsations using networks of stations spread in latitude and longitude or both. They may be local, covering distances as short as 100 km (Baransky 1985), or spread across continents (Hayashi 1981). With the approach of the Solar Terrestrial Energy Program (STEP) and the International Solar Terrestrial Physics Program (ISTP) in the 1990s, it is important that there is adequate ground-based ULF wave information available from networks for correlation with spacecraft particle and wave data.

The availability of reasonably priced microcomputers has provided an economical means of gathering multicomponent magnetometer data and also undertaking preprocessing functions where desirable. Such a system has been developed for the world-wide recording of ELF

Schumann resonances by Sentman (1987). The University of Newcastle has recently developed an induction magnetometer system around a PC XT/AT computer for recording Pc1-5 geomagnetic pulsations at low, middle and high latitudes. Five of these systems have been operating successfully in the field over the last year in Eastern Australia, and more recently at the Australian Antarctic station at Macquarie Island and the New Zealand station, Scott Base. Systems will be installed at the remaining ANARE stations, Casey, Davis and Mawson, in the 1990-91 austral summer.

## 6.2 THE INDUCTION MAGNETOMETER

A block diagram of the induction magnetometer system is shown in Figure 1. The system is based on an earlier CP/M based digital induction magnetometer for recording Pc1 pulsations (Fraser and McNabb 1985). The present system records the two horizontal components of the earth's magnetic field. For simplicity, only one channel of the system is shown. A three component system is under development to provide recording of the vector field.

The sensor coils comprise two bobbins, each 24 cm in length, with total windings of 190K - 300K turns, depending on the application. A core of reannealed grain-oriented mu-metal 1.22 m long threads the coils. A calibration winding of 3K turns is also wound on the bobbins. Typical inductance and resistance of the coil system are 17 kH and 48 kΩ respectively.

The preamplifier and main amplifier (Figure 2) are housed along with the coils in a weatherproof cylindrical polythene container. The low noise preamplifier input stage is an Intersil 7652 chopper amplifier operating in the non-inverting mode to minimise noise and has a gain of 1000. The output is also fed back to the calibration coil, through a buffer amplifier, to provide negative magnetic feedback. This allows the frequency response of the coil/preamplifier to be programmed by the feedback network, and stabilises the operating point against thermal, mechanical and ageing effects. The preamplifier is followed by a fourth order Bessel high pass filter. The main stage amplification includes precision offset compensation. This is followed by a high-pass filter to remove any unwanted low frequencies, and then a balanced output buffer stage which drives a 50-100 m cable and feeds the signal back to the PC recording system. The frequency and phase response of the coil-preamplifier system are plotted in Figure 3. It can be seen that the 3dB bandwidth is 10 mHz - 0.4 Hz. The response has been rolled off slowly between 3-10 mHz so that Pc5 and Pi2 signals can also be observed without overloading the preamplifier. Thus the effective bandwidth response to natural geomagnetic signals is 3 mHz - 0.4 Hz, covering the Pc2-Pc 5 bands and part of the Pc1 band. Noise of the entire detector system is less than two least significant bits of the digitiser over the range 0.3 - 0.03 Hz. The phase response lies between $\pm 40°$. The wide and flat frequency and phase responses for this induction system are achieved essentially through the optimisation of the frequency dependent magnetic feedback process. Component changes may be made to alter this bandwidth which, in the present case, has been chosen to study low latitude Pc2-4 pulsation signals.

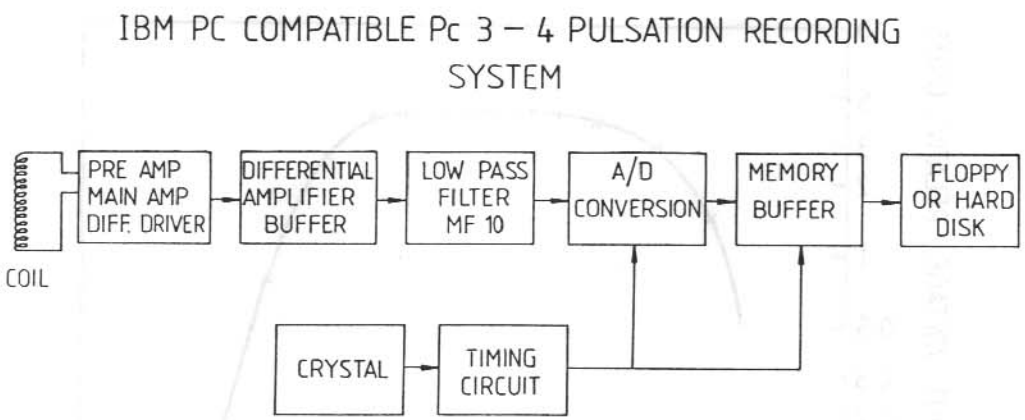


Figure 1. Block diagram of the recording system. Only one signal channel is shown.

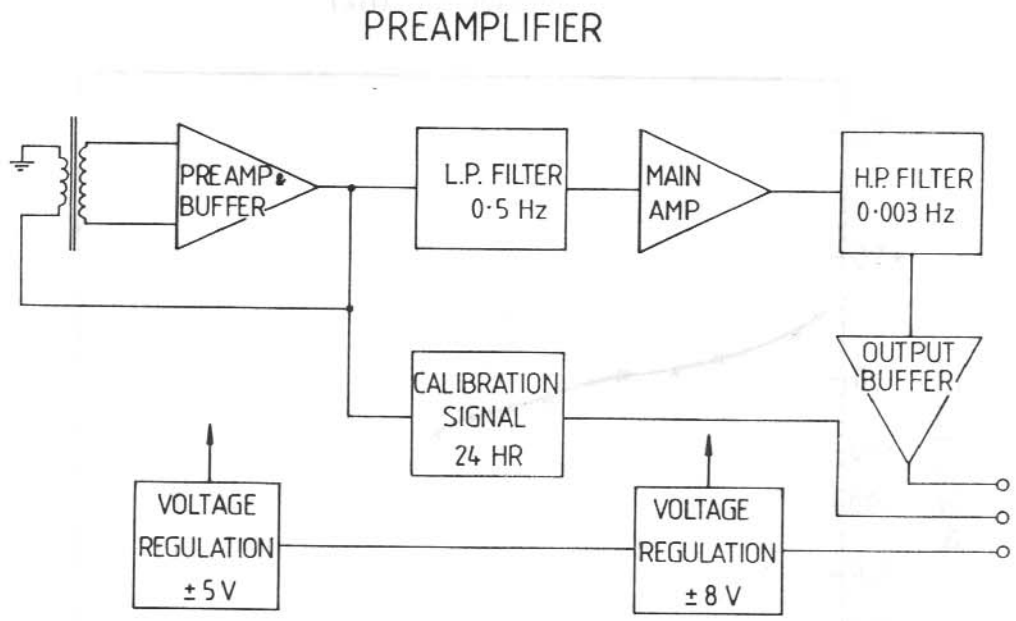


Figure 2. Block diagram of the induction coil preamplifier system.

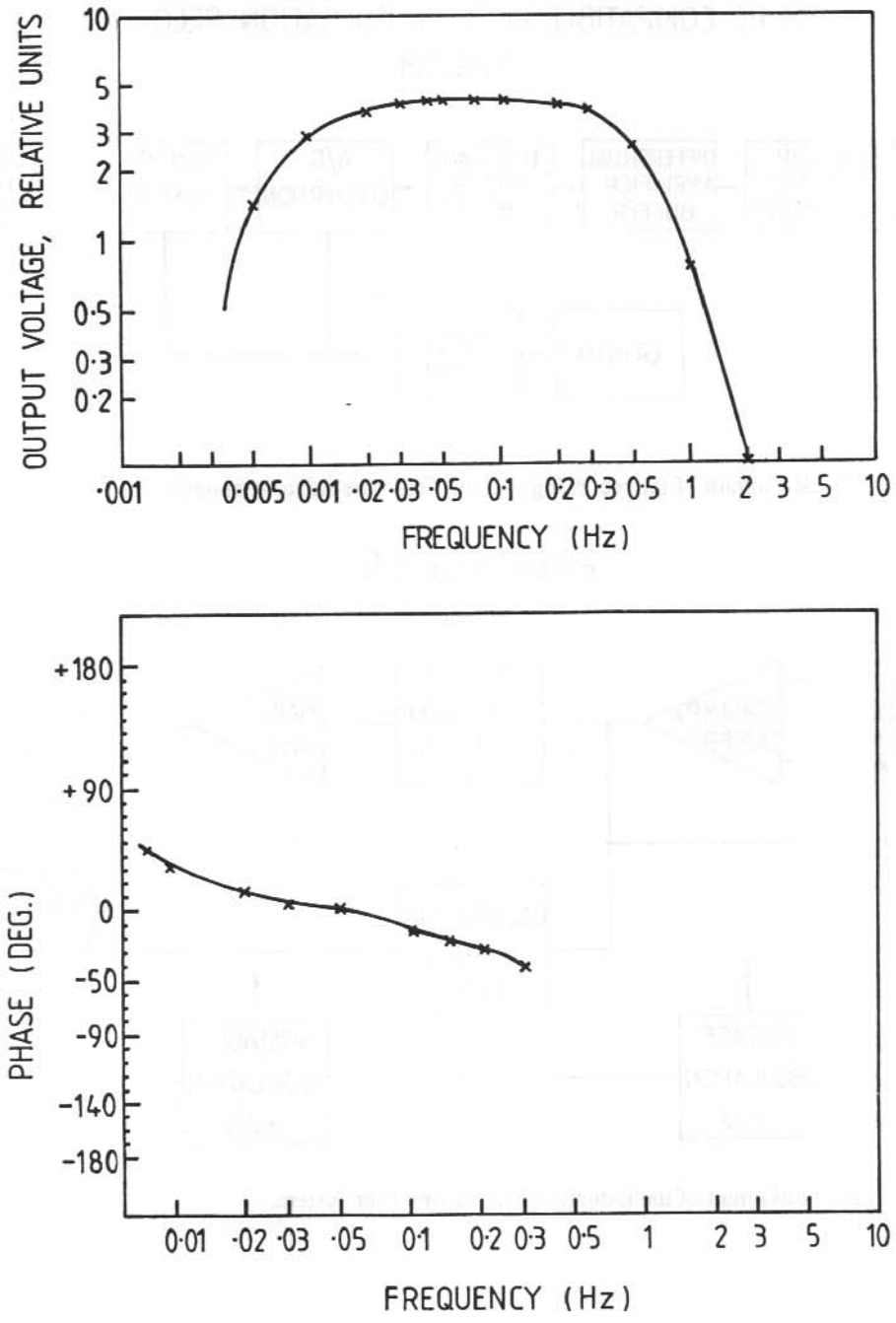


Figure 3. The frequency and phase response of a coil-preamplifier system to record Pc2 5 pulsations.

The analogue-to-digital conversion is carried out in a custom-made card which plugs in to a full slot in any compatible XT/AT microcomputer. This card includes input filtering, A/D conversion and buffer memory storage; all being controlled by the computer clock. The heart of this clock is a crystal-oven unit providing an accuracy of 1 in $10^7$ or about 1 ms per day. The custom made card is the furthest card in the computer in Figure 4, where the crystal oven is easily seen. The signal from each amplifier data channel is fed into a differential input amplifier which provides substantial immunity from any common mode noise induced in the cables to the sensors. A low-pass digital filter removes frequencies above the Nyquist in order to prevent aliasing. The cut-off frequency of this filter changes automatically when the sampling rate is altered. Data can be digitised at any rate from 0.125 $s^{-1}$ up to 16 $s^{-1}$ in binary steps. The present systems use 8 bits but a 12 bit version is under development. In order to obtain acceptable time resolution for Pc3-4 interstation phase studies at middle and low latitudes a data rate of 2 $s^{-1}$ is presently used, providing a Nyquist frequency of 1 Hz. The minimum detectable magnetic field variation is 0.03 nT and the dynamic range of the amplifiers is 48 dB. With 8 bit digital conversion this relates to 0.03 nT $bit^{-1}$ and a full scale signal of 8 nT. The memory buffer size can be set over a binary range of 128 - 1024 bytes and at a sample rate of 2 $s^{-1}$ these limits correspond to 64 s and 8 min 20 s respectively. Data are downloaded onto a 360 Kb or 1.2 Mb floppy disk but hard disk, streaming tape or other media may be used to increase storage capacity. A 1.2 Mb disk lasts 21 days when recording two component data continuously at 0.25 $s^{-1}$.

### 6.3 TIMING SYSTEM

The heart of the recording system is an oven controlled crystal with an accuracy of 1 in $10^7$ which drives the computer clock. This clock is used to synchronise all processes, including A/D conversion and frequency and amplitude calibrations. The clock can be reset to zero error directly from the keyboard in 1 s and 1/100 s steps by comparison with WWV, a local time standard transmission (VNG) or a telephone time service. These reference signals are accessed via the parallel printer port. During the recording process time is displayed continuously on the VDU screen in hours, minutes, seconds and hundredths of seconds, along with the file information.

### 6.4 CALIBRATION

It is very important to maintain a daily monitor of the amplitude and phase responses of each signal channel of the recording system, especially for polarisation and interstation phase studies. An inbuilt calibrator provides four frequencies over the signal response band. An automatic 24 hour calibration may be initiated at a preset time providing the sequence of four frequencies. The calibrator may also be operated manually by keyboard commands. The frequency and duration of these signals are controlled by the digitisation rate.

Figure 4. A PC-XT computer with the custom-built A/D card shown in the background.

## 6.5 DISPLAY FUNCTIONS

One advantage of the PC-based data logging system is its ability to display two channels of current buffer data in the form of amplitude waveforms and fast Fourier transform (FFT) derived power spectra. This allows even inexperienced operators to check data quality visually during the recording process. The amplitude-time records are displayed in the upper and middle left panels for the north-south and east-west components respectively. The corresponding FFT spectra are shown on the two right-hand panels.

A sample screen page is shown in Figure 5. The bottom left-hand corner shows the clock error display in units of 1/100 s. The marker can be reset to zero error by comparison with an external time standard using the keyboard. A threshold detector is available to allow for the storage and/or printing of memory buffer loads with a peak spectral power density above a preset level. This is indicated by the dashed horizontal lines on the spectra in Figure 5. For continuous recording the level is set at zero. A typical Pc3-4 train of pulsations recorded at Gloucester and a power spectrum of part of this record are shown in Figure 6.

The keyboard functions available include the following:

- Dump screen to printer
- Turn FFT off/on
- Reset the internal clock in 1 s and 1/100 s steps
- Set threshold detection level
- Close files and exit

The software incorporates an automatic reboot system in case of power failure. The crystal controlled inbuilt clock incorporates a backup battery supply and will run for several hours during power failure, without loss of time or date information.

## 6.6 PREPROCESSING

The use of a standard PC microcomputer provides computing power which is available for preprocessing. With the use of multiple disk/tape recording media the preprocessed data may be separately recorded for later specialised analysis.

Although the preprocessing options have not been utilised to their fullest extent at our field stations, the following are possible:

- Calculation of the 2 x 2 spectral matrix in the plane of the earth's surface or the 3 x 3 matrix for vector fields. This can save later processing or provide data compression when a high sample rate is required.

- Polarisation parameters. The ellipticity, azimuth and sense of rotation may be calculated from the spectral matrix.

- High-speed data capture. The system may be programmed to operate in a high sample rate mode for a limited time, dependent on storage availability.

- Remote operation. By connection to telephone lines via a modem, it is possible to remotely monitor the operation of the system and reset software controlled recording and preprocessing parameters. Data may also be transferred back to the home laboratory.

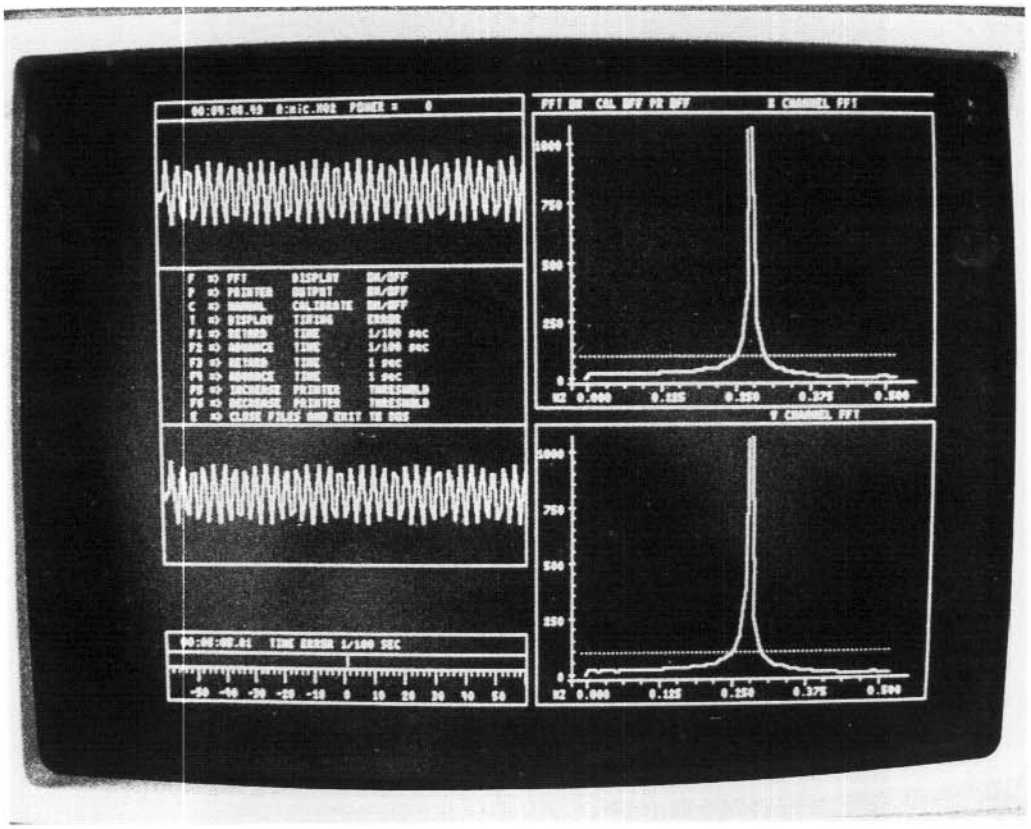

Figure 5. A VDU screen display of the buffer data. Two amplitude-time waveforms and FFT spectra are shown for a f~0.25 Hz test signal.

Date = 08/09/89 Use arrow keys to move marker Segment start date 08/09/89
Time = 08:52:19.00 Press <enter> to select Segment start time 09:33:21.00
File Name = A:/Glo.Dat Press F2 to exit segmentation
Component = X

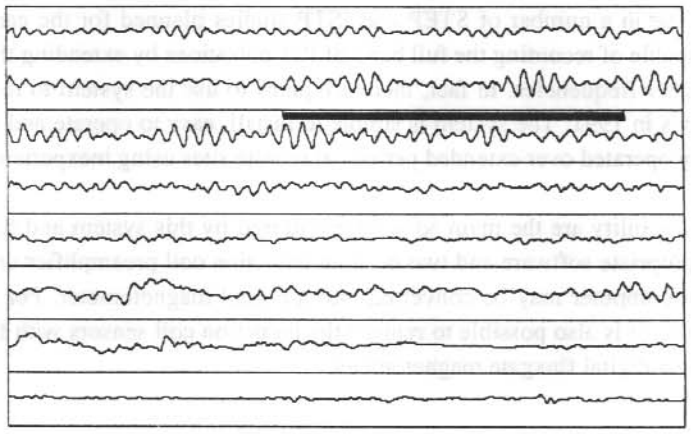

Filename: A:/Glo.Dat Single Component Power

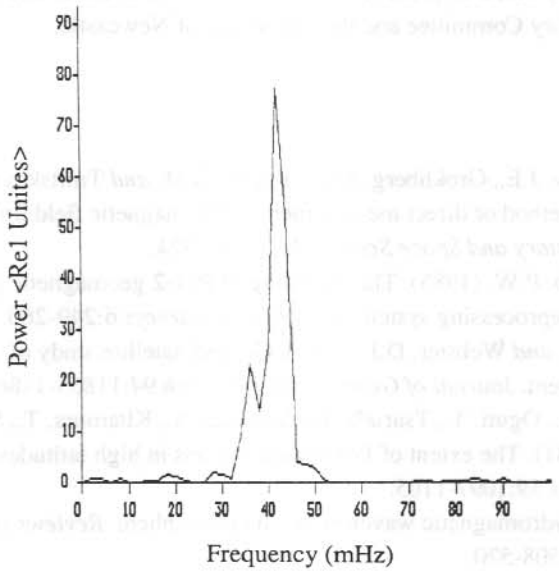


Figure 6. (Upper). A typical daytime amplitude time record of the N-S component at Gloucester, NSW. The predominant signals are Pc3-4 pulsations. The sample rate is 2 s and each panel covers 512 points or 17 min 04 s. The amplitude range of each panel is ± 2.9 nT. (Lower). A power spectrum of the segment of signal spanning 256 points and indicated by the thick line in the upper figure.

## 6.7 CONCLUSIONS

The PC-XT/AT based microcomputer induction magnetometer provides a simple, flexible and inexpensive system for recording Pc2-5 geomagnetic pulsations at ground-based stations. It will be of particular use in a number of STEP and ISTP studies planned for the early 1990s. The system is also capable of recording the full band of Pc1 pulsations by extending the preamplifier bandwidth to higher frequencies. In fact, there are plans to use the system to record the lower ELF band at Davis in 1991. The system is simple to install, easy to operate and reliable. It has been successfully operated over extended periods at remote sites using inexperienced operators.

Simplicity and flexibility are the main advantages offered by this system and for the cost of a plug-in card, appropriate software and two or three induction coil preamplifier units, a standard PC-XT/AT microcomputer may be converted into a digital magnetometer. For improved low frequency response, it is also possible to replace the induction coil sensors with fluxgate heads, thereby providing a digital fluxgate magnetometer.

## 6.8 ACKNOWLEDGMENTS

This work is supported by research grants from the Australian Research Council, the Australian Antarctic Science Advisory Committee and the University of Newcastle.

## 6.9 REFERENCES

Baransky, L.N., Borokov, J.E., Grokhberg, M.B., Krylor, S.M. *and* Troitskaya, V.A. (1985). High resolution method of direct measurement of the magnetic field lines' eigen frequencies. *Planetary and Space Science 33*:1369-1374.

Fraser, B.J. *and* McNabb, P.W. (1985). The recording of Pc1-2 geomagnetic pulsations using a microprocessor preprocessing system. *Geophysical Surveys 6*:249-260.

Fraser, B.J., Kemp, W.J. *and* Webster, D.J. (1989). Ground-satellite study of a Pc1 ion cyclotron wave event. *Journal of Geophysical Research 94*:11855-11863.

Hayashi, K.,Kokubun, S., Oguti, T., Tsuruda, K., Machida, S., Kitamura, T., Saka, O. and Watanabe, T. (1981). The extent of Pc1 source regions in high latitudes. *Canadian Journal of Physics 59*:1097-1105.

Hughes, W.J. (1983). Hydromagnetic waves in the magnetosphere. *Reviews of Geophysics and Space Physics 21*:508-520.

Orr, D. (1973). Magnetic pulsations within the magnetosphere: a review. *Journal of Atmospheric and Terrestrial Physics 35*:1-50.

Perraut, S., Gendrin, R., Roux, A., *and* Villedary, D. (1984). Ion cyclotron waves: direct comparison between ground-based measurements and observations in the source region. *Journal of Geophysical Resesearch 89*:195-202.

Sentman, D.D. (1987). PC monitors lightning worldwide. *Computers in Science 1*:25-30.

# 7. CORRELATION OF CUSP REGION Pc 3 PULSATIONS WITH SOLAR WIND PARAMETERS

J. V. Olson, P.E. Struckman and C.P. Price
Geophysical Institute and Physics Department
University of Alaska
Fairbanks Alaska 99775-0800
USA

ABSTRACT

This is a summary of an investigation of the correlation between the properties of Pc 3 pulsations detected at cusp latitudes and solar wind parameters. Three months of (wintertime) data from Cape Parry, Canada, located at cusp latitudes, were correlated with solar wind parameters. The correlation between Pc 3 power levels and solar wind parameter states were found to be time dependent, reflecting the temporal variability of the solar wind. Using multivariate statistical techniques, three states of the solar wind were identified exhibiting strong, moderate and no correlation with Pc 3 power. The states were differentiated principally by the solar wind velocity and the interplanetary magnetic field (IMF) By. In a study of large amplitude Pc 3 pulsations a correlation was found between the frequency of the pulsation and the magnitude of the IMF with $f = (5.8 \pm 0.2)|B|$. This correlation was found only for intervals in which the IMF cone angle was less than 45°. Pc 3 power levels were also found to correlate with the velocity of the solar wind for velocities above about 400 km $s^{-1}$; no correlation was found for velocities below 400 km $s^{-1}$.

## 7.1 INTRODUCTION

Pc 3 pulsations are nearly ubiquitous in the dayside magnetosphere and have been found to be especially prominent near the dayside cusp where their presence has been suggested as a primary cusp diagnostic (Troitskaya 1985, Olson 1986). Several studies of Pc 3-4 pulsations at high latitude ground sites have found correlation with the pulsation energy and the state of the solar wind (Lanzerotti et al. 1986, Yumoto et al. 1987, Wolfe et al. 1987). Generally, these studies have found that the Pc 3 power correlates best with the velocity of the solar wind, Vs, and secondarily with various components of the interplanetary magnetic field (IMF). The correlation with solar wind velocity has been used to suggest the importance of the Kelvin-Helmholtz instability in generating the pulsations or enhancing their transmission through the magnetopause. In a series of studies using satellite data, Engebretson et al. (1986, 1987, 1990) find Pc 3 pulsations to be present in the low altitude cusp irrespective of its latitude as it moves with magnetic activity and presumably in response to the IMF. They find correlation of Pc 3 power with the IMF Bx, or what is equivalent, the cone angle, $\theta_{XB}$, and velocity Vs. They also find the frequency of packets of Pc 3 radiation in the cusp to be directly proportional to the magnitude of the IMF.

It has been known for some time that the characteristics of pulsations detected at mid-latitudes in the Pc 3-4 band are correlated with parameters in the solar wind (Greenstadt et al. 1981 and Odera 1986 for reviews). The earliest studies were conducted with data from mid-latitude pulsation stations and two prominent correlations were found. First, the Pc 3 signal strength is correlated with the solar wind velocity and second, the frequency of Pc 3 waves are correlated with the magnitude of the interplanetary magnetic field (Gul'elmi 1974, Greenstadt et al. 1981, Odera 1986 and references therein). Correlations of mid-latitude pulsation amplitude in the Pc 3-4 band with the IMF cone-angle, $\theta_{XB} = \cos^{-1}(B_x/|B|)$, are often detected (Greenstadt and Olson 1976, Russell et al. 1983, Verö and Holló 1978, Yumoto 1985, Engebretson et al. 1986) and sometimes not detected (Wolfe et al. 1987, Yumoto et al. 1987).

The correlation between Pc 3 frequency and the magnitude of the IMF led Gul'elmi (1974) to suggest a source of ion-cyclotron waves in the upstream solar wind with energy provided by beams of protons reflected from the bow shock. Smith et al. (1985) and Sentman et al. (1981) have shown that ion-cyclotron waves can be generated in the foreshock plasma. Amplitude correlations with solar wind velocity have led to the suggestion by many authors that the source of the Pc 3 energy might be associated with the generation of Kelvin-Helmholtz waves at the magnetopause although, as Greenstadt et al. (1981) point out, there are many other mechanisms which might account for a dependence of magnetospheric parameters on solar wind velocity. The cone-angle correlation has been used as evidence for the beam-driven ion-cyclotron wave source (Gul'elmi 1974) as well as for a possible indication of waves generated at the earth's bow shock (Greenstadt 1972, Greenstadt et al. 1981). While, as it shall be seen in the results of this study, the correlations described above are found also in the Pc 3 radiation near the cusp, there is, as yet, no understanding as to why there should be a simultaneous connection of Pc 3 properties with three such disparate sources.

## 7.2 CORRELATION OF AVERAGE Pc 3 POWER WITH THE SOLAR WIND

During the winter of 1983-84 as part of a campaign to study cusp pulsations, induction coil and fluxgate magnetometer data were taken at Cape Parry, Canada. Located at geomagnetic latitude 73.8° and longitude 270.5° with L = 14.2, Cape Parry was chosen since the magnetospheric cusp is expected to be overhead at noon, magnetic local time. Details of the instrumentation are given in Olson (1986). As Figure 1 shows, the onset of daytime pulsations at Cape Parry normally begins about four hours before local noon and ceases about four hours after noon. It is this daytime increase in Pc 3 pulsations that is associated with the presence of the magnetospheric cusp overhead. The evidence given by Troitskaya (1985) and Olson (1986) supports the suggestion that enhanced Pc 3 power at these latitudes does indicate the presence of the cusp. However, without correlated optical and/or satellite data the exact location of the cusp is not known. Based upon this association the authors have chosen to use the hourly averaged power in the Pc 3 band for an eight hour interval centered on local noon as an indication of cusp activity. Tonegawa et al. (1985) have pointed out that cusp associated Pc 3 are observed at the ground over a wider azimuthal range than the cusp is expected to cover. It is recognised that this

selection criterion will include some time intervals during which the cusp is not present overhead, but without an independent diagnostic there was no information which would allow a different selection criterion.

Using the criterion above, daytime data spanning three wintertime months, 1 November 1983 through 31 January 1984, were chosen for analysis. Hourly averaged values of solar wind parameters for the same period were obtained from the National Space Science Data Center and contained data taken by IMP 8 and ISEE 3 spacecraft. The hourly averaged Pc 3 power was correlated with hourly averaged solar wind velocity, Vs, the GSM components of the interplanetary magnetic field (IMF), the field magnitude |B|, the cone angle $\theta_{XB} = \cos^{-1}(B_x/|B|)$, the azimuthal angle $\phi = \tan^{-1}(B_z/B_y)$, and the geomagnetic indices Kp and Dst. Local daytime data (1600-2400 hours UT) from 1 November 1983 to 31 January 1984 were analysed for pulsations. An estimate of the Pc 3 power was made by averaging the spectral estimates in the band between 25-50 mHz over one hour. The average Pc 3 power was correlated with hourly averaged solar wind data provided by the NSSDC. Full solar wind coverage was available for 337 of the hours used in the three month period examined, approximately 46% coverage.

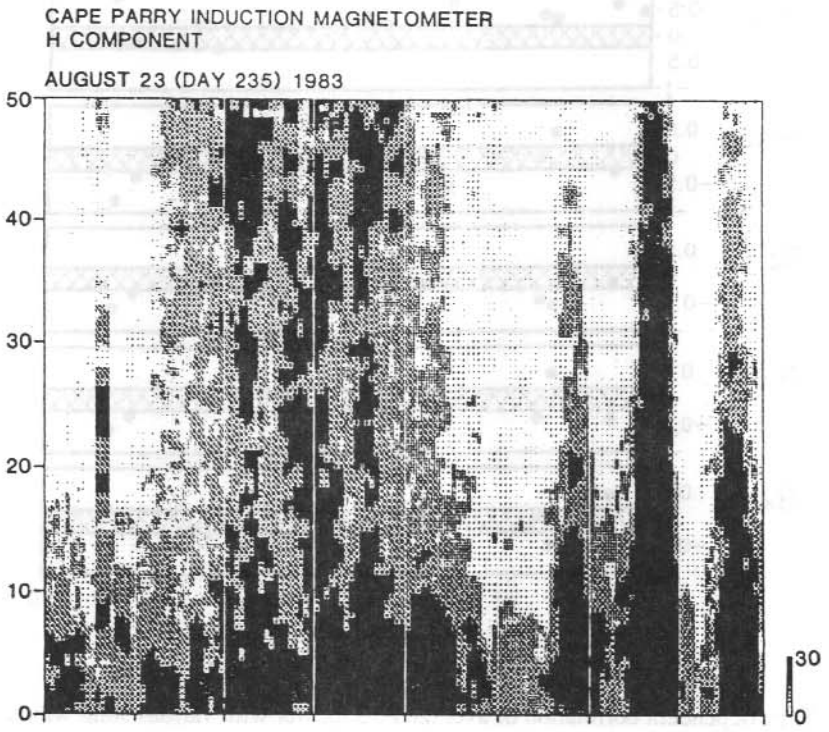


Figure 1. A spectrogram of the variations characteristic of dayside activity at Cape Parry. Notice that activity in the Pc 3-4 band begin several hours prior to noon and continue for several hours afterward (Olson 1986).

The difference in correlation between intervals lead to the study of the level of correlation as a function of time. The correlation coefficients of Pc 3 power with the GSM components of the IMF $B_x$, $B_y$, $B_z$, the total field magnitude |B|, the solar wind velocity, Vs, IMF cone angle $\theta_{XB}$, and the geomagnetic indices Kp and Dst have been plotted as a function of time in Figure 2.

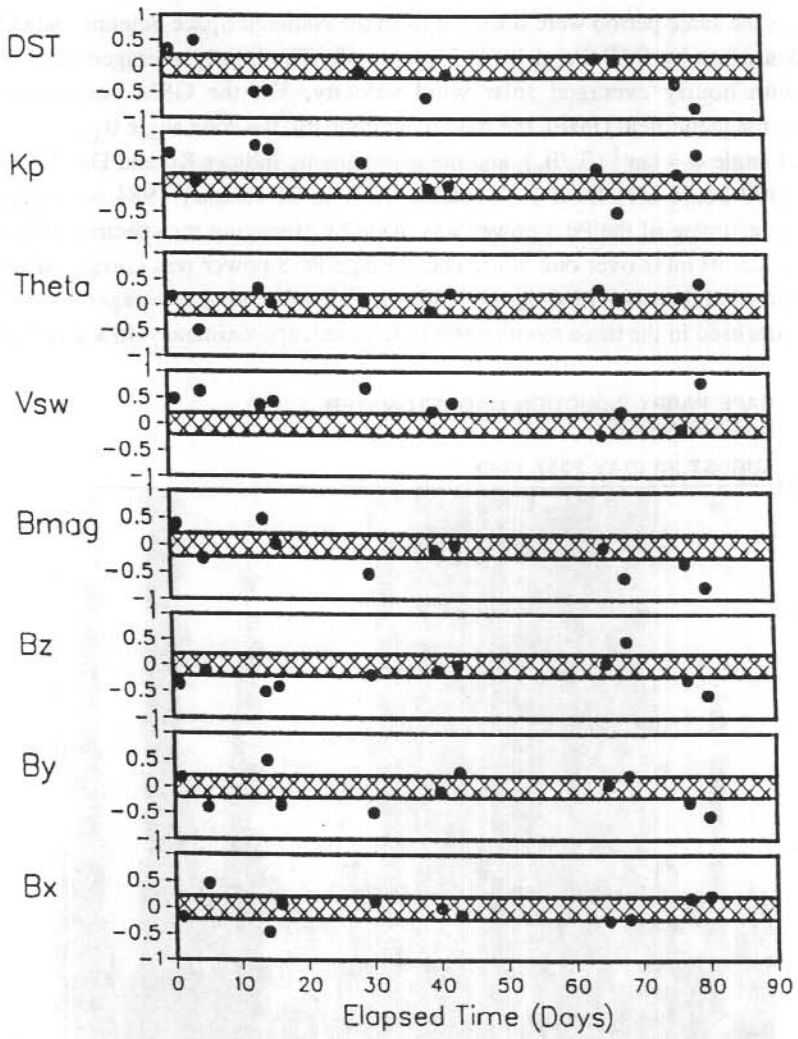


Figure 2. Time dependent correlation of average Pc 3 power with various solar wind and magnetospheric parameters. The shaded region represents the limits of no significant correlation.

The shaded region represents the level of correlation expected from statistical noise. Each point represents the correlation computed over a five day interval. This was done by creating time series for each of the hourly averaged solar wind parameters using the data available during the daytime hours of five consecutive days. These time series were then correlated with a time series of hourly averaged power from the same interval. Note that the solar wind velocity showed the strongest correlation, but that even it did not correlate significantly during some periods of time. Clearly the correlations are a function of time.

The next goal was to try and specify the characteristic states of the solar wind which produced the different levels of correlation with Pc 3 power at the cusp. The data were sorted into groups using K-means clustering (Johnson and Wichern 1982, or Dixon 1985). The data were assembled into cases which included the one hour averages of Pc 3 power, solar wind velocity and the three components of the IMF. (Both cartesian and spherical representations of the field were used with similar results). In this Euclidean 5-space distances between cases were calculated and a visual output was produced (not shown here). By inspection of this output three dominant groups were identified. With this information multiple discriminant analysis was used to sort the cases into two, three and four cases. The technique used is described in Jennrich (1977). Again, three clusters were indicated and excellent agreement was found between the assignments of cases to clusters between these two methods. These clusters have been used to identify states of the solar wind which provide the correlations observed.

The statistical characteristics of the three clusters are given in Table 1. Cluster 1 is characterised by a high solar wind velocity; a rather even distribution in Bx, By and |B|, and cone angle $\theta_{XB}$ and positive Bz and the azimuthal angle $\phi$. Cluster 2 is characterised by a moderate solar wind velocity; relatively low power; a generally negative Bx, positive By; even distribution in Bz, |B|, and $\phi$; and $\theta_{XB} < 90°$. Cluster 3 is characterised by low to moderate solar wind velocities; generally positive Bx and negative By and Bz; an even distribution in |B|; $\theta_{XB} < 90°$ and $\phi < 10°$.

Table 2 shows the correlations of Pc 3 power within each cluster. Cluster 1 exhibits positive correlation between Pc 3 power and solar wind velocity, By and $\theta_{XB}$; and negative correlation with Bx, Bz and $\phi$. In cluster 2, Pc 3 power correlates positively with the solar wind velocity and By; negatively with Bz and $\phi$. Finally, cluster 3 shows negative correlation with solar wind velocity and no other significant correlations. A stepwise multiple linear regression analysis was used to order the importance of the solar wind parameters in producing the separation between the clusters. The ordering was found, in order of importance, to be: the solar wind velocity, Vs, By, $\phi$, $\theta_{XB}$, Pc 3 power, Bz and Bx.

With this analysis the authors have gained some insight into the time dependence of the level of correlation between cusp Pc 3 pulsation power and the solar wind parameters. As the characteristics of the solar wind change with time the level of correlation can be expected to vary. Most of the variation in correlation can be explained by identifying three states of the solar

wind which lead to intervals of strong correlation, moderate correlation or no correlation. The solar wind parameters are ordered in importance with Vs, By, $\phi$ and $\theta_{XB}$ most important. Strong correlation (cluster 1) is obtained for a high velocity solar wind with negative By and positive Bz. The weakest correlation is obtained with low solar wind velocities, and negative By and Bz.

One should be careful in the interpretation of these results since as the solar wind changes the sources of Pc 3 power may change, the character of the transmission path may change and the cusp may move with respect to the observer. Some of the variability, especially in the dependence on By and Bz, may be produced by changes in location of the cusp with respect to the ground observer. This shall be discussed further in the summary section.

## 7.3 CORRELATION OF PEAK Pc 3 POWER WITH THE SOLAR WIND

It is the authors view that the Pc 3 pulsations observed in cusp regions at the ground have their sources external to the magnetosphere. With the data set described above, the second phase of the investigation was an attempt to separate out explicit dependences which might give some clues as to the generation of Pc 3 and the control of the passage of Pc 3 power into cusp region.

For this study, in order to be more certain of including cusp pulsations, Cape Parry induction coil magnetometer data taken between 1920 and 2120 UT (an hour on each side of magnetic local noon) were analysed. The peak power and the corresponding frequency for each interval were found. This selection criterion was introduced to help eliminate intervals when the cusp was not nearby and to focus on the properties of the largest Pc 3 signals, presumably coherent wave packets. Again, hourly averages of the interplanetary magnetic field and solar wind velocity were obtained from the National Space Science Data Center

Table 1. Sample statistics of the parameters contained in the 3 principal clusters in the correlation of average Pc 3 power with solar wind parameters. Each cluster represents a distinct state of the solar wind.

Mean $\pm$ Standard Deviation

| Parameter | Cluster 1 | Cluster 2 | Cluster 3 |
|---|---|---|---|
| Pc3 Power (dB) | 69.56 $\pm$ 8.84 | 53.85 $\pm$ 6.16 | 63.58 $\pm$ 11.00 |
| $B_x$ (nT) | 1.18 $\pm$ 4.55 | -2.65 $\pm$ 2.91 | 2.74 $\pm$ 2.89 |
| $B_y$ (nT) | -1.68 $\pm$ 3.23 | 4.78 $\pm$ 3.11 | -3.79 $\pm$ 3.36 |
| $B_z$ (nT) | 1.73 $\pm$ 1.98 | 0.48 $\pm$ 2.86 | -3.05 $\pm$ 2.40 |
| $V_{sw}$ (km/s) | 630 $\pm$ 60 | 422 $\pm$ 48 | 414 $\pm$ 63 |
| $B_{mag}$ (nT) | 6.19 $\pm$ 1.82 | 7.16 $\pm$ 2.24 | 6.94 $\pm$ 2.88 |
| $\theta$ | 83.1° $\pm$ 49.3° | 115.1° $\pm$ 26.2° | 64.6° $\pm$ 24.4° |
| $\phi$ | 86.0° $\pm$ 96.4° | 8.0° $\pm$ 53.3° | -135.9° $\pm$ 39.1° |

Table 2. Correlations of average Pc 3 power with solar wind parameters within each cluster identified in this study. See text for details.

| Parameter | Correlation Coefficient Cluster 1 | Cluster 2 | Cluster 3 |
|---|---|---|---|
| $B_x$ | -0.57 | -0.11 | -.016 |
| $B_y$ | 0.55 | 0.22 | -0.02 |
| $B_z$ | -0.50 | -0.36 | 0.03 |
| $V_{sw}$ | 0.21 | 0.22 | -0.31 |
| $B_{mag}$ | -018 | 0.15 | 0.15 |
| $\theta$ | 0.52 | 0.19 | 0.15 |
| $\phi$ | -0.52 | -0.44 | -0.09 |
| $\sigma = \frac{1}{\sqrt{N}}$ | 0.140 | 0.110 | 0.11 |

Pc 3 peak power is plotted versus solar wind velocity in Figure 3. For solar wind velocities less than 400 km $s^{-1}$, there is no apparent relationship between amplitude and solar wind velocity. However, for solar wind velocities greater than 400 km $s^{-1}$, the two quantities appear highly correlated. A least squares fit was calculated to the data for solar wind velocities in excess of 400 km $s^{-1}$. This line was found to be $P = 0.0421 * V_s + 31.4$, where P is the power in decibels and $V_s$ is the solar wind velocity in km $s^{-1}$. The linear correlation was quite high, $r = 0.83$, compared to the level of significance $\sigma = 0.19$. The ratio of variance explained by the linear fit to the total variance was found to be $r^2 = 0.69$.

An interesting feature of this plot is that for solar wind velocities below ~ 400 km $s^{-1}$, the Pc 3 power does not appear to correlate with the velocity. This is suggestive, since for the magnetopause to be unstable with respect to the Kelvin-Helmholtz instability, the relative velocity between the plasmas on either side of the boundary must exceed a critical velocity. This critical velocity is dependent on the ambient magnetic field and the density through the Alfvén velocity, and on the angle between the relative velocity and the ambient field (Southwood 1968). However, a number of the properties of the shock, magnetosheath and magnetosphere depend upon velocity and it may be possible to explain Pc 3-Vs correlations without reference to the Kelvin-Helmholtz instability.

Satellite studies by Engebretson et al. (1986) found evidence that the frequency of Pc 3 detected in the cusp region by a low-altitude satellite was proportional to the magnitude of the IMF. The data near local noon was used to test for the same relationship in this data. The least squares fit between the frequency and the magnitude of the IMF was found by constraining the line to pass through the origin. This led to the relationship $f = (5.8 \pm 0.2) * |B|$, in good agreement with the result of Engebretson et al. (1986): $f = 5.88 * |B| + 0.0013$. The linear correlation coefficient was found to be $r = 0.99$, and $r^2 = 0.99$. This is the line plotted in Figure 4.

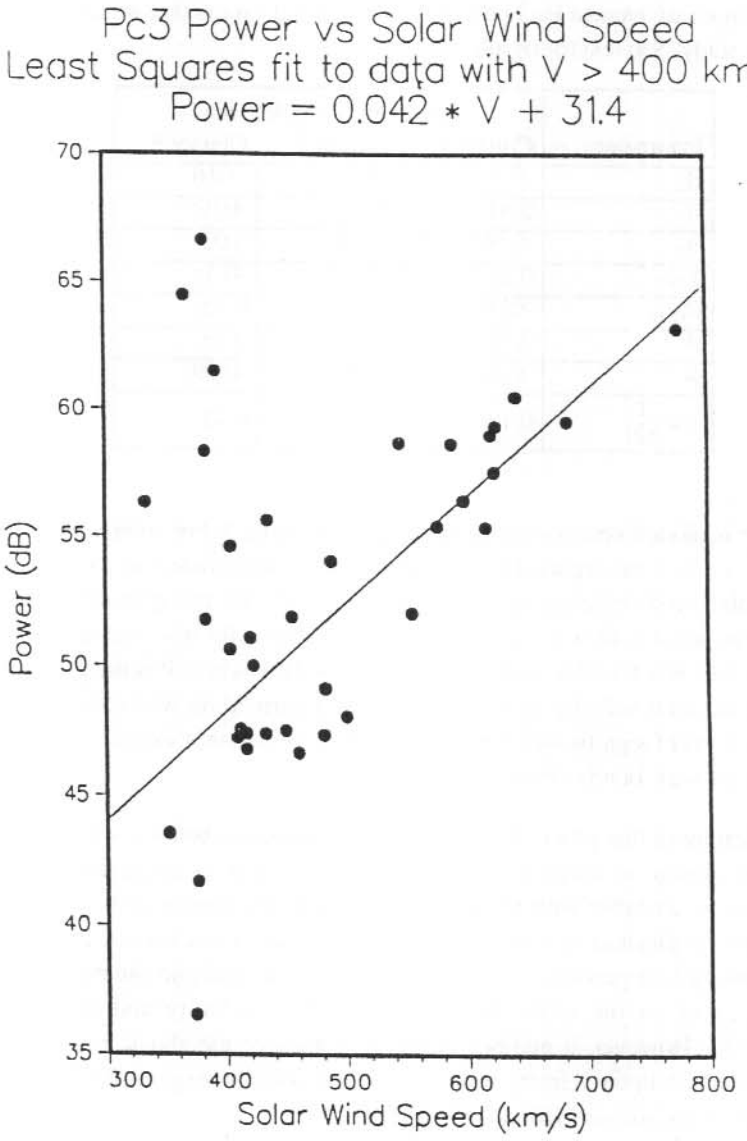


Figure 3. Peak Pc 3 power versus solar wind speed. Note the linear correlation with velocity above the 400 km $s^{-1}$ threshold.

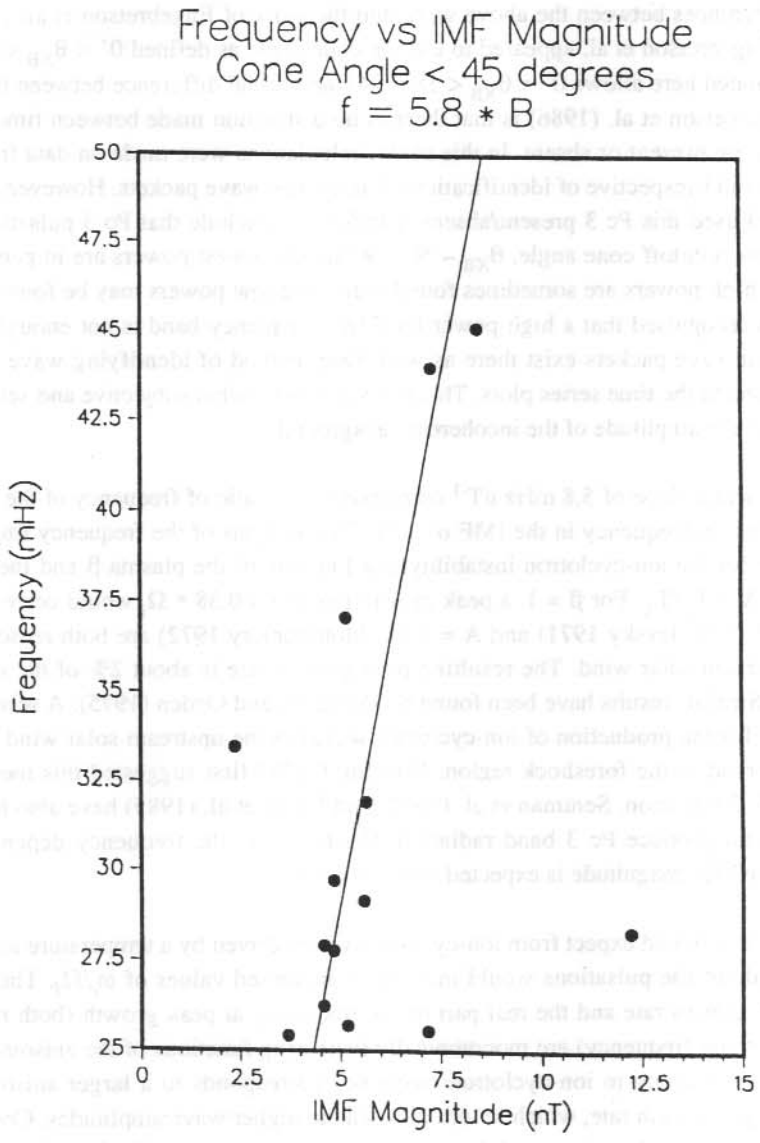


Figure 4. The frequency of Pc 3 pulsations detected near local noon versus the magnitude of the IMF for times when $\theta_{XB} < 45°$.

Several differences between the above work and the work of Engebretson et al. (1986) should be noted. Engebretson et al. appeared to use the cone angle as defined $0° < \theta_{XB} < 90°$ whereas the data scanned here allows $0° < \theta_{XB} < 180°$. An additional difference between this study and that of Engebretson et al. (1986) is that there is no distinction made between times when Pc 3 pulsations were present or absent. In this study, calculations were made on data filtered for the frequency band irrespective of identification of individual wave packets. However, Engebretson et al. (1986) used this Pc 3 present/absent criterion to conclude that Pc 3 pulsations were not present above a cutoff cone angle, $\theta_{XB} \sim 50°$. While the lowest powers are in general found at $\theta_{XB} \sim 90°$, high powers are sometimes found there, and low powers may be found at low cone angles. It is recognised that a high power level in a frequency band is not enough to establish that coherent wave packets exist there as well. One method of identifying wave packets is to visually examine the time series plots. This method is somewhat subjective and selection would depend upon the amplitude of the incoherent background.

The experimental slope of 5.8 mHz $nT^{-1}$ corresponds to a ratio of frequency of the pulsations to the ion-cyclotron frequency in the IMF of 0.38. The real part of the frequency ($\omega_r$) at the peak growth rate for the ion-cyclotron instability is a function of the plasma $\beta$ and the temperature anisotropy $A = T_\perp/T_\parallel$. For $\beta = 1$, a peak growth rate at $f = 0.38 * \Omega_i$ would correspond to $A \sim 1.75$. $\beta = 1$ (Kovalevsky 1971) and $A = 1.75$ (Montgomery 1972) are both reasonable values for the upstream solar wind. The resulting peak growth rate is about 2% of the ion-cyclotron frequency. Similar results have been found by Davidson and Ogden (1975). A second source of free energy for the production of ion-cyclotron waves in the upstream solar wind is the proton beams observed in the foreshock region. Gul'elmi (1974) first suggested this mechanism as a source of Pc 3 radiation. Sentman et al. (1981) and Smith et al. (1985) have also found that the instability can produce Pc 3 band radiation. Furthermore, the frequency dependence of the waves on the IMF magnitude is expected to be $f \sim 6 * |B|$.

In addition, one would expect from ion-cyclotron waves driven by a temperature anisotropy that the amplitude of the pulsations would increase at increased values of $\omega_r/\Omega_i$. This is expected because the growth rate and the real part of the frequency at peak growth (both normalised to the ion-cyclotron frequency) are monotonically increasing functions of the anisotropy. A larger ratio of real frequency to ion-cyclotron frequency corresponds to a larger anisotropy, which implies a larger growth rate, which in turn may lead to higher wave amplitudes. Consequently, a weak correlation is then expected between the frequency normalised to the ion-cyclotron frequency and the amplitude of the wave. The correlation is expected to be weak since the ion-cyclotron instability is convective. So, the wave amplitude is dependent on both the size and the anisotropy of the source region. Although not shown here, a weak correlation has been found in this data between frequency normalised to the ion-cyclotron frequency and the amplitude of the wave, as expected by waves generated by the ion-cyclotron instability driven by a temperature anisotropy. However, the number of cases begins to dwindle and the statistical significance of the result is not high.

## 7.4 DISCUSSION

While the total winter-time cusp region data set was found to exhibit a weak correlation between Pc 3 power and solar wind velocity, and no correlations with the components of the IMF, smaller intervals were discovered which showed both strong and weak correlations with these parameters. One principal result of this study is the recognition that the state of the solar wind, and therefore the correlation level with Pc 3 pulsations, is time dependent. This recognition allows one to understand other apparently conflicting reports. For example, the cone angle correlation found by some investigators and not found by others as mentioned in the authors introduction. Of course, the variability of the solar wind has been recognised since the earliest studies were performed on spacecraft able to measure solar wind properties. Nevertheless, studies continue to be published which make use of only very limited data sets.

It has been found that peak Pc 3 power near the noon-time cusp to be highly correlated with the solar wind velocity for velocities greater than about 400 km $s^{-1}$. For lower velocities, the power appears to be uncorrelated. These characterstics suggest that the Kelvin-Helmholtz instability may be important to either the production or modification of Pc 3 pulsations. It is necessary for distinguishing between mechanisms which may be sources of pulsations and those which modify the pulsations by changing the characteristics of the transmission of the pulsations to the observer. In this case, the velocity correlation and its apparent threshold are properties inherent in the Kelvin-Helmholtz instability operating at the magnetopause. However, there are other mechanisms through which such a velocity correlation could be produced apart from the Kelvin-Helmholtz instability. Greenstadt et al. (1981) point out that the velocity effect could be produced in three ways. First, the higher Mach number flow associated with high velocities could produce a more complex shock structure and change the location of the shock with respect to the magnetopause. This would change the distance over which waves would need to be convected in the magnetosheath before they intercepted the magnetopause. Second, shock produced variations which might propagate upstream in a relatively slow flow might be convected downstream in a faster flow adding to the spectrum impacting the magnetosphere. Third, high solar wind streams are known to increase magnetospheric activity which might appear in band-pass filtered data sets as Pc 3 band energy. Any or all of the above mechanisms might occur alone or in combination with changes in the Kelvin-Helmholtz instability.

For cone angles $\theta_{XB} < 45^{\circ}$ it was found that $f \simeq 5.8 * |B|$, is in agreement with the analysis of cusp pulsations by Engebretson et al. (1986). Similar relationships have been found in investigations of mid-latitude data (Greenstadt et al. 1981 and Odera 1986). It has been found that this proportionality of 5.8 mHz $nT^{-1}$ is consistent with what would be expected from ion-cyclotron waves generated upstream of the bow shock driven either by a temperature anisotropy or by beams of protons reflected from the bow shock (Gul'elmi 1974 and Sentman et al. 1981). In addition, a weak correlation between frequency normalised to the ion-cyclotron frequency and the amplitude of the pulsations as expected by ion-cyclotron waves driven by a temperature anisotropy is found. Other factors which occur in the upstream flow may produce the correlation

with $\theta_{XB}$. The change in the nature of the shock as $\theta_{XB}$ changes means that for small $\theta_{XB}$ the nose of the bow shock may be a quasi-parallel shock producing a rich magnetosheath pulsation spectrum. The flow lines leading from the nose sweep past the entire magnetopause give the largest opportunity for the transmission of pulsations to the magnetosphere or the excitation of boundary pulsations. Note that low $\theta_{XB}$ might be expected to reduce the occurrence of the Kelvin-Helmholtz instability over much of the magnetopause since the instability is least likely when the magnetic fields are parallel across the magnetopause (Lee and Olson 1980).

The relationship between frequency and IMF magnitude suggests that the ion-cyclotron instability is likely to be a major source of low cone angle Pc 3 pulsations. Similar results were obtained for cusp Pc 3 by Engebretson et al. (1986) and the correlation at lower latitudes has been well documented. The same relationship is found to occur in the upstream plasma as well (Russell and Hoppe 1981) making the association a tempting one to base a model of sources upon. Ion-cyclotron waves generated in the upstream solar wind (through protons reflected from the bow shock or through a temperature anisotropy) could account for the experimental slope.

Apart from sources of pulsation energy which might produce the correlations, it has been observed, one should also consider the transmission paths by which the pulsations reach the ground and the dependence of these paths on solar wind parameters. The transmission of ULF waves through the magnetopause has been studied by Wolfe and Kaufmann (1975). They found that the magnetospheric spectrum near the subsolar point could be explained by transmission of the magnetosheath spectrum through the magnetopause but that beyond 35° it could not. They suggested surface waves were increasingly important along the flanks of the magnetosphere. Kwok and Lee (1984) modeled the magnetopause as a rotational discontinuity that certain Alfvén and magnetosonic waves could be amplified upon transmission. Even here it is difficult to assess the importance of the magnetopause surface in modifying and in adding to the spectrum of pulsations seen within the magnetosphere.

This study confirms and extends the information known about Pc 3 at the cusp and together with results from studies at mid- and low-latitudes produces a consistent view of dependence of pulsation amplitudes on the state of the solar wind. However, it seems premature, even with the quantity of data analysed in these studies, to conclude simply that the Kelvin-Helmholtz instability or upstream waves are the clear choice as the source of ground Pc 3. Further progress will come with studies which correlate suites of ground instruments such as photometers and magnetometers. This will allow the experimenter to locate the pulsation spectrum with respect to the cusp, and with extensive correlations with low-altitude satellites which will not only locate the cusp but give a measure of the pulsation spectrum within the cusp.

## 7.5 ACKNOWLEDGMENTS

This work represents one aspect of the research carried out under grants from the National Science Foundation and from the Office of Naval Research. The authors would like to

acknowledge Dr R. Smith for his helpful comments and Dr D. Hawkins for his help in the interpretation of multivariate statistical results. J. Olson would like to thank Dr B. Fraser and Dr F. Menk for useful discussions and the use of facilities at the University of Newcastle, NSW where parts of this manuscript were prepared. Satellite data used in this work were provided by the NSSDC. Additional data were provided by Dr C.T. Russell of UCLA.

## 7.6 REFERENCES

Davidson, R.C. *and* Ogden, J.M. (1975). Electromagnetic ion cyclotron instability driven by ion energy anisotropy in high-beta plasmas. *Phys. Fluids 18*:1045.

Dixon, W.J. (Ed.). (1985). *BMDP statistical analysis software manual*. University of California Press, California.

Engebretson, M.J., Meng C.-I., Arnoldy, R.I. *and* L.J. Cahill, L.J. Jr. (1986). Pc 3 pulsations observed near the south polar cusp. *Journal of Geophysical Research 91*:8909-8918.

Engebretson, M.J., Zanetti, L.J., Potemra, T.A., Baumjohann, W., Luhr, H. *and* M.H. Acuna, M.H. (1987). Simultaneous observation of Pc 3-4 pulsations in the solar wind and in the earth's magnetosphere. *Journal of Geophysical Research 92*:10053-10062.

Engebretson, M.J., Anderson, B.J., Cahill, L.J. Jr., Arnoldy, R.L., Rosenberg, T.J., Carpenter, D.L., Gail, W.B. *and* Eather, R.H. (1990). Ionsopheric signatures of cusp latitude Pc 3 pulsations. *Journal of Geophysical Research 95*:2447-2456.

Greenstadt, E.W. (1972). Field-determined oscillations in the magnetosheath as possible source of medium-period, daytime micropulations. In: *Proceedings of Conference of Solar Terrestrial Relations, University of Calgary*.

Greenstadt, E.W. *and* Olson, J.V. (1976). Pc 3, 4 activity and interplanetary field orientation. *Journal of Geophysical Research 81*:5911-5920.

Greenstadt, E.W., McPherron, R.L. *and* Takahashi, K. (1981). Solar wind control of daytime, mid-period geomagnetic pulsations. In: Southwood, D.J. *and* Reidel, D. (Eds). *ULF Pulsations in the Magnetosphere*.

Gul'elmi, A.V. (1974). Diagnostics of the magnetosphere and interplanetary medium by means of pulsations. *Space Science Review 16*:331.

Jennrich, R.I. (1977). Stepwise discriminant analysis. In: Ralston, A. *and* Wilf, H.S. (Eds). *Statistical Methods for Digital Computers*. Wiley and Sons, New York.

Johnson, R.A., *and* Wichern, D.W. (1982). *Applied Multivariate Statistical Analysis*. Prentice-Hall, New Jersey.

Kovalevsky, J.V. (1971). The interplanetary medium. *Space Science Review 12*:187-257.

Kwok, Y.C. *and* Lee, L.C. (1984). Transmission of magnetohydromagnetic waves through the rotational discontinuity at the earth's magnetopause. *Journal of Geophysical Research 89*:10697-10708.

Lanzerotti, L.J., Maclennan, C.G. *and* Medford, L.V. (1986). Study of a Qp/GP event at very high latitudes. *Journal of Geophysical Research 91*:375-380.

Lee, L.C. *and* Olson, J.V. (1980). Kelvin-Helmholtz instability and the variation of geomagnetic pulsation activity. *Geophysical Research Letters 7*:777.

Montgomery, M.C. (1972). Average thermal characteristics of solar wind electrons. In: Sonett, C.P., Coleman, P.J. Jr. *and* Wilcox, J.M. (Eds). *Solar Wind.* National Aeronautic and Space Administration, Washington D.C..

Odera, T.J. (1986). Solar wind controlled pulsations: a review. *Reviews of Geophysics 24*:55-74.

Olson, J.V. (1986). ULF signatures of the polar cusp. *Journal of Geophysical Research 91*:10055-10062.

Russell, C.T. *and* Hoppe, M.M. (1981). The dependence of upstream wave periods on the interplanetary magnetic field strength. *Geophysical Research Letters 8*:615-617.

Russell, C.T., Luhmann, J.G., Odera, T.S. *and* Stuart, W.F. (1983). The rate of occurrence of dayside Pc 3-4 pulsations: the L-value dependence of the IMF cone angle effect. *Geophysical Research Letters 10*:663.

Sentman, D.D., Edmiston, J.P. *and* Frank, L.A. (1981). Instabilities of low frequency, parallel propagating electromagnetic waves in the earth's foreshock region. *Journal of Geophysical Research 86*:7487-7497.

Smith, C.W., Goldstein, M.L., Gary, S.P. *and* Russell C.T. (1985). Beam-driven ion cyclotron harmonic resonances in the terrestrial foreshock. *Journal of Geophysical Research 90*:1429-1434.

Southwood, D.J. (1968). The hydromagnetic stability of the magnetospheric boundary. *Planetary and Space Science 16*:587.

Tonegawa, Y., Fukunishi, H., Lanzerotti, L.J., Maclennan, C.V., Medford, L.V. *and* Carpenter, D.L. (1985). Studies of the energy source for hydromagnetic waves at auroral latitudes. In: Nagata, T. (Ed.). *Energetics and Dynamics of the Middle and Upper Atmosphere at High Southern Latitudes. Memoirs of National Institute of Polar Research 38.*

Troitskaya, V.A. (1985). ULF wave investigations in the dayside cusp. *Advances in Space Research 5*:219.

Verö, J. *and* Holló, L. (1978). Connections between interplanetary magnetic field and geomagnetic pulsations. *Journal of Atmospheric and Terrestrial Physics 40*:857-865.

Wolfe, A. *and* Kaufmann, R.L. (1975). MHD wave transmission and production near the magnetopause. *Journal of Geophysical Research 80*:1764-1775.

Wolfe, A., Kamen, E.L., Lanzerotti, L.J., Maclennan, C.G., Bamber, J.F. *and* Venkatesan, D. (1987). ULF geomagnetic power at cusp latitudes in response to upstream solar wind conditions. *Journal of Geophysical Research 92*:168-174.

Yumoto, K. (1985). Low-frequency upstream waves as a probable source of low-latitude Pc 3-4 magnetic pulsations. *Planetary and Space Science 33*:239-249.

Yumoto, K.A., Wolfe, A., Terasawa, T., Kamen, E.L. *and* Lanzerotti, L.J. (1987). Dependence of Pc 3 magnetic energy spectra at South Pole on upstream solar wind parameters. *Journal of Geophysical Research 92*:12437-12442.

## 8. AN UPDATE ON THE SUNDIAL CAMPAIGNS

P.J. Wilkinson
IPS Radio and Space Services
PO Box 1548
Chatswood NSW 2057

ABSTRACT

SUNDIAL campaigns are held every nine months and analysis of the data collected takes place after the campaigns. The primary objective of SUNDIAL is to improve the predictive capacity in the solar terrestrial environment. This note indicates where the analysis of these campaigns has reached to date.

### 8.1 INTRODUCTION

SUNDIAL is partially funded by the USA National Science Foundation and aims at producing a comprehensive understanding and an associated predictive capability for the relationships controlling the quiet and disturbed ionosphere. The key concept is coupling of energy and mass in the sun-earth system.

This broad objective is focussed in campaigns which produce data sets suitable for suitable testing state-of-the-art physical models of the ionosphere, thermosphere and magnetosphere. There have been SUNDIAL campaigns every nine months since 1986. Campaigns are scheduled in advance and normally last up to 7 days. Each campaign usually lasts between one and two weeks and to date there have been six (Table 1). During campaigns data is collected for a core data period with the incoherent radars and globally with several types of equipment, including ionosondes.

During the post-campaign analysis stage, solar surface and solar wind data are used to define the current state of the solar terrestrial medium near the earth and then the other data collected are used to describe the effects within the global ionosphere. Having established a feel for the global conditions, attention is directed at explaining the observations using first principles physical models of the ionosphere, thermospheric wind fields and the magnetosphere.

Complete models for the entire solar terrestrial environment do not yet exist, but by seeking cooperative analyses using several levels of model, it is hoped that some modelling facility will be developed.

Thus, a segment of each campaign is selected for initial intensive study. While physically interesting features immediately attract attention, intensive study implies modelling and current models require a large array of input data. This breaks the early study into a compromise

between physically interesting features, which may be analysed for their intrinsic interest, and adequate data coverage necessary for global modelling. At the heart of this process is a belief that nothing can be treated successfully in isolation from the global state.

The rest of this paper outlines work carried out so far on these campaigns and concludes with some specific examples from campaign two.

Table 1. Sundial campaigns.

| | |
|---|---|
| Campaign 1 | 5 to 13 October 1984<br>• Results and analysis complete |
| Campaign 2 | 22 September to 4 October 1986<br>• Results complete and articles are with the journal for publication in 1990 |
| Campaign 3 | 26 May to 7 June 1987<br>• will be used for modelling comparisons<br>• but solar wind data is still hard to obtain for this period |
| Campaign 4 | 14 to 22 March 1988<br>• a third equinoctial campaign<br>• a large volume of USSR data was obtained for this period |
| Campaign 4 | 4 to 14 December 1988<br>• data analysis has not started on this period |
| Campaign 6 | September 4 to 8 October 1989<br>• Planned seasonal change study<br>• includes major storm period starting 29 September |

## 8. 2 SOME RESULTS FROM THE CAMPAIGNS

Although Campaign one, 5 to 13 October 1984, encountered early organisational difficulties, a series of papers were completed in 1988 (Annals Geophysicae No. 16(1)). These papers treat general issues on predictions, types of ionospheric modelling, comparison between models and data, low and high latitude electric fields and the state of the middle and low latitude ionosphere.

The second campaign, 22 September to 4 October 1986, extended the range of topics studied by adding ionospheric trough dynamics, electric field penetration to low latitudes and thermospheric

winds. This last topic, neutral winds, was an important addition to the SUNDIAL campaigns. Direct measurements were obtained using Fabry-Perot interferometer and incoherent scatter radars. These measurements are an important link for modelling, but there is no global wind data set available. This makes any source of wind information valuable. Indirect measurements were, therefore, investigated as part of the campaign using two different analysis methods.

Indirect meridional wind estimates can be made using ionosonde data. The M(3000)F2 data are converted, using Dudeney's (1983) transformation, to give an estimate of the F region ionisation peak height.

Rishbeth et al (1978) showed that for small changes in the meridional wind, hmF2 and the wind are linearly related. Using this idea, a relationship was formulated with the FLIP ionospheric model (Richards 1990) and the relation.

$$u=(hmax - ho) / alpha$$

where u is the meridional wind speed, hmax is the F layer peak height and ho is the peak height for zero meridional wind. The value of alpha is found by running the model for a few wind speeds: say -50, 0 and +50 $ms^{-1}$. Once alpha is known, from the model, hmF2 can be calibrated to give the meridional wind velocity.

Meridional winds were estimated for the data collected and for hmF2 obtained from the International Reference Ionosphere, IRI (Miller et al. 1990). Comparison of these showed remarkable good agreement. Furthermore, comparisons with the meridional wind estimated from the HWM87 wind model (Figure 1) were also good. While these are only intercomparisons of model data with indirect data, the consistency is promising, since the IRI results directly from the CCIR M(3000)F2 maps, and there is an international wish to validate these maps independently.

An alternative modelling experiment (Sica et al. 1990) also resulted in deducing a meridional wind field. The input wind field was adjusted until the peak height of the F region electron density for a set of global stations was matched. The resultant wind field was reasonable and all stations were matched well. However, a similar experiment with no neutral wind at night produced good agreement when the protonospheric flux into the ionosphere was varied (Figure 2). Since the protonospheric flux changes needed were well within the accuracy bounds for present protonospheric flux measurements, it suggests indirect measurements of the meridional wind must be interpreted with care.

## 8.3 SUMMARY

As shown, in Table 1, there are now a number of campaigns available for study. While many of the early data collection and exchange problems have been overcome, some data sets, such as solar wind and interplanetary magnetic field measurements remain hard to obtain.

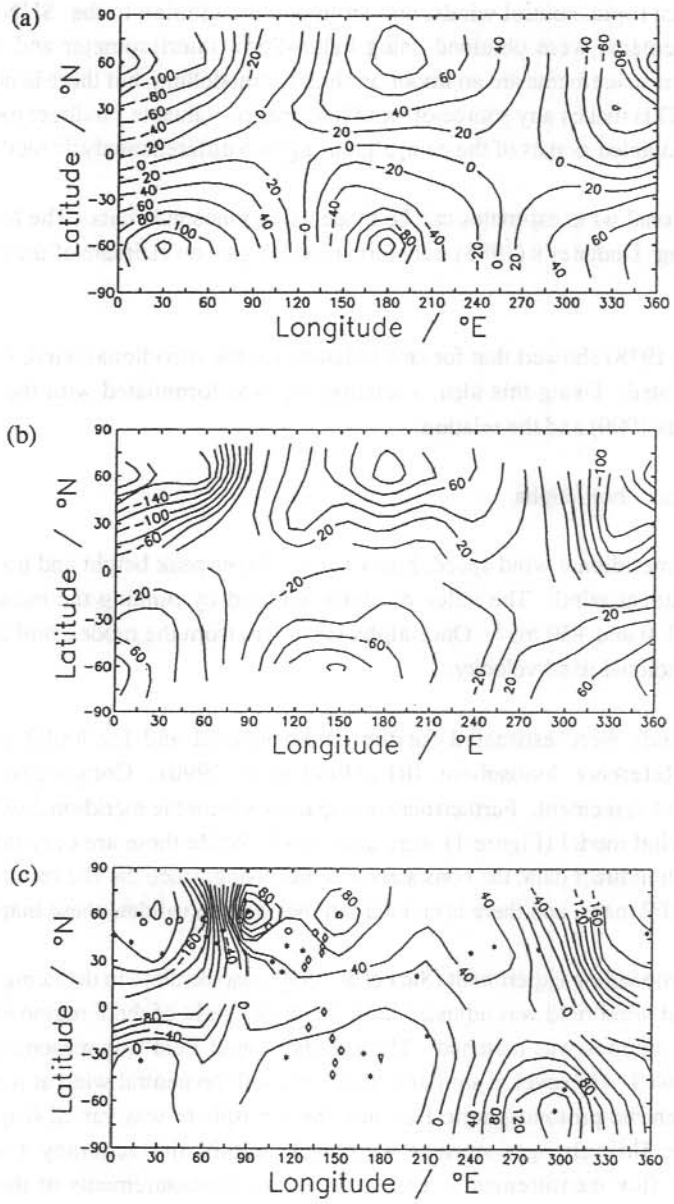


Figure 1. (a)Meridional neutral wind speed ($ms^{-1}$) from the HWM87 model. Input parameters are appropriate for 27 September 1986 at 00 UT. (b) Meridional neutral wind speed ($ms^{-1}$) derived from the IRI model calculations of hmF2. (c) Meridional neutral wind speed ($ms^{-1}$) at 00 UT derived from ionosonde hmF2 estimates made using Dudeney's transformation. The windspeeds have been averaged over 15 days, from 21 September to 5 October 1986. The symbols indicate the locations of the ionosonde stations.

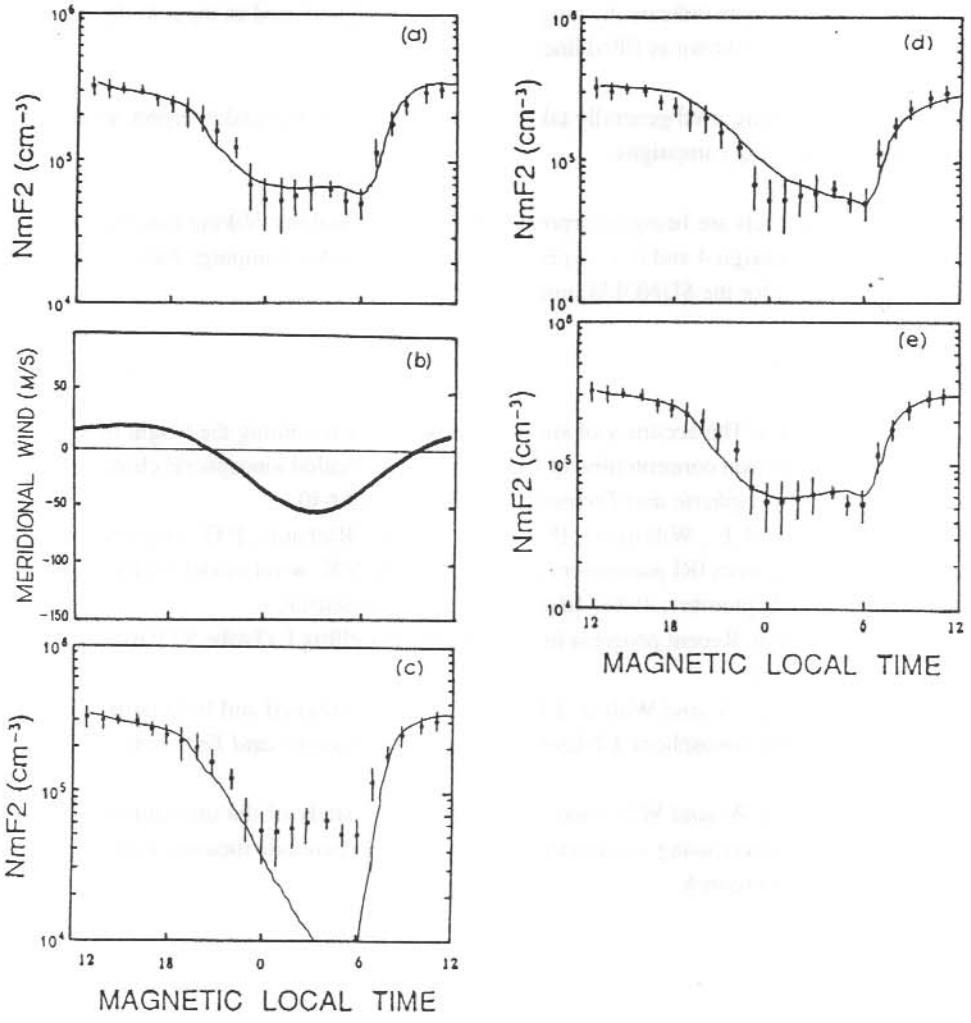


Figure 2. Several comparisons were made between data recorded at a composite station, obtained by averaging the nmF2 for a set of European stations, and results from the Utah State University ionospheric model. The model was run in four modes shown in the four frames of the figure. (a) The results for the best wind field shown in Figure 2b. (b) The wind field that fitted best. (c) The case where there is no neutral wind at night. (d) The case where there is no night neutral wind, but the protonospheric flux is adjusted until the model results fit the data best. (c) The case where half the best wind and half the best fit protonospheric flux is used.

In all cases, the error bars indicate the range of data averaged and used as input to the model. The model calculations are shown as filled lines.

The major models being used generally take considerable time to run and interpret, which will add some delay to analysing campaigns.

However, new data sets are being incorporated for some campaigns; Viking data for campaign 2; USSR data for campaign 4 and new experiments such as a rocket campaign have been proposed. The outlook is good for the SUNDIAL initiative.

## 8.4 REFERENCES


Dudeney, J.R. (1983). The accuracy of simple methods for determining the height of the maximum electron concentration of the F2 layer from scaled ionospheric characteristics. *Journal of Atmospheric and Terrestrial Physics 45*:629-640.

Miller, K.L., Hedin, A.E., Wilkinson, P.J., Torr, D.J. *and* Richards, P.G. (in press). Neutral winds derived from IRI parameters and from the HWM87 wind model for the SUNDIAL campaign of September, 1986. *Advances in Space Research.*

Richards, P.G. (1990). Recent progress in ionospheric modelling LaTrobe STP meeting, February, 1990.

Rishbeth, H., Ganguly, S. *and* Walker, J.C.G. (1978). Field-aligned and field perpendicular velocities in the ionospheric F2-layer. *Journal of Atmospheric and Terrestrial Physics 40*:767-784.

Sica, R.J., Schunk, R.W. *and* Wilkinson, P.J. (in press). A study of the undisturbed mid-latitude ionosphere using simultaneous, multiple-site ionosonde measurements. *Journal of Geophysical Research.*

# 9. OUTSTANDING SOLAR EVENTS OF THE PRESENT SOLAR CYCLE AND THEIR EFFECTS

P.J. Wilkinson[1] and P.S. McIntosh[2]

[1]IPS Radio and Space Service
PO Box 1548
Chatswood NSW 2057
Australia

[2]NOAA Space Environment Laboratory
Boulder Colorado 80303
USA

ABSTRACT

The current cycle of sunspot activity (#22) is near its maximum. Solar flare activity in 1989 produced the most serious terrestrial effects since the record cycle 19 of the International Geophysical Year (1957-58). Events in the period August-October 1989 produced relativistic particles capable of penetrating Earth's atmosphere to the ground. These rare Ground Level Enhancements (GLEs) were among the most intense on record and were a hazard for supersonic transport and spacecraft. The intense geomagnetic storm associated with unprecedented solar flare activity in March is now accepted as the cause of a major disruption to the electric power distribution system in Quebec. Aurora with this storm were reported at tropical latitudes, including the north coast of Australia. However, on other occasions during the year geomagnetic storms, particles, and ionospheric activity were poorly correlated with the sunspot number, radio flux or the frequency and intensity of the X-ray flares.

## 9.1 GENERAL STATUS OF CYCLE 22

The continuous record of sunspot cycles extends back to 1749, the beginning of continuous monthly averaged sunspot numbers. The cycle in progress in 1749 was given the serial number of #0, so that the first cycle observed in its entirety was #1. The present cycle 22 began with the minimum in the 12 month smoothed monthly sunspot number which occurred in September, 1986. The solar indices rose so quickly in 1987-1988 that this cycle very early exceeded all other recorded cycles including cycle 19 in its early stages. Until February 1990, the difference in magnitudes between cycles 19 and 22 (Figure 1) was so slight that the cycles could be considered to be essentially of the same magnitude in sunspot number or 10.7cm radio flux. Since cycle 19 produced some memorable flares with great geomagnetic storms and intense high-energy particle events it was a worry that cycle 22 might repeat this performance. Activity in 1989 proved this worry was well-founded.

Sunspots occur in groups with a bipolar magnetic-field configuration, within a larger entity considered to be an active region. Near sunspot maximum over 500 groups appear each year. Only a small fraction of these groups produce flares large enough to have effects of consequence. The active regions which produce numerous and intense X-ray flares are more frequent near sunspot maximum but do not only occur then. Energetic regions may occur within a year of sunspot minimum (Figure 2). The number of major active regions in 1989 was higher than the corresponding year of the previous solar cycle, adding to the impression that cycle 22 was especially intense.

Four active regions in 1989 produced eruptive events with terrestrial effects greater than any event of the past 30 years. Sunspot numbers and the X-ray flare activity reached high levels several times throughout the year; therefore, a high sunspot count or a high X-ray intensity is insufficient to predict the terrestrial consequences of solar activity. These events extended the range of known solar behaviour, showing that the history of solar observations is still relatively short.

The cumulative sum of all particles emitted from the sun in a given period is called the fluence. The yearly fluences of particles with energies exceeding 30 MeV for cycles 19 to 21 are shown in Figure 3 organised with respect to solar maximum. The fluence for cycle 22 (1989) is shown as a single point. Significantly, only two years exceed the 1989 level (1960 and 1972) and both years occur after their respective solar maxima. One major solar event in August 1972 contributed virtually all the cycle 20 fluence. Based on these observations, it is still possible that cycle 22 is yet to produce its most active particle events.

Relativistic particles can be produced during major solar flares. These are the highest energy particles reaching the earth from the sun and are sometimes called solar cosmic rays. Particles with relativistic energies can penetrate deep into the earth's atmosphere and may even be detected at ground level. When this happens it is called a ground level enhancement, or GLE. These are evidence of very energetic processes on the sun. Figure 4 shows the annual number of GLEs recorded since 1950 superimposed on the solar cycle. Two points are clear. First, the number of GLEs is not related closely to any particular phase of the solar cycle and second, more GLEs were observed in 1989 than in any previous years since measurements commenced.

Already cycle 22 has reached two milestones in establishing itself as a major solar cycle; it has exhibited a record rise from minimum to twelve month smoothed sunspot numbers exceeding 150 and has also produced a number of very energetic events resulting in major proton events at the earth and several geomagnetic disturbances. The rest of this paper looks at these events.

## 9.2 EVENT SUMMARY

### *9.2.1 March 1989*

On March 6, the region with serial number #5395 produced an X15 flare (that is, a flare having a peak intensity at 1 - 8 Å of 15 x $10^{-4}$ watts metre$^{-2}$) as it rotated into view from the backside of the sun. Between then and March 17, two days before rotating off the visible solar disk, an almost continuous sequence of flares occurred (Figure 5). It was this long sequence of flares that produced the record X-ray output (XR = 57) shown in Figure 2. Of all these flares, three, March 6, 10 and 17, stand out.

The March 6 flare produced protons and other energetic particles at geosynchronous orbit. Although they were slow in reaching the earth, taking between 24 and 48 hours to arrive and had a slow onset at all energies, once the particle flux increased it stayed above threshold levels until after March 17. Particle energies were, however, insufficient to cause a GLE.

Embedded in this period of high particle flux came the next major flare of interest on March 10 which further increased the geostationary orbit particle fluxes. Accompanying this flare was a very large coronal mass ejection (CME) which arrived at the earth between 60 and 72 hours after the flare. This CME caused a major geomagnetic disturbance and will be the subject of further research.

Finally, on March 17 there was a large flare of moderate duration from which protons arrived very quickly at the earth.

The period from roughly the beginning of March 1989 to the end of the first week in April was the most magnetically active period during 1989. X-ray bursts were numerous, yet only the great burst on 10 March was followed by a geomagnetic storm. The continuation of minor storms after region 5395 was gone suggests sources other than flares for the enhanced activity during most of March. Observations of coronal mass ejections and solar wind variations are incomplete and/or unavailable for this period, making it difficult at this time to explain all of the March geomagnetic activity.

### *9.2.2 June 1989*

In June the large values of monthly mean 10.7 cm flux (Figure 6a) and sunspot number (196) were higher than any since cycle 19, and were among the 13 largest monthly values ever recorded. Such high values reflect the presence of an unusual number of solar active regions, some of which were extremely large in area. Solar flares as large as X-ray class X4 occurred with these sunspots; but, none of the flare activity resulted in enhanced energetic particles or significant geomagnetic activity. Ionospheric activity measured with the Australian Regional T-index (Figure 6b) peaked in 1989 at the time of the peak radio and sunspot activity in June; but,

the ionospheric index clearly does not follow the solar flux in detail. Thus, the June activity illustrates the need to have more than the standard solar indices in order to anticipate geophysical disturbances.

*9.2.3 August 1989*

On August 16, region 5629 produced the largest X-ray flare yet recorded (Figure 7). It saturated the GOES-7 satellite monitoring system, giving an X-ray class in excess of X20 and had a duration exceeding 24 hours. In addition, the background X-ray flux at geostationary orbit was high - almost at M-class flare levels. The flare produced a sharp increase in protons with energies exceeding 80 MeV, including GeV protons which produced a GLE. However, lower energy particles were not altered significantly as the proton background flux was already high as a result of previous activity.

*9.2.4 September 1989*

Particle flux and particle energies exceeded the August activity when region 5698 produced an X9.8 (Figure 8a) flare as it disappeared beyond the west limb of the sun on September 29. This active region had begun an ominous development as early as 21 September when a pair of strong, opposite polarity sunspots began enlarging and approaching each other. Such behaviour is rare, and occurred in previous sources of high-energy particles.

Protons from the September 29 event reached Earth within 15 minutes, corresponding to speeds almost half the speed of light. The resulting ground-level particle event (GLE) was the largest to be observed in 30 years. Radiation alarms aboard the supersonic transport triggered (Figure 8b) for the first time since regularly-scheduled high-altitude flights began. Events this energetic are a major hazard for man in space.

*9.2.5 October 1989*

Solar rotation brought region 5698 back into view by October 14 as an uninteresting solar region, except for a foreboding new set of sunspots developing at its eastern extremity. This new area, region 5747, took on the characteristics of a great flare producer by October 17, prompting a forecast of a large proton event by one of the authors, while attending the third Workshop on Solar-Terrestrial Predictions at Leura NSW, Australia. Two days later, on October 19, a great proton flare indeed occurred, producing yet another GLE. Flaring continued in this region, with additional particle events, resulting in the largest ever particle fluence for a single solar active region. In fact, this one region produced more protons than were observed at Earth during all of solar cycle 20!

The great flare of October 19 was followed only a day later by a major geomagnetic storm and aurora were visible over much of Australia.

## 9.3 RETROSPECT

Geomagnetic storms are now known to have an imperfect association with large solar flares, and the events of 1989 illustrate this point very well (Table 1). Neither X-ray intensity nor particle flux from solar flares correlate perfectly with the occurrence of the major geomagnetic storms. The coronal mass ejection (CME), difficult to detect without space-borne coronagraphs, may explain most of the storms. These events produce shocks, high density clouds of material, and turbulent, twisted magnetic fields embedded in these clouds. These conditions interact with the Earth's magnetosphere, providing the physical cause of the disturbed geomagnetic conditions. The large solar flare is only sometimes associated with the CME, and then more as a consequence than a cause of the event.

The occurrence of a large flare, even when there is evidence of a CME, often is not followed by a geomagnetic storm, as this collection of events proves. Only the flares of March 10 and October 19 were followed by geomagnetic storms, and these were the only events of Table 1 that were near the centre of the solar disk. Without more detailed observations than now available, it can only assume the other, and sometimes larger, events directed CME away from Earth.

The detection of particles from flares, and the time of their arrival at Earth, are also controlled by the geometries of the solar conditions, as well as by whether particles were accelerated in the first place. Particles slowly increased after the great March 6 flare at the sun's east limb, presumably because the particles had to diffuse across field lines at the sun in order to escape along field lines that were connected to Earth. Flares in the western half of the sun more often are magnetically connected with Earth, allowing particles to reach Earth quickly. These events illustrate this statistical relationship. The occurrence of particles with energies sufficient to give GLE certainly bears no simple relationship to the conventional measures of flare magnitude. It is expected that complex factors involving the strength and geometry of solar magnetic fields determine the acceleration and release of such rare particles.

Ionospheric storms, as seen from the Australian regional ionospheric index (Figure 6b), occurred throughout the year, with storms accompanying the major magnetic storms on August 29, September 26 and October 21. The ionospheric indices, both observed and predicted, are shown in Figure 9. The two indices are generally within 20 index points of each other. The August 29 disturbance was predicted exactly. The other two major storms were incorrectly predicted. It is clear that ionospheric storms have even less dependence upon flare magnitude than on geomagnetic activity, and that factors in addition to solar parameters are essential to a successful ionospheric prediction.

## 9. 4 SUMMARY

The events of a single year in solar cycle 22 have illustrated the full range of effects solar activity can have on the Earth. New bench marks have been set on the authors knowledge of the extremes of solar activity. Man's activities were seriously disrupted by the March and October events, reminding us of our vulnerability to solar activity. With even more, and possibly greater, events yet to come from this large sunspot cycle it is imperative that solar terrestrial research and services receive full support in order to minimise the costs of solar-induced disruptions. Some skill already exists in solar-terrestrial predictions. The lessons from the 1989 events promise to bring further improvements.

Table 1. Major solar-geophysical events of solar cycle 22.

| Date 1989 | Time (UT) solar disk Location | X-ray magnitude | Proton arrival time (UT) | Start GLE (UT) | Major Geomagnetic storm |
|---|---|---|---|---|---|
| March 6 | 1345-1624 N35 E69 | X15 | gradual 08/1735 | - | |
| March 10 | 1848-2158 N31 E22 | X4.5 | increase ~11/000 | - | YES |
| March 17 | 1729-1932 N33 W60 | X6.5 | 2000 | - | |
| August 16 | 0100-0210 S16 W88 | X20 | 0130 | 0200 | |
| September 29 | 1047-1435 >W90 | X9.8 | 1200 | 1200 | |
| October 19 | 1229-2013 S27 E10 | X13 | 1315 | 1315 | YES |
| October 24 | 1739-2118 S30 W55 | X5.7 | 1830 | 1900 | |

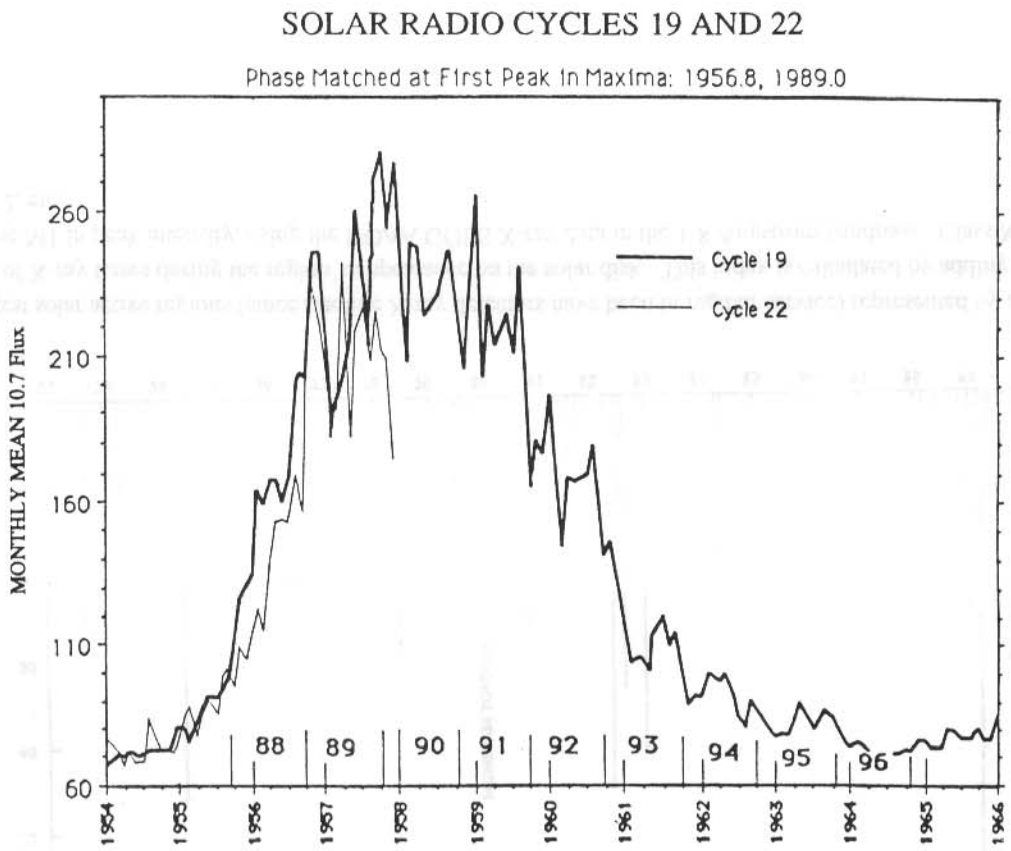


Figure 1. Monthly mean (unsmoothed) values of radio flux for cycle 22 have been overlaid with those from the only observed cycle of comparable shape and magnitude. The two cycles have been matched in phase by the best fit between details of the rising portions of their curves: solar minimum at beginning of the cycle, plateau in rise at the value of 160, and the occurrence of the first local peak at tend of the time of rapid rise. Radio flux at 10.7 cm is closely correlated with sunspot number, but more likely to be physically related to solar output.

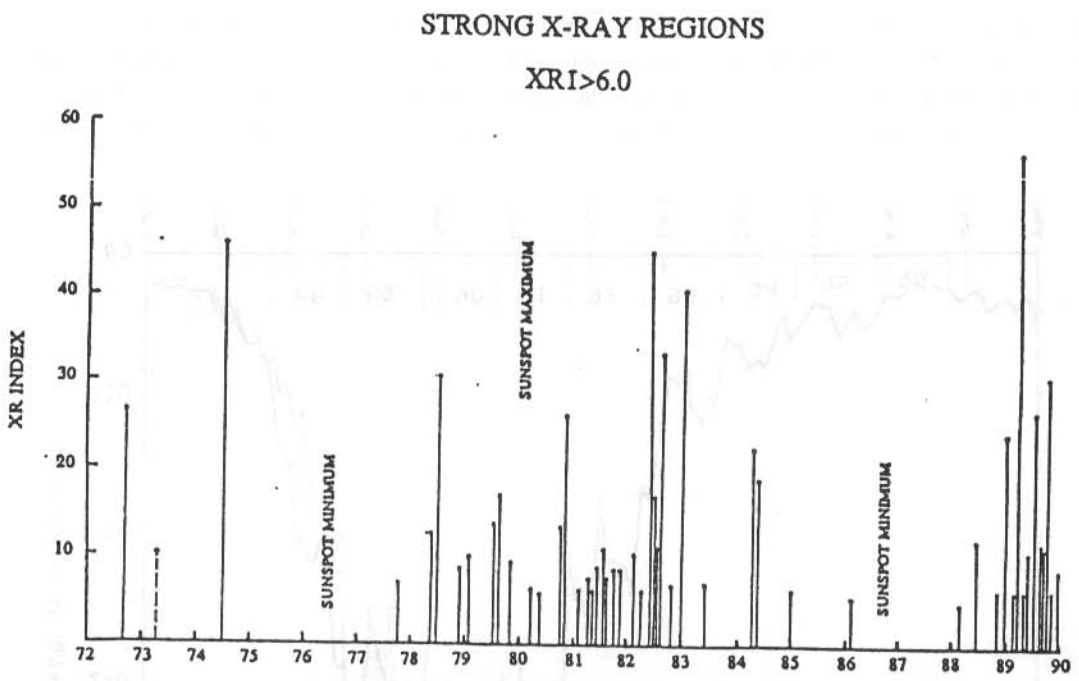


Figure 2. The strongest solar active regions (since satellite X-ray detectors have been in regular service) represented by an index derived from the total output of X-ray flares during the region's appearance on the solar disk. This index is calculated by adding the multipliers of all X-ray flares exceeding M1 in peak intensity, using the NOAA GOES X-ray data in the 1-8 Angstrom bandpass. Class M2 flares count for 0.2, Class X2 count 2, etc.

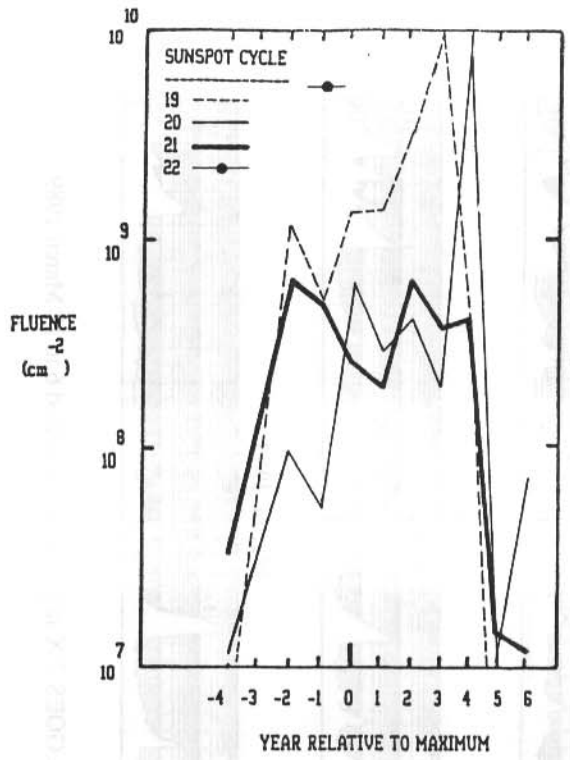


Figure 3. The yearly fluences of particles with energy in excess of 30 MeV organised with respect to solar maximum. Cycle 22 is shown as a point. Note that the vertical axis is logarithmic.

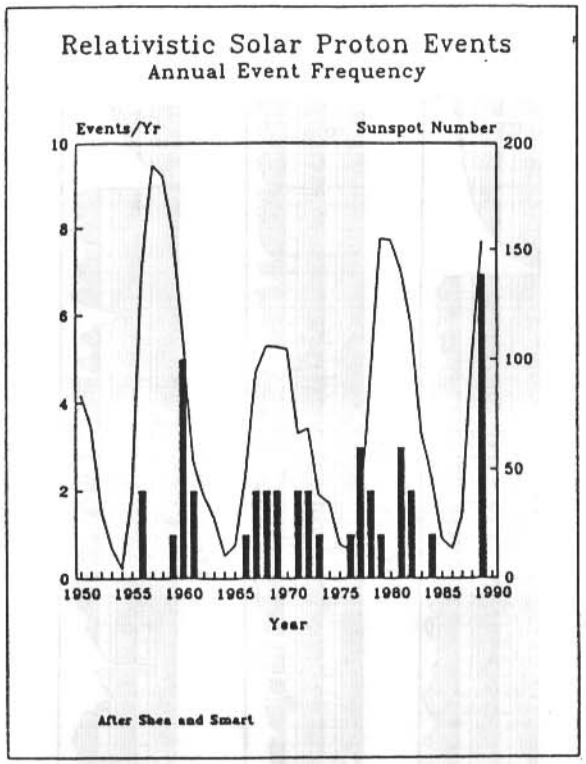


Figure 4. The number of ground level enhancements recorded annually since 1950. The sunspot cycle is added as a reference. (Figure from Shea and Smart 1989, Leura STP meeting).

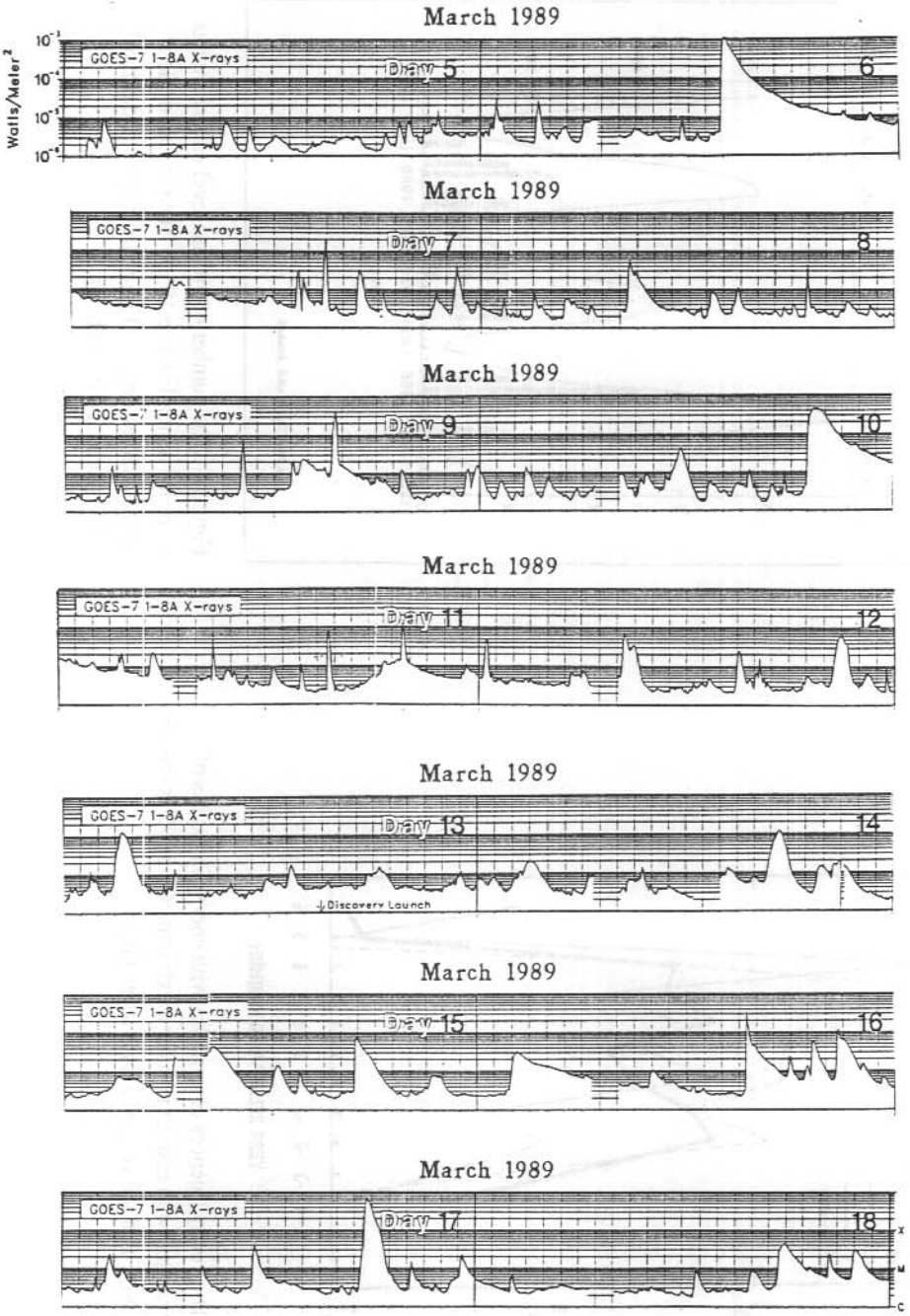


Figure 5. Time series of the GOES-7 X-ray data for the period 6 to 17 March 1989.

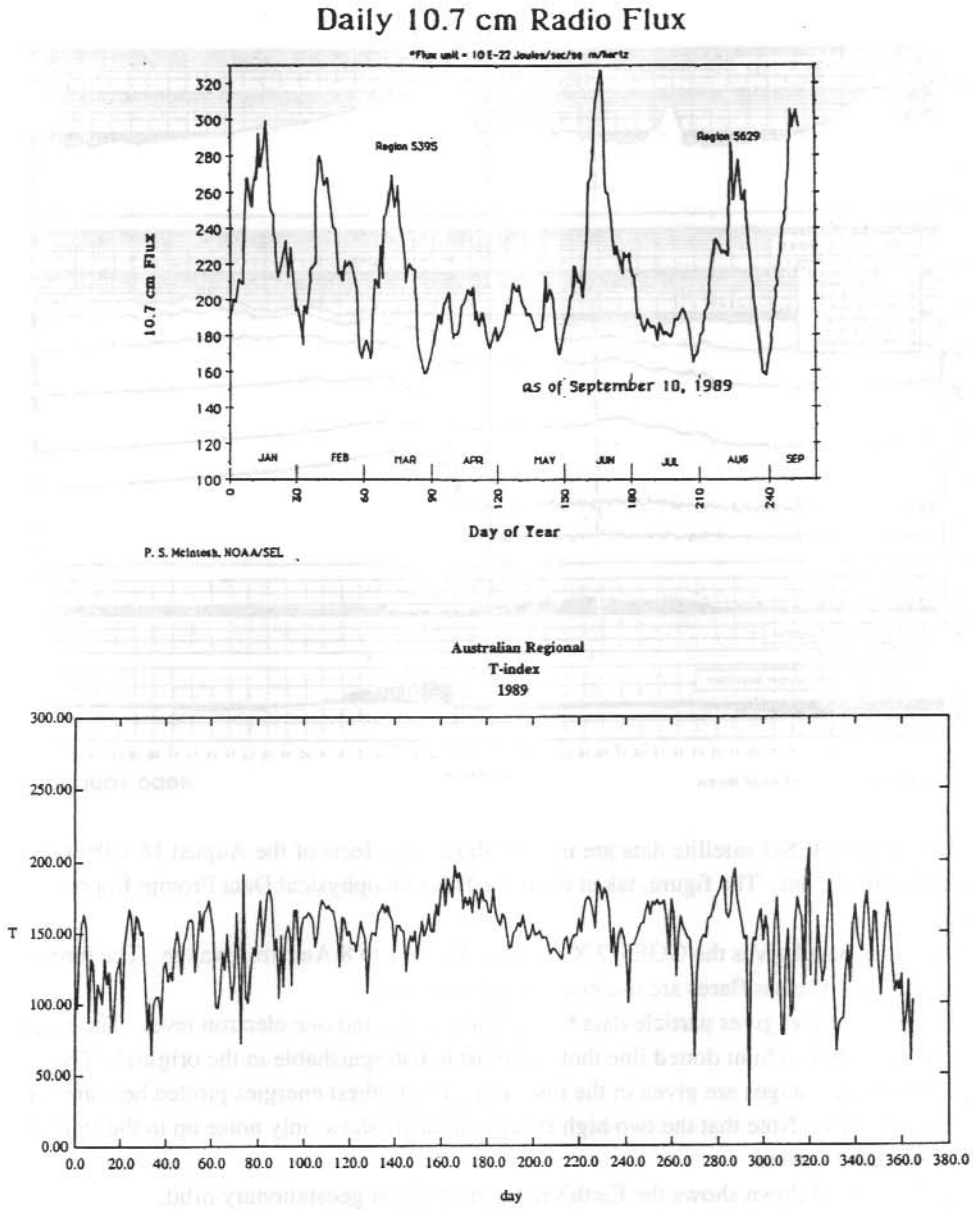


Figure 6. (a) gives the solar 10.7cm flux intensity up until September 1989 and (b) gives the Australian regional ionospheric index for 1989.

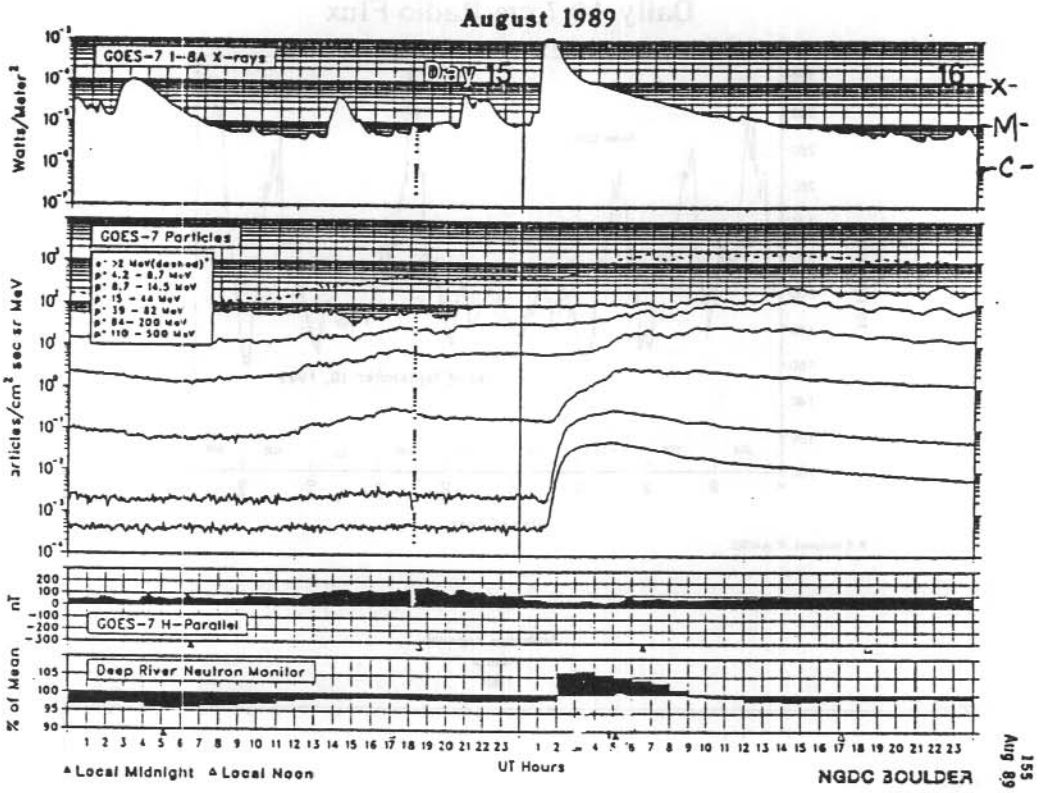


Figure 7. The GOES-7 satellite data are used to show the effects of the August 16 1989 flare at geosynchronous orbit. The figure, taken from the Solar-Geophysical Data Prompt Reports includes:

i. The upper panel gives the GOES-7 X-ray flux in the 1 to 8 Angstrom range. The threshold for X,M and C class flares are marked as reference points.

ii. The middle panel gives particle data for 6 proton levels and one electron level. The electron level appears as a faint dotted line that is almost indistinguishable in the originals. The proton energy ranges are given in the inset key. The highest energies plotted here are for 110-500 MeV. Note that the two high energy channels show only noise up to the start of the August 16 event.

iii. The next panel down shows the Earth's magnetic field at geostationary orbit.

iv. Finally, the bottom panel is a ground-based record showing the neutron monitor record for Deep River. The enhancement after the start of the flare is the GLE.

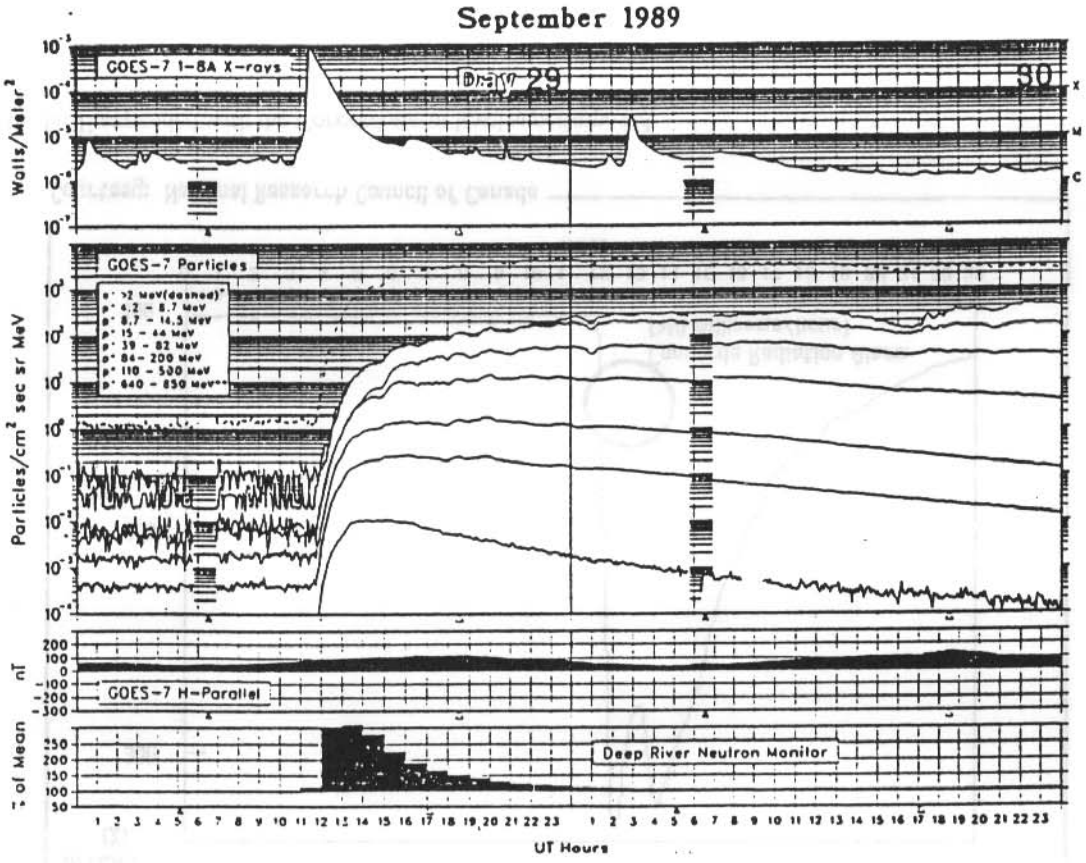


Figure 8a. Shows a similar plot for the September 29 1989 flare (see spike in the X-ray flux at 1130UT). The GLE is clearly evident in the Deep Diver neutron data, and the vertical scale used covers twice the range of the previous figure. Also, note there is an additional high energy particle channel covering the range 640 to 850 MeV. Figure 8b on following page.

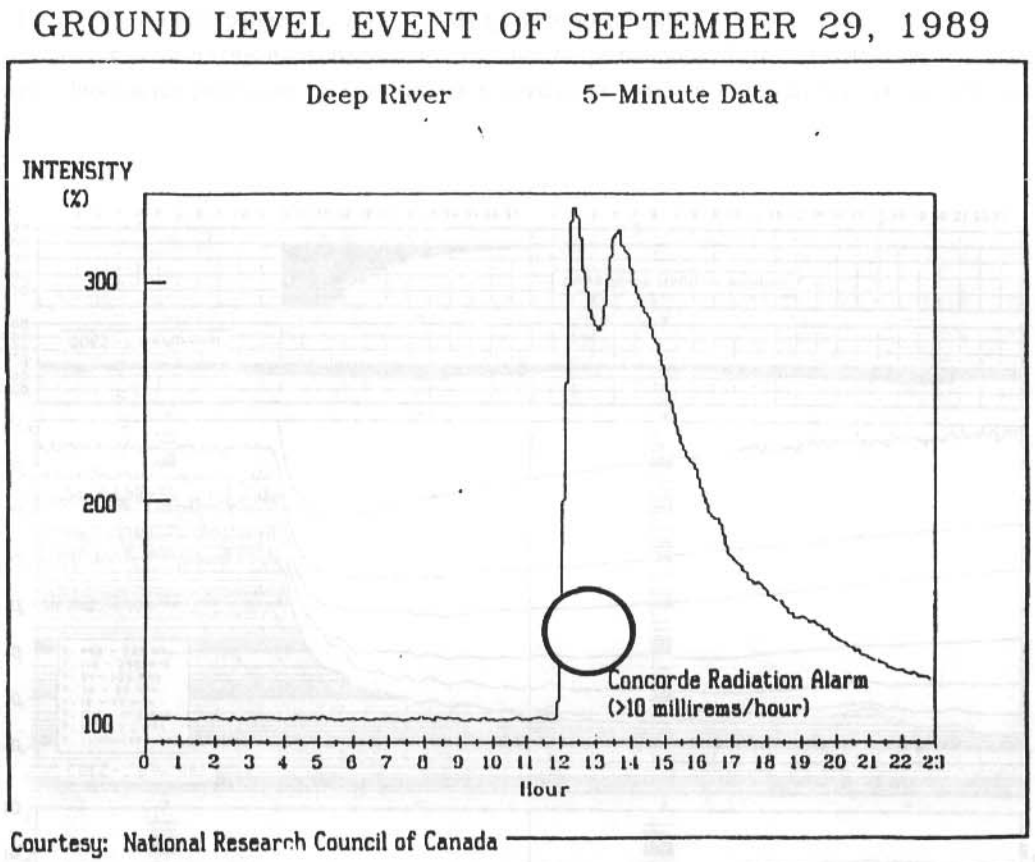


Figure 8b. Gives the GLE expanded with the Concord alarm level superimposed.

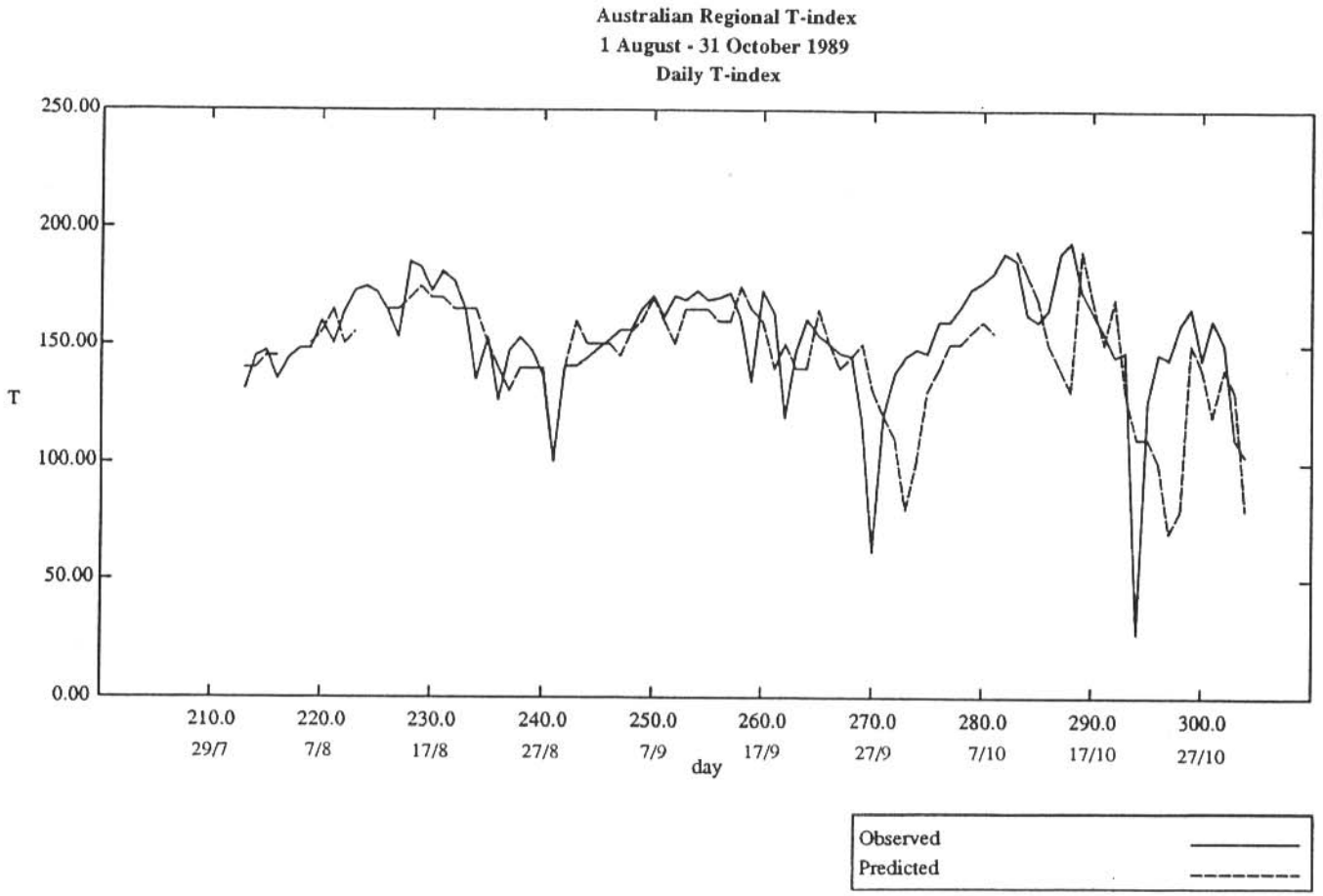


Figure 9. The ionospheric index (solid line) for the Australian region for August to October and the predicted indices (dashed line) are superimposed. Major depressions in F2 region ionisation occurred on 29 August, 27 September and 21 October 1989.

# 10. PARTICLE EFFECTS ON HIGH LATITUDE IONOGRAMS

P.J. Wilkinson and L. Grant
IPS Radio and Space Services
PO Box 1548
Chatswood NSW 2057

ABSTRACT

It is well known that particle precipitation can produce layers of ionisation in the ionosphere. These layers are more common at high latitude and are seen on ionograms as particle E and retardation-type sporadic E. In addition, if the particle energy is high enough the D region is ionised causing increased absorption which can prevent any ionospheric traces being observed with an ionosonde. All these types of trace are scaled regularly at the Australian high latitude bases of Macquarie Island, Mawson, Davis and, more recently, Casey. By studying the scaled data it is possible to make comments about the extent of particle precipitation and, possibly, about the energy spectrum of the particles observed.

This paper will summarise some exploratory results for the Australian bases to establish whether the data is likely to be useful.

## 10.1 INTRODUCTION

Particle precipitation forms an additional ionisation source at high latitudes, compared with mid-latitudes, the effects of which can be detected at the ground using a variety of instruments; from auroral emissions to radio reflections. In the paper only returns observed on ionosondes will be considered.

Ionosondes are most sensitive to particles which do not penetrate below 80 km and one of the main advantages of ionosonde methods for studying precipitation phenomena is that they detect a definite band of particle energy (Dudeney and Piggott 1978). Ionosonde events have been associated with auroral activity by several workers (King 1965). Using scaled ionosonde data, this paper looks at the particle effects observed in the E-region of the ionosphere for the Australian high latitude stations of Casey, Davis, Mawson, Macquarie Island and Hobart.

## 10.2 E LAYERS FORMED BY PARTICLES

If a continuous, steady flux of mono-energetic particles is incident on the atmosphere then it is well known that this will form an ionised layer. Robinson and Vondrak (1985), using Rees (1963) code, showed the layer height $h_{max}E$, in kilometres, is proportional to the particle energy En, measured in keV, and the peak electron density foE, with the units Megahetz, of the layer is proportional to the particle flux. Thus, for electrons:

$$h_{max}E = -13.6 \ln(En) + 128 \text{ km} \quad (1)$$

$$foE = 3.18 \Phi^{1/4} \quad (2)$$

where the flux $\Phi$ is measured in ergs $cm^{-2}$ $sec^{-1}$.

Evidently (2) is very close to experimentally determined results. Thus, the height and maximum electron density of the layers formed this way can give information about the incident particles. The ionising particles may be either electrons or protons. Both (Robinson and Vondrak 1985) have been observed to produce ionised layers. Early work appears to assume energetic electrons are the primary source, but the source particle cannot be identified on the basis of ionisation measurements alone. As a rule of thumb, protons of 8 keV will produce a layer which peaks at the same height as one formed by 1 keV electrons. In the remainder of this report, electrons will be assumed primarily responsible for the observed ionisation.

*10.2.1 Particle effects on ionograms*

Several types of layer are possible and different names have been given to the different types. Two broad groups will be considered in this paper; those thought associated with the diffuse aurora and those associated with the active aurora.

Layers associated with the diffuse aurora are likely to be thick, like the normal E layer and blanket, preventing higher layers with lower ionisation from being seen. The layers may be seen anywhere within the field of view of the ionosonde; either overhead or at oblique incidence. When observed directly above a station the layer is called Es type k and retardation Es, or Es type r, when seen obliquely. These types have been collectively called auroral-E, night-E and more recently particle-E, although not all authors adopt this nomenclature. Some prefer to regard Es-r as a different grouping. In this paper particle-E will be used as the collective name for these layers and Es-k and Es-r will be used when reference to the specific scaled type is needed.

The principle difference between particle-E and normal E is the temporal and spatial variability of the source for the layer. Because E-region chemistry is rapid, the particle layers produce temporal and spatial histories of the particle sources forming them. Particle-E has been identified with the continuous aurora and provided the ionising flux is large enough to produce layer ionisation densities equal to 2 or 3 MHz (about $10^5$ electrons $cm^{-3}$) then an all-sky-camera would record a continuous aurora.

Other more complex E-layer ionisation forms are found during discrete aurora. These forms are variable and often associated with extensively spread echoes on ionograms. They are called auroral Es or Es-a.

A third common type is a flat type sporadic E, or Es-f, layer that is often densely ionised but, appears not to be thick. Evidently (Dudeney and Piggott 1978) the height and top frequency for this flat layer can be interpreted in the same way as the thick particle layer. However, this is a more speculative topic and is not developed here.

When particle energies are sufficiently high, the lower D-region is ionised, resulting in an increase in absorption which prevents any ionogram returns being observed. This is called a B condition. The particle energies are probably of the order of 20 keV.

There are a range of precipitating particle energies and flux signatures that can be observed on ionograms. At any one time, a mixture of types may appear, but as will be shown later, consistent average behaviour is found.

*10.2.2 Scaling ionograms which have particle effects*

Scaling high latitude ionograms seems, at times, to be an art form. The ionograms are complex, show significant spread and appear to invite quite arbitrary interpretation. The issue is not this bad. While rules may cause bias and appear to force the data reduction along uninteresting paths, there is moderate evidence for consistency. However, it does seem at times that the only unambiguous ionogram to scale is a B condition. For Mawson, even this proves not be the case due to massive local radio frequency interference.

Several conventions exist

Particle layers, with minimal spread, are split into two groups; Es-k and Es-r as already indicated. There are several ways of distinguishing between types k and r. The primary difference is that Es-k is overhead and Es-r is seen obliquely. The scaler must use secondary information to decide which type is predominant as shown in Figure 1.

Generally:
- if a layer shows retardation at the high frequency end, it is a thick particle layer and is type k or r,
- if the low frequency F layer trace also shows retardation, the underlying thick layer and the F layer are probably both directly above the station, so the E region layer is either the normal E or particle E, Es-k.

When a layer is immediately overhead, the virtual height of the layer can be used as an estimate of the actual peak height and hence the source particle energy. However, for oblique layers the apparent virtual height will be greater than the actual height so the inferred energy will be a lower bound.

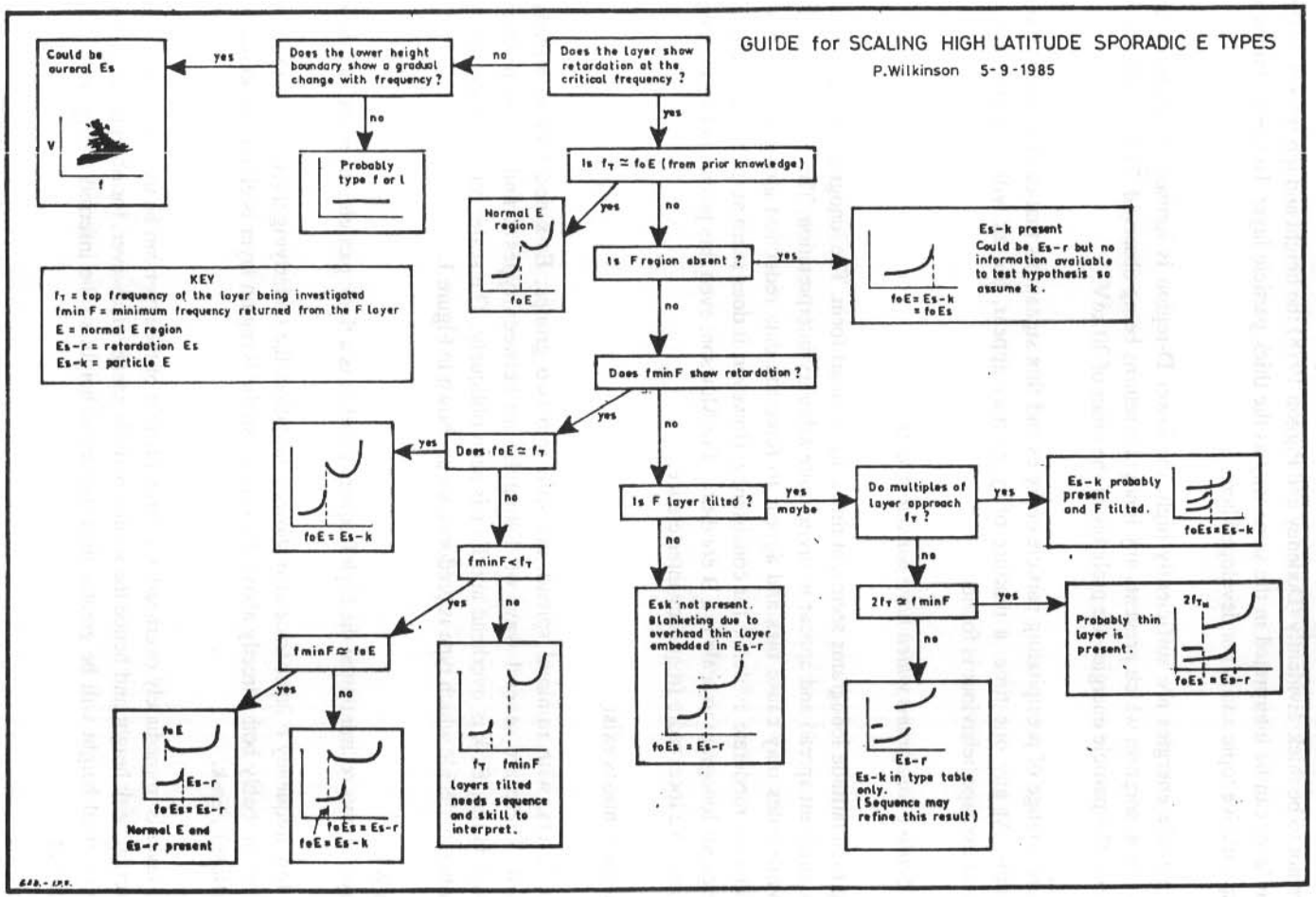


Figure 1. A guide to high latitude sporadic E types is used by scalers at IPS to assist them in interpreting high latitude Es types. The guide was produced in 1985 and outlines the logical arguments scalers used at that time. It is also consistent with international scaling conventions.

Dudeney and Rodger (1985) found evidence for meridional structure in Es-a and, less frequently, in Es-r which will distort the particle fluxes deduced for a location. Their model produces apparent retardation effects as a result of increasing target range. Neither of these problems are of immediate concern, but may place limitations on final applications.

Another important convention is that all these layers are regarded as sporadic E and scaled as sporadic E; i.e. as foEs, fbEs, h'Es and types of Es. For each ionogram, data for only one Es layer is recorded; the layer with the highest critical frequency, foEs. This means that even for a complex auroral ionogram only one layer is recorded; the layer produced by the largest particle flux. There is an exception to this rule, although the exception does not seem to have universal approval or understanding. When Es-k is observed, it is always scaled in the foE table and is described by k. Only if Es-k is the maximum foEs is it also scaled as foEs. This important exception has been created because Es-k can be used unambiguously to give particle energy and flux.

## 10.3 THE ANALYSIS

Average layer statistics were calculated for the virtual height and critical frequency observed each hour as well as the probability of the maximum critical frequency exceeding 3MHz. This was calculated without allowance for obscuration by more dense lower layers.

Two Es types were considered, particle-E and auroral Es. Some exploratory studies were also carried out to compare Es-k with Es-r.

Data were split into seasonal averages and averages for different levels of magnetic activity. Three magnetic levels were considered $ap < 6$, $6 < ap \leq 35$ and $35 < ap \leq 90$. A fourth, $ap > 90$, had virtually no data in it.

Results are presented in magnetic coordinates, magnetic time and geomagnetic latitude. This is consistent with the idea that magnetic control is fundamental to particle effects.

## 10.4 RESULTS FOR THE PARTICLE-E LAYER AT MAWSON

As mentioned, this layer is associated with the continuous aurora. Rather confusingly, the best work on this subject refers to it as the auroral E layer (Buchau et al. 1972). Their work, involving airborne ionosonde soundings across the auroral oval showed that a continuous particle produced layer is always present. The layer follows the auroral oval and during quiet periods forms a band that is roughly 3° wide. During more active conditions the equatorward boundary moves further equatorward as the auroral oval expands. Fluxes lie in the range 2 to 2.5 MHz in quiet periods and 2 to 4 MHz in more active periods.

For Mawson, the vast majority of particle-E data collected is Es-r. A comparison of particle-E, scaled as foE, and scaled for foEs was made. Also Es-r was compared with both.

*10.4.1 Energy*

Both h'E-k and h'Es-k (Figure 2) show quite similar height variations for different seasons. There was little evidence for consistent seasonal variation although summer post-midnight heights were generally lower than for other seasons (winter equinox). Es-r showed this behaviour also.

Generally, particle E was not seen near magnetic noon. Two hours after magnetic noon, particle E appears with average heights between 130 and 135 km. Only summer is different, with heights of the order of 125 to 130 km. A gradual fall is n the average height which accelerates roughly one to three hours after magnetic midnight when heights fall between 125 and 120 km.

When all the Mawson data are used, then Es-r (Figure 3) follows roughly the same pattern, although the heights observed are generally less than Es-k. This is unexpected, and is probably because comparable data sets have not been used. At this stage, Es-k and Es-r require more study to establish the value of Es-k as a separate sporadic E type.

Differences between average heights are marginal for the three magnetic activity levels considered. Es-r also shows similar behaviour compared to the seasonal changes mentioned in the previous paragraph.

The height variation is consistent with a hardening particle source which occurs almost entirely in the early morning hours and has been noted by other workers. The strong summer seasonal effect is probably a normal E-region effect. When the normal E-region is present, the two sources will sum together and the normal E-region height will be recorded as the particle E height.

*10.4.2 Fluxes*

In Figure 4 there is a clear seasonal effect with summer fluxes being highest and winter fluxes usually lowest. The diurnal effect is most obvious during day-light hours and is probably due to normal E layer production being added in to the particle source. The effect is least around local midnight and in the pre-dawn period.

The fluxes increase substantially as the magnetic activity increases, the extent being greatest in the pre-magnetic midnight period.

The diurnal and seasonal effects are probably due to normal E-layer effects. The strong magnetic effect is the feature of prime interest. It shows that while the source energy spectrum may not change, the flux of particles does.

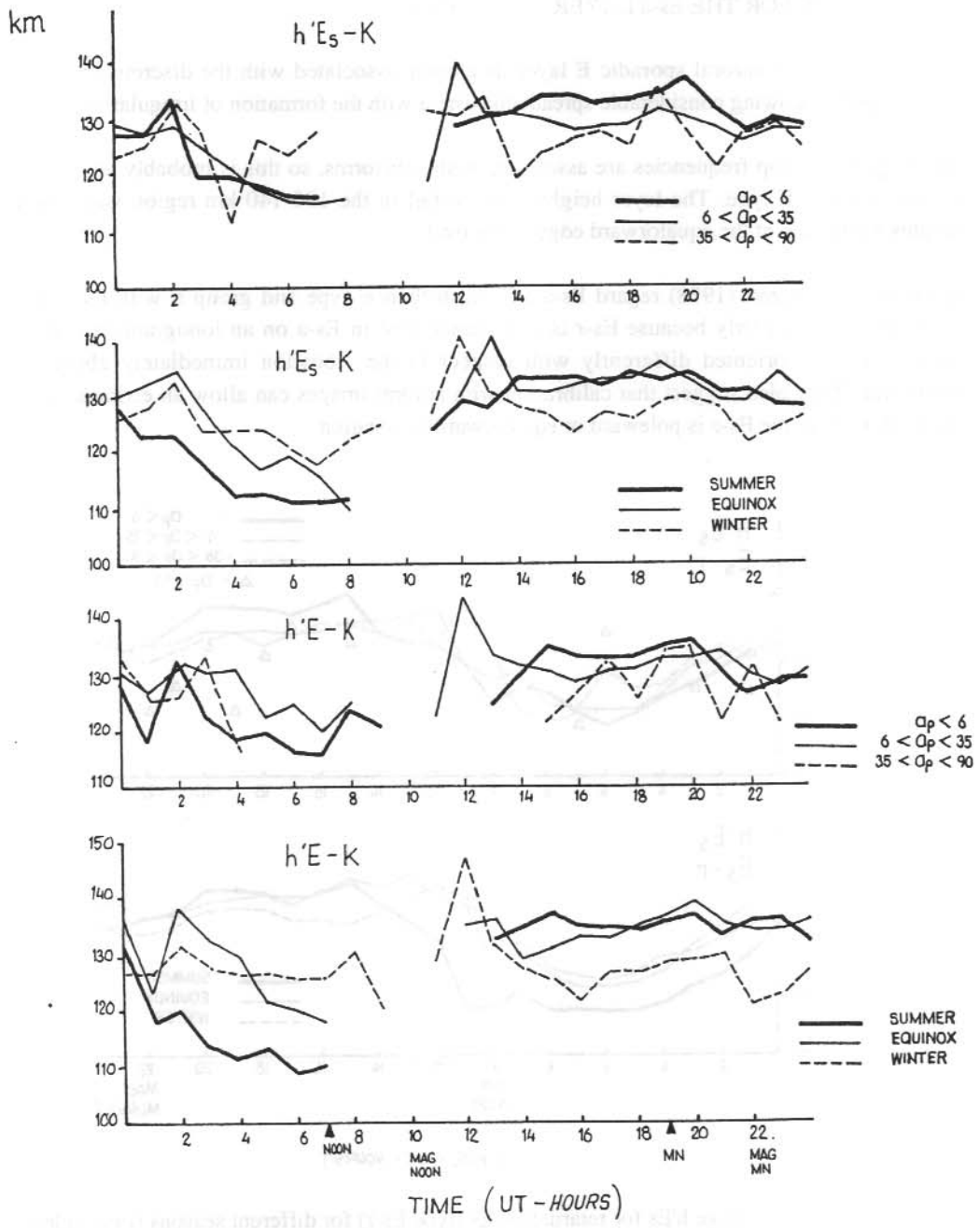


Figure 2. Mawson average h'Es and h'E for particle E (type Es-k) for different seasons (lower plot) and different levels of magnetic activity (upper plot).

## 10.5 RESULTS FOR THE Es-a LAYER AT MAWSON

The Es-a layer, or auroral sporadic E layer, is closely associated with the discrete aurora. It varies rapidly, showing considerable spread, consistent with the formation of irregularities.

The largest Es-a top frequencies are associated with substorms, so this is probably an activity driven sporadic E type. The layer heights tend to fall in the 100-140 km region with lower heights being seen at the equatorward edge of the oval.

Dudeney and Piggott (1978) regard Es-a as a 'disturbance' type and group it with Es-r. The association arises partly because Es-r is often embedded in Es-a on an ionogram and partly because Es-r is oriented differently with respect to the location immediately above an ionosonde. They also suggest that calibration with auroral images can allow an estimate to be made of whether the Es-a is poleward or equatorward of a station.

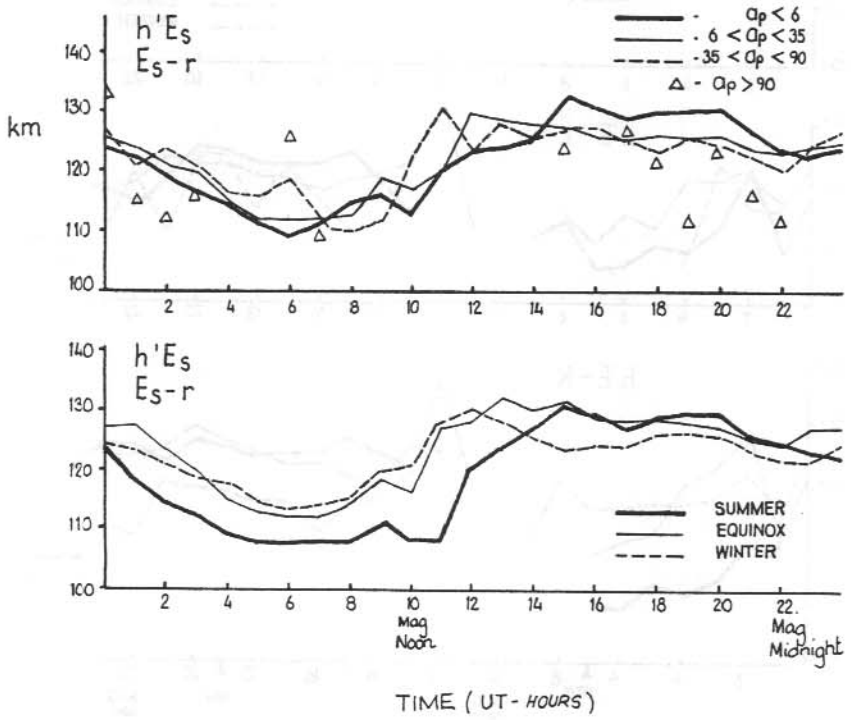


Figure 3. Mawson average h'Es for retardation Es (type Es-r) for different seasons (lower plot) and different levels of magnetic activity (upper plot).

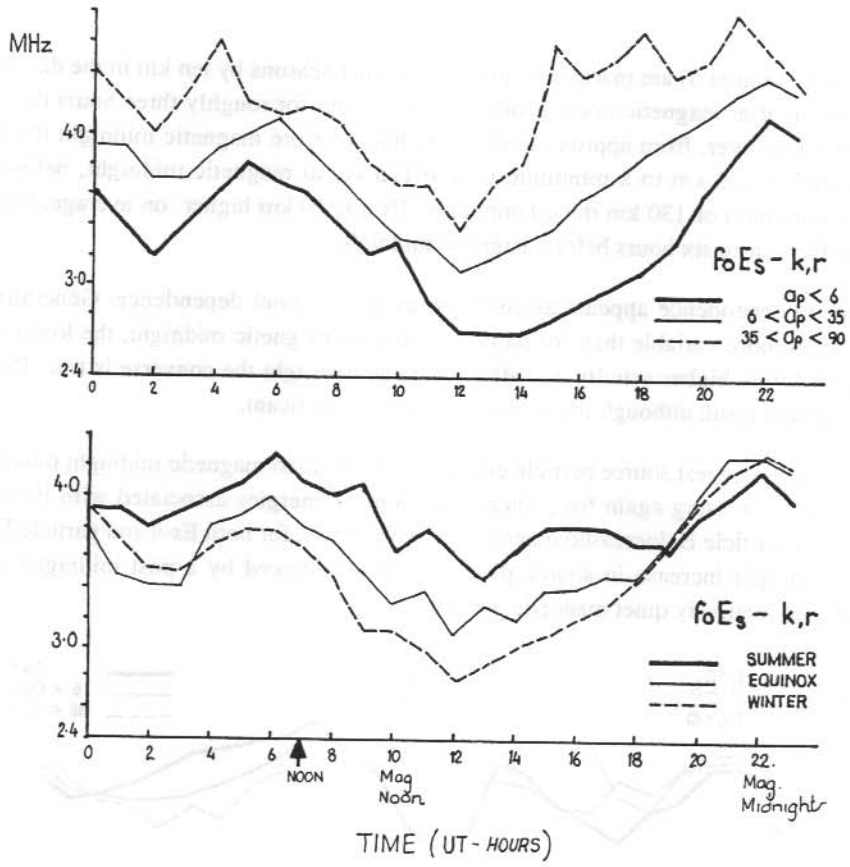


Figure 4. Mawson average foEs for particle E (types Es-k and r together) for different seasons (lower plot) and different levels of magnetic activity (upper plot).

Piggott (private communication) suggested that if there is any spreading associated with E region traces, then auroral-Es is present. Probably many scalers would endorse this rule, although they will tend to associate Es-a with large scale spreading. Auroral Es can produce reflections at oblique incidence and may have virtual ranges of 700 km which may confuse scalers into thinking they are dealing with the F-region.

Bearing these difficulties in mind, it is believed that relationships between energy and flux considered for Es-k also hold for Es-a.

*10.5.1 Energy*

Winter heights (Figure 5) are marginally lower than other seasons by ten km in the daytime and maybe five km after magnetic noon. From magnetic noon, for roughly three hours the heights are variable. However, from approximately eight hours before magnetic midnight the heights fall from around 140 km to a minimum of 120-125 km at magnetic midnight, before rising again to a maximum of 130 km three hours later. Es-a is 10 km higher on average, than Es-r, apart from the four to six hours before magnetic midnight.

The magnetic dependence appears as confused as the seasonal dependence. Generally, Es-a statistics seem more variable than for particle E. Before magnetic midnight, the lower heights are associated with higher activity and after magnetic midnight the converse is true. Particle E showed a similar result although it was not statistically significant.

The Es-a heights suggest source particle energy increases up to magnetic midnight then falls off briefly before increasing again for a short time. Source energies associated with Es-a appear lower than for particle E. Increased magnetic activity shows, for both Es-a and particle E, a pre-magnetic midnight increase in source particle energy followed by a post midnight decrease compared with relatively quiet magnetic periods.

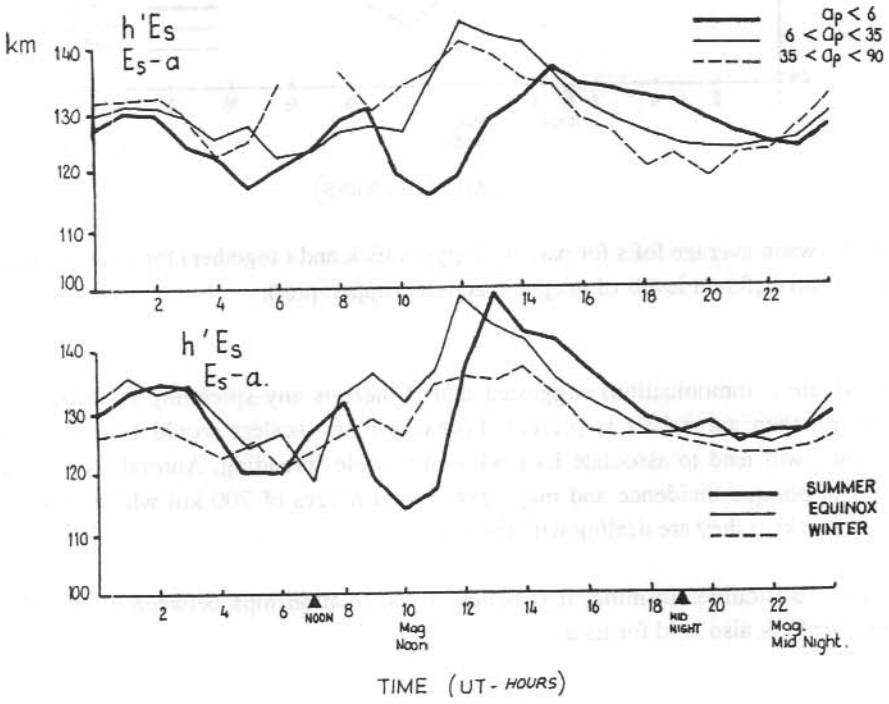


Figure 5. Mawson average h'Es for auroral Es (type Es-a) for different seasons (lower plot) and different levels of magnetic activity (upper plot).

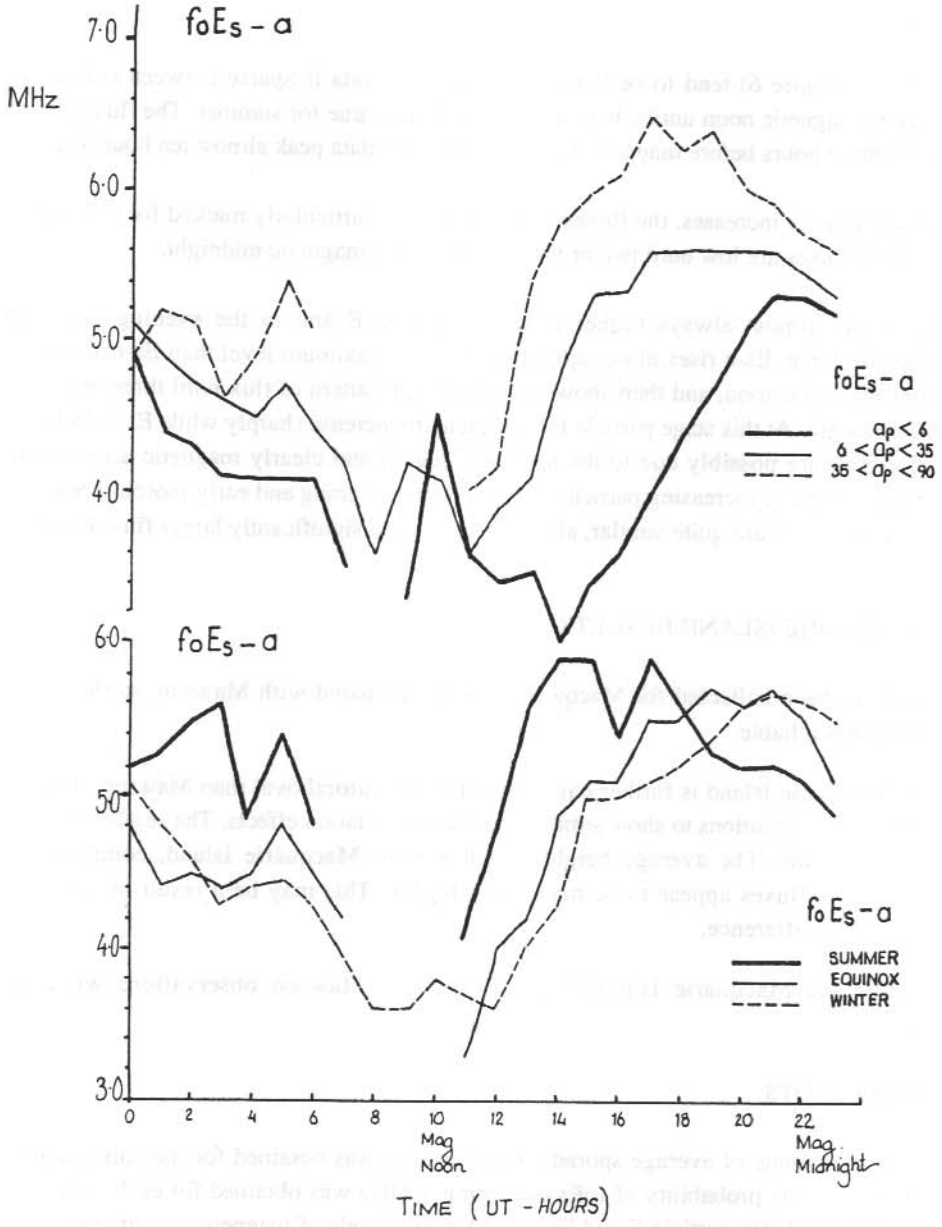


Figure 6. Mawson average foEs for auroral Es (type Es-a) for different seasons (lower plot) and different levels of magnetic activity (upper plot).

*10.5.2 Fluxes*

Winter fluxes (Figure 6) tend to be lower than summer. Data is sparse between two to four hours prior to magnetic noon until a hour after noon. This is true for summer. The fluxes tend to peak one to three hours before magnetic midnight. Summer data peak almost ten hours earlier.

As magnetic activity increases, the fluxes increase. This is particularly marked for low ($ap < 6$) activity where fluxes are low until two or three hours before magnetic midnight.

Es-a fluxes are almost always higher than for particle E and in the evening hours, the differences are large. Es-a rises more rapidly towards its maximum level than Es-r, in the four hours after magnetic noon, and then shows a very similar pattern of flux until three hours after magnetic midnight. At this stage particle E fluxes tend to increase sharply while Es-a declines. Seasonal effects are possibly due to the normal E region and clearly magnetic activity has a major effect, generally increasing particle fluxes. The late evening and early morning behaviour of Es-a and particle E are quite similar, although Es-a has a significantly larger flux of particles associated with it.

## 10.6 MACQUARIE ISLAND RESULTS

Less data have been collected for Macquarie Island, compared with Mawson, so the average statistics are less reliable.

Although Macquarie Island is further equatorward of the auroral oval than Mawson, it is close enough for the two locations to show similar particle precipitation effects. The results (Figures 7 and 8) confirm this. The average heights are lower for Macquarie Island, compared with Mawson and the fluxes appear to be marginally higher. This may be a result of the sample rather than a real difference.

At this state the Macquarie Island data supports the Mawson observations with small differences.

## 10.7 POLAR PLOTS

Finally, some estimate of average sporadic E occurrence was obtained for the Australian high latitude stations. The probability of foEs exceeding 3 MHz was obtained for each station with the data subdivided into particle E and Es-a and for two levels of magnetic activity ($ap < 6$ and $6 < ap \leq 35$). The result of this analysis (Figure 9) were then displayed as polar plots; the radials of the plot giving geomagnetic latitude and the circumference gives the station magnetic local time. Contours were then drawn at the 10% probability levels.

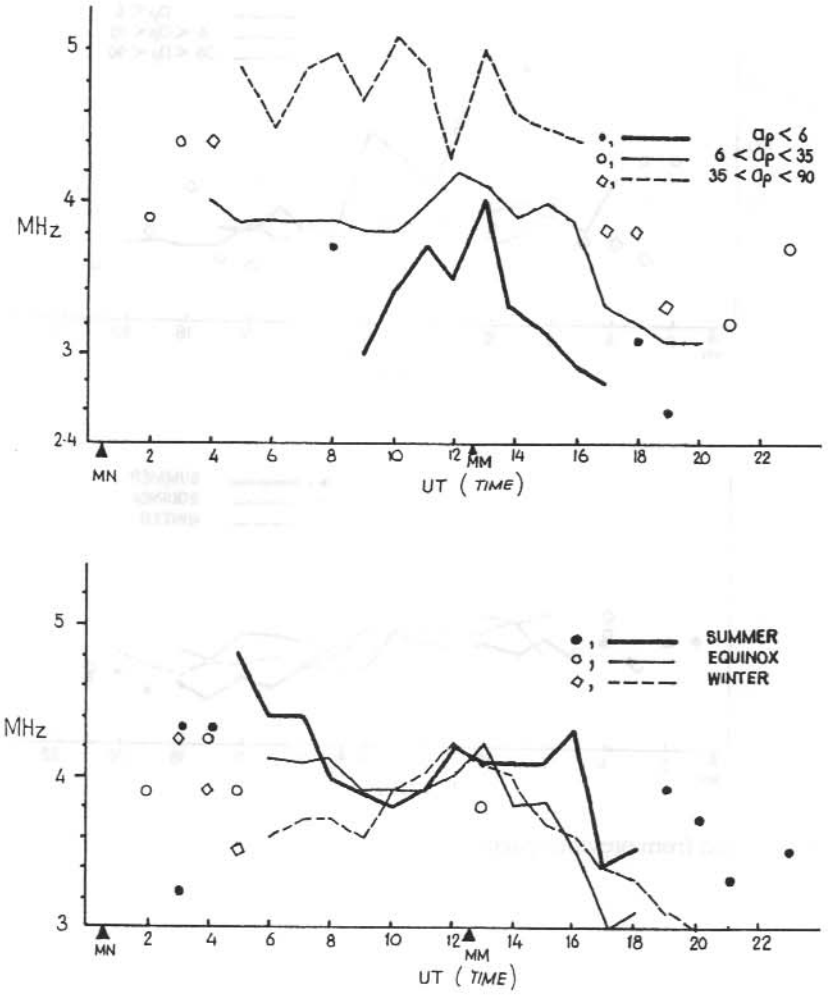


Figure 7. Macquarie Island average h'Es (left hand side) and foEs (next page) for particle E (type Es-k,r) for different seasons (lower plots) and different levels of magnetic activity (upper plots). (continued on next page)

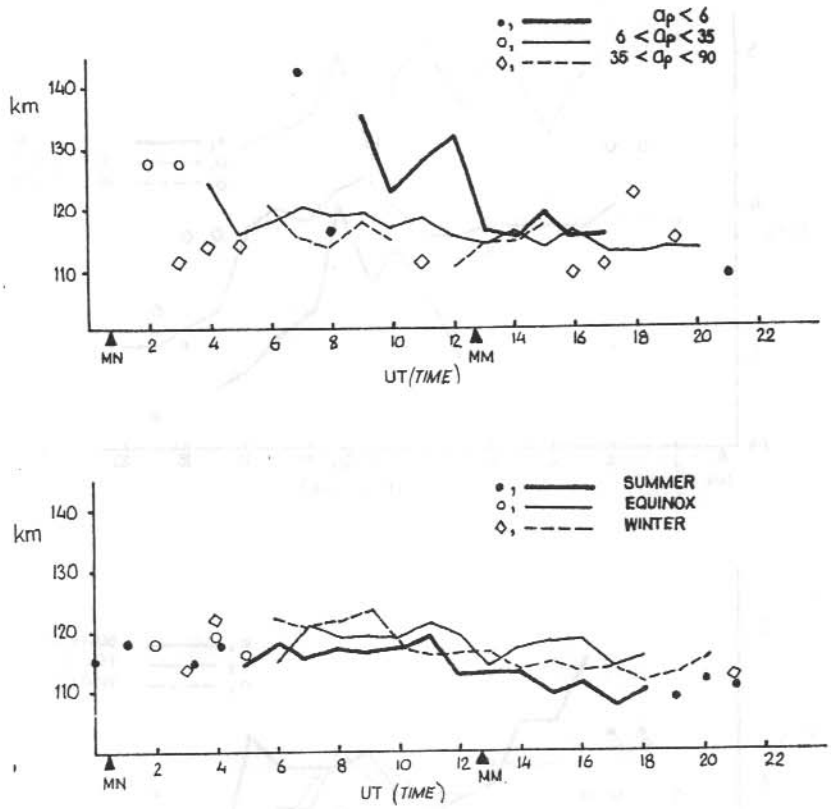


Figure 7. (continued from previous page)

*10.5.2 Fluxes*

Winter fluxes (Figure 6) tend to be lower than summer. Data is sparse between two to four hours prior to magnetic noon until a hour after noon. This is true for summer. The fluxes tend to peak one to three hours before magnetic midnight. Summer data peak almost ten hours earlier.

As magnetic activity increases, the fluxes increase. This is particularly marked for low (ap < 6) activity where fluxes are low until two or three hours before magnetic midnight.

Es-a fluxes are almost always higher than for particle E and in the evening hours, the differences are large. Es-a rises more rapidly towards its maximum level than Es-r, in the four hours after magnetic noon, and then shows a very similar pattern of flux until three hours after magnetic midnight. At this stage particle E fluxes tend to increase sharply while Es-a declines.

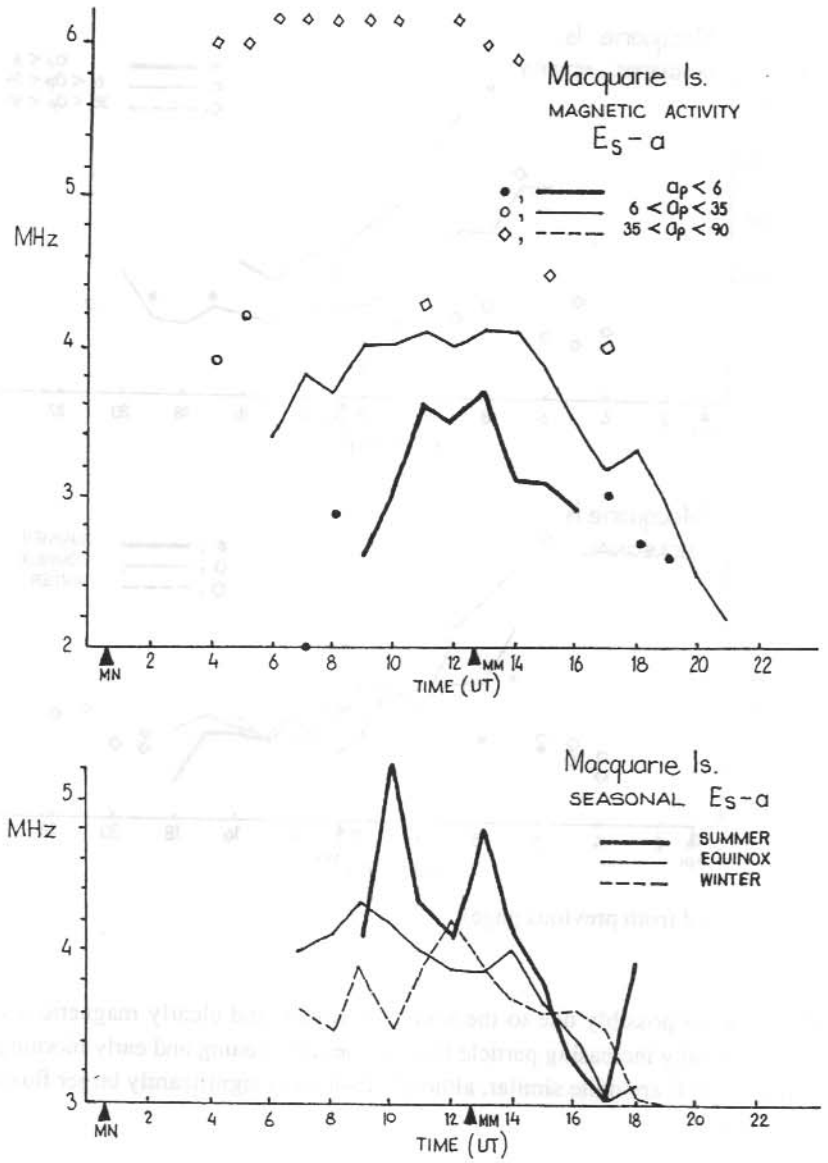


Figure 8. Macquarie Island average h'Es (left hand side) and foEs (next page) for auroral Es (type Es-a) for different seasons (lower plots) and different levels of magnetic activity (upper plots). (continued next page)

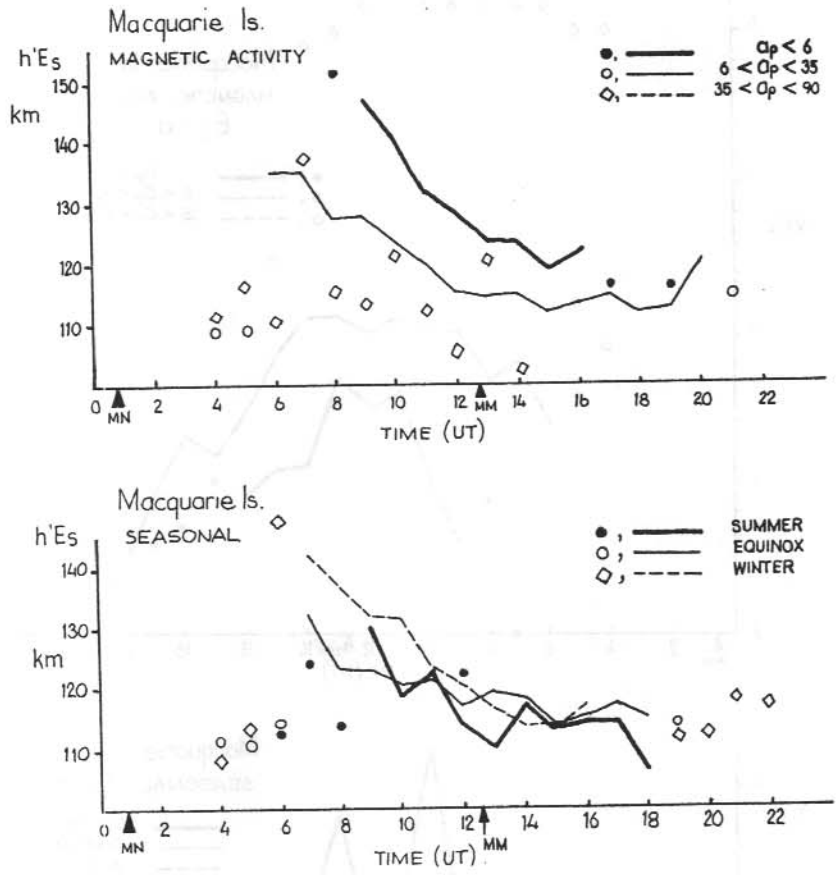


Figure 8. (continued from previous page).

Seasonal effects are possibly due to the normal E region and clearly magnetic activity has a major effect, generally increasing particle fluxes. The late evening and early morning behaviour of Es-a and particle E are quite similar, although Es-a has a significantly larger flux of particles associated with it.

## 10.6 MACQUARIE ISLAND RESULTS

Less data have been collected for Macquarie Island, compared with Mawson, so the average statistics are less reliable.

Although Macquarie Island is further equatorward of the auroral oval than Mawson, it is close enough for the two locations to show similar particle precipitation effects. The results (Figures 7 and 8) confirm this. The average heights are lower for Macquarie Island, compared with

Mawson and the fluxes appear to be marginally higher. This may be a result of the sample rather than a real difference.

At this state the Macquarie Island data supports the Mawson observations with small differences.

## 10.7 POLAR PLOTS

Finally, some estimate of average sporadic E occurrence was obtained for the Australian high latitude stations. The probability of foEs exceeding 3 MHz was obtained for each station with the data subdivided into particle E and Es-a and for two levels of magnetic activity ($ap < 6$ and $6 < ap \leq 35$). The result of this analysis (Figure 9) were then displayed as polar plots; the radials of the plot giving geomagnetic latitude and the circumference gives the station magnetic local time. Contours were then drawn at the 10% probability levels.
From this, Es-a has a lower probability of occurrence than particle E. Since Es-a is associated with active conditions, there is a strong likelihood that particle energies harden sufficiently to produce high absorption. This could result in a reduction in the amount of Es-a observed.

The maximum probability of occurrence for particle precipitation occurs in the evening period for Mawson. However, there is a second maximum in particle E at Davis in the pre-magnetic noon period which could be cusp related.

There is a minimum in occurrence for all stations between one and three hours after magnetic noon.

The general shape of the probability contours is preserved as magnetic activity increases, suggesting the data set is internally consistent.

Finally, there is almost no particle E and Es-a seen at Casey, as expected. These types are uncommon in the polar cap region, but flat type Es is more common and is also thought to be associated with particle precipitation. This possibility was not considered here.

## 10.8 SUMMARY

The ionosonde may be a useful additional source of information on the energy spectrum and source of particles precipitating into the high latitude ionosphere. As shown, particles will produce ionisation at different levels in the atmosphere and, depending on their energy, layers will form at different heights. Layers that will be of particular interest occur in the height region 100 to 200 km. Precipitation at higher altitudes was not considered here and those forming at altitudes less than 90 km will cause absorption, preventing ionograms from being recorded.

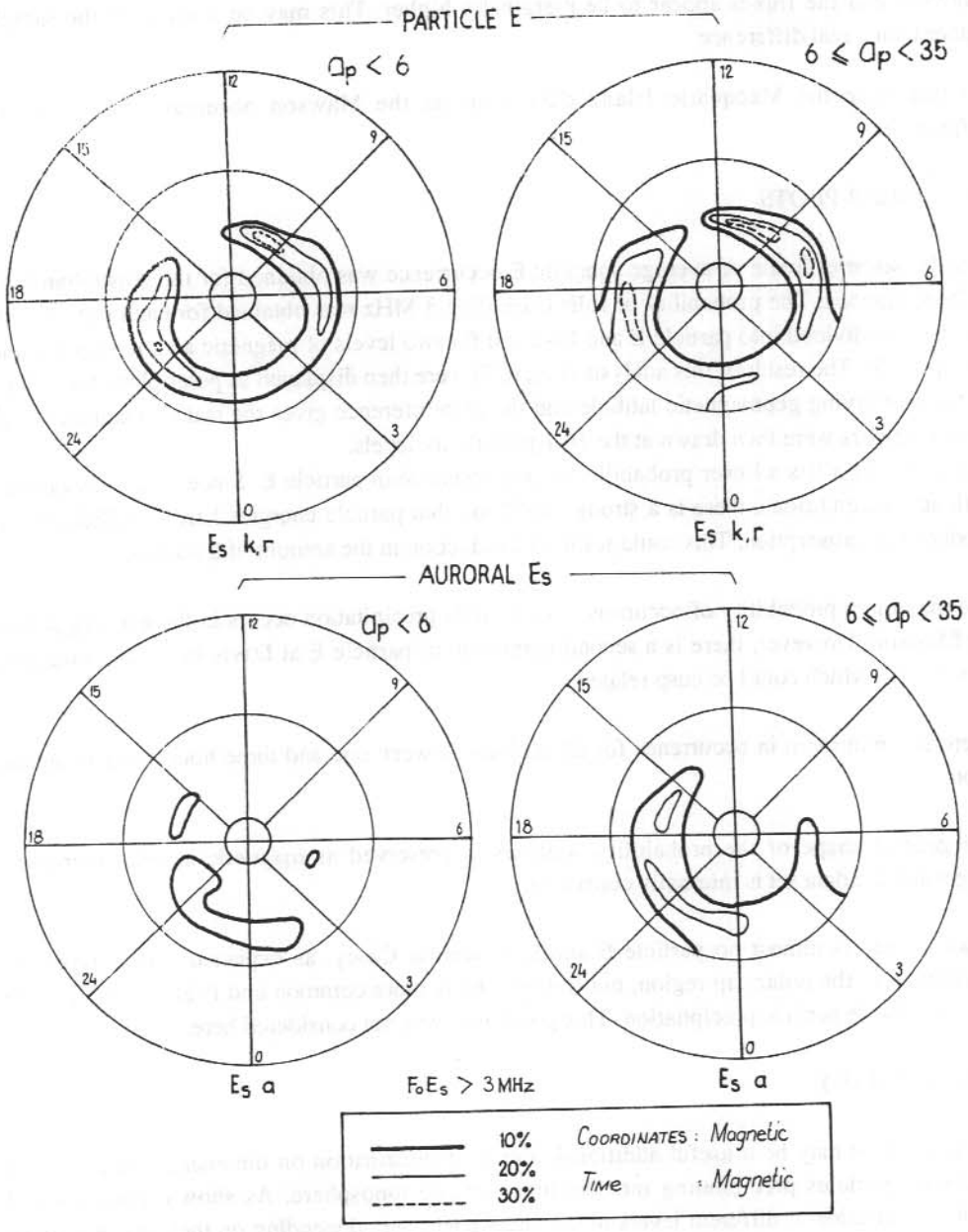


Figure 9. Polar plots of the occurrence of foEs > 3 MHz for particle E and auroral Es. See text for an explanation of these plots.

Two major problems occur with the ionosonde data discussed here that need to be taken into account when interpreting the statistical results.

First, only one Es type is scaled - the one giving the highest foEs value. In terms of particle precipitation effects, this is the layer with the largest flux. At the very least, the statistics must be adjusted for the possible presence of additional layers. This has not yet been done although it should not produce substantial changes to the comments made here.

Second, and potentially more important, if precipitating particles with different energies are present, then the highest energy particles may predominate. For instance, if the D region is ionised, then no ionogram will be recorded. Thus, the ionosonde is a selective window on incoming particle energies. Provided the energies are not too high, the information may be useful, but statistical results will have to be treated with care. All the statistics given here have been adjusted for major absorption effects by counting B-condition ionograms as frames when

no data could be collected. Since interference was treated in a similar way, and the major interference at Mawson, which occurred at clear preferred times, did not distort the statistics, this approach is probably reasonable.

The grouping of the different sporadic E types is probably artificial. However, there is a lot of data scaled in this way so it is worth investigating its value before abandoning it. The labelling schemes used are difficult to deal with. The auroral E layer of Buchau et al. (1972), is probably most correct where there is ample information available to identify the different layers present on the ionogram. However, it does appear that Es-k and Es-r are more alike than Es-r and Es-a.

Thus, Dudeney and Piggott (1978) are not correct in treating these two types together. Again, there are good arguments that they could put to refute this point.

The primary intent of this study was to establish that the sporadic E data for Australian high latitude ionosonde stations were self consistent. The issue is, can a normal scaler with inadequate information do a better job, and is the data scaled so far useful. The work reported on here suggests consistency between stations, at least indicating the scaling is reasonably homogeneous. Thus, further analysis is worthwhile.

## 10.9 REFERENCES


Buchau, J., Gassmann, G.J., Pike, C.P., Wagner, R.A. *and* Whalen, J.A. (1972). Precipitation patterns in the Arctic ionosphere determined from airborne observations. *Annales de Geophysique* 28:443-453.

Dudeney, J.R. *and* Piggott, W.R. (1978). Antarctic Ionospheric Research. *Upper Atmosphere Research in Antarctica.*

Dudeney, J.R. *and* Rodger, A.S. (1985). Spatial structure of high latitude sporadic E. *Journal of Atmospheric and Terrestrial Physics* 47:529-535

King, G.A.M. (1965). The aurora and the night-E layer. *Journal of Atmospheric and Terrestrial Physics* 27:426-428.

Rees, M.H. (1963). Auroral ionisation and excitation by incident energetic electrons. *Planetary and Space Science 11*:1209-1218.

Robinson, R.M. *and* Vondrak R.R. (1985). Characteristics and sources of ionization in the continuous aurora. *Radio Science 20*:447-455.

# 11. IONOSPHERIC ABSORPTION AT CASEY STATION, ANTARCTICA

Bo Wen[1] and G.B. Burns[2]

[1]China Research Institute for Radiowave Propagation
Xin Xiang, Henan
People's Republic of China

[2]Antarctic Division
Kingston Tas 7050
Australia

ABSTRACT

A standard riometer at 30 MHz has been used to study ionospheric absorption at Casey station, Antarctica (geographic coordinates 66.2°S, 110.4°E; invariant magnetic latitude 80.6°S) during 1989. Data has been digitally collected at ten second intervals and Quiet Day Curves (QDCs) determined using the 'Inflection Point Method' of Krishnaswamy et al. 1985. The accuracy with which the QDC can be determined will be discussed and preliminary results on the diurnal absorption variation at this high latitude site will be presented.

## 11.1 INTRODUCTION

Riometers have been used to study absorption in the the upper atmosphere since the instrument was introduced in 1959. In spite of the large effective 'field-of-view' of standard riometers, they have been used to make significant contributions to upper atmospheric geophysics (Hargreaves 1969).

A riometer is a sensitive HF radio receiver. They are used to measure cosmic radio noise at a frequency generally between 20 and 50 MHz. Most commonly a zenith-oriented, broad beam-width antenna is utilised.

Cosmic radio noise originates principally from galactic radio stars. When it traverses the ionosphere a portion of the signal may be absorbed. Since the galactic radio flux is constant over a long period of time, any change in the received signal intensity at the same local sidereal time on different days for any given site, can be considered as due to changes in ionospheric absorption.

In this paper, a standard riometer is used to study the diurnal absorption variation at Casey station, Antarctica.

## 11.2 LOCALE, EQUIPMENT AND DATA

The geographic coordinates of Casey are 66.2°S, 110.4°E and its invariant magnetic latitude is 80.6°S. This corresponds to an L value of 37.8. Local magnetic time is given approximately by UT plus 6.6 hours. Casey is essentially a polar cap station. At magnetic noon it may be close to the magnetic cusp.

During 1989 a riometer was installed at Casey. This riometer operates at 30.1 MHz. The antenna is a vertically-directed, centre-fed dipole with 3 dB points located approximately 32° off-vertical. Data from the riometer was collected digitally on an LSI11 based computer system at a rate of one 'instantaneous' sample every ten seconds. A calibration sequence is initiated at 1630 UT each day. During 1989, this sequence consisted of two minutes duration at each of five equally spaced noise diode currents from 0 to 5 mA.

In the first five months of 1989 the calibration sequence indicated that the riometer was non-linear by a variable amount at low signal levels. This precluded determination of a QDC during this period. In October the riometer was non-operational for a period of about ten days due to an antenna failure. For a further total period of about two weeks in October, two Polar Cap Absorption (PCA) events persistently reduced the signals below the quiet level. It was not possible to determine a QDC for this month. From November on, a graphics card in a newly installed computer system operated in the same room as the riometer introduced an intermittent 0.2 dB offset into the signal recorded. No QDCs were evaluated from this time.

The data set used in this paper is from June to September 1989 inclusive. During this period data losses were minimal and did not effect the extraction of QDCs on a monthly basis.

## 11.3 QUIET DAY CURVES

Cosmic radio noise received on the riometer at Casey during quiet times varies quasi-sinusoidally with respect to local sidereal time. The sidereal diurnal variation in the riometer signal during quiescent times is known as the Quiet Day Curve. It is with respect to the QDC value at the same sidereal time that the absorption level at any time is calculated. The accuracy to which the QDC can be determined thus directly effects the accuracy of the calculated absorption levels.

Various methods have been adopted over the years to determine QDCs. A method which is particularly suitable for application to large digital data sets is the 'Inflection Point Method' initially introduced by Krishnaswamy et al. 1985. There are three stages to determining the QDC by the Inflection Point Method. The first step is to put the data into time bins of local sidereal time and, for each time bin, to determine the number of points over a month which fall into each of a full range of equal width signal strength bins. Theoretically, the smaller the time bin the better defined will be the QDC. However, since only a finite number of samples can be collected, if the bin size is too small, then an insufficient number of points are used in the distribution. Expressed

another way, there is an increase in the significance of statistical noise for smaller time bins. Conversely, if the time bin size is too large, the variation of the QDC over the width of the time bin may become significant and effect the result determined. The best balance of these factors that could determine was to select a time bin size of 15 minutes.

The second step in the process of determining the QDC is to determine the QDC value for each time bin from the distribution of the number of samples in the signal strength bins. In the inflection point method, the QDC point at a given time is defined as the inflection point on the high signal side of the distribution for that time (Krishnaswamy et al. 1985). An ideal distribution looks like the example shown in Figure 1. In this idealised example, there is only one inflection point on the high signal side of the curve. The quiet day point is thus uniquely defined. When real data are used, there may be a few local maxima and associated multiple inflection points on the high signal side of the distribution. An example is shown in Figure 2 in which there are three local maxima and three associated inflection points. To handle this situation a threshold for the ratio of the local maximum to the peak value was chosen. This ratio was defined as 'r'. At each local maximum after the true maximum, the ratio was calculated of its value to that of the peak value in the distribution. The 'starting point' was then moved for the evaluation of the inflection point to the last local maximum which exceeds our chosen ratio. From evaluating the data it was found that the value for the ratio, r, which yields the subjectively evaluated 'best' result lies between 0.5 and 0.8. Monthly QDCs were evaluated choosing a ratio value between these limits. The choice of the ratio value between these limits was made month by month based on a subjective judgement of the appearance of the QDC. For the month of the data shown in Figure 2, an r value of 0.5 was chosen. Marked in Figure 2 are the quiet day value chosen for an r value of 1.0 (i.e. the first inflection point after the peak in the distribution) and the value chosen for an r value of 0.5 (the accepted quiet day value for this data).

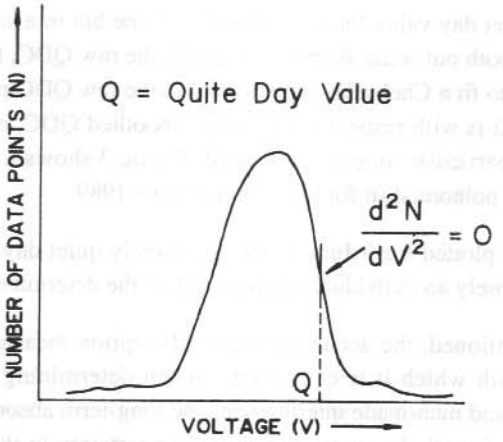


Figure 1. The definition of the quiet day value (Q) by the inflection point method for a number-amplitude distribution for a given sidereal time bin as introduced by Krishnaswamy et al. 1985. This diagram is reproduced from Krishnaswamy et al. 1985.

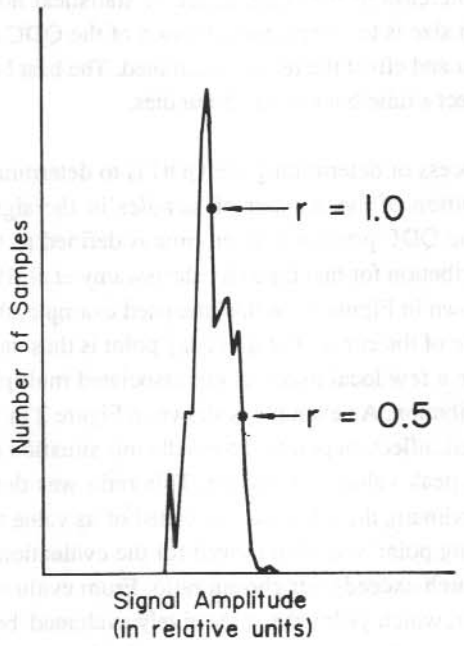


Figure 2. A distribution with multiple inflection points. The computed quiet day value changes depending on the inflection point chosen. Indicated are the inflection points chosen for 'r' values (see text) of 1.0 and 0.5. The value chosen with r set to 0.5 is subjectively considered to be more appropriate.

After determining the quiet day value for each 15 minute time bin in a sidereal day, there was a raw QDC. In order to smooth out some sharp variations in the raw QDC, the third and final stage in evaluating the QDC is to fit a Chebyshev polynomial to the raw QDC points and to interpolate to one minute accuracy. It is with respect to this final smoothed QDC, evaluated monthly, that absorption levels at any particular time are evaluated. Figure 3 shows a comparison of the raw QDC with the Chebyshev polnomial fit for the month of June 1989.

In Figure 4, the data was plotted for 9 June 1989, a relatively quiet day, against the June 1989 QDC. This shows how closely an individual day may follow the determined QDC.

As has already been mentioned, the accuracy of any absorption measurement depends on the accuracy of the QDC with which it is compared. When determining the QDC, the binning process, both solar noise and man-made interference, and long-term absorption (PCA events) can all effect the accuracy achieved. As an estimate of the uncertainty in the QDCs, the QDCs are compared with those of adjacent months. In Figure 5 all four QDC are shown superimposed and displaced from each other. This comparison leads us to claim that the QDCs evaluated are accurate to the order of 0.2dB.

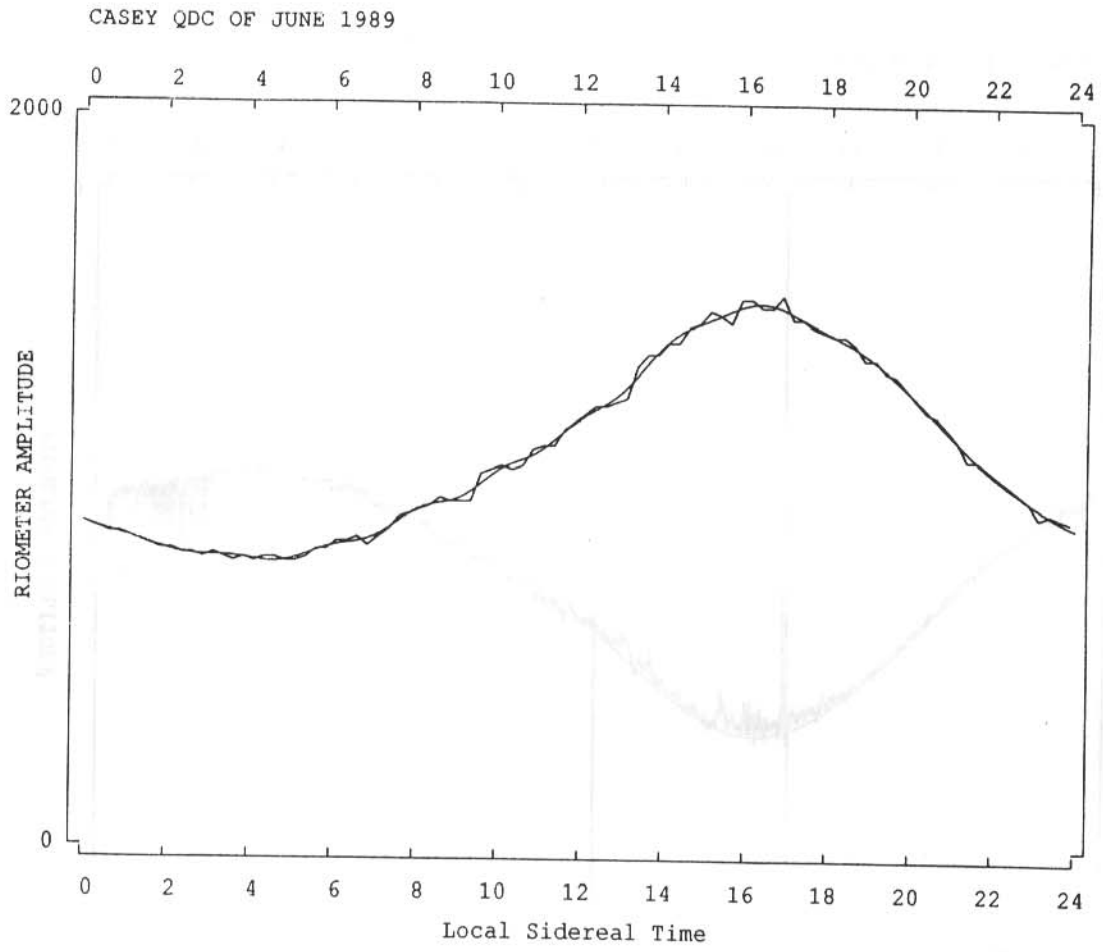


Figure 3. A comparison of the raw June QDC with the smoothed QDC which is obtained by a Chebyshev polynomial fitting program.

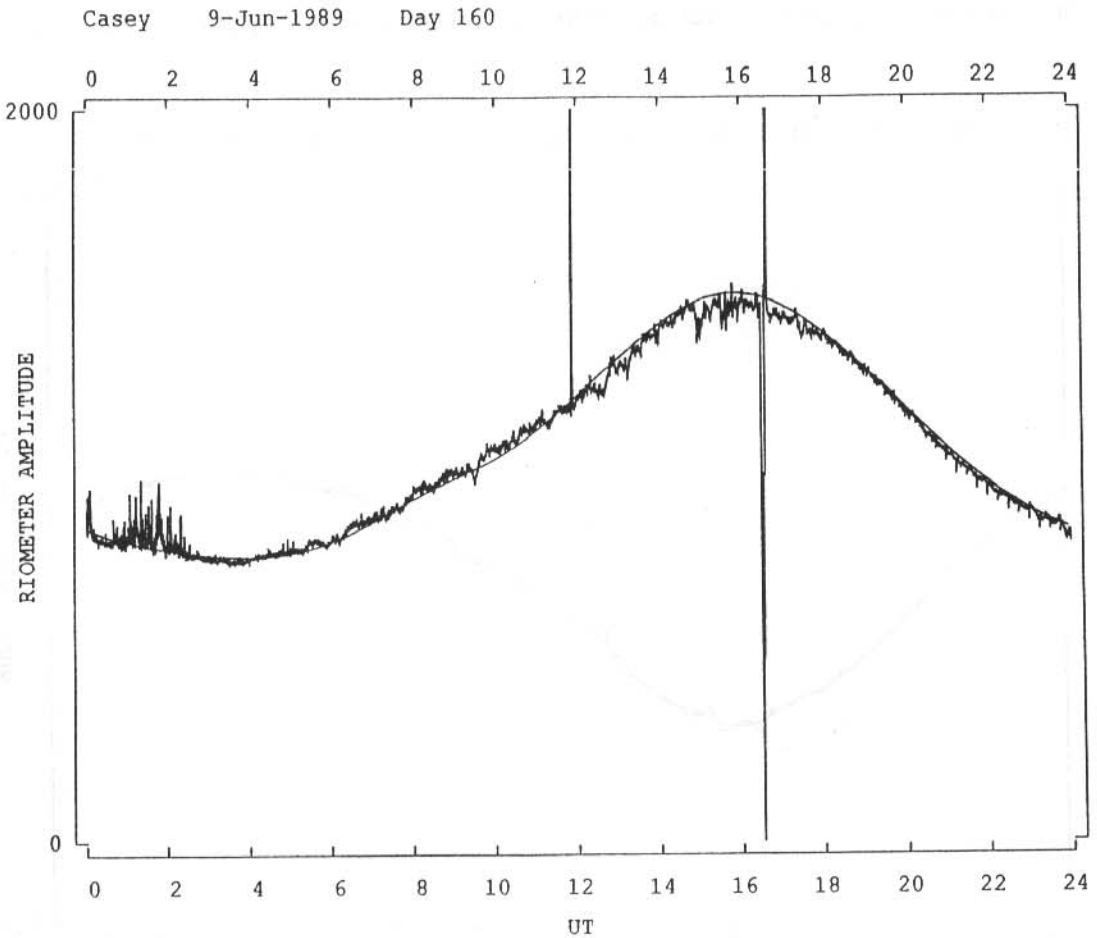


Figure 4. A comparison of an individual relatively quiet day, 9 June 1989, with the smoothed QDC for June. There is good agreement between the two curves. The daily calibration sequence occurs at 1630 UT.

## 11.4 DIURNAL VARIATIONS IN ABSORPTION AT CASEY

The absorption, A (in dB), at a particular time is defined as

$$A = 10 * \log(Q/R) \qquad (1)$$

where R is the signal strength at the time and Q is the monthly QDC value at the corresponding sidereal time.

In the initial data set, there are six digital data values collected each minute. To reduce the amount of data that had to be handled for an average absorption evaluation, one point every minute was selected. It is stressed that there has been no averaging in this selection, thus the points evaluated are still 'instantaneous' absorption values from which percentages can be accurately estimated. The initial digital riometer data were reduced to absorption values, one value per minute, by applying the equation stated above to the selected points. After reducing the data, all data is manually excluded, which were interfered with by anthropogenic sources and direct solar radio noise emissions. The data during times of Polar Cap Absorption were also excluded. It is believed these data are best treated separately from other forms of absorption.

In determining the percentage occurrence of absorption it is important that all times of 'no absorption' are included in the calculations. Times of 'no absorption', have included all times when the calculated absorption level is within our estimated uncertainty of 0.2 dB above the QDC. All data more than 0.2 dB above the QDC is rejected as due to interference and is not included in the averages.

The diurnal variation in the percentage of time for which the absorbtion exceeded given levels (0.3 dB, 0.5 dB and 1.0 dB) are shown in Figures 6, 7 and 8. The time of occurrence of magnetic noon and magnetic midnight are also labelled. In all three figures, there is only one peak in the pecentage occurrence and that is occurs between 5 and 10 UT. The minima occur around 16 to 20 UT. This suggests that the absorption at Casey is generally higher during the daytime hours than at night.

Casey is a generally a 'polar cap' station, but at magnetic noon it may be very close to the magnetic cusp. Note that in Figures 6, 7 and 8 the absorption peak occurs after magnetic noon. Perhaps the absorption that are recorded is associated with the post-noon cleft region rather than directly with the cusp. Figure 9 shows the riometer signal from 15 July 1989 plotted against the QDC for July. This Figure shows a typical daytime absorption event recorded between 5 and 7 UT.

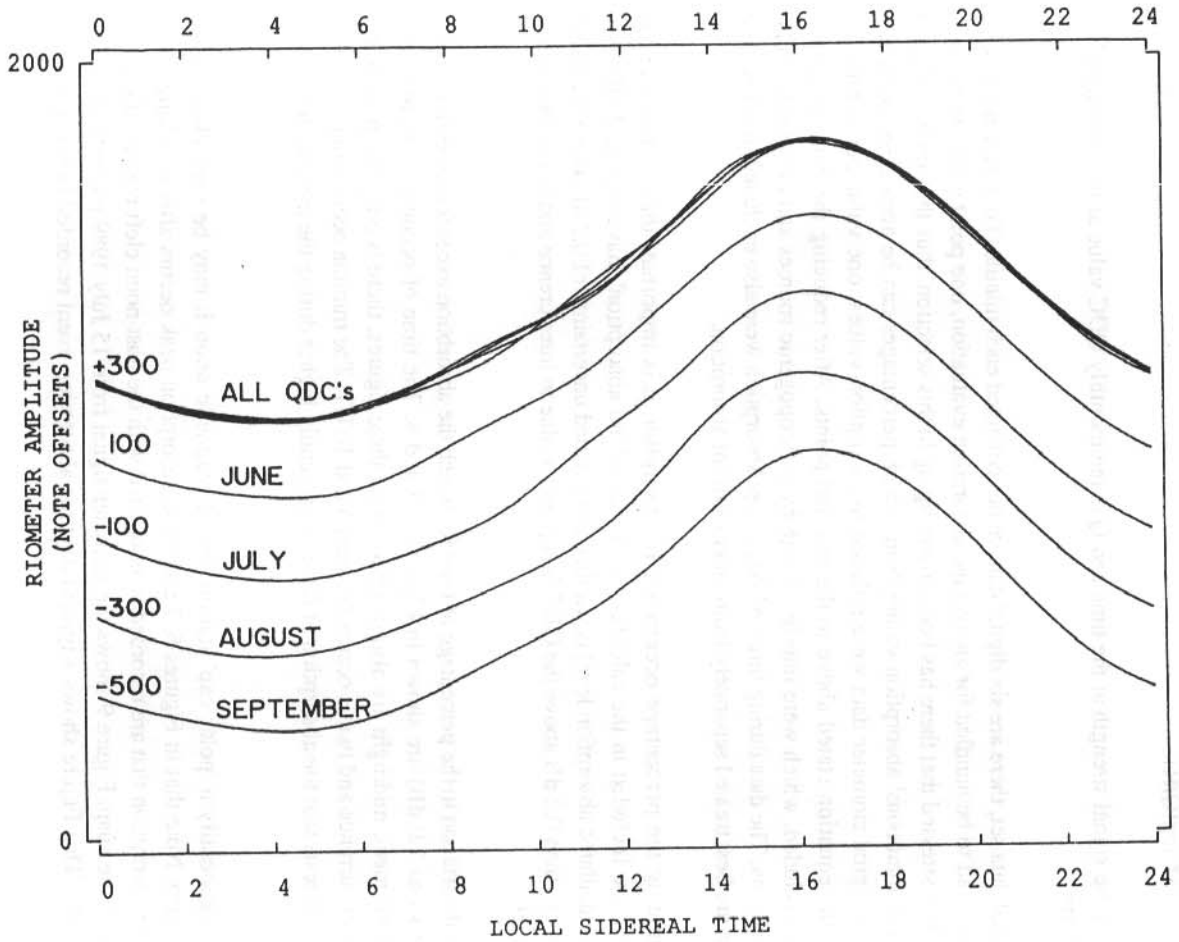


Figure 5. A comparison of the four monthly QDCs calculated. The upper most plots are a superposition of all four QDCs showing the extent of monthly variations. Below this each monthly QDC is plotted individually.

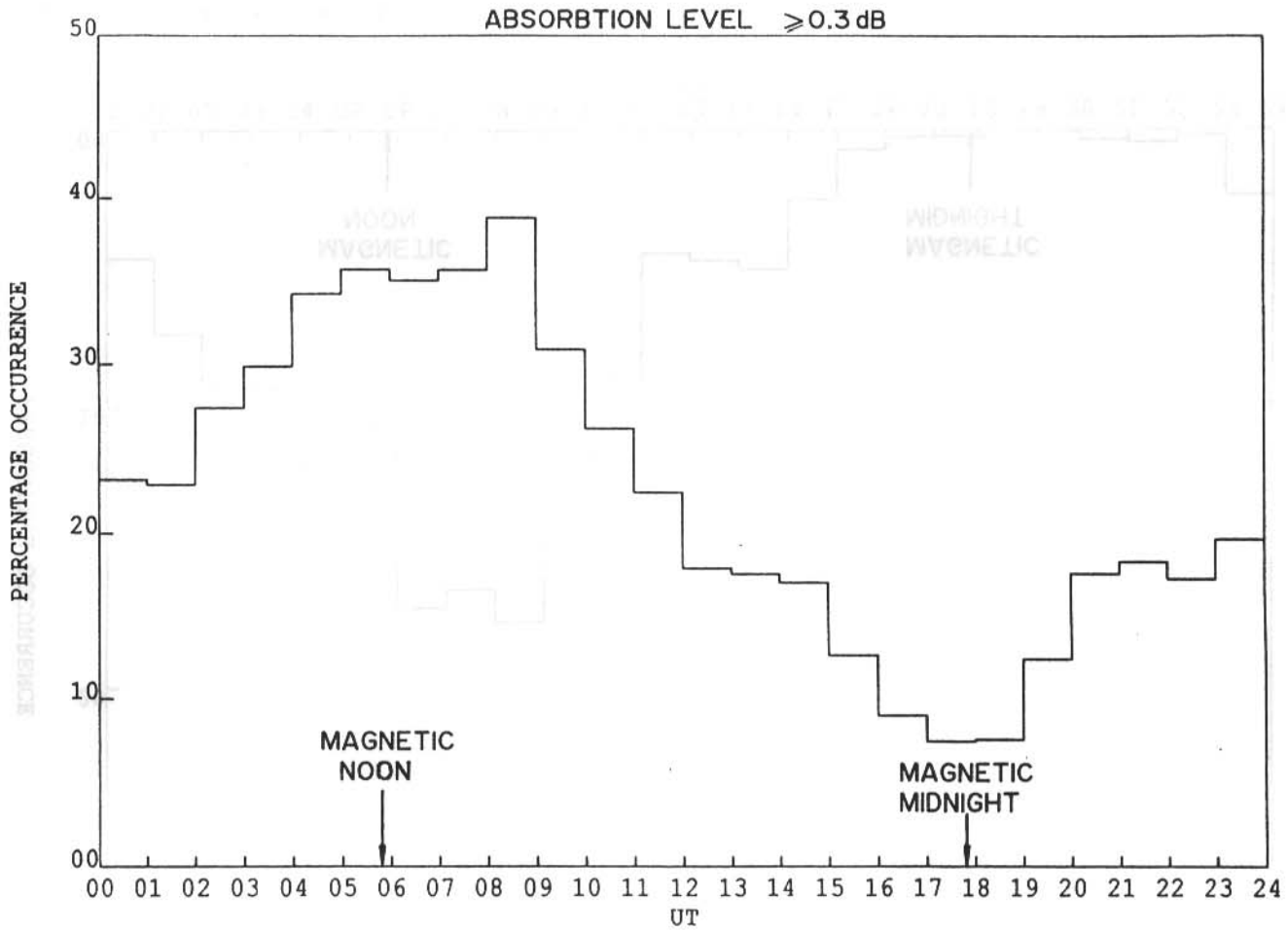


Figure 6. The diurnal variation of the percentage of time that the absorption exceeded 0.3 dB.

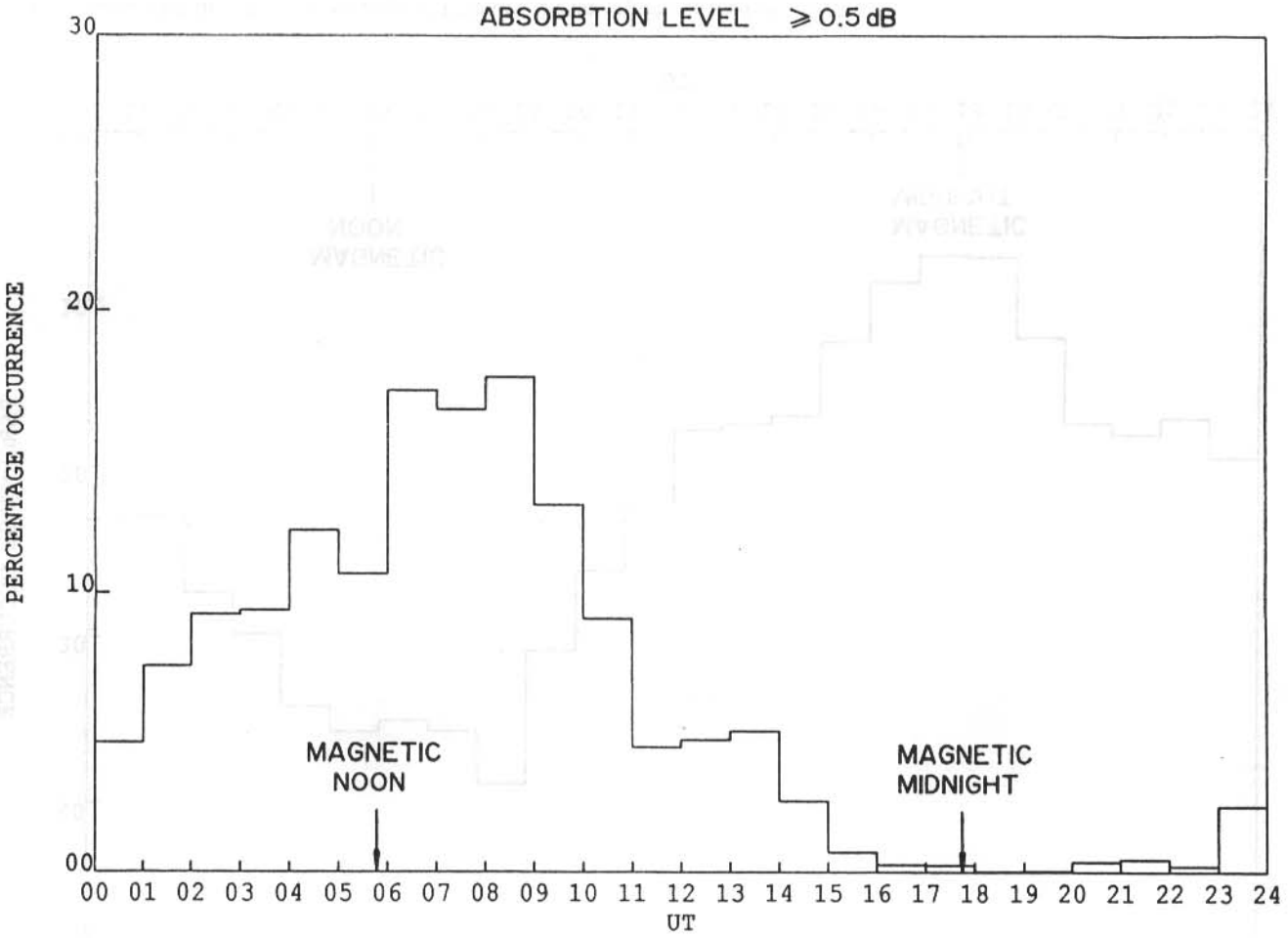


Figure 7. The diurnal variation of the percentage of time that the absorption exceeded 0.5 dB.

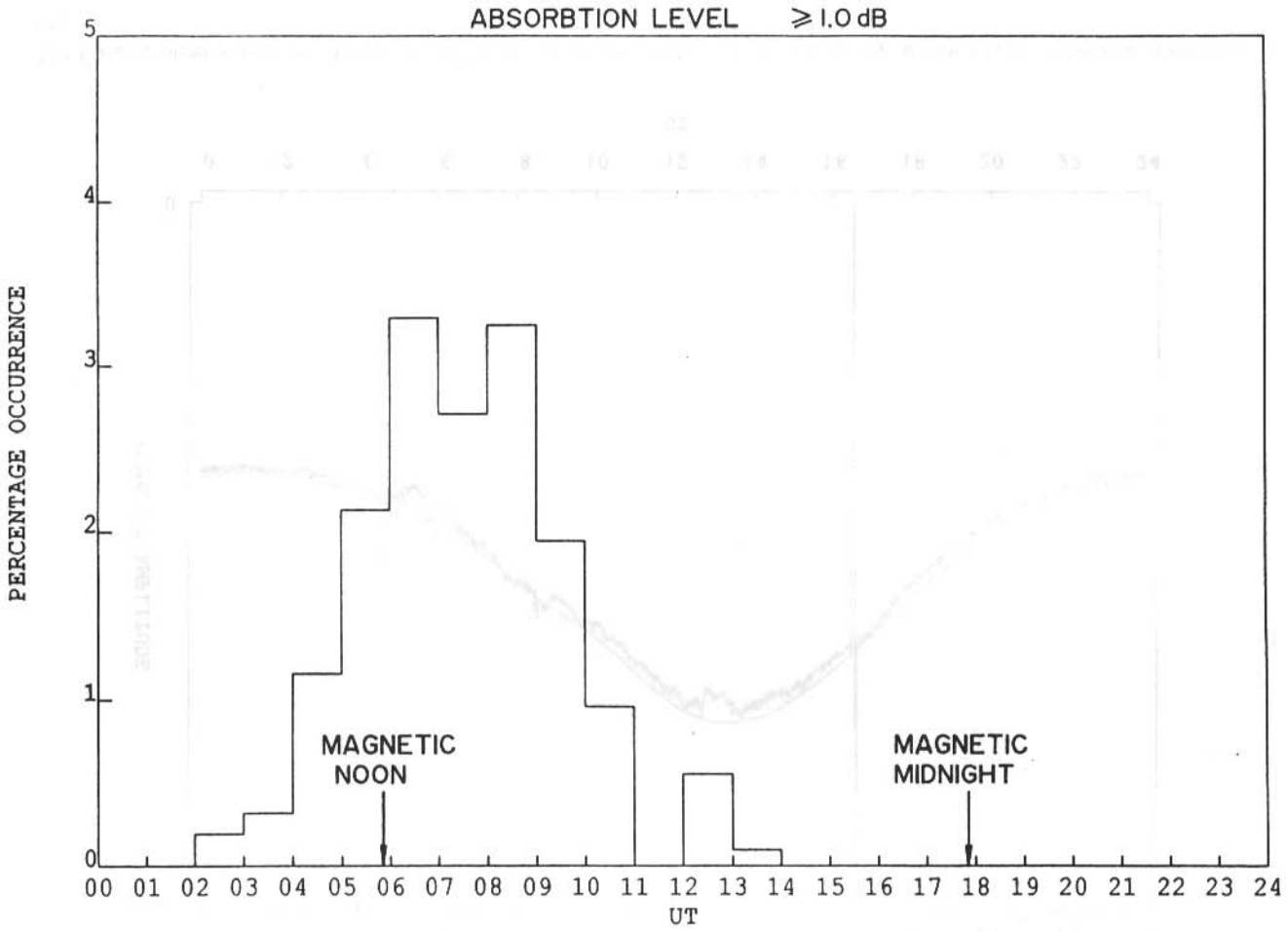


Figure 8. The diurnal variation of the percentage of time that the absorption exceeded 1.0 dB.

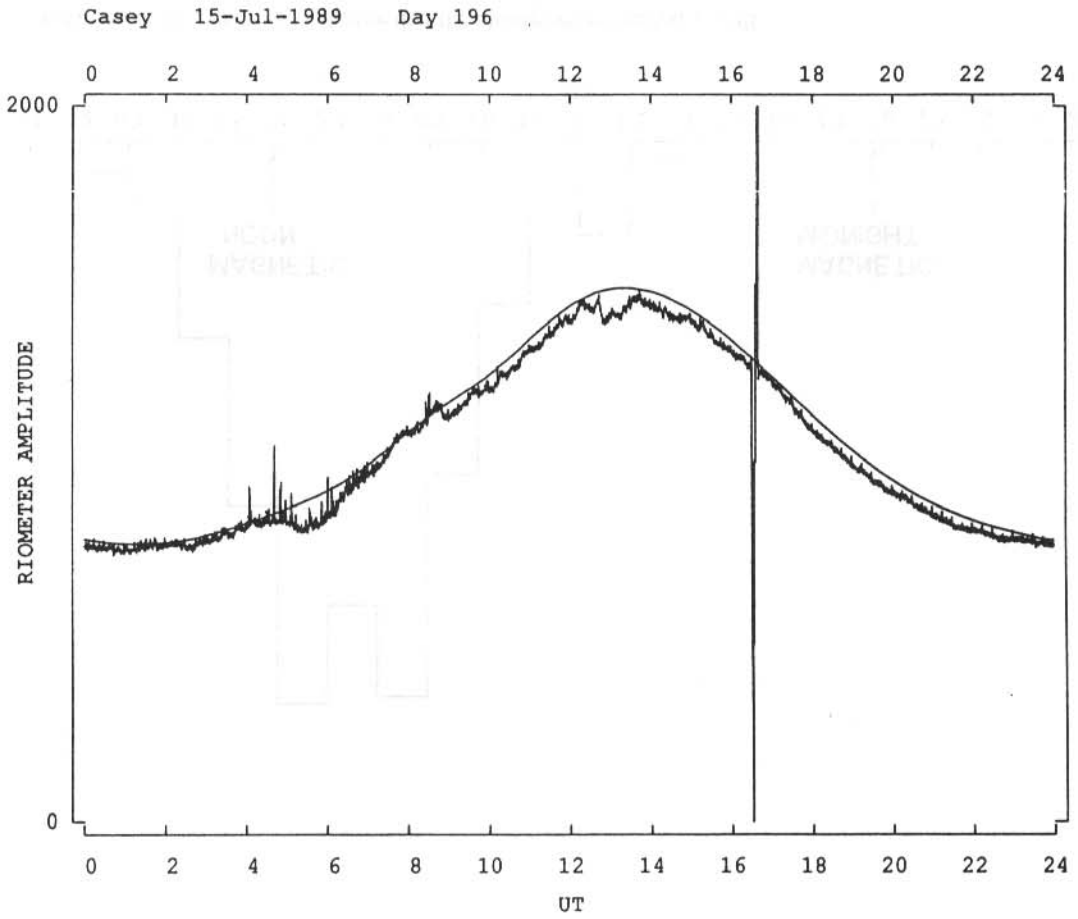


Figure 9. The Casey riometer data for 15 July 1989 plotted against the QDC for that month. This shows a typical daytime absorption event around 5 UT.

It may have been expected that midnight break-up events may progress as far poleward as Casey yielding low percentage occurrences of high levels of absorption. Figures 7 and 8 show that even at modest absorption levels in excess of 0.5 dB and 1.0 dB there are no events recorded around magnetic midnight over this four month period at Casey. It should be noted that the period covered by this analysis is a period of generally high solar activity.

## 11.5 A PERIODIC ABSORPTION EVENT

Riometer data is generally interpreted as measuring absorption due to particle precipitation. When enegetic particles penetrate into the lower E and D regions of the atmosphere they cause enhancements in the ionisation at these levels which in turn enhance the absorption of the cosmic noise on its passage through to the riometer antenna on the ground. Riometer absorption events are generally classified into three types, solar flare absorption (SFA), polar cap absorption (PCA) and auroral absorption (AA). These events are distinguished by characteristics that are the result of the different sources of the increased ionisation in the lower E and D regions. SFA is caused by solar X-rays, PCA is generally caused by energetic protons of solar origin and AA is due to auroral electron precipitation.

Figure 10 shows an event recorded on 10 June 1989. The event perhaps started as early as 4 UT, but specific intererest is that between 12 and 18 UT. There are several times when the riometer signal is significantly above the QDC. It is impossible to explain this event solely in terms of particle precipitation because the QDC is significantly exceeded by what appear to be natural variations in the riometer signal. The data for this day are also presented as absorption levels with respect to the QDC in Figure 11. A negative absorption value corresponds to times when the QDC level was exceeded. Figure 11 shows that the QDC level was exceeded by up to 0.4 dB. An interesting feature of this data is its quasi-periodic nature. Between 16 and 18 UT the period of the ocillations are between 10 and 20 minutes. Although, at this stage no attempt was made to explain these periodic variations in absorption level, it may be signicant that the oscillations are recorded on top of a significant background absorption level.

## 11.6 ACKNOWLEDGMENTS

This research is the result of a cooperative project between Antarctic Division, Australia and the Chinese National Committee for Antarctic Research, Peoples Republic of China. The authors thank both organisations for their support of this research. Our gratitude also to Dr David Watts, who provided the programs adapted for this analysis.

## 11.7 REFERENCE

Krishnaswamy, S., Detrick, D.L., *and* Rosenberg, T.J. (1985). The inflection point method of determining riometer quiet day curves. *Radio Science 20*:123-136.

Hargreaves, J.K. (1969). Auroral absorption of HF radio waves in the ionosphere: a review of the first decade of riometry. *Proceedings of the IEEE 57*:1348-1373.

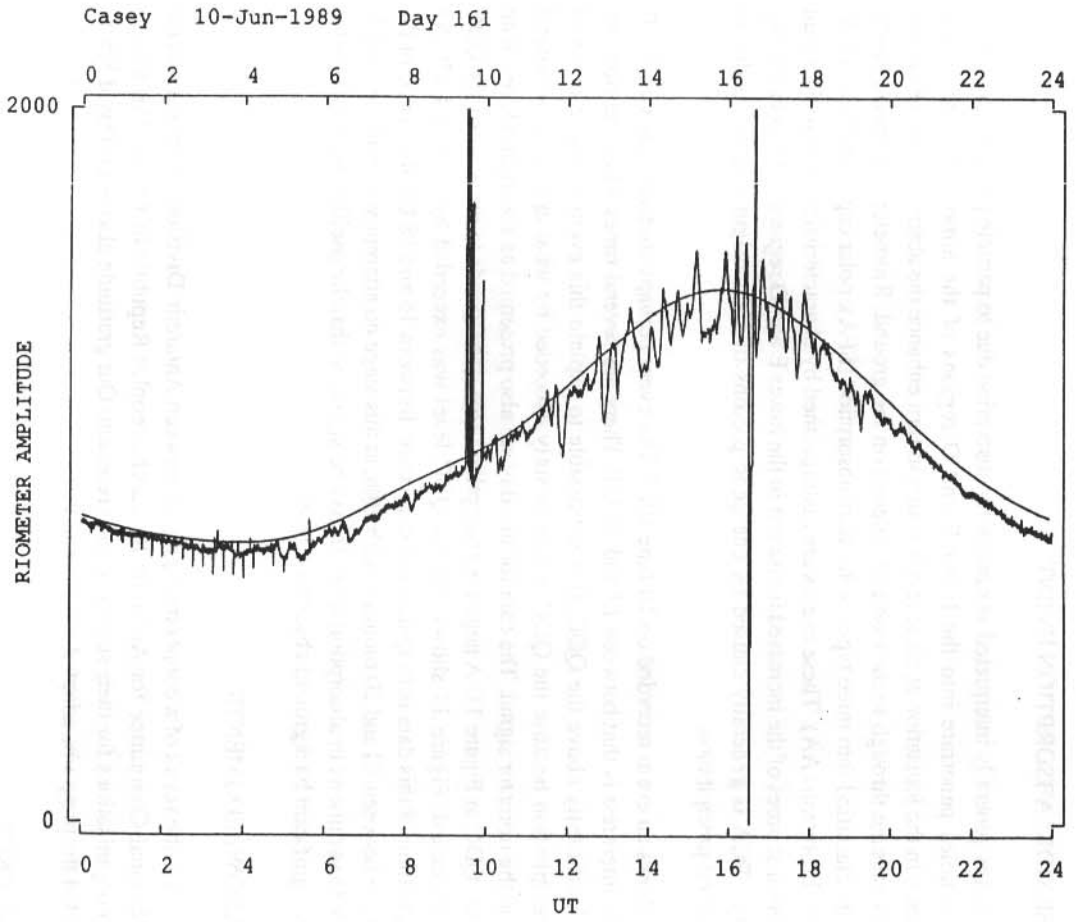


Figure 10. A specific periodic event which occurred on 10 June 1989. Between 12 UT and 18 UT there are several portions of the data which are significantly above the QDC. This feature cannot be explained solely by particle precipitation effects.

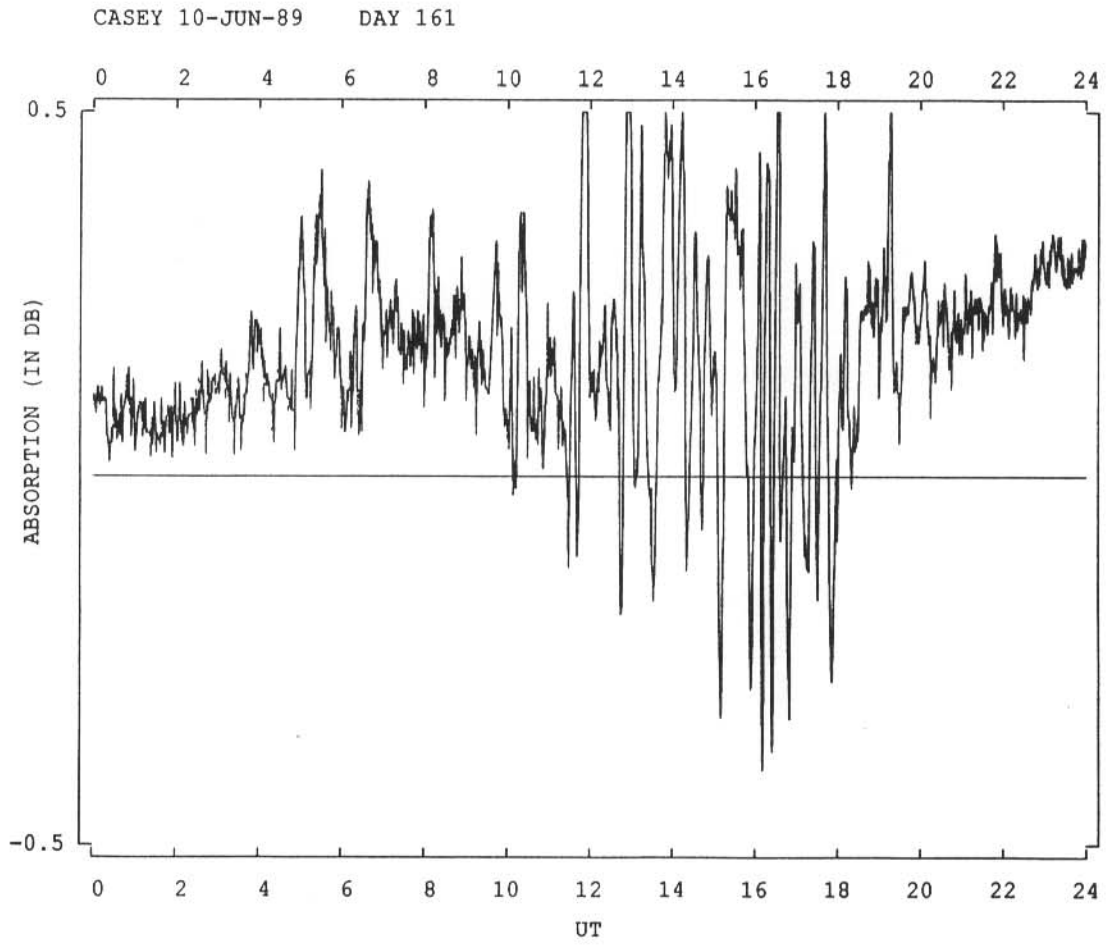


Figure 11. The absorption values for the event shown in Figure 10. Note that negative absorption values correspond to data above the QDC.

# 12. DAYTIME HIGH-LATITUDE TROUGHS AND THEIR POSSIBLE ASSOCIATION WITH TRAVELLING IONOSPHERIC DISTURBANCES

G.G. Bowman
Department of Physics
University of Queensland
St Lucia Qld 4072
Australia

ABSTRACT

A further analysis of ionograms from Ellsworth, Antarctica has shown that trough magnitudes are a function of geomagnetic activity. The trough activity is more intense and the onset times are earlier for higher geomagnetic activity. For $\Sigma K_p \cong 30$ the troughs are observed at Ellsworth around 1600 local time (LT) whereas for $\Sigma K_p \cong 10$ they are not observed until around 2100 LT.

The principal features of these 'so called' daytime troughs, namely modulated height rises, electron-density depletions and spread-F occurrence during recovery, are compared with similar features observed for midlatitude spread-F events. Evidence is presented to suggest that these troughs are a consequence of the passage of travelling ionospheric disturbances which originate around noon in the polar-cusp region (generally located at approximately 80° corrected geomagnetic latitude). The different onset times are seen as a consequence of disturbance speeds also being a function of geomagnetic activity.

## 12.1 INTRODUCTION

As this paper is concerned with high-latitude regions, it is appropriate that corrected geomagnetic coordinates be used (CGlat and CGlong, Hakura 1965). At Ellsworth local time (LT) = UT - 3 hour while magnetic time (MT) = UT - 3.5 hour (Penndorf 1965). It is now obvious that ionospheric ionisation depletions (troughs) observed in latitudes extending from polar to sub-auroral regions cannot all be associated with the projection of the plasmapause to ionospheric heights. The troughs most likely to be so associated are the light-ion troughs (Taylor and Walsh 1972). In Figure 4 of Rodger and Pinnock (1982), it is shown that trough locations and movements in the late afternoon and early evening hours are not consistent with the corresponding plasmapause parameters. This present paper will be concerned principally with the 'so called' daytime trough (Whalen 1987, 1989, Ben'kova 1980). It occurs mainly in the afternoon especially for stations poleward of (say) 65° CGeom. However, despite the use of this term it can be recorded at lower latitudes in the early evening hours for low geomagnetic activity (Figure 7 - to be discussed later). The work by Bowman (1969) using ionograms from Ellsworth, Antarctica (62.6°S, 21.5°E CGeom.) during the International Geophysical Year has been extended to investigate the day to day changes in the magnitude of the ionisation distortions (troughs) and the way the magnitude varies with geomagnetic activity. Bowman

(1969) will hereafter be called paper 1. A comparison will also be made between the characteristics of a spread-F event at Townsville, Australia (28.34°S, 224.2°E CGeom.) with small-scale trough events at Ellsworth. Finally, consideration will be given to the possibility that these daytime troughs result from the passage of travelling ionospheric disturbances (TIDs) generated in polar cusp regions around local midday.

## 12.2 DAY TO DAY VARIABILITY OF DAYTIME TROUGH SIZES

The day to day variability in the strength of the disturbances responsible for the troughs has been investigated. These strengths were being estimated (using a method to be described) for three of the months of 1958 (April, May and September). These estimates involve the equatorward slope recorded by ionograms (which are relatively free of spread traces) during the early stages of the passage of a trough. This variation in trough magnitudes will be compared with local times of onset as well as with geomagnetic activity. It was not practical to estimate trough sizes from $f_0F_2$ values near the centres of troughs because of difficulties (except on a few occasions, see paper 1) in identifying the traces on the spread ionograms representative of vertical incidence.

The magnitude of the equatorward slope can influence the nature of ionograms recorded. Consider the effects on ionograms of both a moderate and a large ionospheric height rise over a period of an hour or so and produced by a disturbance moving horizontally. Figure 1(a) shows a height rise with a slope of 15°while Figure 1(d) illustrates a much larger slope of 45°. After the passage of a moderate monotonic height rise (dashed lines on Figure 1(a)) an ionogram will record the main trace (trace 1 on Figure 1(b)) plus an extra off-vertical trace (trace 2) from the sloping isoionic contours. The small extra range of trace 2 means that in all probability trace 1 and trace 2 will overlap (as illustrated). If, however, the slope is modulated (e.g. by a wavetrain of a travelling ionospheric disturbance (TID)) significantly larger tilted surfaces will appear (Figure 1(a)). Therefore, when the slope (with modulation) has moved an appropriate distance from the recording site, additional traces (duplicate traces) will be recorded leading to a certain degree of range spread. The duplicate traces are illustrated as traces 2,3 and 4 on Figure 1(c) (called a type B event). All the ionograms illustrated diagrammatically on Figure 1 represent O-ray traces only. Similar arguments can be made for the large height rise (Figure 1(d)) with however, somewhat different relative positioning of the main and duplicate traces on the ionograms. Figure 1(e) shows, for no modulation of the slope, a main trace (vertical incidence) with a h'F value around 600 km (trace 1) while the duplicate trace from the sloping surface (trace 4) has a much smaller h'F value (around 460 km). With the isoionic contours of the slope modulated with wavy patterns, additional duplicate traces are recorded as Figure 1(f) shows (called a type A event). Here, unlike the ionogram shown in Figure 1(c) for a moderate height rise, the larger the off-vertical angle for signals responsible for a particular trace, the smaller the virtual ranges recorded for that trace. This configuration of traces (Figure 1(f)) occurs for well-defined troughs as paper 1 illustrates.

The onset of the trough at Ellsworth can be easily identified (paper 1) by the fact that the virtual ranges of the second-hop trace are not twice those of the first-hop trace. This results from the relatively steep equatorward edge. Although not precise as retardation effects vary from one event to another, nevertheless,the method adopted which uses this discrepancy in ranges, is thought to give at least an approximate measure of the magnitude of any particular event. This measure is given by the relationship $\Delta h' = 2h'_1 - h'_2$ where (for a frequency of 4 MHz) $h'_1$ is the virtual range of the first-hop trace while $h'_2$ is the virtual range of the second hop trace. For 18 days of the 91 days of April, May and September of 1958 there were no records or the records were not suitable. The remaining 73 days were divided into four sets according to the maximum value recorded of $\Delta h'$ for each event. The limits for each set are shown in Table 1 together with the number of events in each set. This table also shows very approximate estimates of the range of angles associated with each set for a virtual height of the first hop reflection point set arbitrarily at 300 km. No discrepancy could be found between $2h'_1$ and $h'_2$ on 24 of the days (set 4). Any tilted surface which did occur would need to be relatively small (say less than 15°). An estimate of the limiting value of $\Delta h'$ for this event has been put at 15 km. These 24 days will be called, at least tentatively, 'non-trough' days.

Set 1 events can be classed as large-scale troughs while sets 2 and 3 events will be called medium-scale troughs. The term 'small-scale troughs' will be discussed later. Figure 2(a) shows the average $\Sigma K_p$ value for the days of each set. It is seen that the magnitude of the trough disturbance is a function of geomagnetic activity the more pronounced events occurring for high activity. For set 4, when no troughs were detected, the average $\Sigma K_p$ value is low (14). As found for other investigations (paper 1, Kohnlein and Raitt 1977), Figures 2(b) and 2(c) show that trough onset times are later for lower geomagnetic activity. Medium-scale troughs (sets 2 and 3) are recorded for $\Sigma K_p$ values from 10 to 40 (Figure 2(b)) while large-scale troughs only occur for $\Sigma K_p$ greater than 20.

Because they represent troughs with steep equatorward edges all the large scale troughs exhibit, at the time of maximum disturbance, ionogram trace arrangements similar to that shown by Figure 1(f). These will be called type A ionograms. However, only a proportion of medium-scale troughs record type A ionograms. The other medium-scale events record what will be called type B ionograms. These ionograms have multiple traces similar to those recorded for spread-F events (Figure 1(c)). The relative occurrence of type A and type B ionograms for sets 1, 2 and 3 are shown at Table 2, where it can be seen that for all troughs type A ionograms are seen for 61% of the time. In view of discussion to follow it seems important to note that 39% of trough ionograms (for sets 1, 2 and 3) show spread traces not unlike those observed in midlatitudes.

## 12.3 EXAMPLES OF TROUGH SIZES

Figure 3 is an example of a large-scale daytime trough. It has been adapted from Figure 7(a) of paper 1 with the isoionic contours adjusted to illustrate better normal-incidence reflection for the three signals which produce the off-vertical traces with zenith angles of 17°, 23° and 38°.

The massive electron-density depletion is obvious from the isoionic contours. The zenith-angle information was available because of interference effects produced by an iceshelf (Bowman 1968). Thus, this example and others of similar type (paper 1) illustrate the experimental evidence for the modulation by wavelike structures of the equatorward edge of daytime troughs. Using a method described in paper 1 (involving measurements taken at Ellsworth) the speed of movement of this disturbance (Figure 3) was found to be 94 m $s^{-1}$. It will be seen later that the time of arrival of this disturbance (Figure 3) is consistent with a disturbance generated in the cusp region at midday and travelling equatorward at 94 m $s^{-1}$.

Figure 4 illustrates what might be called a medium-scale daytime trough event. N(h) analyses on ionogram traces have given true reflection ranges for signals which are responsible for the various traces (main traces and duplicate traces) which were recorded during the passage of this disturbance. In addition, interference patterns (Bowman 1968) visible on some traces allowed zenith angles-of-arrival of these traces to be determined. Trial and error adjustments of the horizontal scale to achieve the best fit for all the available information produced the plot of isoionic contours shown on Figure 4(b), thus implying a speed of movement of 111 m $s^{-1}$. The drop in $f_0F_2$ of about 2 MHz (Figure 4a) at the trough centre is much smaller than that observed for the large-scale trough (Figure 3). Figures 4(a) and 4(b) also show, during the recovery phase of the disturbance, the existence of a tongue of ionisation similar to those which have been observed in midlatitudes (Bowman and Dunne 1981, 1984).

As explained earlier, small equatorward slopes were not detected because of the insensitivity of the method used (a very approximate estimate of 15° as a lower limit of detection was proposed in the previous section). Although the days when no slope was detected have been called non-trough days, Figure 5 suggests that small-scale troughs probably exist on some or all of these so called 'non-trough' days. The five minute separation between ionograms (for Ellsworth) on the regular world day of September 6, 1958 allowed N(h) analyses which detected an ionospheric disturbance which could possibly be called a small-scale trough. Figure 5(a) shows the isoionic contours resulting from these analyses. There appears to be a modulated height rise and an abrupt step in $f_0F_2$ at the start of the height rise (Figure 5b). Also, as shown on Figure 5(c), range spread is associated, particularly at around 2100 LT, where it is significant (about 120 km wide). If movement is involved, as seems likely, the angle $\theta$ (illustrated) will represent the background slope. Since the speed of movement is not known, the plot on Figure 5(a) is not to scale and the magnitude of $\theta$ is unknown. In the next section the characteristics of this event will be compared with a similar midlatitude event involving spread-F occurrence. The line drawn through the observations on Figure 2(b) allows an approximate estimate of the expected

time of arrival of a trough for any particular $\Sigma K_p$ value. Since $\Sigma K_p$ on September 6, 1958 was 14, if a trough exists it can be expected around 1930 LT. Therefore, since this is roughly the time of onset of the height rise on Figure 5(a), it is probably not unreasonable to regard this event as a small-scale trough.

## 12.4 SMALL-SCALE TROUGHS AT MIDLATITUDES

In recent times increasing evidence is becoming available to suggest that there are precursors to midlatitude spread-F events in the form of modulated height rises (Bowman 1986, 1990; Bowman and Monro 1988). Furthermore, electron-density depletions are also associated with these midlatitude events. Five minute ionograms for a lower midlatitude station, Townsville, on August 15, 1989, have allowed isoionic contours to be determined (using N(h) analyses) prior to and during the occurrence of a spread-F event. These contours are shown by Figure 6(b) where a background height rise with modulation can be seen. The $f_0F_2$ reduction (Figure 6a) of about 1.7 MHz with a minimum at the height maximum in the isoionic contours has been called a small-scale trough on the diagram. This classification seems reasonable since the overall behaviour of the ionosphere at Townsville on this occasion is not any different from that observed for the daytime large-scale trough illustrated by Figure 3, except that the ionosphere is much more disturbed for the large-scale event. Both events have modulated height rises, electron-density depletions and spread-F occurrence particularly during the recovery phase. Figure 6(c) shows the degree of range spread for the Townsville event. The tilted isoionic contours marked AB, CD and EF on Figure 6(b) provide surfaces which reflect radio signals to any transmitter and produce duplicate traces at different ranges on ionograms. Therefore, spread ionograms similar to the one shown by Figure 1(c) can be expected.

## 12.5 A POSSIBLE ASSOCIATION WITH TRAVELLING IONOSPHERIC DISTURBANCES (TIDs)

An early paper on spread-F occurrence at a midlatitude station (McNicol et al. 1956) reports on an extensive investigation of ionospheric structure movements at these times. For 87 events speeds in the range 42-97 m $s^{-1}$ were found. It seems quite reasonable to call these movements TIDs, which it now seems likely (Dyson et al. 1970) are associated with atmospheric gravity waves (AGWs) in the neutral atmosphere. Subsequent investigations have supported the evidence for moving structures at these times by considering the changing ranges of the duplicate traces which can be observed regularly on mid latitude ionograms (Bowman 1986, Bowman and Monro 1988). The figures to be discussed in this section are drawn to support the idea that the daytime troughs discussed in this paper might result from AGWs generated in the polar-cusp region near midday. The AGWs will be observed in the ionosphere as TIDs. The similarity of daytime trough events with midlatitude events which, as just discussed, seem to be associated with TIDs gives support to this idea, as does the existence of wavelike structures in the macroscale height rises for both regions.

Although the data points show a considerable spread, Figure 9 of paper 1 indicates the relationship which exists between the speeds of transit of these daytime troughs at Ellsworth and their times of onset. Figure 7 considers the generation of a disturbance (for each of five different speeds ranging from 50 m $s^{-1}$ to 150 m $s^{-1}$) at a CGlat of 80° (position $C_0$) and a CGlong of (say) Ellsworth at noon. The sun direction stays fixed while as the earth rotates the position $C_0$ changes (at hourly intervals) to $C_1$, $C_2$ etc. up to $C_6$ when the magnetic time is 1800 hours. As the disturbances travel equatorward, they can be located at different latitudes for each hour and each speed. These positions for each speed reveal arcs on the CGlat magnetic time plot. The average value of $\Sigma K_p$ for each of these speeds is shown indicating the relationship between speeds and geomagnetic activity. As the earth is imagined as rotating Ellsworth will move on the diagram at a CGlat of 62.6°. It is shown plotted at the approximate time of onset for the large-scale trough on April 27, 1958. The 94 m $s^{-1}$ curve which was the speed measured at Ellsworth passes through this position. The arcs derived by assuming uniform speeds of travel of disturbances from near polar regions are consistent with those determined by other workers (Muldrew 1965, Whalen 1987, Ben'kova 1980).

Figure 8 considers the relationship between disturbance speeds and onset times in a different way. Parts of Figures 10 and 14 of paper 1 are reproduced here at Figure 8(a) and 8(c) respectively. The curve relating speeds to onset times on Figure 8(a) represents a reasonable estimate of the scattered points on Figure 10 of paper 1. The onset times for 6 different speeds are used as the starting points to plot (see straight lines on Figure 8(b)) the disturbance positions (assuming equatorward propagation) at times earlier than the onset times at Ellsworth. Figure 8(b) shows that these straight lines converge at approximately 80° CGlat and at a time around midday. Thus, the relationship between speeds and onset times (Figure 8(a)) is consistent with the proposed generation of disturbance near the cusp at noon.

The measurements reported by Whalen (1987) for the daytime trough indicated that trough activity was detected simultaneously at 16 stations, thus, suggesting that the arc is (except for different geomagnetic activity) a permanent feature fixed on the earth relative to the orientation of the sun. The geomagnetic activity for this day was very high ($\Sigma K_p = 40$) following a storm sudden commencement at 00h 35m UT on that day. In view of the high geomagnetic activity it does not seem unreasonable to suggest that disturbances of the type which have been proposed here are generated in quick succession as the position of noon changes throughout the day. This would lead to a series of independent disturbances which will exist simultaneously at different CGlatitudes. Figure 9 is an attempt to show an instantaneous picture of the earth with troughs at 6 locations (P to U) for disturbances generated earlier (at hourly intervals) at midday ($C_0$ to $C_5$) as the sun rotates with respect to the earth. If equatorward propagating TIDs are responsible for daytime troughs, the fact, as this present analysis shows, that they are seen on many days at a fixed location suggests that even for moderate geomagnetic activity, generation must occur at frequent intervals during any day.

## 12.6 DISCUSSION

As stated earlier, daytime troughs and spread-F events in lower midlatitudes have remarkably similar characteristics. As it seems likely that TIDs are responsible for these lower midlatitude events it does not seen unreasonable to propose that TIDs are also responsible for the daytime troughs. The speeds of movement at these widely-separated locations are comparable (McNicol et al. 1956, Bowman 1969, Rodger and Pinnock 1982). Furthermore, precipitation in the cusp region at noon is well documented (Tsunoda et al. 1989) so that a credible source for TIDs exists in these high-latitude regions. Figure 7 shows that the assumption that TIDs are involved leads directly to the daytime-trough arc on a CGlat/magnetic-time plot, as is observed.

The isolated troughs which are found inside (poleward) of the principal trough region which Muldrew (1965) called the main trough, have remained unexplained. Commenting on these supplementary troughs Sharp (1966) states

> "Muldrew describes a series of 'high-latitude troughs' in addition to the main trough, but a given high-latitude trough is not as stable or consistent a feature of his data as the main trough. In the data it was often observed that many peaks and valleys poleward of the midlatitude trough, some of which are nearly as prominent as the midlatitude trough".

In view of the results for the spread-F event shown on Figure 6 for Townsville (28.3° CGlat), it is just possible that these high-latitude troughs are in fact sundry spread-F events.

Bowman (1990) has suggested, for midlatitude spread-F events, that large-amplitude AGWs saturate and break producing electron-density depletions (due to mixing, King 1966) and resultant height rises. If the proposed association between daytime troughs and midlatitude spread-F events is correct, breaking AGWs may explain the characteristics of these daytime troughs.

## 12.7 ACKNOWLEDGMENTS

This work is supported by the Australian Research Council. The Townsville ionograms were kindly supplied by the IPS Radio and Space Services of Australia.

## 12.8 REFERENCES

Ben'kova, N.P., Kozlov, Ye. F., Mozhayev, Am. M., Osipov, N.K. *and* Samorokin, N.I. (1980). Main ionospheric trough in the daytime sector, according to vertical sounding. *Geomagnetism and Aeronomy 20*:571-573.

Bowman, G.G. (1968). Directional characteristics of ionosonde interference patterns from the Filchner ice shelf. *Journal of Atmospheric and Terrestrial Physics 30*:1115-1134.

Bowman, G.G. (1969). Ionization troughs below the $F_2$ -layer maximum. *Planetary and Space Science 17*:777-796.

Bowman, G.G. (1986). Some $F_2$ layer-sporadic-E relationships. *Annales Geophysicae 4A*:55-60.

Bowman, G.G. (in press). A review of some recent work on mid-latitude spread-F occurrence as detected by ionosondes. *Journal of Geomagnetism and Geoelectricity*.

Bowman, G.G. *and* Dunne, G.S. (1981). Some initial results on mid-latitude spread-F irregularities using a directional ionosonde. *Journal of Atmospheric and Terrestrial Physics 43*:1295-1307.

Bowman, G.G. *and* Dunne, G.S. (1984). Grossly-distorted isoionic contours associated with spread-F occurrence at mid-latitudes. *Journal of Atmospheric and Terrestrial Physics 46*:1193-1205.

Bowman, G.G. *and* Monro, P.E. (1988). Mid-latitude range spread and travelling ionospheric disturbances. *Journal of Atmospheric and Terrestrial Physics 50*:215-223.

Dyson, P.L., Newton, G.P. *and* Brace, L.H. (1970). In situ measurements of neutral and electron density wave structure from the explorer 32 satellite. *Journal of Geophysical Research 75*:3200-3210.

Hakura, Y. (1965). Tables and maps of geomagnetic coordinates corrected by the higher order spherical harmonic terms. *Journal of Radio Research Laboratories* (Japan) *12*:121-155.

King, G.A.M. (1966). The ionospheric disturbance and atmospheric waves, I - general discussion. *Journal of Atmospheric and Terrestrial Physics 28*:957-963.

Kohnlein, W. *and* Raitt, W.J. (1977). Position of the mid-latitude trough in the topside ionosphere as deduced from ESRO4 observations. *Planetary and Space Science 22*:600-602.

McNicol, R.W.E., Webster, H.C. *and* Bowman, G.G. (1956). A study of 'spread-F' ionospheric echoes at night at Brisbane, I, Range spreading (experimental). *Australian Journal of Physics 9*:247-271.

Muldrew, D.B. (1965). F-layer ionization troughs deduced from Alouette data. *Journal of Geophysical Research 70*:2635-2650.

Penndorf, R. (1965). The average ionospheric conditions over the Antarctic. *Geomagnetism and Aeronomy, Antarctic Research Series 4*:1.

Rodger, A.S. *and* Pinnock, M. (1982). Movements of the mid-latitude ionospheric trough. *Journal of Atmospheric and Terrestrial Physics 44*:985-992.

Sharp, G.W. (1966). Midlatitude trough in the night ionosphere. *Journal of Geophysical Research 71*:1345-1356.

Taylor, H.A.(Jr) *and* Walsh, W.J. (1972). The light-ion trough, the main trough, and the plasmapause. *Journal of Geophysical Research 77*:6716-6723.

Tsunoda, R.T., Livingston, R.C., Vickery, J.F., Heelis, R.A., Hanson, W.B., Rich, F.J. *and* Bythrow, P.F. (1989). Dayside observations of thermal-ion upwellings at 800 km altitude: an ionospheric signature of the cleft ion fountain. *Journal of Geophysical Research 94*:15277-15290.

Whalen, J.A. (1987). Daytime F-layer trough observed on a macroscopic scale. *Journal of Geophysical Research 92*:2571-2576.

Whalen, J.A. (1989). The daytime F-layer trough and its relation to ionospheric - magnetospheric convection. *Journal of Geophysical Research 94*:17169-17184.

Table 1. The number of events in sets divided in terms of $\Delta h'$. Also listed are very approximate estimates of the range of angles associated with each set for a vertical height of the first hop reflection point set arbitrarily at 300 km.

| SET | $\Delta h' = 2h'_1 - h'_2$ (km) | EVENTS | APPROXIMATE MINIMUM SLOPE |
|---|---|---|---|
| 1 | $\Delta h' \geq 75$ | 11 | $\geq 37°$ |
| 2 | $\Delta h' \geq 50 < 75$ | 16 | $\geq 31 < 37°$ |
| 3 | $\Delta h' \geq 15 < 50$ | 22 | $\geq 15° < 31°$ |
| 4 | $\Delta h' < 15$ | 24 | $<15°$ |

Table 2. The division of the sets of troughs defined in Table 1, in terms of type A and type B (see text) ionograms.

| SET | TYPE A | TYPE B | PER CENTAGE TYPE A |
|---|---|---|---|
| 1 | 11 | 0 | 100 |
| 2 | 10 | 6 | 63 |
| 3 | 9 | 13 | 41 |
| TOTAL | 30 | 19 | 61 |

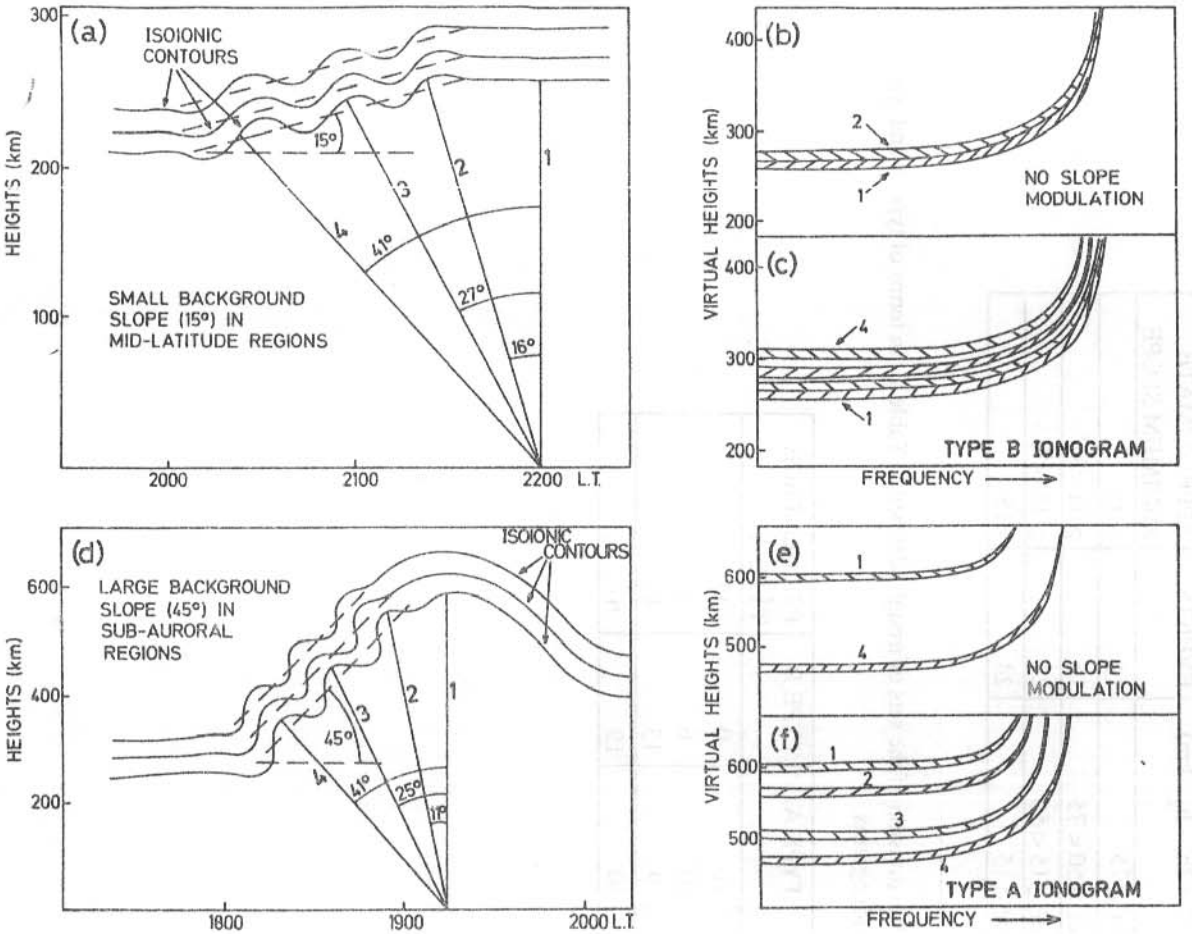


Figure 1. Height rises ((a) small and (d) large) with and without modulation. O-ray ionograms - (b) and (c) for small and (e) and (f) for large height rises.

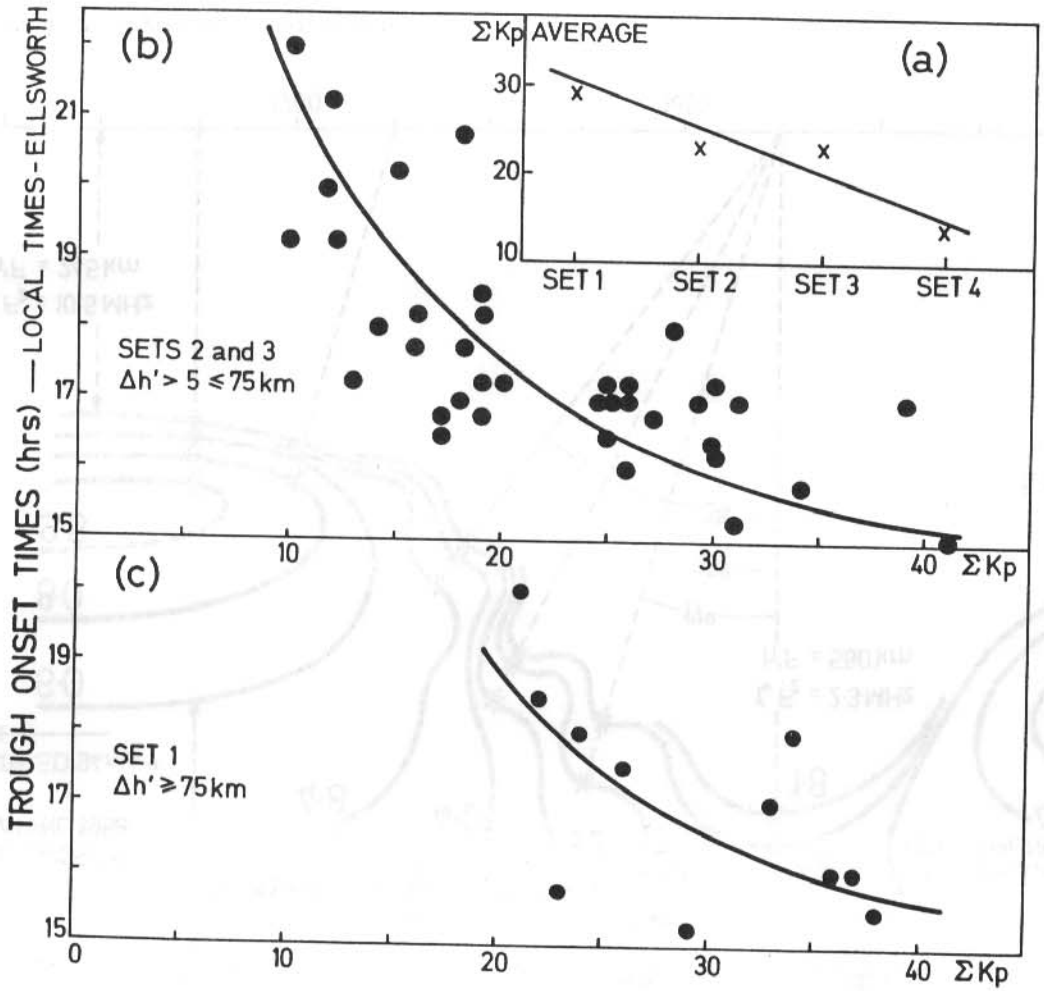


Figure 2. (a) Trough magnitudes versus $\Sigma K_p$. $\Sigma K_p$ versus onset times for (b) medium-scale troughs and (c) large-scale troughs.

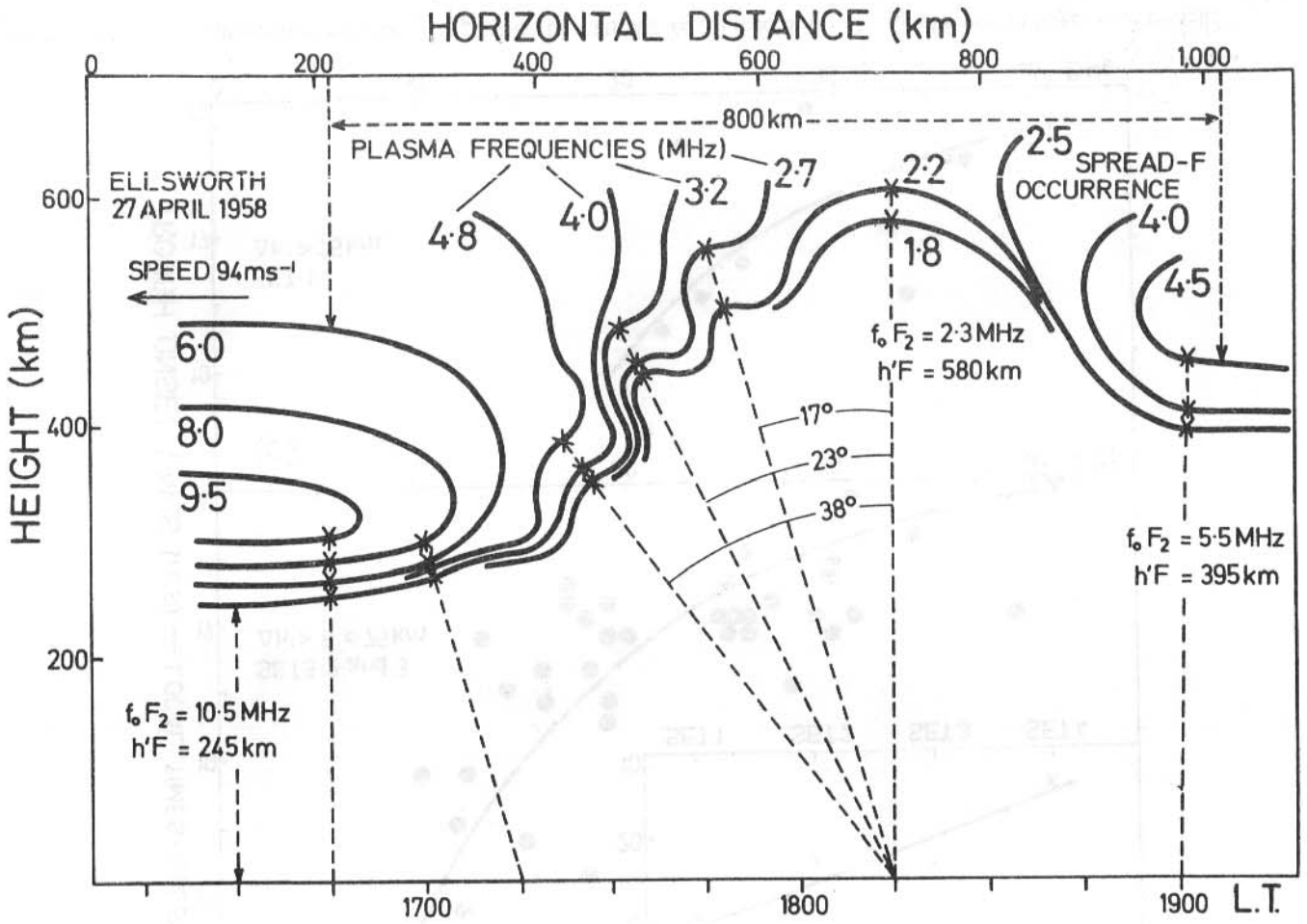


Figure 3. An example of a large-scale daytime trough.

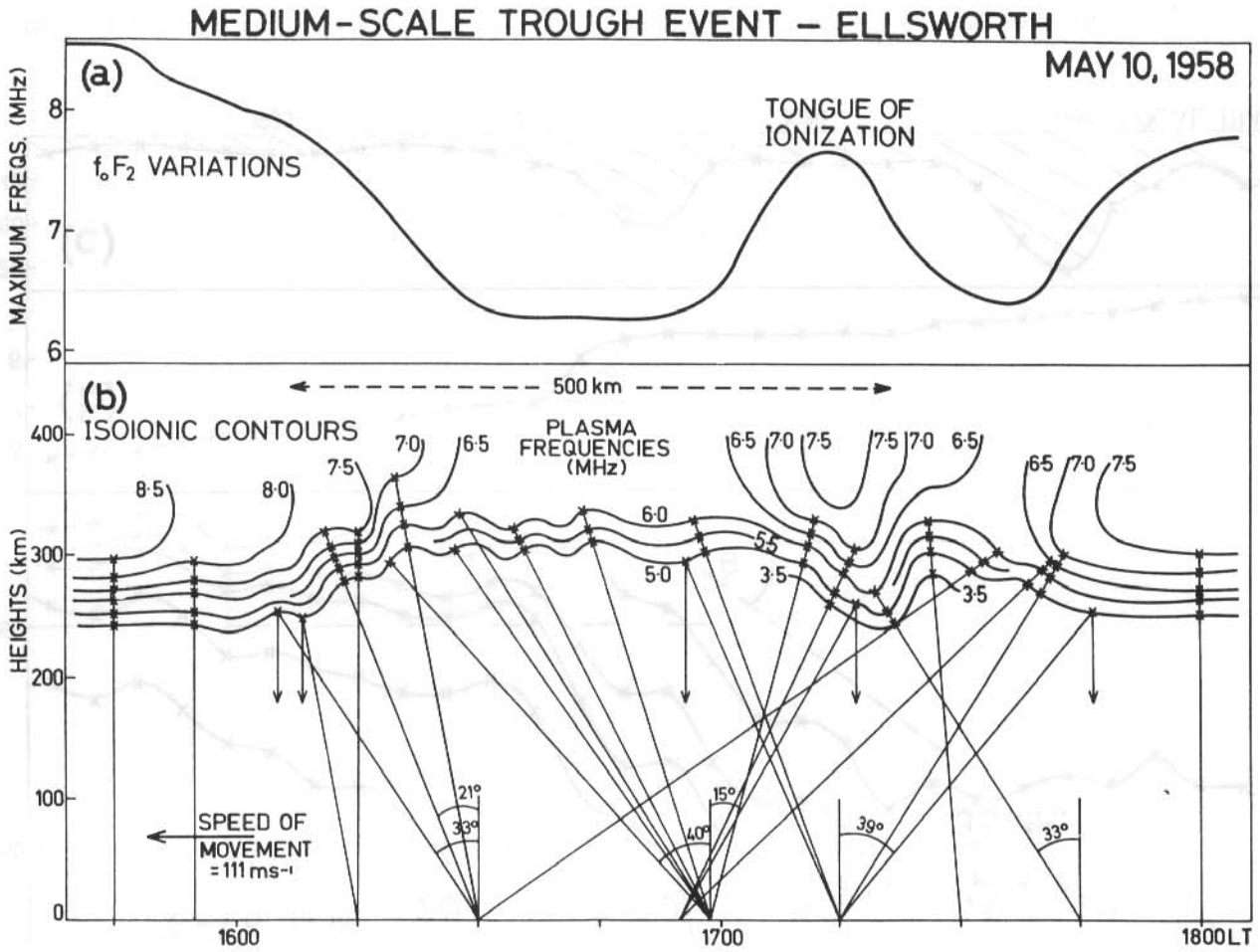


Figure 4. (b) An example of a medium-scale daytime trough and (a) related $f_0F_2$ variations.

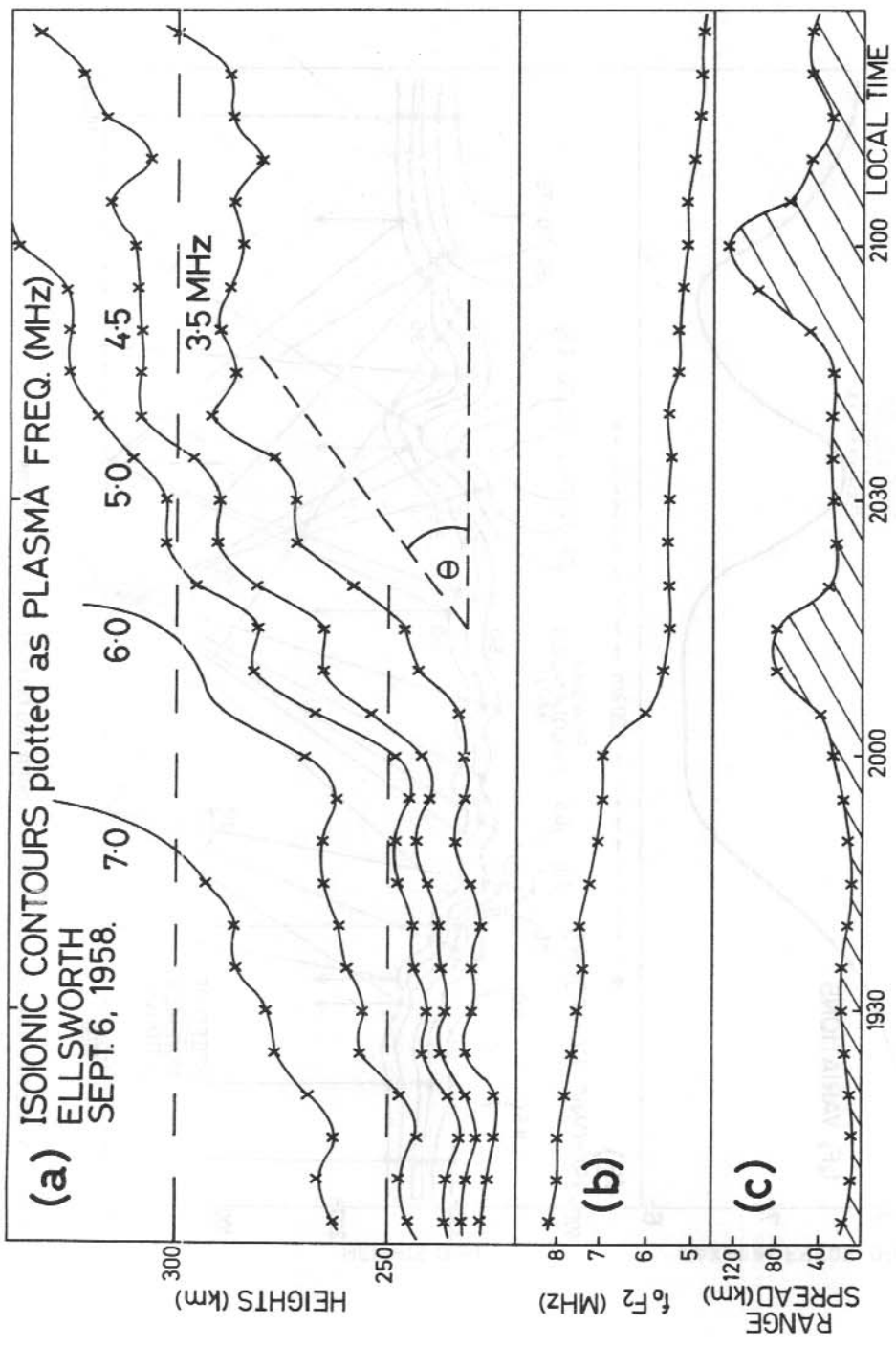


Figure 5. (a) An example of a small-scale daytime trough with associated (b) $f_0F_2$ variation and (c) range-spread width.

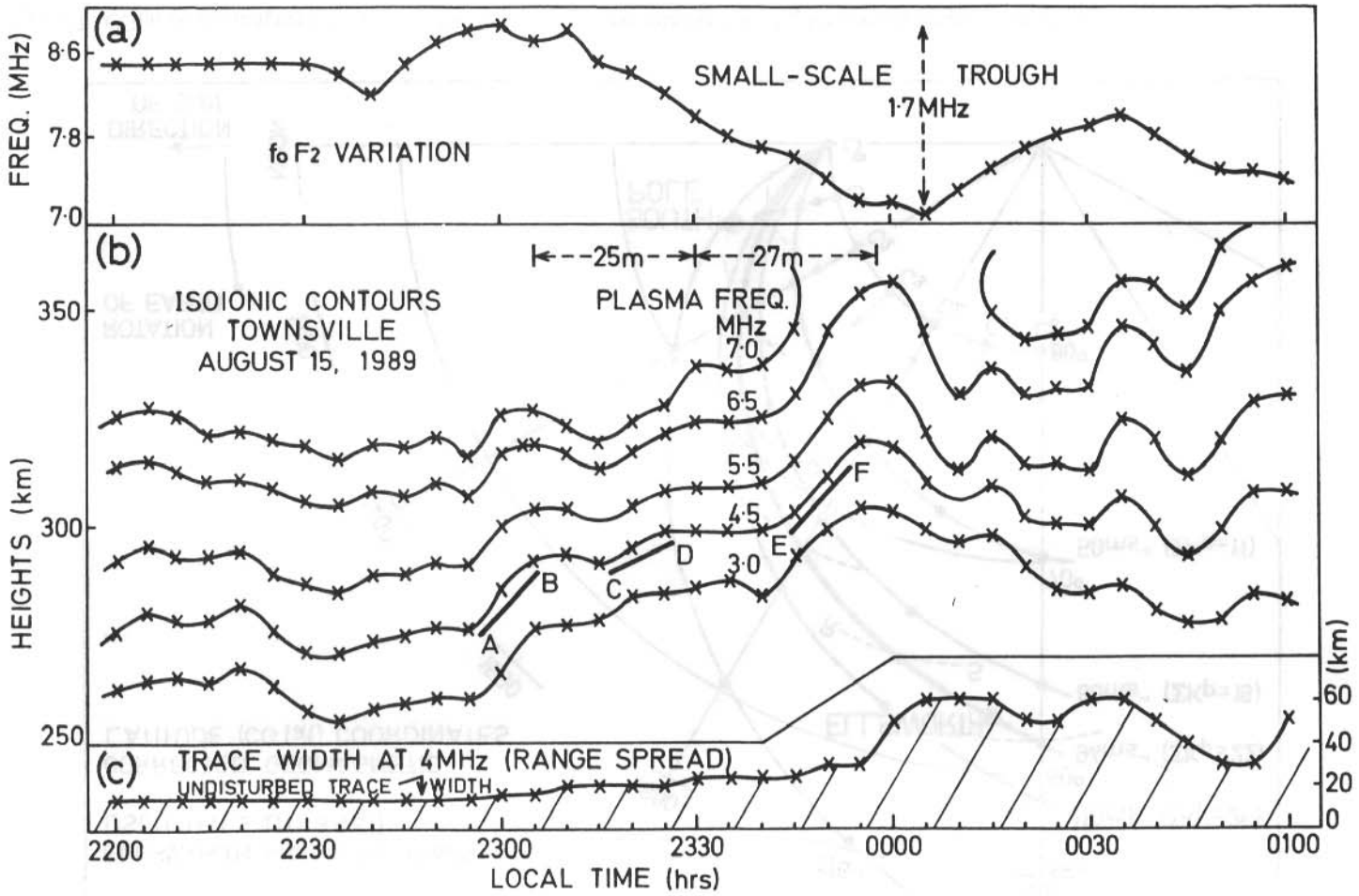


Figure 6. (b) Small-scale trough at Townsville with associated (a) $f_0F_2$ variations and (c) range-spread width.

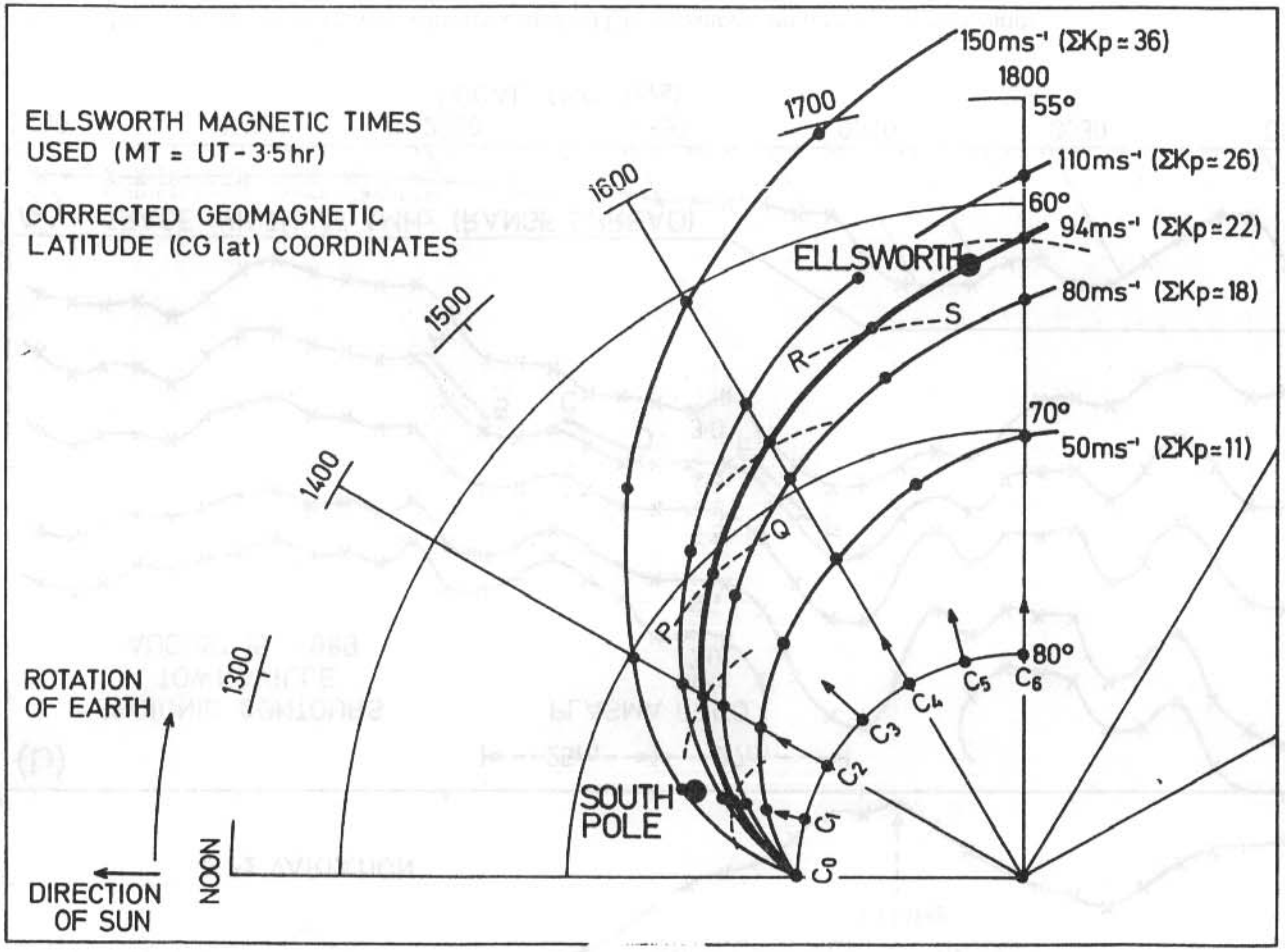


Figure 7. CGlat versus magnetic times plots for disturbances generated at point $C_0$ for various propagation speeds.

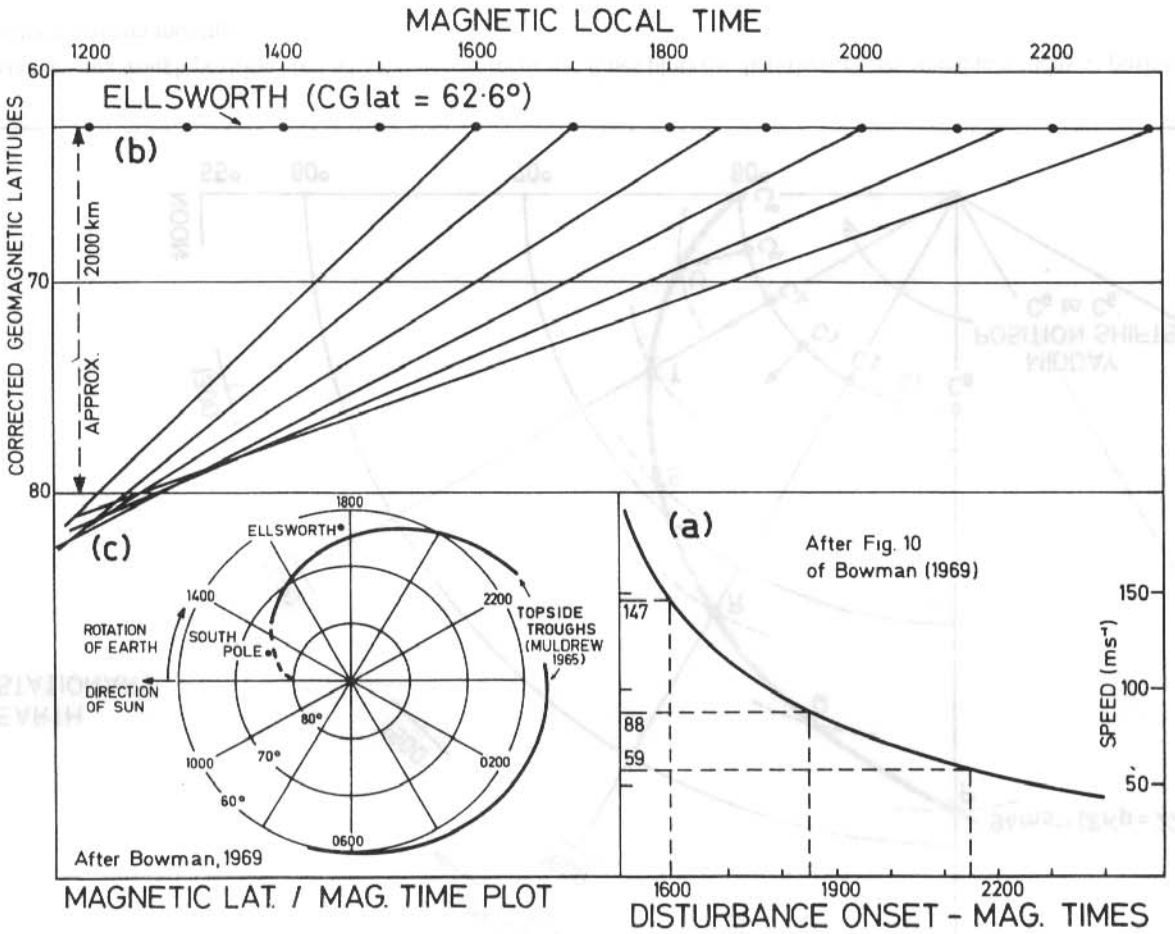


Figure 8. (b) Plot showing magnetic time versus disturbance positions (in CGlats) poleward of Ellsworth for various propagation speeds and onset times at Ellsworth shown by (a). (c) shows main trough position by Muldrew (1965).

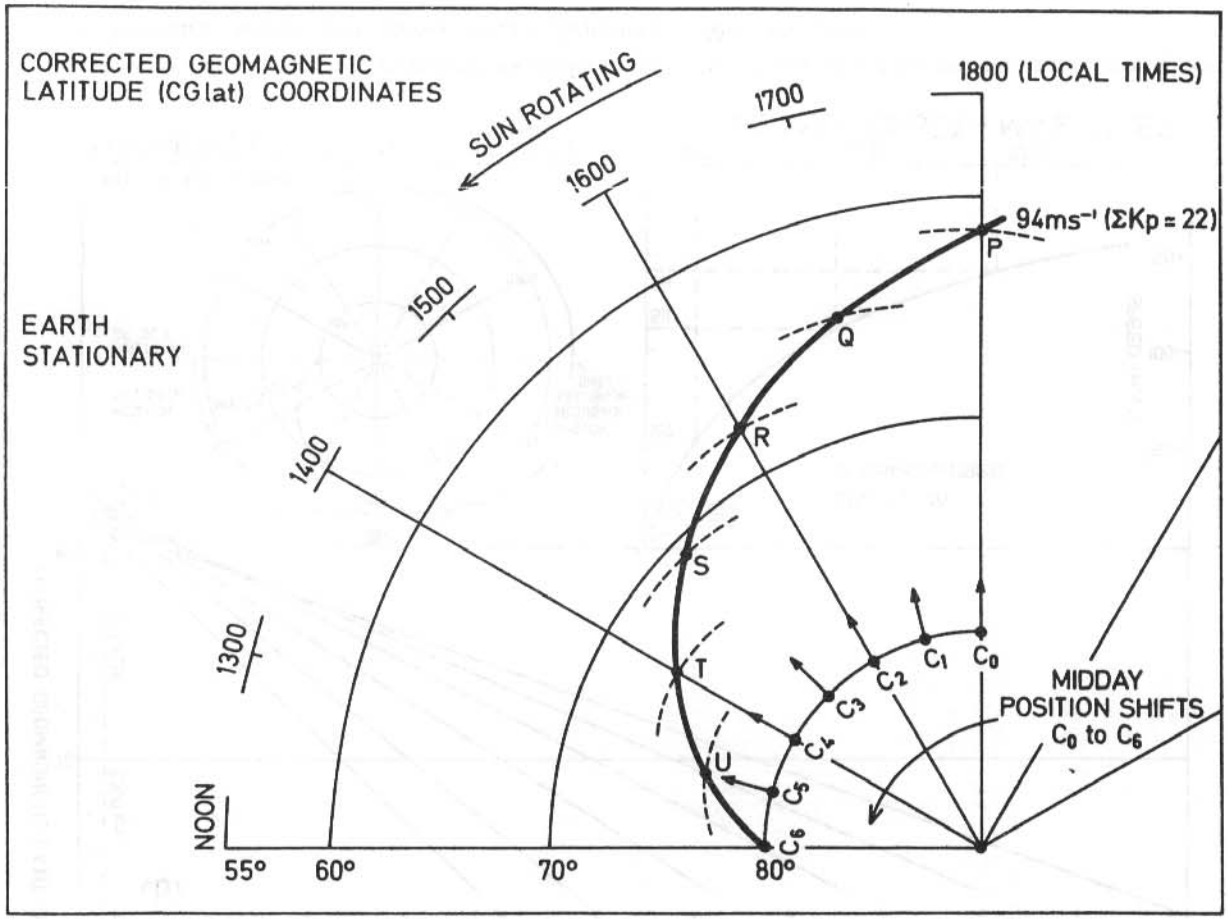


Figure 9. Instantaneous trough positions (on a CGlat versus magnetic times plot) for disturbances generated at midday at positions $C_0$ to $C_6$ for earth stationary and sun moving.

# 13. FIELD-ALIGNED CURRENTS OBSERVED IN THE INNER MAGNETOSPHERE AND THEIR MAGNETIC SIGNATURE ON THE GROUND

J. Wu and R.J. Stening
School of Physics
University of New South Wales
Kensington NSW 2033
Australia

ABSTRACT

ISEE-2 magnetometer data and ISEE 1/2 particle data from the first half of 1978 were examined to search for signatures of field-aligned currents in the earth's inner magnetosphere (2.6-9.5 Re, L=4.8-13.1). Eighteen field-aligned current sheet 'events' were found. Most of them occur during magnetic disturbed periods (AE = 226-724 nT). The surface current densities range from 12 to 113 mA $m^{-1}$ and are compatible with magnitudes measured at low altitudes by Triad. Twelve events appear in pairs of current sheets with currents flowing both towards and away from the earth (corresponding to the usual pattern of Region 1 and Region 2 Birkeland currents). In nearly every 'event' the appearance of a field-aligned current coincides with, or is adjacent to gradients in the proton flux (32-50 Kev and 80-126 Kev).

Using the Tsyganenko-Usmanov magnetospheric field model (Tsyganenko and Usmanov 1982) to trace the field line from where the field-aligned current signature was observed down to the ground, it was found that all of these field lines fall in a range from 62°-73° magnetic latitude. All the facts above indicate that the field-aligned currents in the inner magnetosphere are located on or adjacent to the boundary of the plasma sheet. Geomagnetic field data on the nightside, measured by about 10 observatories for each 'event', were used to study the magnetic field behaviour on the ground. Even though it was found that both Region 1 and Region 2 currents from the ISEE data were in the inner magnetosphere, the ground magnetic signatures favour only Region 1 currents and also indicate the transient nature of the current flows.

## 13.1 INTRODUCTION

Birkeland currents or field-aligned currents play a fundamental role in the dynamic processes of energy coupling between the magnetosphere and the polar ionosphere and may make important contributions to geomagnetic variations at night-time. In the recent two decades the observation of Birkeland currents have been extended from the polar region (Iijima and Potemra 1978, Potemra et al. 1979) to the inner magnetosphere (Kelly et al. 1986), synchronous altitude (Nagai 1982) and the outer magnetosphere (Fairfield 1973, Frank et al. 1981).

The large-scale characteristics of Birkeland currents have been determined from polar orbit satellite magnetic field data (Iijima and Potemra 1978). The flow regions of Birkeland currents

coincides with the auroral oval and have been designated as 'Region 1', located on the poleward side, and 'Region 2', located on the equatorward side (hereafter referred to as BR1 and BR2). The BR1 current flows into the ionosphere in the morning sector and away from the ionosphere in the evening sector. The BR2 current flows in the opposite direction at any local time.

The basic flow pattern of Birkeland currents remains unchanged during geomagnetic active (|AL|>100 nT) and inactive (|AL|<100 nT) periods, although, the flow regions widen and shift to lower latitudes during a disturbed period (Iijima and Potemra 1978). The average latitude width of the BR1 plus BR2 regions is about 6° (Zmuda et al. 1974). The average current density, surface current density and total current of the Birkeland currents are about 1μA $m^{-1}$, 0.1 A $m^{-1}$ and $10^6$ A respectively ( for 2-≤$K_p$≤4+) and the BR1 total intensity is larger than that of BR2 (by 20-25%).

By using ISEE 1 and 2 magnetometer data in the inner magnetosphere, Kelly et al. (1986) indicated that large-scale currents are found at the outer boundary and inner edge of the plasma sheet flowing in the directions expected for both BR1 and BR2. This occurs because the plasma sheet is connected magnetically to the auroral oval. The Birkeland currents have a sheetlike structure and occur during substorms when the AE index exceeds 200 nT.

The magnetic signature of field-aligned currents observed at geosynchronous altitude was always that expected from a BR1 current system and was associated with substorms (Nagai 1982).

## 13.2 DATA AND COORDINATE SYSTEM

The orbits of the ISEE 1 and 2 spacecraft (perigee=600 km, apogee=23 earth radii, I=23° are suitable for field-aligned studies in the inner magnetosphere. Their inbound segments are near the geomagnetic equator while the outbound segments are at middle latitude. The annual precession of the ISEE orbits permits a survey of the nightside plasma sheet during the first half of each year. Figure 1 shows the approximate position of the ISEE orbit at different times of the year (adapted from Ogilvie 1982). In the present report, the authors will search for field-aligned currents in the inner magnetosphere using ISEE data and focus their attention on magnetic signatures on the ground caused by field-aligned currents.

The ISEE 2 magnetic field data and merged ISEE 1/2 particle data from the first half of 1978 (January 26 to June 18) shall be used. The magnetic fields are measured by the magnetometer of the University of California, Los Angeles (Russell 1978) and the values have been averaged over 64 seconds. The particle data are provided by the Medium Energy Particles Experiment of Williams, NOAA/ERL/SEL (Ogilvie and Banks 1977), which are five minute average values and include two energy channels for protons (32-50 keV and 80-126 keV).

In order to find the signature of the field-aligned current in the inner magnetosphere, the authors need to plot the variation of the detrended magnetic field in the Dipole Coordinate System near perigee for each orbit. There are 60 orbits in the first half of 1978. The Dipole Coordinate System is a curvilinear system. If the vector position of the spacecraft is $\mathbf{R}$ and $\mathbf{B_m}$ is the model magnetic field vector at the position of the spacecraft then the $\hat{\mathbf{z}}$ axis lies along the model magnetic field vector ( $\hat{\mathbf{z}} = \mathbf{B_m}/|\mathbf{B_m}|$), $\hat{\mathbf{y}}$ is the normalized cross product of $\hat{\mathbf{z}}$ and $\mathbf{R}$ ($\hat{\mathbf{y}} = \hat{\mathbf{z}} \times \mathbf{R}/|\hat{\mathbf{z}} \times \mathbf{R}|$) and $\hat{\mathbf{x}}$ completes the right-hand Cartesian coordinate ( $\hat{\mathbf{x}} = \hat{\mathbf{y}} \times \hat{\mathbf{z}}$). So both $\hat{\mathbf{y}}$ and $\hat{\mathbf{z}}$ lie approximately in the L shell with the $\hat{\mathbf{y}}$ axis pointing towards geomagnetic east and the $\hat{\mathbf{z}}$ axis north. The $\hat{\mathbf{x}}$ axis defines the local normal to the L shell.

'Detrended' means the observed fields have been detrended by using a certain magnetospheric magnetic field model (here the quiet time Olson-Pfitzer 1977 Magnetospheric Field Model is used). If the model is correct the remaining magnetic field should have contributions only from the field-aligned currents (and the cusp currents if the spacecraft is crossing the cusp area). Detrending is necessary because the perturbation caused by the field-aligned current is small compared to the model magnetic field in the inner magnetosphere.

The magnitude and direction of the equivalent Birkeland currents can be determined from the observed transverse magnetic disturbances (the $\Delta B_y$ component in the detrended Dipole Coordinate System) according to Maxwell's equation (Anderson and Vondrak 1975):

$$\mathbf{J} = 1/\mu_0 \nabla \times (\Delta \mathbf{B})$$

where $\mu_0$ is the permeability of free space. In this case $J_z = \frac{1}{\mu_0}\frac{\partial}{\partial x}(\Delta B_y)$. When the current flows towards the earth the current magnitude is positive. The surface current density (the current density integrated over the thickness of the current sheet) can be obtained directly from $\Delta B_y$.

## 13.3 SATELLITE OBSERVATION OF FIELD-ALIGNED CURRENTS

Using the criteria L>3.5, magnetic latitude 20°-50°, LT = 18:00-06:00 (which is where the night-time plasma sheet is located), by observing variations in the east-west magnetic field component $B_y$, 'events' were identified which may be caused by field-aligned currents. It should noted that $B_y$ component perturbations could also be caused by substorm dynamics and ULF waves (Kelly et al. 1986). To exclude these perturbations, the authors require also that, $\Delta B_y > \Delta B_x$ and $\Delta B_z$ so that they were satisfied that the sheetlike field-aligned currents assumption. In order to check the location of the field-aligned currents the particle data was also examined. A gradient in particle flux is the main characteristics of the plasma sheet boundary (Park et al. 1984).

To satisfy the criteria above, 18 field-aligned current sheet 'events' were found during the period from January 26 to June 18, 1978. In every 'event' the appearance of a field-aligned current did coincide with, or was adjacent to, gradients of the particle flux.
Figure 2(a) shows the detrended magnetic field versus time plot in the Dipole Coordinate System for February 19, 1978 from 0230 to 0500 UT. The triangular magnetic perturbation $B_y$ is caused by a pair of sheet-like field-aligned currents. One was observed between 0327-0335 UT and the other 0335-0419 UT, with surface current density 104 mA $m^{-1}$ flowing toward the earth and 115 mA $m^{-1}$ flowing away from the earth, respectively. The corresponding proton flux is shown in Figure 2(b). The proton flux shows a very large decrease after the crossing of the current sheet. This decrease can be interpreted as a spatial gradient indicating that the spacecraft was near the outer boundary of the plasma sheet. Figure 2(c) shows the ISEE 2 trajectory in the magnetic latitude - R plane during this interval. Both current sheets were observed in the evening sector with R=2.7, L=4.9, ML=42° and R=3.3, L=6.47 ML=44° respectively. The spacecraft was near perigee and outbound when crossing the plasma sheet.

Figure 3(a) shows another plot for February 16, 1978, this time from 1800-2030 UT. Again a triangular magnetic perturbation $B_y$ is observed, indicating the crossing of a pair of sheet-like field-aligned currents, one between 1857-1902 UT and the other between 1902-1930 UT with a surface current density 14 mA $m^{-1}$ flowing toward the earth and 31 mA $m^{-1}$ flowing away from the earth. Figure 3(b) shows the corresponding proton flux. A spatial gradient in the proton flux during 1857-1930 UT is clearly seen. Figure 3(c) shows the ISEE 2 trajectory in the ML-R plane for this interval. Again the spacecraft was near perigee and outbound when crossing the plasma sheet. All 18 events were found during the outbound segment.

For comparison, Figure 4 shows an example of a quiet time magnetic field variation on January 26 from 0730 to 1000 UT. No perturbations were observed in any component.

A computer code of the Tsyganenko-Usmanov magnetospheric field model (Tsyganenko and Usmanov 1982) was developed. The model formulae contain 28 input parameters representing the dynamic magnetospheric field responding to different levels of geomagnetic activity. Using this model to trace the field lines from where the field-aligned current signature was observed by the spacecraft down to the ground, it was found that for all of these events the field lines fall in a range from 62° to 73° ML. This is where the auroral zone is located and also the expected position of the projection of the plasma sheet on to the polar region. All the pieces of evidence above indicate that the 18 field-aligned current events are located on or near the outer boundary of the plasma sheet.

Table 1 summarises the average properties of the 18 current sheet events and the corresponding geomagnetic index and spacecraft location (always in the mid-latitude region between 23° to 46° ML). The L value ranged from 4.84 to 13.1. The sheet current density ranged from 12 to 115 mA $m^{-1}$ with an average of 36 mA $m^{-1}$. Table 1 also shows where the satellite's field line intersects with the ground, traced according to the Tsyganenko-Usmanov magnetic model. It

was found that most of the current sheets occur during a magnetic disturbed period (AE = 226 - 724 nT). The one exception is the March 7 event for which AE values were only 115 and 35 nT. From Table, 1 it is seen that in 6 events the spacecraft encountered only a single current (marked S) with current flowing away from the earth corresponding to the flow direction of the BR1 current in the evening sector. There are 9 events in which the spacecraft crossed a pair of current sheets (marked D) with a current sheet flowing towards the earth first and then a second current flowing away from the earth. This corresponds in the evening sector to BR2 and BR1 currents respectively. In the remaining 3 events the spacecraft detected multiple field-aligned current sheets (marked M in Table 1). An example is shown in Figure 5 which is the detrended magnetic field for March 7, 1978 from 2100 to 2330 UT. The third current sheet (2233 - 2249 UT) can be interpreted as filamentary structure. In general, the field-aligned current patterns observed by the ISEE 2 spacecraft agree with low-altitude measurements (Iijima and Potemra 1978).

## 13.4 GROUND BASED OBSERVATIONS

In this section, the contribution of Birkeland currents to ground-based magnetic observations at night-time will be discussed. There is no doubt that the closure of the Birkeland currents in the polar ionosphere is via the auroral electrojet, but its closure in the magnetosphere is not well understood. There is some agreement that the BR1 current connects to the magnetopause or boundary layer. Some authors suggest that the BR2 current connects to the inner edge of the plasma sheet (Potemra 1979, Stern 1983). According to Heikkila (1978) and Sugiura (1975) BR1 is a part of the distant tail current and BR2 closes via a ring current. In general BR2 is nearer to the earth, but the total intensity of BR1 is always larger than that of BR2 (Potemra 1979).

Referring to the schematic diagram in Figure 6 (adopted from Clauer and McPherron 1974), if BR1 has a larger total intensity than BR2 and is a part of the distant tail current (like the situation at the beginning of a substorm expansion phase), then the magnetic perturbation on the northern hemisphere nightside ground station will be:

1. A symmetric positive perturbation in the northward component of the magnetic field at low and mid-latitude stations (due to the segment AB which is equivalent to a reversal of part of the tail current).

2. A negative perturbation in the northward component of the magnetic field at auroral stations (due to the segment CD which represents the westward auroral electrojet).

3. An eastward field perturbation (due to the segment DA) in the premidnight sector and a westward perturbation in the postmidnight sector (due to BC) with a crossover near the midnight meridian for stations equatorward of the auroral zone. For stations poleward of the auroral zone the situation is opposite.

4. A negative Z perturbation at stations equatorward of the auroral zone and a positive Z perturbation at stations poleward of the auroral zone.

For the stations in the southern hemisphere both (1) and (2) are true but opposite for (3) and (4).

If the contribution of BR2 were larger than that of BR1 then the magnetic perturbations will be in the opposite sense.

A ring current will produce similar negative southward perturbations at all stations in the nighttime sector. If the total intensity of the ring current were larger than that of the Birkeland currents, a negative southward perturbation would dominate on the nightside at low and mid-latitudes. If their total intensities were comparable, then an east-west component perturbation will be seen. By comparing the relative magnitudes of perturbation in the north-south component and the east-west component, the relative importance of the ring current and the Birkeland currents; and also the relative importance between BR1 and BR2 currents can be determined.

Figure 7 shows (H,D,Z) magnetic observations at the ground stations for February 19, 1978 from 0200 to 0800 UT. The spacecraft was crossing the field-aligned current sheet during 0327-0419 UT or 2052-2143 LT. The intersection of the spacecraft magnetic field line with the earth's surface was between 64°-65° MLAT and 350°-360° MLON as shown in Table 1 (here MLAT is magnetic latitude and MLON magnetic longitude). The authors have magnetic records from 14 stations for this event. Their locations are shown in Table 2. These will be grouped into two local time sectors. In Figure 7, the top eight stations are in the evening-midnight sector and the bottom seven stations are in the midnight-morning sector. In the evening sector, the H component increased rapidly near 0330 UT by 25-150 nT from College to Argentine Island, but decreased by 500 nT at Fort Churchill. The D component increased by 40-300 nT from College to San Juan at the same time but decreased at Fort Churchill and Argentine Island. In the early morning sector most stations are near the auroral zone - the H component decreased by 35-200 nT at Narssarssuaq, Leirvogur, St. Johns and Halley Bay but increased at only M Bour near 0330 UT. The D component increased by 30-60 nT at Godhavn, Narssarssuaq, Hermanus and Halley Bay but decreased at St. Johns and M Bour.

The Z component at Meanook, St. Johns, Fredericksburg and Boulder decreased by 10-80 nT but at Argentine Island and Halley Bay increased by 50 nT during the event. Mid-latitude stations like San Juan, Tucson, M Bour and Hermanus and the polar cap station Godhavn have little Z signature. On the other hand Z components at auroral stations like Narssarssaq, Leirvogur, Fort Churchill and College are too variable to interpret because of local auroral activity.

As Figure 8 has shown, the magnetic records from all these stations coincide with the picture expected from a BR1 current system.

A 'demarcation' between positive D excursions and negative D excursions has been identified by Nagai (1987) and Nagai et al. (1987) during substorms. In this observation, this demarcation occurs between Fredericksburg and St. Johns, that is between 350° and 21° magnetic longitude and this is just the longitude of the field line intersecting the space observation.

Figure 9 shows another event, that of March 29, 1978. As Table 1 shows, for this event the field line passing through the satellite intersects the ground at magnetic latitude 66° and magnetic longitude 224° (all the stations examined are located equatorward of the field-aligned current sheet). Again the magnetic records support the picture expected from a BR1 current system. The magnetic records for all the 18 events have been checked. Six of them have no signature (marked NS in Table 1). For two events, the appropriate nightside geomagnetic data were not available (marked ND). The other ten events are like the February 19 event and are all in favour of the BR1 current system including those cases where only a single current sheet is seen. In most events (12 of 18), both BR1 and BR2 sense currents exist in the inner magnetosphere. The necessary magnetic records for 10 of these 12 events were examined. Six of these ten events have clear signatures which are typical of a BR1 current. For these six events the average surface current density is 38 mA $m^{-1}$ and the AE index is 401 nT, but these parameters are rather smaller for the four events which have no obvious signatures (these have an average surface current density of 17 mA $m^{-1}$ and an average AE index of 272 nT). It seems that the more intense the current density is, the more likely the magnetic signature of the field-aligned current will be observed at the ground station. A similar relation to the substorm activity index AE is also seen.

## 13.5 DISCUSSION AND CONCLUSIONS

Kelly et al. (1986) used high resolution ISEE 1 and 2 magnetometer data to search for evidence of field-aligned currents in the earth's inner magnetosphere at both nighttime and daytime (their study concentrated on the structure and the motion of the current sheets). In the same period from January 26 to June 18 they found eight events in the nighttime (the same events listed in the first half of Table 1). But a total of 18 events were picked up. For eight events similar properties to Kelly et al. (1986) were obtained. The other ten events which were added are generally smaller in current density, with an average surface current density of 25 mA $m^{-1}$ (the eight events had an average current density of 48 mA $m^{-1}$), but their existence has been confirmed by both particle data and field line tracing tests. Also, five of them appear to have a significant magnetic signature on the ground.

This study shows that both earthward and outgoing large-scale field-aligned currents were found on the outer boundary of the plasma sheet in the inner magnetosphere. Their flow picture coincides with the usual pattern of 'Region 1' and 'Region 2' Birkeland currents at low latitude. This is expected because the plasma sheet is connected magnetically to the auroral oval: this has been fully confirmed by the field line tracing test using Tsyganenko-Usmanov magnetospheric field model. As shown above, the average surface current density was 36 mA $m^{-1}$. Taking the

average current sheet thickness of 1600 km observed by Kelly et al. (1986), an average current density of 22.5 mA $m^{-2}$ in the inner magnetosphere was obtained. The magnetic fields in the inner magnetosphere and polar ionosphere are assumed to be 1000 nT and 50000 nT. According to the conservation of total current intensity and magnetic field flux on any cross section along the field-aligned current sheet, the current density in the polar ionosphere would be 1.13 mA $m^{-2}$ which is comparable to that observed at low latitude (Iijima and Potemra 1978). All this evidence suggests that the large-scale field-aligned current sheet observed in the inner magnetosphere is the continuation of the Birkeland currents observed at low altitude. It was expected that, even though currents with directions, were found as expected for both the BR1 and BR2 system in the inner magnetosphere, the ground magnetic signatures will favour only the BR1 current system.

As Table 1 shows, six events (6/18 = 33%) were found in which a single current sheet with only the BR1 sense was encountered. The accumulated current density of 18 events was 697 mA $m^{-1}$ for BR1 and 526 mA $m^{-1}$ for the BR2 sense current from Table 1. It seems that the occurrence rate of BR1 sense currents and accumulated total current of the BR1 sense is larger than that of BR2. This supposition matches the fact that the total current of the BR1 system was observed to be larger than that of BR2 by 20-25% at low altitudes (Iijima and Potemra 1978). This supposition also agrees with the work of Ohtani et al. (1988). Their study focuses on the average or net field-aligned current by searching for steplike changes of magnetic direction in the near-tail region ($B_T$<200 nT). They also found the current in the near-tail plasma sheet boundary layer could be identified as the BR1 current system.

It is clear from Figure 7 that the change of H and D components first started at Fredericksburg, San Juan and Argentine Island, then other stations, and College is the last to change. Considering their local time, it indicates that the disturbance spread from local midnight to the evening and morning sides. Most of the magnetic records appear as a short disturbance period of one hour or so. This suggests that the Birkeland current (or its intensification) in the inner magnetosphere is primarily a transient phenomenon and may relate to processes within the plasma sheet (Wiens and Rostoker 1975).

## 13.6 ACKNOWLEDGMENTS

The authors thank C.T. Russell for providing the ISEE 2 magnetometer data. The 'ISEE A and B Data Pool Tapes' were provided by the World Data Centre A for Rocket and Satellites. Ground magnetic data were obtained from the World Data Center A for Solar-Terrestrial Physics, Boulder. Author, J. Wu, very much appreciates the hospitality of the School of Physics, University of New South Wales during her stay as a Visiting Fellow.

## 13.7 REFERENCES


Anderson, H.R. *and* Vondrak, R.R. (1975). Observation of Birkeland current at auroral latitude. *Reviews of Geophysics and Space Physics 13*:243-262.

Clauer, C.R. *and* McPherron, R.L. (1974). Mapping the local time-universal time development of magnetospheric substorms using mid-latitude magnetic observations. *Journal of Geophysical Research 79*:2811.

Fairfield, D.H. (1973). Magnetic field signatures of substorms on high-latitude field line in the nighttime magnetosphere. *Journal of Geophysical Research 78*:1553-1562.

Frank, L.A., McPherron, R.L., DeCoster, R.J., Burek, B.G., Ackerson, K.L. *and* Russell, C.T. (1981). Field-aligned currents in the earth's magnetotail. *Journal of Geophysical Research 86*:687-700.

Heikkila, W.J. (1978). Electric field topology near the dayside magnetopause. *Journal of Geophysical Research 83*:1071-1078.

Iijima, T. *and* Potemra, T.A. (1978). Large-scale characteristics of field-aligned currents associated with substorm. *Journal of Geophysical Research 83*:599-615.

Kelly, T.J., Russell, C.T. *and* Walker, R.J. (1986). ISEE 1 and 2 observations of Birkeland currents in the earth's inner magnetosphere. *Journal of Geophysical Research 91*:6945-6958.

Nagai, T. (1982). Observed magnetic substorm signatures at synchronous altitude. *Journal of Geophysical Research 87*:4405-4417.

Nagai, T., Singer, H.J., Ledley, B.G. *and* Olsen, R.C. (1987). Field-aligned currents associated with substorms in the vicinity of synchronous orbit. 1. The July 5, 1979, substorm observed by SCATHA, GOES 3 and GOES 2. *Journal of Geophysical Research 92*:2425-2431.

Nagai, T. (1987). Field-aligned currents associated with substorms in the vicinity of synchronous orbit 2. GOES 2 and GOES 3 observations. *Journal of Geophysical Research* 92:2432-2446.

Ogilvie, K.W. (1982). Data from ISEE-1 for the IMS period. In: Russell, C.T. *and* Southwood, D.J. (Eds). *The IMS source book, guide ti the international magnetospheric study data analysis*. American Geophysical Union.

Ogilvie, K.W. *and* Banks, M.D. Jr. (1977). *Note on the ISEE A and B Data Pool Tape*. NASA/GSFC X-692-77-129.

Ohtani, J., Kokubun, S., Elphic, R.C. *and* Russell, C.T. (1988). ISEE observations in the plasma sheet boundary layer. *Journal of Geophysical Research 93*:9709-9720.

Park, G.K., McCarthy, M., Fitzenreiter, R.J., Etcheto, J., Anderson, K.A., Anderson, R.R., Eastman, T.E., Frank, L.A., Gurnett, D.A., Huang, C., Lin, R.P., Lui, A.T.Y., Ogilvie, K.W., Pederson, A., Reme, H. *and* Williams, D.J. (1984). Particle and field characteristics of the high-latitude plasma sheet boundary layer. *Journal of Geophysical Research 89*:8885-8906.

Potemra, T.A. (1979). Current systems in the earth's magnetosphere - A review of U.S. progress for the 1975-1978 IUGG quadrenniel report. *Reviews of Geophysics and Space Sciience 17*:640-656.

Potemra, T.A., Iijima, T. *and* Saflekos, N.A. (1979). Large-scale characteristics of Birkeland current. In: Akasofu, S-I. *and* D. Reidel (Eds). *Dynamics of the Magnetosphere*. Dordrecht, Holland. Pp165-199.

Russell, C.T. (1978). The ISEE 1 and 2 Fluxgate magnetometers. *Institute of Electrical and Electionics Engineers Transactions on Geoscience* GE *16*:239-242.

Stern, D.P. (1983). The origins of Birkeland current. *Reviews of Geophysics and Space Science 21*:125-138.

Sugiura, M. (1975). Identifications of the polar cap boundary and the auroral belt in the high-altitude magnetosphere - A model for field-aligned currents. *Journal of Geophysical Research*. 80:2057-2068.

Tsyganenko, N.A. *and* Usmanov, A.V. (1982). Determination of the magnetospheric current system parameters and development of experimental geomagnetic field models based on data from IMP and Heos satellites. *Planetary and Space Science* 30:985-988.

Wiens, R.G. *and* Rostoker, G. (1975). Characteristics of the development of the westward electrojet during the expansive phase of magnetospheric substorms. *Journal of Geophysical Research 80*:2109-2128.

Zmuda, A.J. *and* Armstrong, J.G. (1974). The diurnal variation of the region with vector magnetic field changes associated with field-aligned current. *Journal of Geophysical Research* 79:2501-2502.

Table 1. Properties of field-aligned current, spacecraft location, geomagnetic index and the intersection point of magnetic line with the earth's surface. (*Data were missing from tape.)

| Date | Time | Spacecraft Location | | | | Surface Current Density (mA/m) | Direction of Current Type in/out of Ionos. | | Intersection on the ground MLAT | MLON | AE (NT) | Magnet. Record |
|---|---|---|---|---|---|---|---|---|---|---|---|---|
| | | R | ML | L | LT | | | | | | | |
| Jan 31 | 0017-0135 | 4.7 | 39 | 7.8 | 0031 | 23 | out | S | 64 | 80 | 262 | NS |
| Feb 2 | 1027-1031 | 3.9 | 32 | 5.5 | 2319 | 25 | in | D | 68 | 280 | 286 | BR1 |
| | 1046-1050 | 4.7 | 33 | 6.7 | 2348 | 25 | out | | 70 | 284 | 309 | |
| Feb 14 | 0914-0918 | 3.9 | 34 | 5.6 | 2228 | 15 | in | M | 67 | 283 | 153 | NS |
| | 0918-0924 | 4.1 | 34 | 6.0 | 2240 | 25 | out | | 70 | 287 | 153 | |
| | 0940-0944 | 4.9 | 34 | 7.4 | 2309 | 29 | Out | | 72 | 288 | 275 | |
| | 0954-1034 | 5.8 | 34 | 9.4 | 2338 | 24 | in | | 72 | 288 | 275 | |
| Feb 19 | 0327-0335 | 2.7 | 42 | 4.9 | 2052 | 104 | in | D | 62 | 350 | 324 | BR1 |
| | 0335-0419 | 3.3 | 44 | 6.7 | 2143 | 84 | out | | 75 | 0 | 394 | |
| Mar 3 | 0226-0229 | 2.8 | 45 | 5.8 | 2028 | 60 | in | D | 64 | 356 | 232 | NS |
| | 0229-0239 | 3.1 | 46 | 6.5 | 2050 | 34 | out | | 65 | 359 | 232 | |
| Mar 7 | 2149-2154 | 4.5 | 37 | 7.3 | 2231 | 12 | in | M | 66 | 91 | 115 | BR1 |
| | 2201-2211 | 5.1 | 37 | 8.8 | 2295 | 35 | out | | 66 | 92 | 115 | |
| | 2233-2249 | 6.2 | 37 | 12.4 | 2335 | 20 | in | | 68 | 90 | 35 | |
| Mar 15 | 0115-0118 | 2.6 | 45 | 5.3 | 1932 | 101 | in | D | 64 | 353 | 406 | BR1 |
| | 0121-0128 | 3.0 | 46 | 6.4 | 2006 | 113 | out | | 66 | 359 | 406 | |
| Apr 15 | 0334-0349 | 4.0 | 43 | 8.0 | 1853 | 61 | out | S | 68 | 287 | 406 | BR1 |
| Feb 16 | 1857-1902 | 4.7 | 25 | 5.9 | 2329 | 14 | in | D | 63 | 155 | 519 | NS |
| | 1902-1930 | 5.4 | 24 | 6.7 | 2349 | 40 | out | | 64 | 156 | 519 | |
| Feb 21 | 1332-1400 | 4.9 | 23 | 6.0 | * | 19 | in | D | 67 | 221 | 233 | NS |
| | 1426-1430 | 5.9 | 23 | 7.3 | | 32 | out | | 69 | 221 | 233 | |
| Feb 28 | 2032-2038 | 9.5 | 23 | * | 2427 | 19 | out | S | 67 | 141 | 624 | ND |
| Mar 5 | 1213-1216 | 3.9 | 25 | 4.8 | 2132 | 13 | in | M | 64 | 218 | 534 | ND |
| | 1234-1245 | 4.9 | 25 | 6.2 | 2210 | 27 | out | | 67 | 221 | 397 | |
| | 1245-1256 | 5.3 | 25 | 6.7 | 2222 | 16 | in | | 68 | 222 | 397 | |
| Mar 27 | 0153-0204 | 4.2 | 45 | 6.6 | 2204 | 16 | out | S | 73 | 10 | 724 | BR1 |
| Mar 29 | 1025-1048 | 5.2 | 27 | 6.9 | 2047 | 24 | out | S | 66 | 224 | 446 | BR1 |
| Mar 31 | 1953-2033 | 5.7 | 35 | 10.2 | 0227 | 16 | out | S | 69 | 89 | 186 | NS |
| Apr 3 | 0431-0441 | 3.6 | 41 | 6.4 | 1910 | 34 | in | D | 67 | 285 | 672 | BR1 |
| | 0441-0451 | 4.0 | 42 | 7.5 | 1932 | 29 | out | | 67 | 288 | 672 | |
| Apr 24 | 1706-1714 | 3.8 | 37 | 6.0 | 1919 | 36 | out | D | 66 | 84 | 696 | BR1 |
| | 1714-1721 | 4.1 | 36 | 6.4 | 1932 | 27 | in | | 66 | 86 | 696 | |
| Apr 27 | 0200-0245 | 3.5 | 44 | 7.1 | 1741 | 42 | in | D | 66 | 282 | 486 | BR1 |
| | 0245-0342 | 5.5 | 44 | 13.1 | 1905 | 31 | out | | 72 | 290 | 353 | |

Table 2. Location of ground magnetic stations.

| Station Name | Code Name | Geomagnetic Co-Lati., N. | Geomagnetic Longitude, E. |
|---|---|---|---|
| Fort Churchill | FCC | 21.32 | 305.02 |
| College | CMO | 25.07 | 258.14 |
| Meanook | MEA | 28.05 | 302.92 |
| Fredericksburg | FRD | 40.59 | 353.57 |
| Boulder | BOU | 40.96 | 318.22 |
| Tucson | TUC | 49.50 | 313.83 |
| San Juan | SJG | 60.61 | 4.61 |
| Argentine Island | AIA | 143.96 | 4.37 |
| Godhavn | GDH | 10.43 | 34.62 |
| Narssarssuaq | NAQ | 19.23 | 38.70 |
| Leirvogur | LRV | 20.11 | 72.19 |
| St. Johns | STJ | 31.78 | 22.94 |
| M Bour | MBD | 69.09 | 56.40 |
| Hermanus | HER | 123.58 | 81.98 |
| Halley Bay | HBA | 156.04 | 25.20 |
| Yakutsk | YAK | 38.80 | 194.93 |
| Irkutsk | IRT | 49.13 | 175.83 |
| Yuzhno Sakhalinsk | YSS | 52.83 | 207.91 |
| Gnangara | GNA | 133.01 | 187.40 |
| Toolangi | TOO | 136.34 | 222.30 |
| Macquarie Island | MCQ | 150.75 | 244.40 |
| Sitka | SIT | 29.77 | 277.09 |
| Honolulu | HON | 68.65 | 267.96 |

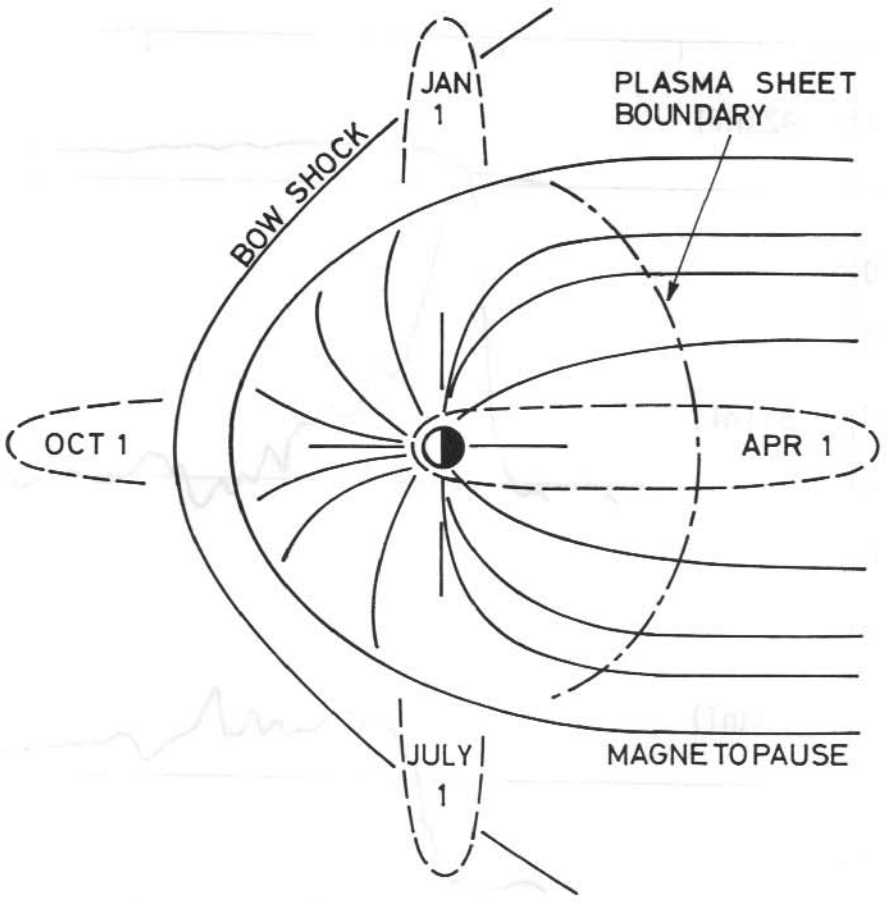


Figure 1. A diagram of the magnetosphere, projected onto the ecliptic plane, showing the approximate positions of the ISEE orbit at different times of the year.

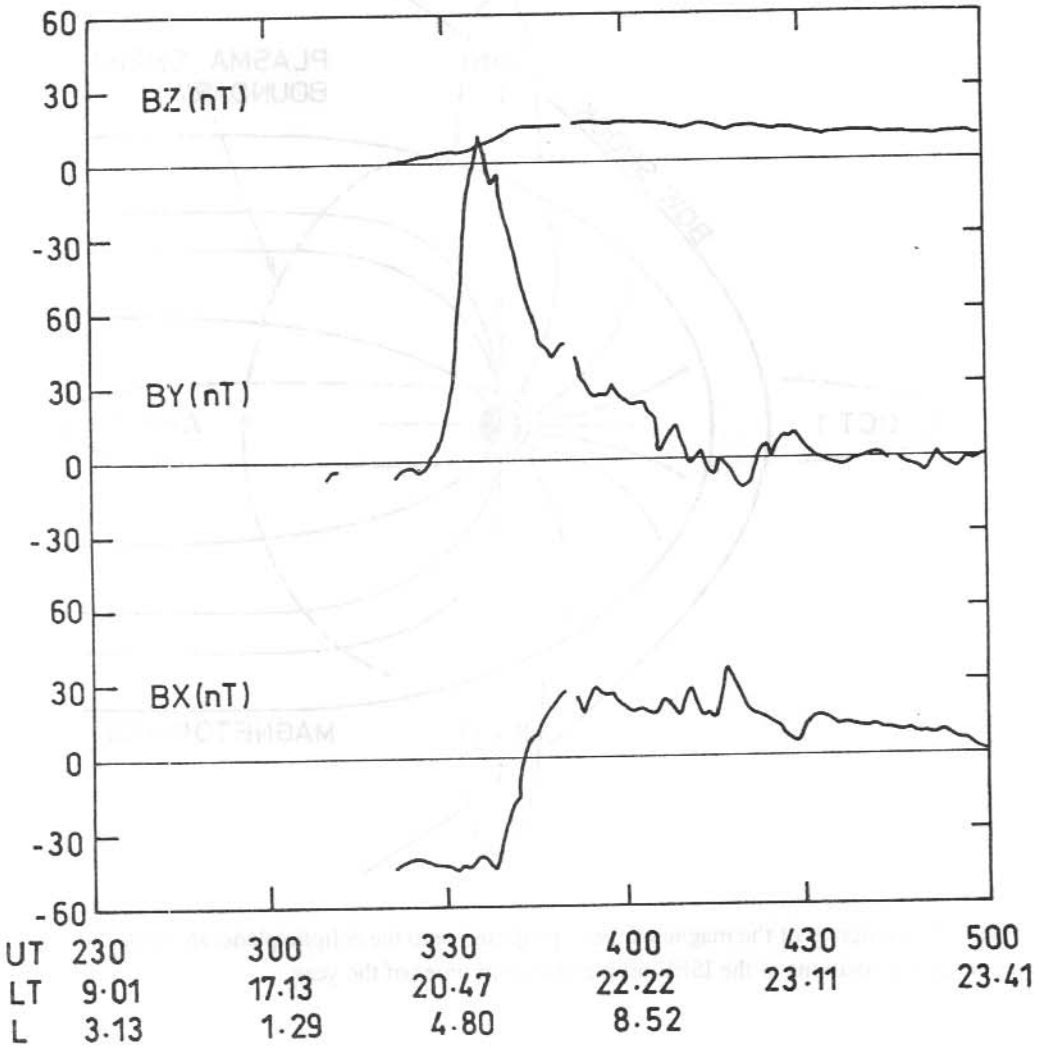


Figure 2(a). The detrended magnetic field versus time plot for February 19, 1978 from 0230-0500 UT. A pair of field-aligned current sheets were observed during 0327-0354 UT.

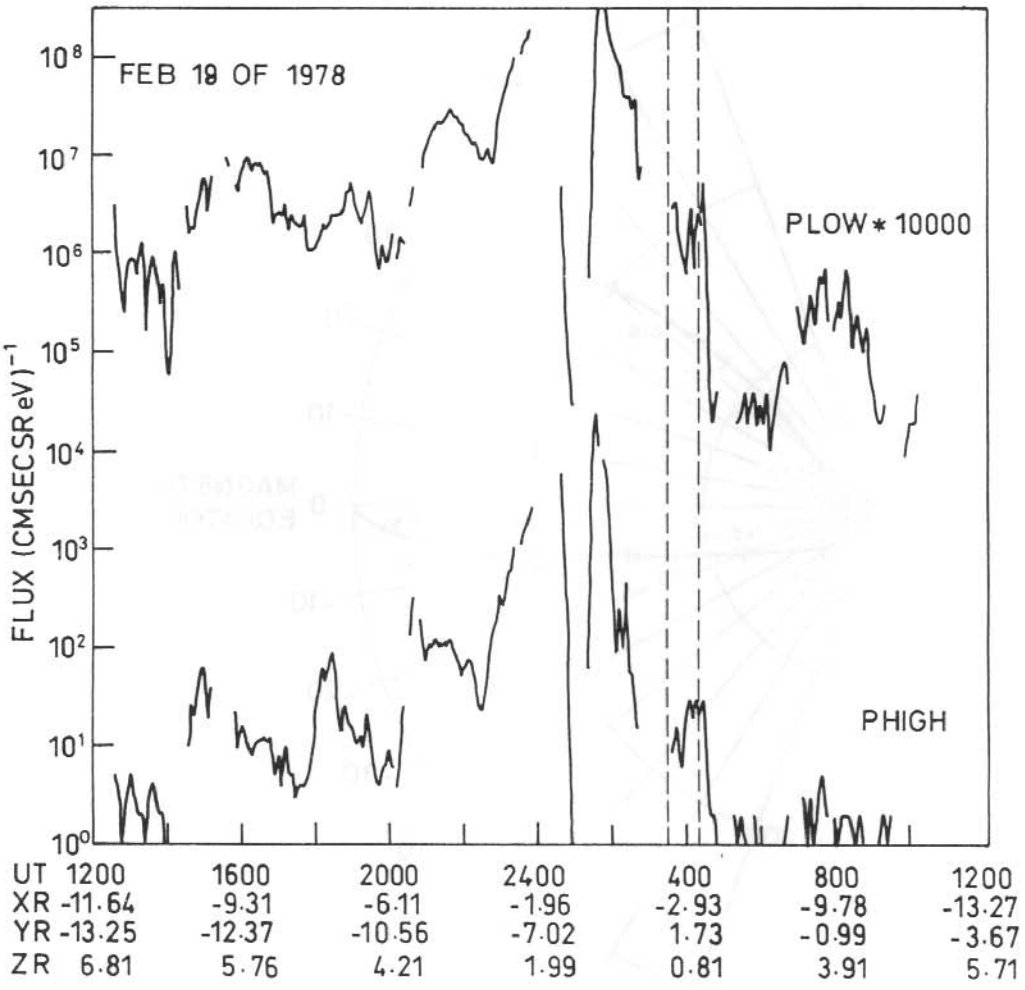


Figure 2(b). Plasma wave and medium energy particle observations from 1200 UT, 18 February to 1200 UT, 19 February 1978. The data shown are 80-125 keV proton (PHIGH) and 32-50 keV proton (PLOW) fluxes. The dashed lines represent the time interval during which the field-aligned current crossing occurred in (a).

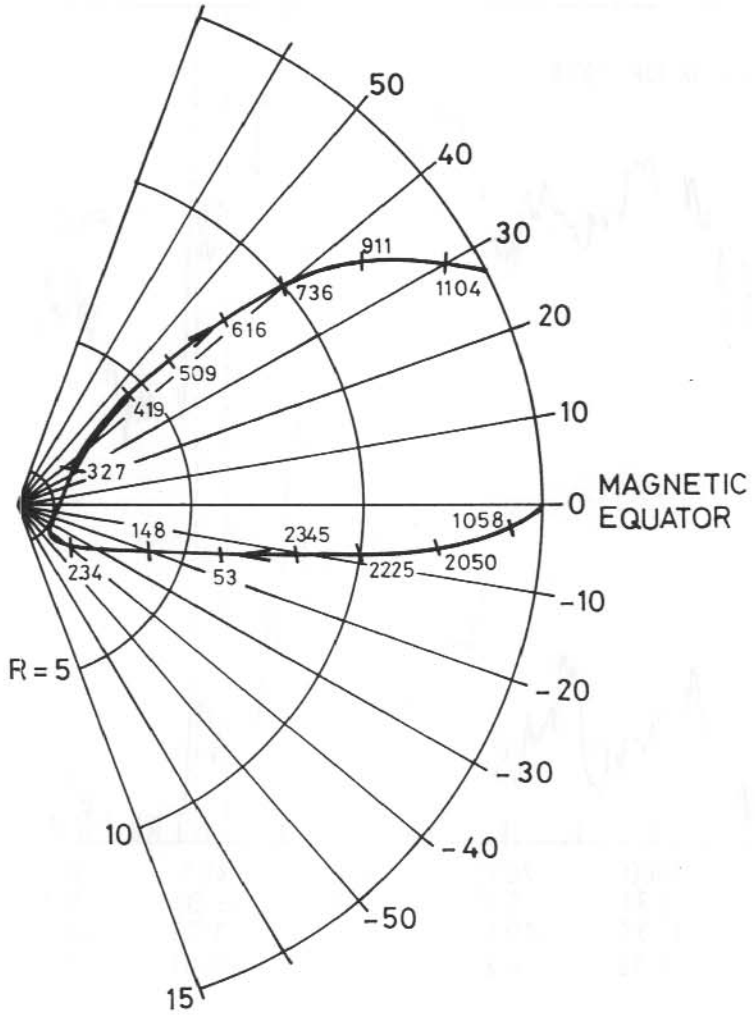


Figure 2(c). The ISEE 2 trajectory in the ML-R plane near perigee (0300 UT, February 19, 1978) of orbit 51. The heavy trace indicates the interval between 0327-0354 UT when the field-aligned current sheets crossing occurred.

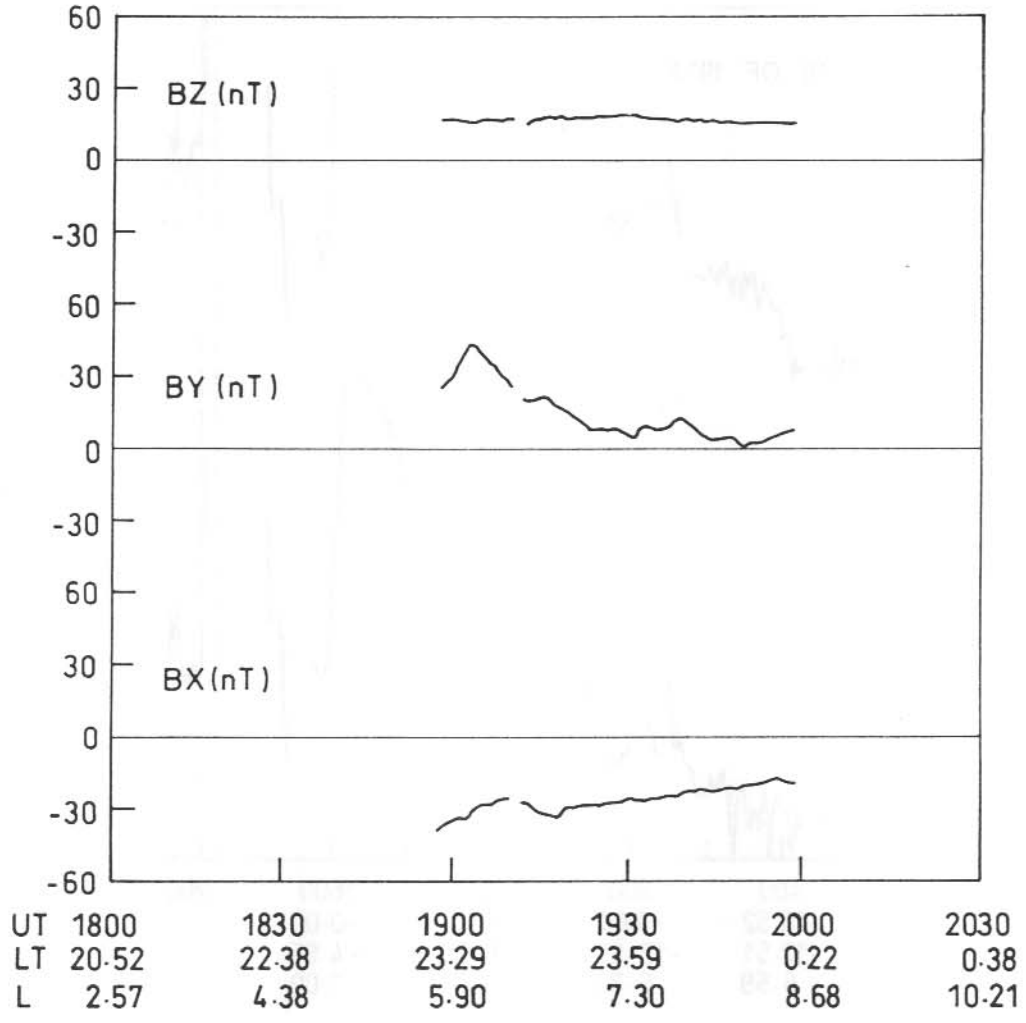


Figure 3(a). The detrended magnetic field versus time plot for February 16, 1978, from 1800-2030 UT. A pair of field-aligned current sheets were observed during 1857-1930 UT.

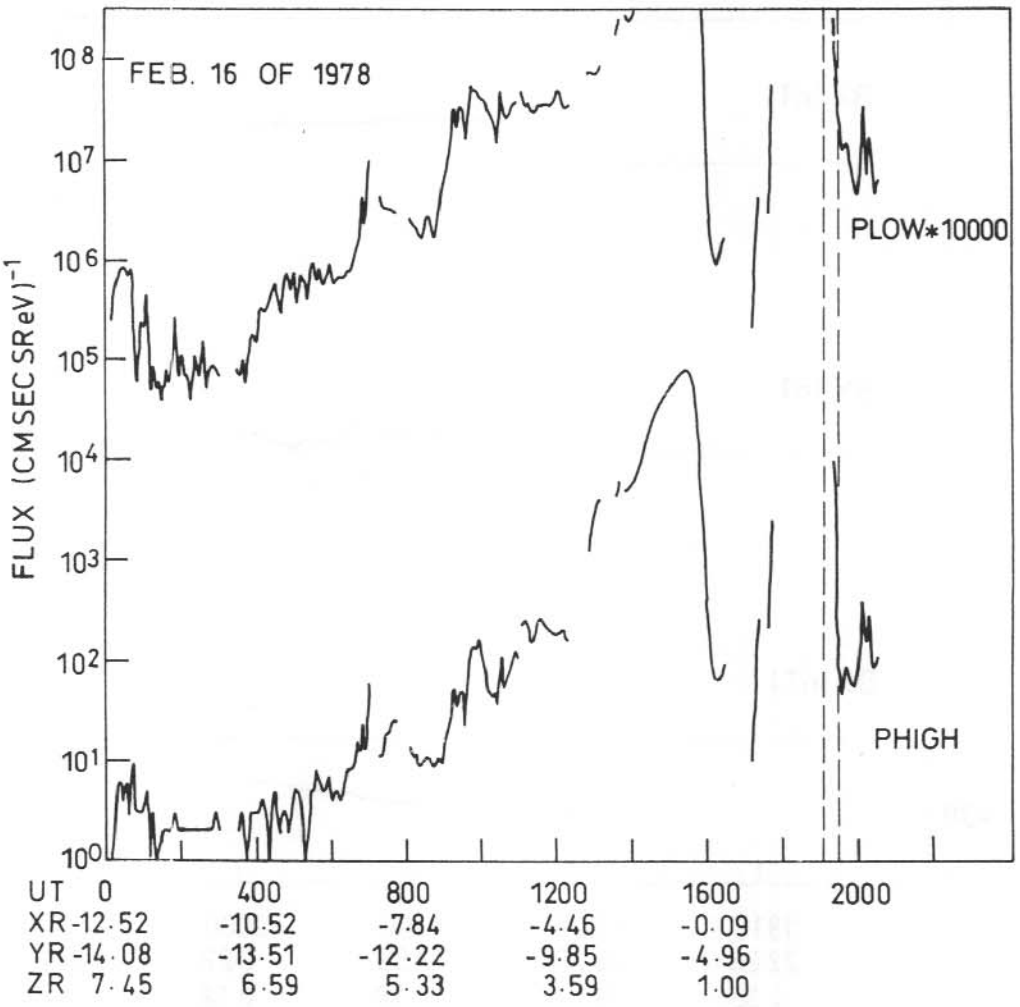


Figure 3(b). Plasma wave and medium energy particles observation from 0000 UT, February 16 to 0000 UT, February 17, 1978. As for Figure 2(b).

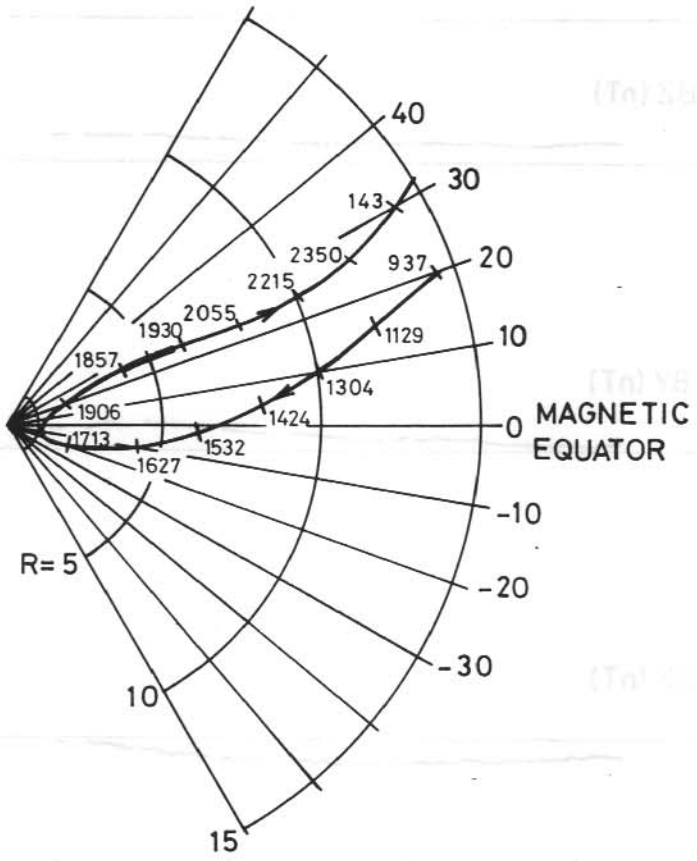


Figure 3(c). ISEE trajectory in ML-R plane near perigee (at 1739 UT, February 16, 1978) of orbit 50, heavy trace indicating the interval between 1857-1930 UT when the field-aligned current states crossing occurred.

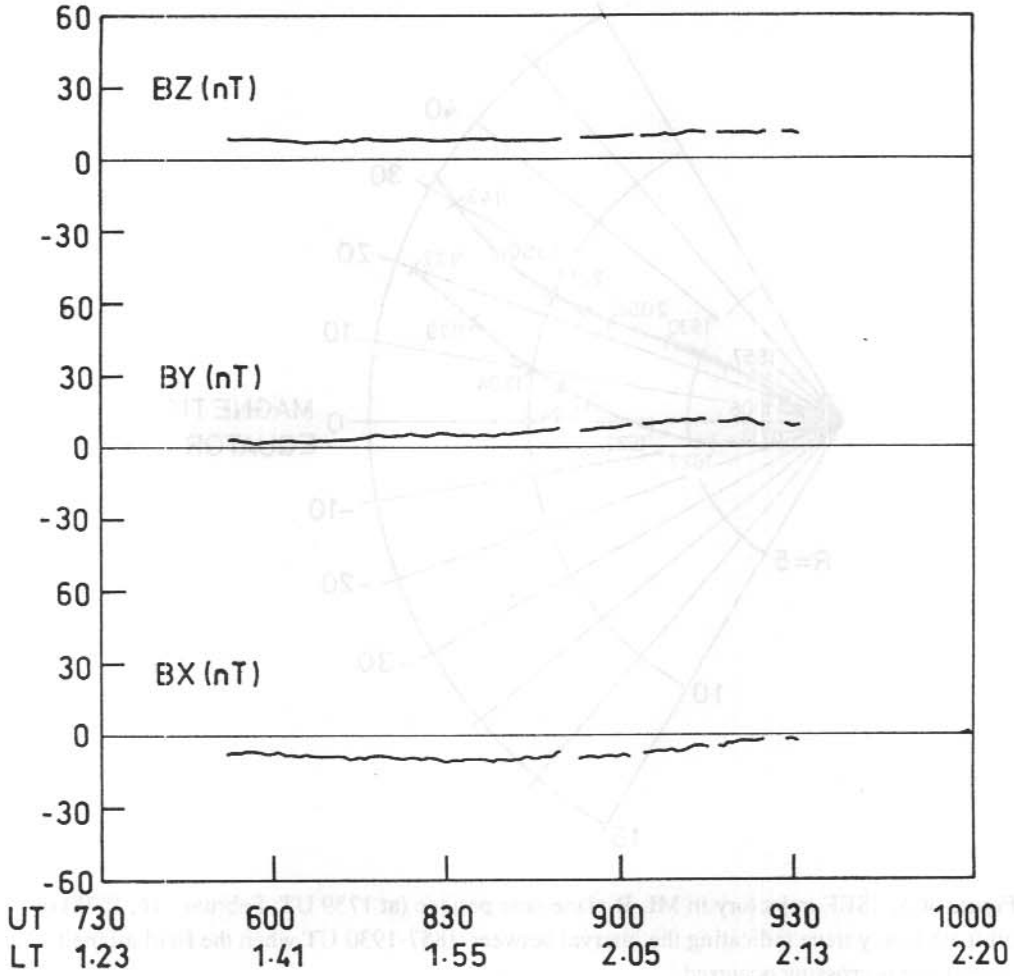


Figure 4. The detrended magnetic field versus time plot for January 16, 1978.

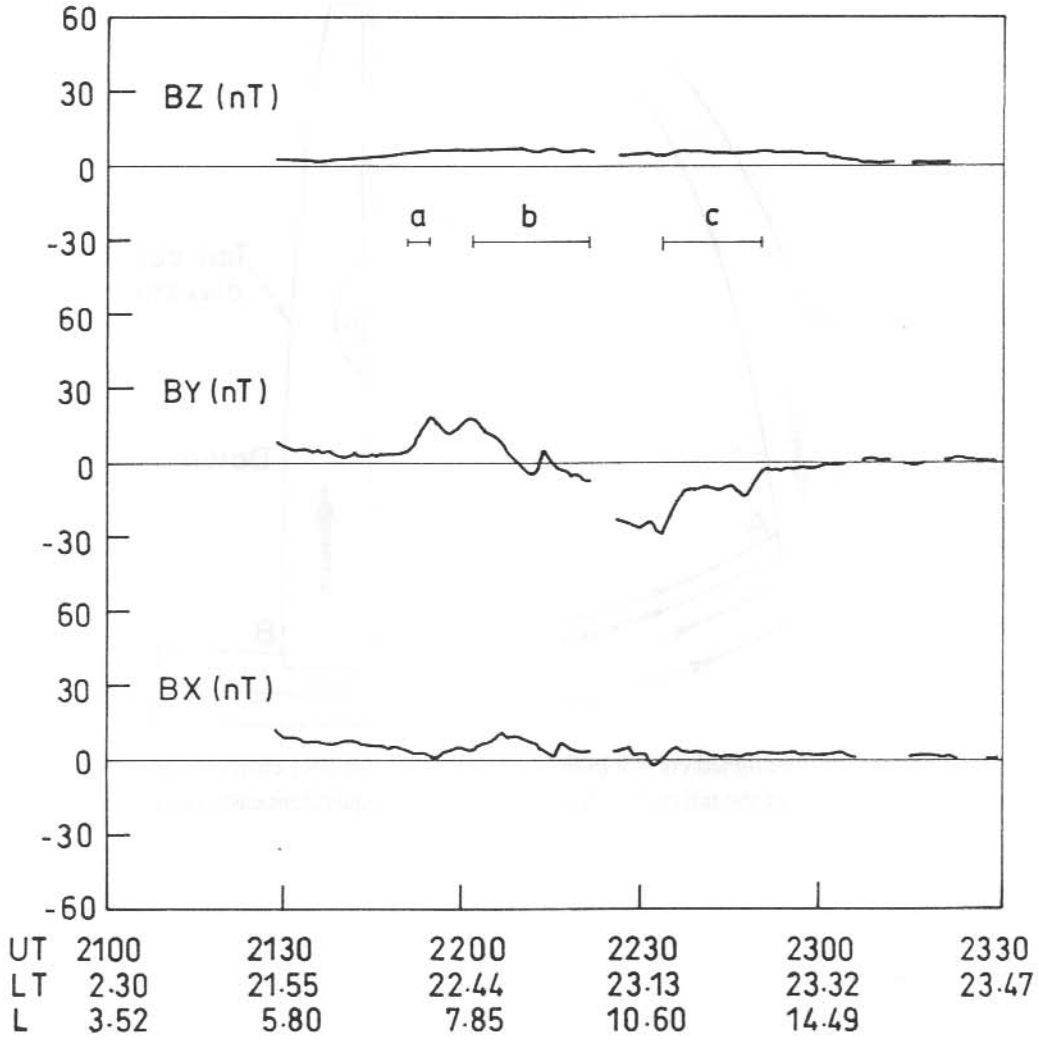


Figure 5. The detrended magnetic field versus time plot for March 7, 1978, from 2100 to 2330 UT. Multiple field-aligned current sheets were observed during 2149-2249 UT. The third current sheet (2233-2249 UT, marked c) can be interpreted as filamentary structure.

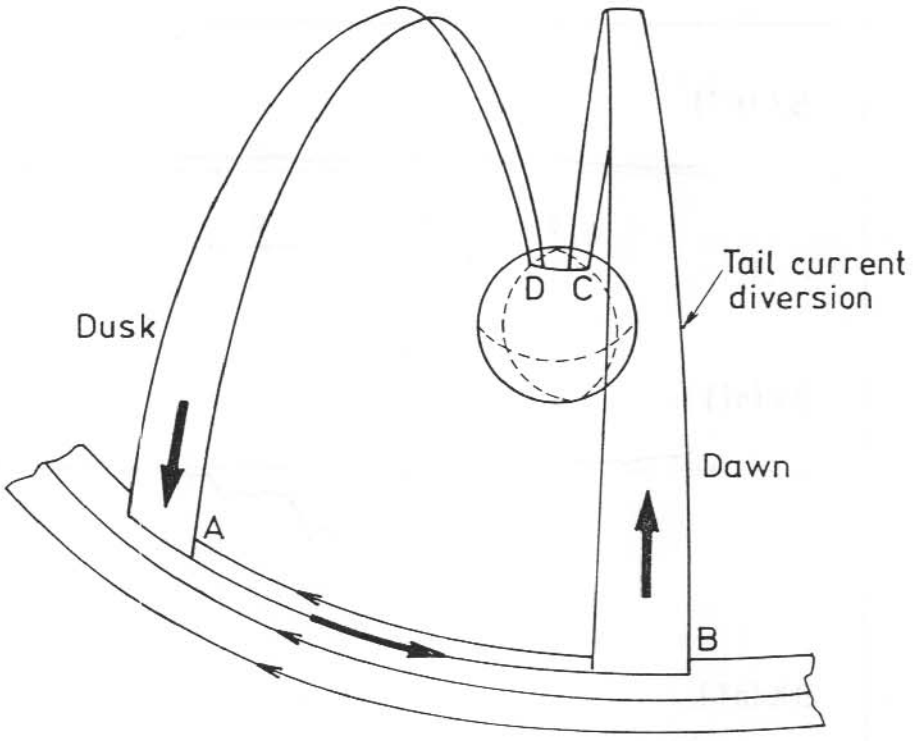


Figure 6. The net field-aligned current in the nightside when the BR1 current exceeds the BR 2 current. The diversion of the tail current is represented by an equivalent eastward tail current.

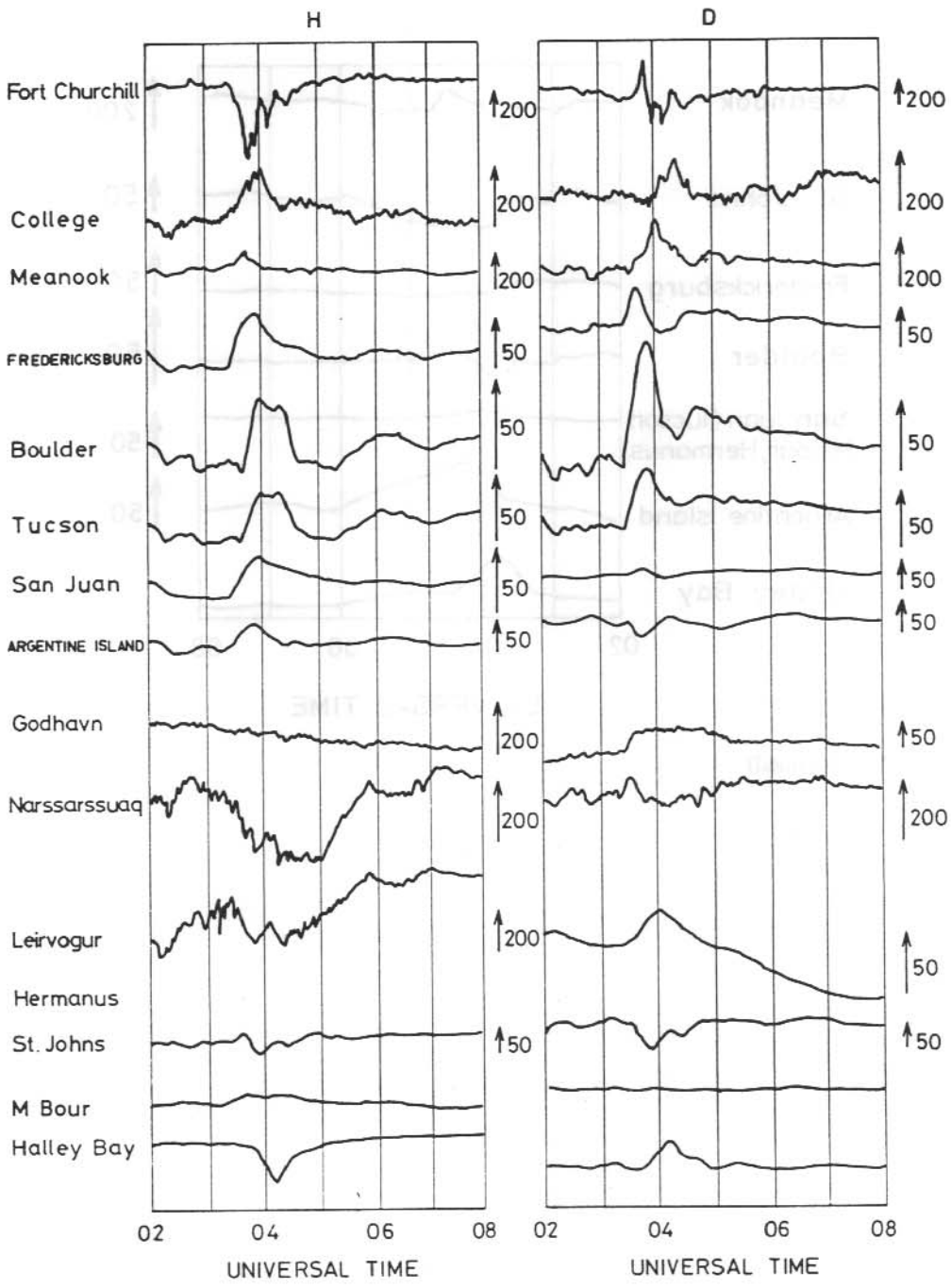


Figure 7. Magnetic components (H, D, Z) observed at ground stations for February 19, 1978 from 0200 to 0800 UT. Arrows indicate the scales in nanotesla. (continued on next page)

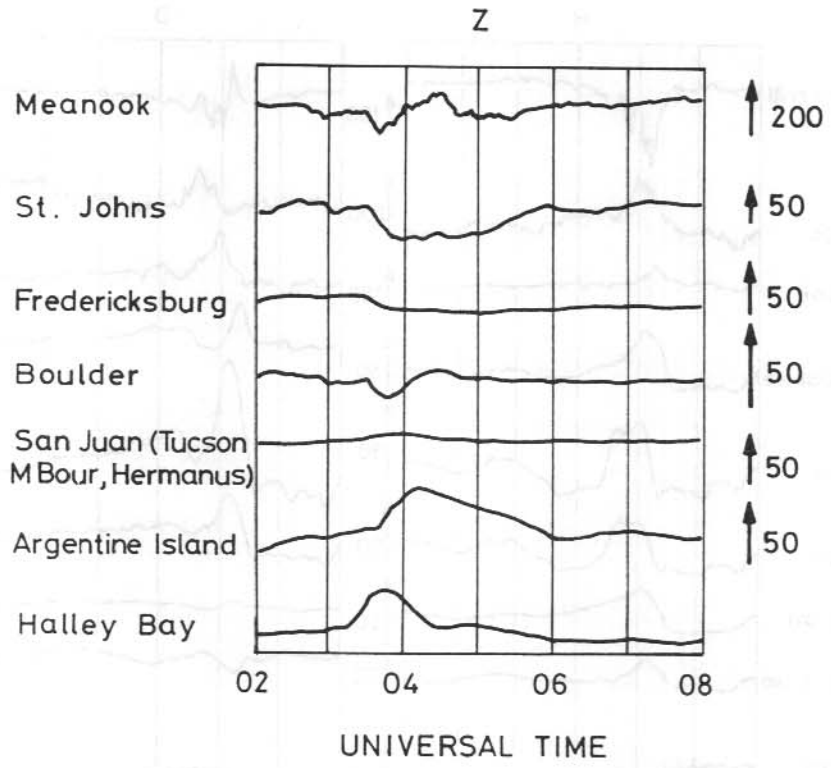


Figure 7. (continued)

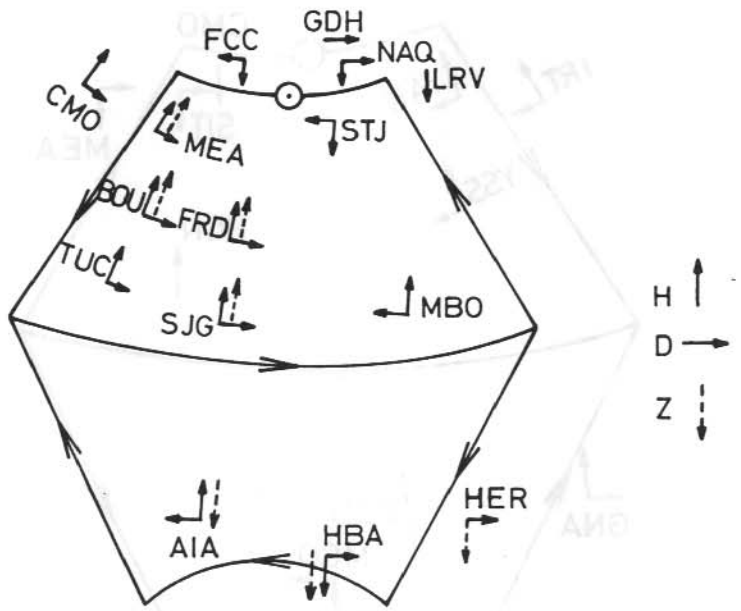


Figure 8. Schematic magnetic perturbation directions (H, D, Z) from stations in Table 2 near 0330 UT, February 19, 1978. H points northward along the earth's magnetic dipole, D eastward along constant magnetic latitude and Z downward along the radial distance. Open arrows show the inferred source of the magnetic perturbation - a BR1 current system. A circle with a dot indicates the intersection of the field line passing through ISEE 2 with the ground.

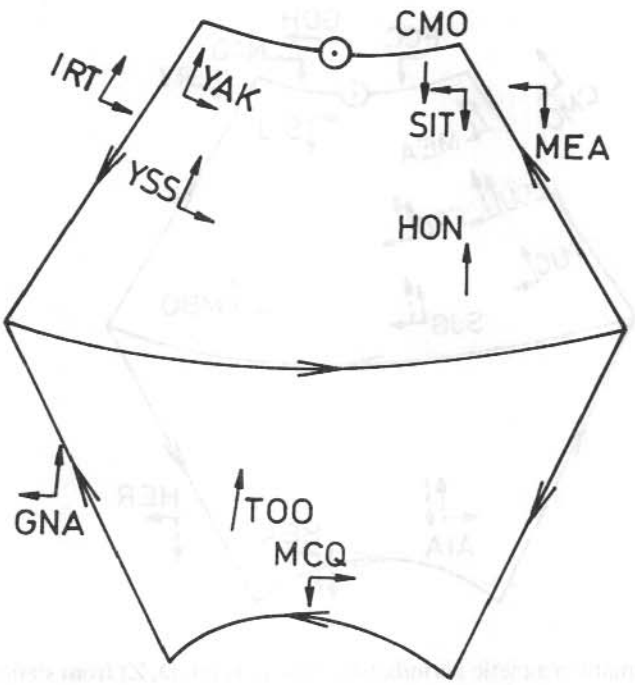


Figure 9. Schematic magnetic records (H, D, Z) from stations in Table 2 near 1025 UT, March 29, 1978, as in Figure 8.

# 14. DIURNAL AND SEASONAL VARIABILITY OF THE SOUTHERN HEMISPHERE MAIN IONOSPHERIC TROUGH USING THE DIFFERENTIAL-PHASE METHOD: SOME RESULTS AND CONCLUSIONS

M. Mallis and E.A. Essex
Physics Department
La Trobe University
Bundoora Vic 3083
Australia

ABSTRACT

The primary aims of this research were to first identify the southern hemisphere ionospheric main-trough and then to undertake a morphological study of various trough features. The differential-phase technique was used for ionospheric trough studies; this being conducted for the first time in the southern hemisphere. The main findings of this work have been the unexpected high incidence of daytime and summertime troughs and the relative low incidence of troughs for the winter and autumnal equinox seasons when compared to the northern hemisphere trough. An attempt to explain some of these features in the light of the high-latitude convection theory is offered. Case studies are given for all seasons to highlight these findings.

## 14.1 INTRODUCTION

In the context of this study, the word trough shall be taken to mean the 'main-trough' unless otherwise stated. The trough usually manifests itself as a sharp decrease in night-time ionisation density in both hemispheres with steep poleward and equatorward walls. Although the trough is predominately a nocturnal feature, with a 95% occurrence frequency (Ahmed et al. 1979), it has been reported in the pre-dusk, dawn and noon-time sectors (Tulunay and Grebowsky 1978, Pinnock 1985). Mendillo and Chacko (1977) claim an 88% observation occurrence frequency based on topside electron density profiles. Mostly topside sounders and some ground based measurements have been employed in the past to identify and measure trough characteristics. It has been found that the trough has a mean position of $L \sim 4$ and is in the order of 10° wide in latitude. The trough minimum is found at about an invariant latitude ($\Lambda$) of 65° in the evening hours decreasing to about $\Lambda < 60°$ at later local times. The trough consists of a circumpolar region fixed in space with respect to the sun, not unlike the auroral oval, and moves equatorwards or polewards in relation to the degree of magnetic activity (Köhnlein and Raitt 1977).

In this paper differential-phase derived ionospheric total electron content (TEC) data were used in determining the location, shape, spatial and temporal characteristics of the main-trough. Trough parameters such as trough width and location were analysed for seasonal and diurnal

trends. To this end purpose designed computer programs were constructed which automated the process of measuring these parameters from TEC records. A detailed morphological study of the trough was conducted over the course of 12 months from February 1988 until January 1989 inclusive using a receiving site at Macquarie Island (GG: 54.5°S, GM: 64.5°S, L = 5.38), a sub-auroral station. More than 6000 satellite passes were recorded and processed. It is found that when compared to the northern hemisphere trough, the southern hemisphere trough has a different seasonal and diurnal structure which cannot be easily explained.

## 14.2 EXPERIMENTAL THEORY, DESIGN AND SETUP

The differential-phase method basically involves measuring the phase-path difference ($\Psi$) of two received transmissions of 150 and 400 MHz initially transmitted coherently from polar orbiting NNSS satellites. With a knowledge of the satellite orbital path, it is possible to deduce TEC throughout the orbit for a vertical column of ionosphere centred at a height of 400 km (the ionospheric point); hence a latitudinal snapshot of ionospheric TEC vertical profile is possible. By computing the rate of change of phase-path difference ($d\Psi/dt$) between these transmissions over some finite time interval, it is possible to find the electron content ($\int_o^{h_s} N\,dh$) beneath the ionospheric point. $\int F dt$ can be approximated by the following equation:

$$\int F dt \approx \frac{1}{\lambda_o} \frac{K_1}{2f_o^2}\left(1-\frac{1}{m^2}\right) sec\chi_m \left(\int_o^{h_s} N\,dh + D\right) \qquad (1)$$

where $F = \dot{\Psi}/\lambda_o$, $\chi_m$ is the angle made between the ray path (from satellite to observer) and the vertical at the ionospheric point, $K_1 = 80.69$ and $D$ is a constant (TEC baseline value) to be determined from other methods. For the NNSS satellite series $f_o = 149.988$ MHz and $m = \frac{8}{3}$. Substituting for $m, f_o$ and $\lambda_o$ and solving for columnar electron content in equation (1) yields

$$\int_o^{h_s} N\,dh = A cos\chi \left(\int F dt + D\right) \qquad (2)$$

where $A = 6.48\ 10^{14}\ (m^{-2})$. $\Psi$ was sampled at a nominal rate of 10 Hz which gives an equivalent spatial resolution of $\approx 0.8$ km. $\int (\dot{\Psi}/\lambda_o)\, dt$ is usually referred to as the refraction 'Doppler-count' and is usually summed over a finite time interval by some satellite receivers ranging from 4.6 to 30 seconds (not the JMR receiver used for this experiment).

Different techniques exist for evaluating $D$ which have been proposed by various workers (Tyagi 1974, Leitinger and Hartmann 1976). The most accurate and successful method is to make use of Faraday-rotation data from geostationary beacon satellites and of ionosonde derived $f_oF_2$ values at the Faraday-rotation sub-ionospheric point (SIP) to help establish a 'baseline' TEC value (Leitinger et al. 1984).

In this study, a commercially available dual frequency geodetic survey satellite receiver (JMR) was used. It was converted to provide $\int$ F dt output which could be logged to a micro-computer. The original JMR design does not permit the output of differential-phase nor Doppler-counts;

this had to be done by specially built circuitry. This circuit simply phase compares the two satellite signals (after removing the vacuum Doppler shift and having been mixed down to a convenient common carrier) which produced a voltage proportional to the phase difference. The output was fed to floppy-disk on a (Forth) micro-computer, high-speed thermal chart recorder and a VDU. One floppy disk could hold up to 48 twenty minute satellite passes recorded at 10 Hz along with 150 and 400 MHz AGC information. This data was later downloaded to a mainframe VAX 8800 computer for post-analysis and conversion to TEC. A typical satellite pass would last for 18 minutes while it traverses the sky. More details regarding the experiment design, installation, theory, data management procedures and results can be found in Mallis (1989a, 1989b).

## 14.3 ANALYSIS AND RESULTS

A method for identifying the trough from the calculated TEC was devised using a model for the trough shape. In the past various definitions of a trough have been made. For example, Tulunay and Sayers (1971) used a trough minimum in electron density while Brace and Theis (1974) used a density level of $10^3$ el $cm^{-3}$ along the equatorial trough wall to define a trough position. Wildman et al. (1976) and Ahmed et al. (1979) used a criteria based on electron density levels to define trough width, depth and wall gradients. In this study a trough minimum in TEC level was used as a guide for trough position, although this may not necessarily correspond to a minimum in the electron density level due to the problem of spatial-filtering. A computer program was developed which handled the task of calculating trough position and other parameters which were used in the statistical compilation.

Because the trough in TEC measurements is not as well defined as *in situ* measurements a model for trough shape was developed so that certain common features could be parameterised and measured. Certain readily identifiable trough features were selected for measurement; these included the latitudinal position of the trough-minimum and the TEC value of this minimum. Figure 1 depicts the basic trough parameters that were identified and determined. The 'full-trough width' is defined as the latitudinal separation of the first occurrence of a TEC peak or plateau when moving away from the trough-minimum position in both directions. In the event of a plasma- or subauroral-blob (Weber et al. 1985) appearing within the trough, this peak is overlooked and the next one chosen. The 'half-trough' width is defined as the latitudinal width of the trough measured from the 3dB points. The 3dB point is defined as the latitudinal position where TEC has fallen to half its maximum peak value measured from where the full-trough width was determined. The poleward and equatorward trough wall gradients were calculated about the 3dB points. The trough-depth is the magnitude of TEC depletion calculated from the trough-minimum to where the full-trough width value was evaluated. An indication of the relative magnitude of a trough to the surrounding ionospheric medium can be gained by taking the ratio trough-depth/(trough-depth + trough-minimum). Values approaching unity indicate that the trough is very pronounced and established. Values approaching zero indicate that the trough is less developed and shallow.

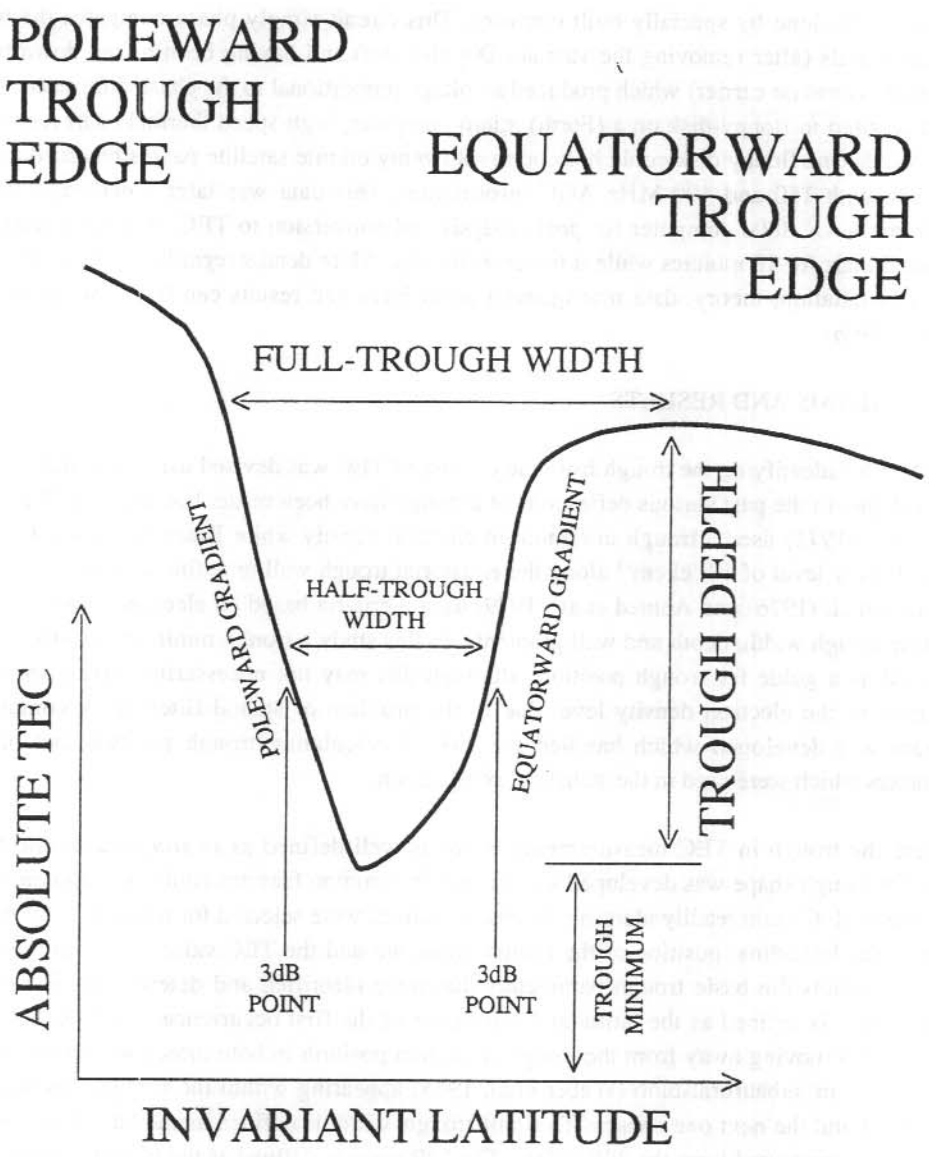


Figure 1. A schematic diagram of a model trough defining basic parameters calculated for all troughs which passed the selection criteria.

The box-plots described below follow the style of Putz and Leitinger (1988) which has been adopted as a more convenient graphical way of representing trough data. This style of plot gives a graphical display of distribution quantities such as skewness and variance which cannot be represented by scatter or histogram plots. Data points that fall within a three hour time interval were subjected to a simple statistical analysis. The upper and lower parts of the box define the upper and lower quartile values respectively which is itself divided by a horizontal median line. The box, therefore, contains 50% of all the data points sampled. A vertical line is drawn from a quartile line to the maximum and minimum values contained in the data set. Horizontal lines placed beyond the quartile lines mark the upper and lower decile values within which 80% of the data set is contained. The total number of data points used in constructing the box-plot is indicated directly beneath the time interval below the time axis and is underlined. All box-plots which are a function of local time have two small vertical arrows. These arrows indicate the position in local time of astronomical sunrise and sunset twilight times. The symbols SR and SS denote sunrise and sunset respectively. No times are listed for the summer season as ionospheric twilight sunrise and sunset times are almost identical at 0000 LT for Macquarie Island.

There is some variability in the number of occurrences listed in a three hour period between some graphs involving any measurements of the trough walls, such as position, width and gradient. This is because there are some times when either the equatorward or poleward trough wall 3dB point could not be defined according to the adopted selection criterion. The reason for this was simply that part of the trough edges were outside the field-of-view (this was ±15° geographic latitude for Macquarie Island) of the differential-phase ground station. When this occurred only the trough position and minimum TEC values could be measured with any certainty. No attempt was made to extract any more information as this could have introduced a bias to the data set. This fact accounts for the discrepancy in occurrence number between successive plots for the same season. No bias is believed to have been introduced into the data set by adopting this procedure.

A distinction is made between the two equinox seasons because there exists a large enough morphological difference to warrant this. The autumnal equinox is taken as the full calendar months of February, March and April. Similarly the winter, vernal equinox and summer seasons are defined as the full calendar months of May, June and July; August, September and October; November, December and January respectively. Figure 2 shows box-plots in which the trough is plotted as a function of local time for all the seasons. Similarly box-plots of the full-trough width, trough-ratio and trough-depth for all seasons are also depicted in Figures 3, 4 and 5.

Figures 6, 7, 8 and 9 depict some examples of absolute TEC as a function of geographic latitude which depict the trough for the autumnal equinox, winter, vernal equinox and summer seasons respectively. Troughs are identified by the letter T. All curves are labelled with a start and stop time in decimal hours (UT). Each plot is labelled (from left to right) with the satellite identifier number, geographic longitude at Macquarie Island, latitude of the satellite pass, plot label, day number and year.

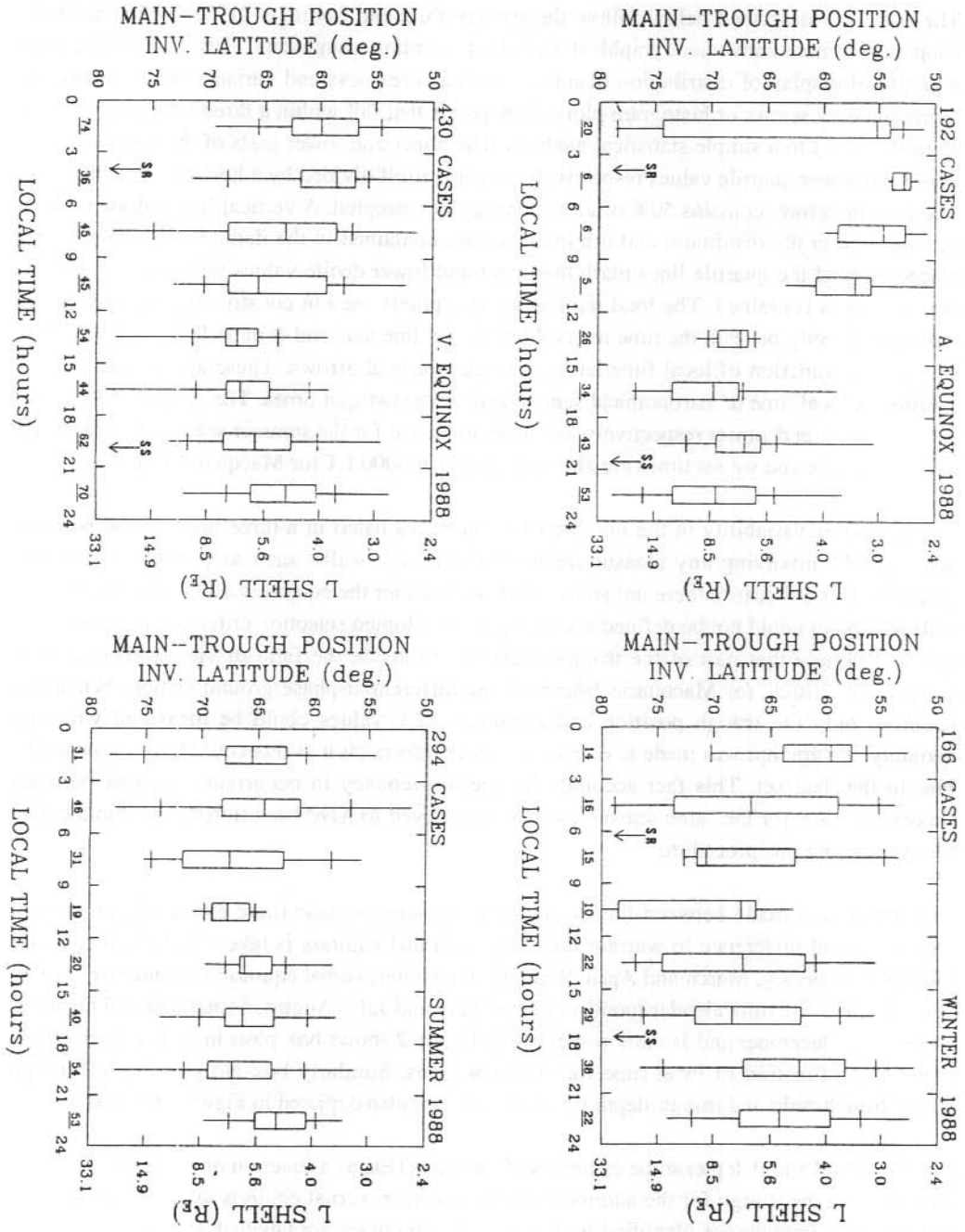


Figure 2. Box-plots of the trough position for all seasons as a function of local time.

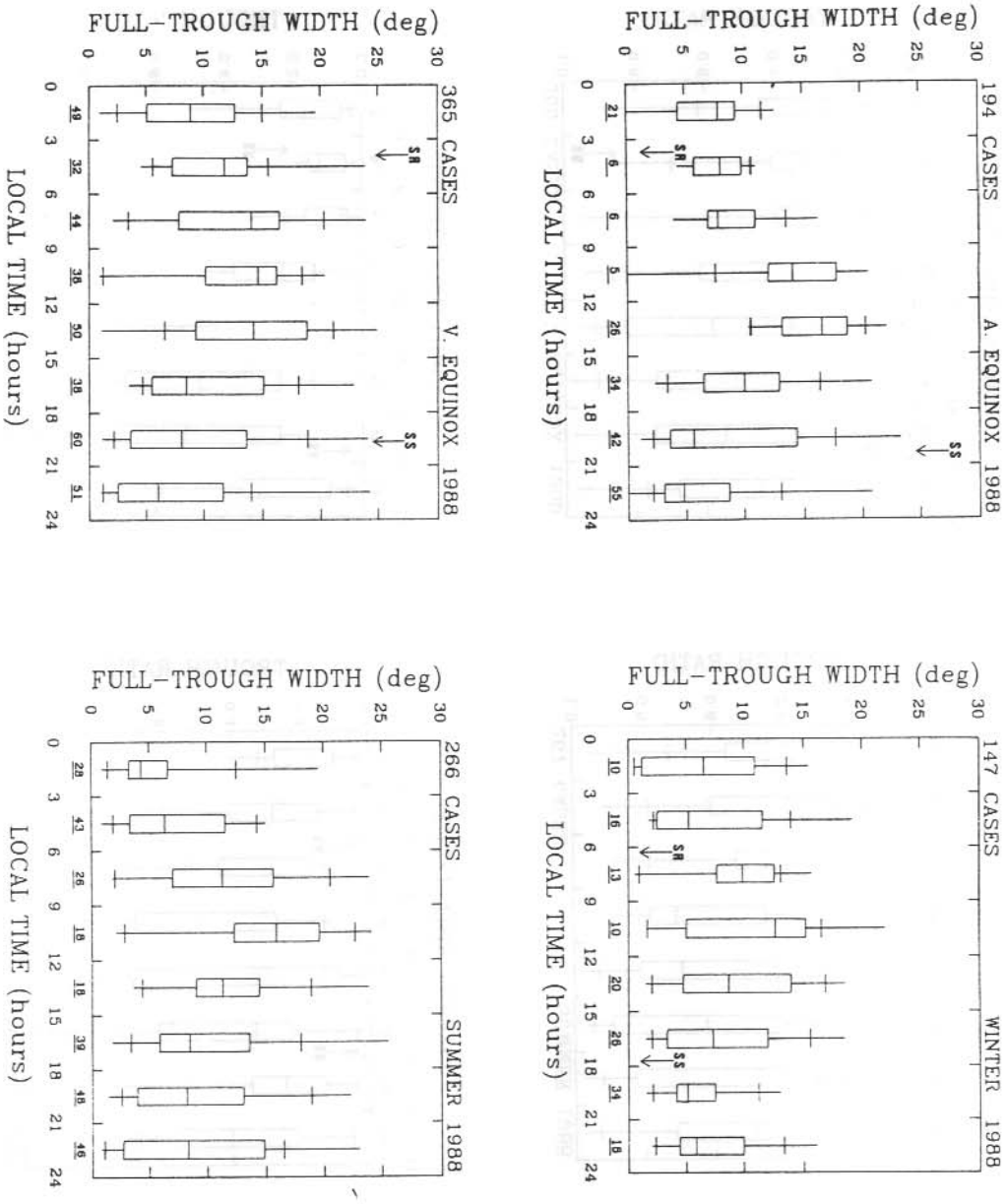


Figure 3. Box-plots of the full-trough width for all seasons as a function of local time.

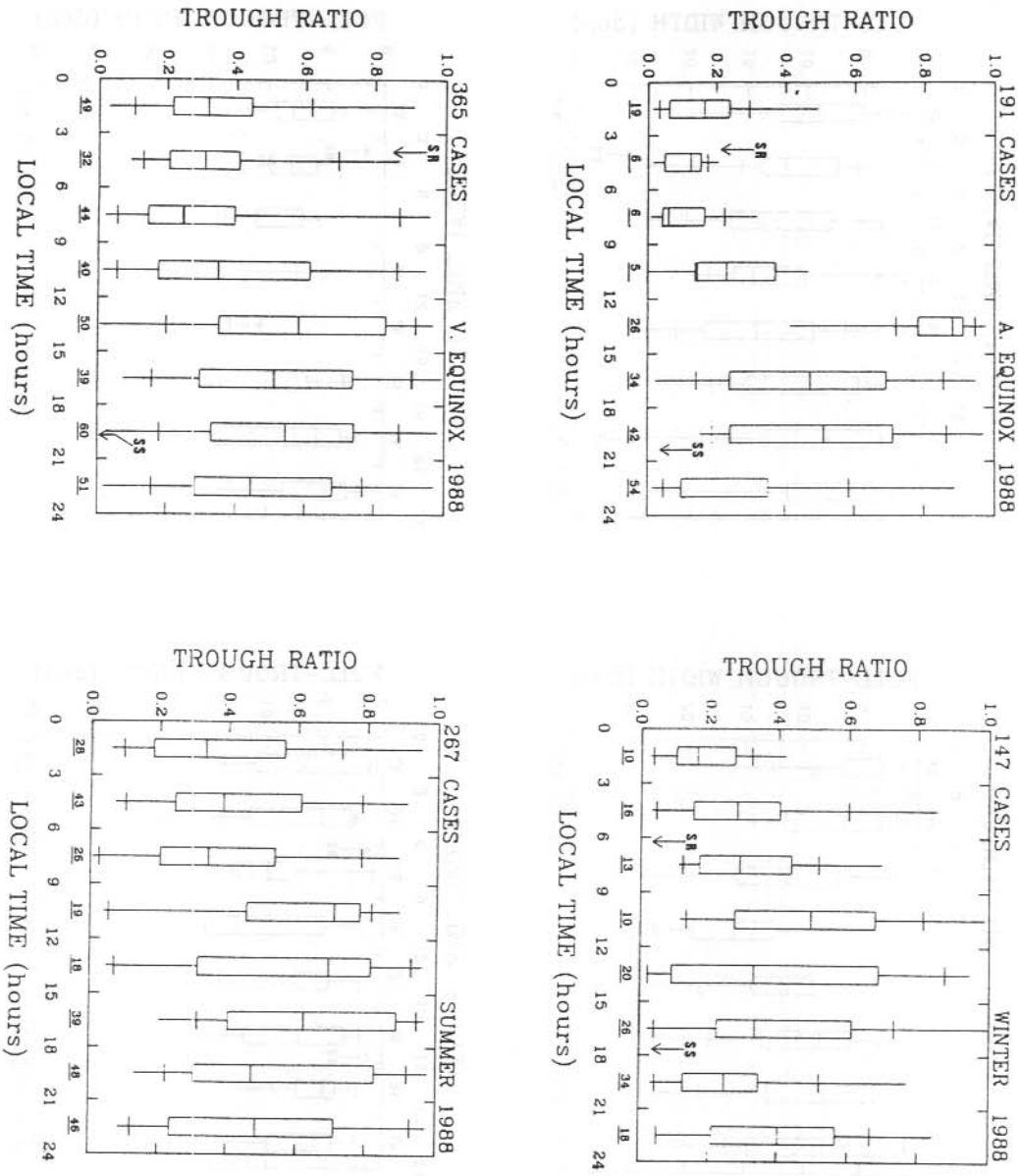


Figure 4. Box-plots of the trough-ratio for all seasons as a function of local time.

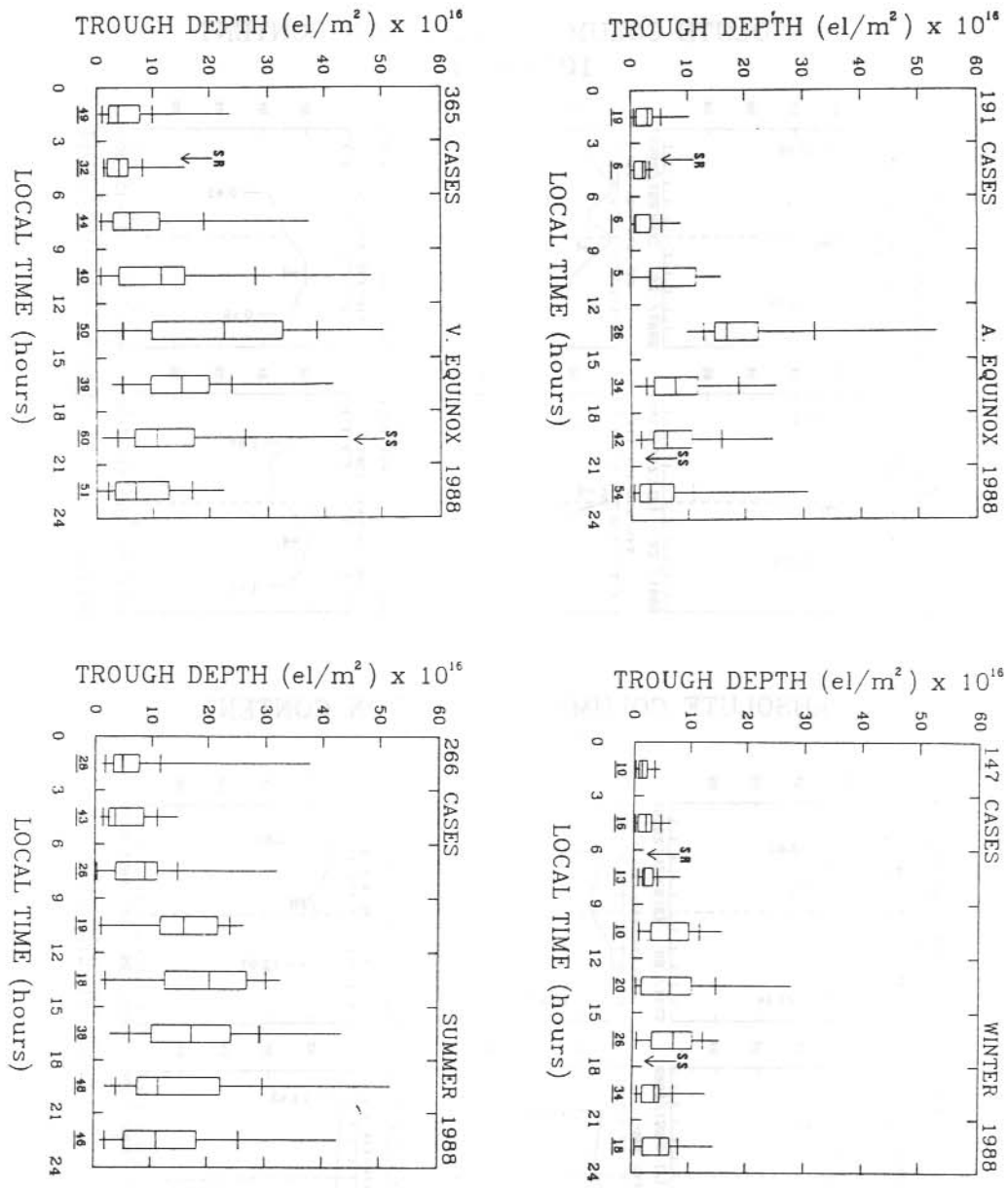


Figure 5. Box-plots of the trough-depth for all seasons as a funtion of local time.

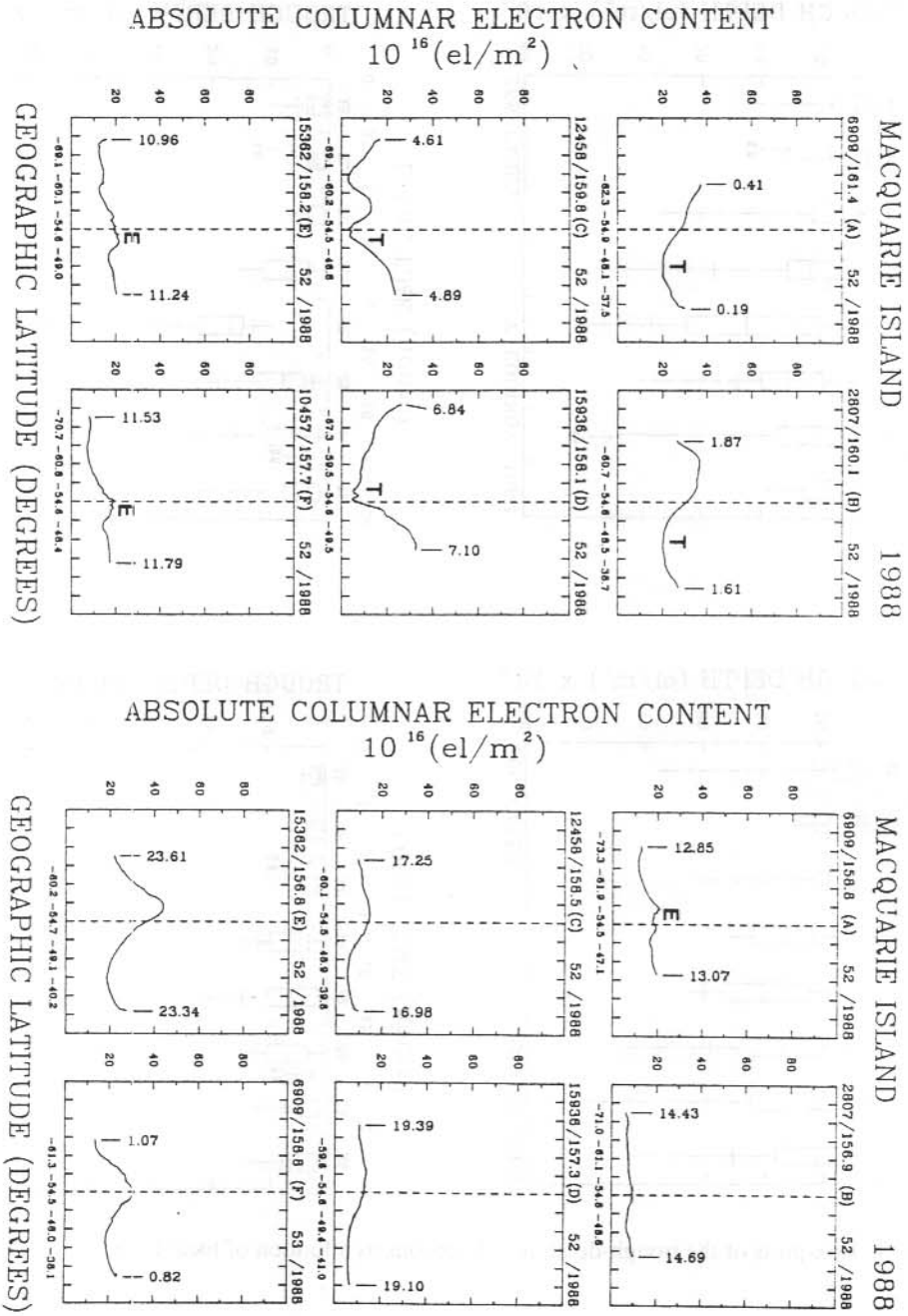


Figure 6. Examples of DP derived absolute TEC for the autumnal equinox from Macquarie Island. T indicates a developing or developed trough and E indicates a localised night-time TEC enhancement.

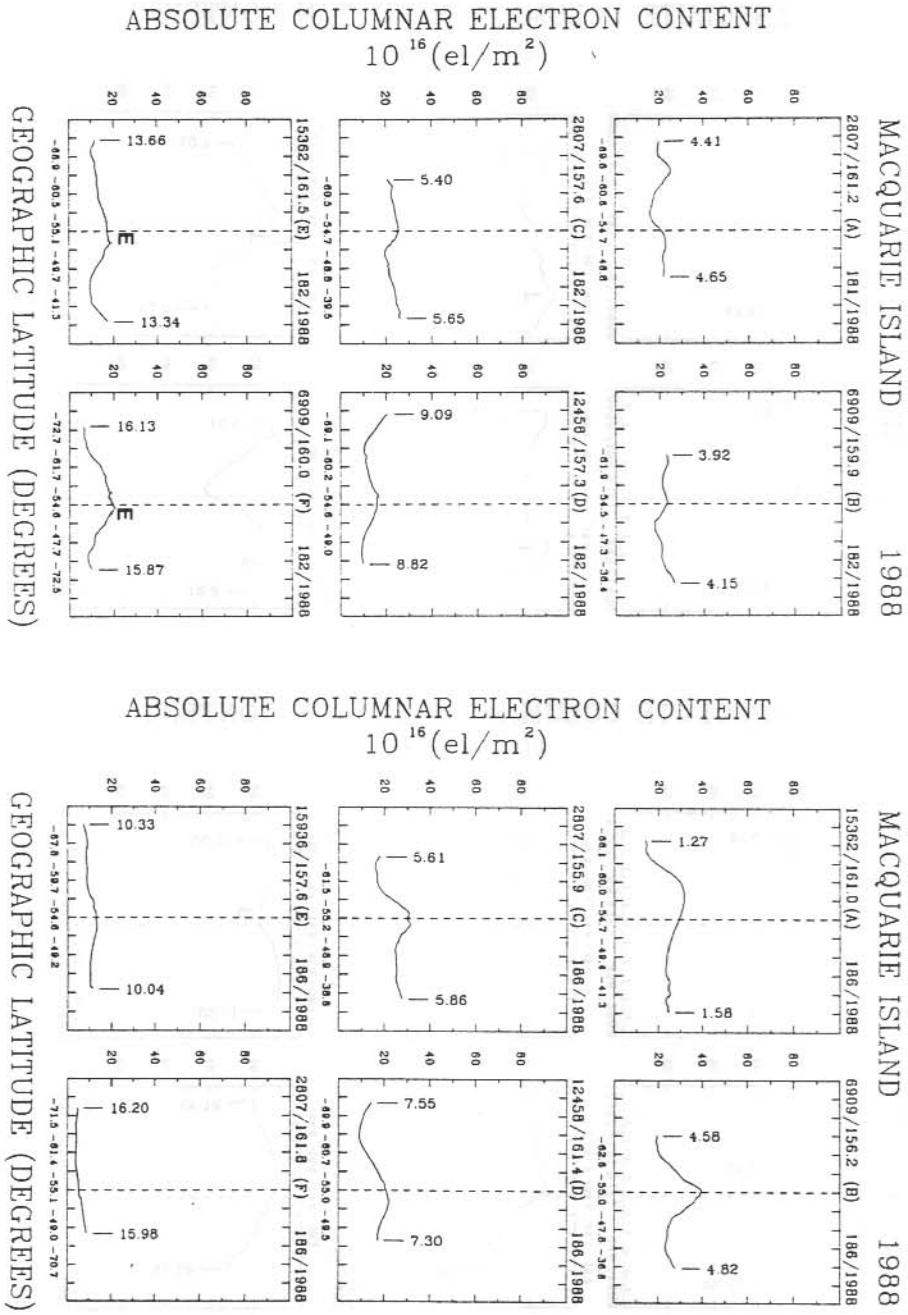


Figure 7. Examples of DP derived absolute TEC for the winter from Macquarie Island. T indicates a developing or developed trough and E indicates a localised night-time TEC enhancement.

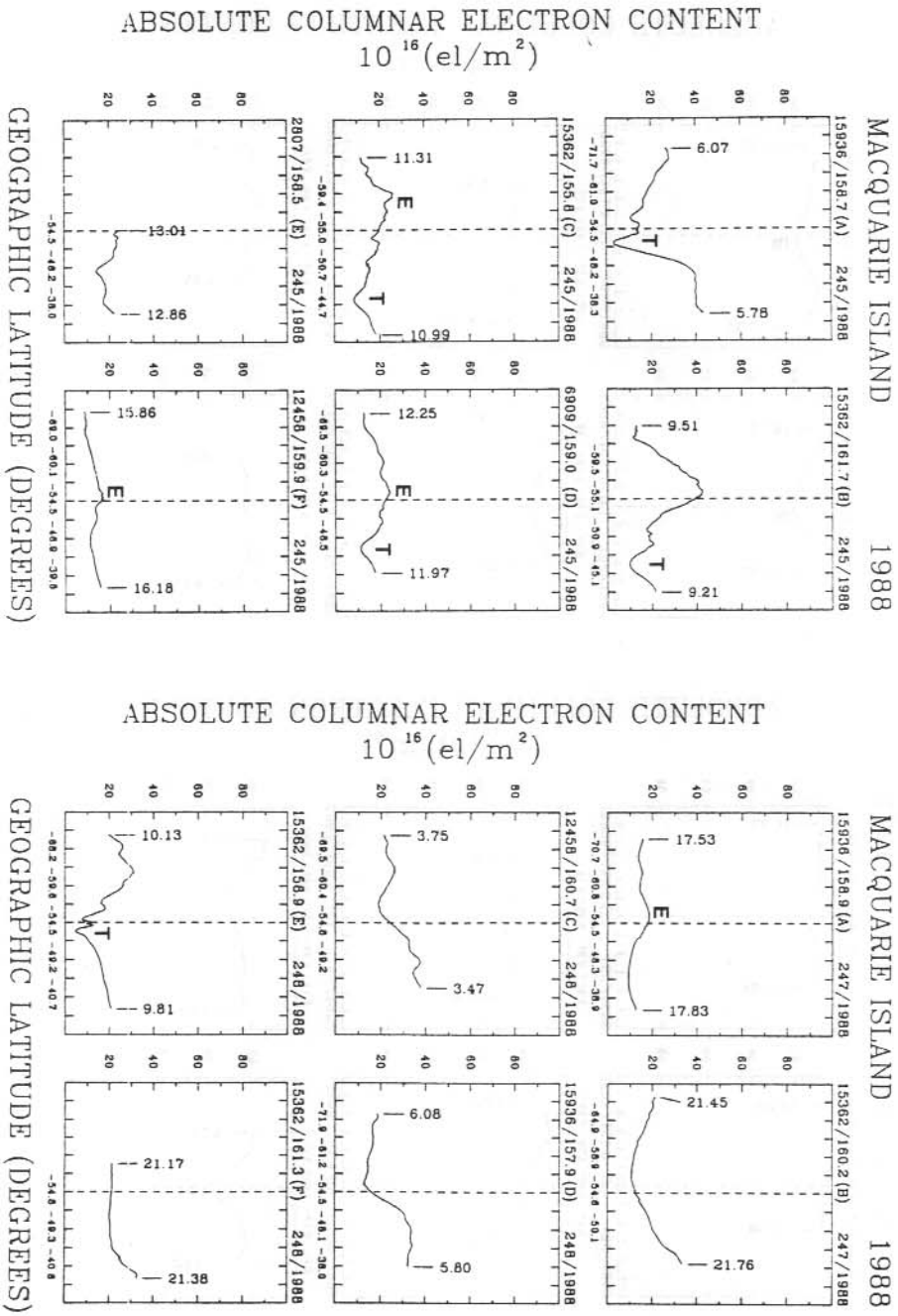


Figure 8. Examples of DP derived absolute TEC for the vernal equinox from Macquarie Island. T indicates a developing or developed trough and E indicates a localised night-time TEC enhancement.

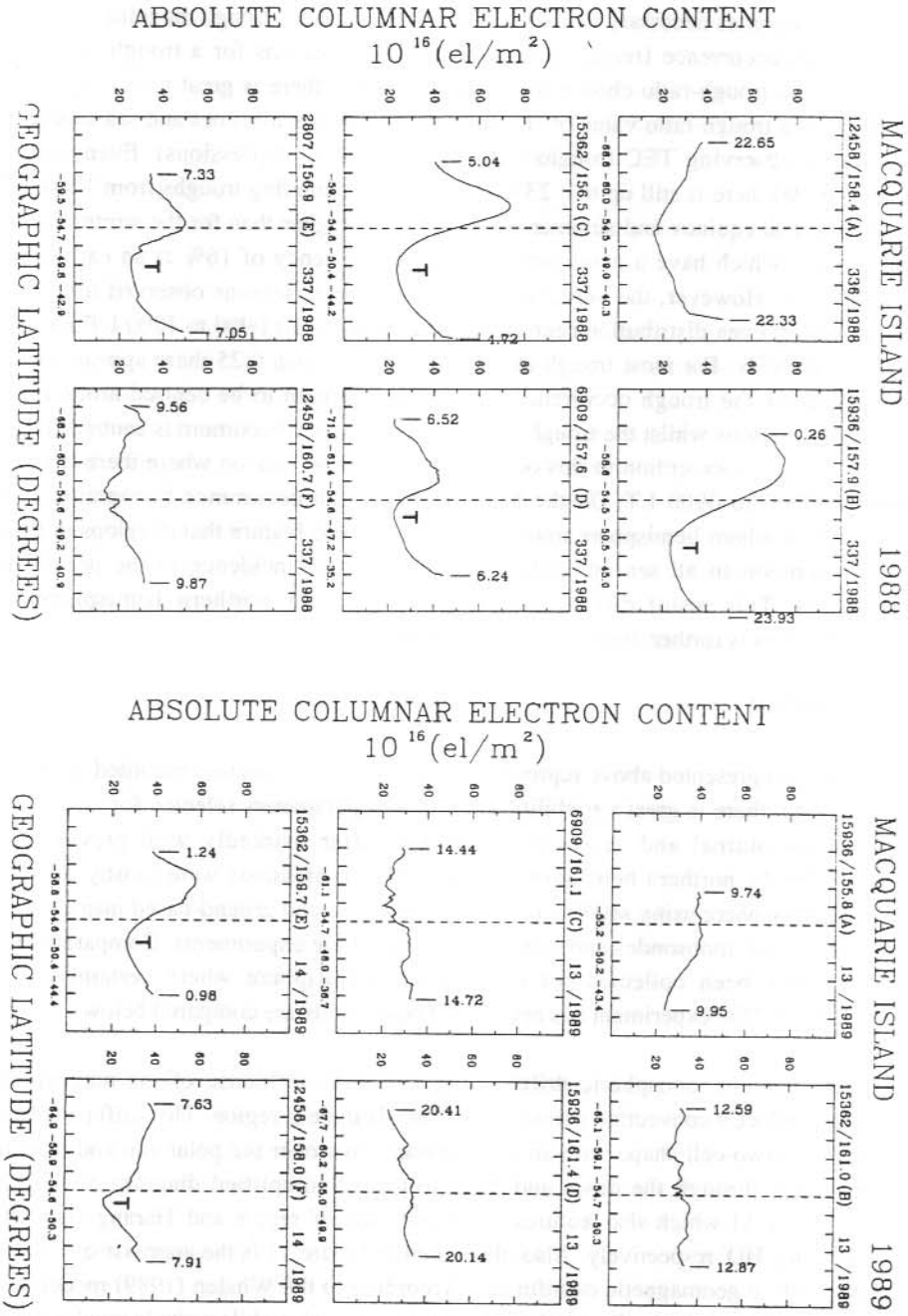


Figure 9. Examples of DP derived absolute TEC for summer from Macquarie Island. T indicates a developing or developed trough and E indicates a localised night-time TEC enhancement.

At this point it becomes necessary to distinguish between various trough magnitudes. Figure 10 depicts a trough occurrence frequency histogram for all seasons for a trough-ratio of 0.50. Depending on the trough-ratio chosen it can be shown that there is great variability in trough onset times. For a trough-ratio value of .10, there is observed at all times and seasons at least a 50% chance of observing TEC troughs (or trough-like TEC depressions). Even selecting a trough-ratio of .90 there is still up to a 23% chance of encountering troughs from 1200 to 1800 LT in the autumnal equinox and summer seasons. This is higher than for the winter and vernal equinox seasons which have a maximum occurrence frequency of 16% at an earlier time of 0900 to 1200 LT. However, the vernal equinox and summer seasons observed troughs at all times in an almost even distribution centred on the time intervals 0900 to 1200 LT and 1200 to 1500 LT respectively. For most trough-ratio values greater than 0.25 there appears an almost universal trend for the trough occurrence frequency minimum to be centred around 0000 to 0600 LT for all seasons whilst the trough occurrence frequency maximum is centred from 0900 to 1500 LT. The only exception to this occurs for the summer season where there is an earlier maximum at 0600 to 0900 LT. On the basis of the trough occurrence histograms it would appear that the southern hemisphere trough is an ionospheric feature that develops in the early to middle afternoon in all seasons with a relatively lower incidence in the pre-dawn and morning hours. This result differs from that reported for northern hemisphere trough measurements. This is further discussed in the next section.

## 14.4 DISCUSSION

The trough results presented above represent one year of data collection recorded at Macquarie Island. Although, there is great variability in all trough parameters selected for attention there are nonetheless diurnal and seasonal trends that differ markedly with previous trough observations for the northern hemisphere. These other observations were mostly obtained for the northern hemisphere using satellite probes and sounders and ground-based instruments such as backscatter radar, ionosondes and some differential-phase experiments. Comparatively little trough data have been collected for the southern hemisphere where certainly no other differential-phase TEC experiment has operated. These results are compared below.

Above about 160 km ionospheric drifts acting under the influence of the magnetospheric electric field produce a convection pattern in the high-latitude F-region. This drift pattern is well represented by a two-cell shape with an anti-sunward flow over the polar cap and returning to the sunward side through the dawn and dusk sectors. A simplified diagram of this flow is depicted in Figure 11 which also features the dayside 'throat' region and 'Harang-discontinuity' labelled 'TH' and 'HD' respectively. Also, illustrated in Figure 11 is the approximate Macquarie Island locus path in geomagnetic coordinates. According to the Whalen (1989) model, a site in an eastern magnetic longitude should observe afternoon troughs while a site located in a western magnetic longitude will observe morning troughs (specifically for the case of a vertical incidence ionosonde) if its diurnal path takes it beneath the high-latitude F-region convection region for the northern hemisphere. The hatched areas indicate regions where the

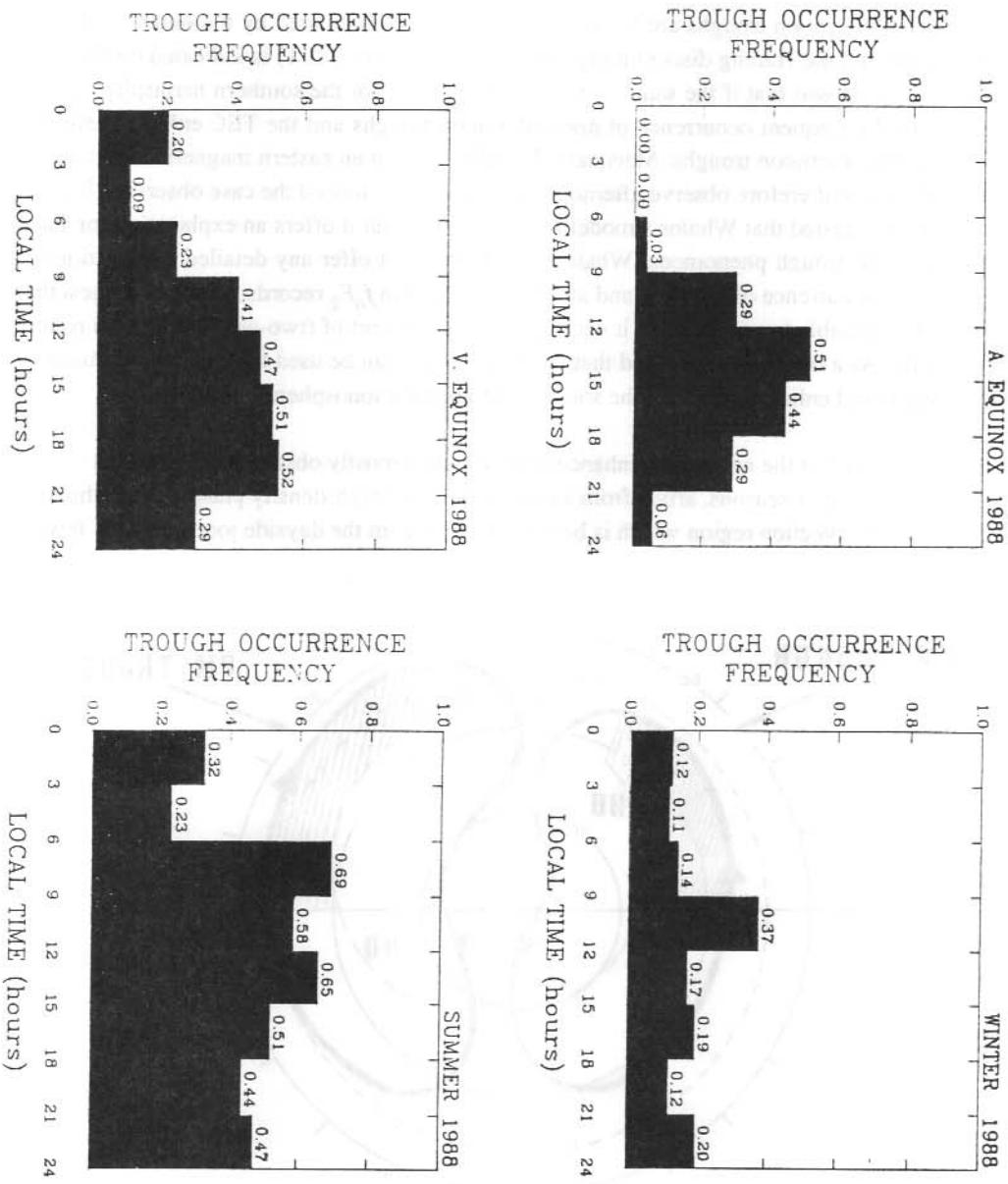


Figure 10. Trough occurrence frequency histograms for all seasons and for a trough-ratio of 0.50.

morning and afternoon troughs are to be observed which are bounded by the outer convection cell flowline and the Harang discontinuity. Magnetic local time (MLT) is indicated on the outer circle. It is proposed that if the same explanation is applied for the southern hemisphere it will account for the frequent occurrence of noon-afternoon troughs and the TEC enhancement that often precedes afternoon troughs. Macquarie Island is sited in an eastern magnetic longitude (at 247°) and should therefore observe afternoon troughs. This is indeed the case observed. It is not necessarily suggested that Whalen's model is correct, only that it offers an explanation for some of the observed trough phenomena. Whalen (1989) does not offer any detailed explanation for the observed occurrence of morning and afternoon troughs in $f_0F_2$ records, but does suggest that it seemed reasonable to propose that it was likely that some sort of (two-cell) convection pattern is operating. As a result it is proposed that the same model can be used to describe the observed TEC troughs and enhancements for the southern hemisphere ionosphere.

It is put forward that the noon TEC enhancement, which is mostly observed in the vernal equinox and summer seasons, arises from a concentration of high-density plasma in the throat region of the convection region which is being funnelled from the dayside ionosphere. A few

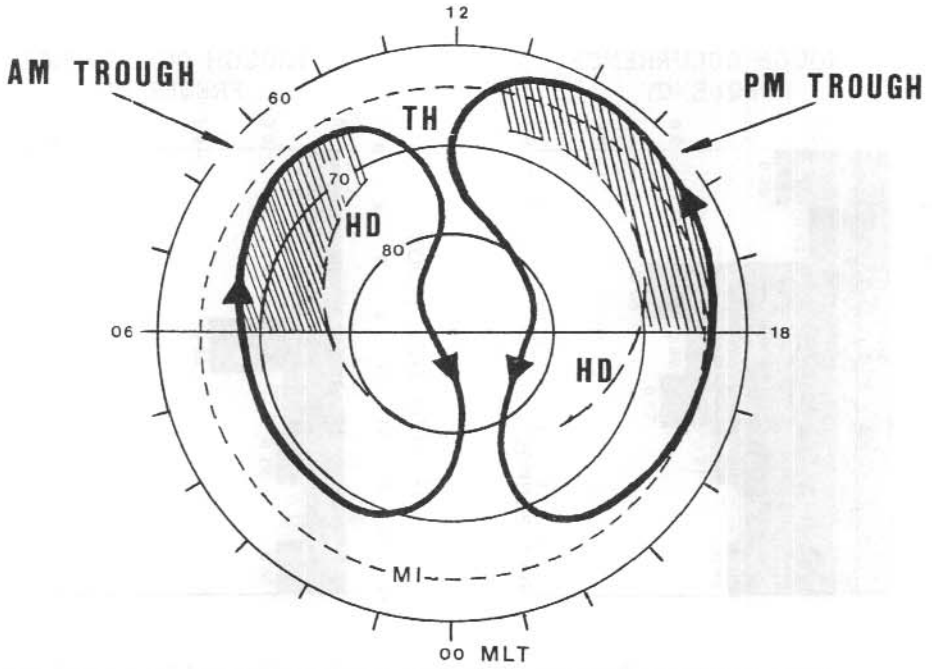


Figure 11. A simplified two-cell convection pattern in geomagnetic coordinates for the southern hemisphere with co-rotation added in a non-rotating frame of reference. The broken circle depicts the locus path of Macquarie Island (MI). The hatched areas indicate the regions of the morning and afternoon troughs. The dayside throat region TH and the Harang discontinuity HD are also depicted.

hours after 1200 LT there is a drop in TEC (possibly as a consequence of having entered a plasma depletion region) resulting from low-density plasma having convected from the nightside and through the dusk sector into the afternoon sector. Although the flux-tube description of this convecting low-density plasma is detailed by Knudsen (1974) and Knudsen et al. (1977), its lifetime in the dayside sector is limited according to theoretical considerations. Often occurring before any TEC enhancement, there is a large-scale and broad trough which only appears in the mid-morning sector for a few hours before local noon. Its occurrence can also be explained by the Whalen model. Low-density plasma convecting from the nightside via the dawn sector and into the dayside sector may survive long enough to be observed as TEC depressions or troughs in differential-phase records. These morning depressions or troughs appear slightly wider in latitudinal extent than afternoon or evening troughs, but the afternoon troughs are generally deeper. Why there should be such a variation is possibly a function of the changing nature of the convection pattern shape and position.

Note that the Sojka et al. (1985) high-latitude ionospheric model exhibits weak winter nocturnal trough for the southern hemisphere. This is also one of the findings where winter troughs had a lower occurrence frequency and were shallower than other seasons from about 2200 to 0200 LT. The large daytime troughs predicted by the Sojka et al. (1985) model are not the same troughs observed at Macquarie Island. They are predicted to occur from 1100 to 1900 UT (≈2100 to 0500 LT). Sojka et al. (1985) claim that processes producing the daytime trough are different from those producing nocturnal troughs. This is claimed to be due to the auroral oval moving to larger solar zenith angles at times when the magnetic pole is on the anti-sunward side of the geographic pole (1100 to 1900 UT for the southern hemisphere). The previous section clearly demonstrates the regular appearance of daytime troughs (even in summer) from 0900 to 1500 LT (=2300 to 0500 UT) in almost direct contrast to the Sojka et al. model prediction.

The Fuller-Rowell et al. (1987) high-latitude ionosphere-thermosphere model also predicts a summer daytime trough that cuts across the southern hemisphere polar cap and into the dayside sector at 0600 UT (Macquarie Island≈1600 LT). The formation of this daytime trough is consistent with some differential-phase TEC observations presented earlier. For the late morning (summer and autumnal equinox season) troughs develop which could be explained by the Fuller-Rowell et al. model. The noontime TEC enhancement is apparent from the model from about 1200 to 1600 LT. The neutral wind vectors for this time correspond to the approach of the throat region on the dayside. It is conceivable that dayside plasma could be funnelled into the throat from lower latitudes by the action of these neutral winds or some other transport process. This higher density plasma redistribution from lower latitudes would enhance TEC values in this region while at the same time lower TEC values just equatorward of the throat region. However, the observed lowering of electron density (hence TEC) equatorward of the noon TEC enhancement is not predicted for the Fuller-Rowell et al. model.
The Sojka et al. (1985) and Fuller-Rowell et al. (1987) models can both be interpreted as explaining some of the TEC observations made from Macquarie Island but a more comprehensive picture still needs to be produced from these models for other times and for all

seasons. Presently, both model descriptions of the southern hemisphere trough are restricted to a single season and/or a single time. It is, nonetheless, encouraging that two different models of the southern hemisphere high-latitude ionosphere have highlighted major differences with the northern hemisphere high-latitude ionosphere and that the occurrence of daytime troughs may not be as uncommon as once thought. While the reasoning behind explaining morning and afternoon troughs in ionosonde records by Whalen (1989) is elegant and even simplistic, it does appear to account for some TEC measurements observed at Macquarie Island.

Local night-time TEC enhancements are sometimes observed at around the throat region and indicate that perhaps poleward convecting plasma from the dayside is entering this region. Ionisation levels can be significantly higher than background levels (up to 100%). Examples of these enhancements observed from Macquarie Island can be observed in Figures 6, 7, 8 and 9 and are labelled as 'E'. These enhancements appear to occur at $\Lambda \sim 70$ to 65° from about 2200 to 0300 LT (≈1200 TO 1700 UT) in all seasons. Whilst dayside TEC enhancements in the throat region display a definite seasonal variation there does not appear to be any such dependence for the night-time TEC enhancement in the throat region.

Although troughs have predominately been reported as a nocturnal feature, there have been reports of daytime F-region troughs (Tulunay 1973, Tulunay and Grebowsky 1978, Grebowsky et al. 1983, Evans et al. 1983, Holt et al. 1983, Pinnock 1985, Whalen 1989). Wildman et al. (1976) report that daytime troughs tend to be narrower and not as well defined as night-time troughs. Tulunay (1973) reports that daytime troughs at 550 km in the winter hemisphere are dependent upon both geographic and geomagnetic longitudes. The poleward edge of the trough is thought to be formed by soft particle precipitation. Pinnock (1985) argues that observational evidence from Halley suggests that local precipitation is not the only possible source for the poleward trough wall. Photoionisation could play a role here or simple convection of plasma from a remote particle precipitation site.

It would appear from the literature that scant observational evidence and even less theoretical support exists which explains the formation of these daytime troughs. However, in recent years there does appear to be a hardening of evidence to suggest that electric fields (of magnetospheric origin) can induce westward ion drift leading to ionospheric troughs forming (Rich et al. 1980 and Evans et al. 1983). In the present study daytime troughs were observed, but measurements of electric fields were not possible.

Given that the afternoon trough is formed, it is difficult to explain how photoionisation does not 'fill-in' the trough. No doubt whatever mechanism(s) form the midday/afternoon trough it must also be powerful enough to counter the effects of this photoionisation. How this occurs depends explicitly on these mechanisms. Trough width, depth, and trough wall gradients maximise for all seasons at about 0900 to 1500 LT before decreasing again. This occurs at a time when photoionisation is also at its maximum. Once the daytime trough is established, by about 1200 LT (≈0200 UT), it then tends to retreat poleward and shrink in width and 'fill-in'. Why and how

this daytime trough forms at all, let alone sustains itself, in the presence of high ionisation levels cannot be explained at present.

## 14.5 CONCLUSIONS

The differential-phase technique for determining absolute vertical TEC has been employed for the first time in the southern hemisphere in a study of the F-region trough. Macquarie Island was established as a receiving site which over the course of a year, during 1988-1989, amassed a combined total of 6345 individual satellite passes. A statistical analysis, for all seasons, of selected trough parameters revealed the following major seasonal and diurnal characteristics:

1. The trough is a more prominent ionospheric feature during early/mid-afternoon and evening hours than in the morning or night hours for all seasons. The autumnal and vernal equinox and summer seasons display a greater trough occurrence frequency and prominence than the winter season.

2. The trough is observable in all seasons and at all times of the day (depending on the selection criteria chosen to distinguish it from other unspecified electron content/density depressions). A seasonal dependence is evident.

3. A regularly occurring pre-noon large-scale trough develops in the vernal equinox and summer seasons which persists into the afternoon. The summer trough is more pronounced.

4. A noon TEC enhancement rapidly develops along the poleward edge of the trough wall of the pre-noon trough at about 1200 to 1300 LT which is more prominent in the summer than the autumnal equinox season and which is almost non-existent in winter.

5. The autumnal equinox and summer noon TEC enhancement diminishes throughout the afternoon and evening hours whilst the pre-noon trough, which had originally accompanied the TEC enhancement, will persist for periods beyond local midnight. The summer and autumnal equinox seasons display this feature more than the winter and vernal equinox seasons.

6. The incidence of day-time troughs is much higher than for the northern hemisphere trough but is much smaller for the post-midnight sector.

7. A night-time TEC enhancement occurs at Macquarie Island latitudes on some nights from 2200 to 0300 LT which is thought to correspond to the passage of the throat region of the two-cell convection pattern.

8. The simple two-cell convection pattern model of Whalen (1989) can be utilised to explain the occurrence of daytime troughs and of the night-time TEC enhancements. Seasonal variations of this might depend on changes in the convection pattern. No attempt has been made to determine exact mechanisms for this.

In conclusion, from the data presented the trough was best explained by invoking a simple two-cell F-region convection pattern model. The model appeared to explain the occurrence and frequency distribution of troughs at all times of the day. Seasonal variations, notably in shape and position, were thought to arise from the changing nature of the plasma convection pattern as well as solar production processes. The most interesting and surprising results of this study have been the occurrence frequency and prominence of daytime troughs which is counter to previous trough findings of the northern (and southern) hemispheres. Whilst an explanation based on convection plasma redistribution is invoked to explain this, no detailed explanation can be offered as it lies outside the scope of this study.

## 14.6 ACKNOWLEDGMENTS

Thanks are extended to the Antarctic Division, and to Mr Robert Polglase, Physics Department, La Trobe University, for making this project possible. This work was funded in part by an Australian Research Committee Grant (ARCG) (now ARC) whilst M. Mallis was the holder of a Commonwealth Postgraduate Research Scholarship and a Fellowship with the Defence Science Technology Organisation (DSTO), Defence Department, Salisbury. The Australian Surveying and Land Information Group supplied the JMR receivers for use in this work.

## 14.7 REFERENCES

Ahmed, M., Sagalyn, R.C., Wildman, P.J. L. *and* Burke, W.J. (1979). Topside ionospheric trough morphology: Occurrence frequency and diurnal, seasonal and latitude variations. *Journal of Geophysical Research 84*:489-498.

Brace, L.H. *and* Theis, R.F. (1974). The behaviour of the plasmapause at mid-latitudes: ISIS 1 Langmuir probe measurements. *Journal of Geophysical Research 79*:1871-1884.

Evans, J.V., Holt, J.M., Oliver, W.L. *and* Wand, R.H. (1983). The fossil theory of nighttime high latitude F-region troughs. *Journal of Geophysical Research 88*:7769-7782.

Fuller-Rowell, T.J., Rees, D., Quegan, S., Moffett, R.J. *and* Bailey, G.J. (1987). Interactions between neutral thermospheric composition and the polar ionosphere: a coupled ionosphere-thermosphere model. *Journal of Geophysical Research 92*:7744-7748.

Grebowsky, J.M., Taylor H.A., Jr. *and* Lindsay, J.M. (1983). Location and source of ionospheric high latitude troughs. *Planetary and Space Science 31*:99-105.

Holt, J.M., Evans, J.V. *and* Wand, R.H. (1983). Millstone Hill measurements on 26 February 1979 during the solar eclipse and formation of a midday F-region trough. *Journal of Atmospheric and Terrestrial Physics 46*:251-264.

Knudsen, W.C. (1974). Magnetospheric convection and the high latitude $F_2$ ionosphere. *Journal of Geophysical Research 79*:1046-1055.

Knudsen, W.C., Banks, P.M., Winningham, J.D. *and* Klumpar, D.M. (1977). Numerical model of the convecting $F_2$ ionosphere at high latitudes. *Journal of Geophysical Research 82*:4784-4792.

Köhnlein, W. *and* Raitt, J. (1977). Position of the mid-latitude trough in the topside ionosphere as deduced from ESRO 4 observations. *Planetary and Space Science 25*:600-602.

Leitinger, R. *and* Hartmann, G. K. (1976). Time and latitude dependence of ionospheric electron content from the combination of NNSS and ATS-6 data. *Beacon satellite group COSPAR, Boston, June 1976.*

Leitinger, R., Hartmann, G.K., Lohmar, F.-J. *and* Putz, E. (1984). Electron content measurements with geodetic receivers. *Radio Science 19*:789-797.

Mallis, M. (1989a). An investigation into the southern hemisphere mid-latitude ionospheric trough. In: Conde, M. *and* Beggs, H. (Eds). *Australian upper atmospheric and space physics research in Antarctica, 1988. ANARE Research Notes Number 69.* Pp. 56-60.

Mallis, M. (1989b). *An investigation of the southern-hemisphere ionospheric main-trough using total electron content measurements.* Ph.D. thesis, La Trobe University, Australia.

Mendillo, M. *and* Chacko, C.C. (1977). The baseline ionospheric trough. *Journal of Geophysical Research 82*:5129-5137.

Pinnock, M. (1985). Observations of a day-time mid-latitude ionospheric trough. *Journal of Atmospheric and Terrestrial Physics 47*:1111-1121.

Putz, E. *and* Leitinger, R. (1988). A proposed model for the TEC main trough in winter and equinox nights. In: Chao Chong (Ed.). *Proceedings of the International Beacon Satellite Symposium, Beijing, China.* Pp 209-216.

Rich, F.J., Burke, W.J., Kelley, M.C. *and* Smiddy, M. (1980). Observations of field-aligned currents in association with strong convection electric fields at subauroral altitudes. *Journal of Geophysical Research 85*:2335-2342.

Sojka, J.J., Raitt, W.J., Schunk, R.W., Parish, J.L. *and* Rich, F.J. (1985). Diurnal variation of the dayside, ionosphere, mid-latitude trough in the southern hemisphere at 800 km: model and measurement comparison. *Planetary and Space Science 33*:1375-1382.

Tulunay, Y.K. (1973). Global electron density distributions from the ARIEL III satellite at mid-latitudes during quiet magnetic periods. *Journal of Atmospheric and Terrestrial Physics 35*:233-254.

Tulunay, Y.K. *and* Grebowsky, J.M. (1978). The noon and midnight mid-latitude trough as seen by ARIEL 4. *Journal of Atmospheric and Terrestrial Physics 40*:845-855.

Tulunay, Y.K. *and* Sayers, J. (1971). Characteristics of the mid-latitude trough as determined by the electron density experiment on ARIEL III. *Journal of Atmospheric and Terrestrial Physics 33*:1737-1761.

Tyagi, T.R. (1974). Determination of total electron content from differential Doppler records. *Journal of Atmospheric and Terrestrial Physics 36*:1157-1164.

Weber, E.J., Tsunuda, R.T., Buchau, J., Sheenan, R.E., Strickland, D.J., Whiting, W. *and* Moore, J.G. (1985). Coordinated measurements of auroral zone plasma enhancements. *Journal of Geophysical Research 90*:6497-6513.

Whalen, J.A. (1989). The daytime F layer trough and its relation to ionosphere-magnetospheric convection. *Journal of Geophysical Research 94*:17169-17184.

Wildman, P. J. L., Sagalyn, R. C. *and* Ahmed, M. (1976). Structure and morphology of the main plasma trough in the topside ionosphere. In: Mendillo, M. (Ed.). *Proceedings of the COSPAR satellite beacon group on the geophysical use of satellite beacon observations, Boston University.*

# 15. UPPER ATMOSPHERE WINDS AND TEMPERATURE DATA FROM MAWSON, ANTARCTICA, 1989

J. French [1,2] and F. Jacka [2]

[1]Antarctic Division
Kingston Tas 7050
Australia

[2]The Mawson Institute for Antarctic Research
University of Adelaide
Adelaide SA 5000
Australia

ABSTRACT

A progress report is presented on the analysis of Fabry-Perot Spectrometer (FPS) and Spaced Antenna, Partial Reflection (SAPR) radar data obtained over the 1989 winter at Mawson, Antarctica. Observations on the sodium (D2, λ589.0 nm) dayglow and twilightglow were made using the FPS to obtain wind and temperature measurements from the 90 km altitude region. The oxygen (λ557.7 nm) night-time emission was also observed for measurements at auroral altitudes. Samples of these data will be presented.

The SAPR radar measures horizontal winds between 60 and 110 km altitude with the aim of determining mean circulation and tidal components. Proposed analysis includes a comparison of the horizontal wind measurements from the SAPR radar at appropriate levels with those obtained from the FPS.

## 15.1 INTRODUCTION

Around 90 km altitude neutral sodium atoms form a layer of vertical thickness about 12 km. During daytime and twilight the sodium resonantly scatters sunlight and emits the λ589.0 / 589.6 nm D lines. With intensity typically about 1 kR this enables measurements of Doppler broadening and shift from which the temperature and wind at this level can be determined.

A layer of atomic oxygen, centred at about 97 km and 7 km thick emits radiation due to the forbidden transition

$$O(^1S) \rightarrow O(^1D) + h\nu_{557.7}$$

via a series of photochemical processes. This airglow emission at λ557.7 nm has a typical intensity of 200 R. However, at polar latitudes, excitation of atomic oxygen also occurs through

particle collisions; this gives rise to an auroral emission at λ557.7 nm which may have intensities of the order of $10^4$R. This emission typically maximises between 100 and 120 km but extends to much greater heights making it difficult to assign an effective height level for the observation. During the summer of 1988-89, the first Fabry-Perot Spectrometer (FPS) observations of the sodium layer in the Antarctic were made at Mawson (67.6°S, 62.9°E) (Greet et al. 1989). The present work continues those observations into the autumn, and again from spring into summer of 1989. During the long nights from autumn through spring, observations were also made on the oxygen λ557.7 nm nightglow.

Winds are also inferred from the drift of irregularities in refractive index in the weakly ionised region up to about 110 km. This involves application of a spaced antenna, partial reflection (SAPR) radar which was operated almost continuously throughout the year at Mawson. The records will be analysed to determine mean circulation and tidal components. A comparison will be made between winds measured with the FPS and with the SAPR radar at corresponding heights.

## 15.2 INSTRUMENTATION

The FPS at Mawson and it's application have been described by Jacka (1984). Two scanning Fabry-Perot etalons with a plate spacing in the ratio of about 10:1, and a blocking filter are used to isolate the emission line profile from the sky spectrum. The instrument was optimised for the λ589.0 nm sodium D2 emission, this being almost twice as intense at the D1 λ589.6 nm emission in the doublet. The high resolution etalon plate spacing was set to give an operating order of 20 358 and the field stop diameter to give an instrument finesse of 21.6. By changing the blocking filter, this setup was also quite adequate for observation of the oxygen λ557.7 nm nightglow. To record an emission line profile the etalon plate spacings were usually scanned in 128 steps (channels) with a 50 msec dwell time in each channel. The pulse rate output from a photomultiplier measuring the signal intensity at each spacing is recorded by a multi-channel analyser. A wavelength step of about 0.2 pm per channel was used so that the 128 channels scanned a wavelength range of 25 pm. The line profile is scanned repeatedly until the signal to noise ratio is acceptably smooth.

For daytime sodium observations the second, low resolution, etalon is included to isolate a single passband of the high resolution etalon. It is necessary to observe both the solar and sky spectra for dayglow observations so that the Fraunhofer absorption can be subtracted from the scattered sunlight component of the sky emission. Normally 10 scans of the sky spectrum and 2 scans of the sun were made, repeated about 40 times to acquire a suitable profile in 45 minutes. For twilight sodium and night oxygen observations the low resolution etalon could be swung out of the beam to increase signal level. Normally about 40 scans of the spectrum were required to obtain a suitable sodium profile at twilight and 100 to 150 scans for the oxygen λ557.7 nm emission overnight. Calibration line profiles were recorded after each sky profile to assess instrument drift.

The Mawson SAPR radar transmits 5 kW, 30 msec pulses from a vertically directed array at 1.94 MHz. Three spaced receive antenna's detect the weak backscatter from irregularities in the refractive index. Each receiver consists of two crossed, half wave dipoles, tuned to resonance at 1.94 MHz. The horizontal motion of the irregularities is deduced from a cross correlation analysis between signals from each antenna. A height range between 60 and 110 km can be measured from the time delay between transmitted and received pulses. Below 60 km there is usually insufficient ionisation to reflect the pulse and above 110 km, it is totally reflected by the ionosphere. A vertical resolution of 2 km is attainable over this range. Data were acquired for two out of every three minutes, analysis being performed for the remaining time.

## 15.3 OBSERVATIONS AND ANALYSIS

### *15.3.1. Data acquired*

Figure 1 shows the days on which sodium dayglow, sodium twilightglow and oxygen nightglow FPS data were recorded in 1989. An obvious limitation of the FPS technique is that observations cannot be made through cloud or in blizzard conditions. Sodium dayglow observations are generally restricted to the long daylight hours of the summer months, and oxygen nightglow observations to the winter months. A long period of no data through May and June was caused by equipment failure. Barring a few short breakdowns the SAPR radar operated continuously throughout the year. Figure 2 illustrates some of the individual records obtained with the FPS on 16 September 1989.

Figure 2(a) illustrates a sodium dayglow line profile and the Fraunhofer absorption curve from the solar spectrum which must first be normalised (Figure 2(b)) and subtracted from the sky profile to leave the sky sodium emission (Figure 2(c)). In the twilightglow, Fraunhofer absorption decreases as the sun sets on the lower atmosphere and the emission feature becomes more prominent (Figure 2(d)). The last solar profile before sunset, or the first on sunrise, can be used to remove the Fraunhofer component in this profile. In Figure 2(e), the sun having set on most of the atmosphere between the observing instrument and the sodium layer, the contribution of Fraunhofer absorption to the profile is so small that the background can be assumed to be flat. Finally in Figure 2(f) the profile has become broadened as the sun sets on the sodium layer and the exothermic reaction of NaO and O contributes to the emission (see later). A typical example of the oxygen nightglow emission is shown in Figure 2(g).

### *15.3.2 Life profile analysis*

The recorded sky emission line profile had been modified somewhat from the original source line profile by the finite bandwidth of the observing instrument. Consider an 'instrument function' as the convolution of an Airy function (for the transmitted intensity for ideal Fabry-Perot plates) with a defect function (as, in practice, the plates are not ideal) and an aperture function (as for a finite transmitted intensity a finite field of view must be observed), then the recorded function will be the convolution of the source function and this instrument function.

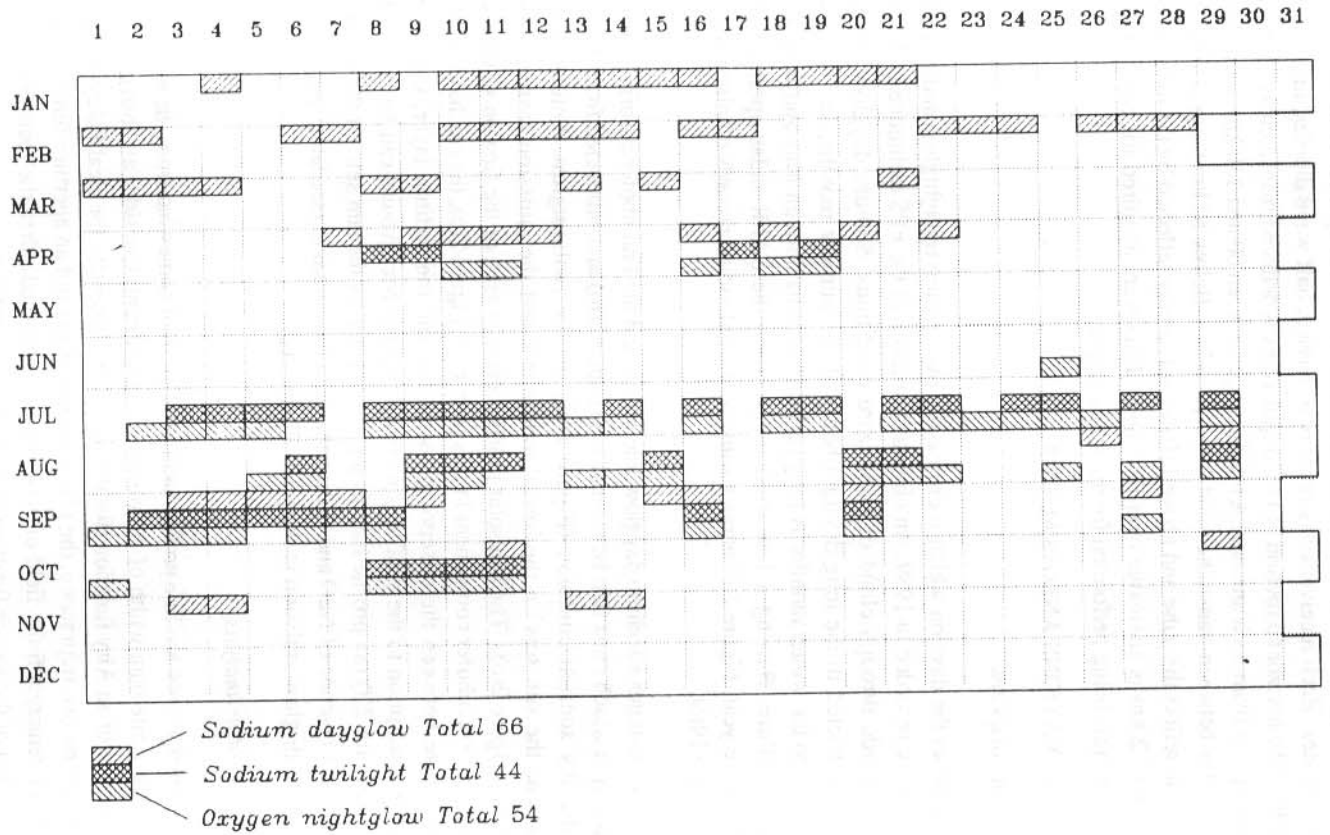


Figure 1. FPS observing days in 1989.

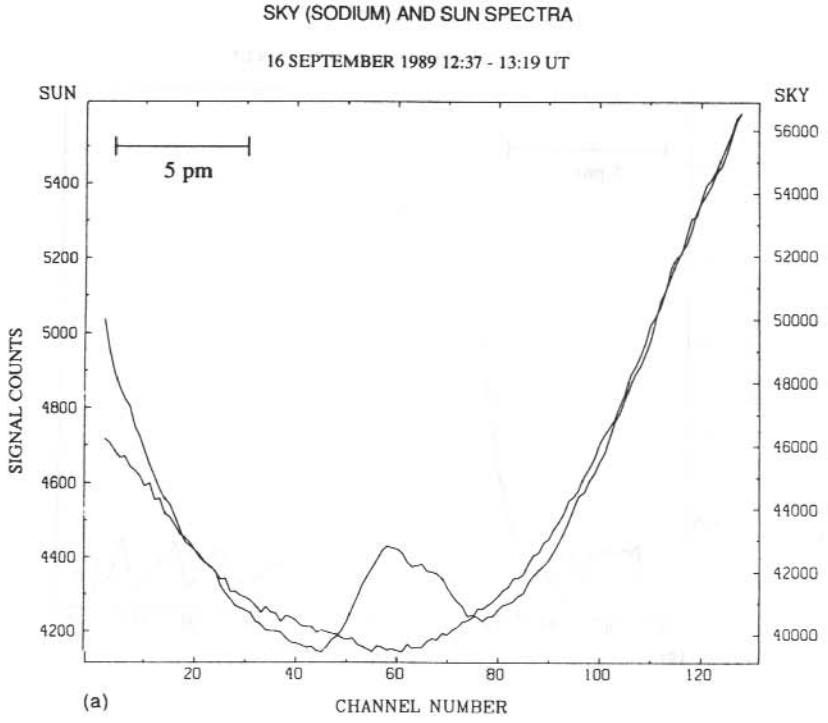


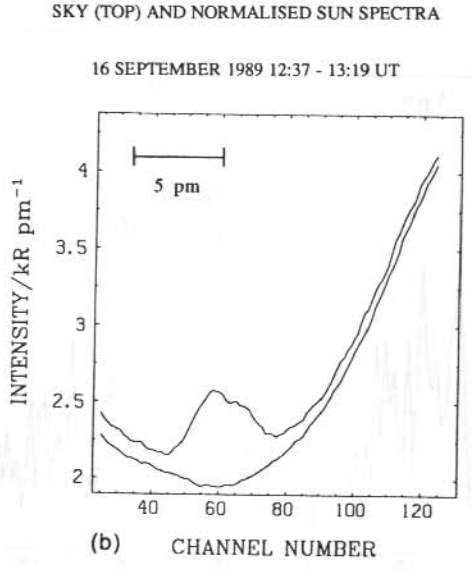


Figure 2(a, b). Examples of the recorded emission profiles from 16 September 1989. (continued)

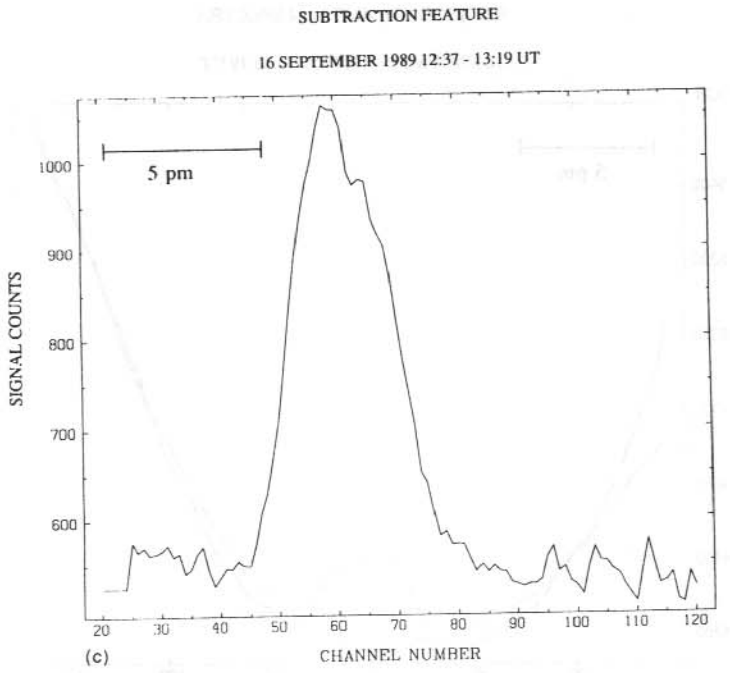


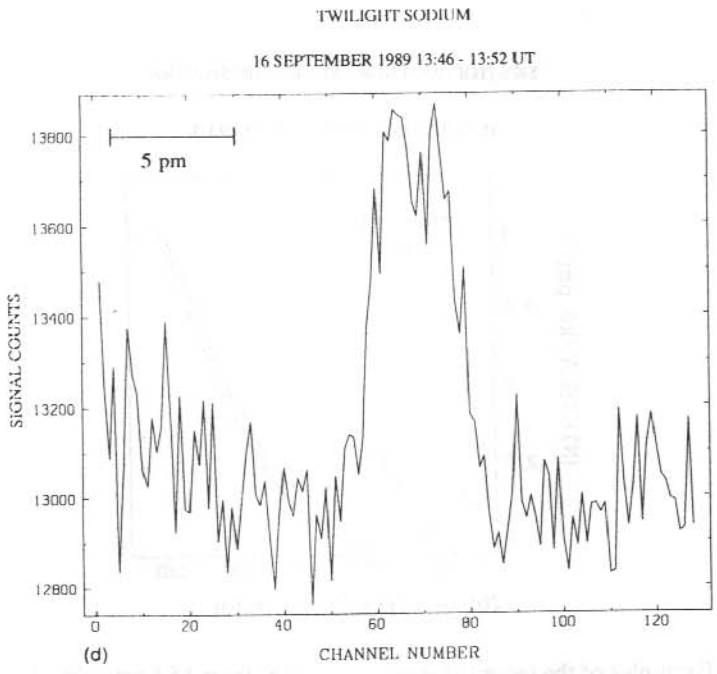


Figure 2(c, d). Examples of the recorded emission profiles from 16 September 1989. (continued)

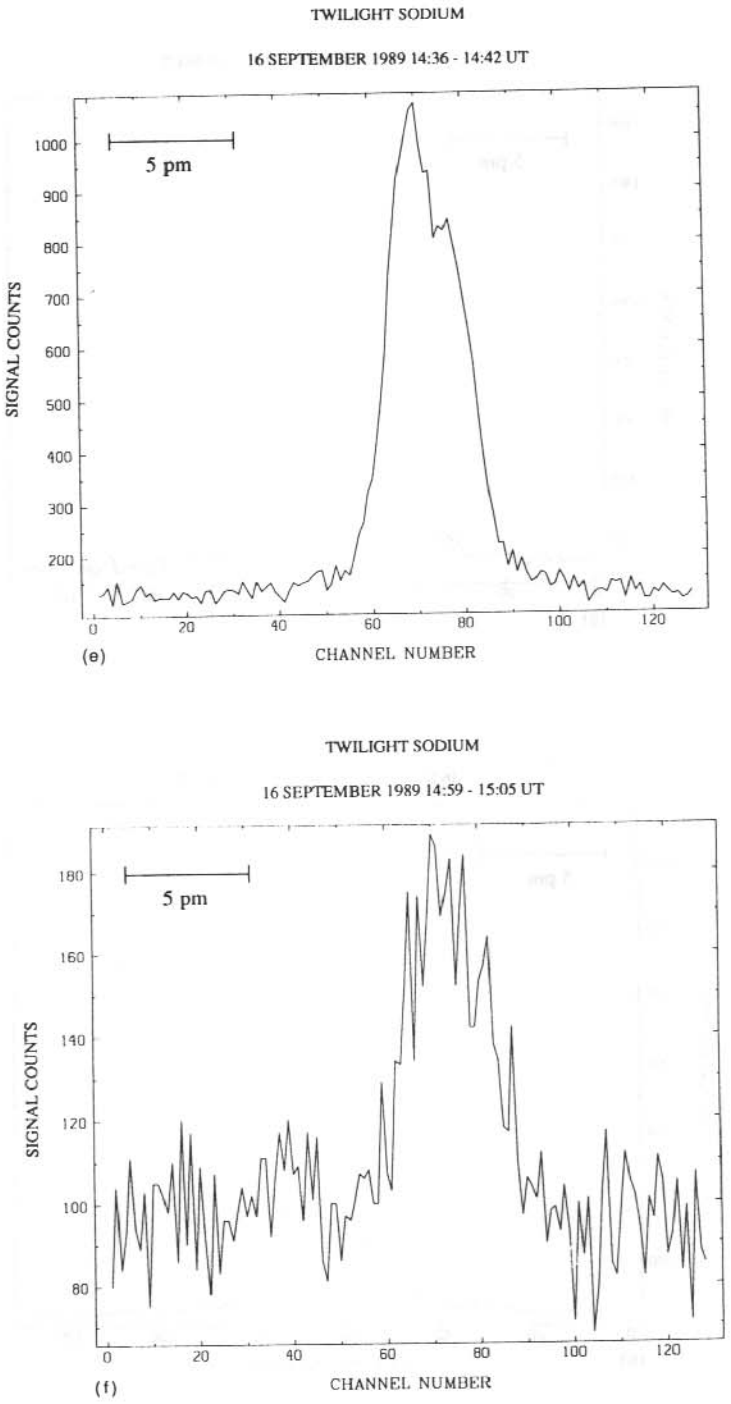


Figure 2(e, f). Examples of the recorded emission profiles from 16 September 1989. (continued)

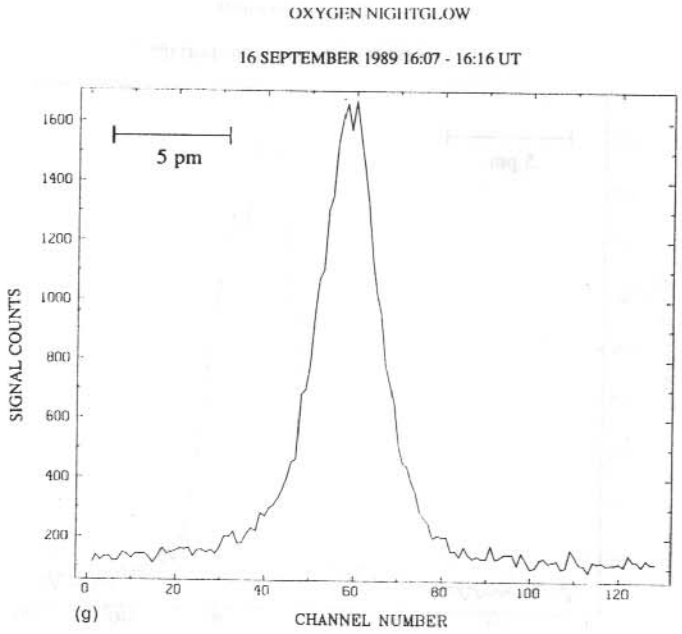


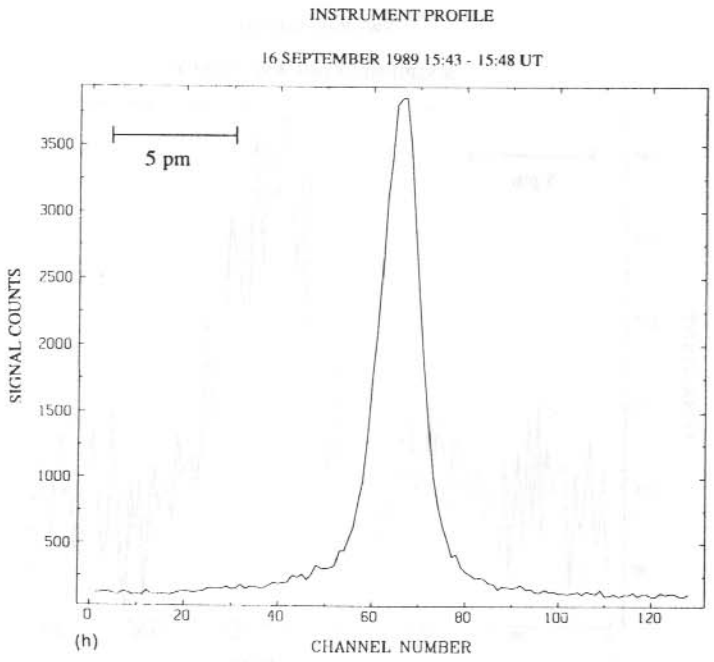


Figure 2(g, h). Examples of the recorded emission profiles from 16 September 1989. (continued)

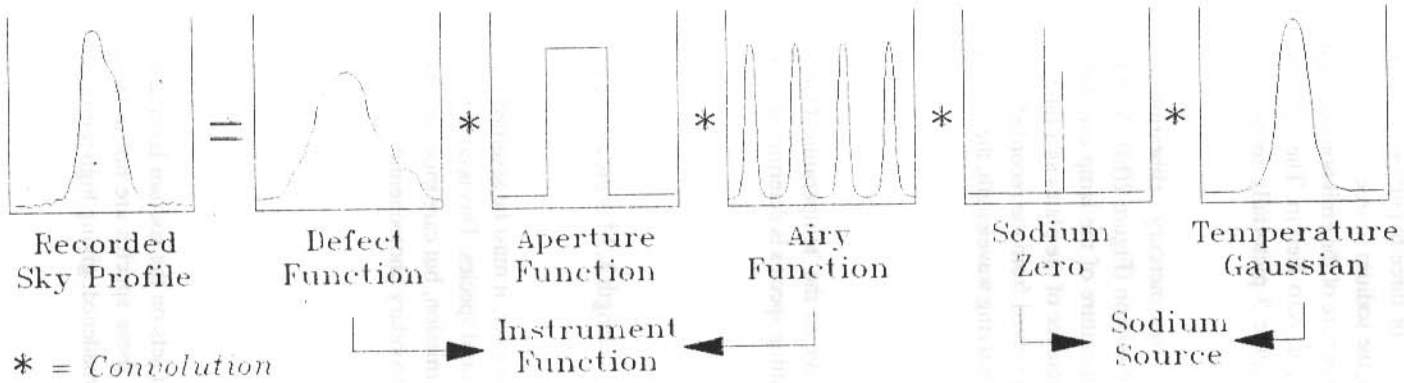


Figure 3. A pictorial representation of the components convolved in the recorded line profile.

In the case of sodium, the emission line profile is further complicated by the existence of hyperfine structure. The sodium D2 line consists of two groups of three hyperfine components separated by about 2.1 pm. Following Greet and Jacka (1988), the sodium source line profile was represented as the convolution of a Gaussian curve at the temperature of the emission and a group of delta functions describing the sodium hyperfine structure at zero Kelvin. The information required is then contained in this 'temperature Gaussian'. Figure 3 pictorially represents this description.

In order to obtain the instrument function, a high signal to noise mercury calibration profile (λ546.1 nm) was obtained at the beginning of each observing session (Figure 2(h)). A gaussian mercury source function can be calculated knowing the temperature of the lamp and the Airy function at λ546.1 nm derived from measurements of the reflectance of the plates as a function of wavelength, or the reflective finesse. If each of these is deconvolved from the recorded mercury profile and the result convolved with an Airy function at the observing wavelength, the instrument function at that wavelength is obtained.

*15.3.3 Temperature analysis*

A least squares fitting routine is used to fit a Gaussian curve to the 'temperature Gaussian' extracted from the recorded profile. The temperature of the emitting species is determined from the width of the emission line profile

$$\delta\lambda = 2\sqrt{(ln2)}\sqrt{\left(\frac{2kT}{M}\right)}\frac{\lambda}{c}$$

where $\delta\lambda$ is the line width at half intensity of the emission at wavelength $\lambda$, M is the atomic mass, k is Boltzman's constant and T is the emission temperature.

For this temperature to be interpreted as the atmospheric temperature, it must be assumed that the emitting species is in thermal equilibrium with the dominant neutral species. This is certainly valid for the oxygen emissions and the resonantly excited sodium emission, but care must be taken in interpreting profiles taken toward the end of twilight as the secondary photochemical excitation mechanism

$$NaO + O \rightarrow Na^* + O_2$$

$$Na^* \rightarrow Na + h\nu_{589.3}$$

with intensity about 40 R becomes more dominant as the sun sets on the sodium layer and the resonant excitation fades. As this is an exothermic process these species are not in thermal equilibrium with the neutral atoms and the profiles become broadened, giving high temperature estimates.

A summer mean temperature of 153±7 K for January 1989 in the sodium layer at Mawson was obtained by Greet et al. (1989). At Mt. Torrens, South Australia, a southern mid-latitude station, a summer mean of 150 K and winter mean of 199 K were obtained (Greet and Jacka 1988). A similar winter warming is expected in the sodium layer over Mawson.

15.3.4 *Wind analysis*

The line of sight component of the wind velocity v is determined from the Doppler shift of the temperature Gaussian line profile.

$$v = \frac{c\,(\lambda-\lambda_o)}{\lambda_o}$$

The rest wavelength $\lambda_o$ is determined for the sodium observations from a sodium hollow cathode calibration lamp. For observations of the λ557.7 nm oxygen emission, lamps are not readily available as the emission involves a forbidden transition. A rest wavelength is determined by taking the mean of observations in the zenith and assuming the mean vertical velocity is zero.

Typical Doppler winds correspond to peak position shifts of fractions of a channel, therefore, any drift in effective etalon spacing must be accurately monitored. Sodium and neon calibration profiles were recorded between observations for this purpose.

Line of sight winds can be converted to horizontal winds by assuming the vertical velocity is zero. Observations were generally made at a zenith angle of 60° in the cardinal points N, S, E and W.

*15.3.5 SAPR radar wind comparisons*

It has generally been assumed in the past that the irregularities of ionisation observed by the SAPR radar drift with the neutral wind, while the FPS directly measures the neutral wind. The aim of this comparison is to assess possible effects of the thermospheric electric field on the drift of the ionisation measured by the radar. This may be particularly evident during periods of high geomagnetic activity.

A few foreseeable problems exist in the comparison of FPS and SAPR radar winds from Mawson. Firstly, the experiments are co-located. The SAPR radar measures winds in the zenith, but a 60° off-zenith observing angle for the FPS corresponds to a radial distance of about 150 km at the sodium layer level. Measurements may differ, if the wind fields are not spacially uniform over this range.

Secondly, winds determined from the aurorally excited λ557.7 nm oxygen emission are usually at or above the maximum height range for the radar. It is possible to use the temperature derived from the oxygen profile to assign a height level for the wind if a temperature profile can be assumed, but again the measurements may differ, if it is considerably higher than 110 km and if the winds vary greatly with height.

Some work has been done on FPS/radar wind comparisons at a mid latitude station (Greet 1988) and some general agreement was found although data were sparse. No previous comparisons of horizontal winds have been undertaken with data from polar latitudes where the effects of electric field at these altitudes may be much more significant. The forthcoming analysis of these data should provide a means to assess the effectiveness of the SAPR radar for measuring the neutral winds.

## 15.4 ACKNOWLEDGMENTS

This project was supported financially by the Australian Research Grants Scheme and logistically by the Australian National Antarctic Research Expeditions (ANARE). The authors are grateful to Mike Dymond, Mark Conde, Pene Greet and the members of the 1989 Mawson ANARE for their assistance and support in this work.

## 15.5 REFERENCES

Greet, P. (1988). *Observations on the Sodium Airglow*. PhD. Thesis, University of Adelaide.

Greet, P., Conde M. *and* Jacka F. (1989). Daytime observation of the Sodium layer with a Fabry-Perot Spectrometer at Mawson Antarctica. *Geophysical Research Letters 16*:871-874.

Greet, P. *and* Jacka, F. (1988). Observations on the Sodium layer using a Fabry-Perot spectrometer: Twilight temperature variations. *Journal of Atmospheric and Terrestrial Physics 51*:91-99.

Jacka, F. (1984). Application of Fabry-Perot spectrometers for measurement of upper atmosphere temperature and winds. *Middle Atmosphere Program Handbook for MAP 13*:19-40.

# 16. THERMOSPHERIC WIND AND TEMPERATURE MEASUREMENTS FROM MAWSON, ANTARCTICA, SPANNING 24 HOURS OF LOCAL TIME

M. Conde[1,2] and F. Jacka[1]

[1]The Mawson Institute for Antarctic Research
University of Adelaide
Adelaide SA 5000
Australia

[2]Antarctic Division
Kingston Tas 7050
Australia

ABSTRACT

A dual scanning Fabry-Perot spectrometer was used to obtain high resolution (R~200 000) spectra of the λ630.0 nm oxygen O($^1$D) thermospheric emission during daylight, twilight and night-time observing conditions at three different phases of the solar cycle. From these spectra estimates were obtained of the neutral temperature and wind velocity in the emitting region - that is, in the altitude range 200-250 km. Temperature results are compared with MSIS-86 values (Hedin 1987). Wind results are compared with the UCL Thermospheric General Circulation Model (Rees and Fuller-Rowell 1988) and the HWM-87 empirical model (Hedin et al. 1988).

Both observed and modelled temperatures increased with increasing solar activity. For each period examined the observed diurnal temperature variation exceeded that of the MSIS-86 model. Possible mechanisms for this are discussed. Observed winds generally agree with model predictions, at least for large-scale features of the flow. Explicitly, sunward winds were observed whilst the observatory lay on the dusk side of the magnetic noon-midnight meridian, whereas anti-sunward winds prevailed around magnetic midnight. These data, together with earlier night-time observations reported by Wardill et al. (1987) and Jones et al. (1987), confirm that F-region neutral winds typically form an anti-cyclonic circulation cell on the dusk-side of the southern polar cap. There is no evidence in the present data of a corresponding dawn-side cyclonic cell, at least in the latitudes observable from Mawson. This is not surprising since the Coriolis force would act to disperse such a circulation in the southern hemisphere. Possible mechanisms are proposed to explain particular features of the observed circulation not predicted by the models.

## 16.1 INTRODUCTION

Energy and momentum inputs to the low and mid-latitude thermosphere vary slowly both spatially and temporally and are relatively well understood, at least for magnetically quiet periods. In contrast, geomagnetic forcing at high latitudes is complex and not yet well described. Three

contrast, geomagnetic forcing at high latitudes is complex and not yet well described. Three dimensional time dependent thermospheric general circulation models (TGCMs) attempt to describe the thermosphere globally, by solving the appropriate energy and momentum equations using empirical descriptions of the terms affected by geomagnetic activity (Fuller-Rowell and Rees 1980, Dickinson et al. 1981). These models have been progressively improved to include self-consistent ionosphere-thermosphere compositional and dynamical coupling, removing some uncertainty in the geomagnetic terms (Fuller-Rowell et al. 1987, Roble et al. 1988). However, terms of magnetospheric origin are still not self-consistently described, a major limitation to modelling accuracy at high latitudes. An alternate approach has been to construct purely empirical models by fitting simple analytic functions to large observational data sets. Examples are the MSIS and 'C-model' temperature and composition models (Hedin 1987, Kohnlein 1980), and the HWM-87 vector spherical harmonic wind model of Hedin et al. (1988). The accuracy of either approach can only be assessed by reference to actual measurements.

Faby-Perot spectrometers have been used extensively to determine thermospheric winds and temperatures, along with the intensity of the emission studied (Jacka 1984, Hernandez and Killeen 1988, Jacka and Vincent 1989). However, the technique has been almost entirely limited to night-time observations. Furthermore, even these observations have been sparse at high southern latitudes (compared to the northern hemisphere). High latitude dynamics are expected to differ significantly between hemispheres because the southern auroral zone is displaced from the geographic pole about twice as far as is its northern counterpart (Smith et al. 1988).

For this project a dual scanning Fabry-Perot spectrometer was employed to provide observations from the southern auroral zone and spanning 24 hours of local time, for three different phases of the solar cycle.

## 16.2 TECHNIQUE

The instrument used was described by Jacka (1984). It consists of two separation-scanned Fabry-Perot etalons of 150 mm and 50 mm working apertures in series with a 0.3 nm bandwidth interference filter and an EMI 9658A photomultiplier. A periscope and solar telescope system allows viewing the sky, in any direction, or the sun. A ground glass diffuser in the solar telescope is used to distribute light uniformly over the field of view from each part of the solar disk when viewing the sun.

High signal to noise spectra were obtained by summing a series of spectral scans in 128 channels of memory, each spanning ~45 pm in wavelength and taking six seconds. During the day two scans of the sun were obtained after each ten scans of the sky, the sun and sky spectra being summed separately. Total integration times were 10-30 min at night and ~1 hour during the day. Absolute intensity calibration of the spectrometer was obtained by viewing a uniform white screen illuminated by a calibrated tungsten lamp.

Recorded night-time spectra were assumed to consist of a Gaussian shaped λ630 nm emission feature broadened by convolution with the instrument transmission function and superimposed on a flat background. The emission intensity, Doppler width and Doppler shift were obtained from each such spectrum using the method of Wilksch (1975). During daytime and twilight the emission is superimposed on an overwhelming and spectrally complex background of scattered sunlight. The method of Conde and Jacka (1989) was used to isolate the emission feature from a pair of sky and sun spectra, allowing determination of the emission parameters described above. This technique is illustrated in Figure 1.

The method described by Wardill (1987) was used to construct horizontal wind vectors from a series of observations in the zenith and at 60° zenith angle along azimuths aligned with geographic north, east, south and west directions. Zenith observations were used to establish a zero velocity wavelength for the emission by requiring that the mean vertical velocity over each observing period was zero. Using this reference, a line-of-sight wind velocity was computed from each recorded spectrum. Multiple days of observations were combined by averaging, for each viewing direction, the line-of-sight velocities in 1.2 hour intervals of universal time. Assuming zero vertical wind contribution to these averaged line-of-sight velocities, the overhead meridional wind component was obtained at 1.2 hour intervals from the mean of the north and south looking horizontal winds; overhead zonal winds were constructed similarly from east and west looking observations.

Three sets of observations were examined: 11 days of daytime and twilight observations from late January and early February 1982, 18 days of night-time, twilight and daytime observations from autumn and spring in 1986, and 13 days of daytime and twilight observations from late December 1988. The three periods occurred at different phases of the solar cycle: the 1982 period just after the peak of solar cycle 21; the 1986 period near solar minimum; and the 1988 period in the rising phase of cycle 22.

## 16.3 THERMOSPHERIC TEMPERATURE

Figure 2(a) shows individual temperature estimates obtained over a 43 hour interval from days 356-358, 1988. A clear diurnal variation is evident, retarded in phase by two to three hours with respect to solar elevation angle. Since the standard error associated with a single daytime temperature estimate was usually greater than 100° K, the data from all observations were averaged in 2.5 hour intervals of universal time for each of the three years. The results are presented in Figure 3, along with corresponding diurnal variations derived from the MSIS-86 empirical model (Hedin 1987) for the location of Mawson and an altitude of 210 km. Solid curves indicate MSIS-86 temperatures for an $A_p$ index equal to the median value during the corresponding observing period; dashed curves indicate MSIS-86 temperatures for $A_p$ =0. Error bars on the observations indicate the standard error in estimating the mean of the points within each averaging interval.

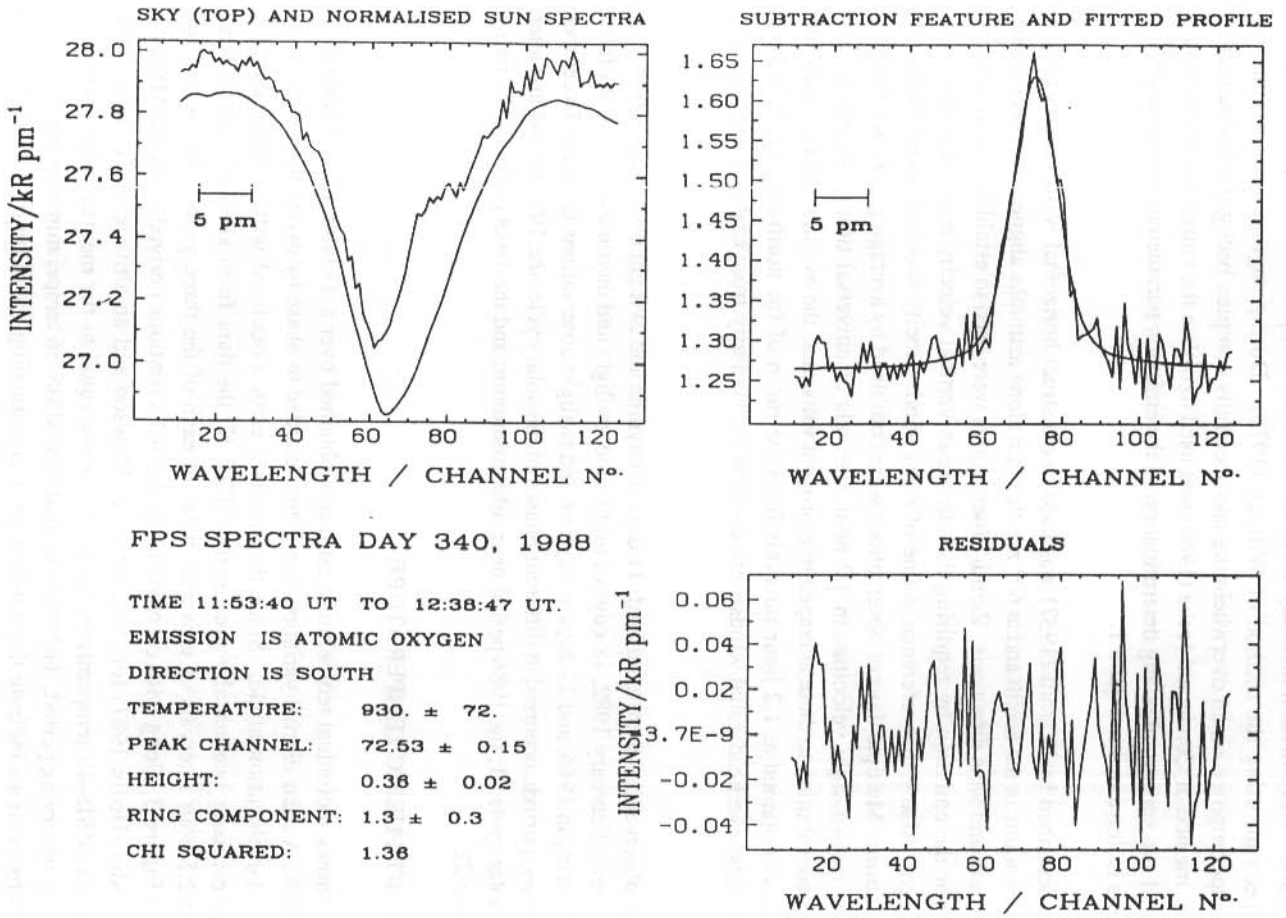


Figure 1. An example of the summary page produced by the daytime analysis program. Subsequent analysis yielded a horizontal wind velocity of 250 $ms^{-1}$, blowing geographic southward, with a standard error of 5 $ms^{-1}$. The horizontal bar labelled 5 pm indicates the wavelength scale.

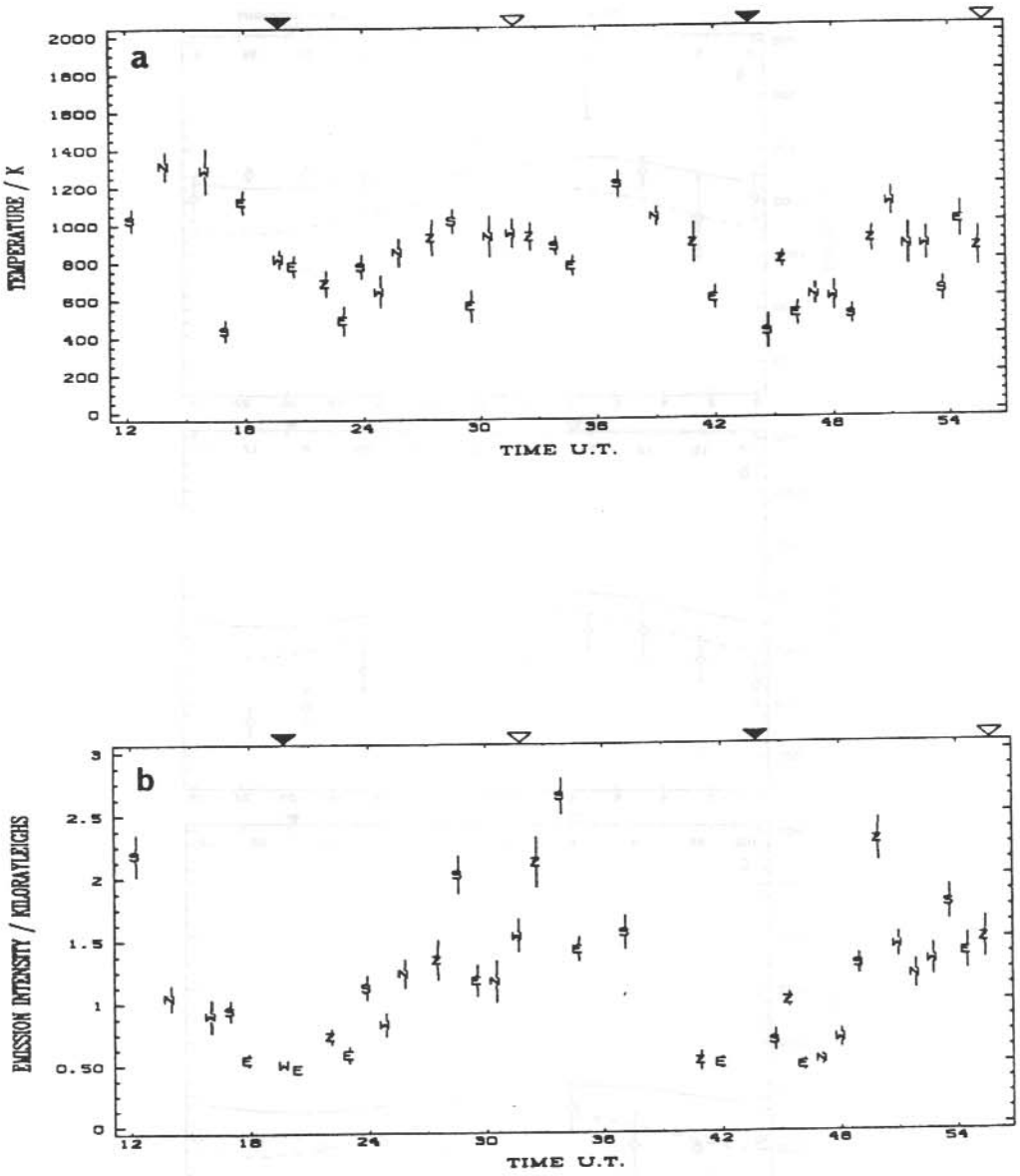


Figure 2.(a). Thermospheric temperature obtained over a 43 hour interval from 12 hours UT on day 356, 1988 to 7 hours UT on day 358, 1988. Letters N, E, S, W, and Z indicate viewing directions of north, east, south, west and zenith respectively. Standard errors are shown as vertical bars. Open triangles indicate times of local midday; filled triangles indicate local midnight.

(b) As for (a), but showing λ630 nm emission intensities. Error bars have been omitted where they do not exceed the height of the plotted symbol.

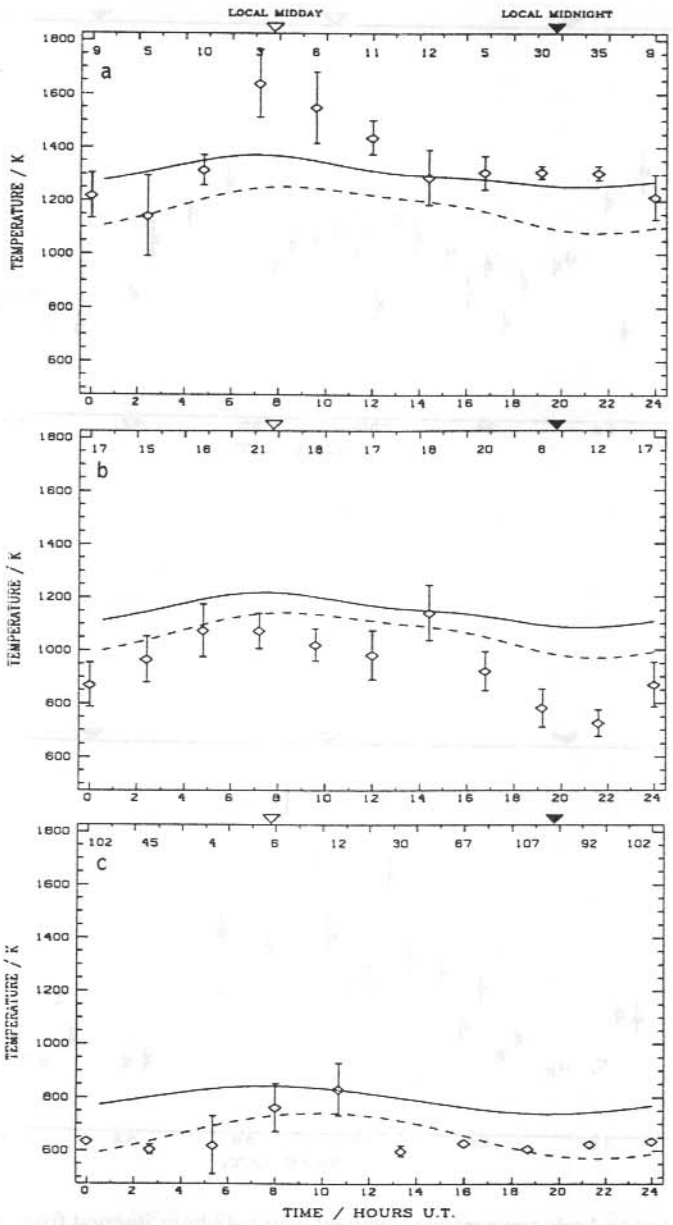


Figure 3(a). 2.5 hour averaged thermospheric temperature results for the 1982 observing period. Error bars, indicating the standard error in estimating the mean of all points within the averaging interval, are shown where they exceed the height of the plotted symbol. Small numbers along the top indicate the number of observations used to compute each average. The solid curve indicates the MSIS-86 model with the appropriate $A_p$ value; the dashed curve indicate MSIS-86 values for $A_p$=0. The 1982 observing period was close to solar maximum. (b) As for (a) but showing thermospheric temperature averages from the 1988 (intermediate solar activity) observing period. (c) As for (a) but showing thermospheric temperature averages from 1986 (low solar activity).

Observed temperatures were greatest in 1982, least in 1986, indicating the expected solar cycle variation in thermospheric heating. The 1986 and 1988 observing periods were magnetically quiet; their median $A_p$ values were 12 and 10 respectively. MSIS-86 temperatures using the appropriate $A_p$ values for these two periods considerably exceed those actually observed, whereas the model does give good agreement for $A_p$=0. Comparisons between MSIS-86 and the UCL-TGCM by Rees and Fuller-Rowell (1988) showed that MSIS-86 over-estimated the geomagnetic heat input relative to the theoretical model under magnetically quiet conditions. They attributed this to inadequate representation of quiet auroral precipitation in their model. However, because the present quiet-time temperature data are also over-estimated by MSIS-86, it is possible that model coefficients describing quiet-time geomagnetic heating are too large.

Observed and modelled daily mean temperatures agree well in 1982; the present observations suggest that geomagnetic heating is better described by the model for magnetically disturbed periods. In contrast, thermospheric temperatures recently derived by Kim et al. (1990) from λ630 nm spectra recorded at 50.6° S geomagnetic latitude during high solar activity were typically 200-300° K greater than MSIS-86 or MSIS-83 model values, on both magnetically quiet and disturbed days. These results demonstrate that inconsistencies between temperatures inferred from λ630 nm emission spectra and the MSIS models remain unresolved, at least at high latitudes. Hedin (1988) compared observations of atomic oxygen number density with corresponding predictions from several empirical atmospheric models and concluded that 'magnetic activity variations remain a critical area needing improvement for all models'. If these deficiencies arise from inadequate observations to characterise changes with magnetic activity then thermospheric temperature variations would also be poorly described.

For each year examined, the measured diurnal temperature variation exceeds that of the model. Thus, the MSIS-86 model may also inadequately describe temperature variations due to the daily passage of Mawson under different regions of geomagnetic heating. Joule heating maximises in the dayside cusp and auroral electrojets, and is least in the midnight sector (maps presented by Ahn et al. 1983, 1989, Rich et al. 1987). Whilst particle heating maximises in the midnight sector (Foster et al. 1986) its input is less than for Joule heating (Ahn et al. 1983 found a factor of four difference was typical). Geomagnetic heating should, therefore, enhance the diurnal temperature variation as compared to that expected from solar ultraviolet heating alone.

A larger than predicted diurnal temperature variation within the mid-latitude thermosphere was also obtained by Cocks and Jacka (1979), from an almost identical experiment to that reported here. Several mechanisms may cause neutral temperatures inferred from the present method to display an erroneously large diurnal variation. Sky brightness varies diurnally by many orders of magnitude; the magnitude of any residual Fraunhofer structure in extracted daytime emission spectra would vary similarly. Were such residuals to appear systematically, e.g. always appearing as a positive feature, the resulting derived temperatures would exhibit an erroneous diurnal variation. However, the daytime analysis routine showed no such systematic error when applied to numerically simulated spectra; this mechanism is therefore considered unlikely to be significant.

If spectral line widths are to indicate atmospheric temperature, the emitting species must be in thermal equilibrium with its surrounding gas. Until recently the radiating $O(^1D)$ population was thought to be well thermalised by collisions (Rees 1989). However, model calculations by Yee (1988) indicated that, for the night-time conditions examined, the $O(^1D)$ velocity distribution may differ significantly from a Maxwell distribution at ambient atmospheric temperature - a fraction of the $O(^1D)$ atoms retain kinetic energy acquired in their formation. Incomplete thermalisation was found to be sufficient to raise the temperatures which would be inferred from $\lambda$630 nm line widths by 50-100° K (in a simulated experiment). Thus, diurnal variation in either the energy spectrum of newly created $O(^1D)$ atoms, or in the degree of thermalisation of the radiating population, could produce a diurnal variation in spectrally inferred temperatures.

Night-time $O(^1D)$ production is due mainly to dissociative recombination of $O_2^+$. This mechanism leaves newly created $O(^1D)$ atoms with an average of ~2 eV of kinetic energy, corresponding to a temperature of ~15,000° K. The important additional daytime $O(^1D)$ production mechanisms, photoelectron impact and photo-dissociation of $O_2$, are not expected to create such a hot population. In the former case, this is because photoelectrons do not efficiently transfer their kinetic energy to the much heavier oxygen atoms. In the latter case most of the dissociation is due to radiation in the wavelength range 130-175 nm; at most ~0.9 eV excess energy per oxygen atom is available if one $O(^1D)$ is created. $O_2$ absorbs radiation at wavelengths shorter than ~70 nm almost totally by photo-ionisation (Rees 1989); excess energy would be taken mainly by the photoelectron. In the approximate wavelength interval 70-100 nm photo-dissociation occurs with a high yield (Rees 1989) and up to 5 eV excess energy is available per oxygen atom if one $O(^1D)$ is created. However, the integrated dissociation-cross-section solar-flux product in this interval is less than ~10% of that in the Schumann-Runge continuum. Overall, the mean energy of newly-created $O(^1D)$ atoms should be characterised by a lower temperature during the day than at night - which would act to suppress, rather than enhance, diurnal temperature variations inferred from the present technique.

Diurnal thermospheric composition changes may produce a diurnal variation in the degree to which the radiating $O(^1D)$ population is thermalised. This is determined by the mean number of momentum-transfer collisions experienced by an $O(^1D)$ atom prior to radiating. A large fraction of thermospheric $O(^1D)$ atoms are lost through 'quenching'. That is, the $O(^1D)$ radiative lifetime exceeds its chemical lifetime throughout much of the emission region. Of species contributing to $O(^1D)$ quenching, electrons may effect $O(^1D)$ thermalisation the most. The daytime F-region electron number density is approximately three orders of magnitude smaller than that of the neutrals, but this is partially compensated by a large electron-quenching rate coefficient which is approximately two orders of magnitude greater than that of $N_2$ (Link and Cogger 1988). Increased daytime electron number density and temperature will increase the $O(^1D)$ quenching rate (and thus decrease its chemical lifetime) without varying the frequency of $O(^1D)$ momentum-transfer collisions. During daytime, the population of radiating $O(^1D)$ atoms would, therefore, have experienced fewer thermalising collisions prior to emitting.

Estimation of the effect of these changes on ground-based thermospheric temperature measurements would require evaluation of a suitable velocity-distribution model, such as that applied by Yee and Killeen (1986) to $O(^1S)$ atoms, over the height range from which significant λ630 nm radiation originates and over a full diurnal cycle. The λ630 nm emission spectra seen by a ground-based instrument at each local time may be obtained by height-integration of the modelled line-of-sight velocity distributions. Finally, these spectra must be submitted to a simulation of the actual experiment used to record and analyse airglow emissions in order to determine what effect the non-thermal distributions have on recovered temperatures.

The last step is important. For example, in an approximate description, Yee (1988) divided the $O(^1D)$ atoms into two sub-populations - those which are totally thermalised and those which retain all excess energy acquired in their creation. A simple calculation shows that at low altitudes (~140 km) the non-thermal population accounts for ~4% of all $O(^1D)$ atoms; this fraction increases at greater heights. Assuming 2 eV excess energy is acquired by each newly-created $O(^1D)$ atom (as in dissociative recombination of $O_2^+$) and an ambient temperature of 1000° K then, with a 4% non-thermal population, the mean $O(^1D)$ kinetic energy is 1.6 times that for a totally thermalised population. A large number of λ630 nm source spectra of this form (96% at 1000° K, 4% at 15,400° K) were submitted to a numerical simulation of the present experiment in its night-time configuration, to investigate its sensitivity to lack of thermalisation. The temperatures returned were only ~60° K above 1000° K. This result is consistent with that obtained by Yee (1988) using a much more sophisticated description of the $O(^1D)$ energy spectrum. A typical spectrometer would appear to be insensitive to incomplete thermalisation because the wavelength interval covered is optimised for the expected thermal line width, and is too small to adequately record the broader non-thermal contribution. When the wavelength interval recorded was doubled in this simulation (to that typical of daytime operation) the mean temperature estimate increased to ~1120° K.

## 16.4 THERMOSPHERIC WIND

Solar wind-magnetosphere interaction generates a large scale electric field, directed in the dawn-to-dusk direction, which is mapped down to ionospheric heights because the electrical conductivity parallel to geomagnetic field lines is very large. The resulting $\underline{E} \times \underline{B}$ force drives a two-cell plasma circulation within the high latitude ionosphere, with anti-sunward flow across the polar cap and sunward return flow around the dawn and dusk sectors of the auroral oval. The direction of the interplanetary magnetic field (IMF) y-component, tangential to the earth's orbit, influences solar wind-magnetosphere coupling and determines the relative sizes of the two plasma circulation cells. Ion-neutral collisions viscuously couple F-region plasma circulation to the neutral wind with a time constant typically around one hour. Therefore, neutral winds also tend to acquire a (smoothed) two-cell flow but, in both hemispheres, the Coriolis force acts to 'disperse' dawn cells; these are expected to be poorly developed.

Figure 4 shows 1.2 hour average observed wind vectors for each of the three years examined, along with predictions from the University College London (UCL) TGCM (Rees and Fuller-Rowell 1988) and the HWM-87 empirical model (Hedin et al. 1988). The large circle in these plots describes the locus of the observatory in invariant magnetic coordinates over 24 hours of magnetic time: i.e. at all points on the circle invariant north is directed radially outward and magnetic noon is at the top. The median $A_p$ values are indicated for each of the three observing periods.

The procedure for determining winds required a continuous series of observations in each of the five viewing directions; only in 1988 was the time coverage sufficiently extensive in all five directions to determine vector winds over an entire 24 hour cycle. The 1982 and 1988 winds, derived from summer-time observations, were determined solely from daytime data. For 1986, night-time data were used exclusively.

Output from 50 runs of the UCL TGCM, representing a wide range geophysical conditions, is distributed for general use by UCL. The simulations used for comparison with the present observations came from this 'standard' set - no special model results were obtained from geophysical conditions exactly corresponding to those prevailing during the observations. Different levels of magnetic activity are represented in the numerical model mainly by varying the assumed high latitude ionospheric electric field and its associated plasma convection pattern (at high activity levels particle precipitation effects must also be included). An equivalent $A_p$ value has been assigned to each simulation presented here based on the cross-polar-cap electric potential applied for that model run. No measurements of the IMF $B_y$ component during the observing periods were able to be obtained. TGCM simulations for the appropriate pressure level, season, solar and magnetic activity levels were examined for both IMF $B_y>0$ and $B_y<0$ cases. Simulations corresponding to low and moderate magnetic activity levels gave very similar results for both IMF $B_y$ configurations. Under magnetically disturbed conditions the IMF $B_y>0$ simulations showed a sunward wind in the (magnetic) dawn-to-noon sector; observations during this period showed no such sunward flow. Since the $B_y<0$ case matched the FPS observations more closely this IMF configuration was used in the comparisons presented here. The HWM-87 model contains no IMF $B_y$, height or F10.7 cm solar flux dependence. Predictions shown are for southern summer with an $A_p$ index equal to the median value for the corresponding observing period.

Observed winds were always anti-sunward around magnetic midnight, due to the combined effects of ion-drag and the pressure gradient force. In each year sunward winds were observed in the afternoon and evening sectors, indicating the passage of Mawson under the ion-drag driven 'westward thermospheric jet stream' associated with the evening auroral oval (Rees et al. 1985). No sunward 'jet stream' was observed on the dawn side; observed magnetic-zonal flow was generally westward throughout the day. This is expected since the Coriolis force acts to disperse clockwise circulation cells in the southern hemisphere. These observed features also appear in the models.

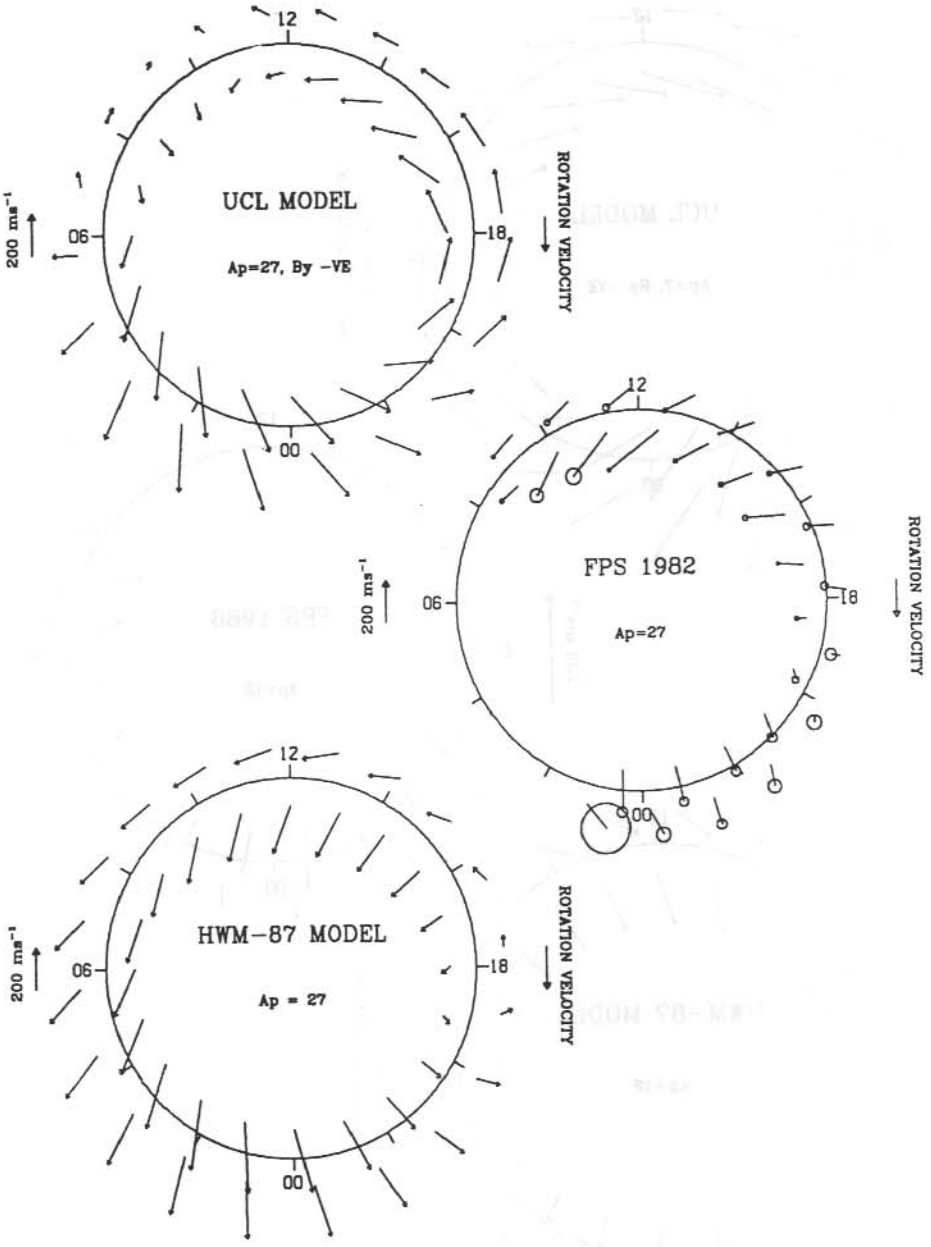


Figure 4(a). Observed and modelled wind vectors for the 1982 period, plotted in magnetic latitude-local time coordinates. In this case meridional components were computed separately from north and south looking observations; the resulting two sets of vectors are indicated by the outer and inner circles of arrows respectively. Model winds at geographic locations corresponding to the regions observed when viewing north and south are plotted similarly.

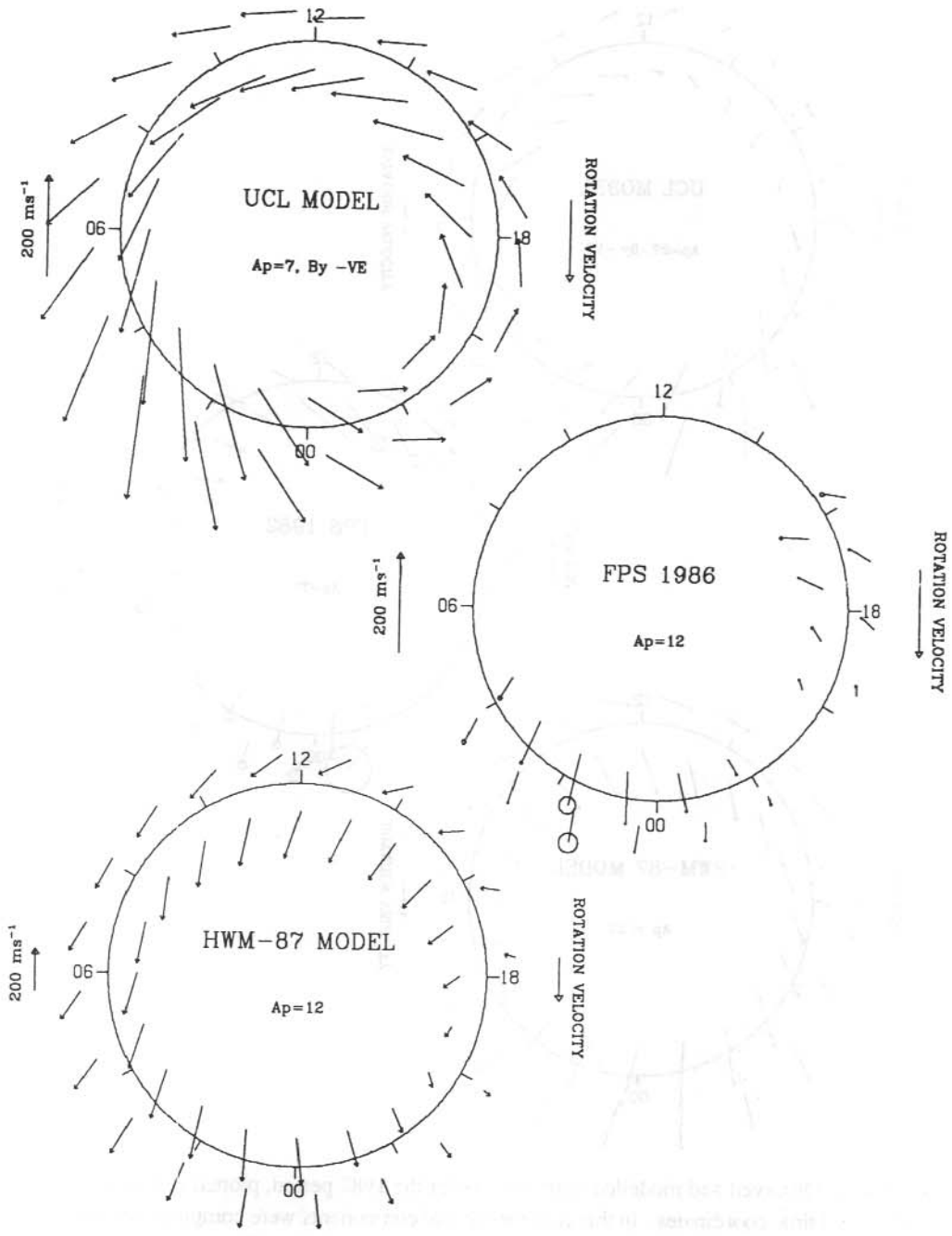


4(b). As for (a), but for the 1986 observing period. Note the scale of the bottom (HWM-87) plot is compressed relative to the other two.

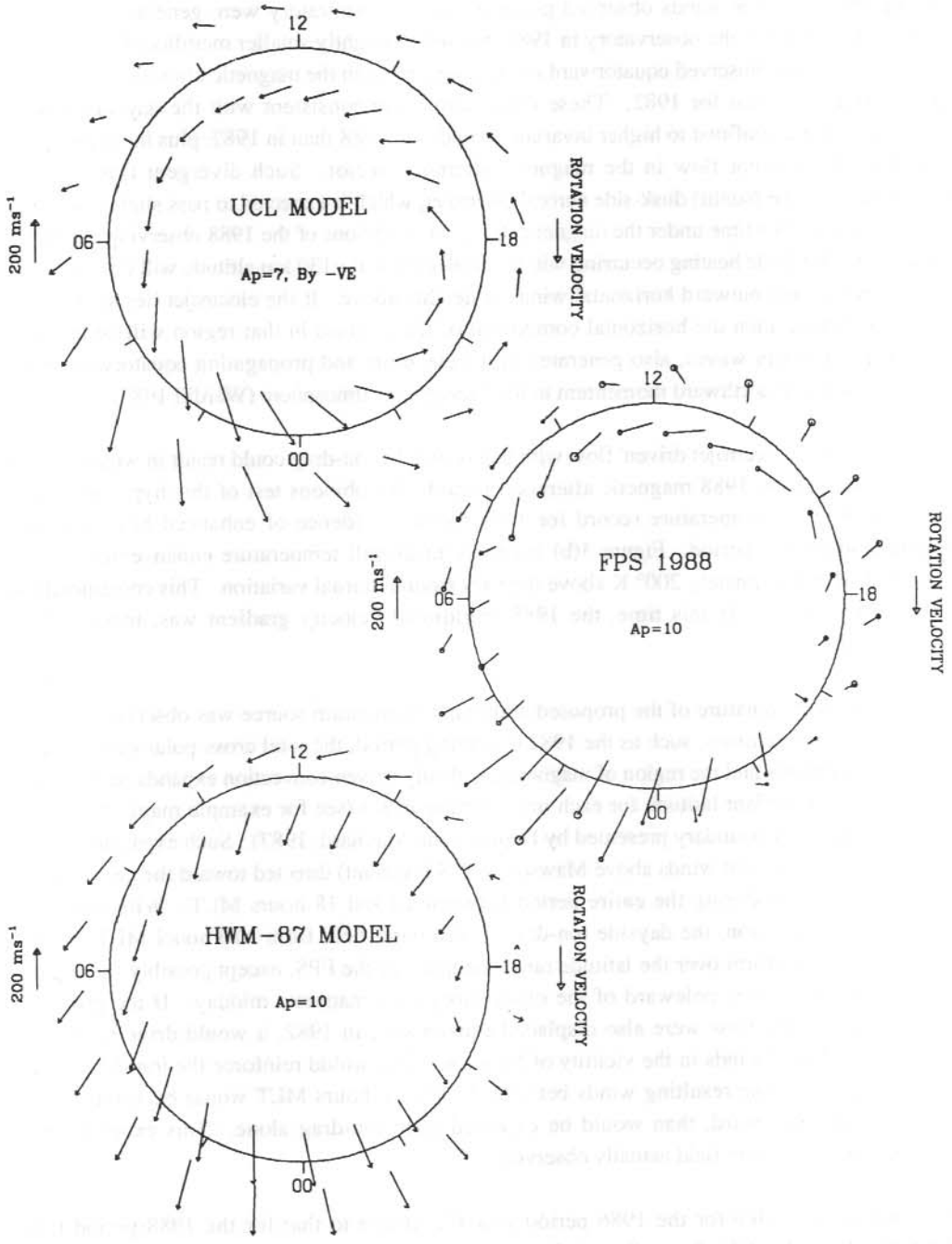


4(c). As for (a), but for the 1988 observing period.

During 1988, dayside winds observed poleward of the observatory were generally similar to those equatorward of the observatory in 1982, but with a slightly smaller meridional component. However, the flow observed equatorward of the observatory in the magnetic afternoon sector was quite different to that for 1982. These observations are consistent with the dayside plasma convection being confined to higher invariant latitudes in 1988 than in 1982, plus the presence of a source of divergent flow in the magnetic afternoon sector. Such divergent flow may be associated with the (sunlit) dusk-side auroral electrojet, which is expected to pass slightly south of Mawson during this time under the magnetically quiet conditions of the 1988 observing period. It is expected that Joule heating occurring within the electrojet at ~130 km altitude will drive upward vertical winds and outward horizontal winds at heights above. If the electrojet lies south of an observing region then the horizontal component of these winds in that region will be directed northward. Gravity waves, also generated in the electrojet and propagating equatorward, may transfer additional northward momentum to the background atmosphere (Wardill 1987).

Superposition of 'electrojet driven' flow with that driven by ion-drag could result in winds similar to those seen in the 1988 magnetic afternoon period. An obvious test of this hypothesis is to examine the FPS temperature record for 1988 for any evidence of enhanced heating in the magnetic afternoon period. Figure 3(b) indicates an overall temperature enhancement at ~14 hours UT of approximately 200° K above the background diurnal variation. This corresponds to ~16.5 hours MLT. At this time, the 1988 meridional velocity gradient was, indeed, most pronounced.

In 1982 no clear signature of the proposed additional momentum source was observed. During magnetically active times, such as the 1982 observing period, the total cross-polar-cap potential difference increases and the region of magnetospherically-driven convection expands equatorward by 2° to 3° of invariant latitude for each unit increase in Kp (see for example maps of the low-latitude convection boundary presented by Heppner and Maynard, 1987). Such expansion would result in ion-drag driven winds above Mawson (70° S invariant) directed toward the geomagnetic west or south-west during the entire period between 10 and 18 hours MLT. With sufficient equatorward expansion, the dayside ion-drag driven wind field from ~10 hours MLT onward would be quite uniform over the latitude range sampled by the FPS, except possibly for slightly greater wind velocities poleward of the observatory near magnetic midday. If the proposed source of divergent flow were also displaced equatorward in 1982, it would drive southward dayside meridional winds in the vicinity of Mawson. This would reinforce the ion-drag driven meridional flow. The resulting winds between 12 and 18 hours MLT would be stronger, and slightly more southward, than would be expected from ion-drag alone. This expectation is consistent with the wind field actually observed.

The median $A_p$ value for the 1986 period was 12, similar to that for the 1988 period (10), although the solar F10.7 cm flux index was only ~70 compared to 150-240 for 1988. Nevertheless, high-latitude winds for 1986 might be expected to be similar to those observed in 1988. The 1986 wind data were derived from single-etalon night-time observations collected

around equinox; these could not be commenced before the onset of darkness at ~16 hours MLT. Despite this there is some overlap in time with the period of meridional wind gradient observed in 1988. No similar gradient appears in the 1986 data. The Joule heat production rate above an observing site is given by

$$u_J = \underline{I} \cdot \underline{E}$$
$$= \Sigma_p E^2$$

where $\underline{I}$, $\underline{E}$ and $\Sigma_p$ are the height-integrated total current density, electric field and Pederson conductivity respectively (Kamide and Kroehl 1987). Joule heating maximises in the E-region where ion recombination rates are large; in the absence of particle precipitation $\Sigma_p$, and thus $u_J$ are over an order of magnitude smaller in non-sunlit regions than in sunlit ones. At the F-region heights sampled by λ630 nm observations, the recombination rate is smaller; ion-drag remains effective after sunset at the altitude of maximum λ630 nm emission. Since the 1986 observations at 16 hours MLT were collected in darkness, it is postulated that Joule heating was not significant relative to ion-drag in driving winds at ~200-250 km. Quiet-time magnetospherically-driven convection (characteristic of the 1986 observing period) would drive a relatively uniform wind field directed magnetic westward or south-westward at ~16 hours MLT. This was observed.

Both of the thermospheric wind models available at the time of writing predict some (magnetic) meridional wind gradient between mid-morning and dusk magnetic local time; it is especially pronounced in the HWM-87 empirical model. However, for both models the mean (overhead) meridional wind is directed toward magnetic south, whereas the 1988 data indicate the overhead meridional wind is directed slightly toward magnetic north.

A consistent feature of the thermospheric wind over Mawson observed both here and previously (Wardill et al. 1987, Jones et al. 1987), is a period of light winds at around 20 hours MLT accompanying the evening transition from anti-sunward to sunward flow. A similar wind abatement appears in the HWM-87 empirical model, although approximately two hours earlier in MLT. The TGCM fails to predict any abatement. TGCM winds at high latitudes are a strong function of the magnetospherically-driven plasma convection pattern, which is a purely empirical input to the model. Ionospheric plasma convection (and hence ion-drag) reverses in direction between 18 and 24 hours MLT, from being sunward at 18 hours MLT to anti-sunward around magnetic midnight. The global pressure gradient due to dayside solar UV heating acts in an antisolar direction throughout the high latitude region. Thus, it is likely that at some time between 18 and 24 hours MLT, the ion-drag and pressure gradient forces will approximately cancel, leading to the observed wind abatement. The degree of cancellation which occurs in a thermospheric model, including the effects of all wind-driving forces, will clearly depend in the particular convection pattern assumed. Failure of the UCL TGCM to predict abatement of the thermospheric wind above Mawson near 20 hours MLT may indicate that the assumed plasma convection is not accurate in this local time sector.

## 16.5 CONCLUSION

Fabry-Perot spectrometer observations of the λ630 nm atomic oxygen emission have enabled measurement of thermospheric temperatures over 24 hours of local time, at three different phases of the solar cycle. Horizontal wind vectors were also obtained; however, only for 1988 was the full diurnal cycle covered.

Thermospheric temperature was observed to increase with increasing solar activity, as expected. However, observed temperatures departed significantly from those predicted by the MSIS model. In particular, the diurnal amplitudes of observed temperature variations exceeded those of the model. Provided that the observations are accurate, the present data may indicate inadequate model representation of geomagnetic heating of the high-latitude thermosphere. However, because an unexpectedly large diurnal amplitude was also obtained by Cocks and Jacks (1979) from a similar experiment at mid-latitudes, it is possible that the Doppler width of the λ630 nm emission does not accurately measure ambient atmospheric temperature in the emitting region. It is proposed that electron quenching of $O(^1D)$ atoms occurs more effectively during the day, possibly resulting in a less well thermalised radiating population, and erroneously high daytime temperatures.

Observed winds were consistently sunward during the magnetic afternoon-to-dusk period and anti-sunward around magnetic midnight. Such flow is consistent with the expected presence of an anti-cyclonic circulation cell centred over the dusk side of the southern polar cap. Where wind data were obtained from the dawn side of the magnetic noon-midnight meridian, anti-sunward flow was observed. These observations suggest that the presence of a corresponding cyclonic cell above the dawn side of the polar cap is not typical.

In one year, 1988, a region of divergent meridional flow was observed during the magnetic afternoon period. It is proposed that this feature was driven by Joule heating occurring within the dusk auroral electrojet, which would pass just south of Mawson during magnetically quiet conditions. Corresponding divergent meridional flow was not observed in the 1982 or 1986 data. Because the 1982 data were collected during a magnetically disturbed period, it is expected that the auroral electrojet typically passed well north of Mawson during the magnetic afternoons of that observing period. The geometry of the resulting driving forces would not produce divergent flow in the vicinity of Mawson. All of the 1986 data were collected under conditions of darkness, under which conditions Joule heating is less effective. Again, divergent meridional flow would not be expected in the magnetic afternoon period.

Finally, in all years examined here, a wind 'abatement' was observed accompanying the transition between sunward flow at dusk to anti-sunward flow at midnight. A similar result was reported by Wardill et al. (1987) and Jones et al. (1987). The UCL TGCM does not contain any such abatement, possibly reflecting an inaccurate model description of magnetospherically-driven plasma flow in the high-latitude F-region.

## 16.6 ACKNOWLEDGMENTS

Thanks are due to the staff and students of the Mawson Institute, in particular Mr. D. Creighton, for the design and construction of parts of the equipment and for many useful suggestions. The 1982 spectra were recorded by N. Jones; some of the 1988 spectra were recorded by Dr. P. Greet. This work was supported by the Australian Research Grants Scheme and the Antarctic Science Advisory Committee grants scheme. Logistic support was provided by the Australian National Antarctic Research Expeditions.

## 16.7 REFERENCES

Ahn, B.H., Akasofu, S.I. *and* Kamide, Y. (1983). The joule heat production rate and the particle energy injection rate as a function of the geomagnetic indices AE and AL. *Journal of Geophysical Research* 88:6275-6287.

Ahn, B.H., Kroehl, H.W., Kamide, Y., Gorney, D.J., Akasofu, S.I. *and* Kan, J.R. (1989). The auroral energy deposition over the polar ionosphere during substorms. *Planetary and Space Science 37*:239-252.

Cocks, T.D. *and* Jacka, F. (1979). Daytime thermospheric temperatures, wind velocities and emission intensities derived from ground based observations of the OI λ630 nm airglow line profile. *Journal of Atmospheric and Terrestrial Physics 41*:409-415.

Conde, M. *and* Jacka, F. (1989). Analysis of day-time observations of the λ630 nm thermospheric emission over Mawson, Antarctica. In: Conde, M. *and* Beggs, H. (Eds). *ANARE Research Notes Number 69*. Pp. 125-138.

Dickinson, R.E., Ridley, E.C. *and* Roble, R.G. (1981). A three dimensional general circulation model of the thermosphere. *Journal of Geophysical Research 86*:1499-1512.

Foster, J.C., Holt, J.M., Musgrove, R.G. *and* Evans, D.S. (1986). Solar wind dependencies of high-latitude convection and precipitation. In: Kamide, Y. *and* Slavin, J.A. (Eds). *Solar Wind-Magnetosphere Coupling*. Terra Scientific Publishing Company, Tokyo.

Fuller-Rowell, T.J. *and* Rees, D. (1980). A three dimensional time dependent model of the thermosphere. *Journal of the Atmospheric Sciences 37*:2545-2567.

Fuller-Rowell, T.J., Rees, D., Quegan, S., Moffett, R.J. *and* Bailey, G.J. (1987). Interactions between neutral thermospheric composition and the polar ionosphere using a coupled ionosphere-thermosphere model. *Journal of Geophysical Research 92*:7744-7748.

Hedin, A.E. (1987). MSIS-86 thermospheric model. *Journal of Geophysical Research 92*:4649-4662.

Hedin, A.E. (1988). Atomic oxygen modelling in the upper thermosphere. *Planetary and Space Science 36*:907-920.

Hedin, A.E., Spencer, N.W. *and* Killeen, T.L. (1988). Empirical global model of upper thermosphere winds based on atmospheric and dynamics explorer satellite data. *Journal of Geophysical Research 93*:9959-9978.

Heppner, J.P. *and* Maynard, N.C. (1987). Empirical high latitude electric field models. *Journal of Geophysical Research 92*:4467-4489.

Hernandez, G. *and* Killeen, T.L. (1988). Optical measurements of winds and kinetic temperatures in the upper atmosphere. *Advances in Space Research 8*:149-213.

Jacka, F. (1984). Application of Fabry-Perot spectrometers for measurement of upper atmosphere temperatures and winds. *Handbook for MAP 13*:19-40.

Jacka, F. *and* Vincent, R.A. (1989). Dynamics of the antarctic upper atmosphere. *Planetary and Space Science 37*:943-954.

Jones, N., Wardill, P. *and* Jacka, F. (1987). Dynamics of the thermosphere over Mawson, Antarctica: II. Dependence on the Y component of the interplanetary magnetic field. In: Burns, G.B. *and* Craven, M. (Eds). *ANARE Research Notes Number 48*. Pp. 121-130.

Kamide, Y. *and* Kroehl, H.W. (1987). A concise review of the utility of ground based magnetic recordings for estimating the joule heat production rate. *Annales Geophysicae 5*:535-542.

Kim, J.S., Murty, G.S.N., Kim, J.W. *and* Kim, Y. (1990). Thermospheric temperature during a high solar activity period. *EOS 71*:1100-1102.

Kohnlein, W. (1980). A model of thermospheric temperature and composition. *Planetary and Space Science 28*:225-243.

Link, R. *and* Cogger, L.L. (1988). A reexamination of the OI 6300-A nightglow. *Journal of Geophysical Research 93*:9883-9892.

Rees, D. *and* Fuller-Rowell, T.J. (1988). The CIRA theoretical thermosphere model. *Advances in Space Research 8*:27-106.

Rees, D., Fuller-Rowell, T.J., Smith, M.F., Gordon, R., Killeen, T.L., Hays, P.B., Spencer, N.W., Wharton, L. *and* Maynard, N.C. (1985). The westward thermospheric jet stream of the evening auroral oval. *Planetary and Space Science 33*:425-456.

Rees, M.D. (1989). *Physics and Chemistry or the Upper Atmosphere*. Cambridge University Press, Cambridge.

Rich, F.J., Gussenhoven, M.S. *and* Greenspan, M.E. (1987). Using simultaneous particle and field observations on a low altitude satellite to estimate joule heat energy flow into the high latitude ionosphere. *Annales Geophysicae 5*:527-534.

Roble, R.G., Ridley, E.C., Richmond, A.A. *and* Dickinson, R.E. (1988). A coupled thermosphere/ionosphere general circulation model. *Geophysical Research Letters 15*:1325-1328.

Smith, R.W., Rees, D. *and* Stewart, R.D. (1988). Southern hemisphere thermospheric dynamics: a review. *Reviews of Geophysics 26*:591-622.

Wardill, P. (1987). *Dynamics of the thermosphere over Mawson, Antarctica*. Ph.D. thesis, University of Adelaide.

Wardill, P., Jones, N. *and* Jacka, F. (1987). Dynamics of the thermosphere over Mawson, Antarctica: I. Diurnal variation and geomagnetic dependence. *ANARE Research Notes Number 48*. Pp. 114-120.

Wilksch, P.A., (1975). *Measurement of thermospheric temperatures and winds using a Fabry-Perot spectrometer*. Ph.D. thesis, University of Adelaide.

Yee, J.H. (1988). Non-thermal distribution of $O(^1D)$ atoms in the night-time thermosphere. *Planetary and Space Science 36*:89-97.

Yee, J.H. *and* Killeen, T.L. (1986). Thermospheric production of $O(^1S)$ by dissociative recombination of vibrationally excited $O_2^+$. *Planetary and Space Science 34*:1101-1107.

# 17. POST-NOON AURORAL ACTIVITY: GROUND-BASED OBSERVATIONS DAVIS, ANTARCTICA, 1988

M. Craven and G.B. Burns
Antarctic Division
Kingston Tas 7050
Australia

ABSTRACT

The morphology of post-noon auroral activity at high latitudes is discussed using ground-based data collected at Davis, Antarctica (68.6°S, 78.0°E geographic, 74.0°S invariant) during the 1988 austral winter. The auroral activity observed is classified into three event types (1) 'kink' aurorae, (2) pulsating aurorae, and (3) aurorae associated with break-up events in the midnight sector.

The authors postulate that 'kink' aurorae are the ground-based signature of the post-noon auroral enhancements that were dramatically depicted in the Viking ultraviolet auroral images. The observation of weak amplitude auroral pulsations was reported with an average period of around 20-30 seconds, in association with Pi(c) magnetic pulsations. It is also shown that main phase auroral break-up activity can intrude into the post-noon sector. Only a brief outline of this phenomenon is presented here.

Occurrence percentages for 'kink' aurorae and pulsating aurorae, and their dependence on Kp level, are presented for the post-noon through evening MLT (magnetic local time) sectors.

## 17.1 INTRODUCTION

Cogger et al. (1977), using data gathered from a scanning auroral photometer onboard the ISIS-2 satellite (Anger et al. 1973), first reported auroral intensity enhancements in the 14-16 MLT sector at geomagnetic latitudes around 72°-76° invariant. They related this activity to the intensity maximum of low energy magnetospheric electrons (E < 150 eV) in the same local time sector (McDiarmid et al. 1975).

The Ultraviolet Imager onboard the Swedish Viking spacecraft dramatically increased the temporal resolution with which it was possible to monitor global auroral activity. Global ultraviolet auroral images were obtainable about once every minute (Anger et al. 1987). One of the major new findings resulting from this enhanced capability, was that emissions in the 14-16 MLT sector can exhibit spatially periodic localised bright regions, resembling beads on a string, which persist for the order of several minutes (Lui et al. 1987). Lui et al. (1987) postulated that these post-noon enhancements may result from the Kelvin-Helmholtz (wind-over-water type) instability at the interface between the low latitude boundary layer (LLBL) and the magnetosheath, on the dayside nose of the magnetosphere. Figure 1 depicts a magnetospheric model indicating these features.

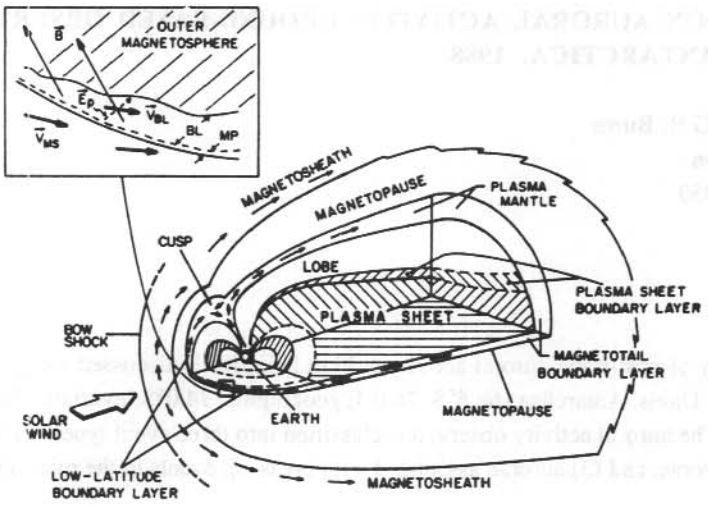


Figure 1. Illustration of the earth's magnetosphere depicting the low latitude boundary layer (LLBL) and the dynamic cusp region. The inset shows how cross-field plasma flow in the boundary layer results in a polarisation electric field which is able to discharge via field-aligned currents (FAC) into the high latitude ionosphere. Abbreviations: MS for magnetosheath, BL for boundary layer, and MP for magnetopause. This Figure is taken from Eastman et al. (1985).

Events, which may be the ground-based signature of these dynamic post-noon auroral enhancements captured by the Viking UV Imager, were observed photometrically from Davis during the 1988 austral winter. Representative data is ppresented later in this paper.

Pulsating aurorae with associated concurrent Pi(c) magnetic pulsations have been routinely observed from auroral zone stations (Heppner 1954, Cresswell and Davis 1966, Campbell 1970, Reid 1976, Arnoldy et al. 1982, Engebretson et al. 1983, Oguti et al. 1984, Burns and Cole 1985). Morphology studies indicate that the phenomenon most commonly occurs following auroral break-up in the midnight sector of the auroral oval, continuing on well into the morning hours. Typical optical intensities have generally been reported as being just above visual threshold limits, at a few kiloRayleigh in the O I line emission at 557.7 nm, with a quasi-periodicity of the fluctuations in the range 2-10 seconds (reviews: Johnstone 1978, 1983).

High latitude pulsations have been reported by Brekke and Pettersen (1971) from photometric observations made at Ny-Alesund (75.7°N inv.). They indicate a pre-noon peak in activity (at around 10 MLT), with pulsation amplitudes generally being around 5% of the total background optical emission, and periods typically of around 20-30 seconds. Reports in the literature of pulsating auroral activity in the post-noon MLT sector were not found.

Auroral zone pulsating aurorae are always accompanied by concurrent magnetic Pi(c) pulsations. This is because the magnetic Pi(c) pulsations are a signature of the ionospheric response to the fluctuating particle precipitation responsible for the optical pulsations (Campbell 1970, Reid 1976, Arnoldy et al. 1982, Engebretson et al. 1983, Oguti et al. 1984, Burns and Cole 1985). The electron precipitation results in an enhanced patch of conductivity in the auroral ionosphere. Under the influence of E-region electric fields, perturbation currents flow. This produces a ground magnetic signature which, under favourable conditions (Burns and Craven 1988), leads directly to a one-to-one correspondence between the auroral pulsations and the magnetic Pi(c) fluctuations (Arnoldy et al. 1982, Oguti et al. 1984, Burns and Cole 1985).

Observations of post-noon pulsating aurorae obtained from Davis during the 1988 austral winter are presented in this paper. Their temporal characteristics are in general agreement with the pre-noon observations of Brekke and Pettersen (1971).

Main phase auroral break-ups and associated substorms have been well documented in the literature, even at high latitudes (Arnoldy et al. 1986). Using observations from South Pole station (75°S inv.), Arnoldy et al. (1986) report that the rapid poleward expansion of discrete auroral forms from the nightside auroral oval results in a burst-like character of optical intensity fluctuations. This activity is always accompanied by large amplitude PiB magnetic pulsations having a 5-20 minutes duration period. The onset times of such bursts is generally well after the commencement of similar outbursts at Siple station (an auroral zone station).

Brief mention will be made in this paper of the nature of such substorm activity observed from Davis during the 1988 austral winter.

Davis station is located at 68.6°S, 78.0°E geog, 74.0°S inv. Geographic noon occurs around 0648 UT, geographic midnight at 1848 UT. Magnetic noon occurs around 0945 UT, with magnetic midnight correspondingly around 2140 UT. This means Davis is situated relative to cusp location such that post-noon ground-based optical observations are feasible during austral winter months.

## 17.2 INSTRUMENTATION

The instrumentation at Davis in 1988 included twin-channel, 30° half-angle, zenith-oriented photometers, to detect auroral emissions in O I at 557.7 nm, and in the $N_2^+$ 1NG(0,1) emission with a band head at 427.8 nm. Two mutually orthogonal induction coils oriented in the H (north) and D (east) local magnetic directions monitor the magnetic fluctuations (Davis has a magnetic variation of some 77°W). Data were sampled at 10 Hz and stored digitally in consecutive files of five minutes duration for subsequent analysis.

An all-sky camera (ASC) was operated whenever local meteorological conditions were such that less than five-eighths of the sky was obstructed by cloud cover. The camera normally cycled in a one frame per minute mode, but could be uprated to record an all-sky image every 20 seconds during periods of special interest.

Fluxgate magnetometer data recording the X (geographic north), Y (geographic south), and the Z (vertically downward), components of the magnetic field were also obtained, together with cosmic radio noise absorption levels, as detected by a standard riometer, operating at 30.4 Mhz. These data were collected digitally at a sampling rate of 0.1 Hz (one datum every ten seconds). Completing the Davis auroral ionospheric monitoring instrumentation was an ionosonde, operated on behalf of the Ionospheric Prediction Service. Ionograms were produced at fifteen minute intervals commencing on the hour, and at five minute intervals on Regular World Days.

The data presented here are that of the photometers, induction coils, and ASC instruments. They cover the period from May 12 to August 21 during the 1988 austral winter. During this period observations were possible to as early as 1030 UT (approximately 1250 MLT). No photometric observations are possible at Davis prior to this time.

It should be noted that the occurrence percentages which are presented in this paper are determined from an examination of the photometer records. The photometer field-of-view is approximately 1° of latitude at an altitude of 120 km.

## 17.3 OBSERVATIONS AND DISCUSSION

In this section a general overview is presented of the observations of the three auroral event types outlined in Section 17.1. Some comments, with reference to relevant current literature, are made concerning the observations.

### *17.3.1 'Kink' aurorae : post-noon enhancements*

The term 'kink' aurorae was adopted for a type of post-noon auroral enhancement observed from Davis. These events develop as curtain-like folds or breaking-wave kinks of enhanced optical emission, appearing along previously quiescent auroral arc systems, as shown on the ASC image in Figure 2. This characteristic form is in agreement with what might be expected from a Kelvin-Helmholtz instability production mechanism. Lui et al. (1988) suggest that their bright spots on Viking images may 'correspond to folds or surges in auroral forms if they are imaged by instruments with higher spatial resolution, such as ground all-sky cameras'. The authors postulate that such events are the ground-based signature of the post-noon localised bright regions witnessed by the Viking UV Imager (Lui et al. 1987).

These kink events have a temporal lifetime of the order of several minutes, and a spatial extent, measured from ASC images for one event as approximately 200 km long by 80 km wide, which is consistent with reports from the satellite observations. Lui et al. (1988) found that their observed bright spots were transient, lasting for a few minutes only. This is consistent with the ASC image sequence depicting a ground-observed Davis kink event shown in Figure 3. Lui et al. (1988) measure the spatial dimensions of the spots as ranging from 50-200 km, in general agreement with the Davis observations.

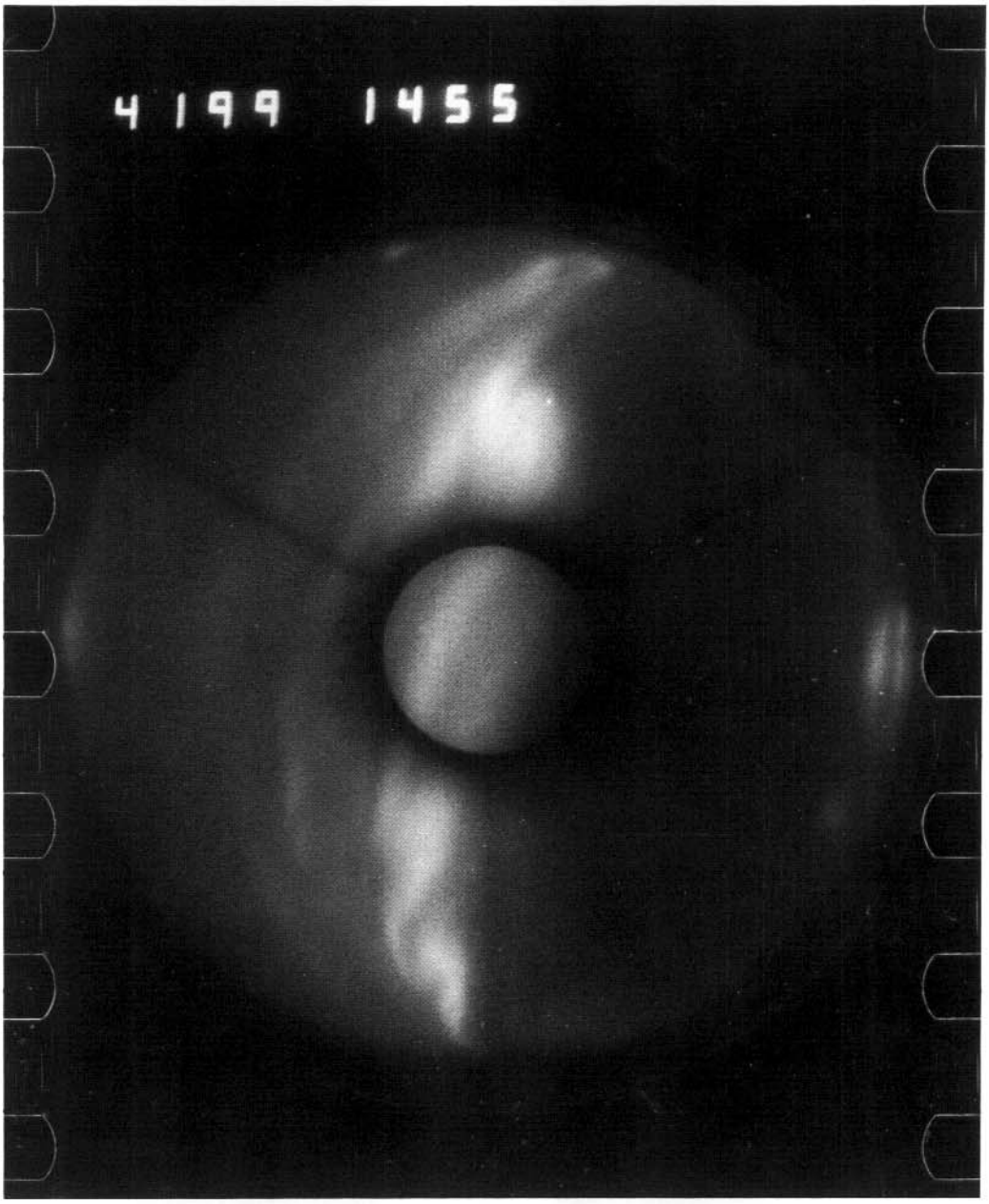


Figure 2. All-sky camera (ASC) image of an auroral kink (bottom centre of picture) which has developed along a previously quiescent auroral arc, was taken on the 17 July 1988 at 1455 UT (approximately 1710 MLT). The fold in the form is quite obvious in this reproduction. (Another fold is evident just above the centre of the frame). Image orientation is such that geographic north is in the 7 o'clock direction, and the southern invariant pole is at 4 o'clock.

From instruments operated at Davis, the kink events here appear to result from low energy particle precipitation (Figure 4). Generally there is no cosmic noise absorption associated with kink events. Cosmic noise absorption, as measured by a riometer, largely manifests itself in the D and lower E regions of the ionosphere where electron-neutral collisions become increasingly important in the quenching of radio waves. Low energy particle precipitation is unable to penetrate to such depths in the ionosphere and is generally considered not to contribute to cosmic noise absorption events. The lack of accompanying magnetic pulsation signals may be more due to the long period nature of the events and the corresponding poor induction coil response characteristics for such low frequencies. No significant activity is recorded by the magnetometer during kink events. The large-scale fluxgate magnetometer signal would however, be expected to respond to any significant enhancements in the overhead ionospheric current systems. Sufficiently low energy particles may not reach ionospheric levels where they could significantly contribute to the ambient conductivities present to generate any major current perturbations.

More quantitative evidence can be obtained from consideration of the photometer data available on these kink events. Although, the authors had been unable to fully calibrate the 427.8 nm channel, they were able to compare the ratios of the 557.7 nm and 427.8 nm intensities for various types of events. The ratio 557.7/427.8 for kink events is typically greater than that for the more energetic break-up events. The 557.7 nm emission is a forbidden transition with a radiative lifetime of about 0.8 seconds. Excited oxygen atoms in their upper $O(^1S)$ state suffer more collisional deactivation lower in the ionosphere. The 427.8 nm emission is effectively instantaneous. Therefore, a higher value for this ratio is a pointer to lower energy particle precipitation. This would be in accord with the connection to low energy particle precipitation in this time sector as reported by McDiarmid et al. (1975).

Peak auroral intensities for the kink events seldom exceed 10 kR in the 557.7 nm oxygen emission, and are more typically less than 5 kR. Lui et al. (1987) claim that their Viking UV Imager post-noon auroral enhancements can reach intensity levels comparable with auroral break-up events. The Davis observations, however, indicate that intensities for kink aurorae are significantly less than those for break-up events. This discrepancy may be a result of different wavelengths involved with the two data suites. There may be some contributing geometrical factors involved due to the spatial integration over the very wide-angle field-of-view of the instruments that were compared.

Lui et al. (1988) suggest, from a preliminary survey, that about one third of the satellite orbits reveal the presence of spatially periodic bright spots on the dayside oval. It was found that kink events have a peak occurrence rate (determined as the chance of being observed in any given 15 minute period) of 30%, in the 16-17 MLT time sector, as depicted in the histogram (Figure 5). There still exists a significant occurrence rate in earlier time sectors. As indicated by Lui et al. (1988) these 'series of bright spots' are not limited to the 14-16 MLT sector, but can extend to the pre-noon sector on some occasions. Photometric observations are, however, not possible at Davis prior to around 1250 MLT.

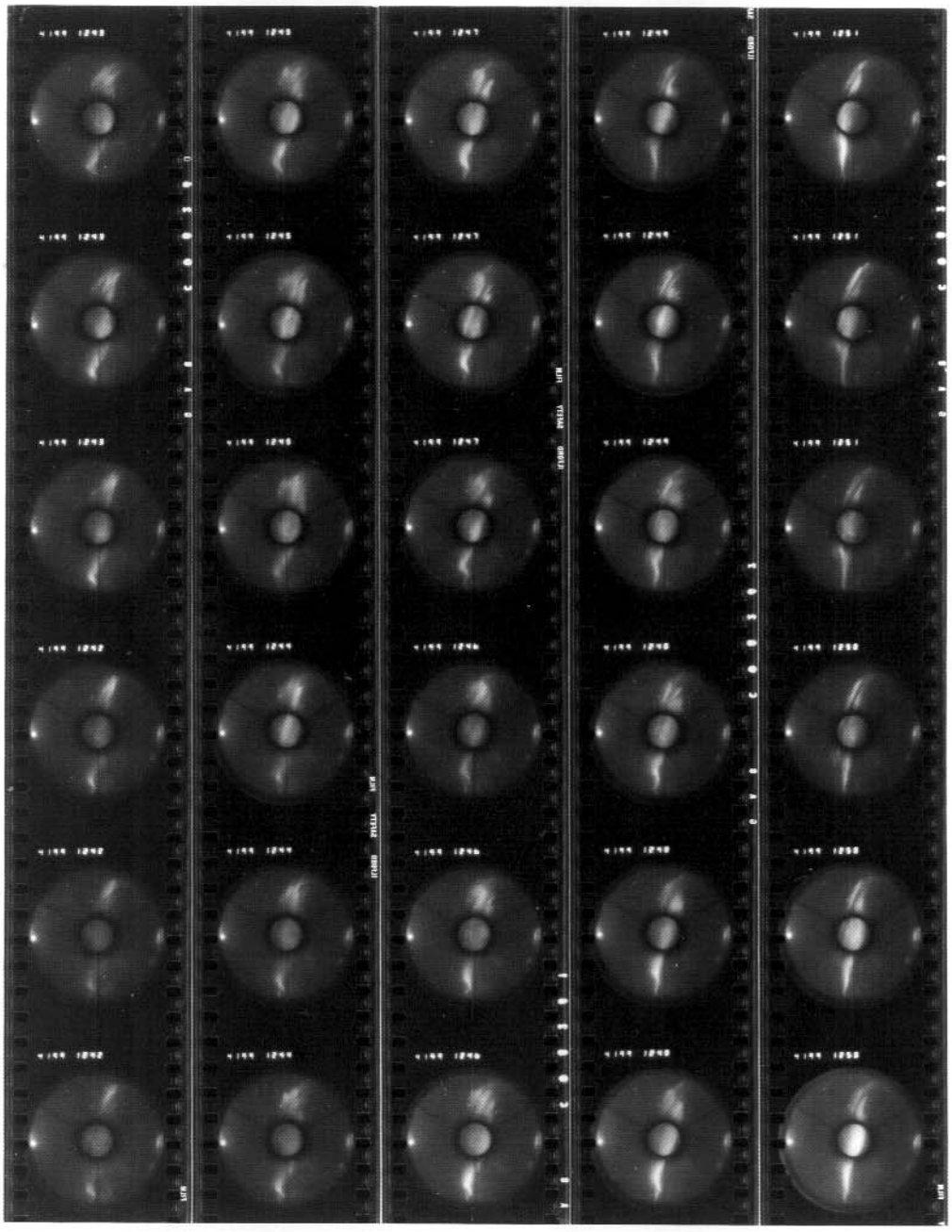

Figure 3. A 20 second resolution ASC image sequence of the development of an auroral kink event taken at Davis on the 17 July 1988. Time increases from the lower left corner to the top right corner of the picture series. The time period covered is from 1242-1251 UT (approximately 15 MLT). ASC orientation is the same as for Figure 2.

As Kp increases, kink events have a percentage occurrence which tends to peak at an earlier time (Figure 6). This may be a manifestation of the latitudinal motion of the entire cusp-cleft regions with changes in the level of magnetic activity and location of kink events relative to these regions.

*17.3.2 Post-noon pulsating aurorae*

Figure 7 displays representative samples of auroral optical pulsations (at 557.7 nm) and associated magnetic pulsation activity, as recorded at Davis 1988. The occurrence of pulsating auroral activity is calculated as the percentage of 10 minute intervals which exhibited pulsations, binned in half-hour time slots. Activity peaked at some 14.5% in the 1330-1400 MLT time sector. While a significant percentage of pulsation activity (12.3%) was observed at the authors earliest observing period (1300-1330 MLT), none was detected later than 1630 MLT. A histogram of the percent occurrence rate of pulsating aurorae appears in Figure 8. In all, pulsating aurorae were observed on 11 of the 89 days during which photometric observations with at least some observing period prior to 1430 MLT were possible.

The pulsation periods observed at Davis are generally around 20-30 seconds. These periods are typically longer than those recorded in the post-midnight auroral zone which are around two to ten seconds. For typical post-midnight auroral zone optical pulsations see for example the observations from Macquarie Island (64.5°S inv.) presented by Burns and Craven (1988). The

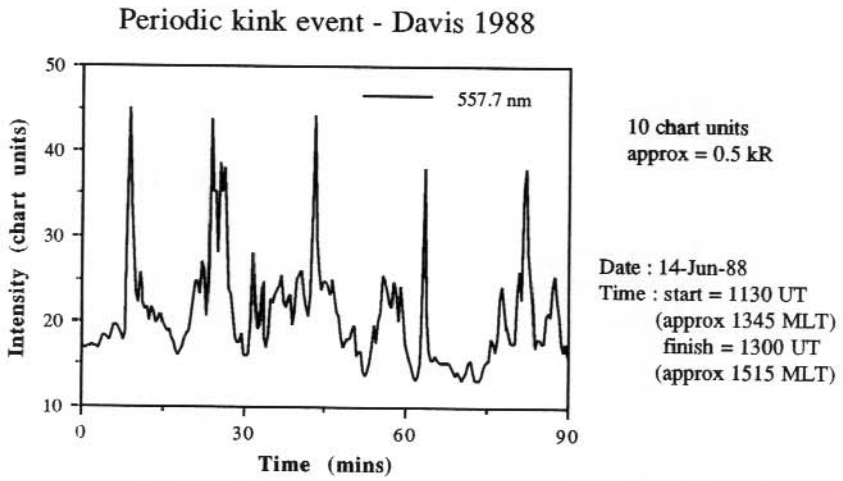


Figure 4. Periodic auroral kink event observed from Davis on the 14 June 1988, 1130-1300 UT (approximately 1345-1515 MLT). The 557.7 nm photometer record shows five major post-noon auroral enhancements of around 1.5 kR intensity on a 1 kR background, with a temporal separation of about 20 minutes between maxima. For the same period, the riometer signal exhibits little or no absorption, while the large-scale magnetic field, as measured by the fluxgate magnetometer, suffers minor deflections only, as shown on following page.

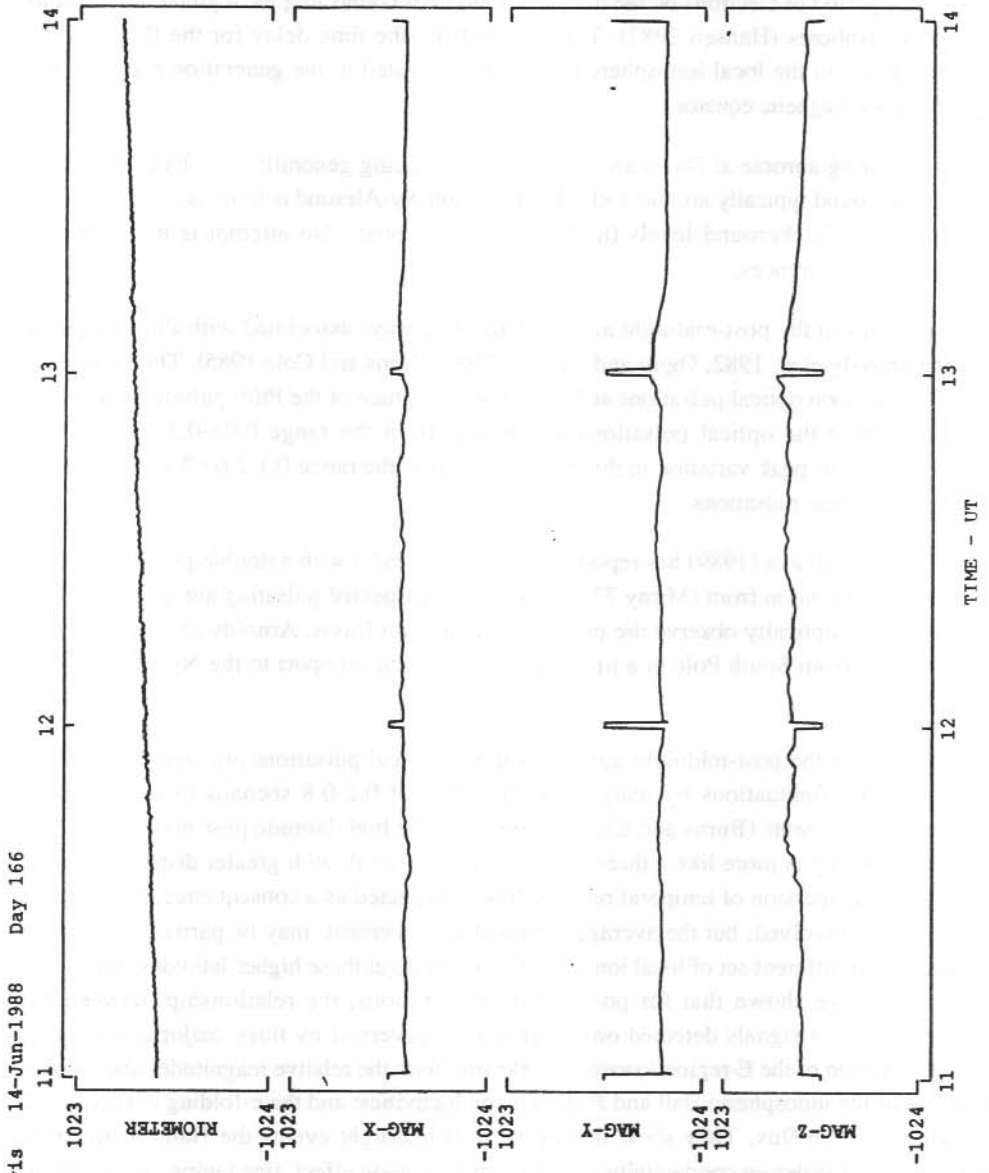


Figure 4. (continued)

pulsation periods recorded at Davis are found to be consistent with the high latitude pre-noon pulsations observed at Ny-Alesund by Brekke and Pettersen (1971). The longer periods associated with high latitude auroral pulsations are in accordance with particle energies of some 200-500 eV (Hansen 1990). In currently accepted theories for the generation of pulsating aurorae (Davidson 1986a, 1986b), the minimum permissible period for pulsations is related to the quarter-bounce period of electrons on the magnetic field lines connecting the high latitude regions in the two hemispheres (Hansen 1987). This results from the time delay for the flux loss via particle deposition in the local ionosphere to be communicated to the generation region in the vicinity of the geomagnetic equator.

Post-noon pulsating aurorae at Davis are of low intensity being generally less than 250 R on a low-level background typically around 1 kR. The pre-noon Ny-Alesund activity was reported as a 5% fluctuation on background levels (magnitudes not quoted). No attempt is made here to account for these differences.

Optical pulsations in the post-midnight auroral zone are always associated with Pi(c) magnetic pulsations (Arnoldy et al. 1982, Oguti and Hayashi 1984, Burns and Cole 1985). This is also the case for the post-noon optical pulsations at Davis. The magnitude of the Pi(c) pulsations recorded in association with the optical pulsations was generally in the range 0.03-0.3 nT $s^{-1}$. This amounts to a peak-to-peak variation in the magnetic field in the range 0.1-2.0 nT for the typical period regime of these pulsations.

It is noted that Troitskaya (1989) has reported high latitude Pi(c) with a double peak occurrence centred on magnetic noon from (Mirny 77.1°S inv.). It is suspected pulsating aurorae match this pattern but cannot optically observe the pre-noon sector from Davis. Arnoldy et al. (1986) also report Pi activity from South Pole in a time sector which lends support to the Ny-Alesund pre-noon observations.

For observations in the post-midnight auroral oval, the optical pulsations are seen to generally lead the magnetic fluctuations by margins of the order of 0.2-0.8 seconds as measured by ground-based instruments (Burns and Craven 1988). For the high latitude post-noon events this temporal relationship is more like a three second lead in general, with greater dispersion in the result. A greater dispersion of temporal relationships is expected as a consequence of the longer pulsation periods involved, but the average temporal displacement may be partially due to the manifestation of a different set of local ionospheric conditions at these higher latitudes. Burns and Craven (1988) have shown that for post-midnight pulsations, the relationship between the magnetic and optical signals detected on the ground is governed by three major contributing factors: the direction of the E-region ionospheric electric field; the relative magnitudes and altitude dependences of the ionospheric Hall and Pedersen conductivities; and the e-folding energy of the precipitating electron flux. They show that in the post-midnight events the Hall conductivity dominates with the Pedersen conductivity acting as a perturbation effect, fine tuning the manner in which the H and D geomagnetic components relate to the optical signal. At high latitudes Hall and Pedersen conductivities peak at higher altitudes with comparable magnitudes (Walker et al. 1978).

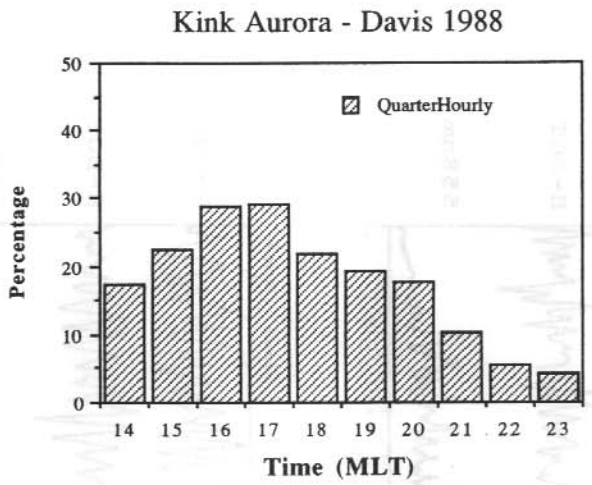


Figure 5. Probability of occurrence of auroral kink events (calculated as the percentage of 15 minute periods which contain activity, collated in 1 hour time bins) at Davis during the 1988 austral winter. The probability of observing kink activity peaks at some 30% around 16-17 MLT. These figures are derived solely from the zenith oriented 1° latitude field-of-view photometer records.

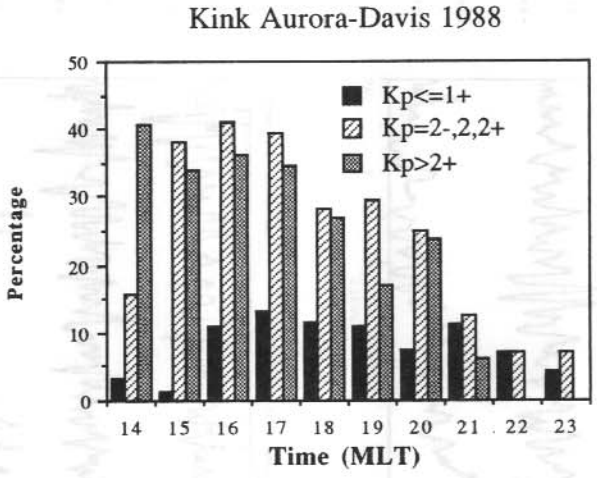


Figure 6. Kp dependence of kink aurora as determined from Davis 1988 photometric data. Kp has been split into three levels of activity chosen to give statistical significance to the figures obtained within each category. For higher Kp values the occurrence rate tends to peak in a slightly earlier MLT sector.

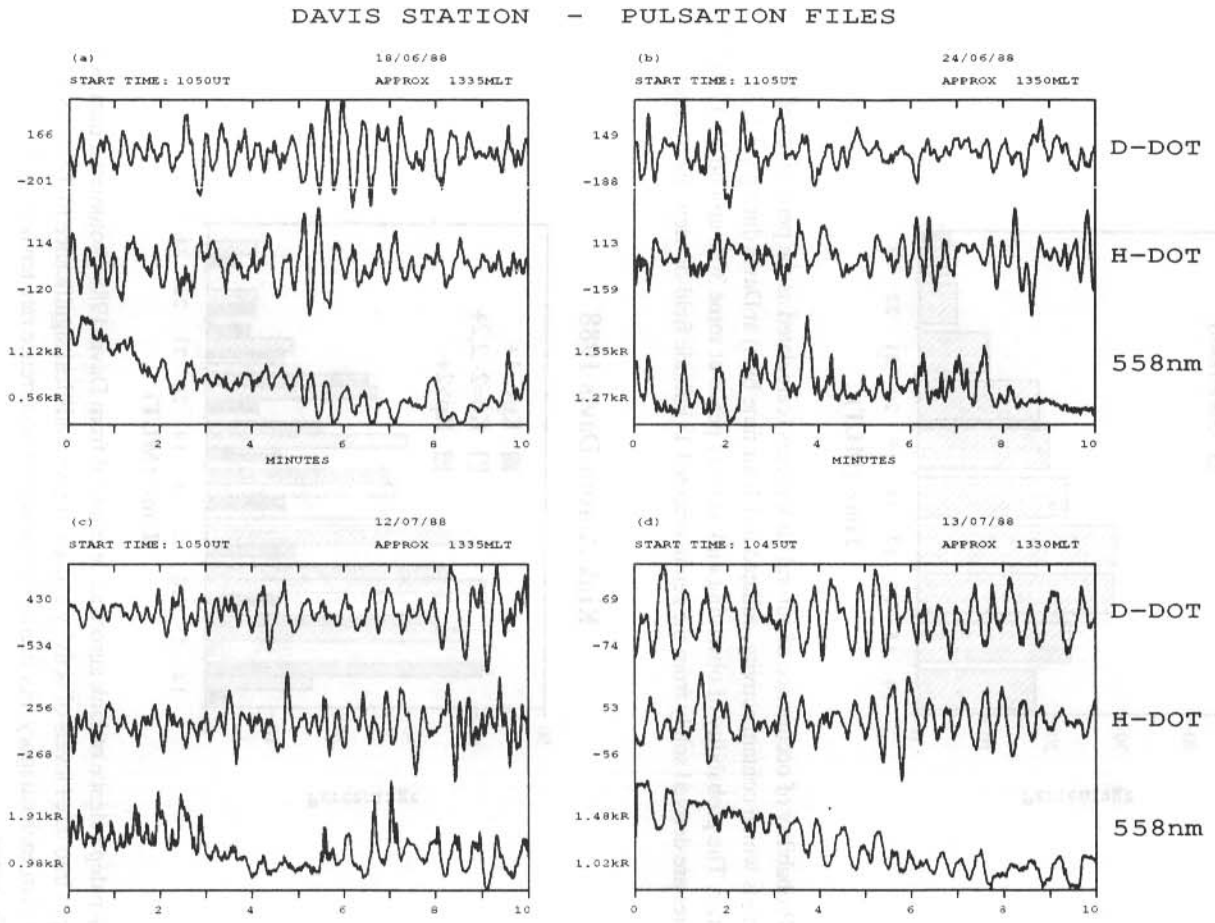


Figure 7. Examples of post-noon high latitude pulsating auroral records from Davis 1988 in the 557.7 nm photometer channel. Periods between 20-30 seconds are clearly evident. Pulsation magnitudes are typically less than 250 R on a 1 kR background. Also shown are the magnetic pulsation H and D files for the corresponding times.

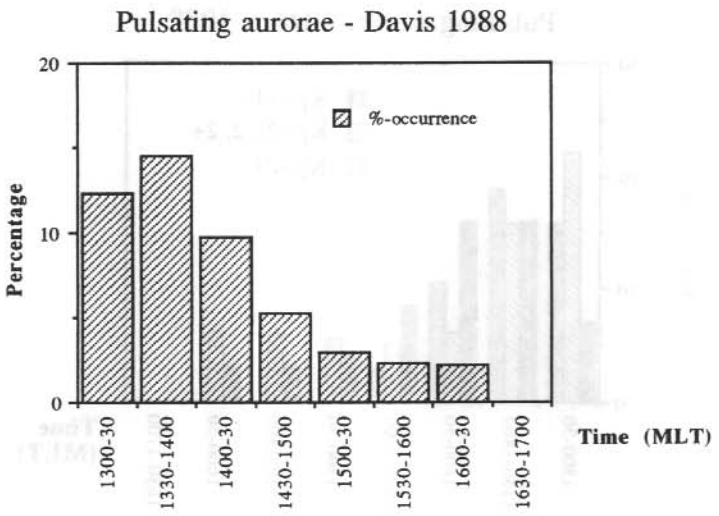


Figure 8. Histogram depicting the rate of occurrence (determined as the percentage of 10 minute periods which contain activity, binned in half hour time slots) of pulsating aurora as observed from Davis 1988. Activity peaks at some 14.5% in the 1330-140 MLT slot. No pulsating auroral events were detected at Davis beyond 1630 MLT.

Pulsating aurorae tend to peak in an earlier time sector as Kp increases. This is shown in Figure 9. The equatorward latitudinal movement of the cusp and cleft regions with increasing geomagnetic activity, means that a station such as Davis will find itself inside the polar cap, and hence under field lines which are open in the magnetosphere, at earlier MLT times in the post-noon sector. Closed field lines are a necessary prerequisite of present theories for the occurrence of pulsating aurorae.

IMP 8 data has been accessed in the form of hourly averages and standard deviations for each of the three components of the IMF (interplanetary magnetic field). Auroral pulsations at Davis were confined to the 1300-1630 MLT sector. During the 1988 austral winter observation period there were some 36 days when IMF data were available for this time sector. On only three occasions were all three of the IMF components positive. These coincide with the only pulsating auroral occurrences during the 36 days of IMF data availability. Bythrow et al. (1988) state that for IMF $B_z$ and $B_y$ both positive the LLBL, whose field lines map into the dayside high latitude regions (Vasyliunas 1979, Bythrow et al. 1981, Eastman et al. 1985), is likely to be populated by magnetosheath particles (energies around 500 eV) residing primarily on closed field lines. It is possible that the quiet magnetospheric condition ($B_z$ positive) is a minimum prerequisite for post-noon high latitude pulsating aurorae.

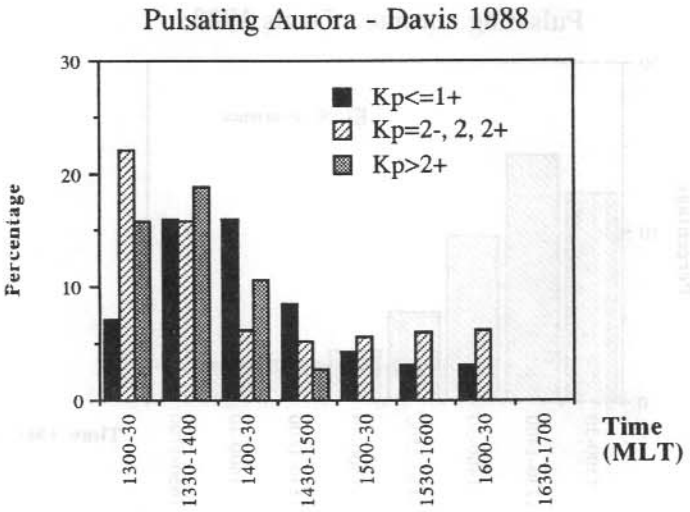


Figure 9. Kp dependence of pulsating aurora from Davis 1988. The data are again split into three levels of Kp activity, and a small trend exists for pulsating aurorae to occur earlier in the afternoon sector as Kp increases.

The Davis observations show that pulsating aurorae do occur for a significant portion of the time in the high latitude post-noon MLT sector. The mechanism for pulsating aurorae is generally agreed to be an electron-cyclotron wave-particle interaction between trapped electron fluxes and VLF waves in the whistler mode, in the vicinity of the geomagnetic equator (Davidson 1986a, 1986b, Hansen 1987). VLF chorus emissions can effect a coherent injection of electrons into the loss-cone for precipitation at ionospheric altitudes. Pulsating chorus elements have been detected on the dayside of the magnetosphere (Cornilleau-Wehrlin et al. 1978). The requirement of trapped electron fluxes on closed field lines, for the production of auroral pulsations, seems to be adequately met. Sonnerup (1980) has presented a theory for the LLBL which involves FAC (field-aligned currents) into the post-noon high latitude ionosphere as Region 1 currents (Iijima and Potemra 1976). That appropriate energy fluxes do exist on closed field lines mapping to the high latitude post-noon sector ionosphere, for appropriate IMF conditions, has already been indicated (Bythrow et al. 1988). It would appear that the Davis results reported here fit with recent magnetospheric observations and the current understanding of the production mechanism for pulsating aurora.

*17.3.3 Auroral break-up events*

Although predominantly a phenomenon centred on magnetic midnight, these break-up events can intrude into the afternoon sector. They are always accompanied by large amplitude PiB magnetic pulsations.

When the Kp level is greater than or equal to 3- it is almost certain that a break-up event will occur at Davis within the three hour period for which the Kp level applies (Figure 10). This figure is still around 67% for a Kp of 2. The level of geomagnetic activity appears to be the controlling factor responsible for the occurrence of break-up events in the afternoon sector.

Much has been reported in the literature on substorm activity and auroral break-up events throughout the auroral zone in all MLT sectors. They are mentioned briefly here only to complete the description of auroral events observed at Davis.

## 17.4 FUTURE RESEARCH

A number of areas of this research are amenable to further studies.

### *17.4.1 Kink aurorae*

1. Absolute calibration of the optical signatures would enable a more accurate determination of the energies of the incident particles. The authors feel confident that they achieved this with the 557.7 nm channel, but unfortunately ran into problems with the 427.8 nm channel due to leakage outside the passband (this proved to be a problem with the spectral range of the calibration lamp and would not significantly manifest itself during auroral observations). Since the electron energies involved in this type of event are quite low (E < 150 eV), it is desirable to also record intensities at 630.0 nm. The ratio of intensities 630.0/427.8 is a much more sensitive indicator of electron energies.

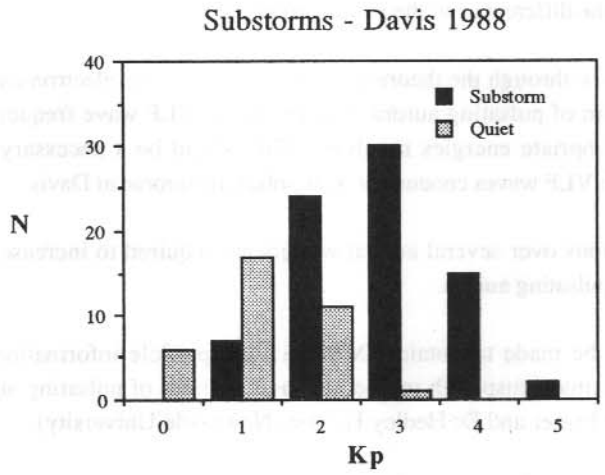


Figure 10. Histogram giving a general overview of the Kp dependence of main phase auroral break-up events observed from Davis 1988.

2. Coordinated ground-based and satellite observations of events is essential to be certain that the kink aurorae presented here are the ground-recorded signature of the Viking UV Imager post-noon bright spots.
3. An auroral TV imager system would be invaluable in this type of research. The authors would then be able to dynamically follow the temporal and spatial development, including drifts, of these events with great precision. This would be an important test of any theoretical modelling of these post-noon auroral enhancements.

*17.4.2 Pulsating aurorae*

1. Fully calibrated optical channels, with inclusion of the 630.0 nm wavelength measurement, would provide a more sensitive indicator of the energetics of pulsation events. It should be possible to look for spectral hardening at optical maxima indicating a spectral hardening of the electron fluxes (as has been found by MacDougall et al. (1981) for the post-midnight optical pulsations).

2. Sonograms of the magnetic pulsation data, which of course are unaffected by the twilight limiting observing conditions on the optical channels, would complete the morphology of the Pi(c) pulsations at such high latitudes. As indicated in Section 17.3.2, it is expected a noon-centred double peak is in occurrence. This would indicate the presence of pre-noon high latitude pulsating aurorae at Davis to supplement the previous Ny-Alesund reports. This study is essential to differentiate between the Pi(c) pulsations and Pc3 pulsations of similar frequency regime also known to occur at high latitude stations (Morris and Cole 1987). Since preparing this work a paper by Engebretson et al. (1990) has appeared which approaches South Pole optical pulsations from a Pc3 standpoint. It is of major importance now to complete this proposed sonogram study in order to highlight the differences in the two approaches.

3. It remains to follow through the theoretical calculations for the electron-cyclotron resonance production mechanism of pulsating aurora. What range of VLF wave frequencies interact with electrons of the appropriate energies involved? This would be a necessary precursor to any attempt to detect such VLF waves concurrent with pulsating aurorae at Davis.

4. Further observations over several austral winters are required to increase the data suite for IMF correlation and pulsating aurora.

5. Attempts should be made to obtain DMSP satellite particle information to pin-point the position of the low altitude cusp with respect to Davis at times of pulsating aurorae (suggestion from Professor Brian Fraser and Dr Hedley Hansen, Newcastle University).

6. There is still a need to follow through the ionospheric current system calculations, as outlined in Burns and Craven (1988) for the perturbations due to the precipitating electron fluxes, for high latitude ionospheric parameters. This will yield a better understanding of the temporal

relationships expected between the optical and magnetic pulsation signals at these higher latitudes, and give a possible means of determining the direction of the ionospheric electric field at these times.

## 17.5 ACKNOWLEDGMENTS

The observations were carried out at the Australian National Antarctic Research Expedition's (ANARE) station at Davis. The authors thank the Director, Antarctic Division, for logistical support. The authors would also like to acknowledge the invaluable discussion on the production mechanism of pulsating aurorae with Dr Hedley Hansen, University of Newcastle. The IMF data was obtained indirectly from the NSSDCA data archives. The authors appreciate the provision of this facility and thank Mr David Steele, ISAS, Saskatoon for accessing the data on their behalf.

## 17.6 REFERENCES

Anger, C.D., Fancroft, T., McNally, J. *and* Kerr, H.S. (1973). ISIS-2 scanning auroral photometer. *Applied Optics 12*:1753-1759.

Anger, C.D., Babey, S.K., Broadfoot, A.L., Brown, R.G., Cogger, L.L., Gattinger, R., Haslett, J.W., King, R.A., McEwen, D.J., Murphree, J.S., Richardson, E.H., Sandel, B.R., Smith, K. *and* Vallance-Jones, A. (1987). An ultraviolet auroral imager for the Viking spacecraft. *Geophysical Research Letters 14*:387-390.

Arnoldy, R.L., Dragoon, K., Cahill, L.J., Mende, S.B. *and* Rosenberg, T.J. (1982). Detailed correlations of magnetic field and riometer observations at L = 4.2 with pulsating aurora. *Journal of Geophysical Research 87*:10449-10456.

Arnoldy, R.L., Cahill , L.J., Eather, R.H. *and* Engebretson, M.J. (1986). Greater than 0.1 Hz ULF magnetic pulsations measured at South Pole. *Journal of Geophysical Research 91*:5700-5710.

Brekke, A. *and* Pettersen, H. (1971). Some observations of pulsating aurora at Spitzbergen. *Planetary and Space Science 19*:536-540.

Burns, G.B. *and* Cole, K.D. (1985). Ionospheric sources of Pi(c) pulsations. *Journal of Atmospheric and Terrestrial Physics 47*:587-599.

Burns, G.B. *and* Craven, M. (1988). Pi(c) magnetic pulsations: their relation to ionospheric currents. *Journal of Atmospheric and Terrestrial Physics 50*:231-241.

Bythrow, P.F., Heelis, R.A., Hanson, W.B. *and* Power, R.A. (1981). Observational evidence for a boundary layer source of dayside Region 1 field-aligned currents. *Journal of Geophysical Research 86*:5577-5589.

Bythrow, P.F., Potemra, T.A., Erlandson, R.E. *and* Zanetti, L.J. (1988). Birkeland currents and charged particles in the high-latitude prenoon region: a new interpretation. *Journal of Geophysical Research 93*:9791-9803.

Campbell, W.H. (1970). Rapid auroral luminosity fluctuations and geomagnetic field pulsations. *Journal of Geophysical Research 75*:6182-6208.

Cogger, L.L., Murphree, J.S., Ismail, S. *and* Anger, C.D. (1977). Characteristics of dayside 5577 A and 3914 A aurora. *Geophysical Research Letters 4*:413-416.

Cornilleau-Wehrlin, N., Gendrin, R., Lefeuvre, F., Parrot, M., Grard, R., Jones, D., Bahnsen, A., Ungstrup, E. *and* Gibbons, W. (1978). ELF electromagnetic waves observed on-board GEOS-1. *Space Science Reviews 22*:371-382.

Cresswell, G.R. *and* Davis, T.N. (1966). Observations of pulsating auroras. *Journal of Geophysical Research 71*:3155-3163.

Davidson, G.T. (1986a). Pitch angle diffusion in morningside aurora 1. The role of the loss cone in the formation of impulsive bursts of precipitation. *Journal of Geophysical Research 91*:4413-4427.

Davidson, G.T. (1986b). Pitch angle diffusion in morningside aurora 2. The formation of repetitive auroral pulsations. *Journal of Geophysical Research 91*:4429-4436.

Eastman, T.E., Popielawska, B. *and* Frank, L.A. (1985) Three-dimensional plasma observations near the outer magnetospheric boundary. *Journal of Geophysical Research 90*:9519-9539.

Engebretson, M.J., Cahill, L.J., Arnoldy, R.L., Mende, S.B. *and* Rosenberg, T.J. (1983). Correlated irregular magnetic pulsations and optical emissions observed at Siple station, Antarctica. *Journal of Geophysical Research 88*:4841-4852.

Engebretson, M.J., Anderson, B.J., Cahill, L.J., Jr., Arnoldy, R.L., Rosenberg, T.J., Carpenter, D.L., Gail, W.B. *and* Eather, R.H. (1990). Ionospheric signatures of cusp latitude Pc3 pulsations. *Journal of Geophysical Research 95*:2447-2456.

Hansen, H.J. (1987) *Wave-particle generation of pulsating aurorae*. Ph. D. thesis, University of Natal.

Hansen, H.J. (1990). (private communication).

Heppner, J.P. (1954) *A study of relationships between the aurora borealis and the geomagnetic disturbance caused by electron currents in the ionosphere*. Ph. D. thesis, California Institute of Technology.

Iijima, T. *and* Potemra, T.A. (1976). The amplitude distribution of field-aligned currents at northern high latitudes observed by Triad. *Journal of Geophysical Research 81*:2165-2174.

Johnstone, A.D. (1978) Pulsating aurora. *Nature 274*:119-126.

Johnstone, A.D. (1983) The mechanism of pulsating aurora. *Annales de Geophysique 1*:397-410.

Lui, A.T.Y., Venkatasan, D., Rostoker, G., Murphree, J.S., Anger, C.D., Cogger, L.L. *and* Potemra, T.A. (1987). Dayside auroral intensifications during an auroral substorm. *Geophysical Research Letters 14*:415-418.

Lui, A.T.Y., Venkatasan, D. and Murphree, J.S. (1989). Auroral bright spots on the dayside oval. *Journal of Geophysical Research 94*(A5):5515-5522.

MacDougall, J.W., Koehler, J.A., Hofstee, J. *and* McEwen, D.J. (1981). Electron energy measurements in pulsating aurora. *Canadian Journal of Physics 59*:1049-1055.

McDiarmid, I.B., Burrows, J.R. *and* Budzinski, E.E. (1975) Average characteristics of magnetospheric electrons (150eV - 200eV) at 1400km. *Journal of Geophysical Research 80*:73-79.

Morris, R.J. *and* Cole, K.D. (1987). Pc3 magnetic pulsations at Davis, Antarctica. *Planetary and Space Science 35*:1437-1447.

Oguti, T. *and* Hayashi, K. (1984). Multiple correlation between auroral and magnetic pulsations 2. Determination of electric currents and electric fields around a pulsating auroral patch. *Journal of Geophysical Research 89*:7467-7481.

Reid, J.S. (1976). An ionospheric origin for Pi1 micropulsations. *Planetary and Space Science 24*:705-710.

Sonnerup, B.U.O. (1980). Theory of the low latitude boundary layer. *Journal of Geophysical Research 85*:2017-2026.

Troitskaya, V.L. (1989). (private communication).

Vasyliunas, V.M. (1979). Interaction between the magnetospheric boundary layers and the ionosphere. In: Battrick, B. (Ed.). *Magnetospheric Boundary Layers Rep. ESA SP-148*:387-393, Noordwijk, Netherlands.

Walker, J.K., Daly, P.W., Pongratz, M.B., Stenbaek-Nielsen, H.C. *and* Whitteker, J.H. (1978). Cleft currents determined from magnetic and electric fields. *Journal of Geophysical Research 83*:5604-5616.

# 18. OPTICAL AURORAL CONJUGACY: HISTORY AND POTENTIAL

G.B. Burns[1,2], D.J. McEwen[2], D. Steele[2] and D. Hearn[3]

[1]Antarctic Division
Kingston Tas 7050
Australia

[2]Institute of Space and Atmospheric Studies
University of Saskatchewan
Saskatoon Sask S7N 0W0
Canada

[3]Physics Department
University of Calgary
Calgary Alberta T2N 1N4
Canada

ABSTRACT

A brief review of ground-based optical conjugacy studies is given. 'Internal' magnetic field models (the International Geomagnetic Reference Field/ Definitive Geomagnetic Reference Field series) and an 'external' magnetic field model (Tsyganenko 1987) are utilised to predict variations in conjugate locations. The Tsyganenko (1987) model is shown to predict diurnal, seasonal, latitudinal, longitudinal (or UT dependent) and 'level of magnetic activity' variations in the locations of conjugate points. The displacements from internal field model calculated conjugate locations are predicted to maximise at high latitudes, for high levels of magnetic activity and in the solstices. The expanded opportunities for optical auroral conjugacy studies presented by high time resolution, UV auroral imagers on satellites are discussed.

## 18.1 INTRODUCTION

That the aurora and the earth's magnetic field are associated became apparent almost as soon as measurements of the magnetic field were made in the northern hemisphere. Auroral displays are accompanied by fluctuations in the magnetic field. The existence of an aurora in the south polar regions was also readily inferred. When it became apparent that electrons hitting the atmosphere from above were the principal cause of auroral glows, a more detailed correspondence of auroral forms in opposite hemispheres was expected.

Electrons, as charged particles, are constrained to move along magnetic field lines in a helical fashion at altitudes above where the electron gyrofrequency exceeds the electron collision frequency. Generally, an electron spiralling into the atmosphere in one hemisphere is, if it does not interact with some atmospheric constituent, 'reflected' by the increasing magnetic field and travels back along the field line to the other hemisphere. A typical auroral electron takes of the

order of 10 s to travel from the auroral region in one hemisphere, along the magnetic field line, to the auroral region in the other hemisphere. Thus, if auroral activity occurs on 'closed' field lines (ie magnetic field lines that intersect the earth in both hemispheres), then a detailed spatial and temporal correspondence of auroral forms in both hemispheres may be expected.

An experimental definition of auroral conjugacy has been given by Wescott (1966).

> 'Conjugacy is said to exist if the similarity of auroral observations is such as to imply a linkage between the hemispheres.'

Optical auroral conjugacy is generally established by showing a similarity in the spatial distribution and temporal development of auroral forms in the two hemispheres. If similarity in these aspects is such that a 'linkage between hemispheres' is accepted, then the experimentally determined conjugate point to a site in one hemisphere can be defined as that point in the opposite hemisphere at which the spatial distribution and temporal development of the auroral forms is most similar.

As has already been noted, it is the earth's magnetic field which provides the 'linkage between the hemispheres'. Models of the earth's magnetic field can thus be used to predict where conjugate points will be located.

The ability to compare predicted and measured observations is essential to the confirmation and development of understanding. Recent advances in satellite auroral imaging instrumentation have significantly increased the potential to experimentally determine conjugate locations by optical techniques. Recent advances in modelling of the earth's magnetic field allow predictions of variations in conjugate locations to be made. Together these advances provide a means to test and improve the understanding of the interaction of the solar wind and the earth's magnetosphere.

## 18.2 'GROUND-BASED' OPTICAL CONJUGACY STUDIES

Optical proof of the detailed correspondence of auroras in opposite hemispheres was difficult to obtain. The southern hemisphere observing sites were (and still are) sparsely located. The relative hemispheric distributions of land and water meant that the northern hemispheric conjugates to existing sites were often difficult or impossible to occupy; the seasonal variations in the hours of darkness between the high latitude regions of the two hemispheres means that only for a limited amount of time are both conjugate sites dark enough for simultaneous auroral observations. Some conjugate sites are further hampered by poor weather conditions.

The first substantive proof of the inter-hemispheric similarity of auroral forms was published by De Witt (1962). De Witt analysed all-sky camera data collected during the International Geophysical Year from the conjugate pairs of Campbell Island/Farewell (Alaska) and Macquarie Island/Kotzebue (Alaska). In the data De Witt viewed, he found four nights from the Campbell Island/Fairwell pair and one night from the Macquarie Island/Kotzebue pair that were suitable for

analysis. De Witt showed that the aurora in opposite hemispheres had similar structure and varied in intensity with time in a consistent fashion.

Bond (1969) found eight useful days of conjugate Macquarie Island/Kotzebue all-sky camera data in the period from October 1962 to March 1963. He concluded that conjugate locations were close to the locations predicted for quiet, pre-break-up aurora, but could be slightly displaced during the later stages of an auroral substrom.

The Macquarie Island/ Alaska region was also the scene of the next major study of optical auroral conjugacy. The researchers, however went to considerable lengths to overcome the problem of poor observing conditions in this region. Aircraft equipped with all-sky and narrow-angle cameras were flown from Christchurch, New Zealand to south of Macquarie Island; and simultaneously along a conjugate flight path in Alaska. During selected days in 1967, 1968, 1970 and 1971, a total of 18 conjugate flights were undertaken. These data showed small differences in the intensity of the aurora in the two hemispheres which were related to the difference in the intensity of the magnetic field at auroral heights in each hemisphere (on average, the northern hemisphere aurora in this magnetic longitude region are some 30% brighter than their southern counterparts; Stenbaek-Nielsen et al. 1973), some displacements of the auroras from 'internal' (Section 18.3 ) magnetic field model predicted conjugate locations, and yielded one dramatic example which showed the field-of-view limitation of ground-based or airborne optical systems (Belon et al. 1969, Stenbaek-Nielsen et al. 1972,1973). The example was of an active aurora in the zenith of the southern hemisphere aircraft and clear skies in the expected conjugate region of the northern hemisphere. The field-of-view of ground-based or airborne optical instrumentation is limited to the order of 10° of latitude at auroral heights, thus displacements of the order of 5° of latitude from the expected conjugate location may be sufficient to move the aurora outside the field-of-view.

Recent ground-based studies of aurora at the conjugate sites of Syowa, Antarctica and Husafell, Iceland have shown the general consistency of broad-scale features, but dissimilarities in fine scale structure. The dissimilarities may be attributed to local acceleration processes (Sato et al. 1986, Fujii et al. 1987, Sato and Saemundson 1987).

Reviews by Nagata (1987) and Rycroft (1987) cover the development of conjugate studies in general.

Ground-based studies of optical auroral conjugacy are limited principally because observations can only be made during the hours of darkness. The seasonal variations in the hours of darkness in the two hemispheres limits the hours that are simultaneously available at conjugate sites for optical observations. This limitation increases in severity at higher latitudes. Readers are referred to Figure 22 in Rycroft (1987), which shows the number of possible hours of ground-based optical conjugate observations per annum for the northern hemisphere. The possible hours of simultaneous observations at conjugate sites also limit ground-based optical conjugacy studies to the night-time auroral oval, generally around the midnight sector. The seasonal variation in the

hours of darkness also means that the potential hours of simultaneous optical conjugacy observations occur predominantly during the equinoxes.

Another limitation to ground-based optical conjugacy observations has been previously alluded to. It is possible for auroral forms to be displaced from expected conjugate locations by an amount sufficient to take the conjugate form beyond the field-of-view of the instrumentation. This means that the researcher may have no idea of the direction or magnitude of the displacement from the expected conjugate location, or indeed if a conjugate auroral form exists.

## 18.3 MAGNETIC FIELD MODELS

The international geomagnetic reference field (IGRF) and definitive geomagnetic reference field (DGRF) series of magnetic field models underpin the coordinate systems most commonly used by auroral physicists. It is important to recognise the advantages and limitations of these models and the various coordinate systems that derive from them. Because these models represent the earth's field as the gradient of a scalar potential they cannot include any current systems within the region to which they are applied. This follows because 'current density' is proportional to the 'curl' of the magnetic field. The 'curl' of the gradient of a scalar function is mathematically a null, thus no current system can exist within the region to which these models are applied. The magnetosphere contains a number of current systems including the ring current, Birkeland (field-aligned) currents, magnetotail currents, and the magnetopause current systems. These current systems give the magnetosphere its day-night asymmetry and its dynamic nature. Essentially the IGRF and DGRF model series, and others of their type, represent the magnetic field the earth would have if there were no interaction with the solar wind. These types of models are known generically as 'internal' field models as they principally represent the field generated by the earth's core currents. Langel et al. (1988) is a recent publication of the IGRF/DGRF series which contains a good evaluation of the accuracy of the models.

The invariant coordinate system commonly utilised by auroral physicists is derived directly from the IGRF and DGRF series models. A coordinate system retains the limitations of the model from which it is derived. Centred dipole (best fit approximation to the IGRF/DGRF model of a dipole passing through the earth's centre) and eccentric dipole (best fit approximation to the IGRF/DGRF model of a dipole not constrained to pass through the earth's centre) models provide simpler analytic approximations to the IGRF and DGRF models. These suffer from the limitations of the 'internal' models from which they are derived and from additional discrepancies associated with the approximations made to achieve analytic simplicity. An excellent review of the derivation of centred dipole and eccentric dipole coordinate systems from IGRF/DGRF models, and a comparison of the differences they yield, has been published by Fraser-Smith (1987).

A consideration of the 'conjugate points' of the various models can give some idea of their advantages and disadvantages. IGRF/DGRF models are defined for a particular epoch. This is because the currents in the earth's core which generate the magnetic field, vary slowly with time in a manner which is not understood. This results in the so-called 'secular' variation. The

coefficients of the spherical harmonic coordinates used in these models are calculated for each five years. Models for different epoches may be interpolated from existing models or extrapolated from the latest model. If an internal field model for a particular epoch is used to trace a field line from a site in one hemisphere towards the other, then the analytic formulation of the models guarantees that the field-line trace will intersect the earth in the opposite magnetic hemisphere. Because of this, internal field models are said to describe 'closed' magneotospheres. The conjugate point reached by this method is the conjugate point that would be defined by the invariant coordinate system derived from the IGRF/DGRF model of that epoch. The conjugate point so defined does not vary diurnally or seasonally, except that a small variation can be expected due to 'secular' variation in the model from epoch to epoch. Figure 1 shows the secular variation in the location of the Macquarie Island (54.5°S 159.0°E geographic, 64.5°S invariant latitude) conjugate point from the time of the 1948 occupation of the island by Australian National Antarctic Research Expeditions (ANARE) through to 1990. The conjugate locations are obtained by field-line tracing the appropriate IGRF/DGRF model, interpolated or extrapolated to give yearly epoches. For later comparison it is noted that the variation in the conjugate location modelled by this means, over the time period indicated, is of the order of 85 km.

Because it essentially defines the conjugate location a site would have if there were no magnetospheric current systems, the invariant coordinate system defined conjugate locations (these are equivalently defined by field-line tracing the IGRF/DGRF model for the appropriate epoch) provides the most rational reference point from which to measure the displacement of measured or predicted conjugate locations. The displacements measured or predicted can be discussed in scientifically useful terms by reference to the magnetospheric current systems that have resulted in the displacement. Care must be taken that measured conjugate displacements are not referenced to predicted conjugate locations that contain significant inherent model approximations in them. As a specific example of the extent to which this may cause confusion consider two model predicted locations of the South Pole conjugate point. The IGRF 1985 model, extrapolated to July/August 1986 (epoch 1986.6) gives a field-line traced South Pole conjugate point of 64.5° N, 293.4° E (geographic; 74.1 invariant latitude, L=13.3). In the eccentric dipole coordinate system for the 1985 epoch, the South Pole conjugate point is located at 68.3° N, 288.8° E (Burns et al. 1990). This is a significant displacement and is not accounted for by the slight difference in epoch for the example given. The discrepancy derives principally from the approximations inherent in the simpler analytic expressions used in the eccentric dipole model (remember that the eccentric dipole model is derived as an approximation to the IGRF model). The displacement between the two model predicted locations is significantly larger than the error acceptable for any meaningful interpretation of predicted or experimentally determined conjugate locations. The eccentric dipole approximations are, as a general rule, more significantly in error in comparison with the IGRF model from which they are derived, the closer the site is to the invariant geomagnetic pole.

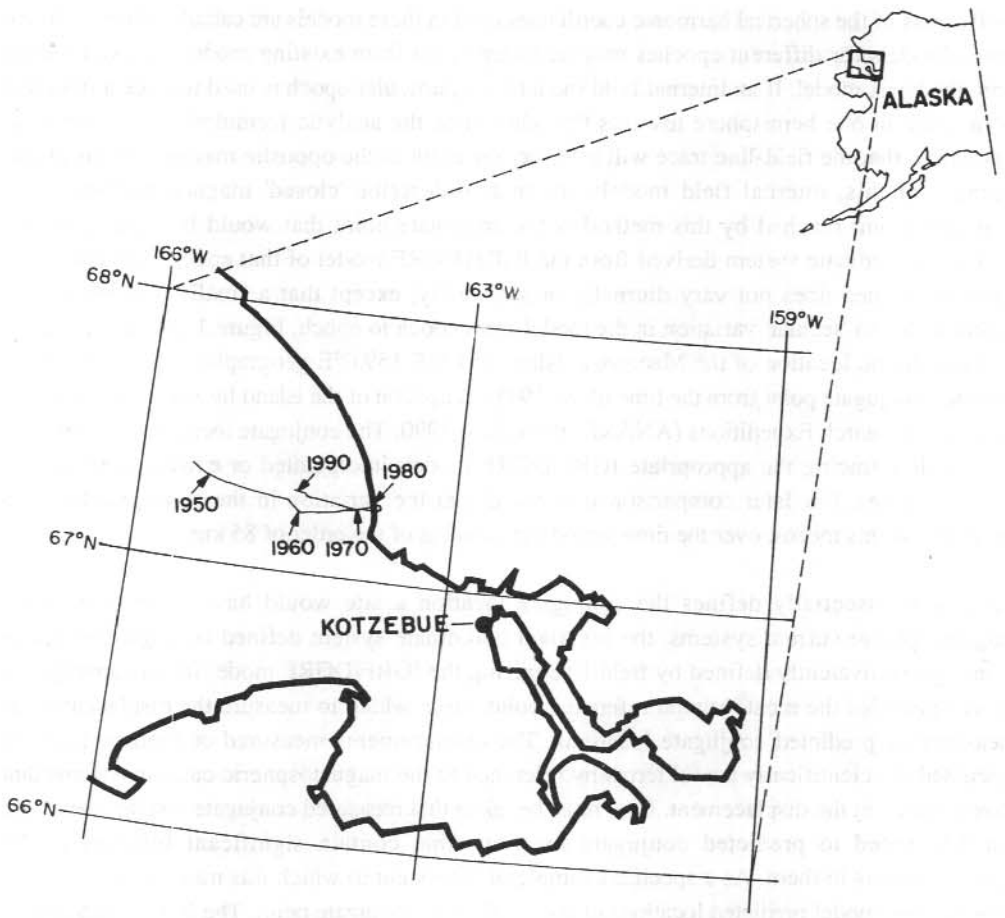


Figure 1. The 'secular' variation of the location of the Macquarie Island conjugate point. The IGRF/DGRF models were extrapolated/interpolated to give the conjugate location from 1948 to 1990. A geographic coordinate system is used to label the map.

'External' magnetic field models incorporate the major magnetospheric current systems as analytic expressions 'best-fitted' to satellite magnetic field measurements (Mead and Fairfield 1975, Tsyganenko and Usmanov 1982, Tsyganenko 1987, 1989). In a magnetic model that realistically incorporates the magnetospheric current systems, the 'field-line traced' conjugate point of any selected site will vary diurnally (as different current systems more significantly influence the field line trace), seasonally (as the range of angles that the earth's magnetic field makes to the sun-earth line varies, changing the relative influences of the current systems) and with magnetic activity (as the various current systems vary in strength and importance).

External magnetic field models have been used to predict variations in the conjugate locations to Siple (Antarctica, 76°S 276°E geographic, 61.1°S invariant latitude, Stassinopoulos et al. 1984) and Syowa (Antarctica, 69.0°S 39.6°E geographic, 66.2°S invariant latitude, Ono 1987). To illustrate some of the predictions and limitations of external magnetic field models, the Tsyganenko (1987) long-field model was utilised. This model consists of a 26 parameter fit to the major magnetospheric current systems for each of five levels of magnetic activity which are each specified as a range of Kp levels. The Tsyganenko model only specifies the current systems and thus must be incorporated with an appropriate internal field model. An appropriate epoch IGRF model was utilised.

In order to interpret some aspects of the Tsyganenko model predictions, it is necessary to understand the 'dipole tilt angle'. Consider the plane defined by the sun-earth line and the line of a centred dipole approximation to the earth's magnetic field. The 'dipole tilt angle' is the angle between the perpendicular to the sun-earth line in this plane, and the line of the dipole field. The angle is defined as positive when the northern magnetic hemisphere is tilted towards the sun. The dipole tilt angle varies between +35° and -35° annually. In the equinoxes it varies diurnally between +12° and -12°. In the southern winter solstice it varies between +35° and +12° diurnally. The importance of the dipole tilt angle is that it sets the angle that the earth's magnetic field makes to the solar wind pressure. It significantly controls the location of the magnetospheric current systems.

Figure 2 shows the Tsyganenko (1987) model predicted diurnal variation, at UT hourly intervals, for the magnetic activity levels and seasons indicated, of the Macquarie Island (54.5°S 159.0°E geographic, 64.5°S invariant latitude) conjugate point. It should be noted that the Tsyganenko model uses data for a range of Kp levels for determining the current system variations as the magnetic activity changes. For the examples introduced here, what is referred to in the figures and the text as the 'Kp 0' Tsyganenko model is derived from satellite magnetometer data obtained when Kp equalled 0 or $0^+$, the Kp 3 model is derived from data obtained when Kp was $3^-$, $3^0$ or $3^+$ and the 'Kp 5' model is derived from data with Kp $\geq 5^-$. An increased displacement from the IGRF predicted conjugate location (shown as a square on the plots) as the level of magnetic activity increases and a greater range of displacement for solstice periods compared to equinox periods (this is equivalent to greater displacements from the IGRF locations for larger dipole tilt angles, for the same UT time) are general features of the model predictions. The general

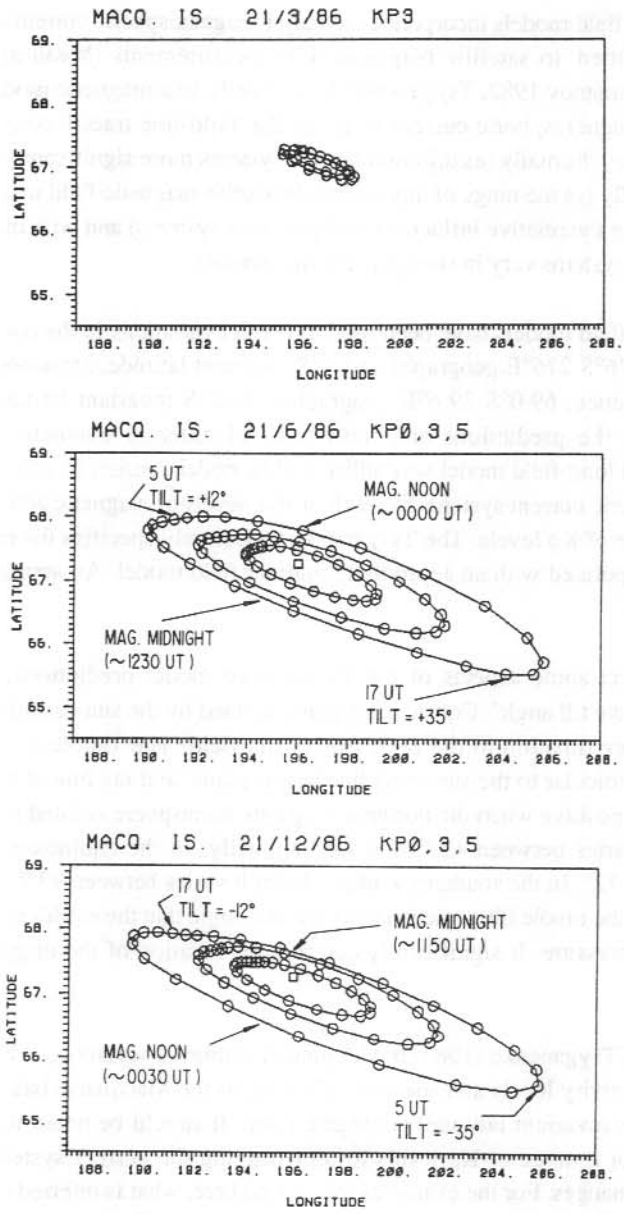


Figure 2. Tsyganenko (1987) model predictions of the diurnal variation in the Macquarie Island conjugate point for dates and levels of magnetic activity. High levels of magnetic activity generate curves with increasingly larger displacements from the IGRF conjugate location (squares). 'Circles' show Tsygannenko model predictions for each UT hour. East latitudes and longitudes shown are northern hemisphere geographic coordinates. The times of magnetic noon, magnetic midnight and maximum and minimum dipole tilt angles (see text) are shown on solstice curves.

restriction of ground-based optical conjugacy studies to the equinox period can be seen to severely limit the range of 'displacements' likely to be observed. The diurnal range of the predicted Macquarie Island conjugate point location for a solstice period and a Kp level of 3 is approximately 450 km. For an equinox period, for the same level of magnetic activity, the predicted diurnal range of the Macquarie Island conjugate point is 150 km. These compare with the range in the 'secular' variation of the Macquarie island conjugate location over a period of 43 years of the order of 85 km, as shown in Figure 1.

Figure 3 shows Tsyganenko (1987) model predictions for the diurnal variation in the location of the Mawson station (67.6°S 62.9°E geographic, 70.1°S invariant latitude) for the 'Kp 0' model and the seasons indicated. The diurnal range in the predicted conjugate points by the 'Kp 0' Tsyganenko model for Maquarie Island is of the order of 240 km and for Mawson is about 670 km. A general result is that the predicted diurnal ranges are larger for stations of higher invariant latitude, other conditions (season and level of magnetic activity) being equal.

Shown in Figure 4 are the predicted diurnal variations in the Mawson conjugate point for three levels of magnetic activity. This appears to be an attempt to push the Tsyganenko model beyond its reasonable limits. For higher levels of activity the predictions become more 'irregular' around 4 and 18 UT. The unrealistic variations shown around these times are most likely due to the difficulties mentioned by Tsyganenko (1987) in specifying the model around the flanks of the magnetosphere (the long model was used in all examples). These difficulties are only portents of the model difficulties with applying this approach to estimating conjugate locations for stations at higher latitudes and for high levels of magnetic activity. Once the influence of magnetospheric current systems is introduced into a model, there is no longer the mathematical constraint on the model ensuring that all field lines traced will reintersect the earth's surface. The model can thus have 'open' field lines. At high latitudes the field line traces generally pass close to, or even through, the magnetospheric current systems. The closer the field line trace comes to these, the more the approximations made by the model in representing the current systems influence the predicted conjugate location.

To show a 'longitude' effect predicted by the Tsyganenko model, and to help show that it is the dipole tilt angle that primarilly influences the model predictions, the authors wish to push things a little further. This effect could perhaps be better shown by choosing better locations to seek conjugate points for, but an initial interest was to investigate the possible diurnal variations in the conjugate points at some specific Antarctic sites. The model predicts that these stations are often on 'open' field lines. In order to get a 'feel' for possible diurnal variations (some of the travesties of the approach will be discussed after it is shown that the 'longitude effect' is apparent in the results) the following approach was adopted. The authors projected back along the great circle line from the south invariant pole (73.7°S 127°E geographic) through the station of interest and continued along this great circle until they reached a location which had an invariant latitude of 65°S. It is for these locations that the diurnal variation of the conjugate point for the southern winter solstice, for the 'Kp 3' model were calculated. The stations that provided the starting point

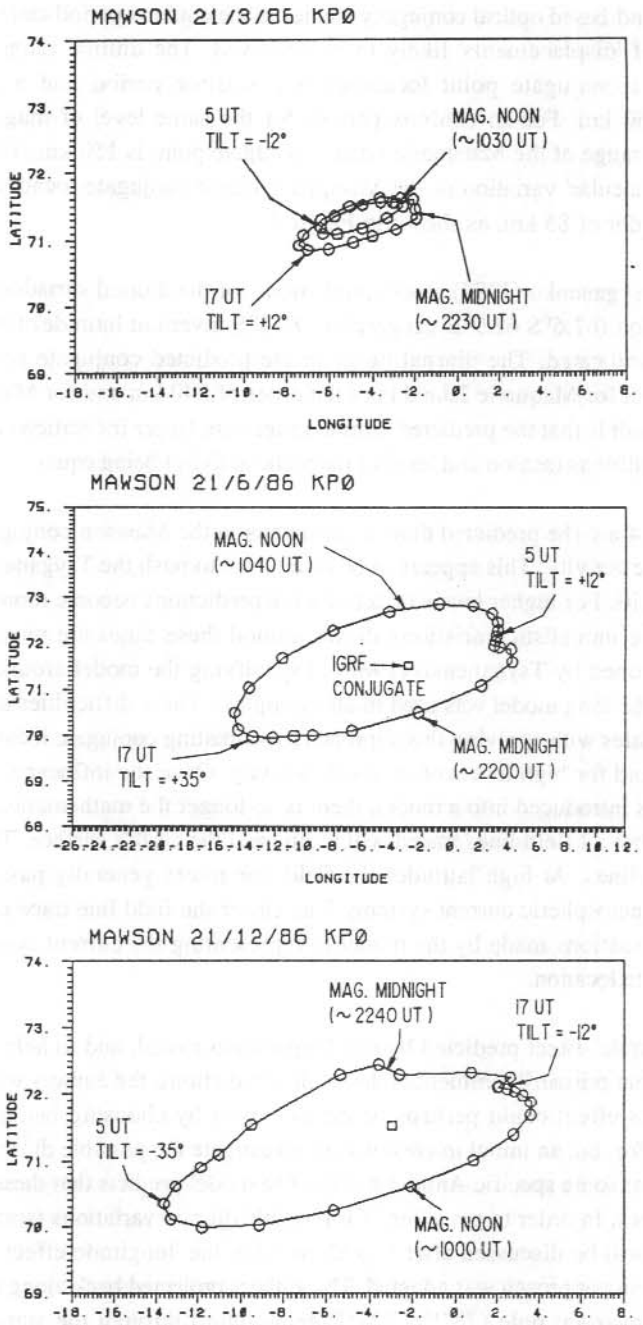


Figure 3. Tsyganenko (1987) model predictions for the diurnal variation in the conjugate locations of the Mawson station for 'Kp 0' and for the dates indicated. The labelling is as per Figure 2.

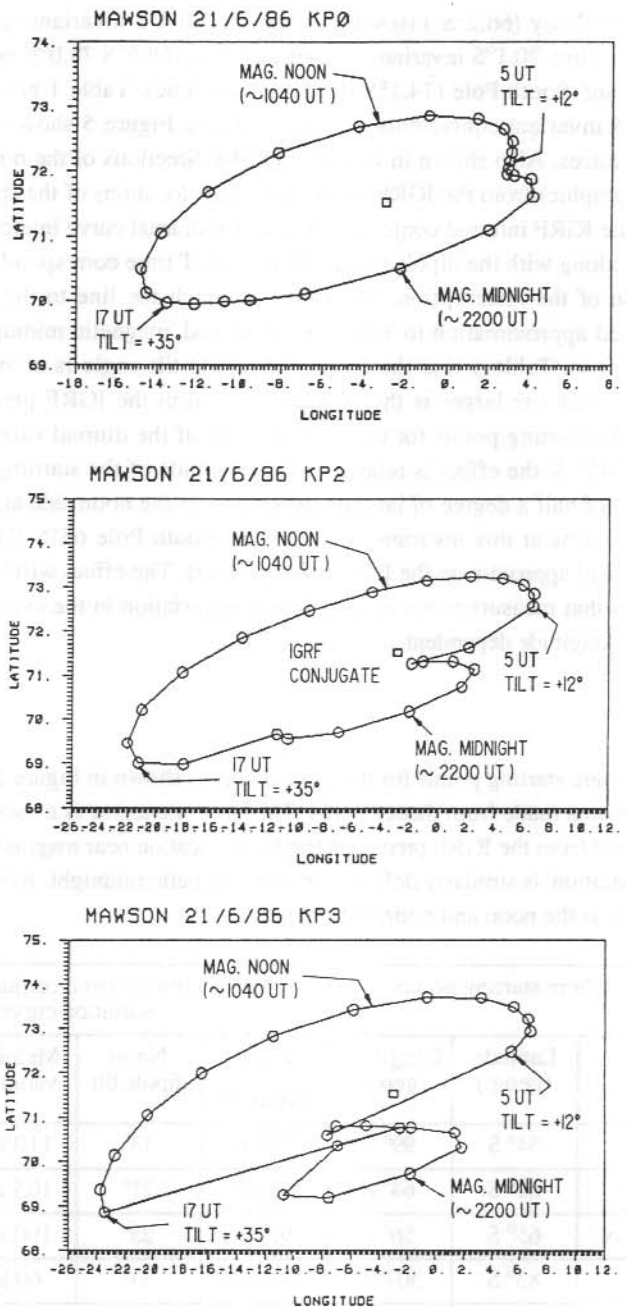


Figure 4. Tsyganenko (1987) model predictions for the diurnal variation in the conjugate location of Mawson station for the southern winter solstice and for three levels of magnetic activity as indicated. The labelling is as per Figure 2.

for this exercise were Casey (66.2°S 110.4°E geographic, 80.6°S invariant magnetic) Mawson (67.6°S 62.9°E geographic, 70.1°S invariant magnetic), Davis (68.6°S 78.0°E geographic, 74.6°S invariant magnetic) and South Pole (74.1°S invariant magnetic). Table 1 gives the geographic location of the '65°S invariant equivalents' of these stations. Figure 5 shows the results of the conjugate field line traces. Also shown in Figure 5 are the directions of the north invariant pole (81.2°N 277°E, geographic) from the IGRF model conjugate locations of the starting points. The displacement from the IGRF inferred conjugate point of the diurnal curve intercepts with this line are listed in Table 1 along with the dipole tilt angles at the UT time corresponding to the time on the diurnal variation of the interception. The times at which the line to the invariant pole is intercepted are a good approximation to 'magnetic noon' and 'magnetic midnight' for the initial sites. It is apparent from Table 1 that the larger the dipole tilt angle is at 'magnetic noon' or 'magnetic midnight', then the larger is the displacement from the IGRF predicted conjugate. Remembering that the starting points for the measurement of the diurnal variations all have an invariant latitude of 65° S, the effect is related to the longitude of the starting point. The effect amounts to in excess of half a degree of latitude difference on the noon side and slightly less for the night side for stations at this invariant latitude (the 'South Pole 65°S Equivalent' and the 'Casey 65°S Equivalent' approximate the limits of the effect). The effect will be larger at higher latitudes and implies that measurements such as seasonal variation in the average cusp location may be significantly longitude dependent.

Table 1. The geographic starting points for the diurnal curves shown in Figure 5 are listed along with some measurements made from those curves. The 'noon variation' is a measure of the poleward displacement from the IGRF predicted conjugate location near magnetic noon (see text) and the 'midnight variation' is similarly defined for near magnetic midnight. Also shown are the 'dipole tilts' (see text) at the noon and midnight times.

| Southern Hemisphere starting points | | | Measurements from conjugate diurnal variation curve | | | |
|---|---|---|---|---|---|---|
| Sites | Latitude (geog.) | Longitude (geog.) | Noon variation | Noon dipole tilt | Midnight variation | Midnight dipole tilt |
| 'Casey 65°S Equiv.' | 54° S | 99° E | 70 km | 13° | 110 km | 34° |
| 'Davis 65°S Equiv.' | 62° S | 64° E | 95 km | 21° | 105 km | 26° |
| 'Mawson 65°S Equiv.' | 65° S | 56° E | 95 km | 23° | 100 km | 24° |
| 'S.P. 65°S Equiv.' | 83° S | 307° E | 140 km | 34° | 60 km | 12° |

It now needs to be noted that the initial aim of getting a 'feel' for the conjugate displacements expected at the high invariant latitude antarctic stations by the method adopted is fraught with strife. At different latitudes different current systems effect the field line trace by proportionally different amounts. The high latitude sites will also be particularly influenced by Birkeland (field-aligned) currents which are perhaps the most difficult to model.

The present generation of external field models are a significant improvement on internal field models in representing the magnetosphere. To be fair, the internal models do not in fact pretend to represent the magnetosphere, but since the coordinate systems was built from these models, it is important to be aware of their acknowledged limitations. It is also important to be aware of the limitations of the present generation of external field models. In attempting to field line trace conjugate points from high latitude sites, one of the difficulties had already been encountered. Generally these sites may be on 'open' field lines as predicted by the model, but occasionally these site may be on 'closed' field lines. Essentially the magnetosphere is more dynamic than the three-hourly Kp index can hope to convey.

Most external field models also do not allow for any interplanetary magnetic field (IMF) $B_y$ and $B_x$ influences on the structure of the magnetosphere (an IMF $B_z$ effect is inherently mixed with the Kp level splitting). Theoretical considerations of merging on the dayside magnetopause and subsequent convection processes predict magnetospheric structures that are dependent on the IMF $B_y$ and $B_x$ components (Reiff and Burch 1985). Hemispheric asymetries have been measured in polar cap convection patterns for different IMF conditions (Heppner and Maynard 1987). The distribution of auroral forms in the northern hemisphere has been shown to be dependent on IMF $B_y$ and $B_x$ orientations (Elphinstone et al. 1990).

External field models predict diurnal, seasonal, latitudinal and longitudinal (or UT) variations in the location of conjugate points. In the next section the potential for optically determining the location of conjugate points is discussed.

## 18.4 SATELLITE UV AURORAL IMAGING SYSTEMS

A significant expansion in the potential of conjugate studies has resulted from the development of high speed UV imaging systems for satellites. These systems make use of the low albedo of the earth at UV wavelengths to image auroral activity in daylight as well as at night. The VIKING UV imager (Anger et al. 1987), a Canadian developed instrument flown on a Swedish satellite, was able to acquire an image of potentially the entire auroral oval in of the order of a second with a possible repetition rate of the order of 20 s. The repetition rate was limited by the satellite spin rate and the method chosen for mounting the camera. Due principally to data rate constraints, in the most common operating mode an image was acquired every minute. This was the first time images at such a high repetition rate were possible. The VIKING images exist only for the northern hemisphere and cover a period of only about one year, however, by using southern hemisphere ground based optical data for observations at the southern end of the field line a lot of

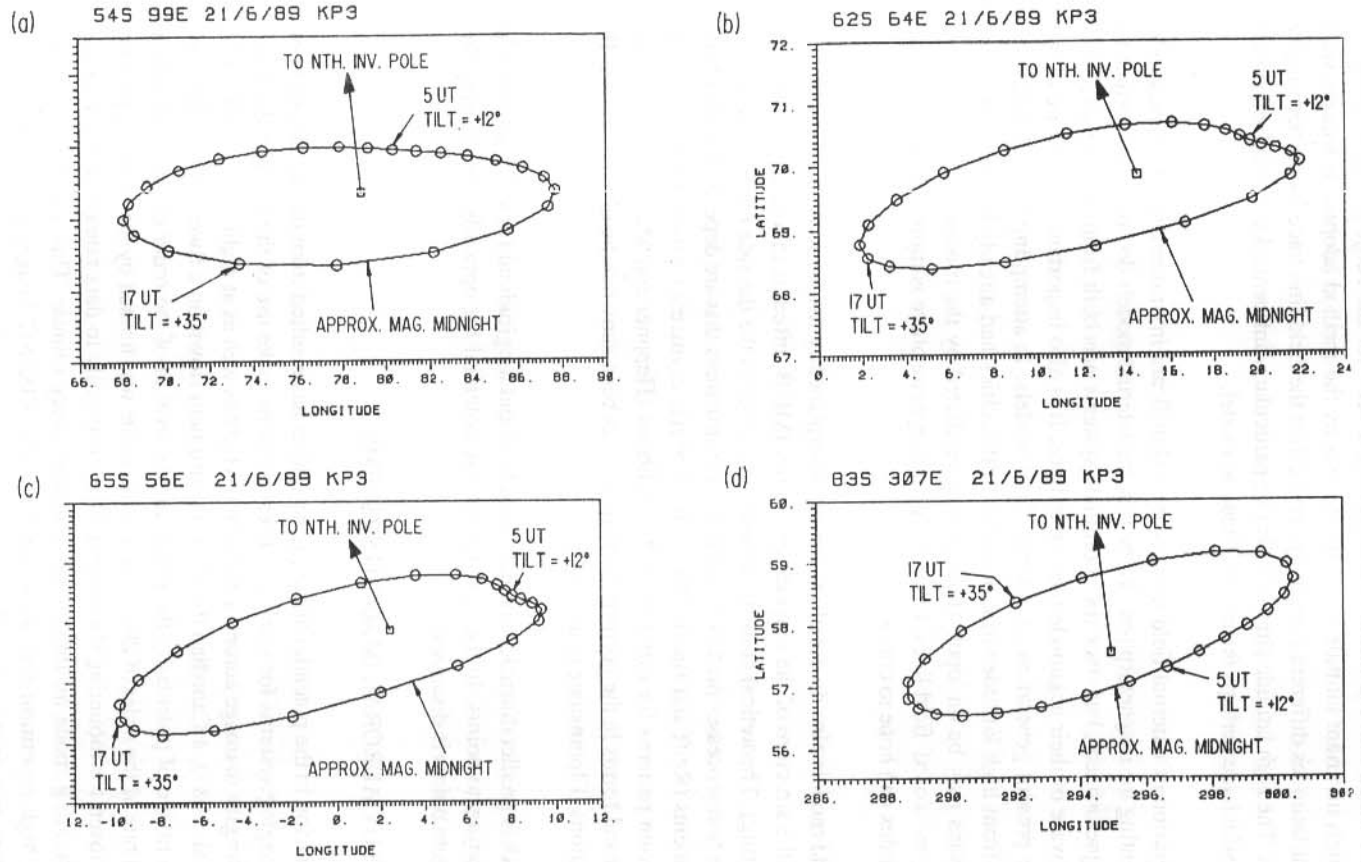


Figure 5. Tsyganenko (1987) model predictions for 'Kp 3', for the southern winter solstice and for the starting points indicated below.
(a). 'Casey 65° inv. equivalent' - 54°S 99°E, geographic; (b). 'Davis 65° inv. equivalent' - 62°S 64°E, geographic
(c). 'Mawson 65°S inv. equivalent' - 65°S 56°E, geographic; (d). 'South Pole 65°S inv. equivalent' - 83°S 307°, geographic
The general labelling is as per Figure 2. The direction to the north invariant pole is on each plot.

the potential for conjugacy studies may be realised. Presently, the Japanese satellite EXOS-D continues to take high time resolution UV images of the aurora in both hemispheres. Further high-time resolution auroral imagers are planned for future satellites including the second Swedish satellite, FREJA, and the Russian INTERBALL satellites.

The fact that the UV imager can image auroral activity in daylight conditions allows the extension of optical conjugacy studies to the dayside auroral oval, high magnetic latitudes and to the winter solstice of the ground-based site.This has been demonstrated using VIKING data by Burns et al. (1990). As shown in the previous section, these are times when, and locations where, conjugate displacements from internal field model predicted locations will be maximised.

For periods of simultaneous satellite and opposite hemisphere ground based observations, if an auroral form is visible from the ground based site, then its conjugate cannot be beyond the field-of-view of a suitably oriented imager. The potentially larger field-of-view means that it is possible to cover the possible range of displacements of the auroral forms. An array of ground instruments, and suitable weather conditions, would be needed to provide an equivalent coverage. With the wide field-of-view potentially available to the satellite auroral imagers, all ground-based optical observatories have the possibility of being utilised for conjugate studies.

A repetition rate for the images of at least the order of a minute is desirable as this is short with respect to the duration of an auroral substorm and can facilitate the identification of conjugate locations by allowing identification of regions in opposite hemispheres at which similar auroral development occurs. It is also highly desirable that the image be rapidly acquired to limit 'blurring' due to the dynamic nature of the aurora. While the time resolution of ground-based optical instrumentation considerably exceeds the present satellite systems, a repetition rate of the order of a minute is sufficient for some discussion of conjugate auroral dynamics to be feasible using these systems.

One limitation which needs to be noted when ground-based instruments are used for comparison with satellite UV images is that, of necessity, the observing wavelengths are different. Particular care needs to be taken when interpreting any variations in intensity between ground-based and satellite UV images.

Auroral imagers with a 'field-of-view' sufficient to ensure that the conjugate point is not displaced beyond its range presently do not have the spatial resolution of ground based instruments. They can, however, have the approximately 50 km resolution necessary to make significant progress on substantial issues relating to the structure of magnetosphere.

## 18.5 CONCLUSION

Studying optical auroral activity at conjugate locations simultaneously provides a stringent test of the understanding of the processes involved in controlling the magnetosphere as a wide range of

symmetries and asymmetries are expected between the hemispheres. There are a number of research areas where optical auroral conjugacy studies may make significant contributions.

Ground-based conjugate auroral studies conducted with high spatial and temporal resolution may facilitate understanding of the importance of local acceleration processes in the control of auroral activity.

External field models which incorporate analytic expressions to represent the major current systems of the magnetosphere predict diurnal, seasonal, latitudinal, longitudinal and magnetic activity level variations in the locations of conjugate points. The displacements from internal field model calculated conjugate locations are predicted to maximise at high latitudes, for high levels of magnetic activity and in the solstices.

Existing external field models are not yet sophisticated enough to include the effects of variations in the IMF $B_y$ and $B_x$ components. These have been shown, and have been predicted, to effect the relative location of the auroral precipitation regions in the two hemispheres. IMF influences on the earth's magnetosphere are generally expected to maximise on the dayside.
The development of high-time resolution auroral UV imagers enables conjugate points to be experimentally determined at these times and locations, where they have been difficult or impossible to determine optically with solely ground-based instrumentation.

By comparing measured conjugate images with what is predicted by the present generation of external magnetic field models, it is potentially possible to determine the relative contribution of the dipole tilt effect and IMF variations to the structure of the magnetosphere. This is a direct testing of the understanding of the processes that shape the magnetosphere, and may provide insights for the future development of magnetic models.

The other significant region of conjugacy study potentially expanded by the advent of high-time resolution UV auroral imagers is the study of the dynamics of the conjugate dayside regions of the auroral oval. This may lead to insights on the transfer of energy from the solar wind to the earth's magnetosphere.

Satellite UV auroral imagers have also significantly expanded the number of ground observatories that can contribute to optical conjugacy studies. Observatories which have conjugate locations which have in the past proved difficult or impossible to occupy on the ground, now have the chance to contribute by utilising the modern generation of satellite imager data.

## 18.6 REFERENCES

Anger, C.D., Babey, S.K., Broadfoot, A.L., Brown, R.G., Cogger, L.L., Gattinger, R., Haslett, J.W., King, R.A., McEwen, D.J., Murphree, J.S., Richardson, E.H., Sandel, B.R. *and* Vallance Jones, A. (1987). An ultra-violet auroral imager for the Viking satellite. *Geophysical Research Letters 14*:387-390.

Belon, A.E., Maggs, J.E., Davis, T.N., Mather, K.B., Glass, N.W. *and* Hughes, G.F. (1969). Conjugacy of visual aurora during magnetically quiet periods. *Journal of Geophysical Research 74*:1-28.

Bond, F.R. (1969). Auroral morphological similarities at two magnetically conjugate stations: Buckles Bay and Kotzebue. *Australian Journal of Physics 22*:421-433.

Burns, G.B., McEwen, D.J., Eather, R.A., Berkey, F.T. *and* Murphree, J.S. (1990). Optical auroral conjugacy: Viking UV imager -South Pole ground station data. *Journal of Geophysical Research 95*:5781-5790.

De Witt, R.N. (1962). The occurrence of aurora in geomagnetically conjugate areas. *Journal of Geophysical Research 67*:1347-1352.

Elphinstone, R.D., Jankowski, K., Murphree, J.S. *and* Cogger, L.L. (1990). The configuration of the auroral distribution for IMF Bz northward 1: IMF Bx and By dependencies as observed by the Viking satellite. *Journal of Geophysical Research 95*:5791-5804.

Fujii, R., Sato, N., Ono, T., Fukinishi, H., Hirasawa, T., Kokubun, S., Araki, T. *and* Saemundsson, Th. (1987). Conjugacy of rapid motions and small-scale deformations of discrete auroras by all-sky TV observations. *Memoirs of National Institute of Polar Research, Japan 48*:72-80.

Fraser-Smith, A.C. (1987). Centred and eccentric geomagnetic dipoles and their poles 1600-1985. *Reviews of Geophysics 25*:1-16.

Heppner, J.P. *and* Maynard, H.C. (1987). Empirical electric field models. *Journal of Geophysical Research 92*:4467-4489.

Langel, R.A., Barraclough, D.R., Kerridge, D.J., Golovkov, V.P., Sabaka, T.J. *and* Estes, R.H. (1988). Definitive IGRF models for 1945, 1950, 1955 and 1960. *Journal of Geomagnetism and Geoelectricity 40*:645-702.

Mead, G.D. *and* Fairfield, D.H. (1975). A quantitative model derived from spacecraft magnetometer data. *Journal of Geophysical Research 80*:523-534.

Nagata, T. (1987). Research of geomagnetically conjugate phenomena in Antarctica since the IGY. *Memoirs of National Institute of Polar Research, Japan 48*:1-45.

Ono, T. (1987). Temporal variation of the geomagnetic conjugacy in Syowa-Iceland pair. *Memoirs of National Institute of Polar Research, Japan 48*:46-57.

Reiff, P.H. *and* Burch, J.L. (1985). IMF By dependent plasma flow and Birkeland currents in the dayside magnetosphere, 2, A global model for northward and southward IMF. *Journal of Geophysical Research 90*:1595-1609.

Rycroft, M.J. (1987). Some aspects of geomagnetically conjugate phenomena. *Annales Geophysicae 5*:463-478.

Sato, N., Fujii, R., Ono, T. Fukinishi, H., Hirasawa, T., Araki, T., Kokubun, S., Makita, K. *and* Saemundsson, Th. (1986). Conjugacy of proton and electron auroras observed near L=6.1. *Geophysical Research Letters 13*:1368-1371.

Sato, N. *and* Saemundsson, Th. (1987). Conjugacy of electron auroras observed by all-sky cameras and scanning photometers. *Memoirs of National Institute of Polar Research, Japan 48*:58-71.

Stassinopoulos, E.G., Lanzerotti, L.J. *and* Rosenberg, T.J. (1984). *Journal of Geophysical Research 89*:5655-5659.

Stenbaek-Nielsen, H.C., Wescott, E.M., Davis, T.N. *and* Peterson, R.W. (1973). Relative motion of auroral conjugate points during substorms. *Journal of Geophysical Research 77*:1844-1858.

Stenbaek-Nielsen, H.C., Davis, T.N. *and* Glass, N.W. (1972). Differences in auroral intensity at conjugate points. *Journal of Geophysical Research 78*:659-671.

Tsyganenko, N.A. *and* Usmanov, A.V. (1982). Determination of the magnetospheric current system parameters and development of experimental geomagnetic field models based on data from IMP and HEOS satellites. *Planary and Space Science 30*:985-998.

Tsyganenko, N.A. (1987). Global quantitative models of the geomagnetic field in the cislunar magnetosphere for different disturbance levels. *Planary and Space Science 35*:1347-1358.

Tsyganenko, N.A. (1989). A magnetospheric magnetic field model with a warped tail current sheet. *Planetary and Space Science 37*:5-20.

Wescott, E.M. (1966). Magnetoconjugate phenomena. *Space Science Reviews 5*:507-561.

# 19. METEOROLOGICAL INFLUENCES ON THE MEASUREMENT OF THE GEOELECTRIC FIELD AT DAVIS, ANTARCTICA

R.G. McLoughlin[1], S. Malachowski[2,1], M. Hesse[1] and G.B. Burns[1]

[1]Antarctic Division
Kingston Tas 7050
Australia

[2]La Trobe University
Bundoora Vic 3083
Australia

ABSTRACT

The results of a preliminary examination of some of the electric field data returned from Davis Antarctica are presented. In particular, examples of meteorological conditions under which the local electric field is not representative of the global 'fair weather' field are illustrated.

## 19.1 INTRODUCTION

At any given point on the globe the local electric field is the resultant of contributions from several sources.

1. The global or 'fair weather' electric field which results from world-wide thunderstorm activity. This is a tropospheric effect which is globally synchronised.
2. Electric fields which originate in the magnetosphere or ionosphere and penetrate down to the surface of the planet. These electric fields vary with local time.
3. Electric fields which result from local sources which may be meteorological or anthropogenic in origin, e.g. wind-blown snow and rain, local thunderstorms, high-voltage transmission lines, etc. These effects may exhibit a periodic signature although it is unlikely in the case of meteorological phenomena. The important thing to note is that these local effects tend to dominate over those of global scale and for this reason it is necessary to choose measuring sites carefully to minimise their impact.

By choosing Davis as a measuring site the authors hoped to minimise local perturbations of the 'fair weather' field by distancing themselves from areas of thunderstorm activity and anthropogenic pollution, and to maximise the chances of observing ionospheric and magnetospheric influences. For example, the footprint of the dawn-dusk polar-cap electric field resulting from magnetospheric convection should have maximum influence at invariant latitudes near 75°. However, objective limits still need to be established for the local meteorological conditions in order to be able to reject data which is likely to be dominated, or contaminated, by local generators. A visual scan has been undertaken of the data and selected those days when the

recorded electric field was influenced by one or other of the simultaneously recorded meteorological parameters. From this subset of the data the authors have been able to determine objective limits on some of the meteorological parameters but, as yet, not on others.

## 19.2 RESULTS AND DISCUSSION

In the following figures some of the relationships typical of the general type observed while scanning the data have been examined. Note that while routine consistency checks are performed on the electric field sensor, the scale values provided for the potential gradient are tentative and derive from a cross calibration against a passive detector which is, as yet, not fully calibrated. Figure 1 shows an example of the data when the electric field and wind speed data exhibit a positive correlation. Note that the electric field seems to lead the wind speed change and recover more quickly. To verify this observation the data for this day was plotted as a scattergram and is shown in Figure 2. The time sequence of the data plotted in Figure 2 is indicated by arrows and highlights the observation that the electric field leads the wind speed. In Figure 3 the authors have concentrated on the electric field and wind speed spikes which are observed in Figure 1 at about 1800 UT. Notice that in this example the electric field lags the wind speed in contrast to earlier events on the same day when it led the wind speed. Despite this phase change a scattergram of the data for the period 1800 UT to 2000 UT, Figure 4 clearly indicates a threshold around 6.5 m $s^{-1}$ for the point at which the local electric field is dominated by wind speed related events. The time sequence for the data indicates that the weak positive correlation between wind speed and electric field occurs during the recovery phase, from about 1830 UT to about 1930 UT in Figure 3. Whether this residual correlation is indicative of a global or local effect, has not yet been determined.

In Figure 5, there is an example of a fairly quiet day, meteorologically speaking, although there is still a noticeable positive correlation of the electric field with wind speed. What is interesting with the data for this day is that there is an apparent negative correlation between the wind speed and the electric field, indicated by the arrows in Figure 6, which seem to occur at low values of the wind speed only. A scattergram of the data for this day is shown in Figure 7 for the period 0000 UT to 0900 UT and clearly illustrates both correlations.

Figure 8 illustrates an example of an occasion when the electric field change correlates with a change in relative humidity. This is a typical case in that the humidity change is accompanied by a temperature change from +0.5°C to -1.5°C. Taken together these changes probably result in a decrease in the conductivity of the air at this time; which results in an increase in the local electric field. When a scattergram was plotted of the Data (Figure 9), there was again evidence for the electric field leading the relative humidity response. It may be that in this instance the lead can be attributed to a slow response on the part of the relative humidity sensor, however, this hypothesis is mitigated by the abrupt rise of the humidity data.

Examples of the electric field response to blizzard and snow shower conditions are shown in Figures 10 and 11. Use was made of the logbook observations of the operator and those kept by the Bureau of Meteorology observers at the station in determining the prevailing meteorological conditions.

## 19.3 CONCLUSION.

From an examination of data such as this over a period of one year (1988), the authors have been able to determine the following relationships between meteorological parameters and the local electric field.

1. For wind speeds in excess of ~ 6 m $s^{-1}$ and durations from tens of minutes to hours, the electric field exhibits a positive correlation with wind speed.
2. For wind speeds less than ~ 3 m $s^{-1}$ and durations of about ten minutes, negative correlations of the electric field and wind speed have been observed.
3. For ambient temperatures near 0°C, the electric field has been observed to increase with increasing relative humidity. This effect is observed to occur in conjunction with a decrease in the ambient temperature and is thought to be due to a change in the local conductivity when small ions act as condensation nuclei for micro-droplet formation.
4. On many occasions the electric field was observed to increase dramatically some hours prior to the onset of blizzard conditions. This is thought to be associated with a lowering in altitude of the high velocity upper level winds, which is the normal sequence of events at Davis as a blizzard approaches.
5. During periods of snow showers the electric field has been observed to undergo a reversal of sign. The frequency of this reversal has been used as an indicator of the intensity of vertical exchange, instability, or turbulence between the region of formation of the precipitation and the earth's surface (Reiter 1977).

## 19.4 REFERENCE

Reiter, R. (1977). Atmospheric electricity activities of the Institute for Atmospheric Environmental Research. In: Dolezalek, H. *and* Reiter, R. (Eds). *Electrical Processes in Atmospheres*. Pp 759-796.

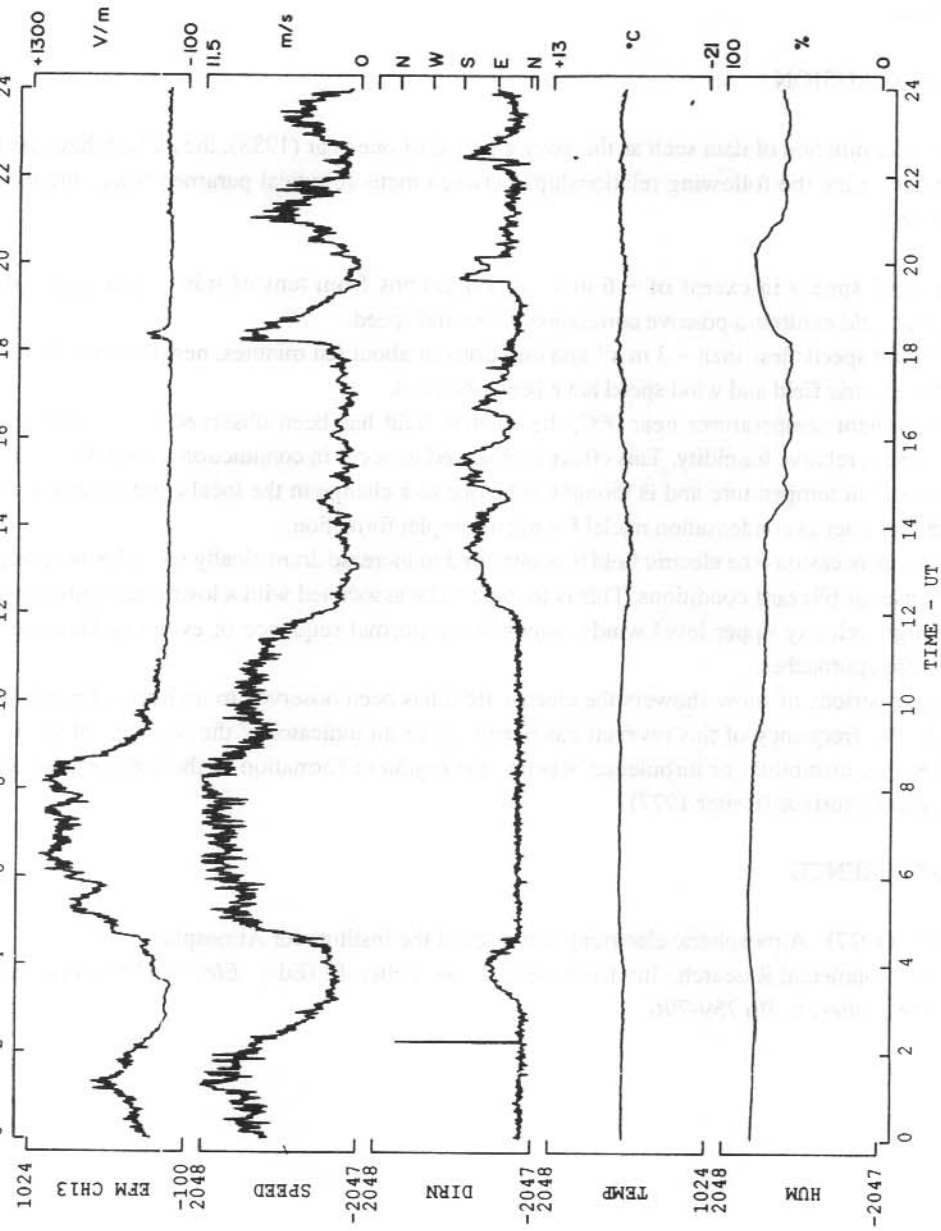


Figure 1. An example of data exhibiting a positive correlation between the electric field and the wind speed at Davis, 20 May 1988.

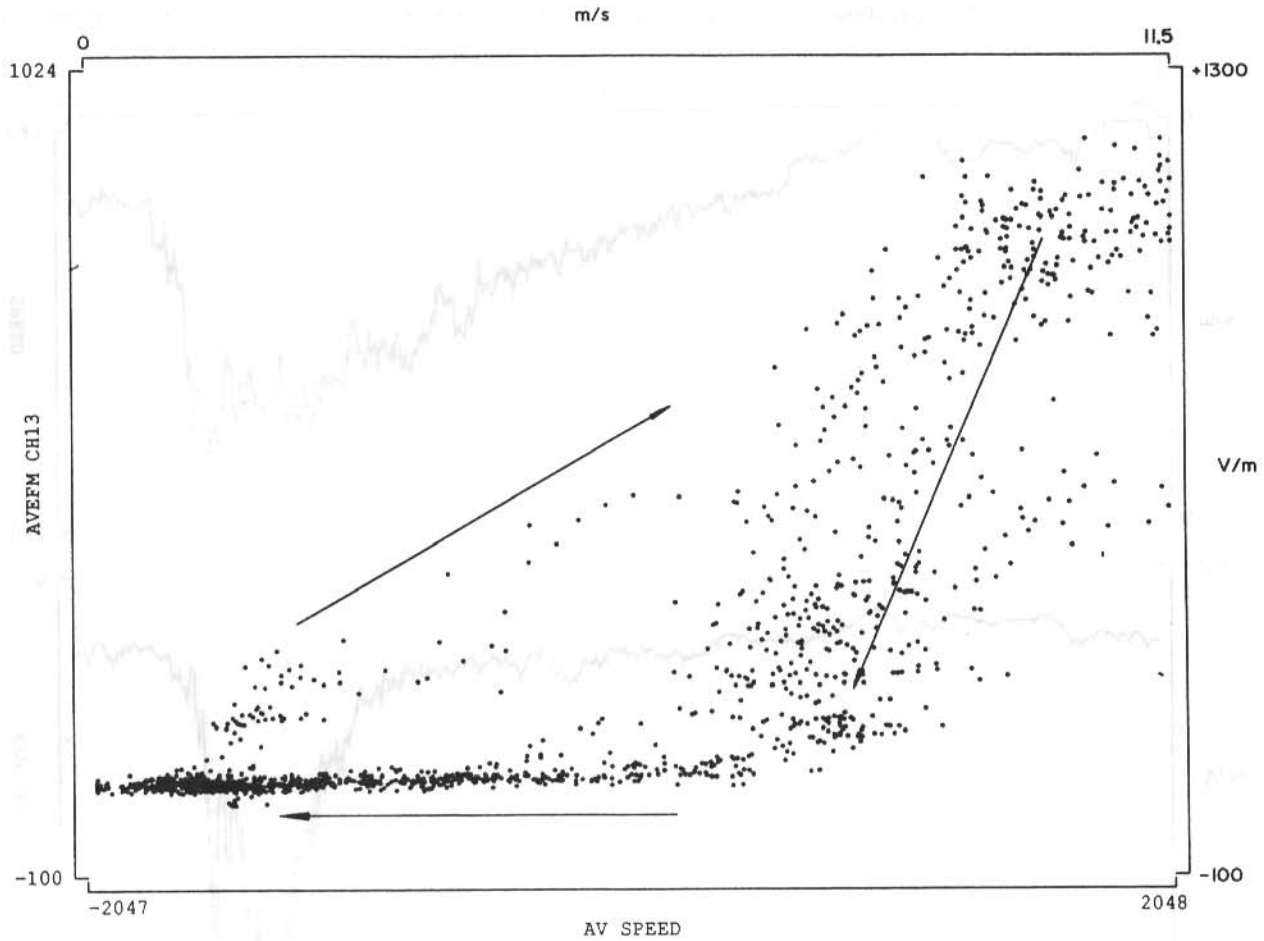


Figure 2. Scattergram of the data plotted in Figure 1. The arrows indicate the time sequence of the points at Davis, 20 May 1988. Data from 0000 to 2400 UT, 1 minute averages.

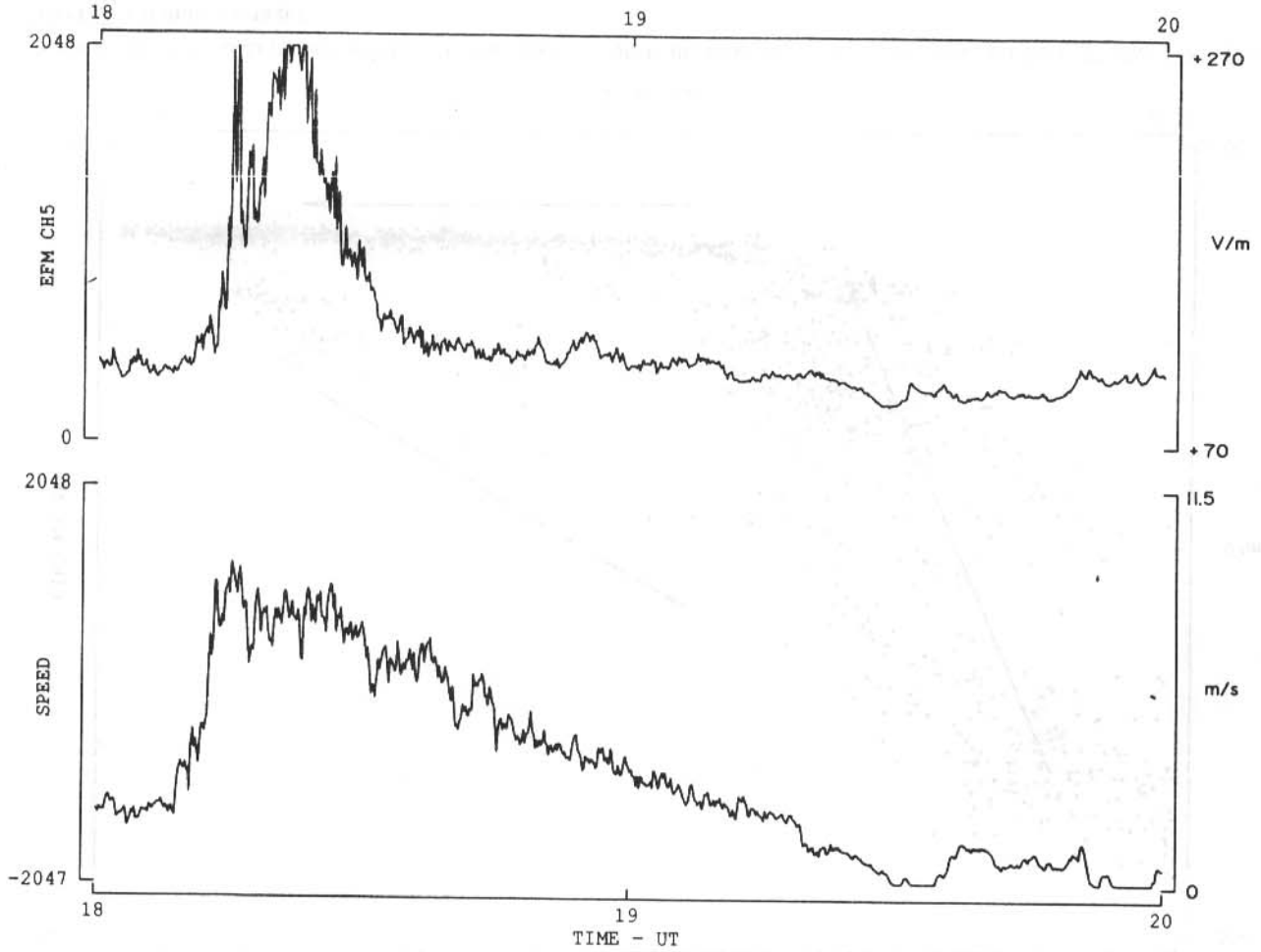


Figure 3. Expanded view of the wind speed and electric field spikes evident in Figure 1 at about 1800 UT.

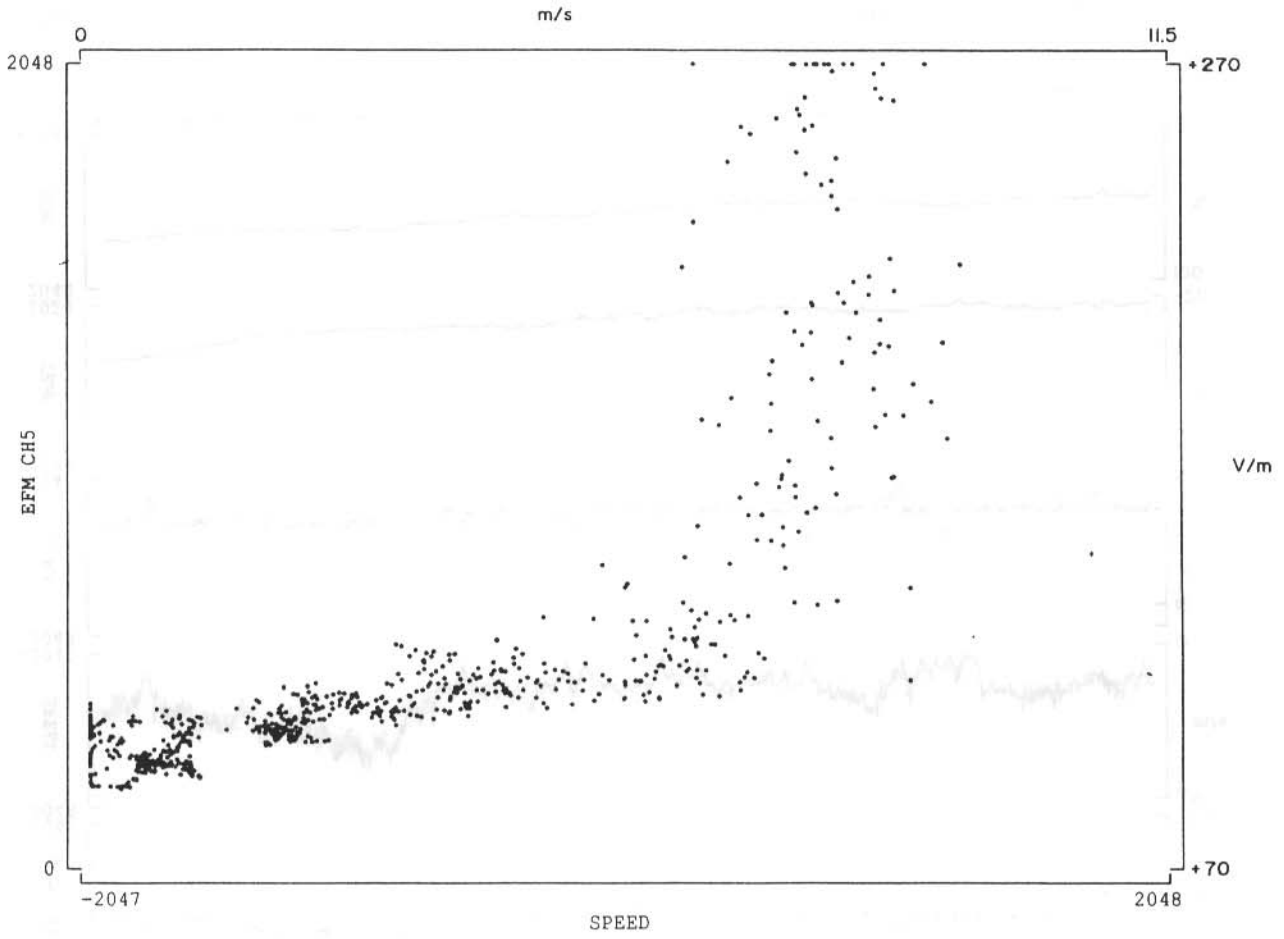


Figure 4. Scattergram of the data plotted in Figure 3 and showing the threshold at about 6.5 m $s^{-1}$, beyond which the electric field is definitely dominated by local effects at Davis, 20 May 1988. Data from 1800 to 2000 UT.

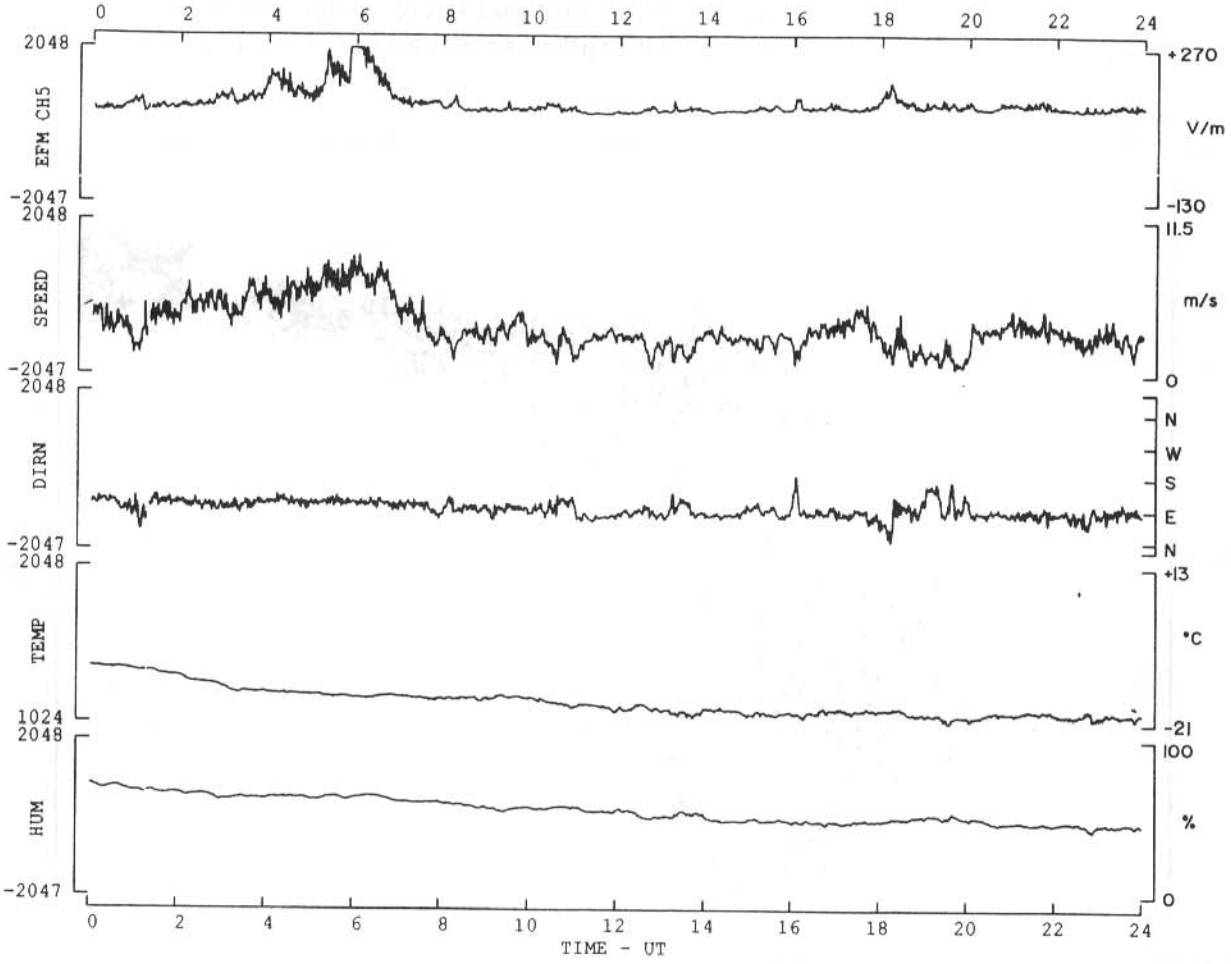


Figure 5. A day exhibiting residual positive correlation between wind speed and electric field at Davis, 24 April 1988.

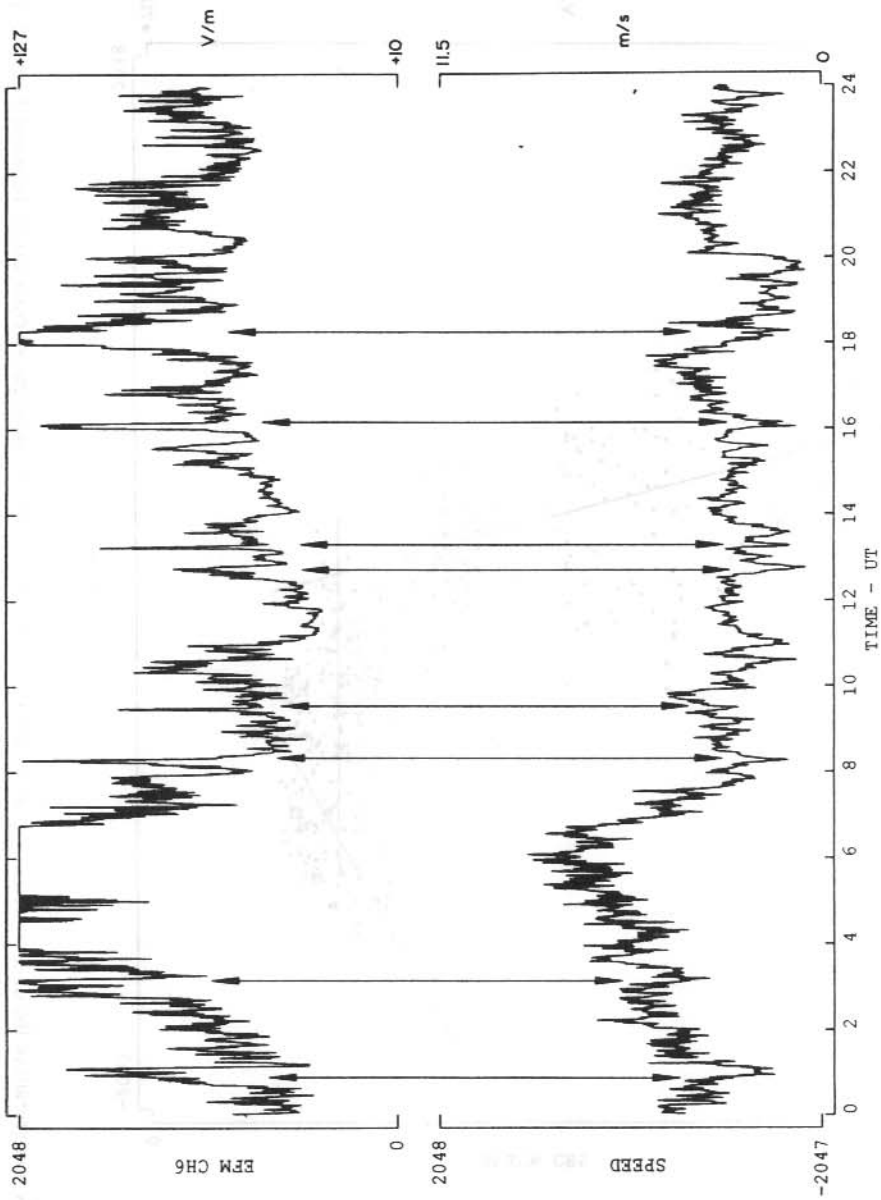


Figure 6. An expanded plot of the data shown in Figure 5 illustrating the negative correlation between wind speed and electric field at low wind speeds at Davis, 24 April 1988.

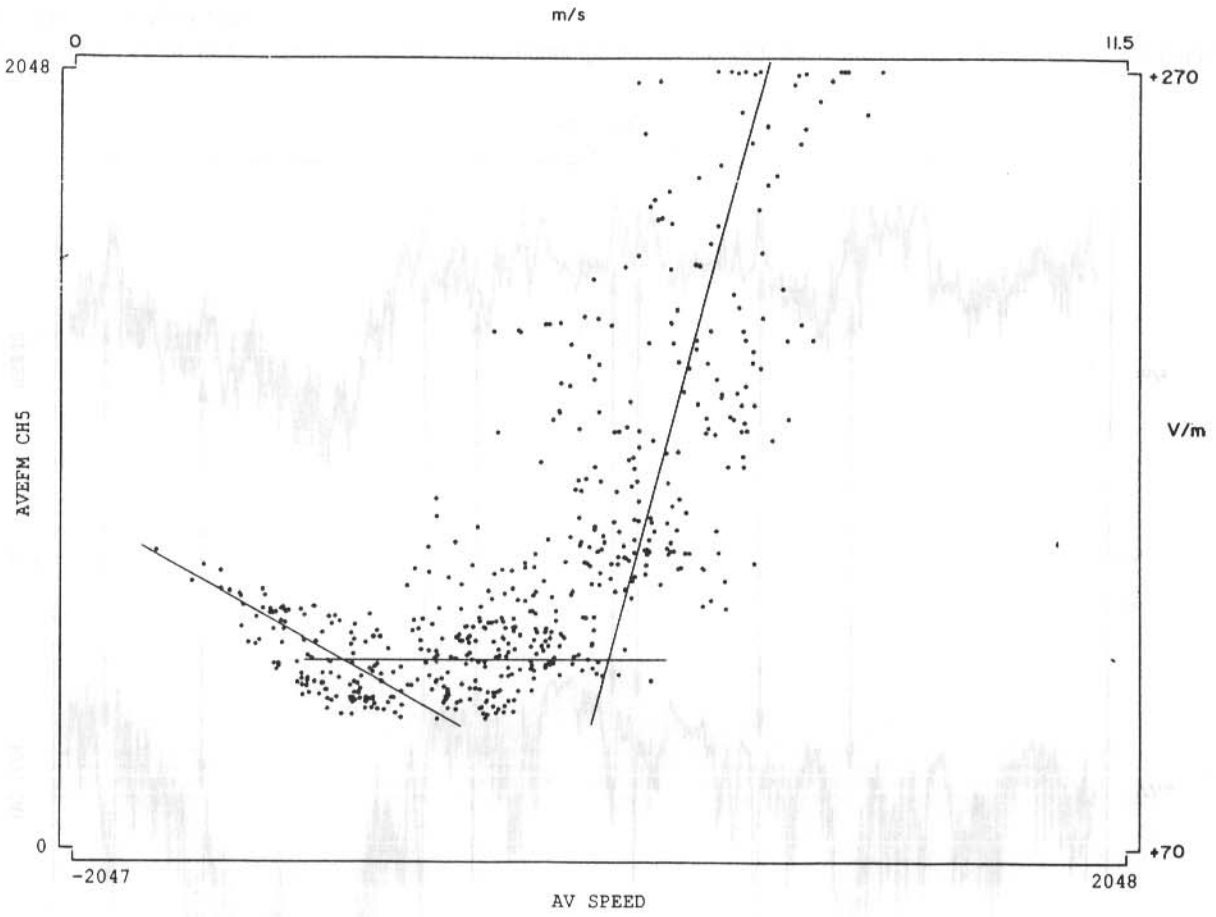


Figure 7. A scattergram of the data plotted in Figure 6 and illustrating both positive and negative correlations between the wind speed and the electric field at Davis, 24 April 1988. Data from 0000 to 0900 UT, 1 minute averages.

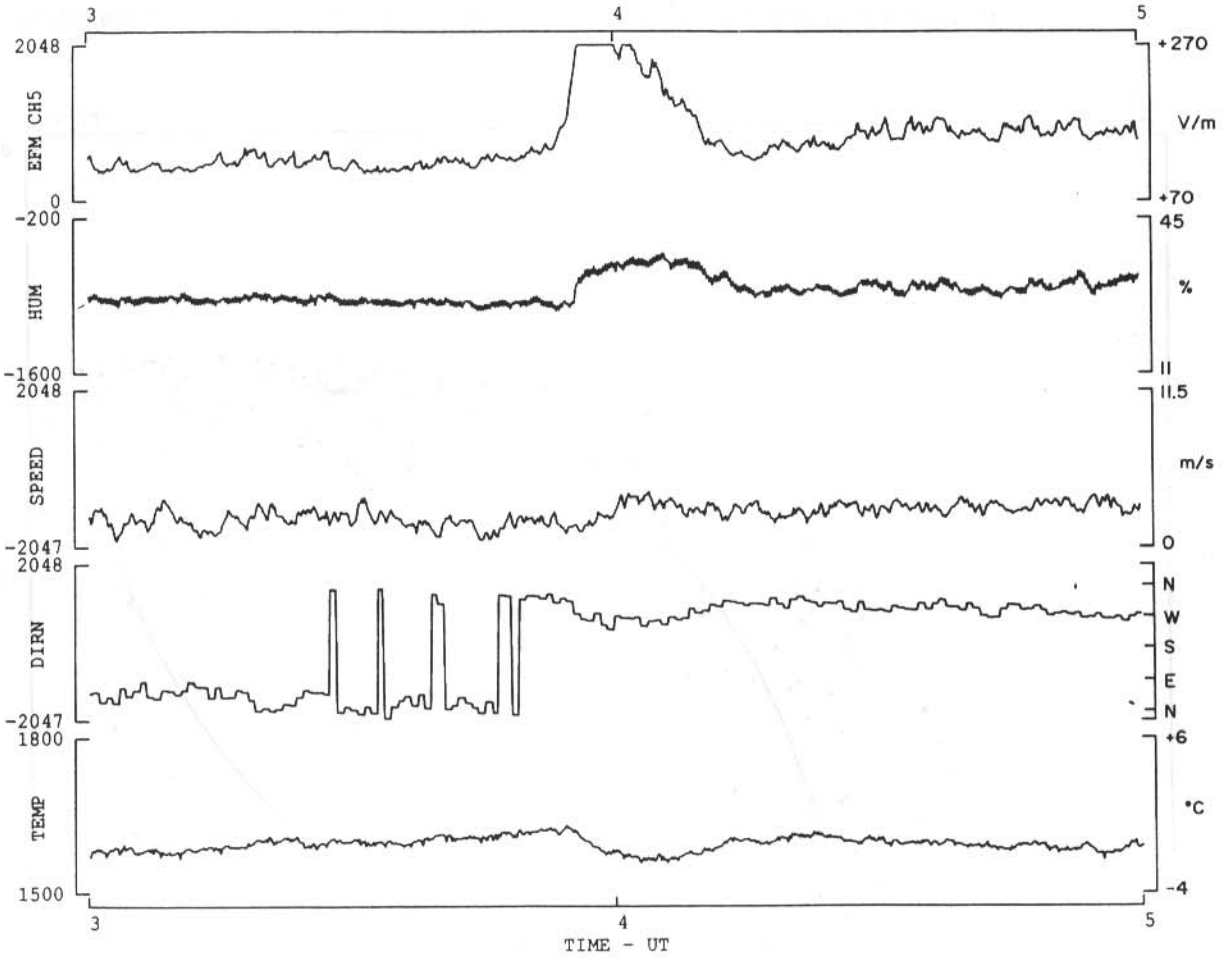


Figure 8. An example of data illustrating the correlation of the electric field and relative humidity at Davis, 3 November 1988.

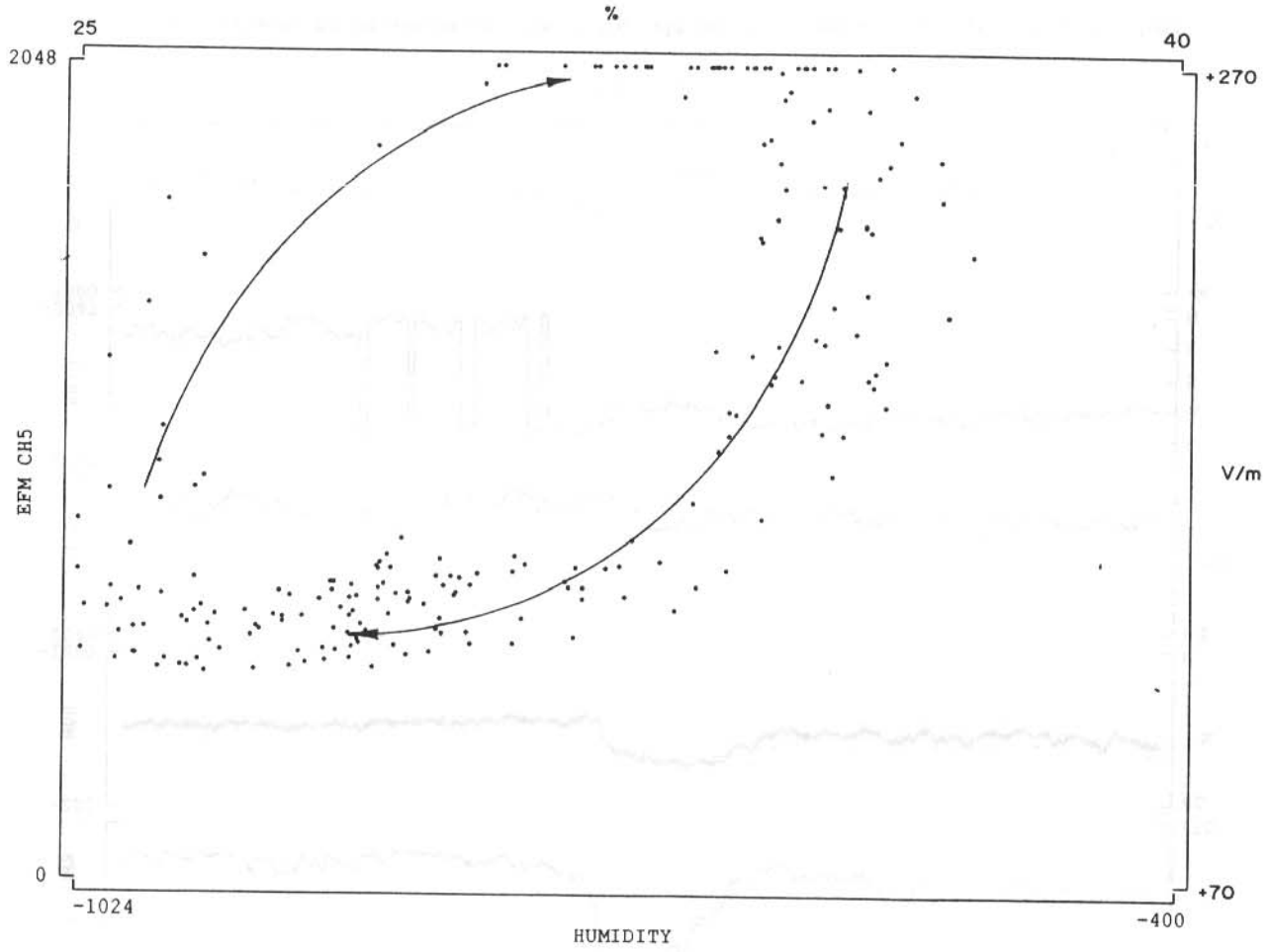


Figure 9. Scattergram of the data plotted in Figure 8 at Davis, 3 November 1988, data from 0348 to 0424 UT.

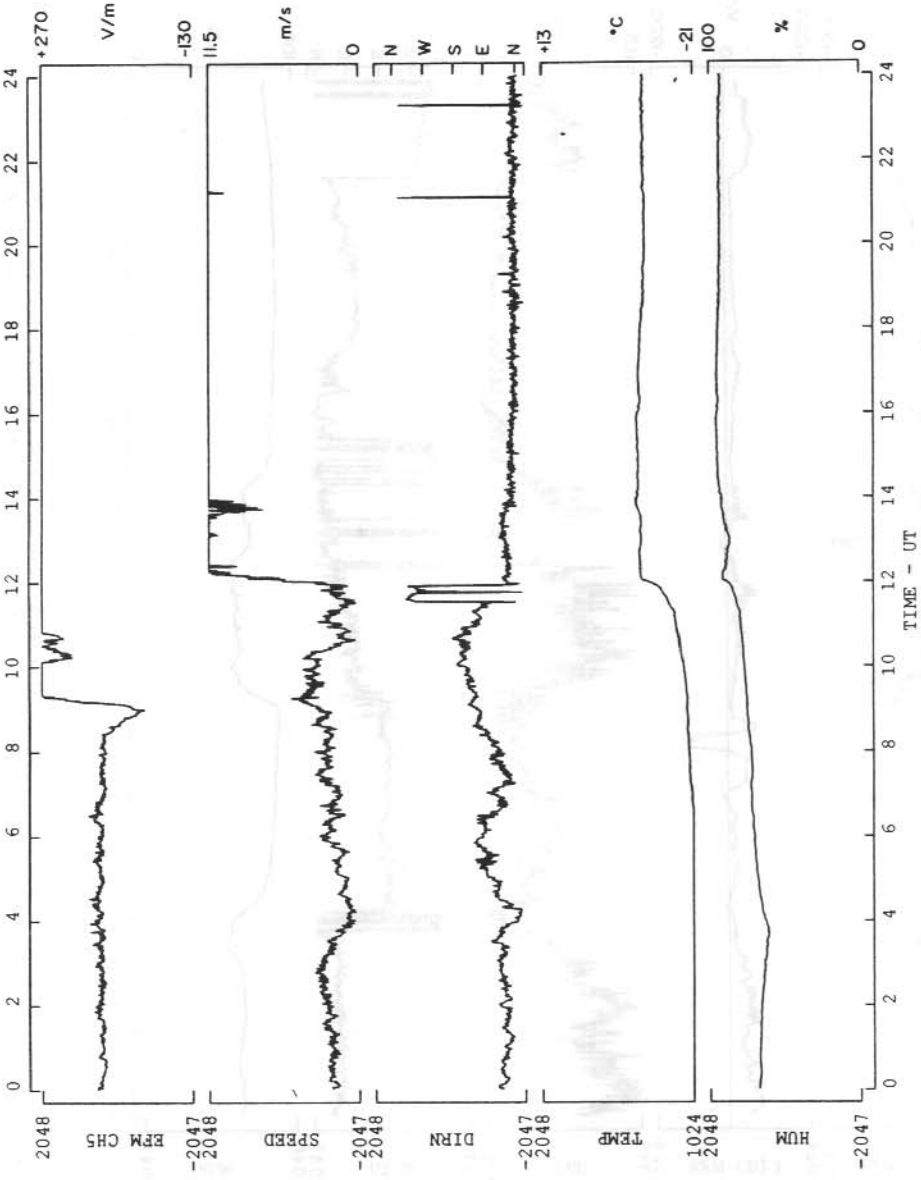


Figure 10. An example of data illustrating an occasion when the electric field response led the wind speed by a matter of hours prior to the onset of blizzard conditions at Davis, 19 May 1988.

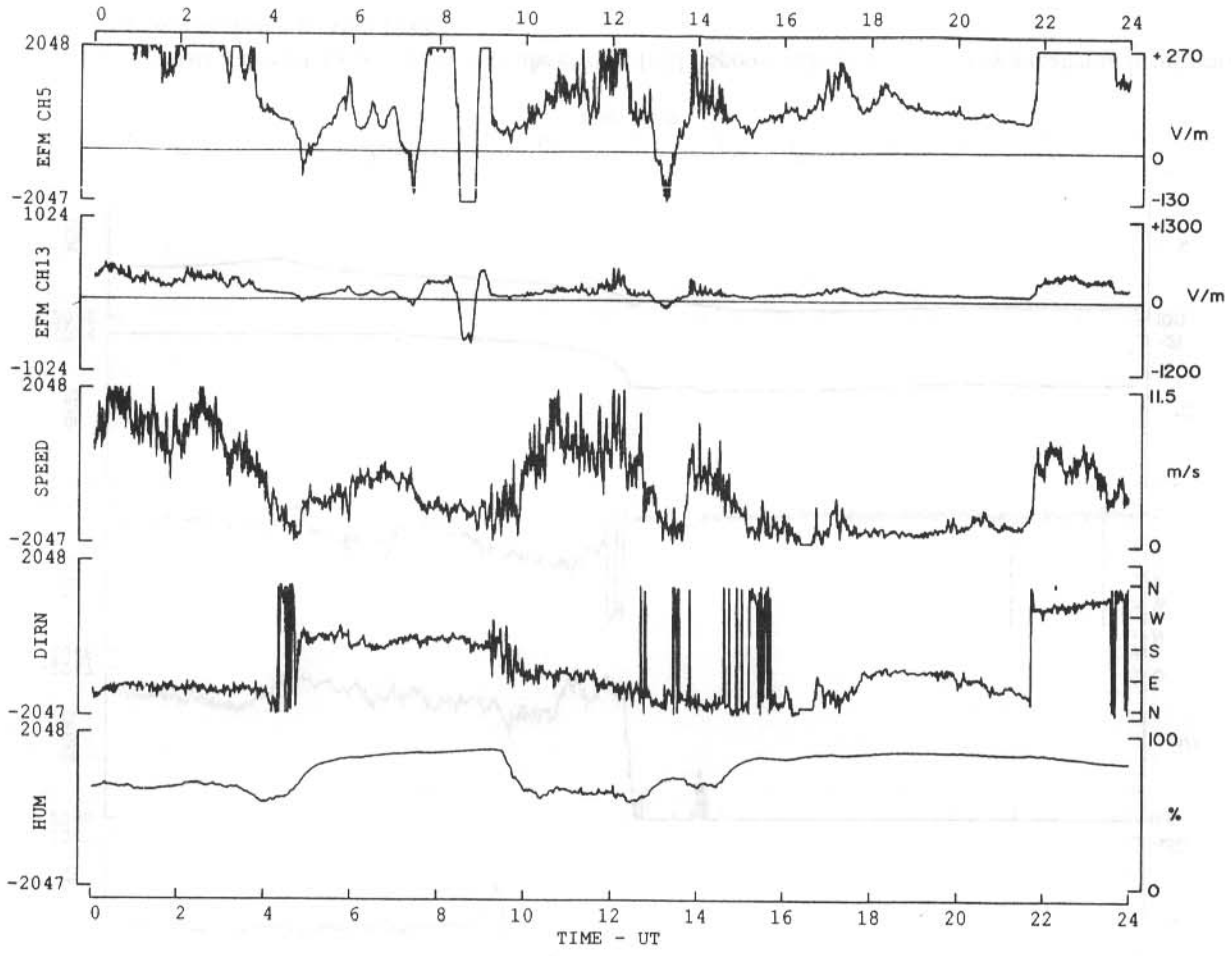


Figure 11. An example of data illustrating the reversal of the electric field during snow shower conditions at Davis, 3 May 1988.

# 20. A METHOD OF COMPARISON FOR ELECTRIC FIELD MEASUREMENTS

S. Malachowski
La Trobe University
Bundoora Vic 3083
Australia

ABSTRACT

In order to realistically compare electric field data sets collected from two different sites, a standard was devised. This consisted of a sphere attached to a very high impedance electrometer. By placing the sphere in reasonable proximity to the electric field measuring machines during calm weather conditions, it is possible to then compare the subsequent time series obtained from the machines. The spherical arrangement is sufficiently simple in geometry to enable calibration.

The principles of the measurement are discussed and results of a comparison between the spherical device and a field mill are shown. The measurement using a sphere is a one-sided potential measurement. The field mill makes a measurement of the field gradient in a differential manner. The difficulties in relating the two are explained.

The electric field present in the lower regions of the atmosphere has many facets. The first few sections of this article provide some background to this phenomenon. They are not intended to review but merely introduce.

## 20.1 THE ATMOSPHERIC ELECTRIC FIELD OF THE EARTH

The atmospheric electric field of the earth is the perpendicular electric field that extends from the bottom of the ionosphere to the ground. The strength of the field decreases exponentially from the ground upwards and is directed towards the earth most of the time.

A list of some of the established and postulated associations between the electric field and other atmospheric phenomena follows. In all cases, no extensive theory has yet been established to explain the effects conclusively.

(1) Geometry. The physical topography distorts the electric field locally (Chalmers 1957).
(2) Local Meteorology. These effects determine the neighbourhood space charge (Chalmers 1957).
(3) Medium Range Meteorology. Specifically clouds. These act as charge sources producing additional electric fields (Imyanitov and Chubarina 1967).
(4) Global Meteorology. Specifically thunderstorms. These act as current sources sustaining the atmospheric electric field.
(5) Ground Based Radioactivity. The conductivity at ground level is affected by this.

(6) Cosmic Neutrons. The conductivity at ground level is affected by this (Israel 1973a).
(7) Solar Magnetic Effects. The changing direction if the solar field has been found to correlate with changes in the electric field (Park 1976).

Typical values of the electric field are presented in Table 1 (Israel 1973a, 1973b).

Table 1. Typical values in the electric environment (Israel 1973a, 1973b).

| Quantity | Value |
|---|---|
| Electric Field | 100 V $m^{-2}$ |
| Electric Current | $10^{-12}$ A $m^{-2}$ |
| Conductivity | $10^{14}$ Ω $m^{-1}$ |

## 20.2 THE GLOBAL ATMOSPHERIC ELECTRIC CIRCUIT

Elster and Geitel discovered ionisation, albeit weak, in the lowermost regions of the atmosphere in the latter part of the last century. An electric field had been known to exist for one hundred years prior to their discovery. Since there is a field and a conductor, by Ohm's Law, a current must flow. The source of this current is postulated to be thunderstorms acting cooperatively over the globe. The word 'postulated' is used as there are still unexplained discrepancies between the total amount of current produced by thunderstorms and the current flowing in non-thunderstorm regions.

This theory arises from the efforts of the Carnegie Mellon Institute of Washington during the first three decades of the century. A vessel named the Carnegie sailed the world making measurements of the electric field and other phenomena. The analysis of the data revealed a diurnal variation that was invariant with respect to geographic position (Bauer 1917). In the early 1930's, the same diurnal curve was established in global thunderstorm occurrence (Whipple 1929).

The subsequent association of the two phenomena has become known as the Global Electric Circuit in which, over most of the earth, where there are no thunderstorms, current flows in such a direction as to decrease the field. In thunderstorm areas, the current is replenished.

## 20.3 THE MEASUREMENT OF AN ELECTRIC FIELD

The adopted method over the last two decades for the measurement of electric field relies on the principle of induction. Conducting material is exposed to the electric field and the degree of induced charge is sensed. The machines that implement this method are described as field mills and fall into two categories.

(1) Varying Degree of Exposure. These mills provide a grounded plate that swings over a floating conductor. A varying charge is induced in the latter due to the changing area of exposure.
(2) Varying Orientation. These mills physically move an isolated conductor around in the field. As the orientation reverses, so does the induced charge.

The output of these devices is a periodic wave whose amplitude is proportional to the electric field. This wave is then sampled at the crest of the wave to determine the field strength.

## 20.4 A DUAL SITE EXPERIMENT

The motivation for establishing a dual site experiment is to investigate the global theory of the electric field. To attack this problem, two similar experiments were implemented at locations separated by thousands of kilometres. The chosen positions were La Trobe University, Melbourne, Australia and Davis station, Antarctica. The geographic locations of these sites are given in Table 2.

Table 2. Experimental site locations.

| Site | Latitude | Longitude |
|---|---|---|
| Davis Station, Antarctica | 68.6° S | 78.0 ° E |
| La Trobe University, Melbourne | 37.45° S | 144.58° E |

The local geometry was noted in Section 20.1 as being one factor that modifies the electric field. Indeed, the device itself that measures the field distorts it. A standard to which both sites could be compared is required.

## 20.5 THE METHOD OF COMPARISON

A minimal requirement is the development of at least a relative standard to which the two sites could be compared. This article is concerned with the development of such a standard and the results of its application.

Electric field measuring devices of the type employed in this experiment produce a characteristic distortion of the electric field being measured. This is generally described as the 'compression factor'. This distortion could, at least in principle, be calculated analytically, as a solution to Laplace's equation in three dimensions. The geometry, however, is intractable and one is left with a numerical approach. This to, is difficult due to the large number of mesh points. For a reasonable representation of a moderately sized instrument something like $10^9$ nodes would be

(1) Varying Degree of Exposure. These mills provide a grounded plate that swings over a floating conductor. A varying charge is induced in the latter due to the changing area of exposure.
(2) Varying Orientation. These mills physically move an isolated conductor around in the field. As the orientation reverses, so does the induced charge.

The output of these devices is a periodic wave whose amplitude is proportional to the electric field. This wave is then sampled at the crest of the wave to determine the field strength.

## 20.4 A DUAL SITE EXPERIMENT

The motivation for establishing a dual site experiment is to investigate the global theory of the electric field. To attack this problem, two similar experiments were implemented at locations separated by thousands of kilometres. The chosen positions were La Trobe University, Melbourne, Australia and Davis station, Antarctica. The geographic locations of these sites are given in Table 2.

Table 2. Experimental site locations.

| Site | Latitude | Longitude |
|---|---|---|
| Davis Station Antarctica | 68.6° S | 78.0 ° E |
| La Trobe University, Melbourne | 37.45° S | 144.58° E |

The local geometry was noted in Section 20.1 as being one factor that modifies the electric field. Indeed, the device itself that measures the field distorts it. A standard to which both sites could be compared is required.

## 20.5 THE METHOD OF COMPARISON

A minimal requirement is the development of at least a relative standard to which the two sites could be compared. This article is concerned with the development of such a standard and the results of its application.

Electric field measuring devices of the type employed in this experiment produce a characteristic distortion of the electric field being measured. This is generally described as the 'compression factor'. This distortion could, at least in principle, be calculated analytically, as a solution to Laplace's equation in three dimensions. The geometry, however, is intractable and one is left with a numerical approach. This to, is difficult due to the large number of mesh points. For a reasonable representation of a moderately sized instrument something like $10^9$ nodes would be

required, as would an exhausting number of dimension measurements. Since this would most certainly have exceeded the time available to complete this project, an empirical technique was examined.

*20.5.1 The use of passive antennas*

Active antennas have been in use for a great number of years in the calibration of measurements of the electric field. During the cruise of the Carnegie, a land based antenna was used for calibration of the shipboard unit (Bauer 1917). The usual configuration was a thin wire suspended above some form of ground plane. In order to reduce the impedance between the wire and ground, a radioactive source was attached to the centre of the wire. This source ionised the air about the wire. Apart from the unpalatable environmental considerations, such a source (usually an isotope of Thorium called Ionium), is capable of generating a cloud of ions that could once again distort the electric field. Typically, an impedance of $10^9\Omega$ was necessary for the metering equipment of the Carnegie years.

In the case of Ionium, the emission is strictly $\alpha$ particles. In air at standard temperature and pressure (STP), one may anticipate the ionisation to extend only a few centimetres from the antenna. This should not cause a problem if the ions stayed there. There are both electric and mechanical forces present capable of upsetting this delicate configuration. The ultimate distribution of charge due to the generated ions is unpredictable unless one goes to the extent of monitoring the space charge near the wire. It would produce its own distortion upon the field.

Such an antenna will distort the field due to its physical presence. However, if it is constructed with a sufficiently simple geometry, this distortion can be accounted for. For example, in the case of the stretched wire antenna mounted parallel to ground, then it can be seen that an equipotential passes through the centre of the wire.

With improving technology, it has been possible to obtain sensing equipment that relies only on the natural ions present in the air as a current source. The field machines used in this project measure $E_z$ over a small region of space, and so, an antenna performing likewise was considered. A possible design then, for a passive antenna, is a sphere. This idea originates in an article by Crozier (1963).

*20.5.2 The suitable size for a passive antenna*

The main restriction on the sensing of a voltage in air is the impedance between the antenna and ground. The antenna functions as a collector for the current flowing in the air, the amount of current collected being dependent upon the size and shape of the antenna. Hence, if a metering system requires $x$ amperes as the minimal current to function (i.e. its bias current), then the antenna must extract roughly $100x$ amperes from the air so that the meter represents the voltage to within one percent.

It can be shown that the field lines that cut a circular area above a sphere with a diameter equal to three times that of the sphere will converge on the sphere. This can be demonstrated by firstly considering the flux of the electric field at the surface of the sphere. The electric field surrounding a free-floating conducting sphere is given by equation (1). The equipotentials surrounding a free floating sphere in a constant electric field are displayed in Figure 1.

$$\tilde{E} = E_0\left(1 + \frac{2a^3}{r^3}\right)\cos\theta\,\hat{r} - E_0\left(1 - \frac{a^3}{r^3}\right)\sin\theta\,\hat{\theta} \qquad (1)$$

The third dimension is not represented here due to symmetry. The flux of the electric field cutting an arc element is given by equation (2).

$$d\Phi = \vec{E}.d\vec{S} \qquad (2)$$

Where $d\vec{S}$ is an arc element and the direction of $d\vec{S}$ is normal to the sphere. The total flux is given by integrating over the top of the sphere as given in equation (3).

$$\Phi = \int_S \vec{E}.d\vec{S} \qquad (3)$$

The electric field is normal to the sphere, and r = a on the sphere. Thus integrating equation (1) under these conditions produces equation (4).

$$\Phi = 2\int_0^{\frac{\pi}{2}} 3E_0 a\cos\theta d\theta \qquad (4)$$

The integral is taken only over the top of the sphere, since the net flux on the other side equals and cancels the flux on the top. The result is then given by equation (5).

$$\Phi = 6aE_0 \qquad (5)$$

Any current flowing on the lines that converge on the sphere will be 'available' for use by a sensing device. The assumption of uniform conductivity of the air is made here. A typical value for the current flowing in the air is $10^{-12}$ Amp $m^{-2}$. The bias current for the available meter (a Keithley Instruments electrometer) is quoted as $10^{-15}$ Amp. To measure to within one percent, a current of at least $10^{-13}$ Amp must be present. The catchment area of the sphere must, therefore, be no less than 0.1 $m^2$. This implies a minimal diameter of 0.12 m. The sphere, chosen with this requirement in mind, and also the availability of spun metal spheres, was approximately three times this size. This increased size permits a fluctuation in the available current by an order of magnitude before the one percent design criterion is exceeded. Correspondingly, it has a larger range effect on the space around it and must be placed further away from the field measuring machine. The meter has an analogue output that is proportional to the potential assumed by the sphere, but with an output impedance sufficiently low to be digitised by a conventional computerised system.

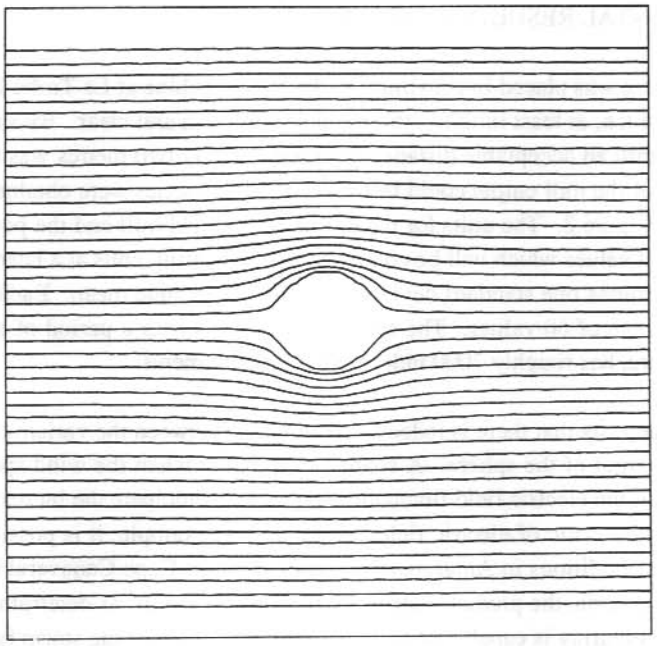

Figure 1. The distortion of the electric field by a free sphere.

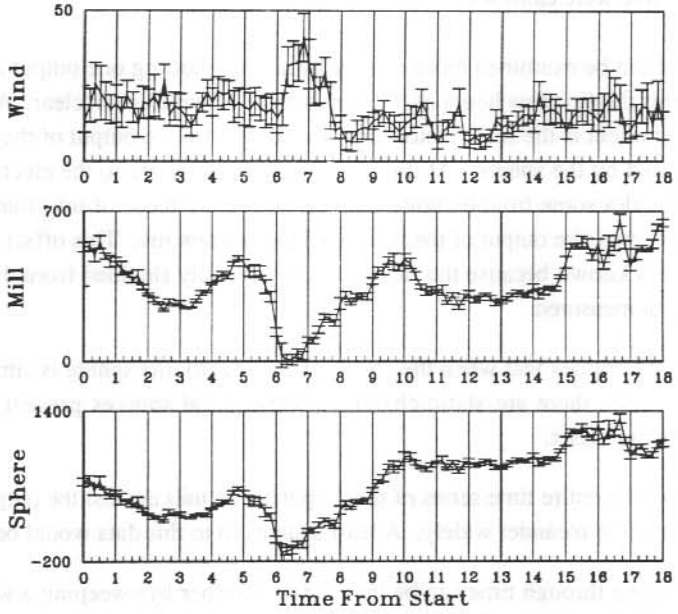


Figure 2. Data collected by 'sphere' and 'mill' at La Trobe.

## 20.6 EXPERIMENTAL RESULTS FROM LA TROBE

The potential sphere was placed in proximity to the field machine at La Trobe University. Days were chosen on which, at least initially, the weather was calm and clear. By simply moving the sphere about the mill an acceptable distance of approximately two metres was found before any sort of deflection of the mill output could be observed. Time series were obtained, an example of which appears in Figure 2. The units for the output of the field mill and the potential sphere are the arbitrary digital values which will be converted to engineering units at a later stage. The error bars are plus and minus one standard deviation about a ten minute mean. Each point in the plot represents an average of 60 values. The time series extends over a period of approximately 19 hours and, therefore, has roughly 7000 independent measurements.

At first glance it appears that there is indeed a relationship between the variation of the output of the mill and the output of the sphere. A change is apparent when the wind speed increases. A point of note is that the electric field fluctuation appears to anticipate the increase in wind speed. This effect is characteristic of electric field variation. For example, it is possible to predict the arrival of blizzard conditions in Antarctica by some minutes. Cape Canaveral in Florida has, as one of the launch criteria, the predicted strength of electrical storms as determined by a field mill array. The field mill array is capable of anticipating the strength of the storm before the onset of high winds. The further discussion of this aspect of the electric field environment is outside the scope of this article. It is mentioned here for the sake of interest only. The prevailing weather conditions at the time were calm winds and clear skies.

These time series can be examined more closely by simply plotting one output against the other. Figure 3 represents the first few hours of this series and a linear trend is clear. A least squares fit is applied. The gradient is the scale factor for converting from the output of the field machine to the voltage assumed by the sphere. At this stage, it does not relate to the electric field directly. The intercept provides some trouble, however. An additional piece of information is that when the electric field is zero, the output of the field machine is a few mv. This offset is due to the mill electronics. This is known because the field mill can be easily shielded from the earth's electric field and the output measured.

The -0.206 V offset implies that when the electric field is zero, the sphere is sitting at some non-zero voltage. Clearly, there are static charges or other local sources present somewhere that produce the annoying offset.

Figure 4 plots over the entire time series of the output of the mill against the output of the sphere. The intercept appears to meander widely. A least squares fit to this data would be meaningless.

The intercept hopping through time can be investigated further by sweeping a window down the time series and calculating the gradient and intercept at each point. A reasonable window was considered to be ten minutes. This represents sixty digital values - a fair statistical sample. This

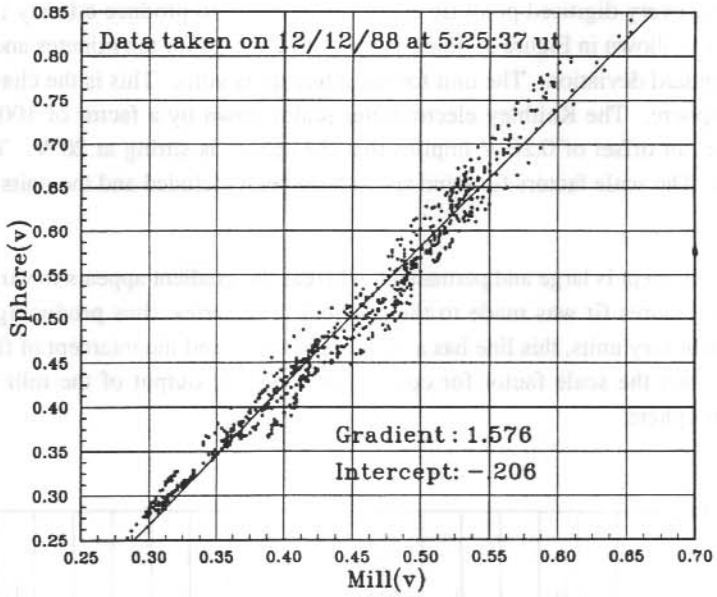


Figure 3. Plot 1 of 'field mill' against 'spherical antenna' (La Trobe).

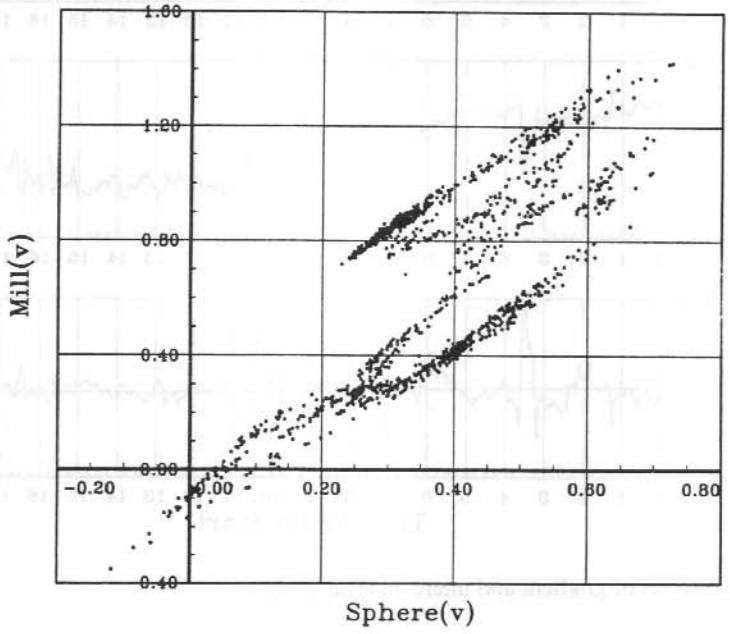


Figure 4. Plot 2 of 'field mill' against 'spherical antenna' (La Trobe).

is stepped along every digitised point (ie every ten seconds) to produce a finely resolved result. The time series is shown in Figure 5. Each point is the average for ten minutes and the error bars display the standard deviation. The unit for the intercept is volts. This is the changing offset of the potential sphere. The Keithley electrometer scales down by a factor of 100 from input to output. Hence, an offset of 0.20 V implies that the sphere is sitting at 20 V. The gradient is dimensionless. The scale factors for wind speed have been included and the units are metres per second.

The change in intercept is large and permanent, whereas the gradient appears to vary about a fixed level. A least squares fit was made to the gradient time series, thus producing a gradient of gradients. In arbitrary units, this line has a gradient of 0.001 and the intercept of this line is 1.58. This figure is then the scale factor for conversion from the output of the mill to the voltage assumed by the sphere.

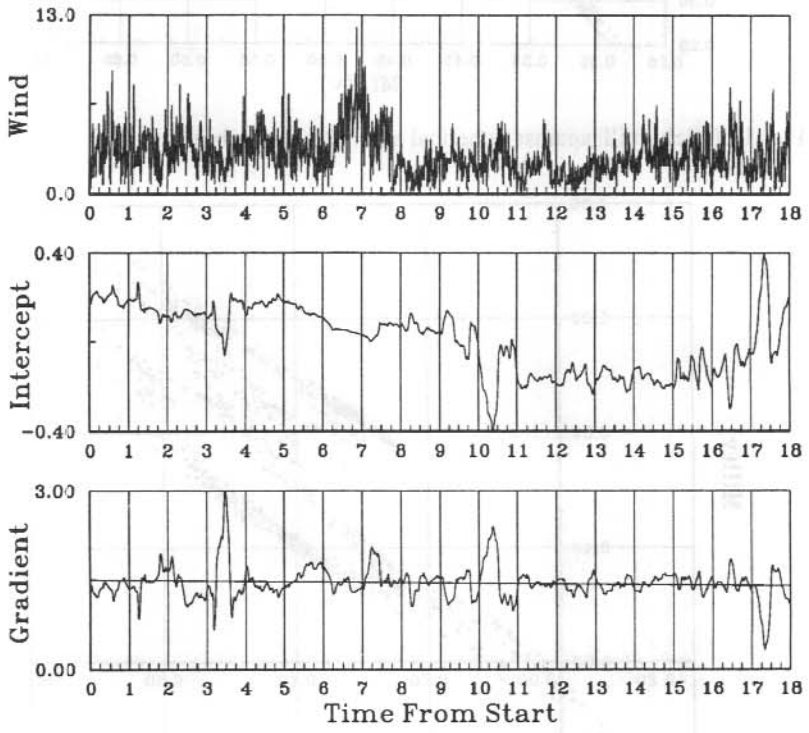


Figure 5. Time series of gradient and intercepts (La Trobe).

*20.6.1 Error estimates of the results from La Trobe*

The size of the errors associated with this method depend upon how linear the fit between the two data sets is. In the latter part of the sample period, the variation in gradient is smaller and this reduces the error estimate. Rather than use a bulk value, such as a $\chi^2$ statistical test of goodness of fit, into which the earlier turbulent periods would add equally, this latter period is selected as the most usable. By visual inspection the empirical equation (6) is arrived at.

$$V_{sphere} = 100 \text{ x } (1.56 \pm 0.03)V_{mill} \qquad (6)$$

Where $V_{sphere}$ is the voltage assumed by the sphere, $V_{mill}$ is the output of the electric field mill and the 100 is the scale factor due to the Keithley electrometer.

This experiment was run over many days and the collective results fell within these error bounds. After a few days, the impedance degrades, probably due to deposition about the insulation between the sphere and the mast and the antenna can no longer be used. Some degree of intuition and experience is required to decide when the results are no longer valid.

20.7 EXPERIMENTAL RESULTS FROM DAVIS

A similar procedure for the site at Davis station, Antarctica was carried out. The same antenna and metering system were transported to the site by ship and placed above the local ground plane there. The level of noise is greater in the Davis experiment and filtering was required. The source of this noise is unknown. The data presented in Figure 6 is the raw unscaled information with the error bars representing standard deviations. Once again the units are the arbitrary digital values.

A similar procedure of phase plotting and gradient time series extraction was carried out. The plot of 'field measuring device' against 'sphere' appears in Figure 7. The data in this case has been low pass filtered. The time evolution of the gradient and intercept appears in Figure 8. A similar behaviour to the La Trobe results can be seen.

*20.7.1 Error estimates of the results from Davis*

In a similar fashion to the procedure carried out on the data from La Trobe, the error estimate was based upon the more quiescent periods of the series. The data is, unfortunately, more noisy giving rise to larger errors. The empirical equation (7) for Davis is:

$$V_{sphere} = 100 \text{ x } (2.0 \pm 0.1)V_{mill} \qquad (7)$$

Where $V_{sphere}$ is the voltage assumed by the sphere, $V_{mill}$ is the output of the electric field mill and the 100 is the scale factor due to the Keithley electrometer.

Similar comments apply to the reproducibility of the Davis data. The test was carried out over several days with equivalent results.

## 20.8 DIFFICULTIES INVOLVED IN THE MEASUREMENTS

The greatest problem is the insulation of the potential sphere from ground. The Keithley meter is capable of measuring impedances up to $10^{18}\ \Omega$. All connectors and cabling must have verified high insulation before their use in the sphere. Using 'clean' techniques akin to those employed in vacuum physics, impedances in excess of $10^{16}\ \Omega$ were obtained. The Keithley meter was used to test the insulations. An instrument of such quality is vital to the development of such a measurement. It was found that the sphere could be left in place for two to three days before degradation of the insulation took place and the voltage declined to zero. It was then necessary to disassemble the insulation and clean it thoroughly, an extremely time consuming process. Any sort of precipitation destroys the measurement permanently and the antenna must be taken down and cleaned. For this reason such a device is not practical for continuous measurement of electric fields. It can be used, however, as shown in preceding sections, as a useful device for comparing data from different sites. In the next section the problem of reduction to absolute values is addressed.

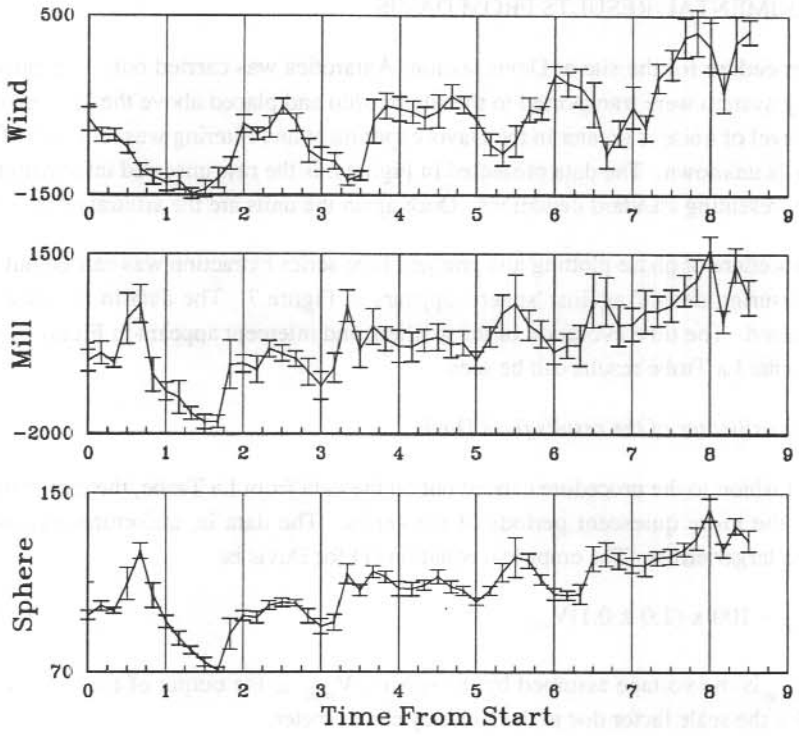


Figure 6. An example of data collected by 'sphere' and 'mill' at Davis.

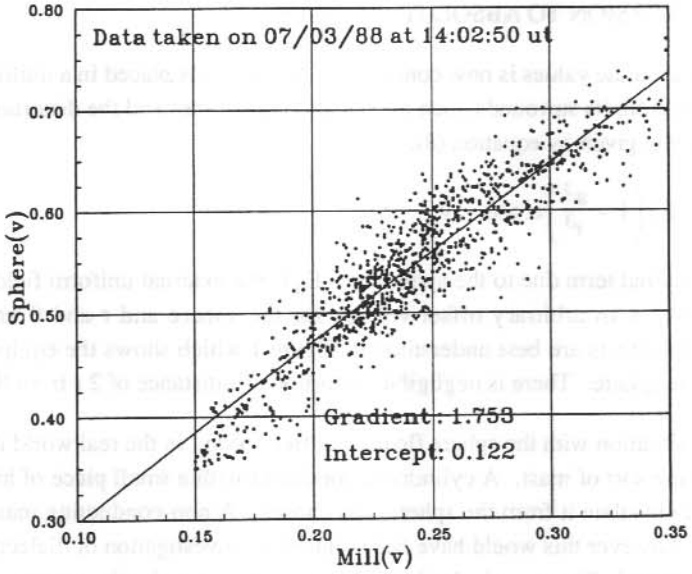


Figure 7. Plot of 'field mill' against 'spherical antenna' (Davis).

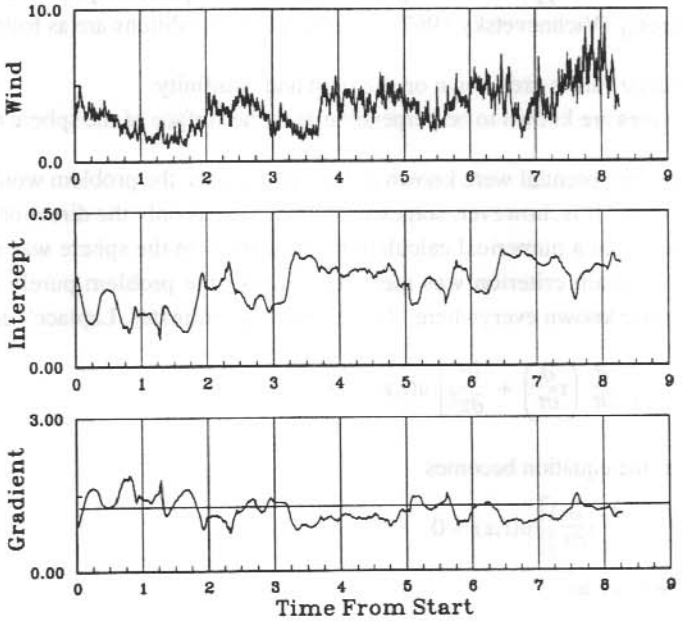


Figure 8. Time series of 'gradiant' and 'intercepts' (Davis).

## 20.9 THE CONVERSION TO ABSOLUTE VALUES

The question of absolute values is now considered. If a sphere is placed in a uniform electric field in space, isolated from its surrounds, then the potential it assumes and the distortion it produces in space is analytically given by equation (8).

$$V(r,\theta) = -E_0\left(1 - \frac{a^3}{r^3}\right)r\cos\theta + V_0 \qquad (8)$$

There is no azimuthal term due to the symmetry. $E_0$ is the external uniform field, a is the radius of the sphere, $V_0$ is an arbitrary offset voltage for the sphere and r and $\theta$ are the spherical coordinates. The effects are best understood in Figure 1 which shows the equipotential lines in the vicinity of the sphere. There is negligible distortion at a distance of 2 r from the sphere.

This is an ideal situation with the sphere floating in free space. In the real world it is necessary to carry it upon some sort of mast. A cylindrical conductor with a small piece of high quality non-polar dielectic to insulate it from the sphere was chosen. A non-conducting mast could perhaps have been used, however this would have necessitated the investigation of dielectic behaviour for some specific material. For numerical calculation, a conductor is simpler to account for.

## 20.10 THE METHOD OF FINITE ELEMENTS

The equation that can be applied to the sphere and mast is Laplace's equation in three dimensions with axial symmetry (Vichnevetsky 1967). The boundary conditions are as follows:

(1) The boundary values are known on the mast and at infinity.
(2) The field lines are known to be perpendicular to the surface of the sphere and mast.

If the gradient of the potential were known on the sphere, then the problem would be described as a 'Robbins' problem. It is, however, somewhat incomplete as only the direction of the gradient is known. In order to do a numerical calculation, a potential on the sphere was assumed and then modified until a certain criterion was met. This makes the problem purely Dirichlet, i.e. the boundary values are known everywhere. In cylindrical coordinates, Laplace's equation is

$$\nabla^2 u(r,z) \equiv \left[\frac{1}{r}\frac{\partial}{\partial r}\left(r\frac{\partial}{\partial r}\right) + \frac{\partial^2}{\partial z^2}\right] u(r,z) = 0 \qquad (9)$$

Multiplying by r, the equation becomes

$$\left[\frac{\partial}{\partial r}\left(r\frac{\partial}{\partial r}\right) + \frac{\partial}{\partial z}\left(r\frac{\partial}{\partial z}\right)\right] u(r,z) = 0 \qquad (10)$$

This may be re-written as

$$\nabla(r\nabla u) = 0 \qquad (11)$$

where $\nabla$ is the Cartesian operator

$$\nabla \equiv \begin{bmatrix} \frac{\partial}{\partial r} \\ \frac{\partial}{\partial z} \end{bmatrix} \qquad (12)$$

Triangular elements were used as a circular arc can be represented with good symmetry and accuracy if a fine enough mesh is applied. A portion of such a mesh appears in Figure 9. The numbering of the nodes starts at the top left and proceeds from left to right down the rows.

Software was developed which implemented a finite element solution. The condition at infinity was approximated with a large enough mesh. The size of the mesh was varied. The real physical distance where there is no discernible disturbance of a measuring device was used as a starting point. When a solution was obtained, the size was increased. This experimentation was carried out until the result did not vary significantly (less than one percent). The fineness of the mesh depends on the desired accuracy. In order to have the condition at the infinite boundary met to within one percent, and the potential of the sphere found to within one volt, a mesh of 200 by 200 nodes was required. With the method of finite elements, this produces a sparse symmetric matrix having 1.6 billion elements. The Gauss-Seidel method with successive over-acceleration was used to solve the matrix. Reich (1949) proved that this method of iteration converges always if and only if the matrix is positive definite. Solutions of elliptic partial differential equations always produce positive definite matrices, and so a result can be found. Since the matrix is sparse, it is not necessary to store all the elements. In effect, there are only something like one million non-zero elements.

In order to determine the potential that the isolated sphere would float to, the sum of squares of the dot products of the unit tangential vector to the sphere and the potential gradient can be calculated and minimised by adjusting the potential of the sphere. This amounts to a 'relaxation' technique for finding the unknown potential. Figure 10 is a flow chart that displays the logic.

A solution was carried out on a VAX 8600, but the computation time was found to be extreme. The code was modified to run on a MPS 3100 which has ten times the computing power of the VAX system. A complete solution on this system took approximately 4 hours.

## 20.11 THE SIMULATION RESULTS

With the size and spacing of the mesh, it is possible to derive the voltage of the sphere to the nearest volt. This voltage corresponds to the impressed electric field. Thus, using the result of empirical equations (6) and (7), the following empirical results are obtained

$$E_{Davis} = 2.6 \times 100 \times (2.0 \pm 0.1)V_{Davis} \qquad (13)$$

$$E_{La\ Trobe} = 1.7 \times 100 \times (1.56 \pm 0.03)V_{La\ Trobe} \qquad (14)$$

Where the E values are the electric field strengths at the respective locations and the V values are the real voltage outputs of the electric field measuring machines. The coefficients of 2.6 and 1.7 are produced by the numerical calculation. Their respective errors are not reported as the experimental error in the 'gradient of gradients' calculation exceeds this error significantly. This relationship 'connects' the two sites and scales them to absolute values.

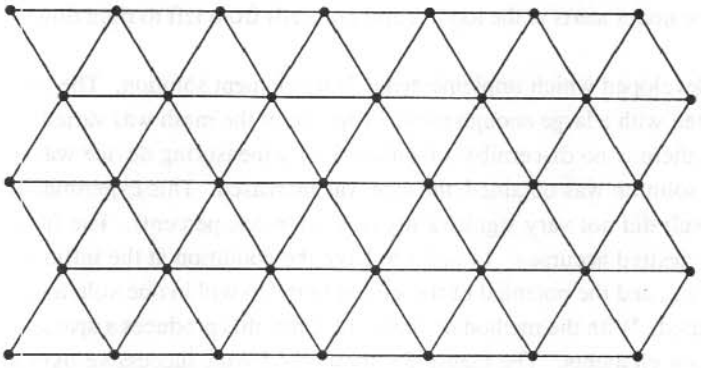

Figure 9. Fine element mesh.

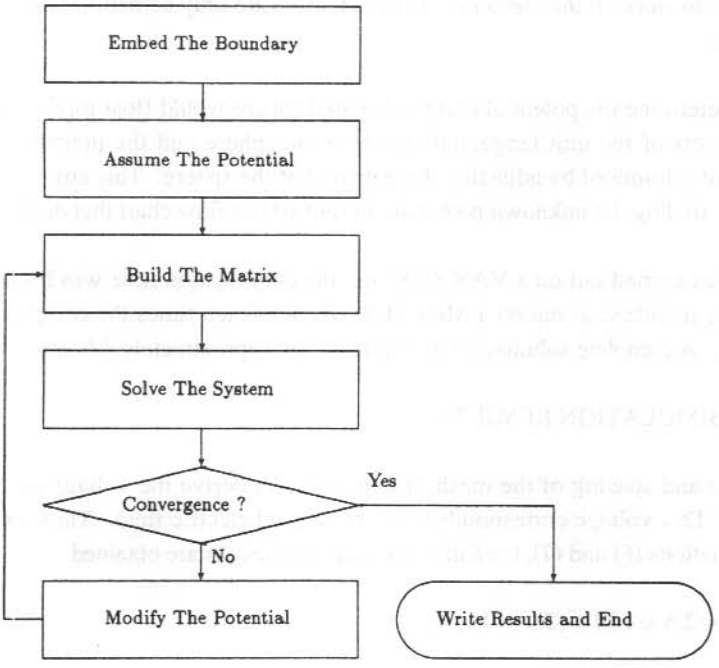


Figure 10. Finite element solution flow.

## 20.12 ACKNOWLEDGMENT

The measurements at Davis station, Antarctica were made by Dr Russell McLoughlin of the Antarctic Division, Kingston.

## 20.13 REFERENCES

Bauer, L.A. (1917). *Researches of the department of terrestrial magnetism,* Carnegie Institution of Washington *3*(175):361-422.

Chalmers, J. (1957). *Atmospheric electricity*. Pengamon Press.

Crozier, W.D. (1963). Measuring atmospheric potential with passive antennas. *Journal of Geophysical Research 68*:5173-5179.

Imyanitov, I.M. *and* Chubarina, E.V. (1967). *Electricity of the free atmosphere*. Israel program for scientific translations.

Israel, H. (1973a). *Atmospheric electricity*. Volume 1. Israel program for scientific translations.

Israel, H. (1973b). *Atmospheric electricity*. Volume 2. Israel program for scientific translations.

Park, C.G. (1976). Solar magnetic effects on the vertical electric atmospheric field at Vostok, Antarctica. *Geophysical Research Letters 3*:475-479.

Reich, E. (1949). On the conversion of the classical interative methods of solving linear simultaneous equations. *American Mathematical Statistics 20*:448-451.

Vichnevetsky, R. (1967). *Computer methods for partial differential equations*. Volume 1. Prentice Hall.

Whipple, F.J.W. (1929). On the association of the diurnal variation of electric potential gradient in fine weather with the distribution of thunderstorms over the globe. *Quarterly Journal of the Royal Meteorological Society 55*:351-361.

# 21. ION-CYCLOTRON AND LOWER ELF WAVE PHENOMENA

B.J. Fraser[1] and D. Sentman[2]

[1]Department of Physics
University of Newcastle
Newcastle NSW 2308
Australia

[2]Institute of Geophysics and Planetary Physics
UCLA
Los Angeles CA 90024
USA

ABSTRACT

The earth's magnetosphere and ionosphere supports the generation and propagation of a multitude of plasma waves, some of which may be observed on the ground. Of particular interest to the University of Newcastle research group, is the development of ground-based and spacecraft diagnostic techniques to probe the plasma properties of these regions using ULF and ELF waves at middle and high low latitudes. Currently, techniques are being developed using ion-cyclotron waves (ICW) (~1 Hz) generated in the vicinity of the plasmapause by the ion-cyclotron instability, and ELF Schumann resonances (3-100 Hz) in the earth-ionosphere cavity. The properties of ICW generation and propagation observed by spacecraft in the magnetosphere are drastically modified by the presence of small concentrations of heavy ions ($He^+$ and $O^+$) in the cold/cool magnetospheric plasma. Each heavy ion species produces cut-off, resonance and crossover frequencies and a stop-band in the wave spectrum. Remote sensing using ground-based Schumann resonance and ELF observations supports the study of global lightning activity, slow and rapid D-region variability, Q-burst interferometry, and naturally occurring lower ELF band phenomena. The first half of this paper is tutorial and describes the basic physics of the ion-cyclotron instability and a study of wave growth in conjunction with ISEE spacecraft data. The second part considers ELF observations and plans for future experiments.

## 21.1 INTRODUCTION

The ultra-low frequency (ULF) waves of interest here are ion-cyclotron waves (ICW) which are generated within the magnetosphere and propagate to the ground where they are seen as Pcl-2 geomagnetic pulsations in the 0.1-5 Hz frequency band. The second half of the paper describes a proposed global study of the properties of naturally occurring electromagnetic noise at the lower end of the extremely low frequency (ELF) band at 3-200Hz. Here the primary emphasis is on the Schumann resonances.

Both the ICW and ELF studies involve cooperative research between the University of Newcastle and the Institute of Geophysics and Planetary Physics at UCLA.

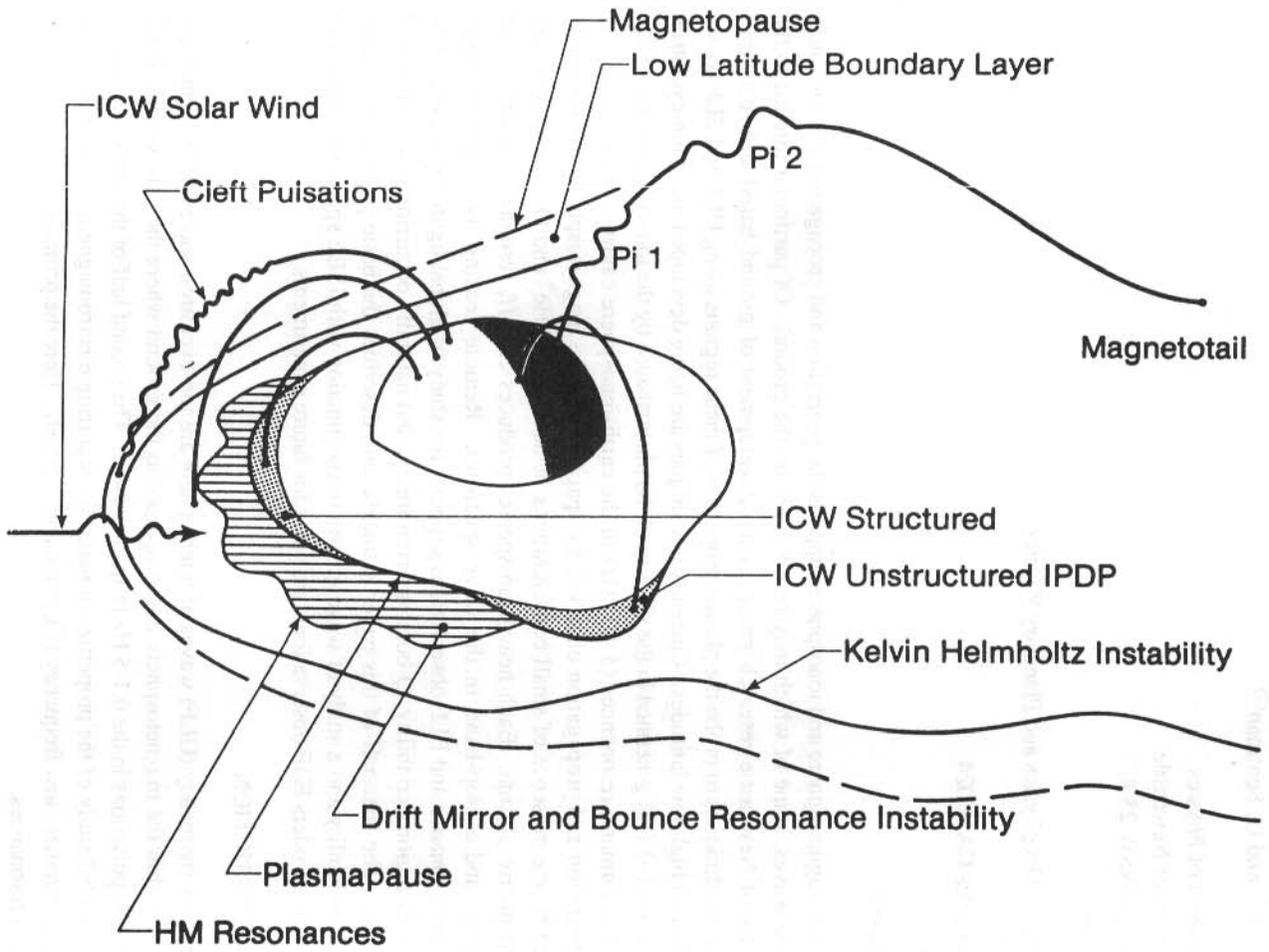


Figure 1. A schematic model of ULF hydromagnetic and ICW waves seen in the earth's magnetosphere (Samson 1990).

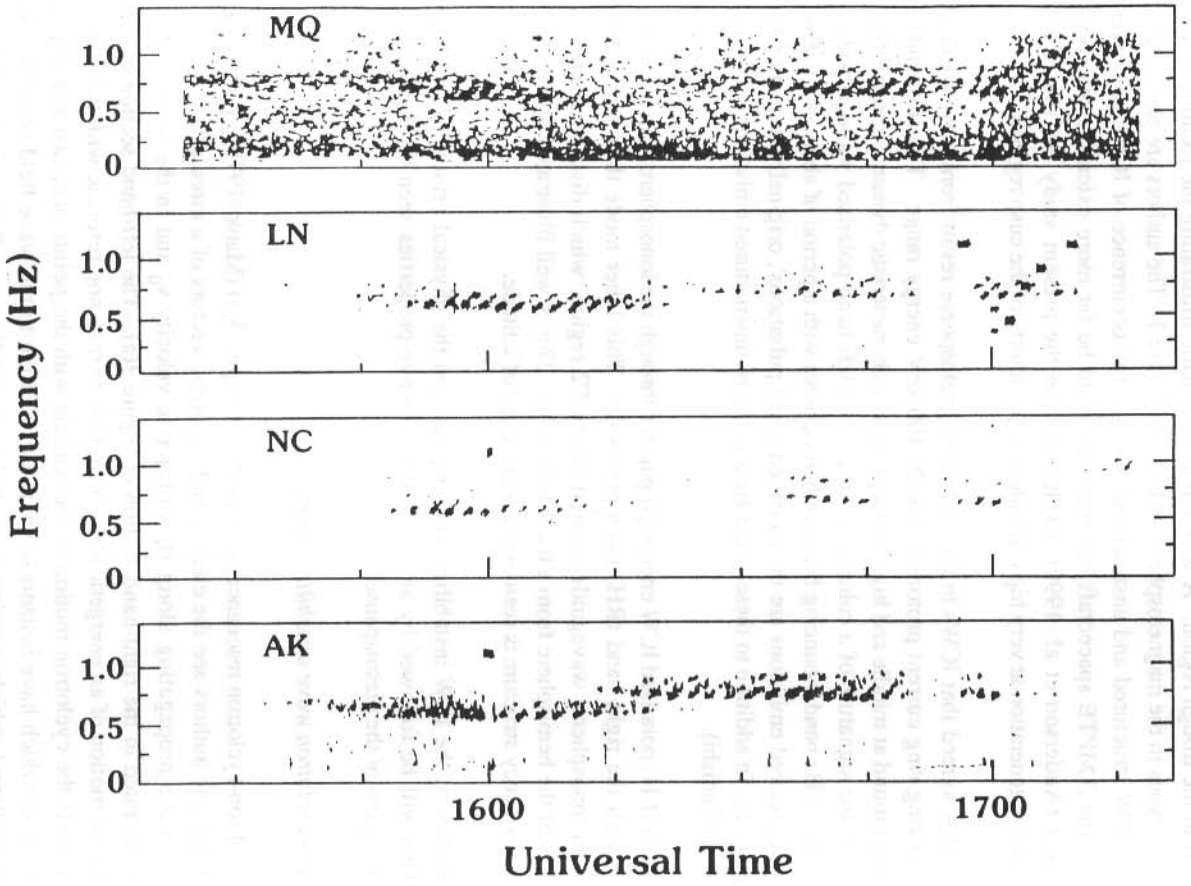


Figure 2. A Pc1 ICW emission recorded at four stations in Australasia between 1540-1710 UT on December 16, 1977. The stations are Macquarie Island (MQ, L=4.3), Launceston (LN, L=2.7), Newcastle (NC, L=1.8) and Auckland (AK, L=1.9).

## 21.2 ION-CYCLOTRON WAVES

The ICWs are generated in the closed field line region of the magnetosphere, particularly near the plasmapause and in the trough region. A wire model schematic illustrating the location of the various ULF wave types in the magnetosphere is shown in Figure 1. The authors are particularly interested in the ICW structured and unstructured waves. The occurrence of ICWs seen over these regions by the AMPTE spacecraft has been shown to be far more extensive than was originally thought (Anderson et al. 1990). Excluded from the present study are the ICWs associated with wave generation at very high latitudes in the vicinity of the cusp regions.

It is now, generally, agreed that ICWs in the middle magnetosphere result from wave particle interactions involving ring current protons in the 20-100 keV energy range. The subsequent ICWs seen on the ground at middle and high latitudes show a characteristic dynamic spectral fine structure, which is the signature of a coherent field-aligned left-hand polarised wave packet of frequency in the 0.1-5 Hz band, bouncing between hemispheres with a period of about one to five minutes. These structured emissions are the so-called 'pearl pulsations', originally so named by Troitskaya (Figure 2). In addition to these, there are a group of unstructured emissions occurring at high latitudes (Fukunishi).

When the left-hand (LH) polarised ICW energy propagates through the ionosphere, it experiences mode coupling with the right-hand (RH) isotropic mode. This latter mode then propagates horizontally in an ionospheric waveguide centred on the F2 region, which distributes energy across wide areas of the hemisphere from a localised source. This is well illustrated by Figure 2 where the same frequency structure is seen over a wide range of latitude.

The basic properties of the ICW instability with emphasis on the physical principles was first considered. This will be followed by an illustration of wave properties seen by the ISEE-1 spacecraft in the region of the plasmapause.

### *21.2.1 Linear ion-cyclotron wave instability theory*

The phenomena of ion-cyclotron resonance is illustrated in Figure 3(a) (Mauk (1978)). Following Mauk's description, the authors see the electric and magnetic vectors of a circularly polarised electromagnetic wave propagating along $B_0$ with phase velocity $v_0$ and in the wave vector direction $\underline{k}$, as illustrated in the right-hand section of Figure 3(a). The left-hand section of the figure illustrates the motion of an energetic ion which may, or may not, resonate with the wave. The circle represents the cyclotron motion of the particle with the points one, two and three, representing particles which have instantaneous phases relative to the wave field patterns. A particle at phase position 1, which experiences the field pattern adjacent to B sees an electric field vector parallel to its perpendicular particle velocity ($\underline{v}_\perp$) and will, at that instant, gain energy. By the same argument a particle at position 3 will lose energy. Consider now a particle at point B on the figure. This particle rotates with cyclotron frequency $\Omega_i$, whereas the field pattern rotates at

frequency $\omega$ as the wave pattern moves along the field line. Since $\omega < \Omega_i$ for ICWs, the particle will gain energy at one instant of time and lose energy at the next instant. As a result there will be no net energy exchange. Now consider the particle located at B at phase position 1, it has a parallel velocity $\underset{\sim}{v}_{\|}$ in the direction antiparallel to $\underset{\sim}{k}$ such that, by the time the particle has reached phase position 2, the particle has moved along $\underset{\sim}{B}_0$ so, that it sees the field pattern initially across from point C. Here at phase position 1, $\delta\underset{\sim}{v}_{\perp}$ is parallel to $\delta\underset{\sim}{E}$ and at phase position 2, $\delta\underset{\sim}{v}_{\perp}$ will again be parallel to $\delta E$. This leads to a continual one-way exchange of energy between the particle and the field. The cyclotron frequency is independent of particle energy and ,therefore, the parallel resonant velocity will also be independent of energy. Thus, all particles which resonate with the wave will be on a vertical line in velocity space, as displayed in Figure 3(b). The resonant velocity is given by

$$kv_{\|} = \omega - n\Omega_i \qquad (1)$$

where n is integer.

It is obvious that the presence of resonant particles does not guarantee an energy transfer since an initial random phase distribution will have just as many particles at phase position 1 gaining energy, as there are particles at phase position 3 losing energy.

It is now important to investigate the interaction between the particle velocity and $\delta B$. From Figure 3(a), the $e\underset{\sim}{v}_{\perp} \times \delta\underset{\sim}{B}$ force will move the resonant particles at phase point 1 parallel to $\underset{\sim}{B}_o$ and those at phase point 3 anti-parallel to $\underset{\sim}{B}_o$. As a consequence $\delta\underset{\sim}{B}$ sorts the nearly resonant particles by phase along the field line relative to the wave field patterns. Figure 3(c) illustrates this argument. If the particle in Figure 3(c) is nearly resonant then the phase $\varphi$ of the particle relative to $\delta\underset{\sim}{B}$ will change only very slowly on a time scale synchronised with the cyclotron or wave frequency. By interacting with $\delta\underset{\sim}{B}$ the particle near phase position 1 tends to drift towards position 2. A particle near position 3 will also tend to drift towards position 2. Therefore, some particles will oscillate around phase position 2, depending on initial conditions, at a trapped particle oscillation frequency ($\omega_t$). The wave trapping of particles in this manner is discussed by Hu and Fraser elsewhere in this volume. It should be remembered that there is still have a problem in creating a situation whereby more particles lose energy than gain energy, since the interaction will move both those particles losing and gaining energy towards the neutral region at phase point 2. The problem can be solved by considering the initial conditions and the dynamics of the nearly resonant particles.

Consider a set of randomly phased particles which have parallel velocities which are slightly slower than the exact resonant velocity. Here the phases advance in a clockwise manner as seen in Figure 3(c). On a time scale much shorter than $\omega_t$ these subresonant particles will bunch near phase point 3, due to interaction with $\delta\underset{\sim}{B}$ and result in a net particle to wave energy transfer. But, there are also super-resonant particles which rotate counter-clockwise, bunch near phase point 1, and remove energy from the wave. Whether the sub-resonant or super-resonant particles dominate depends on the details of the unperturbed energetic ion distribution function.

The energetic ions which resonate with the wave interact with both the electric and magnetic wave fields. Interaction with $\delta\underline{B}$ causes the wave to travel on concentric circles (Figure 3(b)) since this conserves energy. Interaction with $\delta\underline{E}$ results in an energy transfer which pulls the particles off the concentric circles. A typical diffusion path is seen in Figure 3(b). The particles which begin at point I are sub-resonants and will lose energy and, therefore, drift on the diffusion curve to a smaller concentric circle ($|\underline{v}|$) towards the resonant region. The super-resonant particles at point II will gain energy by moving towards the resonant region. Obviously there must be a gradient on the unperturbed distribution function along the particle diffusion paths, such that more particles exist at I than at II, for a net overall particles to wave transfer of energy.

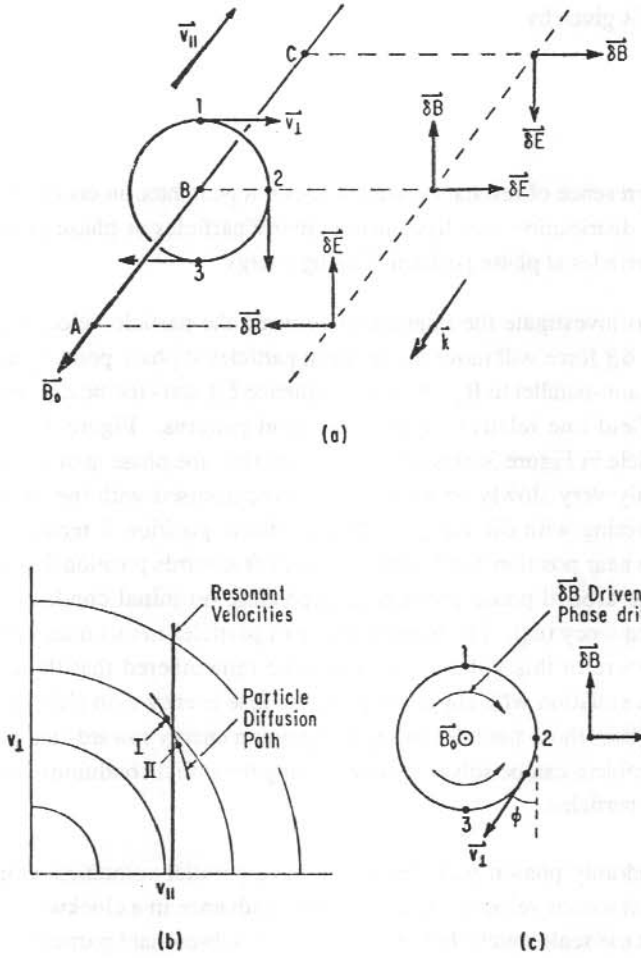


Figure 3. The electromagnetic ion-cyclotron instability (Mauk 1978). (a) Wave-particle interaction configurations. (b) Velocity space cyclotron resonance region and a typical ion diffusion path. (c) Field-particle phase diagram for nearly resonant particles.

In practice, it is found that a simple pitch angle anisotropy will provide the required unstable configuration. It is, however, important to remember that observable waves will result only if the growth rate and interaction time are large enough. It is usual to define the pitch angle anisotropy A for the case $v_\perp > v_\parallel$ as

$$A = [( T_\perp / T_\parallel ) -1] > 1 \qquad (2)$$

ICW growth rates have been well studied in the past and have particular significance near the plasmapause (Kozyra et al. 1984). It is a well-established fact that ICWs are seen on the ground as Pc1 pulsations at middle latitudes some four to seven days following significant geomagnetic storm activity. A scenario to explain this is illustrated in Figure 4 (Kuwashima et al. 1981) where the intersection of the hot ring current ions with cold plasmaspheric particles at geomagnetic storm-times is seen. Greatest overlap is seen during the recovery phase, when Pc1 wave occurrence maximises. For the energetic ions (20-100 keV) with $A > 1$, the increase in cold ion density enhances the instability. In this regard, the role of the $B_o$ field magnitude may also be important, especially at the higher latitudes (Anderson et al. 1990).

*21.2.2 Ion-cyclotron waves near the plasmapause*

A first order understanding of the physics of the ICW instability over a wide range of parameter space may be gained by studying the linear growth rate. This can include multiple heavy ion species in both the energetic anisotropic component and the cold component of the plasma. It is apparent from the plasma data in Figure 5 that the waves are propagating in a multicomponent plasma containing $O^+$, $He^+$ and $H^+$ ions. The presence of $O^+$ and $He^+$ heavy ions introduces cut-offs, resonances and wave polarisation reversals in the Pc1-2 band (Young et al. 1981, Fraser 1985). For quasi-longitudinal LH mode wave propagation in a cold homogeneous collisionless plasma, resonances occur at the cyclotron frequencies, $\omega_{O^+}$ and $\omega_{He^+}$ and wave cut-offs at slightly higher frequencies. LH waves do not propagate in the stop-band between a resonance and a cut-off. This produces a slot in the wave spectra which has been identified in association with both $He^+$ and $O^+$ ions (Young et al. 1981, Fraser and McPherron 1982). Above these frequencies polarisation reversals associated with the $O^+$ and $He^+$ ion presence occur and the LH(RH) wave polarisation changes through linear to RH(LH) for non-zero wave normal angles.

Although a number of theoretical studies have been undertaken which predict wave spectra under various plasma and energetic particle conditions, there have been few direct comparisons with experimental results. In this section the instability is studied using ISEE-1 field and plasma data recorded some $10^o$ off the geomagnetic equator as the spacecraft crosses a broad plasmapause region.

The wave and plasma environment seen by ISEE-1 on an inbound pass near equatorial dusk on August 22, 1978 is shown in Figure 5. The top trace shows the Pc2 cyclotron wave event occurring at 0015-0140 UT. The second trace shows the total field (BT) after the spacecraft passes through the magnetopause at about 2130 UT. A large amplitude 180 s Pc5 wave can be seen. The electron sounder data (NE-) shows a gradual plasmapause commencing at L=8 at 0015

UT and continuing until about 0110 UT. Clearly, the Pc2 waves are observed in the thick plasmapause and within the plasmasphere. The next three plots show the Lockheed RPA 0.1-16 KeV/e warm plasma data for protons ($H^+$), helium ($He^+$) and Oxygen ($O^+$) ions. At 0020 UT there is a 5-fold increase in $O^+$ and a 2-fold increase in $He^+$ concentrations. The bottom tabulations show the relative concentrations of <100 eV/e thermal ions, calculated assuming a flowing Maxwellian. Large concentrations of $He^+$ are seen in the plasmapause/plasmasphere. $O^+$ concentrations are a few percent. The thick plasmapause seen here is associated with substorm onset just prior to 2200 UT and with $K_p$ decreasing from four to one 10 hours later. This is typical of the substorm refilling process in the dusk outer plasmasphere.

Although ICW wave propagation properties near the $O^+$ characteristic frequencies will account for many of the spectral properties observed (Fraser et al. 1986), they cannot explain the absence of wave power between $\omega_{xO}$ and $\omega_{cO}/\omega_O+$, or the decrease in wave frequency on passing through the plasmapause. These properties are associated with the ICW instability where the free energy source is the resonating energetic ring current protons.

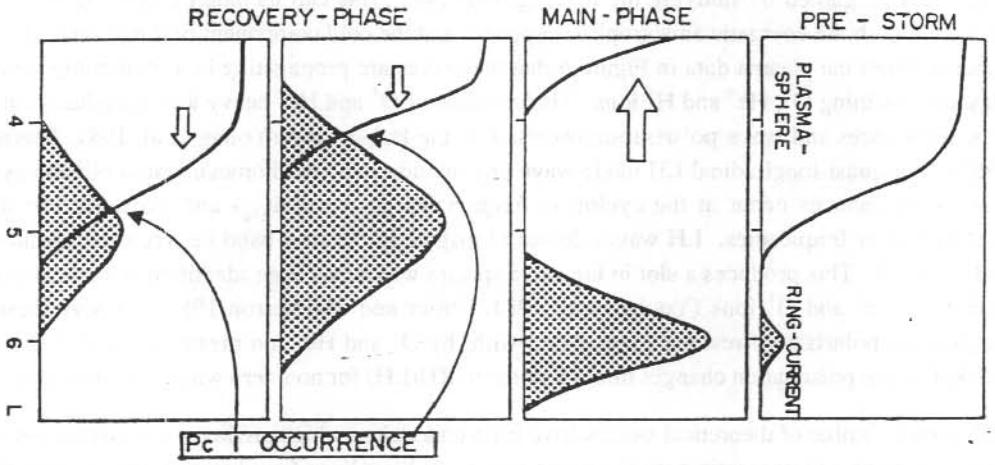


Figure 4. The overlap between the plasmasphere cold plasma with the energetic ring current plasma near the plasmapause (Kuwashima et al. 1981).

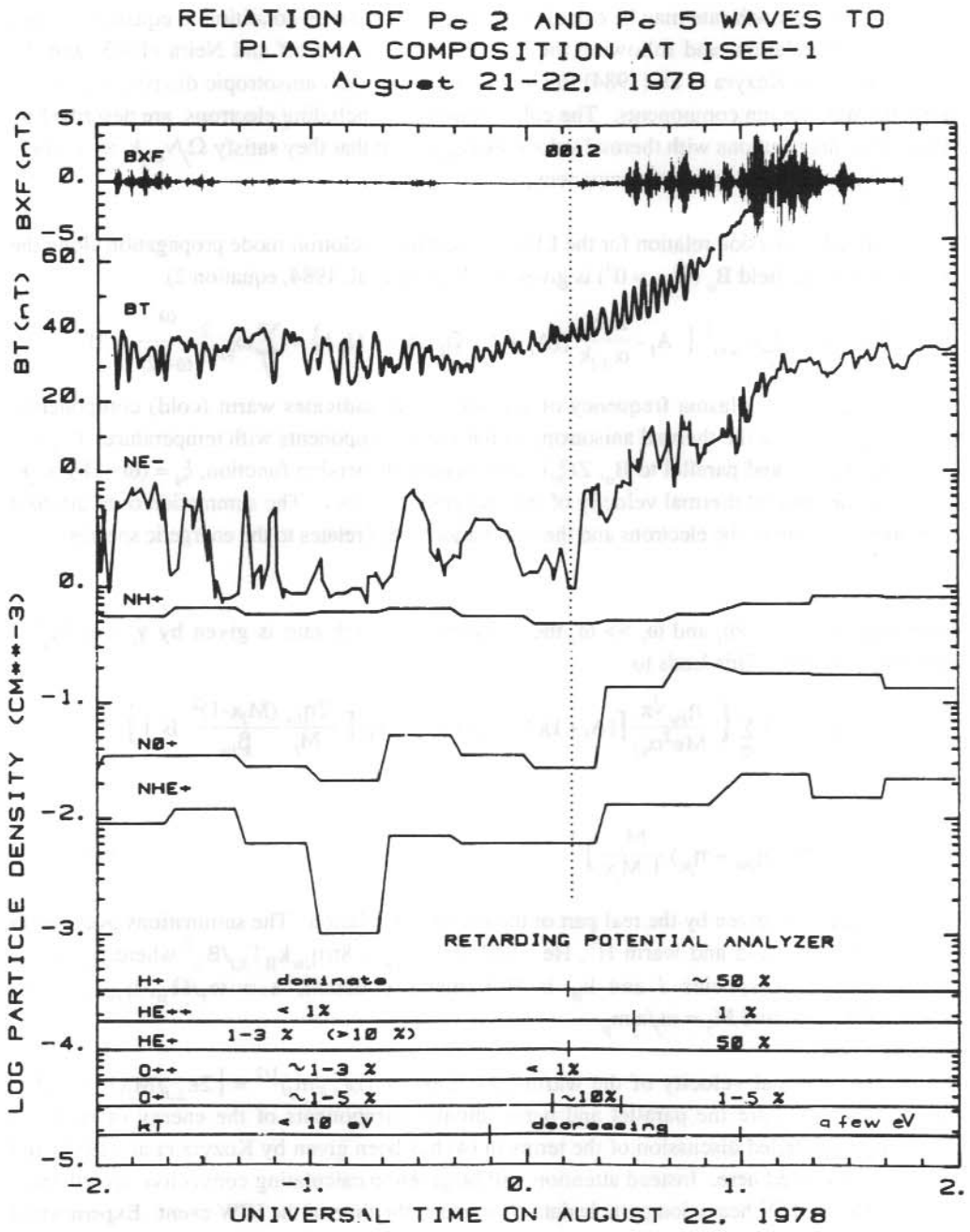


Figure 5. The wave and plasma environment observed in association with Pc2 ICW activity.

The convective growth rate may be calculated using the resonance condition in equation (1) and the dispersion relation, and following the derivation of Gomberoff and Neira (1983) and the modifications by Kozyra et al. (1984) to include bi-Maxwellian anisotropic distributions in the energetic multiple ion components. The cold populations, including electrons, are described by Maxwellian distributions with thermal velocities ($v_{th,j}$) such that they satisfy $\Omega_j/v_{th,j}k >> 1$ where $\Omega_j$ is the cyclotron frequency of component $j$.

The linearised dispersion relation for the LH polarised ion-cyclotron mode propagation along the ambient magnetic field $B_o$ ($\Theta_{kB} = 0^o$) is given by (Kozyra et al. 1984, equation 2)

$$\omega^2 = c^2k^2 - \sum_l \omega_{pl\omega}{}^2 \left\{ A_l - \frac{Z(\xi_l)}{\alpha_{\|\,l}k}\left[(A_l + 1)(\Omega_l - \omega) - \Omega_l\right]\right\} + \sum_j \omega_{pjc}{}^2 \frac{\omega}{\omega - \Omega_j} \quad (3)$$

where $\omega_{pl\omega\,(c)}$ is the plasma frequency of species $l$, w(c) indicates warm (cold) components, $A_l = \left[T_{\perp,l}/T_{\|,l}\right] - 1$ is the thermal anisotropy of the warm components with temperatures $T_{\perp,l}$ and $T_{\|,l}$ perpendicular and parallel to $B_o$, $Z(\xi_l)$ is the plasma dispersion function, $\xi_l = (\omega - \Omega_j)/\alpha_{\|,l}k$, and $\alpha_{\|,l}$ is the parallel thermal velocity of the energetic species $l$. The summation over the cold components $j$ includes the electrons and the summation over $l$ relates to the energetic species.

Assuming $\omega = \omega_r + i\omega_i$ and $\omega_r >> \omega_i$ the convective growth rate is given by $\gamma_s = \omega_i/\Omega_g V_p$ where $V_g = \partial\omega_r/\partial k$. This leads to

$$\gamma_s = \frac{\mu}{V_g} = B \sum_e \left\{ \frac{\eta_{lw}\sqrt{\pi}}{Me^2\alpha_{\|l}}\left[(A_l + 1)(1 - M_l x) - 1\right] \exp\left[ -\frac{2\eta_{lw}}{M_l}\frac{(M_l x - 1)^2}{\beta_{lw}} B \right]\right\}$$

where

$$B = \left[2x^2 \sum_j (\eta_{jw} + \eta_{jc})\frac{M_j}{1 - M_j x}\right]^{-1} \quad (4)$$

where $V_g$ and k are given by the real part of the dispersion relation. The summations over $l$ and $j$ includes all ions (cold and warm $H^+$, $He^+$, and $O^+$). $\beta_{lw} = 8\pi\eta_{lw}k_B T_{\|,l}/B_o{}^2$ where $\eta_{lw}$ is the density of warm species $l$ and $k_B$ is Boltzman's constant, $x = \omega_r/\Omega_p$, $\eta_{jw(c)} = M_j\left(\omega_{pjw(c)}{}^2/\omega_{ppw}{}^2\right)$, and $M_j = m_j/z_j m_p$.

The parallel thermal velocity of the warm ions is $\alpha_{\|,l} = (2\varepsilon_{\|,l}/m_l)^{1/2} = \left[2\varepsilon_{\perp,l}/M_l(1 + A)\right]^{1/2}$ where $\varepsilon_{\|,l}$ and $\varepsilon_{\perp,l}$ are the parallel and perpendicular components of the energy of each ion species $\varepsilon_l$. A detailed discussion of the terms in (4) has been given by Kozyra et al. (1984) and will not be included here. Instead attention will be given to calculating convective growth rates using the $He^+$ and $O^+$ heavy ion particle data observed at the time of the ICW event. Experimental parameters required to evaluate (4) are the ratio of the concentration of each hot and cold species to the hot protons ($\eta_l$), and the anisotropy ($A_l$) and perpendicular temperature ($T_{\perp,l}$) for each ion species. The thermal and warm heavy ion data in Figure 5 are taken to represent the cold and warm ions and their concentrations are listed in Table 1. The unknown parameters needed to

calculate the growth rate are $A_I$ and $T_{\perp,I}$ for each ion species. From a detailed study of the geosynchronous experimental data used by Mauk and McPherron (1980), Young et al. (1981) and Inhester et al. (1984), typical values for these parameters were chosen and are included in Table 1.

Table 1. Parameters used in convective growth rate calculations over four time intervals.

| Time (UT) | 0038-0042 | 0054-0058 | 0103-0107 | 0117-0121 |
|---|---|---|---|---|
| | 1 | 2 | 3 | 4 |
| Particles-Warm ($cm^{-3}$) | | | | |
| $N_{H+}(w)$ | 0.50 | 0.60 | 0.70 | 0.80 |
| $N_{He+}(w)$ | 0.020 | 0.02 | 0.025 | 0.022 |
| $N_{O+}(w)$ | 0.20 | 0.20 | 0.20 | 0.20 |
| Particles-Cold ($cm^{-3}$) | | | | |
| $N_{H+}(c)$ ($cm^{-3}$) | 7.00 | 9.00 | 28.00 | 41.00 |
| $N_{He+}(c)$ | 7.50 | 10.00 | 30.00 | 45.00 |
| $N_{O+}(c)$ | 0.60 | 1.00 | 2.50 | 4.00 |
| $\|B\|$ (nT) | 56.00 | 68.00 | 75.00 | 110.00 |
| Arbitrarily chosen parameters are : $T\perp(H^+)$ = 30 keV; $T\perp(He^+)$ = 10 keV; $T\perp(0^+)$ = 10 keV; $A(H^+, He^+, 0^+)$ = 1.0 | | | | |

A comparison of calculated wave spectra for the four time intervals in Table 1 with observed spectra are shown in Figure 6. All spectra and growth rates are normalised. In all four data intervals, the width of the minimum in the spectral slot is wider than the $\omega_{O^+}$ - $\omega_{cO}$ stop-band, but is the same width as the slot predicted by the wave growth calculations. Thus, heavy ions and the cyclotron wave instability, in addition to wave propagation, play a role in determining the spectral characteristics of the slot. Over the 0103-0107 UT interval, the spectral slot amplitude does not drop to the very low values seen in the other intervals. A significant slot amplitude such as this may be associated with thermal damping effects (Ball 1987). In Figure 6 the modelling of the low frequency (LF) branch describes the data reasonably well over all intervals. However, the LF branch is absent over the 0054-0058 UT interval. In the high frequency (HF) branch large wave amplitudes are seen at frequencies immediately above the slot over the 0054-0058 and 0103-0107 UT intervals and at higher frequencies over the 0038-0042 UT interval. There is no HF branch present over the 0117-0121 UT interval.

branch is absent over the 0054-0058 UT interval. In the high frequency (HF) branch large wave amplitudes are seen at frequencies immediately above the slot over the 0054-0058 and 0103-0107 UT intervals and at higher frequencies over the 0038-0042 UT interval. There is no HF branch present over the 0117-0121 UT interval.

The dynamic characteristics of the Pc2 wave growth process observed as the ISEE-1 spacecraft penetrates the plasmapause and enters the plasmasphere during the evolution of the wave event are also illustrated in Figure 6. It has been noted that the calculated bandwidths of both branches agree well with the observed spectra. Also, the shift to lower frequencies for the 0103 and 0107 UT interval is due to the increase in cold populations associated with the steep inner edge of the plasmapause seen at this time (Figure 5). In terms of wave growth described here, there is no obvious explanation for the absence of wave energy in the high frequency branch after O1 UT. The lack of energy in the low frequency branch before 01 UT may be associated with the low concentrations of the cold populations outside the plasmapause which reduces the wave growth bandwidth.

The electron and ion density data in Figure 7, along with the magnetic field magnitude, were used to determine the Alfven velocity both with ($V_A^+$) and without ($V_A$) heavy ion mass loading (Figure 2). The Alfven velocity is a minimum at the plasmapause when strong convective flows are seen and ion-cyclotron waves are generated. This scenario is not unexpected since wave growth maximises when $V_g$ (or $V_A$) is a minimum (Equation 2), a property which supports the idea that the plasmapause is a favoured region for ion-cyclotron wave generation.

*21.2.3 Summary*

The physics of ion-cyclotron wave interaction has been explained in detail and a realistic application of the theory to ICW's generated and propagating in a multicomponent energetic and cool plasma environment, has been considered. Convective growth rates have been compared with ISEE wave spectra. In particular, left-hand polarised ion-cyclotron waves have been observed by ISEE-1 in a thick plasmapause and the outer plasmasphere during the replenishment of the outer plasmasphere following substorm activity. This is a region of enhanced warm oxygen and helium and thermal helium where strong electric fields and plasma convection are seen, the Alfven velocity is a minimum and Pc2 wave amplitudes are large. The bandwidth of the waves spans the oxygen cyclotron, cut-off and crossover frequencies and multicomponent plasma propagation characteristics including the stop-band are seen in the ISEE-1 data. The predominance of left-hand polarisations in an off-equator location suggests that the spacecraft may be immersed in the generation region. Linear convective growth rate calculations taking into account cold and warm $H^+$, $He^+$ and $O^+$ ions show good agreement with ISEE-1 spectra in the plasmapause and outer plasmasphere. It is, however, important to note that this study of the ICW growth theory does not take into consideration non-linear effects or wave amplification along a growth path.

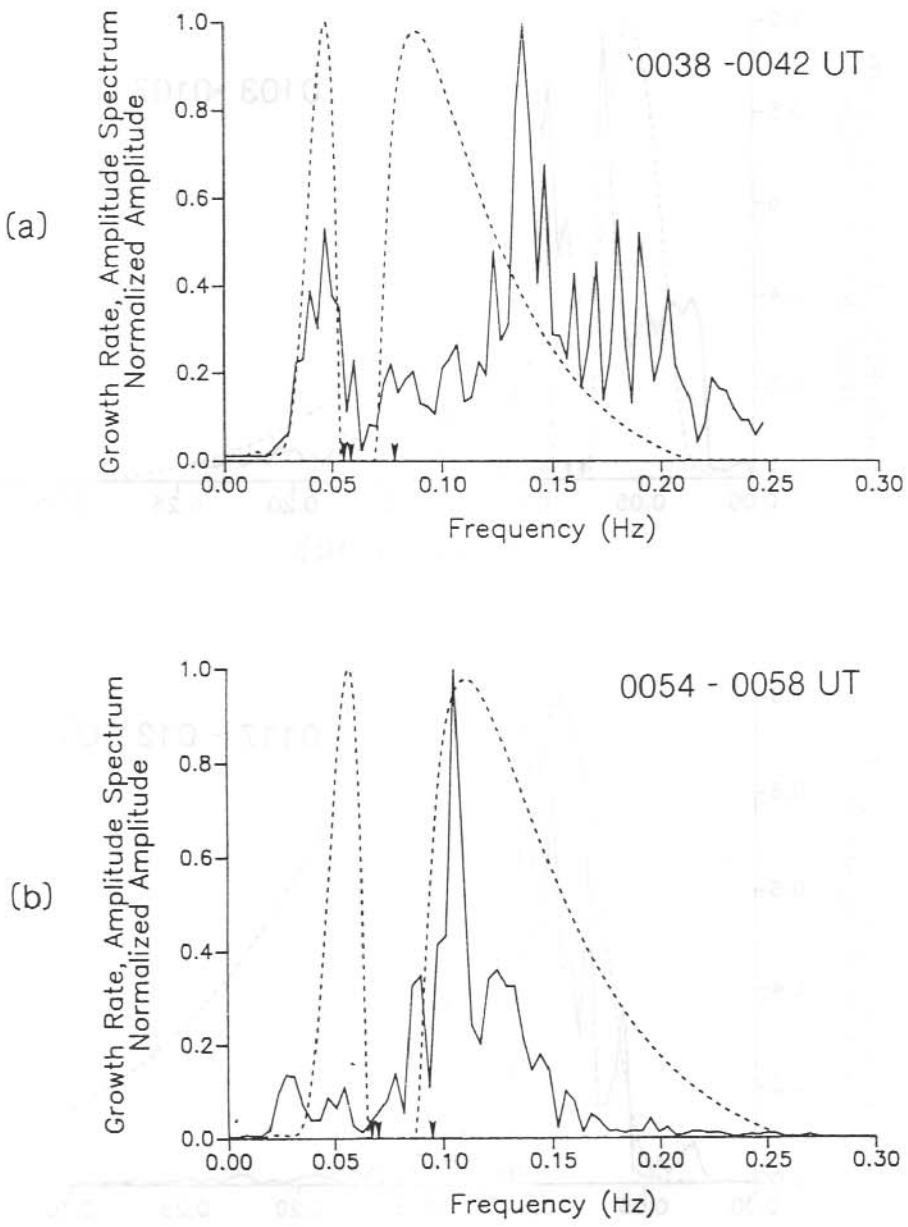


Figure 6. Convective ICW growth rate normalised amplitudes in the vicinity of the $O^+$ characteristic frequencies compared with observed ISEE-1 amplitude spectra over four time intervals. Wave growth calculations in (a) - (d) use data in columns 1-4 of Table 1 respectively. The experimental data was filtered with a cut-off frequency of 0.02 Hz. The three arrows on the frequency axis respectively indicate the local $O^+$ cyclotron frequency, the $O^+$ cut-off frequency, and the $O^+$ crossover frequency. (continued on following page)

(c)

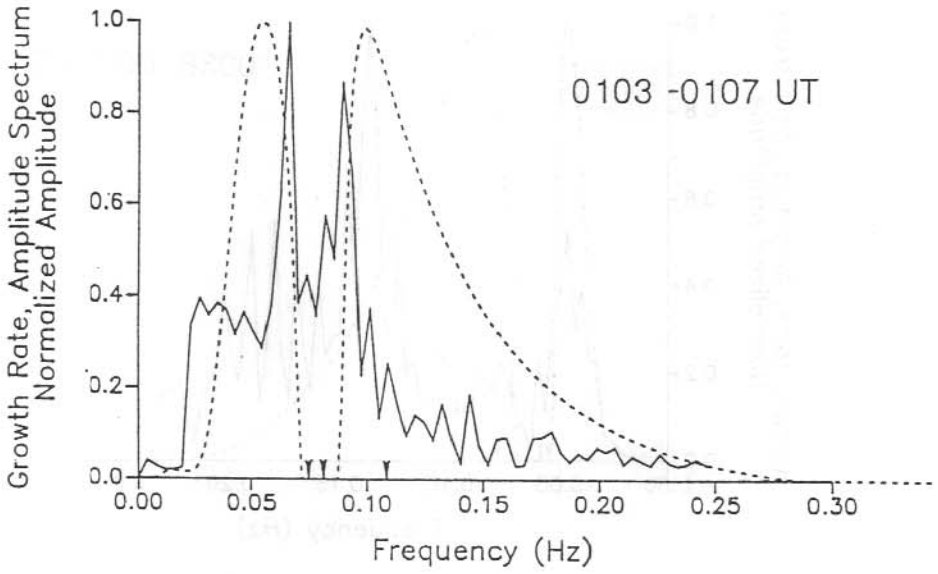


(d)

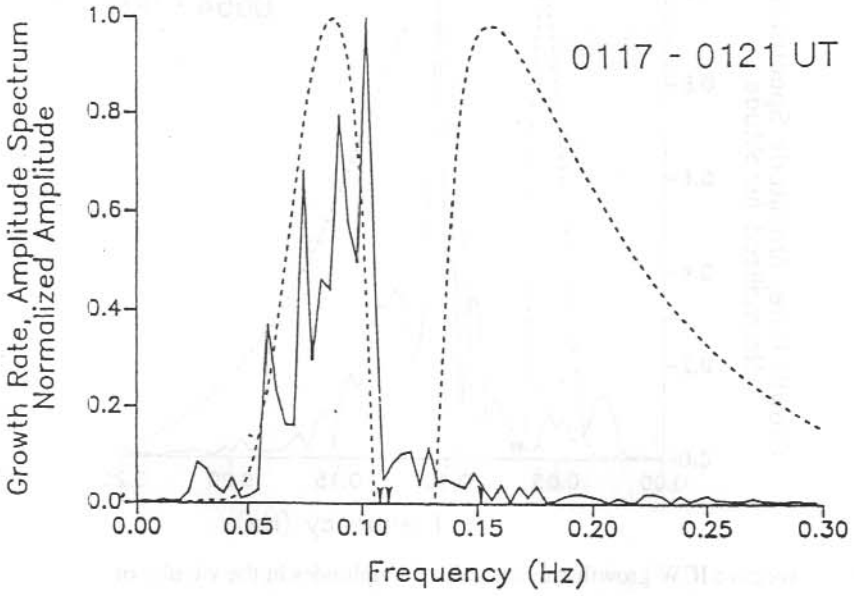


Figure 6 (c, d).

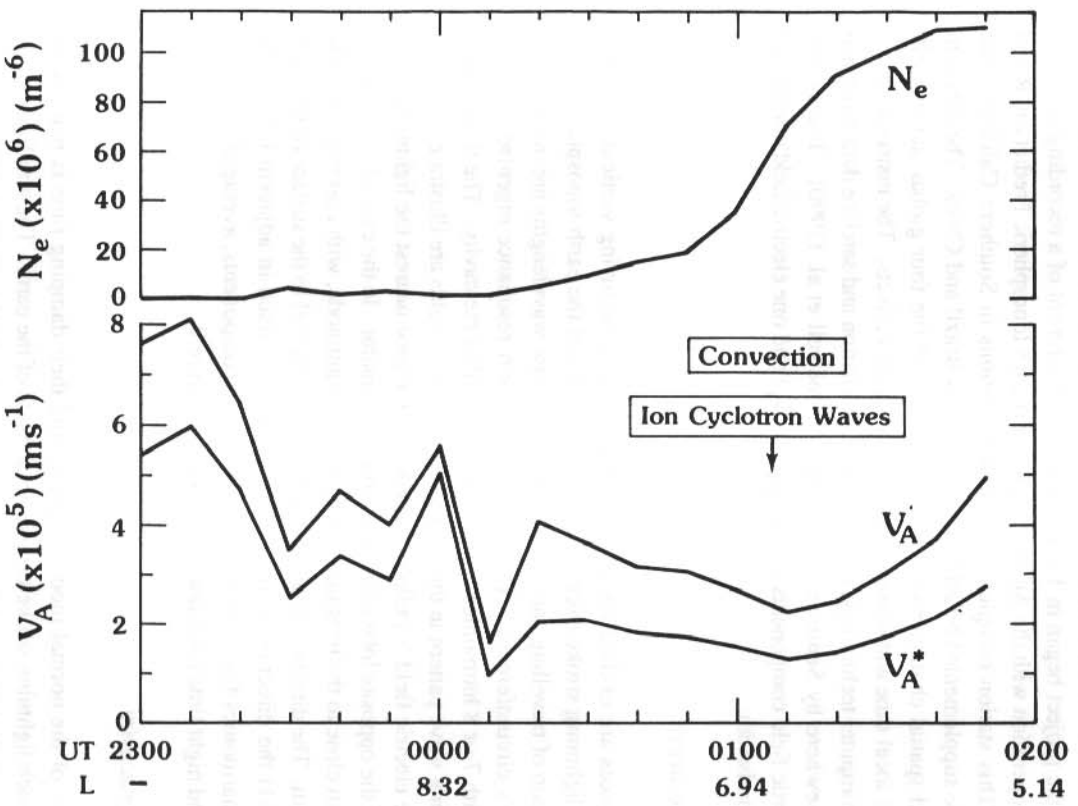


Figure 7. Upper: ISEE-1 electron sounder cold electron density measurements $N_e$ smoothed over 10 minute intervals. Lower: Alfven velocity profiles calculated using smoothed $N_e$ and smoothed total magnetic field measurements. $V_A$ takes into account the measured cool heavy ion mass loading calculated from the concentrations tabulated in the bottom panel of Figure 5 and assuming charge neutrality with $N_e$. The occurrence intervals of the Pc2 ion-cyclotron waves is indicated by the labelled rectangle with the arrow denoting the time of maximum wave amplitude at ISEE-1. The interval of strong plasma convection is also shown.

## 21.3 ELF WAVES IN THE EARTH'S IONOSPHERIC CAVITY

The University of Newcastle is providing a supporting role in a study initiated by IGPP/UCLA to investigate the properties of naturally occurring electromagnetic noise in the extremely low frequency (ELF) band of 3-200 Hz, with primary emphasis on the Schumann resonances. The experimental phase of the project began in 1989 with the establishment of a recording station at Learmonth, W.A. in cooperation with the Australian Government's Ionospheric Prediction, Radio and Space Services. This station complemented similar stations in Southern California and Alaska and will later be supplemented by additional stations in Brazil and China. The aim is to study the temporal and spatial characteristics of ELF waves and the four global stations will permit the separation of local time and seasonal effects from global effects. The instrumentation uses innovative microcomputer technology, real time data acquisition and satellite data links, and has been described elsewhere by Sentman (1987b) and Kennewell et al. (1990). The system records the three magnetic field components ($B_{NS}$, $B_{EW}$ and $B_V$) and one electric field component ($E_r$) over a 3-120 Hz bandwidth.

### *21.3.1 Shumann Resonances*

The Schumann resonances are excited continuously by naturally occurring vertical lightning. Each cloud-to-ground lightning stroke excites the normal modes of the earth-ionosphere cavity and sets up a combination of travelling and standing waves, whose wavelengths are integral sub-multiples of the earth's circumference. The lowest Schumann resonance eigenfrequency is approximately 7 Hz with 7 or 8 harmonics typically excited within the cavity. The three lowest harmonics of the standing wave pattern in the electric and magnetic fields are illustrated in Figure 8. The direction of the electric field is radially outwards in the lobe nearest the lightning stroke and radially inwards in the opposite lobe with nulls along the equator. In the case of the magnetic field there is a minimum close to the lightning source and at an antinode, with maxima where the electric field is minimum. The direction of the magnetic field is parallel to the surface of the earth. For the harmonics (n>1) the direction of the electric field is reversed in adjacent lobes. The spectra of up to eight harmonics for the magnetic and electric components, averaged over three hours under daytime and night time conditions are plotted in Figure 9.

### *21.3.2 Global lightning activity*

Since the spatial extent of the normal modes is global and their damping time is many wave periods, the effects of each lightning stroke extends to all parts of the earth. The amplitude of the resonances is directly proportional to the vertical component of the current moments of the exciting discharges so that measurements of the resonances can, in principle, provide a direct measure of the total global current moment. Single point measurements have been used in the past to obtain current moments, but they make assumptions regarding the spatial distribution of lightning and lateral inhomogeneities in the heights of the ionosphere are not taken into account (Clayton 1980).

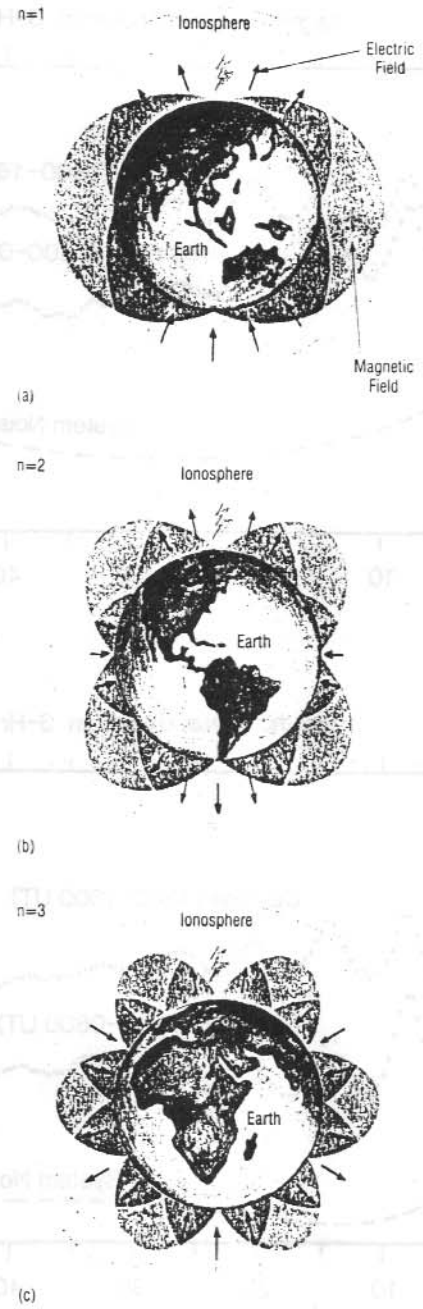


Figure 8. Cross-section of the earth-ionosphere cavity and the spatial patterns in the electric and magnetic fields created by standing waves excited by a single lightning stroke (Sentman 1987b). (a) First harmonic (7 Hz); (b) Second harmonic (14 Hz); (c) Third harmonic (20 Hz).

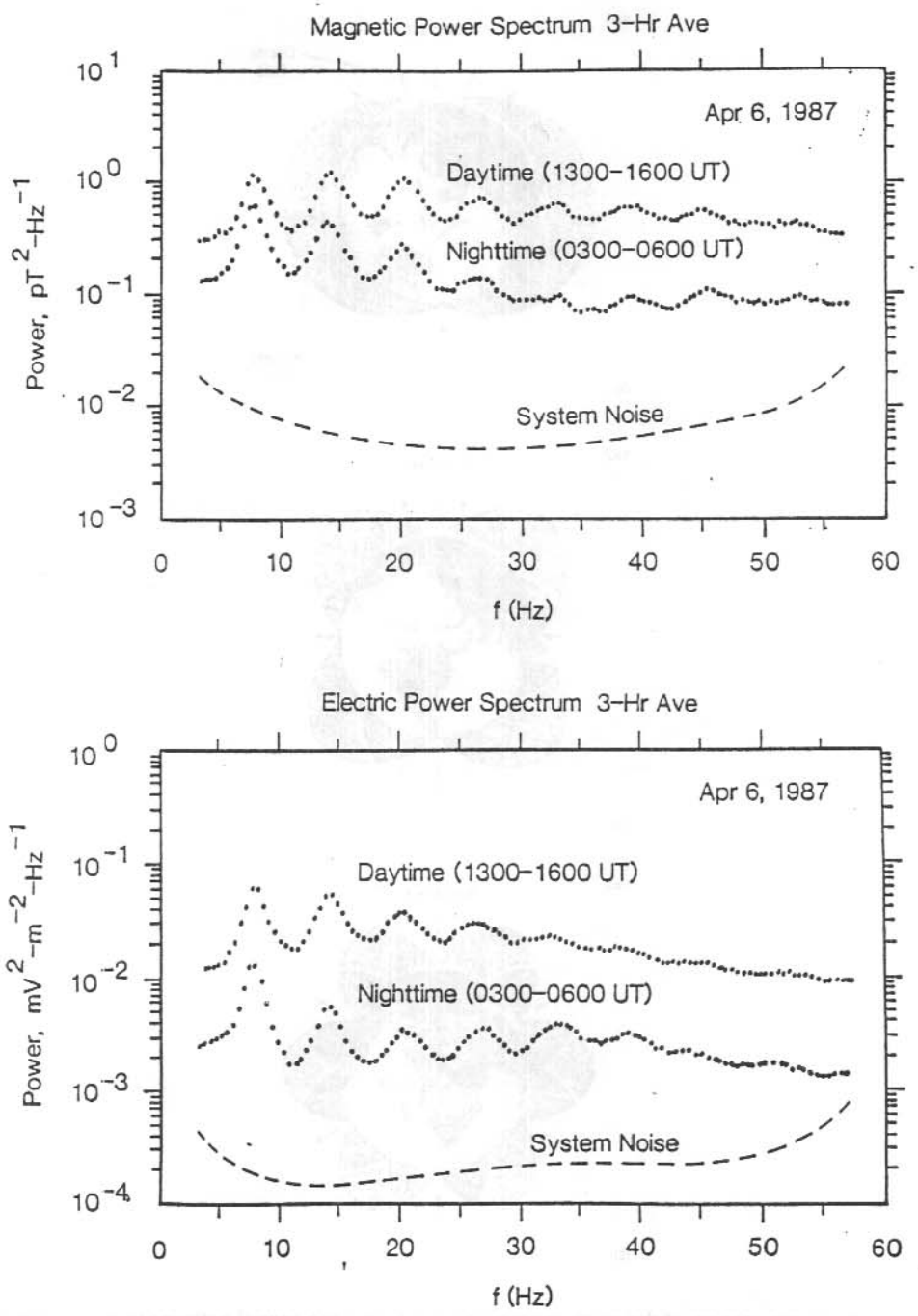


Figure 9. Power spectra of magnetic and electric components, averaged over 3 hours and recorded in Southern California on April 6, 1987 (Sentman 1987a).

This, and other work, illustrate the need to monitor total global lightning activity using a network of stations in order to obtain more accurate measures of these, the principle currents, in the global electric circuit. It is hoped that this may lead to the establishment of a geoelectric index similar to other solar-terrestrial activity indicators.

There are also a number of questions relating to the separation of local time and global effects which need to be studied. Firstly, there is an unexplained factor of two in the diurnal variation of the amplitude of the resonance at a single station (Sentman 1987a). Secondly, the diurnal variation in the resonances should also be independent of local time. This is not so with amplitudes maximising near local noon. This may be partly attributed to the day/night variation in the D-region height. The need for simultaneous measurements from stations widely spaced in local time in order to separate local and global effects and obtain a reliable measure of current moments, is adequately demonstrated.

### *21.3.3 D-region variability*

For a given source and observer location, the intensity of the Schumann resonances is primarily a function of the excitation source intensity, while the eigenfrequency and Q-value mode parameters are properties of the cavity geometry. Because the mode parameters are determined by the characteristics of the D-region forming the upper boundary of the cavity, variations in ionising radiation that maintain the D-region conductivity modulate the effective shape of the cavity and dissipation occurs at its upper boundary. Modulation of the resonances has been associated with sudden ionospheric disturbances (SIDs), X-rays from solar flares and polar cap absorption (PCA) events. Recent research has shown that high speed streams in the solar wind enhance the magnetospheric intensities of $E_e > 1.5$ MeV electrons which precipitate and penetrate deeply into the atmosphere, altering the D-region conductivity sufficiently to perturb the Schumann eigenmodes on a global scale (Baker et al. 1987).

The first tentative visual evidence that solar X-ray flares may have a direct effect on the Schumann resonances is seen in dynamic spectra in Figure 10. Here the second and third harmonics are plotted from data recorded at Gilmore Creek, Alaska, on August 15, 1989. A massive X20 solar X-ray flare commencing at 0100 UT appears to have raised the third harmonic frequency by about one Hertz.

### *21.3.4 Lower ELF phenomena*

In addition to the normal modes constituting the Schumann resonances, there are other electromagnetic wave phenomena that fall within the ELF range of 3-200 Hz which have received little attention in the past. One example is the whistler-like events from 60-120 Hz with a duration of about 1-3 minutes. Examples of these, recorded at 64°N geomagnetic by Heacock (1974), are shown in Figure 11. Some of the emissions show a periodic fine structure, were magnetically polarised in the east-west direction, were anticorrelated with geomagnetic activity and do not

appear to be simply the low frequency extension of VLF whistlers. They also show a maximum daytime rate of occurrence (Figure 11). The source and propagation characteristics of these events are unknown, but they may be associated with cyclotron interaction in the cusp magnetosheath, with subsequent dispersive propagation to the earth. A lower-ELF recording system over the 3-16 Hz band using the microcomputer data logger described by Fraser et al (1991), will commence operation at Davis station, Antarctica, in the 1990-1991 austral summer. It will attempt to observe cusp related ELF phenomena in this frequency range.

### *21.3.5 Q-burst phenomena*

Q-bursts are the signatures of discrete extremely large lightning strokes ($I=10^6$ Ampere) occurring within the earth-ionosphere cavity (Ogawa et al. 1966). They have amplitudes 10-100 times greater than the ambient background, and occur at a rate of about one per minute (Figure 12). Since Q-bursts are the impulsive response of the entire cavity to a distant, but individual, lightning transient, their waveform will depend on the lateral distribution of conductivity in the D-layer and the relative locations of the source and observer with respect to both the conductivity distribution and to each other.

Theoretical work by Bezrodny et al. (1977) has shown that a magnetised ionosphere will produce distortions in the phase surfaces of the eigenmodes. Other asymmetrics in the cavity may result from the latitudinal variation in ionospheric height. These may give rise to spectral splitting. Recent experimental evidence that the Schumann resonances have a substantial elliptically polarised magnetic component (Sentman 1987a) indicates that the side multiplets are being excited, and that the effects of eigenmode distortion are observable. This can be seen in Figure 13 where the polarisation of the magnetic vector is rotated into the principle axis system using maximum/minimum variance techniques and the corresponding power spectra for the x' and y' components show a line splitting in the range $\Delta f = 1.4 - 1.8$ Hz for the first harmonic.

### *21.3.6 Summary*

The brief discussion of Schumann resonances and lower-ELF phenomena presented above, has been aimed at providing an indication of the new remote sensing role in four areas, which involve the physics of the lower ionosphere and its coupling downwards to the neutral atmosphere, and upwards to the upper ionosphere and the magnetosphere. In particular, the authors have considered Schumann resonances in relation to the monitoring of global thunderstorm intensities and the proposal of a new geoelectric index, the variability in D-region conductivity by a solar X-ray flare event, Q-burst activity and naturally occurring ELF wave phenomena in the magnetosphere.

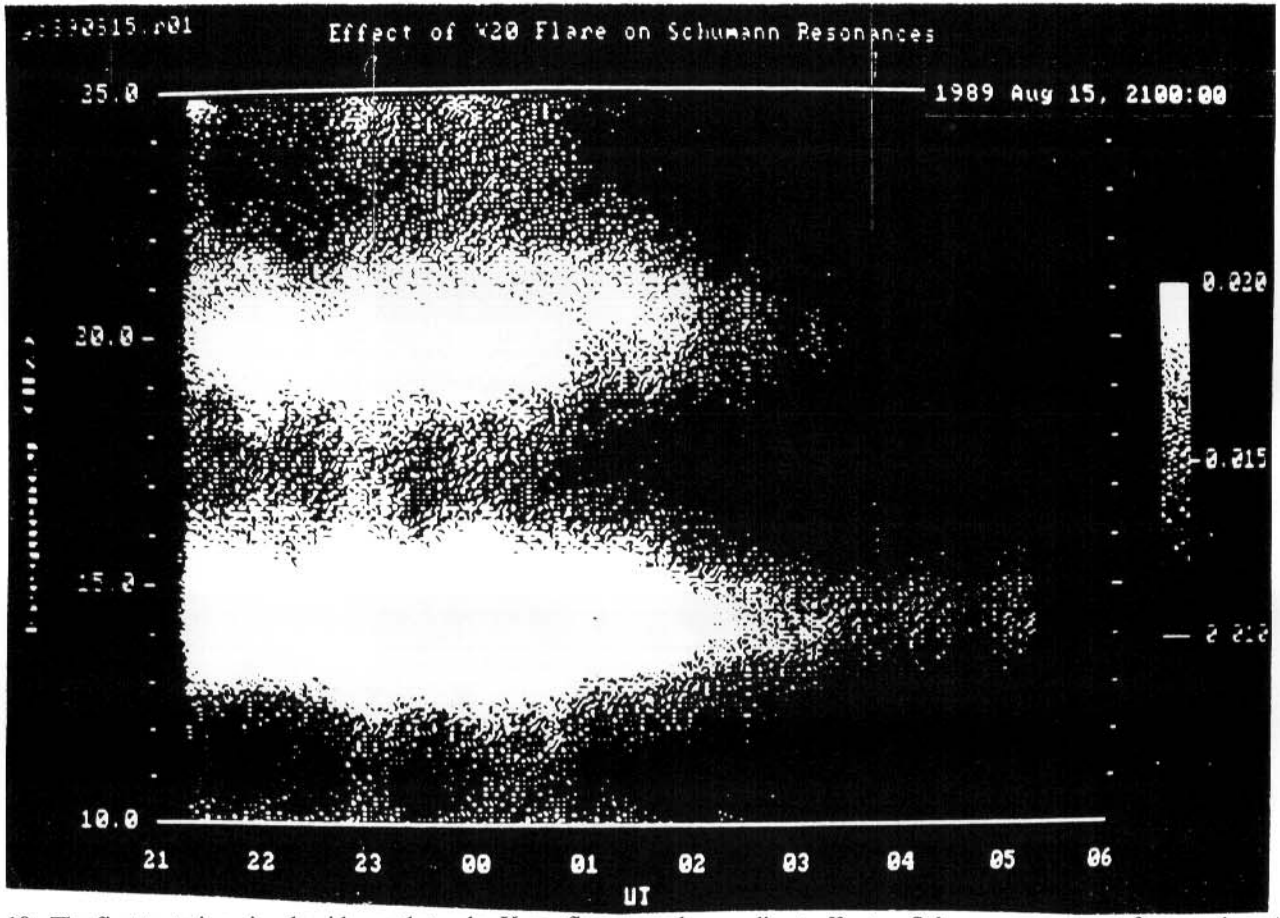


Figure 10. The first tentative visual evidence that solar X-ray flares may have a direct effect on Schumann resonance frequencies. A massive X20 solar X-ray flare commencing at 0100 UT appears to have raised the third harmonic frequency by 1 Hz. (The first harmonic is not shown here.)

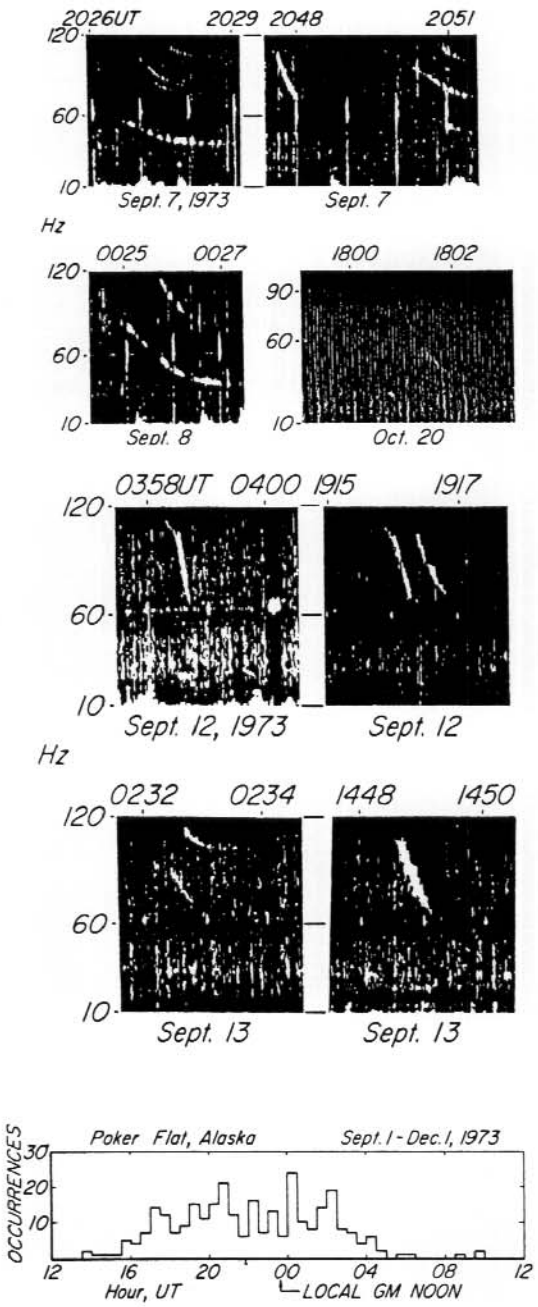


Figure 11. Upper: Examples of whistler-like lower-ELF events seen between 60-100 Hz. Signal amplitudes are near 3 pT.
Lower: The diurnal variation of the occurrence of these events showing a daytime maximum.

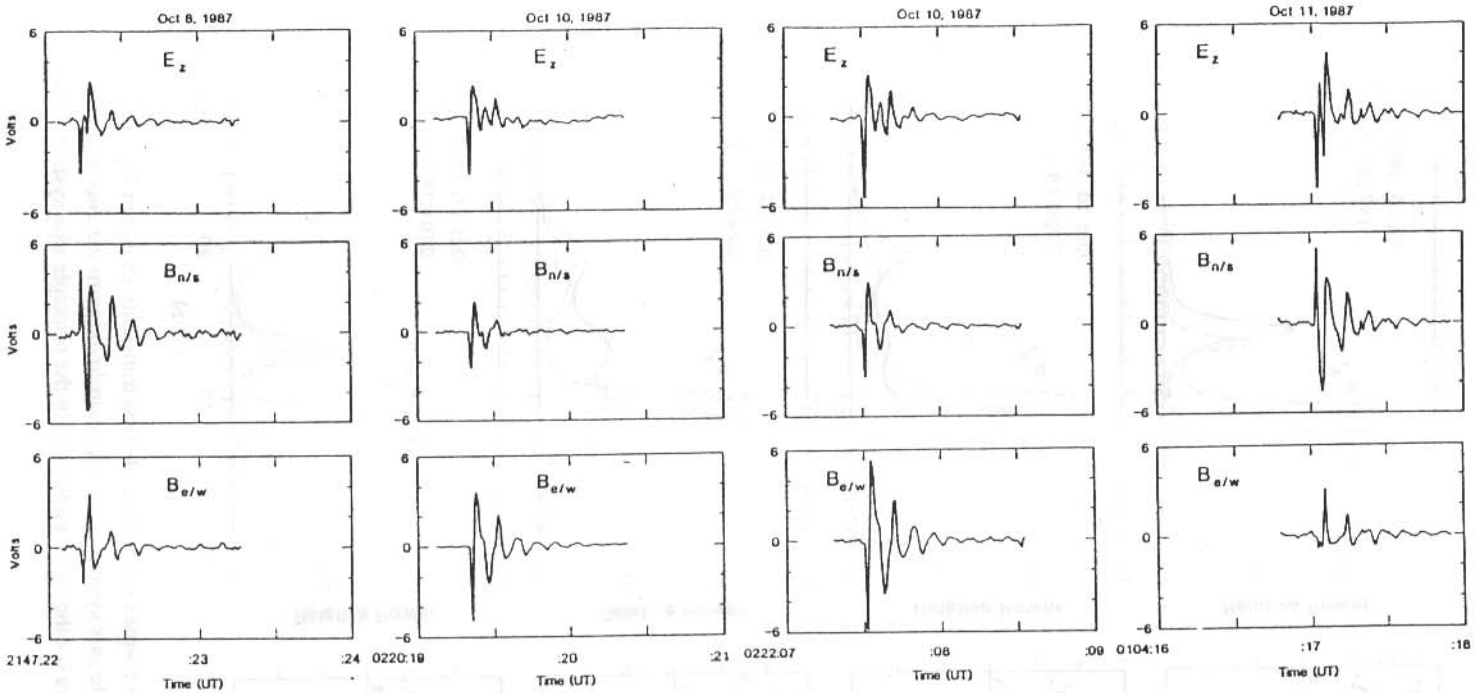


Figure 12. Amplitude-time records of four Q-burst transient events with duration less than one second, seen in the $B_{NS}$ $B_{EW}$ and $E_r$ (or $E_z$) field components.

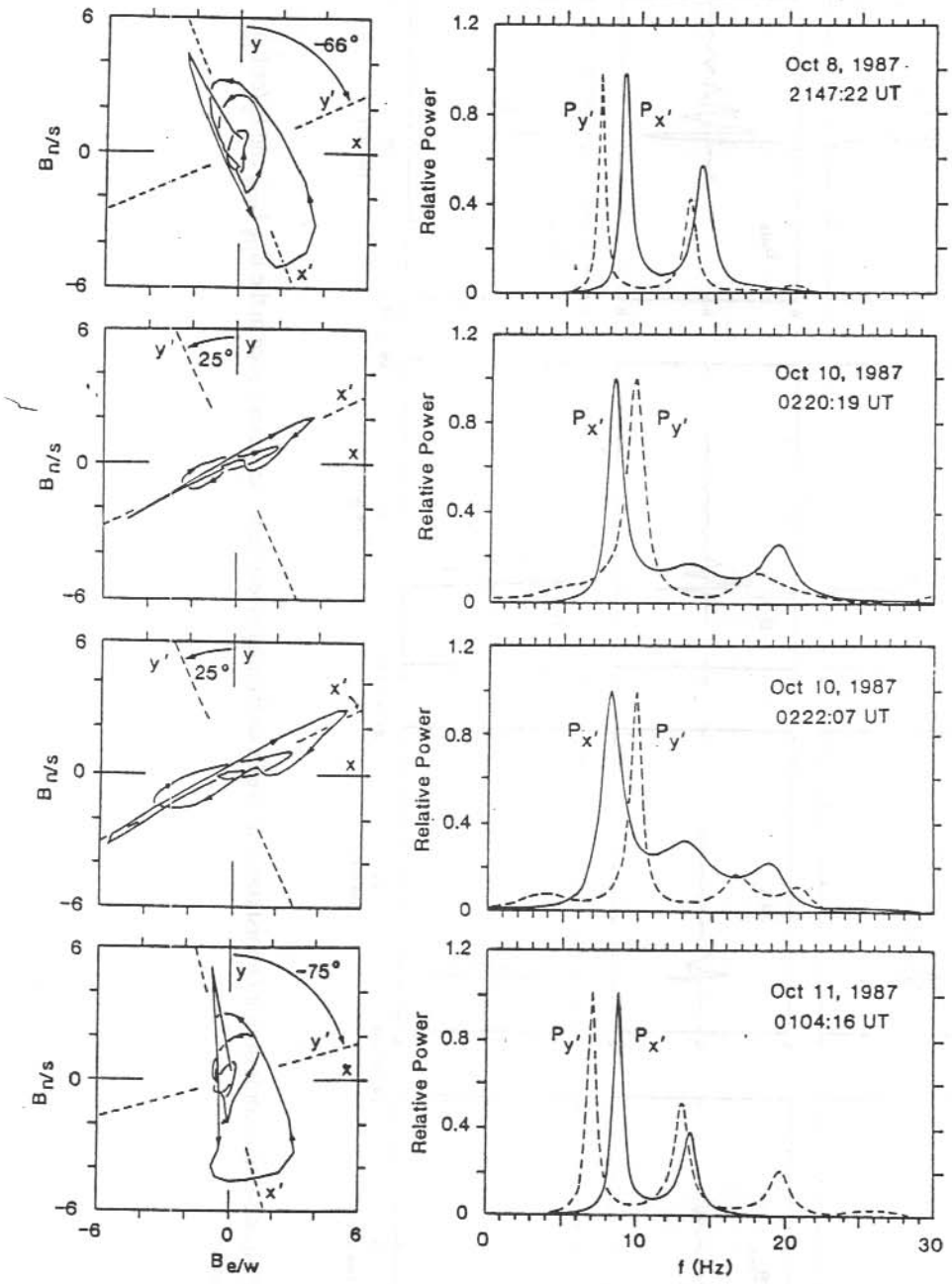


Figure 13. Left panels: Polarisation ellipses of the four Q-burst transients shown in Figure 12. The axes are rotated into the principle axis system using minimum/maximum variance techniques. Right panels: Relative power spectra for the two components in the principle axis system. The line splitting is obvious.

## 21.4 ACKNOWLEDGMENTS

Thanks are due to W. Lennartsson and J. Etcheto for providing ISEE-1 plasma data and to R.L. McPherron and C.T. Russell for ISEE-1 UCLA fluxgate magnetometer data. J. Kennewell, IPS, Learmonth, W.A. provided some of the ELF data. The research was supported at the University of Newcastle by the Australian Research Council and the University of Newcastle.

## 21.5 REFERENCES

Anderson, B.J., Takahashi, K., Erlandson, R.E. *and* Zanetti, L.J. (1990). Pc1 pulsations observed by AMPTE/CCE in the earth's outer magnetosphere. Submitted to *Geophysical Research Letters*.

Baker, D.N., Blake, J.B., Corney, D.J., Higbie, P.R., Klebesadel, R.W. *and* King, J.H. (1987). Highly relativistic magnetospheric electrons: A role in coupling to the middle atmosphere. *Geophysical Research Letters 14*:1027-1030.

Ball, L.T. (1987). Non-relativistic thermal effects on parallel propagating ion cyclotron waves. *Journal of Plasma Physics 38*:117-138.

Bezrodny, V.G., Nikolaenko, A.P. *and* Sinitsin, V.G. (1977). Radio propagation in natural waveguides. *Journal of Atmospheric and Terrestrial Physics 39*:661.

Clayton, M.D. (1980). *Estimation of world-wide thunderstorm activity from Schumann resonance data*. Ph.D. Thesis, University of Rhode Island, Kingston, Rhode Island.

Fraser, B.J. (1985). Observations of ion cyclotron waves near synchronous orbit and on the ground. *Space Science Reviews 42*:357-374.

Fraser, B.J. *and* McPherron, R.L. (1982). Pc1-2 magnetic pulsations spectra and heavy ion effects at synchronous orbit: ATS 6 results. *Journal of Geophysical Research 87*:4560-4566.

Fraser, B.J., McNabb, P.W., Menk, F.W. *and* Waters, C.L. (1991). A personal computer induction magnetometer system for recording geomagnetic pulsations. *ANARE Research Notes Number 80*.

Fraser, B.J., Samson, J.C., McPherron, R.L. *and* Russell, C.T. (1986). Ion cyclotron waves observed near the plasmapause. *Advances in Space Research 6*:223-226.

Fukunishi, H. (1984). Pc1-2 pulsations and related phenomena: Review. In: *Processings of the Conference on Achievements of the IMS, ESA SP-217, ESA STPB, Noordwijk*. Pp. 437-447.

Gomberoff, L. *and* Neira, R. (1983). Convective growth rate of ion cyclotron waves in $H^+$ - $He^+$ and $H^+$ - He - $O^+$ plasma. *Journal of Geophysical Research 88*:2170-2174.

Heacock, R.R. (1974). Whistler-like pulsation events in the frequency range 20 to 200 Hz. *Geophysical Research Letters* 2:77.

Inhester, B., Wedekin, V., Korth, A., Perraut, S. *and* Stokholm, M. (1984). Ground-satellite coordinated study of the April 5, 1979 events: Observations of $O^+$ cyclotron waves. *Journal of Geophysical Research 55*:134-141.

Kennewell, J.A., Sentman, D.D. *and* Fraser, B.J. (1990). ELF monitoring in Australia. In: Paper presented at the Conference on ST & SP, La Trobe University, Melbourne.

Kozyra, J.U., Cravens, T.E., Nagy, A.F. *and* Fontheim, E.G. (1984). Effects of energetic heavy ions on electromagnetic ion cyclotron wave generation in the plasmapause region. *Journal of Geophysical Research 89*:2217-2233.

Kuwashima, M., Toya, T., Kawamura, M., Hirasawa, T., Fukunishi, H. *and* Ayukawa, M. (1980). Comparative study of magnetic Pc1 pulsations between low latitudes and high latitudes: statistical study. *Proc. Third Symp. on Coord. Obs. of Ionosph. Magnetosph. in Polar Regions*. Special issue *18*:101-117.

Mauk, B.H. (1978). *Alfven-ion cyclotron waves and the ion cyclotron instability in the earth's magnetosphere*. Ph.D. dissertation, 145, UC San Diego.

Mauk, B.H. *and* McPherron, R.L. (1980). An experimental test of the electromagnetic ion cyclotron instability within the earth's magnetosphere. *Physics of Fluids 23*:211-217.

Ogawa, T., Tanaka, Y., Miura, T. *and* Yasuhara, M. (1966). Observations of natural ELF and VLF electromagnetic noises by using ball antennas. *Journal of Geomagnetism and Geoelectricity 18*:443.

Samson, J.C. (1990). Geomagnetic pulsations and waves in the earth's magnetosphere. in *Geomagnetism* Vol. 4, ed. Jacobs, J.A., Academic Press, to be published.

Sentman, D.D. (1987a). Magnetic elliptical polarization of Schumann resonances. *Radio Science 22*:595.

Sentman, D.D. (1987b). PC monitors lightning world-wide. *Computers in Science 1*:25.

Young, D.T., Perraut, S., Roux, A., de Villedary, C., Gendrin, R., Korth, A., Kremser, G. *and* Jones, D. (1981). Wave particle interaction near $\Omega_{He^+}$ observed on GEOS 1 and 2. 1, propagation of ion cyclotron waves in $He^+$ rich plasma. *Journal of Geophysical Research 86*:6755-6772.